OUTPUT BANDWIDTH EFFECTS IN SEEDED, HARMONIC CASCADE FELS

W.M. Fawley, G. Penn, A. Zholents, LBNL, Berkeley, California

Abstract

A number of laboratories are studying and/or proposing seeded Harmonic Cascade (HC) FELs as a means both to reach soft x-ray output wavelengths and to provide a degree of longitudinal coherence much greater than that normally possible with SASE devices. While theoretically the output bandwidth of a HC FEL can approach the transform limit given a high quality input seed of reasonable power, there appear to be a number of practical considerations that in many cases can increase the output bandwidth many-fold. In particular, designs that employ dispersive sections following modulator sections in order to increase the amount of coherent harmonic microbunching, can be very sensitive to temporal variations in the electron beam energy, resulting in an output wavelength chirp. Unwanted microbunching induced by the combination of longitudinal space charge instability growth in the linac and CSR in compression sections also can lead to variations in the output radiation phase and amplitude, thus increasing the bandwidth. We give some semi-analytical results for the predicted bandwidth increase for HC configurations and also some detailed numerical simulation results.[1]

PAPER NOT AVAILABLE

---

[1] Work supported in part by the US DOE under Contract no. DE-AC02-05CH11231.

FOURIER OPTICS TREATMENT OF CLASSICAL RELATIVISTIC ELECTRODYNAMICS

G. Geloni*, E. Saldin, E. Schneidmiller and M. Yurkov,
Deutsches Elektronen-Synchrotron (DESY), Hamburg, Germany.

Abstract

We coupled Synchrotron Radiation (SR) theory with laser beam optics. In the space-frequency domain SR beams are described by solutions of the paraxial wave equation. They appear as laser beams with transverse size much larger than the wavelength. In practical situations (e.g. undulators, bends), SR beams exhibit a virtual source, similar to the waist of a laser-beam, strictly related with the inverse Fourier transform of the far-field distribution. The Fresnel formula can be used to propagate the field distribution from the waist to anywhere in space. The general theory of SR in the near-zone developed in this paper is illustrated for the special cases of undulator radiation, edge radiation and transition undulator radiation (TUR). By solving the inverse problem for the electric field we find analytical expressions for near-field distributions in terms of far-field data. A more detailed explanation of this subject is provided in [1].

INTRODUCTION

In previous works we developed a formalism ideally suited for analysis of SR problems, where we took advantage of Fourier Optics ideas [1]. Fourier Optics provides an extremely successful approach which revolutionized the treatment of wave optics problems and, in particular, laser beam optics problems. The use of Fourier Optics led us to establish basic foundations for the treatment of SR fields in terms of laser beam optics. Radiation from an ultra-relativistic electron can be interpreted as radiation from a virtual source producing a laser-like beam. The virtual source is regarded as the analogous of the waist for a laser beam, and often exhibits a plane wavefront. In this case it is specified, for any given polarization component, by a real-valued amplitude distribution of field. The laser-like representation of SR is intimately connected with the ultra-relativistic nature of the electron beam. In particular, paraxial approximation always applies. Then, free space basically acts as a spatial Fourier transformation, and the far-zone field is, aside for a phase factor, the Fourier transform of the field at any position z down the beamline. It is also, aside for a phase factor, the Fourier transform of the virtual source. Once the field at the virtual source is known, the field at other longitudinal positions, both in the far and in the near zone up to distances to the sources comparable with the radiation wavelength, can be obtained with the help of the Fresnel propagation formula. This means that the near-zone field can be calculated from the knowledge of the far-zone field, that is possible because the paraxial approximation applies. The knowledge of the far-zone field completely specifies, through the Fresnel integral, the near-zone field as well. In the case when the electron generating the field is not ultra-relativistic, though, the paraxial approximation cannot be applied. Typically, the wavelength is comparable with the radiation formation length, and it is impossible to reconstruct the near-field distribution from the knowledge of the far-field pattern [2]. An arbitrary SR source is equivalent to several virtual sources inserted between the edges of each magnetic device. This provides conceptual insight of SR sources and should facilitate their design and analysis. In fact, since the analysis of SR sources can be reduced to that of laser-like sources, it follows that any result, method of analysis or design and any algorithm specifically developed for laser beam optics (e.g. the code ZEMAX, see [1]) is also applicable to SR sources. We first apply our method to undulator radiation around resonance. We find the field distribution of the virtual source with the help of the far-zone field distribution and we propagate to any distance of interest. Similarly, we treat edge radiation [1], studying the emission from a setup composed by a straight section and two (upstream and downstream) bends. We derive an expression for the field from a straight section that is valid at arbitrary observation position. Due to the superposition principle, this expression can be used as building block for more complicated setups. We use this idea to analyze a TUR setup consisting of an undulator preceded and followed by straight sections and bends (upstream and downstream). The first study on TUR constituted a theoretical basis for many other studies [1], dealing both with theoretical and experimental issues. More recently, TUR has been given consideration in the framework of large XFEL projects. A method was also proposed [1] to obtain intense infrared/visible light pulses naturally synchronized to x-ray pulses from the LCLS XFEL by means of Coherent TUR. In view of these applications, there is a need to extend the knowledge of TUR to the near zone. We address it here.

FAR-FIELD DATA INVERSE PROBLEM

We represent the electric field in time domain $\vec{E}(\vec{r},t)$ as a time-dependent function of an observation point located at position $\vec{r} = \vec{r}_\perp + z\vec{z}$. In free-space, the field $\vec{E}(\vec{r},t)$ satisfies the source-free wave equation. For monochromatic waves of angular frequency ω the wave amplitude has the form $\vec{E}_\perp(z,\vec{r}_\perp,t) = \vec{\bar{E}}_\perp(z,\vec{r}_\perp)\exp[-i\omega t] + C.C.$, where the frequency ω is related to the wavelength λ by

---

* gianluca.aldo.geloni@desy.de

$\omega/c = 2\pi/\lambda$, and $\vec{\bar{E}}_\perp$ describes the variation of the wave amplitude in the transverse direction. $\vec{\bar{E}}_\perp$ actually represents the amplitude of the electric field in the space-frequency domain. We assume that the ultra-relativistic approximation is satisfied, that is always the case for SR setups. In this case the paraxial approximation applies [1]. This implies a slowly varying envelope of the field with respect to the wavelength. We therefore introduce $\vec{\widetilde{E}}_\perp = \vec{\bar{E}}_\perp \exp\left[-i\omega z/c\right]$. In paraxial approximation and in free space, $\vec{\widetilde{E}}_\perp$ obeys the paraxial wave equation along any fixed polarization component, that is $[\nabla_\perp{}^2 + (2i\omega/c)\partial_z]\widetilde{E}_\perp = 0$, where derivatives in the Laplacian operator $\nabla_\perp{}^2$ are taken with respect to the transverse coordinates. Solving this equation with given initial conditions at z gives

$$\widetilde{E}_\perp = \frac{i\omega}{2\pi c(z_o - z)} \int d\vec{r'} \widetilde{E}_\perp(z, \vec{r'}) \exp\left[\frac{i\omega \left|\vec{r}_{o\perp} - \vec{r'}\right|^2}{2c(z_o - z)}\right] \tag{1}$$

where the integral is performed over the transverse plane. A propagation equation for $\mathrm{F}(z, \vec{u}) = \int d\vec{r'}_\perp \widetilde{E}_\perp(z, \vec{r'}_\perp) \exp\left[i\vec{r'}_\perp \cdot \vec{u}\right]$, that is the spatial Fourier transform of the field, reads instead:

$$\mathrm{F}\left(z, \vec{u}\right) = \mathrm{F}\left(z_s, \vec{u}\right) \exp\left[-\frac{ic|\vec{u}|^2(z - z_s)}{2\omega}\right], \tag{2}$$

where z_s is identified with the position of a virtual source. Identification of the position $z_s = 0$ with a virtual source position is always possible, but not always convenient (although often it is). From Eq. (1) and Eq. (2) a relation follows between the far-zone field distribution, dependent on the observation angle $\vec{\theta}$, and the field distribution at the virtual source position z_s:

$$\begin{aligned}\widetilde{E}_\perp(z_s, \vec{r}_\perp) = \quad & \frac{i\omega z_o}{2\pi c} \int d\vec{\theta} \exp\left[-\frac{i\omega|\vec{\theta}|^2}{2c}(z_o + z_s)\right] \\ & \times \widetilde{E}_\perp(\vec{\theta}) \exp\left[\frac{i\omega}{c}\vec{r}_\perp \cdot \vec{\theta}\right] . \end{aligned} \tag{3}$$

Finally, the transverse components of the envelope of the far field can be written as [1]:

$$\begin{aligned}\vec{\widetilde{E}}_\perp = -\frac{i\omega e}{c^2 z_o} \int_{-\infty}^{\infty} dz' \exp\left[i\Phi_T\right] \left[\left(\frac{v_x(z')}{c}\right.\right. \\ \left.-\frac{x_o}{z_o}\right) \vec{x} + \left(\frac{v_y(z')}{c} - \frac{y_o}{z_o}\right) \vec{y}\right] ,\end{aligned} \tag{4}$$

where the total phase Φ_T is

$$\begin{aligned}\Phi_T = \omega\left[\frac{s(z')}{v} - \frac{z'}{c}\right] + \omega\left(\frac{1}{z_o} + \frac{z'}{z_o^2}\right) \\ \times \frac{\left[x_o - x'(z')\right]^2 + \left[y_o - y'(z')\right]^2}{2c}\end{aligned} \tag{5}$$

and the charge of the electron is $(-e)$. Eq. (4) can be obtained starting directly with Maxwell's equations in the space-frequency domain. Here $v_x(z')$ and $v_y(z')$ are the horizontal and the vertical components of the transverse velocity of the electron, while $x'(z')$ and $y'(z')$ specify the transverse position of the electron as a function of the longitudinal position. Finally, we defined the curvilinear abscissa $s(z') = vt'(z')$, v being the modulus of the velocity of the electron. Eq. (4) can be used to characterize the far field from an electron moving on any trajectory as long as the ultra-relativistic approximation is satisfied. Then, once the far field is known, Eq. (3) can be used to calculate the field distribution at the virtual source. Finally, Eq. (1) solves the propagation problem at any observation position z_o. Note that part of the phase in Eq. (5) compensates with the phase in $|\vec{\theta}|^2$ in Eq. (3) at $z_s = 0$. If Eq. (4) describes a field with a spherical wavefront with center at $z = 0$, such compensation is complete. The centrum of the spherical wavefront is a privileged point, and the plane at $z = 0$ exhibits a plane wavefront. This explains why the choice $z_s = 0$ is often privileged with respect to others.

DISCUSSION

It makes sense to ask what is the range of observation positions where our algorithm applies, and what is the accuracy of our result in this range. We show that the paraxial approximation holds with good accuracy up to observation positions such that its distance d from the electromagnetic sources in the space-frequency domain, when $d \gg \lambda$. To do so, we compare results from the paraxial treatment with results without the help of the paraxial approximation. The paraxial equation must then be replaced with Helmholtz equation $c^2\nabla^2\vec{\bar{E}} + \omega^2\vec{\bar{E}} = 4\pi c^2\vec{\nabla}\bar{\rho} - 4\pi i\omega\vec{\bar{j}}$, $\bar{\rho}(\vec{r}, \omega)$ and $\vec{\bar{j}}(\vec{r}, \omega)$ being the Fourier transform of the charge density $\rho(\vec{r}, t) = -e\delta(\vec{r} - \vec{r'}(t))$ and of the current density $\vec{j}(\vec{r}, t) = -e\vec{v}(t)\delta(\vec{r} - \vec{r'}(t))$. Application of the proper Green's function yields:

$$\begin{aligned}\vec{\bar{E}}(\vec{r_o}, \omega) = -\frac{i\omega e}{c}\int_{-\infty}^{\infty} dz' \frac{1}{v_z(z')}\left[\frac{\vec{\beta} - \vec{n}}{|\vec{r_o} - \vec{r'}(z')|}\right. \\ \left.-\frac{ic}{\omega}\frac{\vec{n}}{|\vec{r_o} - \vec{r'}(z')|^2}\right] \exp\left\{i\omega\left[\left(\frac{s(z')}{v} - \frac{z'}{c}\right)\right.\right. \\ \left.\left.+\left(\frac{|\vec{r_o} - \vec{r'}(z')|}{c} - \frac{z_o - z'}{c}\right)\right]\right\} .\end{aligned} \tag{6}$$

Eq. (6) is an exact solution of Maxwell's equations with boundary conditions at infinity. The exactness of Eq. (6) allows us to control the accuracy of the paraxial approximation. A conservative estimate shows that when $d \gtrsim L_f$ this accuracy is of order $c/(\omega L_f)$, but quickly decreases as $L_f \gg d \gg c/\omega$ remaining, *at least*, of order of $c/(\omega d)$.

The integrand term scaling as $1/R^2$ (with $R = |\vec{r_o} - \vec{r'}(z')|$) can be dropped in Eq. (6) whenever $d \gg \lambda$. This is always the case in paraxial approximation. Note that the inverse field problem cannot be solved without application of the paraxial approximation. In this case we should solve the homogeneous Helmholtz equation with boundary conditions constituted by the knowledge of the field on a open surface (for example, a transverse plane) and additionally, Rayleigh-Sommerfeld radiation condition at infinity (separately for all polarization components). This is not enough to reconstruct the field at any position in space. However, if the paraxial approximation is applicable, the inverse field problem has a unique and stable solution. We recognize a few observation zones of interest. **Far zone.** d is such that $\vec{n} = \mathrm{const}$. **Formation zone.** Defined by $d \lesssim L_f$. **Radiation zone.** The field can be interpreted as radiation. $\mathbf{1/R}-$**zone .** The term in $1/R^2$ can be neglected in Eq. (6). **Reconstruction zone.** The inverse problem based on far-field data can be solved.

In all generality, from Eq. (6) follows that the $1/R-$zone always coincide with the reconstruction zone. Any system of interest is characterized by a size a, a formation length L_f and the radiation wavelength λ. In the case of ultra-relativistic systems $a \gtrsim L_f \gg \lambda$. Then, the near zone is defined by $d \lesssim a$, the formation zone by $d \lesssim L_f$, the radiation zone, the reconstruction zone and the $1/R-$zone by $d \gg (c/\omega)$. Ultra-relativistic cases present an increased level of complexity with respect to others. This complexity is at the origin of several misconceptions. Usually textbooks do not follow a direct derivation of Eq. (6). They start with the solution of Maxwell's equation in the space-time domain, the Lienard-Wiechert fields, and they apply a Fourier transformation:

$$\vec{\bar{E}}(\vec{r_o}, \omega) = -e \int_{-\infty}^{\infty} dt' \left\{ \frac{\vec{n} - \vec{\beta}}{\gamma^2 (1 - \vec{n} \cdot \vec{\beta})^2 R(t')^2} \right.$$
$$\left. + \frac{\vec{n} \times [(\vec{n} - \vec{\beta}) \times \dot{\vec{\beta}}]}{c(1 - \vec{n} \cdot \vec{\beta})^2 R(t')} \right\} \exp\left[i\omega \left(t' + \frac{R(t')}{c} \right) \right] \quad (7)$$

where $\vec{\beta} = \vec{v}/c$. Inspecting Eq. (7) it looks paradoxical that the near field, including velocity and acceleration terms, can be characterized starting from the far zone, including acceleration term only. However, the magnitude of terms in $1/R^2$ and $1/R$ in Eq. (7) does not depend on λ, while that of terms in $1/R$ and $1/R^2$ in Eq. (6) does. Eq. (6) and Eq. (7) are equivalent, as can be shown by addition of the full derivative $d\Phi(t')/dt'$ of a properly chosen $\Phi(t')$ function to the integrand of Eq. (7) (and using $t' = z'/v_z(z')$). Addition of different full derivatives yields an infinite number of equivalent representations for the field, and physical sense can be ascribed to the integral only. The terms in $1/R$ and in $1/R^2$ in Eq. (6) appear as a combination of the terms in $1/R$ (acceleration term) and $1/R^2$ (velocity term) in Eq. (7). They differ from each other. As a result, there are contributions to the radiation from the velocity part in Eq. (7). The presentation in Eq. (6) is most interesting because the magnitude of the $1/R^2$-term in Eq. (6) can be directly compared with the magnitude of the $1/R$-term inside the sign of integral, that is related to the $1/R$-zone and to the reconstruction zone. If one forgets about this fact one would incorrectly conclude that far-field data cannot be used to reconstruct the field in the near-zone.

UNDULATOR LASER-LIKE SOURCE

Let us apply our algorithm in the case of undulator radiation at resonance, i.e. $\omega/(2\gamma^2 c)(1 + K^2/2) = 2\pi/\lambda_w$. Here λ_w is the undulator period, and $K = \lambda_w e H_w/(2\pi m_\mathrm{e} c^2)$, m_e being the electron mass and H_w being the maximum of the magnetic field produced by the undulator on the z axis. Position $z = 0$ is in the undulator center. A well-known, axis-symmetric expression for the distribution of the first harmonic field $\widetilde{E}_\perp(z_o, \theta)$ from a planar undulator in the far-zone as a function of the observation angle θ is

$$\widetilde{E}_\perp = -\frac{K\omega e L_w}{c^2 z_o \gamma} A_{JJ} \exp\left[i \frac{\omega z_o}{2c} \theta^2 \right] \mathrm{sinc}\left[\frac{\omega L_w \theta^2}{4c} \right], \quad (8)$$

where the field is polarized in the horizontal direction, $L_w = \lambda_w N_w$ is the undulator length, N_w the number of undulator periods and $A_{JJ} = J_o[K^2/(4 + 2K^2)] - J_1[K^2/(4 + 2K^2)]$, J_n being the n-th order Bessel function of the first kind. Eq. (8) describes a field with spherical wavefront centered at $z = 0$. Eq. (3) yields the field distribution at the virtual source (also axis-symmetric) [1]:

$$\widetilde{E}_\perp(0, r_\perp) \quad = \quad i \frac{K\omega e}{c^2 \gamma} A_{JJ} \left[\pi - 2\mathrm{Si}\left(\frac{\omega r_\perp^2}{L_w c} \right) \right], \quad (9)$$

$\mathrm{Si}(\cdot)$ being the sin integral function and $r_\perp$ the distance from the z axis on the virtual-source plane. In laser physics, the waist is in the center of the optical cavity and the Rayleigh length is related to the resonator geometrical factor. Our virtual source is in the center of the undulator and the Rayleigh length is related to L_w. In both cases we have a plane phase front, and the transverse dimension of the waist is much larger than λ. Also, the phase of the wavefront in Eq. (9) is shifted of $-\pi/2$ with respect to the wavefront in the far zone in analogy with the Guoy phase shift. Eq. (1) gives the field at arbitrary observation position z_o:

$$\widetilde{E}_\perp = \frac{K\omega e A_{JJ}}{c^2 \gamma}$$
$$\times \left[\mathrm{Ei}\left(\frac{i\omega r_\perp^2}{2z_o c - L_w c} \right) - \mathrm{Ei}\left(\frac{i\omega r_\perp^2}{2z_o c + L_w c} \right) \right] \quad (10)$$

$\mathrm{Ei}(\cdot)$ being the exponential integral function. The field singularity at $z_o = L_w/2$ and $r_\perp = 0$ is related with the use of the resonant approximation. Introducing normalized units $\vec{\hat{r}} = \sqrt{\omega/(L_w c)}\vec{r}_\perp$, $\vec{\hat{\theta}} = \sqrt{\omega L_w/c}\vec{\theta}$ and $\hat{z} = z/L_w$ we obtain the intensity profile at the virtual source

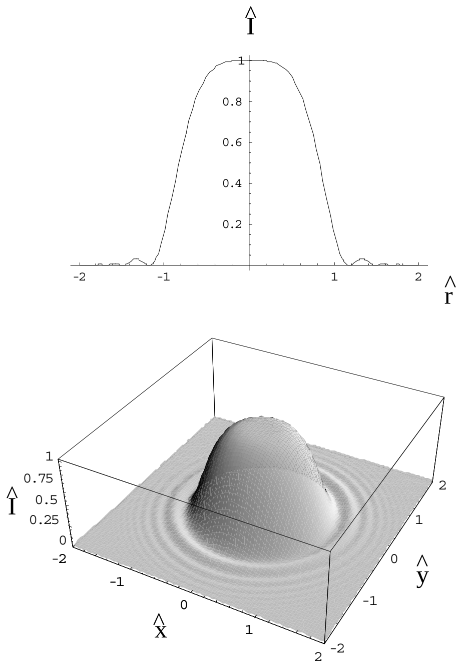

Figure 1: Intensity pattern $\hat{I}$ at the virtual source.

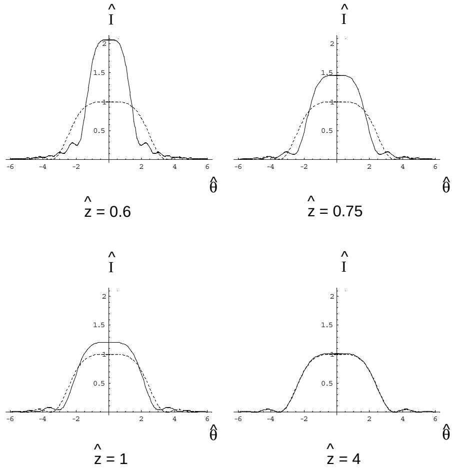

Figure 2: Evolution of the intensity profile as in Eq. (12) (solid lines) compared with far field asymptotic (dashed lines).

$$\hat{I}(0,\hat{r}_\perp) = \frac{1}{\pi^2}\left[\pi - 2\mathrm{Si}\left(\hat{r}_\perp^2\right)\right]^2 , \tag{11}$$

and at any distance $\hat{z}_o$, both in the near and in the far zone:

$$\hat{I}\left(\hat{z}_o,\hat{\theta}\right) = \hat{z}_o^2\left|\mathrm{Ei}\left(\frac{i\hat{z}_o^2\hat{\theta}^2}{2\hat{z}_o-1}\right) - \mathrm{Ei}\left(\frac{i\hat{z}_o^2\hat{\theta}^2}{2\hat{z}_o+1}\right)\right|^2 , \tag{12}$$

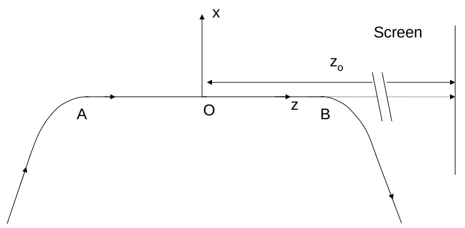

Figure 3: Edge radiation geometry.

where $\hat{\theta} = \hat{r}_\perp/\hat{z}_o$. $\hat{I}$ at the virtual source is plotted in Fig. 1. The evolution of the intensity profile for different z_o, Eq. (12), is given in fig. 2. A virtual source can be used as an input for wavefront propagation codes (as ZEMAX , PHASE, SRW [1]), allowing for the presence of complicate optics, likewise it has been used as an input to Eq. (1) for free-space propagation. Spontaneous SR from an electron beam can be treated as an incoherent collection of laser-like beams with different offsets and deflections (summing up the intensities), while if the electron beam is distributed coherently, radiation can be described as a coherent collection of laser-like beams.

EDGE RADIATION

We consider the system depicted in Fig. 3. An electron enters the setup via a bending magnet, passes through a straight section (segment AB) and exits the setup via another bend. Edge radiation (see references in [1]) is collected at a distance z_o from the center of the straight section. The trajectory and, therefore, the space integration in Eq. (4) consists of the two bends b_1 and b_2, and of the straight section AB. Let L be the length of AB. Points A and B are thus located at $z_A = -L/2$ and $z_B = L/2$. In general, one should sum the contribution due to the straight section to that from the bends. In some cases the presence of the bending magnets can be ignored as if they had zero length, and what may be called ”zero-length switchers approximation” applies. Magnets act like switchers: the first magnet switches the radiation harmonic on, the second switches it off. Switchers may have different physical realizations, depending on the setup. There is no limitation to the length of the switcher. The only common feature between different switchers is that the switching process depends exponentially on the distance from the beginning of the process. Since electrodynamics is a linear theory, when the straight-section contribution cannot be considered a good approximation to the total field, it can still be considered as a fundamental building block for a more complicated setup. This justify our choice to deal with the straight-section contribution to the field only. It is interesting to discuss when the field due to switchers is negligible in our study-case. For $L \gg \gamma^2(c/\omega)$, the formation length for the straight section is $\gamma^2(c/\omega)$, while the formation length for the bend is $((c/\omega)\rho^2)^{1/3}$, ρ being the radius

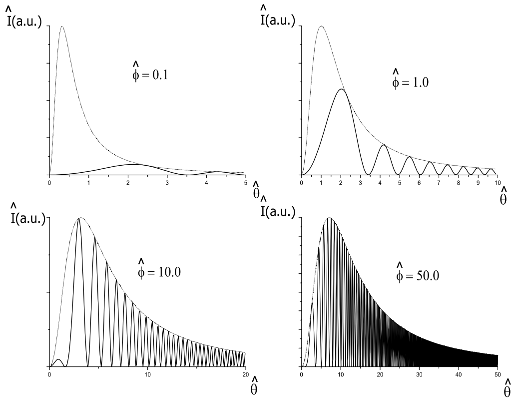

Figure 4: Directivity diagram (solid lines) of the radiation from the setup in Fig. 3 and envelope of the directivity diagram (dotted lines).

of the bend. Let the ratio between the latter and the former be $\epsilon^2 = (\lambda_c/\lambda)^{2/3} \ll 1$, where $\lambda_c = 4\pi\rho/(3\gamma^3)$ is the critical wavelength for SR and $\lambda \gg \lambda_c$, as we are interested in edge radiation. The distance $d_c = \epsilon\gamma^2(\omega/c)$ turns out to constitute an extra characteristic-length for our system. When $d \ll d_c$, the straight section contribution dominates the bending magnet one for $r_\perp > \epsilon\gamma(\omega/c)$, while for other values of $r_\perp$ the two contributions are comparable. When $d \sim d_c$ the zero-length switcher approximation cannot be used. When $d \gg d_c$ we the straight section contribution dominates for $0 < r_\perp \ll ((\omega/c)^2\rho)^{1/3}$, the characteristic size of the radiation being $\epsilon((\omega/c)^2\rho)^{1/3}$. Finally, when $d \gg \gamma^2(\omega/c)$, the straight section contribution dominates for $0 < \theta \ll ((\omega/c)/\rho)^{1/3}$, the characteristic angle of the radiation being $\epsilon((\omega/c)/\rho)^{1/3}$.

Far field pattern of edge radiation

Field contribution calculated along the straight section. Accounting for the geometry in Fig. 3 we have $s(z') = z'$ for $z_A < z' < z_B$. Use of Eq. (4) yields the field contribution from the straight section AB:

$$\vec{\widetilde{E}}_{AB} = \frac{i\omega e L}{c^2 z_o} \exp\left[\frac{i\omega\theta^2 z_o}{2c}\right] \vec{\theta}\, \mathrm{sinc}\left[\frac{\omega L}{4c}\left(\theta^2 + \frac{1}{\gamma^2}\right)\right] . \tag{13}$$

Eq. (13) is describes a spherical wave and explicitly depends on L. The formation length L_{fs} for the straight section AB can be written as $L_{\mathrm{fs}} \sim \min[\gamma^2(c/\omega), L]$. The far-zone asymptotic is independent of such value and always valid at observation positions $z_o \gg L$.

Energy spectrum of radiation. With the help of normalized quantities $\vec{\hat{\theta}} = \sqrt{\omega L/c}\vec{\theta}$ and $\hat{\phi} = \omega L/(\gamma^2 c)$ we may write the directivity diagram $\hat{I}$ of the radiation as $\hat{I} \sim \hat{\theta}^2\ \mathrm{sinc}^2[(\hat{\theta}^2 + \hat{\phi})/4]$. This is plotted in Fig. 4 for several values of $\hat{\phi}$ as a function of the normalized angle $\hat{\theta}$. The natural angular unit is evidently $(2\pi L/\lambda)^{-1/2}$.

There are two asymptotic cases for the problem parameter $\hat{\phi}$: $\hat{\phi} \ll 1$ and $\hat{\phi} \gg 1$. The behavior of the far-field emission is well-known in literature [1]. We take this as the starting point for investigations based on Fourier Optics.

Method of virtual sources

Edge radiation as a field from a single virtual source. Eq. (3) and Eq. (13) yield the virtual source $\vec{\widetilde{E}}(0, \vec{r}_\perp)$:

$$\vec{\widetilde{E}} = -\frac{eL\omega^2}{2\pi c^3} \int d\vec{\theta}\vec{\theta}\mathrm{sinc}\left[\frac{L\omega}{4c}\left(\theta^2 + \frac{1}{\gamma^2}\right)\right] \exp\left[\frac{i\omega\vec{\theta}\cdot\vec{r}_\perp}{c}\right] \tag{14}$$

The Fourier transform in Eq. (14) is difficult to calculate analytically in full generality. An analytic expression for the field amplitude at the virtual source for $\hat{\phi} \ll 1$ reads:

$$\vec{\widetilde{E}}(0, \vec{r}_\perp) = \frac{4\omega e}{c^2 L}\vec{r}_\perp \mathrm{sinc}\left(\frac{\omega}{Lc}\left|\vec{r}_\perp\right|^2\right) . \tag{15}$$

For any value of $\hat{\phi}$, Eq. (15) explicitly depends on L, as the far-field emission does. Using $\vec{\hat{r}} = \sqrt{\omega/(Lc)}\vec{r}_\perp$ the intensity pattern of the virtual source is $\hat{I}(\hat{r}) \sim \hat{r}^2 \mathrm{sinc}^2(\hat{r}^2)$ and is plotted in Fig. 5. The Fresnel formula yields the field in the near and the far zone for $\hat{\phi} \ll 1$

$$\vec{\widetilde{E}} = -\frac{2e}{c}\frac{\vec{r}_\perp}{r_\perp^2} \exp\left[i\frac{\omega r_\perp^2}{2cz_o}\right] \left\{\exp\left[\frac{-i\omega r_\perp^2}{2cz_o(1 + 2z_o/L)}\right]\right. \\ \left. - \exp\left[\frac{i\omega r_\perp^2}{2cz_o(-1 + 2z_o/L)}\right]\right\} , \tag{16}$$

where the singular behavior at $\vec{r}_\perp = 0$ and $z_o \longrightarrow L/2$ cannot be resolved within the paraxial approximation. The intensity profile associated with Eq. (16) is

$$\hat{I} = \frac{1}{\hat{\theta}^2}\left|\left[\exp\left(\frac{-i\hat{\theta}^2\hat{z}_o}{2(1 + 2\hat{z}_o)}\right) - \exp\left(\frac{i\hat{\theta}^2\hat{z}_o}{2(-1 + 2\hat{z}_o)}\right)\right]\right|^2 , \tag{17}$$

where $\hat{\theta} = \hat{r}_o/\hat{z}_o$ and $\hat{z}_o = z_o/L$. A comparison between intensity profiles at different observation points $\hat{z}_o$ is plotted in Fig. 6. When condition $\hat{\phi} \ll 1$, studied until now, is not satisfied, the integral in Eq. (14) can be calculated numerically. The intensity distribution for the virtual source at $\hat{\phi} = 0.1$, $\hat{\phi} = 1$, $\hat{\phi} = 10$ and $\hat{\phi} = 50$ are plotted in Fig. 7. An enlarged plot of the case $\hat{\phi} = 50$ is given in Fig. 8. Fine structures are now evident, consistently with Fig. 4 for the far zone. Once the field at the virtual source is specified for any value of $\hat{\phi}$, Fourier Optics can be used to propagate it. However, we prefer to use an alternative way to solve the field propagation problem for any value of $\hat{\phi}$, capable of giving a better physical insight at $\hat{\phi} \gg 1$.

Edge radiation as a superposition of the field from two virtual sources. The far field in Eq. (13) can be written as $\vec{\widetilde{E}}(z_o, \vec{\theta}) = \vec{\widetilde{E}}_1(z_o, \vec{\theta}) + \vec{\widetilde{E}}_2(z_o, \hat{\theta})$, where

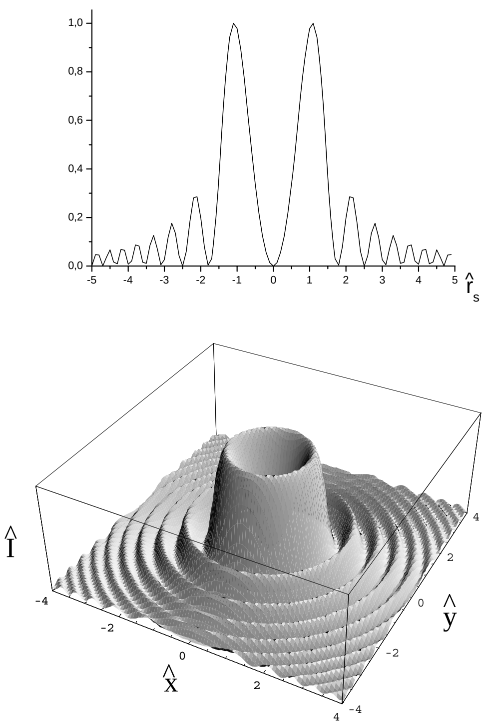

Figure 5: Intensity distribution of the virtual source, $\hat{I}$.

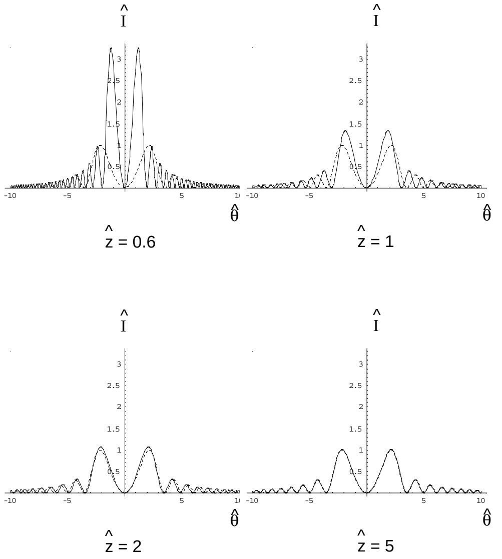

Figure 6: Evolution of the intensity profile for edge radiation for $\hat{\phi} \ll 1$ at different observation distances (solid lines) compared to the far-zone intensity (dashed lines).

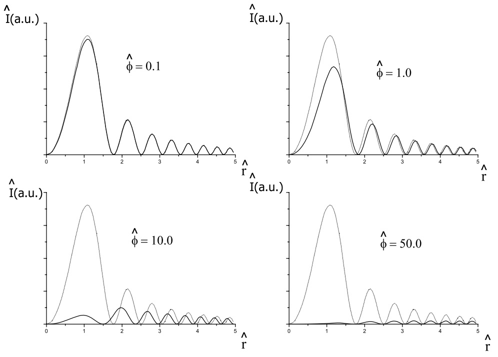

Figure 7: Intensity profiles of the virtual source for different values of $\hat{\phi}$ (solid lines) compared with the case $\hat{\phi} \ll 1$ (dotted lines).

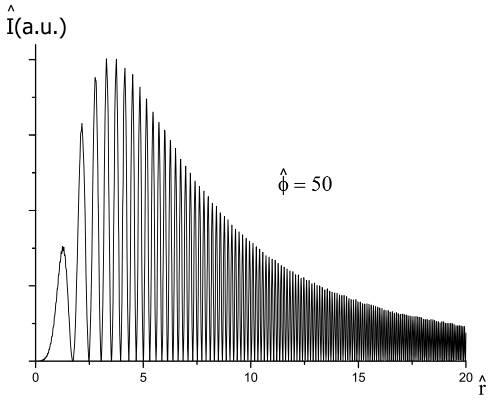

Figure 8: Intensity pattern at the virtual source for $\hat{\phi} = 50$.

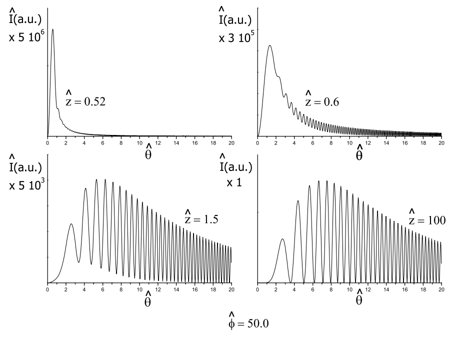

Figure 9: Edge radiation intensity profile at $\hat{\phi} = 50$ for different observation distances.

$$\vec{\tilde{E}}_{1,2}\left(\hat{z}_o,\vec{\hat{\theta}}\right) = \pm\frac{2e\vec{\theta}}{cz_o(\theta^2+1/\gamma^2)} \times \exp\left[\pm\frac{i\omega L}{4c\gamma^2}\right]\exp\left[\frac{i\omega L\theta^2}{2c}\left(\frac{z_o}{L}\pm\frac{1}{2}\right)\right]. \tag{18}$$

The two terms $\vec{\tilde{E}}_1$ and $\vec{\tilde{E}}_2$ represent two spherical waves centered at $z_{s1} = L/2$ and $z_{s2} = -L/2$, corresponding to two virtual sources. Their field distribution is given by

$$\vec{\tilde{E}}\left(\pm\frac{L}{2},\vec{r}_\perp\right) = \mp\frac{2ie\omega}{c^2\gamma}\exp\left[\pm\frac{i\omega L}{4c\gamma^2}\right]\frac{\vec{r}_\perp}{r_\perp}K_1\left(\frac{\omega r_\perp}{c\gamma}\right), \tag{19}$$

where $K_1(\cdot)$ is the modified Bessel function of the first order. It should be noted that Eq. (19) is identical to the well-known frequency-domain expression for the transverse component of the field from an ultra-relativistic electron moving in uniform motion. Both far zone field and the field at the virtual sources exhibit dependence on L through phase factors only. Application of the Fresnel formula allows to calculate the field at any distance z_o in frees space. Using the definition $\vec{\hat{\theta}} = \vec{r}_o/\hat{z}_o$ we obtain $\hat{I} \sim |A_1 + A_2|^2$, where

$$A_{1,2} = \mp\frac{\vec{\hat{\theta}}}{\hat{\theta}}\frac{2i\sqrt{\hat{\phi}}\exp\left[\pm i\hat{\phi}/4\right]}{\hat{z}_o\mp\frac{1}{2}}\exp\left[\frac{i\hat{\theta}^2\hat{z}_o^2}{2\left(\hat{z}_o\mp\frac{1}{2}\right)}\right] \times\int_0^\infty d\xi\xi K_1(\sqrt{\hat{\phi}}\xi)J_1\left[\frac{\hat{\theta}\xi\hat{z}_o}{\hat{z}_o\mp\frac{1}{2}}\right]\exp\left[\frac{i\xi^2}{2\left(\hat{z}_o\mp\frac{1}{2}\right)}\right] \tag{20}$$

In Fig. 9 we plotted results for the field propagation for the case $\hat{\phi} = 50$. Radiation profiles are shown as a function of $\hat{\theta}$ at $\hat{z}_o = 0.52$, $\hat{z}_o = 0.6$, $\hat{z}_o = 1.5$ and $\hat{z}_o = 100.0$. Let us discuss the two limiting cases for $\hat{\phi} \ll 1$ and for $\hat{\phi} \gg 1$. Consider first $\hat{\phi} \ll 1$. The field at any observation distance is given by Eq. (16). There are only two observation zones of interest. **Far zone,** in the limit for $\hat{z}_o \gg 1$ and **Near zone,** when $\hat{z}_o \lesssim 1$. From Eq. (16), the total field results from the interference of the two virtual sources. The transverse size of these sources is $\gamma(c/\omega)$, independently of L. In the center of the setup instead, the virtual source has a dimension $\sqrt{(c/\omega)L}$ (see Eq. (16)). The source in the center of the setup is much smaller than those at the edge, as the two sources at the edges interfere in the center of the setup. Consider now the case $\hat{\phi} \gg 1$. Let $d_{1,2} = z_o \mp L/2$ be the distances of the observer from the edges. One can recognize four regions of interest, that are more naturally discussed in the two-source picture. **Two-edge radiation. Far zone.** When $d_{1,2} \gg L$ we are summing far field contributions from the two edge sources, see Fig. 9 for $\hat{z}_o = 100$. **Two-edge radiation. Near zone.** When $d_{1,2} \sim L$ both contributions from the sources are important, but d_1 and d_2 become sensibly different, see Fig. 9 for $\hat{z}_o = 1.5$. **Single-edge radiation. Far zone.** When $\gamma^2(c/\omega) \ll d_1 \ll L$ the contribution due to the near edge is dominant, see Fig. 9 for $\hat{z}_o = 0.6$. **Single-edge radiation. Near zone.** When $0 \ll d_1 \lesssim \gamma^2(c/\omega)$ we have the near-field contribution from a single edge, and the intensity distribution tends to reproduce the behavior of the square modulus of Eq. (19). See Fig. 9 for $\hat{z}_o = 0.52$.

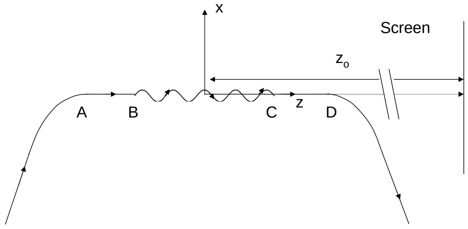

Figure 10: TUR geometry.

TRANSITION UNDULATOR RADIATION

Consider the system in Fig. 10. An electron enters the setup via a bending magnet, passes through a straight section AB, an undulator BC, and another straight section CD. Finally, it exits the setup via another bend. TUR (see references in [1]) is collected at a distance z_o from the origin of the reference system, located in the middle of the undulator. As before we ignore the presence of the bending magnets having already discussed the applicability of the "zero-length switcher approximation".

Far field pattern calculations

Field contribution from the undulator. We first consider the contribution $\vec{\tilde{E}}_u$ from the undulator. We assume a planar undulator and we introduce the longitudinal Lorentz factor $\gamma_z = \gamma/(\sqrt{1+K^2/2})$. Frequencies of interest are $\omega \ll 2\gamma_z^2 ck_w$ (with $k_w = 2\pi/\lambda_w$). As a result one obtains

$$\vec{\tilde{E}}_u = \frac{i\omega e}{c^2 z_o}\int_{z_B}^{z_C} dz' \exp\left[i\Phi_{BC}\right](\theta_x\vec{x}+\theta_y\vec{y}) \tag{21}$$

with

$$\Phi_u = \omega\left[\frac{\theta_x^2+\theta_y^2}{2c}z_o + \frac{z'}{2c}\left(\frac{1}{\gamma_z^2}+\theta_x^2+\theta_y^2\right)\right]. \tag{22}$$

Field contribution from the straight sections. The field contribution from a straight section has been dealt with in the previous Section. Accounting for the proper phase shift, one obtains the contributions $\vec{\tilde{E}}_1$ from AB and $\vec{\tilde{E}}_2$ from CD:

$$\vec{\tilde{E}}_{(1,2)} = \frac{i\omega e}{c^2 z_o}\int_{z_{(A,C)}}^{z_{(B,D)}} dz' \exp\left[i\Phi_{(1,2)}\right](\theta_x\vec{x}+\theta_y\vec{y}) \tag{23}$$

where $\Phi_{(1,2)}$ in Eq. (23) is given by

$$\Phi_{(1,2)} = \omega\left[\frac{\theta^2}{2c}z_o - \frac{L_w}{4c\gamma_z^2} + \frac{L_w}{4c\gamma^2} + \frac{z'}{2c}\left(\frac{1}{\gamma^2}+\theta^2\right)\right] . \tag{24}$$

Total field and energy spectrum of radiation. The contributions from the segments AB, BC and CD are:

$$\begin{aligned}\vec{\bar{E}}_{(1,2)} = {}& \frac{i\omega e L_{(1,2)}}{c^2 z_o}\vec{\theta}\mathrm{sinc}\left[\frac{\omega L_{(1,2)}}{4c}\left(\frac{1}{\gamma^2}+\theta^2\right)\right]\\ &\times\exp\left[\frac{i\omega\theta^2 z_o}{2c}\right]\exp\left[-\frac{i\omega L_w}{4c}\left(\frac{1}{\gamma_z^2}+\theta^2\right)\right]\\ &\times\exp\left[\mp\frac{i\omega L_{(1,2)}}{4c}\left(\frac{1}{\gamma^2}+\theta^2\right)\right] ,\end{aligned} \tag{25}$$

$$\vec{\bar{E}}_u = \frac{i\omega e L_w}{c^2 z_o}\vec{\theta}\mathrm{sinc}\ \left[\frac{\omega L_w}{4c}\left(\frac{1}{\gamma_z^2}+\theta^2\right)\right]\exp\left[\frac{i\omega\theta^2 z_o}{2c}\right] \tag{26}$$

The total field produced by the setup is obtained by summing up these contributions. The resulting energy density of radiation is known in literature [1].

Virtual source specification. Field propagation.

Eq. (25) and Eq. (26) can be interpreted as far field radiation from separate virtual sources with plane wavefronts, located at $z_{s1} = -L_w/2 - L_1/2$, $z_{su} = 0$ and $z_{s2} = L_w/2 + L_2/2$ and characterized by

$$\begin{aligned}\vec{\bar{E}}_{s(1,2)} = {}& -\frac{\omega^2 e L_{(1,2)}}{2\pi c^3}\exp\left[\mp\frac{i\omega}{4c}\left(\frac{L_w}{\gamma_z^2}+\frac{L_{(1,2)}}{\gamma^2}\right)\right]\\ &\times\int d\vec{\theta}\vec{\theta}\mathrm{sinc}\left[\frac{\omega L_{(1,2)}}{4c}\left(\theta^2+\frac{1}{\gamma^2}\right)\right]\exp\left[\frac{i\omega}{c}\vec{\theta}\cdot\vec{r}_\perp\right],\end{aligned} \tag{27}$$

$$\begin{aligned}\vec{\bar{E}}_{su} = {}& -\frac{\omega^2 e L_w}{2\pi c^3}\\ &\times\int d\vec{\theta}\,\vec{\theta}\,\mathrm{sinc}\left[\frac{\omega L_w}{4c}\left(\theta^2+\frac{1}{\gamma_z^2}\right)\right]\exp\left[\frac{i\omega}{c}\vec{\theta}\cdot\vec{r}_\perp\right] .\end{aligned} \tag{28}$$

L_1, L_2 and L_w can assume different values. γ and γ_z are also different. We prescribe the same normalization for all quantities: $\vec{\hat{\theta}} = \sqrt{\omega L_{\mathrm{tot}}/c}\vec{\theta}$, $\hat{\phi} = \omega L_{\mathrm{tot}}/(\gamma^2 c)$ and $\vec{\hat{r}}_\perp = \sqrt{\omega/(L_{\mathrm{tot}}c)}\vec{r}_\perp$. Then, we introduce parameters $\hat{L}_1 = L_1/L_{\mathrm{tot}}$, $\hat{L}_2 = L_2/L_{\mathrm{tot}}$, $\hat{L}_w = L_w/L_{\mathrm{tot}}$ and $\hat{\phi}_w = (\gamma^2/\gamma_z^2)\hat{\phi}$. Finally, we define $\hat{z}_s = z_s/L_{\mathrm{tot}}$. One may check that, in the limit for $\hat{\phi} \ll 1$ and $\hat{\phi}_w \ll 1$ one obtains the same results as for edge radiation from a single straight section. A second region of interest in the parameter space that can be dealt with analytically is for $\hat{\phi} \ll 1$ and $\hat{\phi}_w \gg 1$. In this limit, the contribution from the undulator can be neglected, because the $\mathrm{sinc}(\cdot)$ is strongly suppressed. Then, $\vec{\hat{E}}(\hat{z}_{su}, \vec{\hat{r}}_s) \simeq 0$, where $\vec{\hat{E}} = (\omega e/c^2)\vec{\bar{E}}$. The surviving virtual sources are:

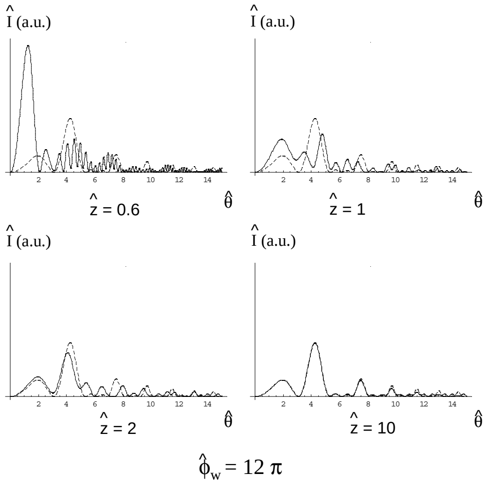

Figure 11: Evolution of the intensity profile for TUR for $\hat{\phi}_w = 12\pi$ (solid lines) and comparison with far-zone intensity (dashed lines).

$$\vec{\hat{E}}_{s(1,2)} = \frac{4\vec{\hat{r}}_\perp}{\hat{L}_{(1,2)}}\exp\left[-\frac{i\hat{L}_w\hat{\phi}_w}{4}\right]\mathrm{sinc}\left(\left|\vec{\hat{r}}_\perp\right|^2/\hat{L}_1\right) . \tag{29}$$

Eq. (29) describes virtual sources characterized by plane wavefronts. Use of the Fresnel propagation formula, Eq. (1) allows reconstruction of the field in the near and in the far zone. The two surviving contributions to the field are:

$$\begin{aligned}\vec{\hat{E}}_{(1,2)} = {}& -\frac{4\vec{\hat{r}}_\perp}{\hat{r}_\perp^2}\exp\left[\mp\frac{i\hat{L}_w\hat{\phi}_w}{4}+\frac{i\hat{r}_\perp^2}{2(\hat{z}_o-\hat{z}_{s(1,2)})}\right]\\ &\times\left\{\exp\left[-\frac{i\hat{L}_1\hat{r}_\perp^2}{2(\hat{z}_o-\hat{z}_{s(1,2)})(\hat{L}_{(1,2)}+2\hat{z}_o-2\hat{z}_{s(1,2)})}\right]\right.\\ &\left.-\exp\left[\frac{i\hat{L}_{(1,2)}\hat{r}_\perp^2}{2(\hat{z}_o-\hat{z}_{s(1,2)})(-\hat{L}_{(1,2)}+2\hat{z}_o-2\hat{z}_{s(1,2)})}\right]\right\}\end{aligned} \tag{30}$$

Eq. (30) solves the propagation problem for the near and the far field when $\hat{\phi} \ll 1$ and $\hat{\phi}_w \gg 1$. The intensity pattern is obtained by summing up contributions in Eq. (30) and taking square modulus of the sum. To give an example we study the case $L_1 = L_2 = L_w = L_{\mathrm{tot}}/3$. The intensity pattern periodically depends on $\hat{\phi}_w \gg 1$ with a period 12π. For illustration, in Fig. 11 we plot the intensity profile for $\hat{\phi}_w = 12\pi$ at different distances $\hat{z}_o$ and we compare these profiles with the far field asymptote.

REFERENCES

[1] References and a more detailed description of this subject are included in: G. Geloni, E. Saldin, E. Schneidmiller and M. Yurkov, DESY 06-127 (2006), downloadable at http://arxiv.org/abs/physics/0608145.

[2] It is not so if near and formation zone do not coincide.

A SCALLOPED ELECTRON BEAM FREE-ELECTRON LASER *

D.C. Nguyen[#], Los Alamos National Laboratory, Los Alamos, NM 87545, U.S.A.
H.P. Freund, Science Applications International Corp., McLean, VA 22102, U.S.A.
W.B. Colson, Naval Postgraduate School, Monterey, CA 93943, U.S.A.

Abstract

Typical high-gain FEL amplifiers employ an electron beam that is “matched” to the wiggler so that the envelope remains constant throughout the wiggler. This paper describes a novel approach in which the electron envelope undergoes scalloping motion along the wiggler because the beams are deliberately mismatched at the wiggler entrance. We present an analysis of the electron scalloping motion and the FEL interaction with a scalloped electron beam. Using MEDUSA simulations, we show the advantages of the scalloped-beam FEL and the properties of the radiation beam it produces.

INTRODUCTION

In high-gain FEL amplifiers, the electron beam radius plays a crucial role in determining the FEL interaction strength. Most FEL amplifiers use a tightly focused electron beam to enhance the FEL interaction, i.e. both the FEL gain and saturated power increase with smaller electron beam radius. A typical FEL employs electron beams that are “matched” to the wiggler so that the envelope remains constant throughout the wiggler. Since the matched beam radius is proportional to $\sqrt{\varepsilon_n}$, a small beam radius requires a small normalized rms emittance.

The use of external magnets to focus the electron beam to a radius smaller than allowed by the normalized rms emittance in order to pinch the optical beam was first suggested by Sprangle *et al*. [1]. In this paper, we suggest the use of natural betatron motion in a weak focusing wiggler, to refocus the electron beam periodically in the wiggler, resulting in pinching near the wiggler exit (Fig. 1). It is possible to select a combination of input laser power and wiggler length such that the FEL saturates near the second waist. Optical guiding causes the radiation beam to follow the electron beam’s motion, resulting in pinching of the radiation beam near the exit [2].

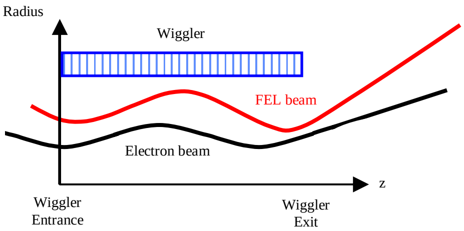

Figure 1: Illustration of a scalloped electron beam FEL with a uniform wiggler.

THEORY

The evolution of the rms radius σ of a relativistic, axi-symmetric beam with equal transverse emittance and equal two-plane focusing can be written as follow

$$\frac{d^2\sigma}{dz^2} = -k_\beta^2\sigma + \frac{2I}{\gamma^3 I_A \sigma} + \frac{\varepsilon_n^2}{\gamma^2\sigma^3}, \tag{1}$$

where k_β is the betatron wavenumber, I the peak current, I_A the Alfven current, γ the relativistic factor, and ε_n the normalized rms emittance. Under steady-state condition, the emittance-dominated rms matched beam radius is

$$\sigma_0 = \sqrt{\frac{\sqrt{2}\varepsilon_n}{k_w a_w}}\ . \tag{2}$$

Using a first order perturbation analysis of Eq. (1) we can show that

$$\sigma = \sigma_0 - \delta_0 \sin(k_\Sigma z) \tag{3}$$

where $\delta_0 = (\sigma_0 - \sigma_{min})$ is the initial deviation from the matched radius, and k_Σ , the scalloping wavenumber, as given by

$$k_\Sigma = 2k_\beta\sqrt{1 - \frac{I}{I_A}\frac{1}{\gamma^2 k_\beta \varepsilon_n}} \tag{4}$$

The power gain length in a high-gain FEL amplifier scales with the electron beam radius as follow [3]

$$L_G = \frac{\gamma}{\sqrt{3}}\left(\frac{I_A}{a_w^2 f_B^2 k_w I}\right)^{1/3}\sigma^{2/3}\left(1+\Lambda_{3D}\right) \tag{5}$$

where f_B is the difference in Bessel functions, and Λ_{3D} is the three-dimensional effect. Since the electron beam radius varies slowly with distance, the FEL power gain length also varies along the wiggler. The saturated power scales inversely with electron beam radius.

$$P_s = \frac{1}{\gamma}\left(\frac{a_w f_B}{2\sqrt{2}k_w\sigma}\right)^{2/3}\left(\frac{I}{I_A}\right)^{1/3}\frac{P_{beam}}{\left(1+\Lambda_{3D}\right)^2} \tag{6}$$

where P_{beam} is the electron beam power. The scalloped beam FEL performance depends on how the electron beam is focused in the wiggler and the scalloping period. We look at two cases: 1) the electron beam waist is focused near the entrance, and 2) the waist is the centre of the wiggler. In the first case, the electron comes to second waist near the wiggler exit and the FEL output power, which scales inversely with radius, is at a maximum. In the second case, the beam radius is largest near the wiggler exit and the output power is at a minimum [4].

---

*Work supported by the Office of Naval Research and the High-Energy Laser Joint Technology Office. Author email: dcnguyen@lanl.gov

SIMULATION

Table I summarizes the FEL and beam parameters used in the MEDUSA simulations. These parameters are chosen for a 1.06-micron wavelength where high-power seed lasers exist. The wiggler is a conventional permanent-magnet design with parabolic pole faces to provide equal two-plane, sextupole focusing. Alternatively, the magnets can be notched to approximate sextupole focusing [5]. We chose an input power of 10^6 W (1 μJ pulse energy and 1 ps FWHM, for instance) to achieve saturation in about 2 m of wiggler length with a matched electron beam. For the scalloped beam FEL, the saturation length is 2.6 m. The scalloping period is about 2 m so the second waist of the electron beam envelope is near the exit of the wiggler in both cases. The effects of using matched- and scalloped-beams in the two-stage wiggler are illustrated in Figs. 2 and 3. The power reaches a maximum of 0.84 GW in the matched case, and 1.03 GW in the scalloped case. The extraction efficiency increases correspondingly from the usual 1% to 1.27%. The only drawback is a 30% increase in the wiggler length required to reach saturation.

Table 1: MEDUSA simulation parameters and results.

Parameters	**Values**
Beam Energy	80.8 MeV
Peak Current	1000 A
Emittance	10 mm-mrad
Energy Spread	0.25%
Wiggler Period	2.18 cm
Wiggler Peak Magnetic Field	8.247 kG
rms Wiggler Parameter	1.187
Wiggler Length	2.6 m
Matched Beam Radius	0.27 mm
Scalloped Beam Minimum Radius	0.16 mm
Scalloping Period	2.05 m
Wavelength	1.058 µ
Peak Injected Power	1 MW
Injected Radiation Waist	0.305 mm
Matched Beam Peak Power	0.84 GW
Matched Beam Efficiency	1.0%
Matched Beam Saturation Length	1.96 m
Scalloped Beam Peak Power	1.03 GW
Scalloped Beam Efficiency	1.27%
Scalloped Beam Saturation Length	2.6 m

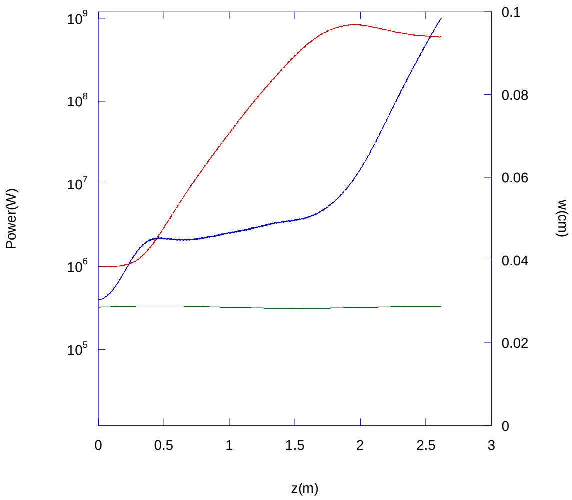

Figure 2: FEL power (red), optical beam radius (blue), and electron beam radius (green) for the matched case.

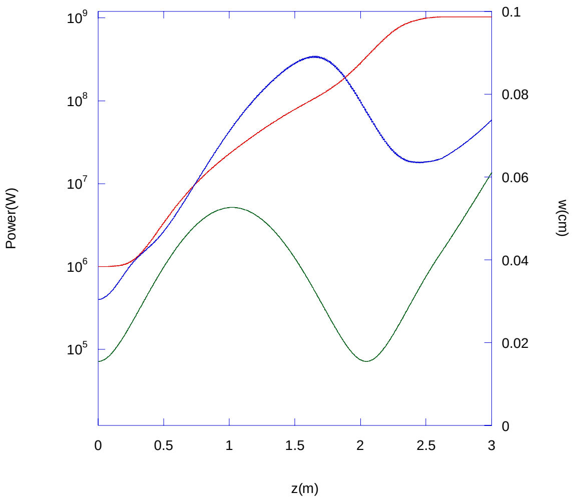

Figure 3: FEL power (red), optical beam radius (blue), and electron beam radius (green) for the scalloped case.

It is noteworthy that the lethargy region is reduced in the scalloped beam FEL as a result of high gain (short gain length) at the wiggler entrance. In the middle of the wiggler, exponential gain is reduced and the reduction in optical guiding causes the radiation beam to expand rapidly. At saturation, the scalloped beam optical waist is larger than the matched beam case. Thus, scalloping the electron beam in a uniform wiggler does not pinch the optical beam to a smaller radius. To significantly pinch the optical beam, we need additional optical guiding, for instance with the addition of a step-taper wiggler.

For seeded FEL amplifiers, it is advantageous to tune the input wavelength while keeping the electron beam energy constant in order to find where the power is maximized. In the matched beam case, the FEL output power increases toward larger detuning, namely longer wavelength at a fixed electron beam energy (or higher electron beam energy at a fixed wavelength) and then drops sharply. In the scalloped beam case, the FEL output power decreases rapidly on both side and the detuning bandwidth is narrower. This is a result of lower FEL gain due to the scalloped electron beam, but the FEL saturated power is higher than the matched beam case.

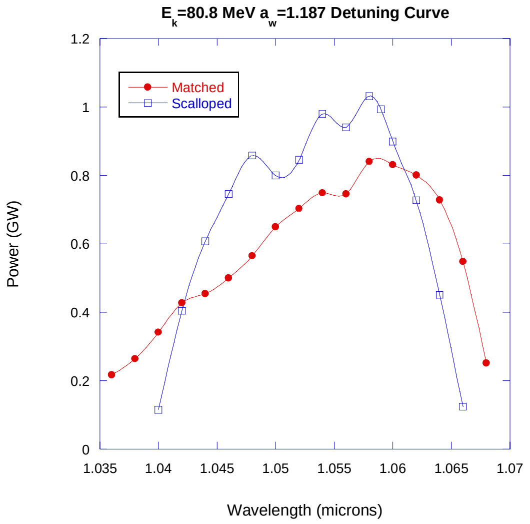

Figure 4: Detuning curves for the matched (red) and scalloped (blue) electron beam FEL.

We also study scalloped beam FEL with a step-taper wiggler to increase the extraction efficiency (Fig. 5). The step-taper starts at z = 1.92 m and the magnetic field is reduced to 8.032 kG while the period remains the same. The FEL peak power grows to 1.45 GW, corresponding to 1.8% efficiency (Fig. 6). The optical beam is pinched to a 0.3 mm radius in the second wiggler segment, compared to a 0.6 mm radius of the uniform wiggler. The optical divergence angle is increased from 0.8 to 1.6 mrad.

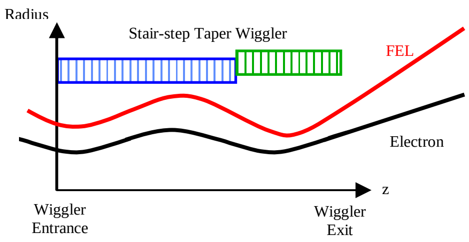

Figure 5: Illustration of a scalloped beam FEL with a step-tapered wiggler.

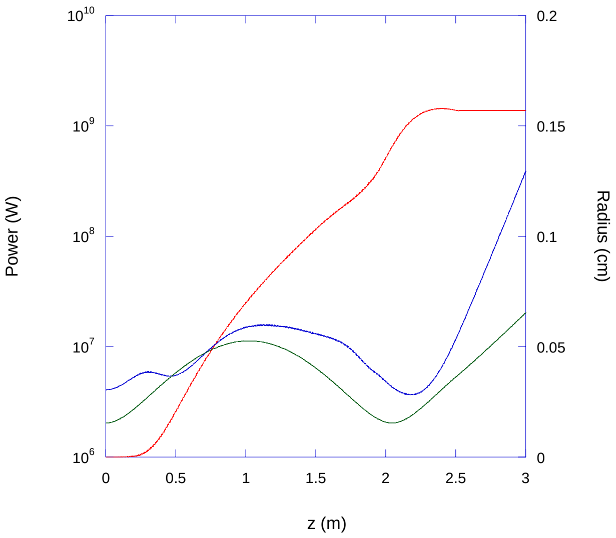

Figure 6: FEL power (red), optical beam radius (blue), and electron beam radius (green) for scalloped beam FEL with a step-tapered wiggler.

SUMMARY AND DISCUSSION

We have studied a new kind of FEL interaction in which the electron beam's envelope undergoes scalloping motion and the exponential gain varies along the wiggler length. For maximum power, the optimum approach is to focus the electron beam near the wiggler entrance and chose a wiggler length that is slightly longer than the scalloping period so that the second waist occurs near saturation. The smaller electron beam radius at saturation increases the saturated power of a uniform wiggler. The scalloped beam FEL detuning spectrum is narrower than the matched beam case. This is indicative of a lower net gain for the scalloped beam FEL.

As a result of this study, we conclude that the use of a scalloped-beam is advantageous even at the expense of a longer wiggler length to reach saturation. In addition, the combination of scalloped electron beams and a step-tapered wiggler can double the output power, and thus the FEL efficiency. The radiation beam is also pinched near the exit and expands rapidly afterward, thereby reducing the risk of damaging optics intercepting the FEL beam.

REFERENCES

[1] P. Sprangle, B. Hafizi, and J.R. Penano, IEEE J. Quantum Electron. 40 (2004) 1739.

[2] D.C. Nguyen, H.P. Freund, and W. Colson, Phys. Rev. ST-AB 9 (2006) 050703.

[3] M. Xie, Proceedings of the IEEE Particle Accelerator Conference, 1995, V.1, 183-185.

[4] P.P. Crooker et al., these Proceedings, paper MOPPH075.

[5] C. Fortgang, Nucl. Instrum. Meth. A393 (1997) 385.

INFLUENCE OF OPTICAL FEEDBACK ON THE COHERENCE PROPERTIES OF FEL OSCILLATORS

S. Bielawski, PhLAM/CERCLA, Villeneuve d'Ascq Cedex;
M.-E. Couprie, CEA, Gif-sur-Yvette;
M. Hosaka, M. Katoh, A. Mochihashi, UVSOR, Okazaki;
C. Szwaj, PhLAM/CERCLA, Villeneuve d'Ascq Cedex

Abstract

When detuned, the output of a FEL oscillator is dominated by a transient amplification of the spontaneous emission noise (SE). Here, we show that FEL oscillators in this situation appear to display a strong sensitivity to optical feedback. From a Dattoli-Elleaume type modeling, we show that a very small amount of reinjected power (typically $\ll 1 \cdot 10^{-8}$ in the case of the UVSOR SR-FEL) modifies dramatically the FEL operation. In particular, we demonstrate experimentally and numerically a strong spectral narrowing, correlated with a disappearance of the laser pulse microstructures. This is also accompanied by a suppression of SR-FEL instabilities for a wide range of parameters (half of the detuning curve). These topics (strong amplification of SE noise, and control using tiny reinjection), are of course more general. We propose a theoretical approach of these questions, using in particular the concept of convective instabilities.

PAPER NOT AVAILABLE

SPACE-FREQUENCY MODEL OF ULTRA WIDE-BAND INTERACTIONS IN FREE-ELECTRON LASERS

Y. Pinhasi*, Yu. Lurie, and A. Yahalom
The College of Judea and Samaria, Ariel, Israel.

Abstract

The principle of operation of intense radiation devices such as microwave tubes, free-electron lasers (FELs) and masers, is based on a distributed interaction between an electron beam and radiation. We developed a three-dimensional, space-frequency theory for the analysis and simulation of radiation excitation and propagation in electron devices and free-electron lasers operating in an ultra wide range of frequencies. The total electromagnetic field is presented in the frequency domain as an expansion in terms of cavity eigen-modes. The mutual interaction between the electron beam and the field is fully described by coupled equations, expressing the evolution of mode amplitudes and electron beam dynamics. The approach is applied in a numerical particle code WB3D, simulating wide band interactions in free-electron lasers operating in the linear and non-linear regimes. The code is used to study the statistical and spectral characteristics of multimode radiation generation in a free-electron laser, operating in various operational parameters. The theory is demonstrated also in the case of ”grazing”, resulting in a wide-band interaction between the electron beam and the radiation.

INTRODUCTION

In this paper we continue development of the previously stated space-frequency, 3D model, which describes broadband phenomena occurring in electron devices, masers and FELs [1, 2, 3, 4]. In the model, the total electromagnetic field is presented in the frequency domain in terms of transverse eigen-modes of the cavity, in which the field is excited and propagates. A set of coupled excitation equations, describing the evolution of each transverse mode, is solved self-consistently with beam dynamics equations.

This coupled-mode model is employed in a three-dimensional numerical simulation code WB3D (see [1, 2] for the details). In the present work, the code is used to study the statistical and spectral characteristics of multimode radiation generation in a free-electron laser, operating in various operational parameters. The theory is demonstrated also in the case of “grazing”, when the group velocity of the radiation mode is equal to the axial velocity of the electrons, resulting in a wide-band interaction between the electron beam and the generated radiation.

THE MODEL

In the frequency domain the total electromagnetic field can be expanded in terms of transverse eigenmodes of the medium in which it is excited and propagates (see [1, 2] for the details). The perpendicular component of the electric and magnetic fields are given in any cross-section as a linear superposition of a complete set of transverse electric filed $\widetilde{\mathcal{E}}_{q\perp}(x,y)$ and magnetic field $\widetilde{\mathcal{H}}_{q\perp}(x,y)$ eigenmodes:

$$\widetilde{\mathbf{E}}_\perp(\mathbf{r},f) = \sum_q C_q(z,f)\, e^{+jk_{z_q}z}\, \widetilde{\mathcal{E}}_{q\perp}(x,y) \quad (1)$$

$$\widetilde{\mathbf{H}}_\perp(\mathbf{r},f) = \sum_q C_q(z,f)\, e^{+jk_{z_q}z}\, \widetilde{\mathcal{H}}_{q\perp}(x,y) \quad (2)$$

here $C_q(z,f)$ is amplitude of the mode q, that may be found from the excitation equations:

$$\frac{d}{dz}C_q(z,f) = \frac{1}{\mathcal{N}_q}\sum_i Q_i\left\{\frac{\mathbf{v}_{\perp i}}{v_{z_i}}\widetilde{\mathcal{E}}^*_{q\perp}(x_i,y_i)+\widetilde{\mathcal{E}}^*_{q_z}(x_i,y_i)\right\}e^{j[\omega t_{z_i}-k_{z_q}z]} \quad (3)$$

Spectral energy distribution of the electromagnetic field is defined in the model as a sum of energy spectrum of the excited modes:

$$\frac{d\mathcal{W}(z)}{df} = \sum_q \frac{1}{2}|C_q(z,f)|^2\, \Re\left\{\mathcal{N}_q\right\} \quad (4)$$

MULTIMODE SUPER-RADIANT EMISSION

To demonstrate the utilization of the model, we present a study of super-radiant emission in a waveguide-based, pulsed beam free-electron maser (FEM), with operational parameters are given in Table 1. Such FEM is expected to operate at millimeter and sub-millimeter (THz) wavelengths. When a FEL utilizes a waveguide, the axial wavenumber of transverse mode q follows the dispersion relation:

$$k_{z_q}(f) = \frac{2\pi}{c}\sqrt{f^2 - f^2_{co_q}} \quad (5)$$

where $f_{co_q} = \frac{c}{2\pi}k_{\perp q}$ is the cut-off frequency of the mode. In synchronism with that mode, the dispersion relation for

---

* e-mail: yosip@eng.tau.ac.il

Table 1: Operational parameters of millimeter and sub-millimeter wave free-electron maser.

Accelerator	
Electron beam energy:	E_k=1÷6 MeV
Electron beam current:	I_0=1 A
Electron beam pulse duration:	T=0.1 pSec
Wiggler	
Magnetic induction:	B_w=2000 G
Period:	λ_w=5 cm
Number of periods:	N_w=20
Waveguide	
Rectangular waveguide:	15×7.5 mm
mode	Cut-off frequency
TE_{01}	20.0 GHz
TE_{21} , TM_{21}	28.3 GHz
TE_{41} , TM_{41}	44.7 GHz
TE_{03}	60.0 GHz

the electron beam is given by

$$k_{z_q}(f) = \frac{2\pi f}{v_{z0}} + k_w \tag{6}$$

where v_{z0} is the average velocity of the accelerated electrons and $k_w = \frac{2\pi}{\lambda_w}$ (λ_w is the wiggler's period). The corresponding curves of synchronism frequency vs. beam energy for the FEM are shown in Fig. 1. Only waveguide modes which have in their field profile components that interacts efficiently with the wiggling electrons are shown. Table 2 summarizes several examined cases resulted from Eq. (6) in the multi-transverse mode operational regime. For each transverse mode q, the acceleration energy E_k can be set to excite two frequencies corresponding to the "slow" ($v_{g_q} < v_{z0}$) and "fast" ($v_{g_q} > v_{z0}$) synchronism frequencies or to the special case of "grazing", where $v_{g_q} = v_{z0}$ and a single synchronism frequency is obtained. Here

$$v_{g_q} = 2\pi \frac{d\,f}{d\,k_{z_q}} = \frac{c^2}{2\pi f} k_{z_q}(f) \tag{7}$$

is the group velocity of the excited mode q.

The effect of super-radiance emerges when the duration of the electron beam pulse is much less then the period of the electromagnetic waves expected to be excited at synchronism frequencies according to Table 2. The waveguide and e-beam dispersion curves when the acceleration energy is $E_k = 2$ MeV are shown in Fig. 2. In this case a single waveguide mode TE_{01} is excited at two separated synchronism frequencies ("slow" and "fast") 46.1 GHz and 149.5 GHz, respectively. The spectral density of energy flux calculated with the code WB3D is shown in Fig. 3a. The spectrum peaks at the two synchronism frequencies with main lobe bandwidth of $\Delta f_{1,2} \approx \frac{1}{\tau_{sp_{1,2}}}$, where $\tau_{sp_{1,2}} \approx N_w \lambda_w \left| \frac{1}{v_{z0}} - \frac{1}{v_{g_{1,2}}} \right|$ is the slippage time. The corresponding temporal wave-packet (shown in Fig. 3b) consist of two "slow" and "fast" pulses with durations equal to the slippage times modulating carriers at their respective synchronism frequencies. Lowering the beam energy to $E_k \approx 1.62$ MeV, results in grazing between the e-beam and the waveguide dispersion curves at a single synchronism frequency 69.6 GHz. The spectrum in the case of grazing, as well as the corresponding temporal wavepacket are shown in Fig. 4.

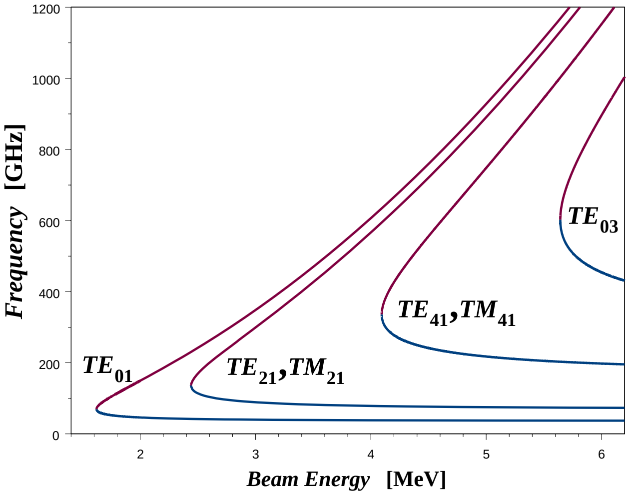

Figure 1: Energy dependence of the dispersion solutions.

As the acceleration energy is increased, transverse modes of higher orders are being excited simultaneously (in addition to the mode TE_{01}) extending the radiation spectrum over a wide rage of frequencies from few tens of GHz to more then THz. Fig. 5 shows the energy spectral densities of the excited waveguide modes as the beam energy is increased.

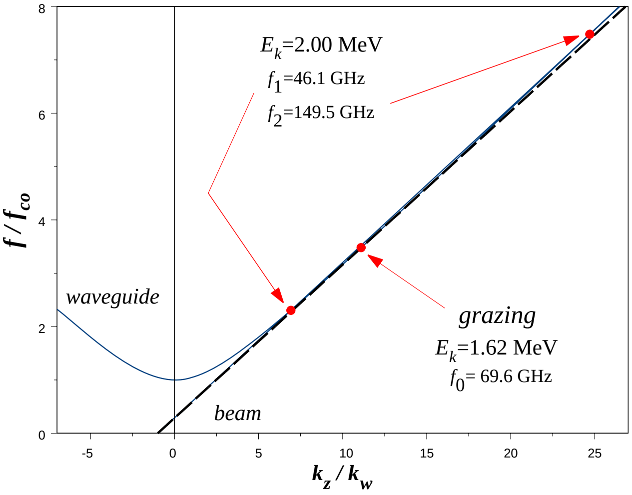

Figure 2: Dispersion solutions for TE_{01} transverse mode for $E_k = 2$ MeV.

Table 2: Synchronism frequencies for several beam energies.

Beam Energy	Synchronism frequencies [GHz]			
[MeV]	TE_{01}	TE_{21},TM_{21}	TE_{41},TM_{41}	TE_{03}
1.62	69.6 (grazing)	—	—	—
2.00	46.1 , 149.5	—	—	—
2.44	42.0 , 230.5	136.2 (grazing)	—	—
3.00	39.8 , 348.4	88.9 , 299.3	—	—
4.09	38.2 , 632.9	78.1 , 592.9	336.1 (grazing)	—
5.00	37.5 , 927.8	75.0 , 890.3	217.5 , 747.8	—
5.60	37.3 , 1151.0	73.9 , 1114.5	203.6 , 984.8	602.6 (grazing)

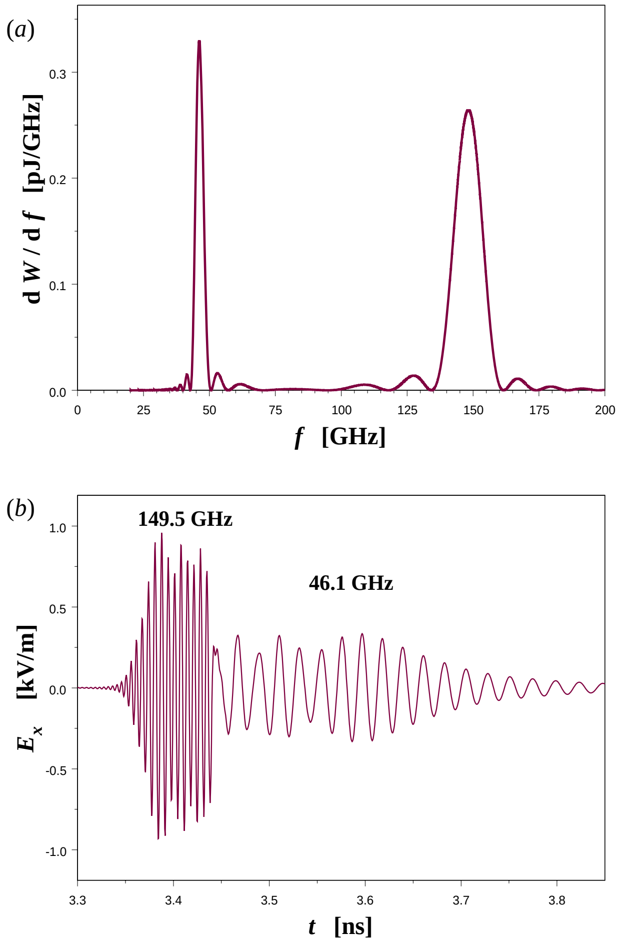

Figure 3: Super-radiant emission from an ultra short bunch when the beam energy is E_k=2 MeV and a single TE_{01} mode is excited: (a) Energy spectrum, and (b) temporal wavepacket.

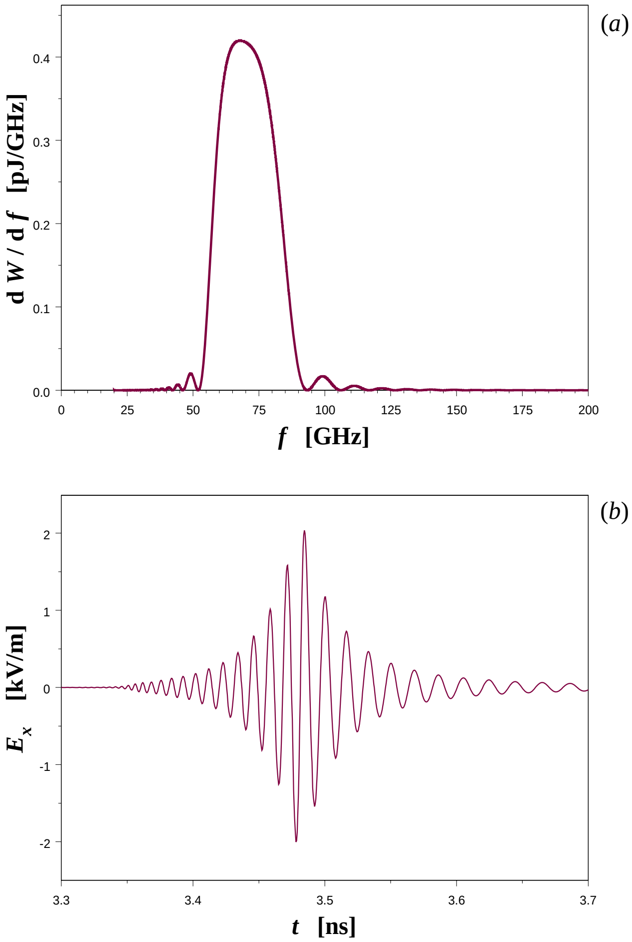

Figure 4: That of Fig. 3, but at grazing condition for mode TE_{01} (the beam energy is $E_k \approx 1.62$ MeV).

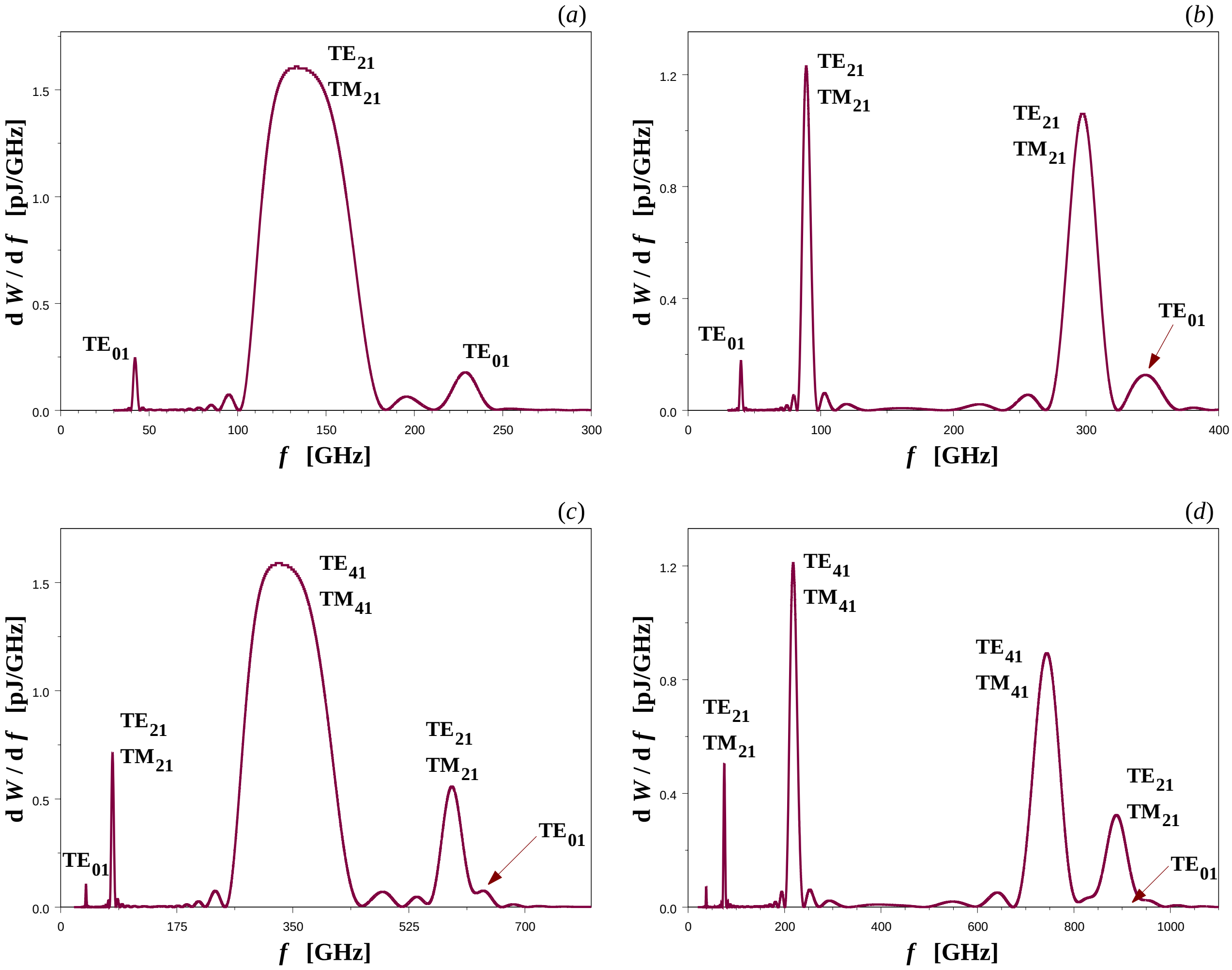

Figure 5: Energy spectra for different acceleration energies: (a) $E_k = 2.44$ MeV (grazing in the TE$_{21}$,TM$_{21}$ modes); (b) $E_k = 3.00$ MeV; (c) $E_k = 4.09$ MeV (grazing in the TE$_{41}$,TM$_{41}$ modes); (d) $E_k = 5.00$ MeV.

CONCLUSIONS

The presented coupled-mode theory, formulated in the frequency domain, enables development of a three-dimensional model, which can accurately describe wide-band interactions between radiation and electron beam in electron devices and free-electron lasers. Space-frequency solution of the electromagnetic equations considers dispersive effects arising from the resonator and gain medium. Such effects play a role also in the special case of grazing, and can not be accurately treated in approximated space-time approaches. We also note that our space-frequency model described here, also facilitates the consideration of statistical features of the electron beam and the excited radiation, enabling simulation of the interaction of a free-electron laser operating in the linear and non-linear regimes.

REFERENCES

[1] Y. Pinhasi, Yu. Lurie and A. Yahalom, Nucl. Instr. and Meth. in Phys. Res. A, **475**, 147 (2001).

[2] Y. Pinhasi, Yu. Lurie, A. Yahalom, and A. Abramovich, Nucl. Instr. Meth. Phys. Res. A, **483**, 510 (2002).

[3] Y. Pinhasi, Yu. Lurie, A. Yahalom, Phys. Rev. E **71**, 036503 (2005).

[4] Y. Pinhasi and Yu. Lurie, Phys. Rev. E **65**, 026501 (2002).

PARAMETRIC OPTIMIZATION OF A X-RAY FEL BASED ON A THOMSON SOURCE*

L. Serafini, A. R. Rossi, V. Petrillo, C. Maroli, A. Bacci, INFN-Milano, Milano, Italy
M. Ferrario, INFN-LNF, Frascati, Italy.

Abstract

We present a study based on a parametric optimization of a Thomson Source operated in FEL mode. This deals with the proposed scheme to use a high intensity laser pulse colliding with a high brightness electron beam of low to medium energy (around 10 MeV). Electrons undulating in the incoming laser field may emit radiation in a FEL coherent mode as far as some conditions are satisfied. A set of simple analytical formulas taking into account 3D effects is derived, in order to express these conditions in terms of three free parameters, namely the wavelength of the colliding laser pulse, the amplitude of the ripples in the time profile of the laser field, and the peak current carried by the electron beam. A few examples of possible operating points are compared with results of 3D numerical simulations, showing the FEL coherent emission of X-rays in the 0.1 to 5 nm range with tens of MeV high brightness electron beams colliding with high intensity ps-long laser beams carrying pulse energies of about 10 J.

INTRODUCTION

It has been recognized by several authors in the past [1,5] that the interaction between a high brightness electron beam and a counterpropagating - head-on colliding - high intensity laser pulse could lead to coherent emission of radiation, in the direction of the electron beam motion, according to a FEL-like mechanism driven by a collective instability that induces exponential growth of the radiation intensity. This coherent part of the emitted radiation overlaps with the spontaneous incoherent radiation generated by the Thomson back-scattering effect. Only recently, however, detailed 3D simulations[6] able to model the FEL collective instability showed the potential existence of this effect under particular conditions of electron beam emittance and current as well as laser field amplitude in the focal region, where the interaction between the two beams occurs. In this paper we derive a set of practical analytical formulas describing the existence of operating conditions in the dynamical range of the system where 3D effects can be mitigated so to allow the onset of the FEL instability, hence the generation of coherent radiation in a SASE-FEL emission mode.

Generally speaking, the situation is at all similar to a conventional SASE-FEL based on a magnetostatic undulator through which the electron beam propagates: the magnetostatic field of the undulator is replaced by the e.m. field of the incoming laser pulse, which causes the electrons to wiggle while they propagate through the pulse. Since the laser field is a classical description of a flux of real photons (to be compared with virtual photons for the case of a magnetostatic undulator), the resonance relationship for a Thomson source is at all similar to the FEL resonance apart for a factor 4 in the denominator.

$$\lambda_R = \frac{\lambda}{4\gamma^2}\left(1 + a_0^2 + \gamma^2\vartheta^2\right) \tag{1}$$

where λ is the wavelength of the colliding laser pulse, γ the kinetic energy of the electron beam (expressed in terms of its dimensionless relativistic factor), λ_R the wavelength of the forward emitted radiation (within a small angle ϑ around the electron beam propagation axis) and a_0 is the laser parameter (dimensionless amplitude of the vector potential associated to the laser field), given by

$$a_0 = 8.5 \cdot 10^{-6}\,\frac{\lambda\sqrt{P}}{R_0} \tag{2}$$

where R_0 is the laser focal spot size and P the peak power in the laser pulse (in TW).

The interaction between the electron beam and the laser pulse is assumed to take place in a drift space where no external forces (focusing or deflecting) act on the two beams, which are tightly focused by their individual final focus lens systems, taking them down to micron-size focal spots. Under the assumption that the laser pulse has a uniform transverse intensity profile of hard edge radius R_0 in the focus position, we can neglect ponderomotive transverse effects on the electron trajectories[7].

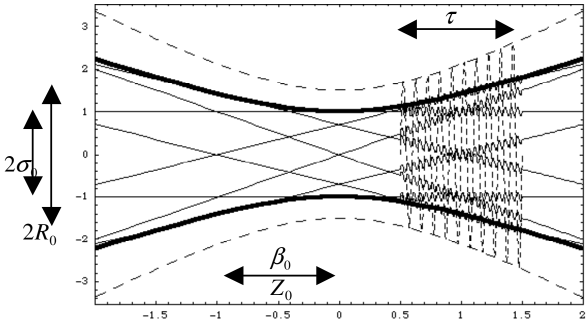

Figure 1: Electron orbits in the focal region (intersecting thin solid lines). Electron beam envelope (bold solid lines) and laser beam envelope (dashed lines) are also shown. Electrons are moving to the right, laser pulse (duration τ) is moving to the left.

As depicted in Fig.1, electrons cross the focus area traveling on rectilinear orbits: when they traverse the laser field their secular trajectories remain rectilinear, with a superimposed slightly wiggling motion.

PARAMETER DEFINITIONS

We break-up the set of parameters describing the whole system into three groups, one for each of the three interacting beams: the electron beam, the colliding laser beam and the emitted FEL radiation beam, respectivley.

The system is described by 11 main free parameters: 4 parameters for the electron beam, summarized in Table 1, 5 parameters for the laser beam, summarized in Table 2, and 2 parameters for the FEL radiation beam, summarized in Table 3. Note that units indicated in the tables are just the ones used for simplicity in the final set of formulas: all intermediate calculations are performed in standard MKS units.

Table 1: Electron Beam parameters

Energy γ	Current **I [A]**	Focal spot **σ_0 [μm]**	Emittance **ε_n [μm]**

There are some other additional parameters which represents ancillary quantities useful for handling the system of conditions relating the 11 main free parameters. These are: the electron beam beta-function in the focus, β_0 , which is defined by the usual relation

$$\sigma_0 = \sqrt{\frac{\varepsilon_n \beta_0}{\gamma}} \tag{3}$$

the electron bunch rms length, σ_z , and the electron beam rms relative energy spread $\frac{\Delta\gamma}{\gamma}$. These last two quantities do not enter in the derivation of the final set of formulas: they are only used for an afterward check on additional ancillary conditions.

Table 2: Laser parameters

Wavelength **λ [μm]**	Power **P [TW]**	Pulse length **τ [ps]**	Focal spot **R_0 [μm]**	Intensity ripples Δ [%]

Additional parameters for the laser beam are the Rayleigh range Z_0 , given by

$$Z_0 = \frac{4\pi R_0^{\,2}}{\lambda} \tag{4}$$

and the laser pulse energy, defined by $U = P\tau$. Note that the definition of the laser ripple parameter Δ is

$$\Delta \equiv \frac{\Delta a_0}{a_0} \tag{5}$$

which represents the fluctuations of laser field amplitude along the pulse, which is assumed to have (at $\Delta = 0$) an ideal flat-top time profile.

Table 3: FEL radiation parameters

Wavelength **λ_R [Å]**	FEL parameter **ρ**

Additional parameters for the FEL radiation beam are the gain length, $L_g = \frac{\lambda}{4\pi\rho}$, and the quantum parameter, $\overline{\rho} = \rho\frac{\gamma\lambda_R}{\lambda_C}$ (with $\lambda_C = 0.024$ Å). As discussed elsewhere[8], as far as $\overline{\rho} \geq 0.5$ quantum effects are negligible ant the system can be described by means of classical FEL-like equations[6].

CONDITIONS FOR FEL EMISSION

Let us now analyze what are the conditions to be satisfied by the 11 main parameters (***γ, I, σ_0, ε_n, λ, P, τ, R_0, Δ, λ_R, ρ***) in order to operate the Thomson source as a Free Electron Laser.

The FEL resonance condition

$$\lambda_R = \frac{\lambda}{4\gamma^2}\left(1 + a_0^2\right) \tag{C.1}$$

The definition of the FEL parameter

$$\rho = \frac{10^{-2}}{\gamma}\sqrt[3]{I\lambda^4 P/\sigma_0^4} \tag{C.2}$$

Two conditions for optimal geometrical beam overlap of the envelopes of the two colliding beams: the first one is to ensure that the electrons will observe transversally constant undulator field

$$R_0 \geq 2\sigma_0 \tag{C.3}$$

and the second one is to minimize the hour-glass effect in the collision of the two beams

$$c\tau \leq 2Z_0 \tag{C.4}$$

Note that we will further check that the condition

$\beta_0 \geq Z_0$ is satisfied (assuring that the electron beam envelope is contained within the laser beam envelope). However, this condition is not explicitely used in order to simplify the following derivation.

We want of course that the interaction between the two beams, *i.e.* the equivalent undulator length, be longer than the FEL saturation length, which is typically set at 10 times the gain length. Hence

$$c\tau \geq 10L_g \qquad \text{(C.5)}$$

Now we must take into account how 3D effects and non-uniformities in the laser filed (which is our undulator field) may affect the FEL instability, avoiding inhomogeneous broadening effects of the gain bandwidth that may damp the onset of the FEL exponential instability. We know that the gain bandwidth of a SASE FEL is set by $\Delta\lambda_R/\lambda_R = 2\rho$. This implies that 3D and non-uniformity effects must produce bandwidth broadening smaller than 2ρ.

For a Fourier trasnform limited laser pulse the spectrum line width is $\frac{\Delta\lambda}{\lambda} = \frac{\lambda}{c\tau}$, therefore $\frac{\Delta\lambda_R}{\lambda_R} = \frac{\Delta\lambda}{\lambda} = \frac{\lambda}{c\tau}$, hence the condition

$$c\tau \geq \frac{\lambda}{2\rho} \qquad \text{(C.6)}$$

The FEL frequency broadening due to fluctuations in the undulator field amplitude, in our case represented by Δ, is given by $\frac{\Delta\lambda_R}{\lambda_R} = \frac{2a_0^2}{1+a_0^2}\Delta$, which in turns implies

$$\Delta \leq \rho\frac{1+a_0^2}{a_0^2} \qquad \text{(C.7)}$$

The transverse motion of the electrons in the focal region, which is mainly determined by the electron beam emittance, produces a random distribution of the angle ϑ in the resonance relationship reported in eq.1, which in turns induces a broadening of the FEL bandwidth. As extensively discussed elsewhere[6,9], the limitation on this random angle can be casted in terms of an upper limit on the emittance. This criterion is generally known as Kim-Pellegrini criterion: it has been generalized in ref.6 to the expression

$$\varepsilon_n \leq \sqrt{\frac{Z_R}{L_G}\frac{\lambda_R\gamma}{2\pi}} \qquad \text{(C.8)}$$

whewre Z_R is the Rayleigh range of the emitted FEL radiation, $Z_R = \frac{4\pi R_0{}^2}{\lambda_R}$.

FINAL SET OF FORMULAS

In order to simplify the derivation of a solution for the system of equations (C.1-C.8) we assume equalities for all the conditions instead of inequalities: this will allow to derive the minimum condition that 8 parameters have to fulfill, expressed as functions of three free parameters. We choose as free parameters the laser wavelength λ, the electron beam current I and the laser ripple parameter Δ.

The electron beam parameters must obey:

$$\varepsilon_n = 0.18\lambda \ \text{(F.1)} \ ; \quad \gamma = 0.05\sqrt[3]{\frac{I}{\Delta^2}} \ \text{(F.2)}$$

$$\sigma_0 = 0.21\lambda/\sqrt{\Delta} \ \text{(F.3)}\ ; \quad \beta_0 = 0.009\lambda\sqrt[3]{\frac{I}{\Delta^5}} \ \text{(F.4)}$$

the ancillary condition $\beta_0 \geq Z_0$, as anticipated, is respected if $I > 576\ \Delta^2$, which is easily satisfied, since Δ assumes values definitely lower than 0.1, while the beam curent I has expected values in excess of several hundreds Amps. Note that the additional condition $\Delta\gamma/\gamma \leq \rho$ has to be satisfied, though it was not explicitely considered in the derivation.

The laser parameters must obey:

$$P = 0.0018/\Delta \ \text{(F.5)}\ ; \quad U = 18.6\lambda/\Delta^2 \ \text{(F.6)}\ ;$$

$$a_0 = 1. \ \text{(F.7)} \ ; \quad \tau = 1.1\cdot 10^{-8}\lambda/\Delta \ \text{(F.8)}\ ;$$

$$Z_0 = 1.6\lambda/\Delta \ \text{(F.9)}$$

The FEL radiation is characterized by:

$$\lambda_R = 200\lambda\sqrt[3]{\frac{\Delta^4}{I^2}} \ \text{(F.10)}\ ; \quad \rho = 0.25\Delta \ \text{(F.11)}\ ;$$

$$L_G = 0.32\lambda/\Delta \ \text{(F.12)}\ ; \quad \bar{\rho} = 10^{12}\lambda\sqrt[3]{\frac{\Delta^5}{I}} \ \text{(F.13)}$$

EXAMPLES

A relevant example is for the case of a CPA Ti:Sa laser system, which is nowadays capable of delivering fs to ps long pulses carrying energies in excess of a J, focused down to micron-size spots. In this case, setting $\lambda = 0.8\ \mu$m, the formula set (F.1-F.13) reduces to the following (expressing Δ in units of %):

$$\varepsilon_n = 0.14\ \mu\text{m}\ ; \quad \gamma = 1.08\sqrt[3]{\frac{I}{\Delta^2}}\ ; \quad \sigma_0 = \frac{1.4}{\sqrt{\Delta}}\ \mu\text{m}$$

$$\beta_0 = \frac{0.015}{\Delta}\sqrt[3]{\frac{I}{\Delta^2}}\ [\mathrm{mm}]\ ;\ P = \frac{0.18}{\Delta}\ [\mathrm{TW}]\ ;$$

$$U = \frac{0.15}{\Delta^2}[\mathrm{J}]\ ;\ \tau = \frac{0.85}{\Delta}\ [\mathrm{ps}]\ ;\ Z_0 = \frac{0.13}{\Delta}\ [\mathrm{mm}]\ ;$$

$$\lambda_R = 3436\Delta\sqrt[3]{\frac{\Delta}{I^2}}\ [\text{Å}]\ ;\ \rho = 2.5\cdot 10^{-3}\Delta\ ;$$

$$L_G = \frac{26}{\Delta}\ [\mu\mathrm{m}]\ ;\ \bar{\rho} = 386\Delta\sqrt[3]{\frac{\Delta^2}{I}}\ .$$

We take into account now two specific examples, one in the classical SASE-FEL regime, the other in the quantum regime: all parameters now depend only on the beam current and the laser ripple parameter.

1) we set $\Delta = 0.15\ \%\ ;\ I = 1500\ A$: we find

$$\varepsilon_n = 0.14\ \mu\mathrm{m}\ ;\ \gamma = 44\ ;\ \sigma_0 = 3.7\ \mu\mathrm{m}\ ;$$
$$\beta_0 = 4.1\ \mathrm{mm}\ ;\ P = 1.2\ \mathrm{TW}\ ;\ U = 6.6\ \mathrm{J}\ ;$$
$$\tau = 5.6\ \mathrm{ps}\ ;\ Z_0 = 0.85\ \mathrm{mm}\ ;\ \lambda_R = 2.1\ \text{Å}\ ;$$
$$\rho = 4.\cdot 10^{-4}\ ;\ L_G = 159\ \mu\mathrm{m}\ ;\ \bar{\rho} = 1.4\ .$$

2) we set $\Delta = 0.05\ \%\ ;\ I = 2500\ A$: we find

$$\varepsilon_n = 0.14\ \mu\mathrm{m}\ ;\ \gamma = 108\ ;\ \sigma_0 = 6.4\ \mu\mathrm{m}\ ;$$
$$\beta_0 = 30\ \mathrm{mm}\ ;\ P = 3.5\ \mathrm{TW}\ ;\ U = 60\ \mathrm{J}\ ;$$
$$\tau = 17\ \mathrm{ps}\ ;\ Z_0 = 2.5\ \mathrm{mm}\ ;\ \lambda_R = 0.35\ \text{Å}\ ;$$
$$\rho = 1.2\cdot 10^{-4}\ ;\ L_G = 531\ \mu\mathrm{m}\ ;\ \bar{\rho} = 0.2\ .$$

The paremeter values predicted for case 1), which is in the calssical regime, are in agreement with the results of 3D simulations reported in ref.6,9, where a 15 MeV electron beam carrying 1.5 kA of current, focused down to 10 µm rms focal spot size, was considered colliding with a Ti:Sa pulse with $a_0 = 0.8$, and a 20 µm spot size, which corresponds to a power of 5.5 TW. The saturation of the FEL instability is reached, for an emittance of 0.44 µm, at 4 ps of laser pulse length, implying the need of 22 J of laser pulse energy and an effective gain length of about 120 µm. The radiation wavelength was 3.64 Å. Since these simulations were performed before deriving the set of formulas reported in this paper, the agreement is only on a general frame. More detailed comparisons between this set of formulas, that are meant to drive the initial choice of parameters for the simulations, and the simulation results, will be the subject of a future work.

As a last remark we report here the results of 1D simulations (performed with a code described elsewhere[10]) evaluating the effects of laser ripples on the growth of the FEL instability, taking same laser and electron beam parameters as for the previously mentioned 3D simulations. The laser amplitude modulation was taken as $\Delta \sin\left(k_{fluct} z + ct\right)$. The FEL saturation intensity is plotted as a function of ω_{fluct}/ω_L ($\omega_L \equiv 2\pi c/\lambda$) for different values of the laser ripple parameter Δ.

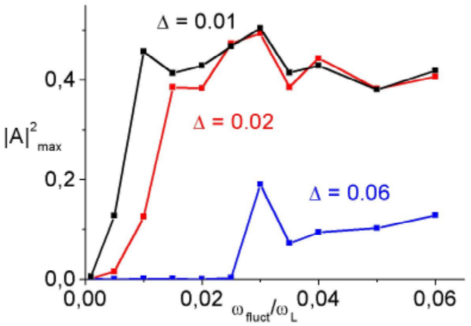

Figure 2: Saturation intensity in presence of laser ripples.

It is clearly visible in Fig.2 how the FEL instability is damped, *i.e.* the exponential growth is no longer attained, when Δ assumes values greater than a few percent, for almost any value of the modulation scale length k_{fluct}. Also, the system seems to tolerate laser amplitude modulations occurring on a scale much shorter than the gain length, as indicated by the fact that the saturation intensity goes to zero for any value of Δ when the scale of the laser modulation gets close to gain length, *i.e.* when $L_G/\lambda = \omega_{fluct}/\omega_L = 1/4\pi\rho = 0.0055$.

REFERENCES

[1] J. Gea-Banacloche, G.T. Moore, R.R. Schlicher, M.O. Scully, and H. Walther, IEEE Journ. of Quantum Electron., **QE-23**, 1558 (1987).

[2] B.G. Danly, G. Bekefi, R.C. Davidson, R.J. Temkin, T.M. Tran, and J.S. Wurtele, IEEE Journ. of Quantum Electron., **QE-23**, 103(1987).

[3] J.C. Gallardo, R.C. Fernow, R. Palmer, and C. Pellegrini, IEEE Journ. of Quantum Electron. **QE-24**, 1557 (1988).

[4] C.B. Schroeder, C. Pellegrini, and P. Chen, Phys. Rev. E **64**, 056502 (2001).

[5] R. Bonifacio *et al.*, FEL-2005 Proceedings, SLAC-R-791, JACoW / eConf C0508213, 71 (2005).

[6] A. Bacci, M.Ferrario, C. Maroli, V. Petrillo, L. Serafini, PRST-AB **9** (2006) 060704.

[7] L. Serafini, *AIP CP* **335**, 666 (1995).

[8] R. Bonifacio *et al.*, Nucl. Instr. and Methods, **A 543**, 645 (2005).

[9] A. Bacci *et al.*, X-Ray Generation with a FEL based on an Optical Wiggler, this conference.

[10] A.Bacci *et al.*, "Collective effects in the Thomson back-scattering between a laser pulse and a relativistic electron beam" EPJAP (in print).

APPLE UNDULATORS FOR HGHG-FELS

J. Bahrdt, BESSY, Berlin, Germany.

Abstract

Cascaded HGHG-FEL facilities have been proposed by several groups. In these machines the beam characteristics of the initial seeding laser like coherence, short time structure and small bandwidth are transformed to shorter wavelengths where seeding lasers are not available. The first stages are equipped with planar devices. For full polarization control the last amplifier and the final radiator can be realized as APPLE devices. The specific demands on the polarizing devices as compared to planar hybrid devices are discussed for the example of the proposed BESSY HE-FEL to be operated at 1nm. The field optimization procedure requires specific strategies. An improvement of the magnetic material is helpful in this context. The small good field region implies tight geometrical tolerances. Gap and phase dependent focussing effects have to be compensated. Other important issues are the complexity of the control system and the radiation protection system.

INTRODUCTION

FEL facilities are powerful sources for ultra short pulses and longitudinally and transversely coherent radiation in the soft X-ray and X-ray regime. Three X-ray FELs based on the SASE principle are currently under construction [1-3].

In the soft X-ray regime various seeding schemes have been proposed and realized which improve the spectral characteristics and the time structure. A cascaded HGHG FEL [4,5] starts with the coherent radiation of a high power Ti:Sapphire laser which interacts with the electron beam in a modulator. In a dispersive section the energy modulation is converted to a spatial modulation. The following radiator takes advantage of the higher orders of the electron beam bunching producing a seed for the next stage. Several stages can be cascaded achieving frequencies down to 1nm.

The number of stages can be reduced if the seed wavelength of the first stage is already in the few 10s nm regime which can be accomplished using the HHG process [6].

Only the light of the last radiator will be delivered to the experiment. All other undulator modules serve to provide a sufficient bunching of the electron beam in the last stage. For simplification all these modules can be realized as planar devices though they might be slightly longer than helical devices. The last radiator has to provide the full flexibility concerning the polarization control. APPLE type structures are suitable for this purpose. In this paper we concentrate on the design of APPLE undulators to be used as final radiators. We discuss the technical challenges and their solutions. For illustration we will apply the parameters of the proposed BESSY Soft X-Ray FEL.

The tolerances for HGHG and SASE FEL undulators are similar for comparable photon energies. The complexity of a HGHG undulator system is, however, higher. A 200m SASE undulator consists of 40 identical 5m modules whereas a cascaded FEL can be composed of 18 modules with 9 different lengths and 5 different period lengths (BESSY HE-FEL). This affects the concept of series production and modularity, the control system and the operation.

In contrast to an X-ray FEL undulator system the undulator focussing is an important issue for soft X-ray systems (in particular for polarizing devices) because the electron energies are generally lower.

MAGNETIC STRUCTURE

APPLE undulators provide the highest fields among all variably polarizing insertion devices. A single pass FEL permits the installation of a circular beam pipe without performance loss. In this geometry additional magnetic material can be arranged at the side of the vacuum chamber. Additionally, the angle of magnetization can be rotated by 45° (APPLE III [7]). The demagnetizing fields are slightly higher for an APPLE III than for an APPLE II (figure 1). The magnetic stability can be recovered with another magnet grade and the field gain is still about a factor of 1.4 as compared to an APPLE II [7].

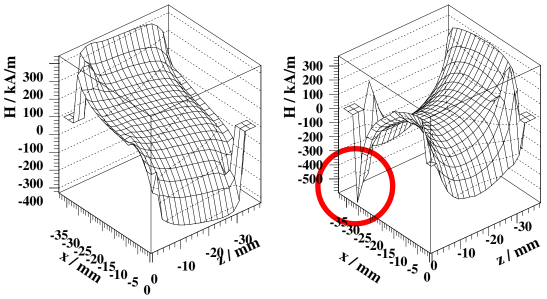

Figure 1: Difference of reverse fields between APPLE III and APPLE II design for the example of the planned BESSY UE50 (LE- and ME-FEL). Left: A-magnet (long. magnetized), right: B-magnet (vert. magnetized).

Today APPLE undulators can be built with the same field quality as planar devices using specific sorting and shimming techniques. At BESSY the magnets of the APPLE undulators are characterized individually with respect to the dipole moment (automated Helmholtz coil) and the inhomogeneities (stretched wire system). The data are used in a simulated annealing code which minimizes the phase errors and reduces the multipoles by a factor of 5-10 as compared to an unsorted structure [8]. The field quality of devices consisting of 1000 magnets can be predicted with an accuracy of about 1.5 Gm (figure 2).

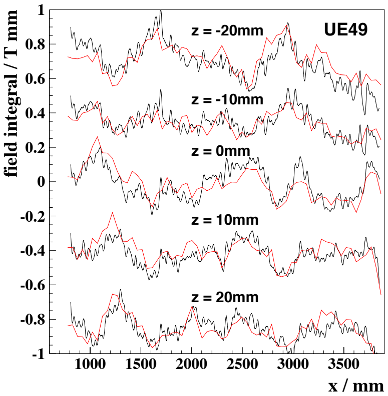

Figure 2: Prediction from single block characterization (red) and Hall probe measurements (black) of the BESSY UE49 field integrals at five transverse positions.

The field properties are optimized with various techniques:

- trajectories: block movements
- shift dependent terms: Fe-shims
- shift independent terms: permanent magnet arrays at both ends of the devices.
- dynamic multipoles: Fe-shims

Details can be found in [8,9,10]. The required magnet quality of FEL undulators can be achieved with state of the art techniques which can, however, be rather time consuming and are not suitable for a series production.

MAGNET MATERIAL

The new FEL facilities will consist of many undulator segments with totally 10.000s of individual magnets. Today, permanent magnets have typical remanence and angle errors in the order of 1-2% and 1-2°, respectively, where the distributions within one batch can be significantly narrower. The inhomogeneities are important as well and determine the field quality at small gaps. In principle, the required magnet field performance can be achieved with a detailed characterization of the magnets, sorting and shimming. The production process can, however, significantly be simplified if the magnet quality can be improved.

Triggered by the need for high quality magnets for the European X-Ray FEL at DESY and the BESSY Soft X-Ray FEL a BMBF funded joint collaboration between DESY, BESSY and Vacuumschmelze has started. The collaboration has the goal to reduce remanence and angle errors by a factor of 5-10 and to improve the block homogeneity. At a certain level the quality is determined by the geometrical tolerances of the blocks and hence, these tolerances have to be reduced to a level of 10µm. Magnet measurement equipment built at BESSY and DESY has been shipped to the magnet manufacturer who will use the machines to optimize the production process. BESSY provides a stretched wire system for the characterization of block inhomogeneities whereas DESY has built an automated Helmholtz coil system.

The north south effect (field difference between two opposite sides of a block) is not a useful quantity in particular for APPLE devices where the electron beam is located close to a magnet corner. Block inhomgeneities can be determined by cutting the magnet into slices and measuring the slices in a Helmholtz coil. Results are shown in figure 3 where a systematic variation of the magnetization angle over the position inside the magnet is plotted. The systematic trend can be minimized with an appropriate setting of the production parameters.

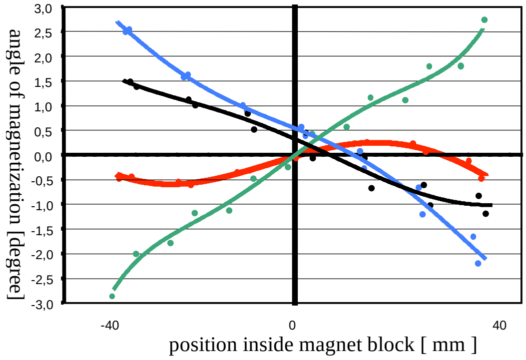

Figure 3: Variation of the magnetization angle inside four individual magnet blocks. The blocks have been produced with different production parameters (by courtesy of Vacuumschmelze, Hanau).

The magnet cutting and the characterization of the slices is time consuming. Similar information can be gathered with the new stretched wire setup in a much shorter time from the complete magnet. The magnet is moved with respect to a single wire in a distance of 5-10mm and induced voltages are measured (figure 4). Measurements from different sides give the information on the magnetization distribution inside the magnet.

Since the measurements are done in a strong field gradient a good positioning accuracy is essential. Temperature stabilized linear motors with absolute encoders and air bearings allow for fast and precise movements. Fe shieldings around the motors reduce the electrical noise.

Figure 4: Stretched wire system for the measurement of magnet block inhomogeneities.

Figure 5 shows a reproducibility of 3.0e-4 Tmm for magnets with the magnetization vector parallel to the wire (A-magnets) and 1.5e-3Tmm for magnets with an orientation perpendicular to the wire (B-magnets). In case of the B-magnets the measurement noise is dominated by a contribution which is proportional to the main signal. A positioning accuracy <4.0µm and a temperature stability of <0.2° is needed to bring the electrical noise to this level.

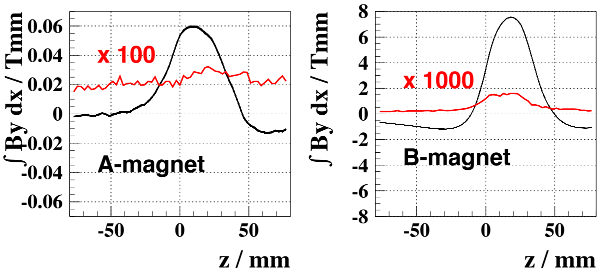

Figure 5: Reproducibilities of the stretched wire system. One hundred blocks of both types have been measured (black) and sigma values (red) have been determined. The distance to the single wire is 10mm and the block dimensions are 40x40x<u>28</u>mm^3.

TOLERANCES

The tolerances for HGHG and SASE FELs are different from those of storage ring IDs. A good overlap between the photon and electron beam ($\Delta x \le 0.1$ x ($\sigma_{eelctron}$, σ_{photon})) defines the maximum trajectory walk off. For a Pierce parameter of 0.001 (BESSY HE-FEL) a maximum variation in the K-parameter of ±5 x 10^{-4} can be tolerated ($\Delta E < 0.16$ x bandwidth). This defines the following tolerances: The temperature dependence of the magnet remanence of 0.0011 / °C requires a temperature stability $\Delta T \le \pm 0.1$°C. The gap positioning accuracy must be $\Delta gap \le \pm 1$µm and the transverse alignment tolerance has to be $\Delta x \le \pm 40$µm. The largest contribution to ΔK / K is attributed to the transverse alignment error (see below). The phase error due to energy spread dominates the total phase error if

$$\Delta\Phi_{rms} \le \frac{\sigma_\gamma}{\gamma}\frac{1}{\rho\sqrt{3}}$$

Assuming an energy spread of 2 x 10^{-4} the tolerance for the phase error of the magnetic field is $\Delta\Phi_{rms} < 6.6°$ for the BESSY HE-FEL. Apart from quadrupole terms (see later in this paper) static or dynamic multipoles are less important for single pass devices.

The trajectory errors can be measured and minimized with state of the art measurement and shimming techniques. Phase errors below 5° can be achieved even for the complicated APPLE II design without explicit phase shimming as demonstrated for the six BESSY APPLE II devices. A gap positioning accuracy of ±1.5µm has already been achieved [7] (see also next chapter). In the following, we will concentrate on the challenging transverse alignment tolerances.

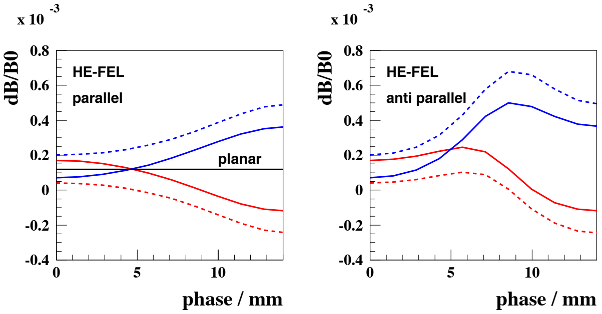

Figure 6: Relative field variation 0.1mm horizontal (red) and vertical (blue) off axis for APPLE III (solid) and APPLE II (dashed) undulator operating in the parallel (left) and antiparallel (right) mode.

The good field region of an APPLE device is significantly reduced as compared to a planar device (figure 6) though it is larger for the APPLE III design as compared to the APPLE II.

In figure 7 the transverse charge distribution of the BESSY FEL electron beam is compared to the field variations in various operation modes. For a maximum transverse displacement of 40µm more than 2σ of the electron beam are within ΔK / K < 5 x 10^{-4}.

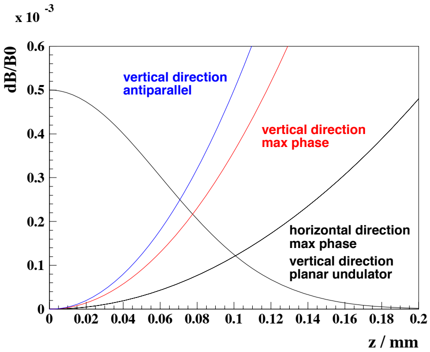

Figure 7: Averaged transverse size of the BESSY FEL electron beam compared to the field roll off for various operation modes.

Figure 8 shows all possible girder misalignments. They are classified as follows:

1. No circle: this movement is uncritical.
2. Black circle: the motion can be minimized with a stiff support structure. The motion is not driven by any force.
3. Blue circle: the movements are well controlled with a closed loop servo system.
4. Red dotted circle: The movement shifts the field amplitude and the center of the good field region. It shows up for antiparallel motion where longitudinal and transverse forces between the upper and lower magnet girders are present.
5. Red circle: The movement enhances ΔK / K. It shows up for antiparallel motion.

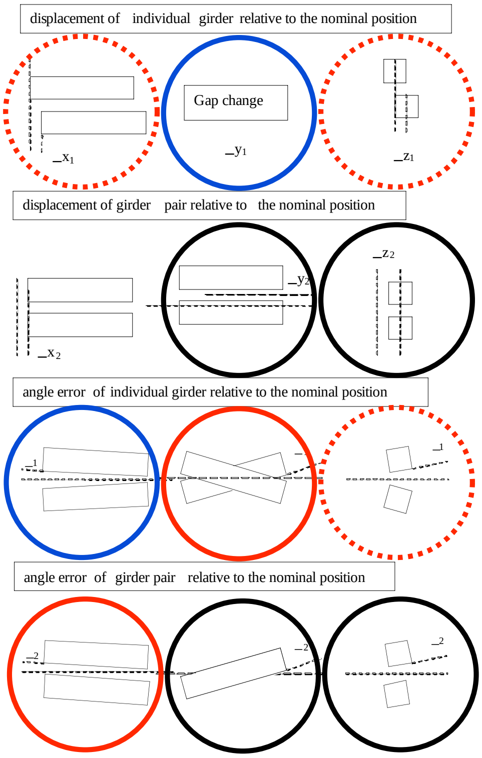

Figure 8: Classification of geometrical tolerances.

SUPPORT AND DRIVE SYSTEM

The tolerances discussed in the previous section define the mechanical design of the support and drive system.

Gap Accuracy

The gap setting has to be done with a closed loop servo system which uses a direct gap reading. The encoders have to be located in a vertical line with the electron beam to avoid Abbe's comparator error [7] (figure 9). Differential thermal expansion coefficients of the support structure (Fe) and the magnet girders and the measurement system (Al) result in a temperature dependent gap error of only 1.1μm/°C for the system described in [7] and can be ignored if compared to the thermal variation of the magnet material remanence.

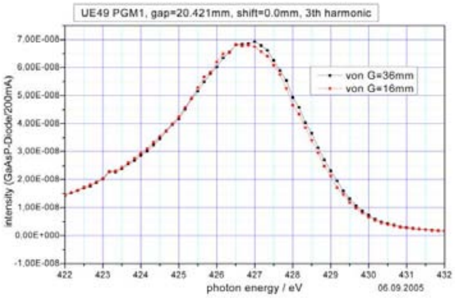

Figure 9: Approaching the third harmonic of the BESSY UE49 from two different directions results in a very small energy shift which corresponds to a gap error of only ±1μm. The device employs the new measurement system described in [7].

In principle an APPLE II type final amplifier of a HGHG cascade can be realized as a fixed gap device. The energy and polarization tuning can be performed by magnet row movements [11]. The BESSY final amplifiers will be of the APPLE III type. In this case the gap drive is necessary to install and remove the modules from the beam pipe without breaking the vacuum.

The magnets are assembled onto Aluminum girders with a length of up to 4m. They are gimbal-mounted to permit a tapering and to cope with the different thermal expansion coefficient of the Fe-support structure. The straightness of the assembling surfaces of such girders can be within ±8μm resulting in a gap variation of only ±15μm (figure 10). This remaining gap variation can be reduced to ±6μm using appropriate mechanical shims under the magnet holders.

The bending of the magnet girder can be minimized by choosing appropriate locations for the support. The bending can be further reduced by more than one order of magnitude with four supports instead of two using two crossbars inside the magnet girders. This has been demostrated for the BESSY undulators UE46, UE49 and UE112.

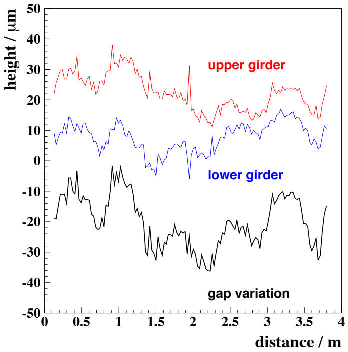

Figure 10: Straightness of upper and lower UE112 magnet girder and corresponding gap variations.

Bearings

In antiparallel mode strong longitudinal and transverse forces between the upper and lower magnet girder show up. The transverse forces can be supported with transverse flexible joints connecting the girders to the support structure. These joints have to permit a longitudinal motion (thermal expansion) and an intentional longitudinal taper of the girders.

The longitudinal forces produce a torque around the vertical axis and around the horizontal (transverse) axis where the strength depends on the location of the joints that keep the girders longitudinally in place. As a result the girders rotate and ΔK / K on axis is enhanced. The transverse motion can be kept within the acceptable limits with stiff joints between the girders and the support structure. The vertical parallel inclination of the girders can principally be compensated using four motors for the gap drive. Such a drive system can also compensate for the residual transverse girder crossing via a deliberate inclination of the girders. This concept implicates however a complication of the control system and the gap measurement arrangement. Another solution is the positioning of the longitudinal fixed bearing vertically at the height of the magnets and longitudinally close to the drive system for the row phase. This arrangement eliminates any torque around the transverse axis (figure 11) and hence, any girder inclination or girder bending.

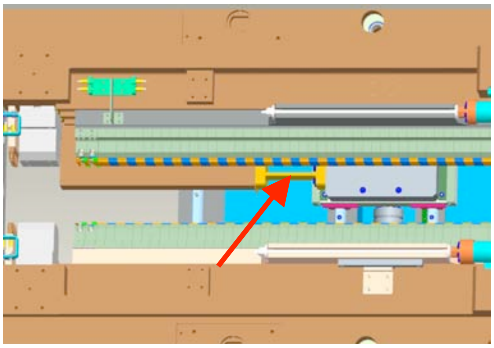

Figure 11: The vertical location of the longitudinal bearing (red arrow) is chosen such that there is no torque around the transverse axis.

Support Structure

The support structure of an APPLE undulator operating in the antiparallel mode has to cope with the strong longitudinal and transverse forces which are absent in a planar or elliptical device.

The support structure can be either a welded structure or a cast structure. The latter one has several advantages:

- The structure can be made extremely stiff without additional effort because literally any shape can be realized.
- A bionic optimization can be applied where material is added at locations with large stress and removed at locations of low stress (figure 12).
- The complete support structure can be cast and milled as a single piece.
- The procedure is suitable for series production since wooden forms can be used for many casts. Modular forms can be adapted to different undulator lengths.

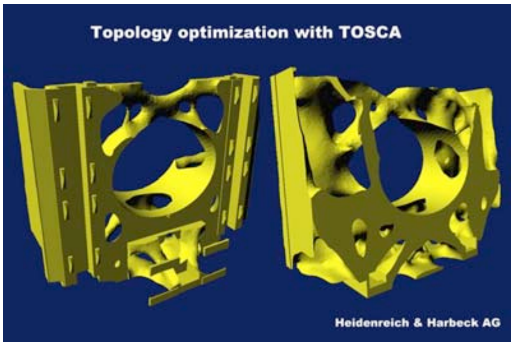

Figure 12: Bionic optimization of the support structure of the BESSY UE112 undulator (by courtesy of Heidenreich und Harbeck AG).

All BESSY undulators are based on cast iron structures. The last APPLE device (UE112) has a single piece support structure (figure 13) which significantly simplifies the assembling procedure.

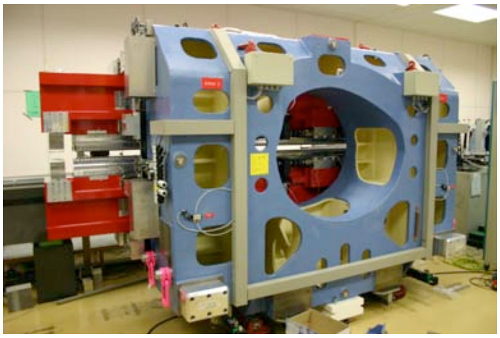

Figure 13: The support structure of the 4m long UE112 is made from a single piece of cast Fe.

Alignment

The magnet centers of all final amplifier modules have to be aligned with an accuracy of ±40µm with respect to each other (assuming APPLE type devices). This can not be accomplished with standard alignment tools. Beam based alignment techniques have to be applied instead. For this purpose the modules have to be assembled onto moveable supports with an accuracy of 10µm.

UNDULATOR FOCUSSING

An undulator is a series of alternating dipole magnets which shows an edge focusing. Planar devices focus in the vertical direction. This second order effect can not be described with normal 2-dimensional multipoles. Polarizing devices show also a horizontal defocusing under certain operating conditions which results in an additional focusing in the vertical plane. For Halbach fields the focusing strength in the horizontal plane is given by:

$$K_x = \frac{2\cdot e^2}{(\gamma mc)^2} k_{x-eff}{}^2 \cdot k^2 \cdot \sum_{n=1}^{\infty} (B_{xn}^2 + B_{yn}^2)$$

$$k_{x-eff}{}^2 = \sum_{n=1}^{\infty} \frac{B_{xn}{}^2 \cdot k_{xxn}{}^2 / n! + B_{yn}{}^2 \cdot k_{xyn}{}^2 / n!}{B_{xn}{}^2 / n! + B_{yn}{}^2 / n!}$$

and similar for the vertical plane (summation over the Fourier components *n*). The focusing strength in the antiparallel mode can not be described in this compact form since the fields are not of the Halbach type.

These effects influence the beam size and it has to be considered whether the transverse overlap between the electron beam and the photon beam is still maintained. Figure 14 shows the variation of the horizontal and vertical beam size for the BESSY HE-FEL. The values change by more than a factor of two which is not acceptable. For the BESSY ME- and the LE- FEL the effects are larger by factors of 9 and 45, respectively, due to the larger period length and larger field (ME- and LE-FEL) and the lower beam energy (LE-FEL). Obviously, additional quadrupoles are essential to keep the beam size within acceptable limits and they have to be adapted during gap drive and row phasing.

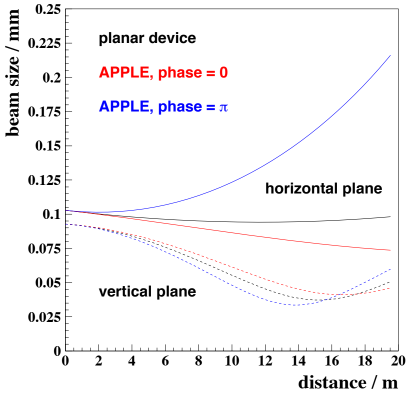

Figure 14: Horizontal (solid) and vertical (dotted) beamsize within the final amplifier of the BESSY HE-FEL at smallest gap without additional quadrupoles. The data are given for different operation modes of an APPLE III device and for a planar device.

MOTION CONTROL

A cascaded HGHG FEL requires a sophisticated motion control system. Each HGHG stage consists of a modulator and a radiator (maybe several submodules), steerer to compensate residual dipole errors, quadrupoles for tune compensation and phase adapting units between the modules. Between two stages fresh bunch dispersive sections are installed. All components have to be driven in synchronism. Reproducibility is essential and can be realized with closed loop servo systems for motion control, permanent magnet phase adapting units and quadrupoles and air coils to avoid hysteresis effects.

In the following we describe the BESSY system as one possible solution. Other hardware and software concepts are also possible.

Figure 15 shows the control system of a single undulator, the BESSY UE112, which can be adapted to the FEL requirements. The undulator control program runs on a VME-bus based computer called IOC. It is a reliable system and many interface cards are available on the market. The user interface does not run on the IOC but on an independent workstation, which communicates with the IOC via ethernet. In principle, one IOC can control all modules (modulator, radiator, etc.) of one HGHG stage. Four of these systems are required for the BESSY four stages HE-FEL. A fifth IOC operates as a master to synchronize the individual IOCs.

A PLC is useful for a low level safety control of the system checking parameters like air pressure (needed for the brakes), inclination of magnet girders, hard and software limit switches etc.

EPICS is used as a robust and reliable software framework for the undulator control software. All sources are available and it is actively developed in many research laboratories. Many drivers have been written. Useful tools are available such as an archiver for the process variables or a network protocol for the distribution of the process variables. GUIs can be easily built with a “point and click” tool.

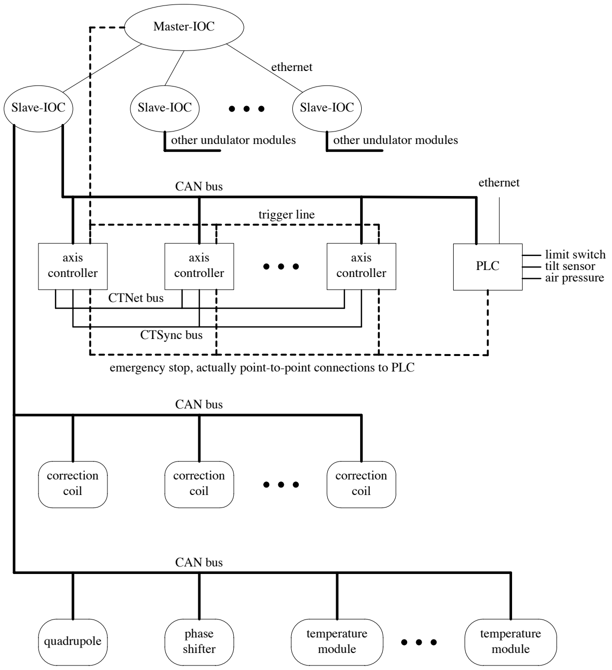

Figure 15: Control system of the BESSY UE112.

Each motor has its own detached motor controller which is connected to the IOC via CAN bus. Absolute linear encoders simplify reference procedures. Modern motor controllers as used for the UE112 can operate several tasks with different priorities. User defined parameters can be stored permanently in the controller and can even be modified during motor movement. The motor controllers can communicate among each other and with the IOC via CTNet (ruggedized version of ARCNet) and a synchronization between the modules can be realized via CTSynch.

BEAM PROTECTION SYSTEM

The electron beam can cause a demagnetization of the undulator magnets if it propagates severely off axis [12-14]. The electrons produce a shower of secondary electrons and photons in the vacuum chamber which may deposit energy into the magnets. Detailed experiments have been done to study the influence of various parameters on the process like the geometry, material, working point of the magnets, temperature etc. [15]. A reduced dose (electron energy > 20MeV) of 70 kGy produces already a remanence loss of 1% in a typical magnet material with a coercivity of 1800 kA/m [16].

For the layout of a beam protection system the maximum beam charge which may be dumped into the vacuum chamber without loss of performance has to be determined. In the following we discuss the consequences on the spontaneous radiation spectrum. Simulations for the impact on the stimulated radiation will be done in the future using GENESIS. Two scenarios have been studied where the electron beam hits the vacuum chamber under grazing angles of 1mrad and 0.1mrad, respectively. Due to the small vacuum apertures larger angles are unlikely. Monte Carlo simulations with GEANT [17] have been done for both cases. The deposited charge was 300.000 nC. The magnets have been subdivided into 5x5 (1mrad case) and 7x7 (0.1mrad case) segments (figure 16). Doses have been evaluated for each of the segments.

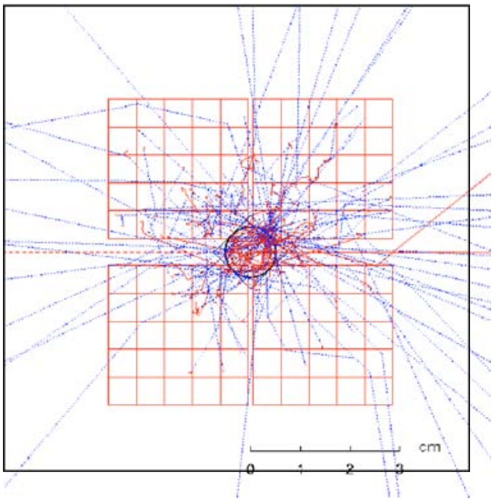

Figure 16: Monte Carlo simulations with GEANT. The geometry for the BESSY HE-FEL with APPLE III magnets (red) and a circular vacuum pipe (blue) has been used. Secondary electrons (red) and photons (blue) are plotted as well.

In the 1mrad case a maximum reduced dose of 700kGy has been detected close to the vacuum pipe. This corresponds to a maximum demagnetization of 10%. Based on the doses in each magnet segment the corresponding remanences have been evaluated. Then, the undulator on axis field has been derived from the contributions of all segments (totally about 70.000 segments). The field reduction close to the point of interaction is 1.6% (figure 17).

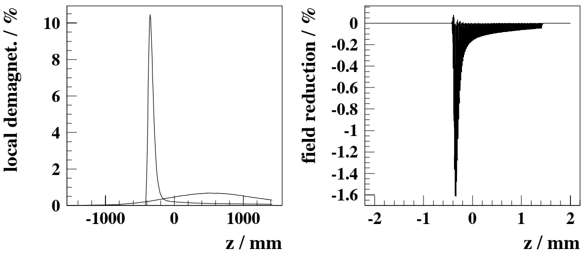

Figure 17: Maximum demagnetization of magnet segments (left) for 1mrad and 0.1mrad angle of incidence and field variation (right) for 1mrad.

In the 0.1mrad case the region of interaction is spread out over more periods and the local degradation is much lower. Since the magnet degradation extends over several periods the trajectory errors are negligible even for the 1mrad case (figure 18). The averaged phase error introduced in this case is 7° (figure 18) which results in a shift of the first harmonic and a splitting of the fifth harmonic (figure 19).

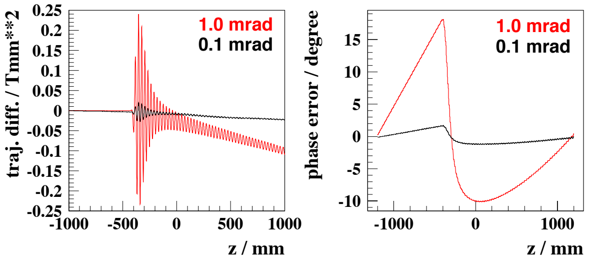

Figure 18: Trajectory errors for angles of incidence of 0.1mrad and 1mrad (left) and phase errors for both cases.

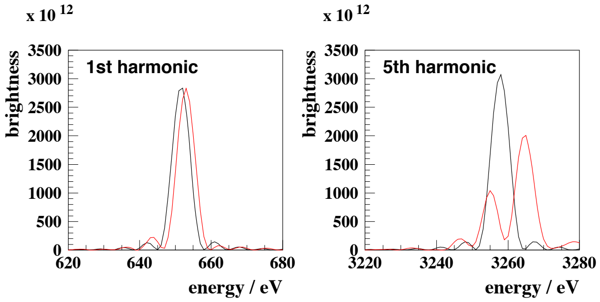

Figure 19: Spectra of the first (left) and fifth (right) harmonic for the unperturbed case (black) and the degraded magnets (red).

Even if the undulator is used only at the first harmonic the spectral shift has to be avoided. The simulations show that a deposited charge of 30.000nC (1mrad) shifts the first harmonic by only $\Delta E/E=2x10^{-4}$ which is acceptable.

The simulations show that a collimating system for the off axis particles as well as for the off energy particles is essential for a safe operation. The dog-leg collimator for the planned BESSY Soft X-Ray FEL collimates the beam transversally to ±30σ and energetically to 5%.

Fibre monitors are needed for several purposes: i) A fast interlock system which can switch off the gun laser has to be triggered, ii) information on the total deposited dose is required to estimate the lifetime of the magnets, iii) information on the longitudinal distribution of the deposited radiation helps to detect the hot spots. Two types of fast monitors have been tested at FLASH: i) Cerenkov monitors [18] and ii) fibres for optical time domain reflectometry used in power-meter mode [19]. The latter ones can be used also for spatially resolved measurements. Fibre Bragg gratings can be used as high dose radiation sensors on the scale of many kGy [20].

They provide also information on the spatial distribution of the dose.

CONCLUSION

Various technological aspects for using APPLE undulators in HGHG FELs have been discussed. Experiences gained with APPLE undulators at 3rd generation light sources have been extrapolated and strategies to meet the tight tolerances of HGHG FEL insertion devices have been proposed.

New concepts for the magnet field optimization, for the motion control, for a new support structure and for radiation dose monitoring have already been tested and will be further improved at a 3rd generation facility.

ACKNOWLEDGEMENT

The author thanks M. Scheer for doing the GEANT simulations and H.-J. Bäcker, W. Frentrup, A. Gaupp, S. Gottschlich, G. Pfeiffer, B. Schulz for many fruitful discussions.

REFERENCES

[1] TESLA-Technical Design Report, TESLA X-FEL, Technical Design Report, 2002-9, 2002.

[2] Linac Coherent Light Source (LCLS), Conceptual Design Report, SLAC-R-593, 2002.

[3] T. Shintake, Nucl. Instr. and Meth. in Phys. Res. A, 507 (2003) pp 382-397.

[4] L. H. Yu, Nucl. Instr. and Meth. in Phys. Res. A, 483 (2002) pp 493-498.

[5] X. J. Wang et al., Proceedings of the 26th International FEL Conference, Trieste, Italy, 2004, pp 209-211.
C. Bochetta et al., Proceedings of the 27th International FEL Conference, Stanford, CA, 2005, pp 632-685.
The BESSY Soft X-ray Free Electron Laser, Technical Design Report March 2004, eds.: D. Krämer, E. Jaeschke, W. Eberhardt, ISBN 3-9809534-08, BESSY, Berlin (2004).
J. Bahrdt et al., Proceedings of the EPAC 2006, Edinburgh, Scotland, pp 59-61.
M.-E. Cuprie et al., Proceedings of the 27th International FEL Conference, Stanford, CA, 2005, pp 55-58.
A. Andersson et al., Proceedings of the 26th International FEL Conference, Trieste, Italy, 2004, pp 190-192.
D. Wang et al., Proceedings of 2005 PAC, Knoxville, Tennessee, pp 1961-1963.
J. Wu, Z. Huang, Proceedings of the 27th International FEL Conference, Stanford, CA, 2005, ppxx.
J. Qi-ka et al., Proceedings of the 26th International FEL Conference, Trieste, Italy, 2004, pp 494-497.

[6] O. Tscherbakoff et al., Proceedings of the EPAC 2006, Edinburgh, Scotland, pp 47-49.
G. Lambert et al., Proceedings of the EPAC 2006, Edinburgh, Scotland, pp 44-46.
J. A. Clarke, Proceedings of the EPAC 2006, Edinburgh, Scotland, pp 181-183.
Gullens et al., Proceedings of the EPAC 2006, Edinburgh, Scotland, pp 142-144.

[7] J. Bahrdt et al., Proceedings of the 26th International FEL Conference, Trieste, Italy, 2004, pp 610-613.

[8] J. Bahrdt et al., Nucl. Instr. and Meth. in Phys. Res. A, 516 (2004) pp 575-585.

[9] J. Bahrdt et al., Proceedings of the International Conference on Synchrotron Radiation Instrumentation, Daegu, Korea, 2006.

[10] J. Bahrdt, G. Wüstefeld, Proceedings of the EPAC 2006, Edinburgh, Scotland, pp 3562-3564.

[11] T. Schmidt et al., Proceedings of the International Conference on Synchrotron Radiation Instrumentation, Daegu, Korea, 2006.

[12] P. Colomp, T. Oddolaye, P. Elleaume, “Partial Demagnetization of ID6 and Dose Measurements on Certain Ids”, Machine Technical Note 1-1996/ID, 1996.

[13] M. Petra et al., Nucl. Instr. and Meth. in Phys. Res. A, 507 (2003) pp 422-425.

[14] P. Colomp, T. Oddolaye, P. Elleaume, “Demagnetization of Permanent Magnets to 180 MeV Electron Beam”, Technical Report ESRF/MARCH-ID/93-09, European Synchrotron Radiation Facility, ESRF March 1993.

[15] T. Bizen, T. Tanaka, Y. Asano, D.E. Kim, J.S. Bak, H.S. Lee, H. Kitamaru, Nucl. Instr. and Meth. in Phys. Res. A 467-468 (2001) pp185-189.
M. Marechal, T. Shintake, SRI2003, Conference Proceedings, AIP 705, (2004) pp 282-285.

[16] H. Schlarb, “Collimation System for the VUV Free-Electron-Laser at the TESLA Test Facility”, Thesis Work, Universität Hamburg, DESY-THESIS-2001-055, Nov. 2001.

[17] GEANT, Detector Description and Simulation Tool, Computing and Networks Division, CERN Geneva Switzerland.

[18] E. Janata, M. Körfer, H. Schlarb, Nucl. Instr. and Meth. in Phys. Res. A 253 (2004) 256-261.

[19] H. Henschel, J. Kuhnhenn, M. Körfer, F. Wulf , Nucl. Instr. and Meth. in Phys. Res. A, 507 (2003) pp 422-425.

[20] K. Krebber, H. Henschel, U. Weinhand, „Fibre Bragg Gratings as high dose radiation sensors”, Meas. Sci. Technol. 17 (2006) pp 1-8.

ELECTRON BEAM ALIGNMENT STRATEGY IN THE LCLS UNDULATORS*

H.-D. Nuhn#, P.J. Emma, G.L. Gassner, C.M. LeCocq, F. Peters, R.E. Ruland, Stanford Linear Accelerator Center, 2575 Sand Hill Road, Menlo Park, CA 94025, U.S.A.

Abstract

The x-ray FEL process puts very tight tolerances on the straightness of the electron beam trajectory (2 µm rms) through the LCLS undulator system. Tight but less stringent tolerances of 80 µm rms vertical and 140 µm rms horizontally are to be met for the placement of the individual undulator segments with respect to the beam axis. The tolerances for electron beam straightness can only be met through beam-based alignment (BBA) based on electron energy variations. Conventional alignment will set the start conditions for BBA. Precision-fiducialization of components mounted on remotely adjustable girders and the use of beam-finder wires (BFW) will satisfy placement tolerances. Girder movement due to ground motion and temperature changes will be monitored continuously by an alignment monitoring system (ADS) and remotely corrected. This stabilization of components as well as the monitoring and correction of the electron beam trajectory based on BPMs and correctors will increase the time between BBA applications. Undulator segments will be periodically removed from the undulator Hall and measured to monitor radiation damage and other effects that might degrade undulator tuning.

Table 1: LCLS undulator parameters

Parameter	symbol	value	unit
min. fundamental wavelength	λ_r	1.5	Å
undulator period length	λ_u	3.0	cm
nom. undulator parameter	K	3.	
peak field	B_{pk}	1.25	T
undulator segment length	L_s	3.4 5	m
number of segments	N_s	33	
full undulator length	L_s	132	m
nom. undulator full pole gap	g	6.8	mm
long break length	L_l	0.898	m
short break length	L_s	0.470	m
number of quadrupoles	N_Q	33	
number of BPMs	N_{BPM}	33+3	

INTRODUCTION

The undulator system for the Linac Coherent Light Source (LCLS), under construction at the Stanford Linear Accelerator Center (SLAC), is comprised of 33 identical 3.4-m-long undulator segments, separated from each other by short and long breaks. Every third break is long. The space provided by these breaks is used to place devices for controlling and monitoring the electron beam. A parameter summary is given in Table 1.

COMPONENT DESCRIPTION

The components relevant to the SASE (self-amplified spontaneous emission) lasing process in the LCLS undulator system include

- Undulator Segments
- Segment Slide Supports
- Quadrupoles
- Beam Position Monitor (BPM) System
- Girder Motion Supports
- Beam Finder Wire (BFW) Devices
- Fixed Girder Supports
- Vacuum chamber
- Alignment Diagnostic System (ADS) Sensors
- Temperature Sensors
- Air Temperature Stabilization

A brief description for each of these components is provided in this section

Undulator Segments

The undulator segments [1] are fixed-gap permanent magnet planar undulators with a period length of 3 cm and a nominal *K* value of about 3.5, and are mounted inside a 3.4-m-long Ti strongback of circular cross section. The undulator gap is arranged such that the electron wiggle motion is in the horizontal plane. The upper and lower pole face planes are canted with respect to each other by an angle of 4.5-mrad, which makes the *K* value dependent on the electron beam's horizontal position in addition to its dependence on the vertical position for the regular planar undulator. Each undulator will be operated at a different effective *K* value to compensate for energy losses during the radiation process and to optimize the SASE process. The magnetic axis, i.e., the ideal average beam trajectory, through the undulator segment will be determined during the tuning of the device and fiducialized to tooling balls on the device body. Undulator magnet tuning will be done in the Magnet Measurement Facility (MMF), which has been specially built for this purpose.

Segment Slide Supports

Each undulator segment is mounted on two parallel horizontal slides that allow remotely controlled repositioning of the segment relative to the electron beam and a full translation to a 'removed' position at 8 cm.

---

[*] Work by U.S. Department of Energy contract DE-AC02-76SF00515

[#] nuhn@slac.stanford.edu

Quadrupoles

The quadruple magnets in the LCLS undulator system are arranged in a FODO lattice. They are designed to operate with an integrated quadrupole field gradient of 3 T over the entire LCLS operational energy range between 4.3 GeV to 13.6 GeV. Each quadrupole magnet has dipole correction coils integrated into its design to provide independently controllable horizontal and vertical dipole fields superimposed on the quadrupole fields.

The quadrupole magnets are based on electromagnetic technology, each with its own power supply, and their integrated gradient can be changed in the range between 0 T and 4 T. By varying the gradient, the quadrupoles can be used to measure the transverse distance of the electron beam trajectory from the magnetic center of the quadrupoles, which is fiducialized to the magnetic center of the upstream undulator segment. This enables control of the alignment of the electron beam to the magnetic axis of the undulator segment at its down stream end, where the quadrupole magnet is located. The electromagnetic technology also provides the options of modifying the focusing optics.

Beam Position Monitor (BPM) System

The electron beam position monitor system uses RF cavity BPMs. It has been demonstrated that this type of BPM can provide relative beam position information at better than 1 µm resolution in the 0.2-1 nC charge range, at which the LCLS electron bunches will be operated. Their circular cavity body, machined to have a well-defined mechanical center, will be used in the alignment of this component. One BPM is located just downstream of each quadrupole magnet. An additional 3 BPMs of the same type are mounted upstream of the first segment to monitor the horizontal and vertical launch position and angle of the electron beam.

Girder Motion Supports

Each undulator segment and its beamline components are mounted on a remotely moveable support structure, called a girder [2]. The remote motion is controlled through cam shafts [3] and allows changing the horizontal and vertical position as well as yaw, pitch, and roll of the girders. The components mounted on each of the 33 identical girders include an upstream Beam Finder Wire (BFW) device, two horizontal slides supporting one undulator segment, a downstream quadrupole magnet, an RF cavity BPM, and a Cerenkov radiation detector, as well as the supports for the vacuum chamber throughout the girder, and the mounting plates for the Alignment Diagnostic System (ADS) sensors. The BFW device, the undulator segment, and the quadrupole are fiducialized in the MMF. The complete girder assembly will initially be aligned on the Coordinate Measurement Machine (CMM), which has been specially designed for that purpose. The undulator segment is mountable on and removable from the girder with the vacuum chamber in place and without compromising the alignment of the vacuum chamber. Segments will be swapped on the girder for magnetic measurements and will be interchangeable without the need for renewed CMM alignment.

Beam Finder Wire (BFW) Devices

The BFW device is a special wire scanner [4], with only two positions for the horizontal and vertical wire pair: the wires will be either in a well reproducible “in”-position, in which they can be brought in collision with the electron beam, or they will be in a “park”-position, where they won’t affect the electron beam. The locations of the wires in the “in” position will be fiducialized to tooling balls mounted on the device body.

Each BFW device enables control of the alignment of the electron beam at its up-stream end. After all quadrupoles are aligned using BBA (see below), the girder can then be moved to bring the wires of the BFW device into collision with the beam, which will complete the alignment of the undulator segments relative to the beam axis. The BFW device will provide a means to accomplish a beam-based undulator segment alignment from the control room without the need for tunnel access. The BFW device is only needed for occasional verifications. The alignment can be achieved at even tighter tolerance levels using portable Hydrostatic Leveling System (portable HLS) and portable Wire Position Monitor (portable WPM) devices without the need for the electron beam to be present [5]. The use of these devices requires, however, extended tunnel access and will be used prior to the beam–based commissioning process. It is expected that the ADS (see below) will be used to monitor the girder positions from then on.

Although not their primary purpose, the BFW wires will also provide transverse beam profile and rms size information. This functionality will be preserved as long as the wire diameter is not larger than about twice the rms beam width. With an rms beam width of 36 µm, a maximum wire diameter of 40 µm is a reasonable upper limit and the choice of a Carbon wire will adequately limit beam loss on the downstream undulators [6]. The transverse position of the wires will be monitored with the cam mover readback system and also, at sub-micron resolution but at a slower rate, with the ADS. Local BPMs can also be used to measure and compensate for any shot-by-shot trajectory jitter during the scan.

Fixed Girder Supports

Each girder is supported by two thermally isolated, sand-filled pillars, with manual adjustments at the top (Figure 4), which allow pre-alignment of the cam movers.

Vacuum chamber

The vacuum chamber of the LCLS undulator system has a 5 mm×12.5 mm rectangular inner cross section through the undulator segments and circular (both 8 mm and 10 mm diameter) cross sections in the breaks. The interaction of the electron beam with the vacuum chamber generates longitudinal and transverse wakefields. The amplitude of the latter is limited by keeping the beam at the center of the chamber with a ±200 µm tolerance. The vacuum chamber will not be moved when the undulator segment is horizontally repositioned on the slides.

Alignment Diagnostic System (ADS) Sensors

The alignment of the girders will be continuously monitored by the ADS, which is a combination of a Wire Position Monitor (WPM) system and a Hydrostatic Leveling System (HLS), both permanently installed. There are four sensors for each of the two subsystems mounted on each girder, two each close to either end of the undulator segment. The sensors are supported by a mounting plate. The HLS is most sensitive to vertical positioning, while the WPM is best for horizontal positioning.

Temperature Sensors

The temperature will be monitored at several control points on girder components, at girder supports, and at the mounting plates of the ADS sensors.

Air Temperature Stabilization

The temperature of the LCLS undulator tunnel is controlled by a constantly flowing, thermally regulated, air stream [7]. The air enters upstream of the first girder and is blown through the 170-m-long tunnel in downstream direction. Temperature monitoring is done at the entrance point. As the air travels through the tunnel it is expected to pickup heat from the tunnel equipment at a rate of less than 50 W/m. The system is designed such that the air temperature will stay in the range of 19.5° C-20.5° C at all times along the entire undulator system. The undulator *K* value has been measured to change by 0.015% over a temperature range of 0.28° C.

TOLERANCES AND ALIGNMENT STRATEGY OVERVIEW

The purpose of the undulator system is to enable the SASE process, which is based on the interaction between an electron bunch and its spontaneous undulator radiation.

For obtaining and maintaining high gain in the SASE process, it is important that the electron bunch is in good overlap with the radiation field and that the individual electrons maintain a well defined phase relationship with that field. The radiation field is initially produced in the first undulator segment and will proceed in a straight line, while the electron beam trajectory will deviate from a straight line in the presence of magnetic and electric fields. The ideal undulator magnetic field will generate tiny periodic deviations from the straight line, which are necessary for the SASE process; the first and second field integrals over each undulator segment are ideally zero. Problems arise from off-axis fields of misaligned quadrupoles and undulator segments, the earth's magnetic field [8], other environmental fields, as well as from errors in the undulator fields that create finite field integrals or increase the electrons' path lengths through the undulator. The primary mitigation tool includes tuning [9], (for undulator field errors and earth's magnetic field), and shielding, (for environmental fields as well as earth's magnetic field).

The remaining error-fields (off-axis fields in quadrupoles and undulator segments, remnants of undulator field errors, the earth's magnetic field, and the environmental field) will be corrected through beam based alignment, which compensates the net effect of these fields by adjusting the transverse positions of the quadrupoles, through girder motion and by adding small dipole correction fields through trim coil adjustments. This process will automatically take the largest error field source, (e.g., misaligned quadrupoles), out of the system by moving the centers of the quadrupole magnets to a *goal* position, close to a common straight line. The *goal* position will be slightly away from that line, just enough to compensate for other remaining error sources. Thus, the *goal* position of each quadrupole will be precisely defined through the BBA process, and will be deviating from the electron beam trajectory (beam axis, defined by BBA) by about 20 µm (rms), a calculated number based on error amplitude estimates.

Table 2: Alignment tolerances for component alignment on girders for the LCLS undulator system

	Value	**Unit**
Horizontal Alignment of Quadrupole and BPM to Segment (rms)	125	µm
Vertical Alignment of Quadrupole and BPM to Segment (rms)	60	µm
Horizontal Alignment of BFW to Segment (rms)	100	µm
Vertical Alignment of BFW to Segment (rms)	55	µm

For best FEL performance, the effective magnetic centers of all quadrupoles need to be within ±2 µm of their *goal* position in both the horizontal and vertical directions. Additionally, the magnetic axes of the undulator segments need to be aligned to the beam axis to an accuracy of 140 µm (rms) horizontally and 80 µm (rms) vertically.

Table 3: Alignment tolerances for girder alignment in the LCLS Undulator Hall

	Value	**Unit**
Initial rms uncorrelated x/y quadrupole alignment tolerance wrt straight line	125	µm
Longitudinal Girder alignment tolerance	±1	mm
Undulator Segment yaw tolerance (rms)	240	µrad
Undulator Segment pitch tolerance (rms)	80	µrad
Undulator Segment roll tolerance (rms)	1000	µrad

The precise alignment of the quadrupoles can only be achieved using a beam based alignment method (energy scan) while the relative alignment (see Table 2) of the undulator segments to the quadrupoles and the BFW devices is aided by mounting the components on common, remotely movable girders (see above). The tolerances for the conventional alignment of the girders in the tunnel are reasonably achievable (see Table 3).

ALIGNMENT DIAGNOSTIC SYSTEM

The ADS continuously tracks changes in the transverse position, tilt, yaw, and roll of all girders to better than 1 µm [10]. This position information together with temperature measurements on the girders will be used to calculate the motion of the geometric centers for BPMs and quadrupoles to better than 2 µm (rms) with respect to the ADS sensors.

The information will be used between BBA applications to correct for girder/quadrupole position changes due to ground motion and temperature fluctuations and to correct the offset used in evaluating the BPM readings.

Wire Position Monitor (WPM) System

The WPM system is based on two 140-m-long stretched wires, running parallel to the beam line axis on one side of the Undulator as illustrated in Figure 1.

The wire position monitors are mounted to the girders kinematically, as shown in Figure 1. The vertical position of monitors has to be adjustable at different girders according to the wire sag of about 15 cm. Each girder will be equipped with four wire position monitors, two on each end. With this geometry, positions of each girder can be measured in horizontal and vertical direction with respect to both stretched wires. Pitch, roll and jaw of the girders will be calculated. Transverse position of quadrupoles can be determined within 0.5 µm (rms) by measurements of support temperatures within ±0.1 K.

As extensive test measurements have shown [11], the readout resolution of the WPM system is much better than 100 nm and instrument drifts are lower than 100 nm per day.

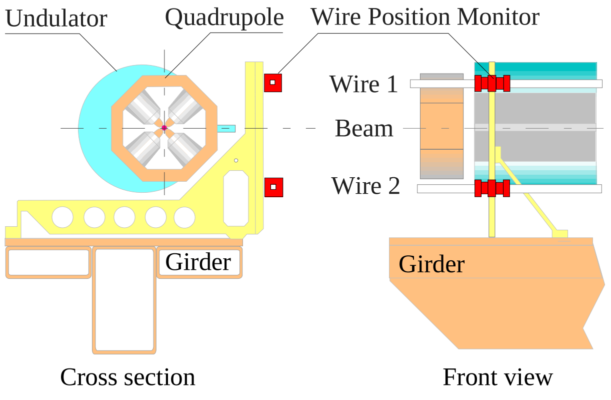

Figure 1: Functional cross section diagram of wire arrangements for the WPM system

Due to the unavoidable large sag of long wires, the uncertainty of the wires in vertical direction will be higher than one micrometer, which is the required design objective for the quadrupoles. Therefore, the vertical position of both wires will be correlated to the horizontal plain defined by the Hydrostatic Leveling System.

Hydrostatic Leveling System (HLS)

The HLS system is based on a system of water pipes also covering the entire 140-m-long undulator system.

Four sensors are mounted to the sides of each girder. The sensors are located at the same position as the WPM system sensors on each side of the girder.

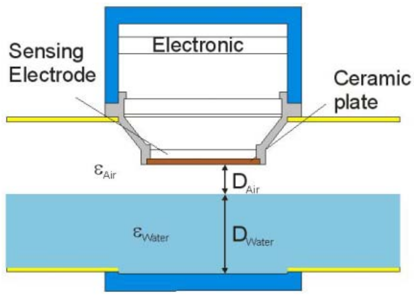

Figure 2: Functional cross section diagram of an HLS capacitive sensor

The system consists of two types of HLS sensors, which complement each other. One sensor type is based on capacitive measurements, which has the advantage of being widely used and having a lower purchase cost, see Figure 2. The repeatability of the sensor is 1 µm with an accuracy of 5 µm over the 5 mm measurement range. A disadvantage of this sensor type is that capacitive sensors drift by about 1 – 2 µm per month due to aging of electronic components. Ideally, the determination of the absolute distance between the sensing electrode and the water surface would require knowing the exact dielectric constants involved and the exact distance between the sensing electrode and the other electrode (vessel geometry). However, it is not possible to determine these values with sufficient accuracy to derive height readings directly from the capacitances of the sensors. Therefore, a calibration is performed by measuring the capacitance at different water levels and referring them to actual height readings.

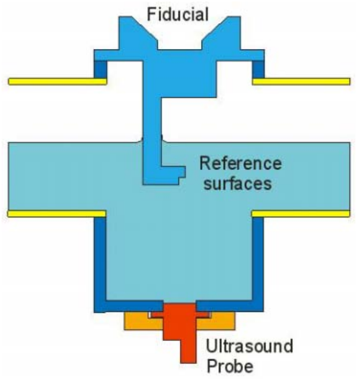

Figure 3: Functional cross section diagram of an HLS ultrasound sensor.

The second type of sensor is based on ultrasonic runtime measurements, see Figure 3. The measurements are self calibrating and therefore no drifts are expected. The repeatability of the sensor is 1 μm with an accuracy of 5 μm over the 5 mm measurement range. The ultrasound sensors measure the runtime to the two reference surfaces of the probe and to the water surface. This provides information about the water level with respect to the external fiducial of the probe. The ultrasound sensors, once mounted to the girder, are measured with the CMM. They are used to set the height of the girder in the tunnel during the conventional alignment step. Since the ultrasound sensors provide actual height differences to the water surface they can be used to calibrate the capacitive sensors.

MONITORING ELEMENTS SUMMARY

Monitoring elements are used to detect girder position as well as electron beam position. The following list provides a summary:

- Hydrostatic Leveling System (HLS)
  - monitors y, pitch, and roll
- Wire Position Monitoring System (WPM) [11]
  - monitors x, (y), (pitch), yaw, and roll
- Temperature Sensors
  - in support of HLS/WPM readout corrections, undulator K corrections, and component motion interpretation
- Beam Position Monitors[*]
  - monitors x and y positions of the electron beam
- Quadrupoles*
  - can be used to measure x and y offsets of the electron beam with respect to the quadrupole center

ALIGNMENT CONTROLS

A number of manual (local) and remote adjustments are available for the alignment of the beamline components of the LCLS undulator system.

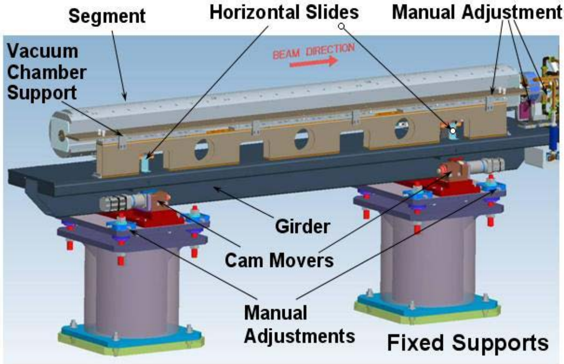

Figure 4: Undulator segment supports

Local Controls

Alignment of the cam supports is done using the manual adjustment controls on top of the support pedestals (see Figure 4). Relative alignment of girder components to the magnetic axes of the undulator segments (on the CMM) is done by using the manual adjustable supports of the quadrupole, BPM and BFW components, which provide a range of ±2 mm in the horizontal and vertical directions with a resolution of 2 μm. The height of the magnetic axes of the undulator segments above the segment supports is controlled by permanent shims created specially for the undulator after the tuning process and permanently bolted to its bottom. This makes all undulator segments interchangeable with each other.

Remote Controls

The transverse positions of the girders are (remotely) controlled based on cam mover technology

- during initial conventional alignment (see above)
- for quadrupole position control, i.e., beam steering during BBA.
- for BFW scans
- for compensation of ground motion effects etc.

The motion range is such that each quadrupole magnet can be moved ±0.7 mm in any transverse direction from its neutral position. The motion control allows moving a single quadrupole independently in the horizontal and vertical direction without affecting the adjacent quadrupoles and without introducing roll to the girder assembly. All girder components will be moved together when a quadrupole is repositioned so that the BFW device, the undulator segment, the quadrupole, the BPM and the vacuum chamber will stay aligned relative to each other. The horizontal position of the undulator segment is remotely controlled for

- field strength adjustment (change of K)
- reduction of radiation exposure during commissioning (full roll-out position),
- measurement of FEL gain as function of z (full roll-out position),
- measurement of K using spontaneous radiation from only two adjacent, interfering undulators [12].

CONVENTIONAL ALIGNMENT

The conventional alignment of the undulator system focuses on bringing the quadrupole magnets into a straight line at tolerances specified in Table 3.

To achieve this goal, the first step is to establish a monument network inside the undulator hall. This set of coordinates assigned to the network points serves as the representation of the coordinate system and is the basis for all component set-ups. In practice, the points are nests compatible with 1.5" spherical tooling. They can be equipped with SMRs (Spherically Mounted Retroreflectors) for laser tracker observations, or solid sphere based rods for leveling observations. Simulations have been made with a regular pattern of both floor and wall targets. Figure 5, below, represents the middle section of the undulator hall with the red rectangles representing quadrupoles. A floor point is installed in the

---

[*] Transverse Locations Tracked by HLS and WPM

middle of the tunnel at every other quadrupole location. The laser tracker positions are placed in front of the other quadrupoles with a staggered offset from the beamline. The tracker observations (purple lines) have a-priori standard deviations based on recent experiences and standard observation practices: 30 µm for the distances and an inverse function of the distance for the two angles (30 µm and 50 µm at one meter for the horizontal and the vertical, respectively). The weight of the leveling observations (green lines) is based on 50 µm as a-priori standard deviations.

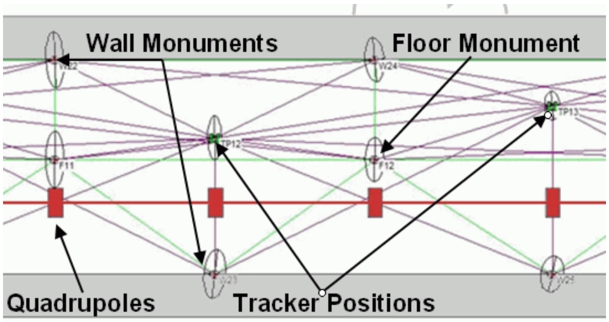

Figure 5: The undulator hall network, used in Simulation, is shown relative to quadrupole locations. Floor and wall monuments as well as tracker positions are shown. The largest semi-major axis of the error ellipses is below 50 µm.

Figure 5 shows the resulting error ellipse at 1 sigma for a free-net approach. All semi-major axes are below 50 µm. This free-net approach assumes that the location and orientation of the LCLS undulator coordinate system [13] has been established through the inclusion of a number of points known in the SLAC linac system.

Once the network is established, the points can be used for the markings on the floor, the alignment of the fixed support pillars and finally the pre-alignment of the girders. For all these tasks, total station set-ups are performed. A solid resection of the instrument, based on at least two floor monuments and three wall monuments, can guarantee the necessary requirement for point determination. Depending on the duration of the installation and the characteristics of the floor curing, an additional survey of the monument network will be observed to control and update the coordinates.

After the undulator segments are installed, a final mapping of all monuments and all fiducials is performed. The scenario for the laser tracker position and methodology is identical to the one used to derive the monument network. The fiducials of the girders, undulator segments, quadrupoles, BFW devices and HLS ultrasound sensors are observed from multiple laser tracker stations. Leveling observations between monuments and selected fiducials are added. The adjustment of all observations is again performed with a free-net approach. Finally the measurements with the laser tracker and the digital level are combined with the portable HLS and WPM observations. If moves are required, they can be checked by the ADS readings and do not require a full remapping of the undulator hall.

BEAM-BASED ALIGNMENT

The electron beam trajectory through the FEL undulator must be straight to a level of about 2 µm over one FEL gain length (~5 m). This level is difficult to achieve using standard component survey methods, and therefore requires a special electron Beam-Based-Alignment (BBA) algorithm [5] which samples undulator BPM readings at three different beam energies (13.6, 6.5, and 4.3 GeV). Changing the linac energy will require a change in many magnetic components upstream of the first undulator to keep the beam matched to the undulator optics, and to keep the horizontal and vertical position and angle of the trajectory at the entrance to the undulator independent of energy. The latter will be monitored by a set of three RF cavity BPMs located between the last quadrupole of the linac-to-undulator beam transport line and the first undulator segment. Detailed simulations have been made, which indicate that adequate beam-based alignment can be achieved if undulator quality and beam stability are within the tight tolerance specifications described here.

BBA will use quad motion and dipole trims for beam corrections. The BBA algorithm uses the off-axis field in the quadrupoles for trajectory correction. Changes are applied through cam-based girder motion, which will automatically align the quadrupoles in the process. Thus, the main source of the original trajectory errors, i.e., quadrupole misalignment, will be taken out by BBA. Secondary sources, such as undulator field errors, the earth's magnetic fields, and other environmental fields are expected to be small and will require slight off-center positioning of the quadrupoles to generate the required correction field on beam axis. The largest of these corrections can then be partially taken over by dipole trim correctors, which are integrated in the quadrupole design. Their range is equivalent to ±100 µm of quadrupole motion. The BPMs must have a relative position measurement resolution of <2 µm rms in order to achieve trajectory straightness adequate to support 1.5-Å FEL operations. This resolution definition implies that the BPM readback offsets (electrical or mechanical) must be stable to <2 µm over the one hour required to accumulate the BBA data.

TOLERANCE ZONES

A systematic plan for trajectory correction during operation has been developed based on tolerance zones and different levels of correction. This plan integrates the results of global tolerance studies, which predict an amount of FEL power loss as a function of the size of the errors, with a sequence of correction operations with increasing disruption to the FEL beam. Starting at the completion of a full BBA session, there will be continuous trajectory feedback systems running at 120 Hz, based on LTU (Linac-To-Undulator transport line) BPMs, and at 0.1 Hz, based on undulator BPMs,

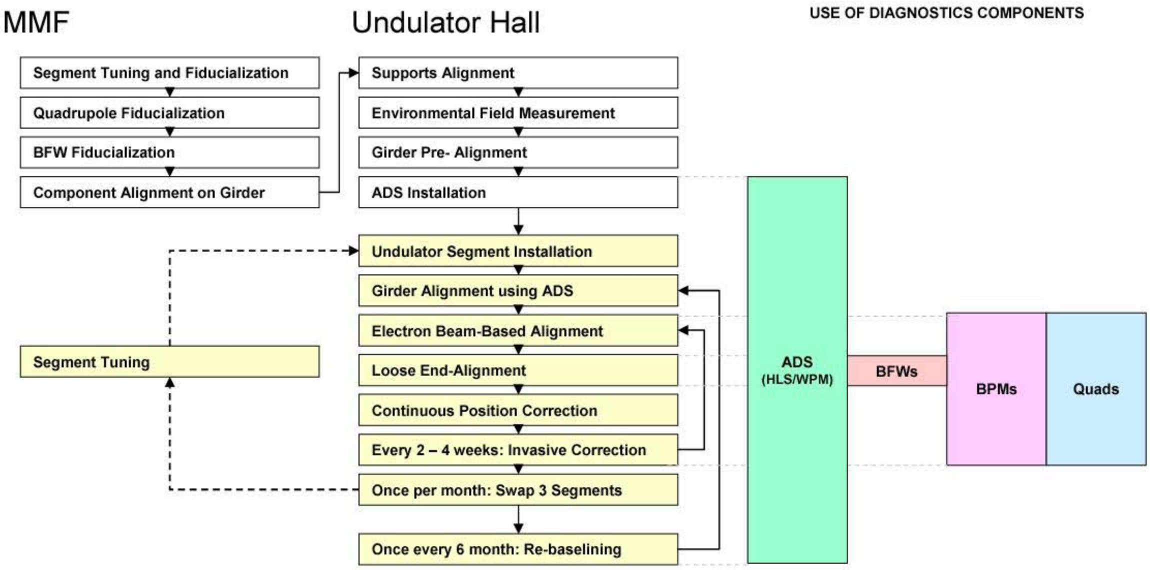

Figure 6: Alignment Function Diagram.

which are tracked by the ADS (Zone 1). Every few hours (Zone 2) small girder position corrections, based on ADS measurements, will keep the quadrupoles at their *goal* positions to restore most, but not all, of the beam power which is expected to sag by up to 10%. This can be done without disruption of the FEL beam. Once a day (Zone 3), re-adjustment of the FEL beam pointing direction may be done. Once a week or less (Zone 4), a full BBA session will be used to get back to the original tolerance zone, which will interrupt FEL beam delivery for less than an hour. Before the BBA is applied, the FEL power level is expected to drop by no more than 25%. Full BBA should fully restore the FEL power to the original level. At an interval of roughly once every six months (Zone 5), a cam mover may range-limit and a planned access will be used to reset cam blocks as necessary.

ALIGNMENT FUNCTION DIAGRAM

The main function block of the undulator alignment system is given in Figure 6. Alignment functions are performed in the Magnet Measurement Facility (MMF) and in the Undulator Hall (UH). Alignment tasks performed in the MMF include the tuning and fiducialization of the undulator segments as well as the fiducialization of the quadrupoles and the BFW devices. The components are then mounted on the girder and aligned. The alignment is checked on the CMM, which is also located in the MMF. The undulator segments are stored separately from the girders until they are installed in the UH. In preparation for the girder installation, fixed support pillars are installed in the UH and aligned. The girders are then installed and pre-aligned on the fixed support pillars after the environmental magnetic field has been measured and recorded along the entire undulator line. After installation of the ADS system, the continuous measurement and recording of the girder positions will start. The undulator segments are then mounted onto the horizontal slides on top of the girders, and the quadrupoles are aligned onto a straight line with conventional alignment. Then, portable WPM and HLS systems [14] will be used for a precise alignment of the undulator segments between neighboring quadrupole magnets.

Every few hours small girder position corrections based on ADS measurements will keep the quadrupoles at their goal position (which will be reset after BBA) to better than ±2 µm over a 1-hour period and to better than ±5 µm over a 24-hour period, in order to support BBA. The next alignment steps involve the electron beam. BBA based on BPMs and quadrupoles under observation of the ADS will be used to straighten the electron beam trajectory to the level required to achieve FEL gain. At this point, continuous position corrections based on BPM readings will start. The BPM readings will be corrected for any device motion, as reported by the ADS.

The BFW devices can now be used to check the alignment of the upstream end (‘loose end’) of the undulator segments.

Every 2-4 weeks, the procedure loops back to BBA (one iteration, rather than the initial three, may be sufficient), which requires interrupting beam delivery.

Once per month, three undulator segments will be swapped out of the tunnel and brought back to the MMF to be checked for detuning effects, such as radiation damage. At the same time, three of the six replacement undulator segments, which will have been prepared ahead of time, will be installed in the empty slots. As mentioned above, the undulator magnets are mechanically shimmed that the magnetic axis will come to lie in the same *x*, *y* location when placed onto a given girder. Every six months, when cam movers might have run out of range due to the expected continuous ground motion, there will be a maintenance shutdown for re-baselining, i. e., realignment of the cam movers using the manual adjustments on top of the support pillars.

SUMMARY

The X-ray FEL demands very tight tolerances on magnetic field quality, electron beam straightness, and undulator segment alignment. These tolerances can be achieved through BBA procedures based on BPMs and quadrupoles (with energy scan) as well as BFW devices.

Relative component alignment to the required tolerances will be achieved through common girder mounting. Main tasks of the conventional alignment and motion systems are:

- Component fiducialization and alignment on girder
- Conventional alignment of girders in Undulator Hall as prerequisite for BBA.

The ADS measures and enables the correction of girder movement due to ground motion, temperature changes, and cam mover changes. A strategy is in place for using the monitor systems and the controls in order to establish and maintain a straight FEL trajectory.

ACKNOWLEDGEMENTS

It is a pleasure to acknowledge contributions by Argonne National Laboratory’s LCLS team.

REFERENCES

[1] I. Vasserman, R. Dejus, P. Den Hartog, E. Moog, S. Sasaki, E. Trakhtenberg, and M. White, "LCLS Undulator Design Development." *FEL2004 Proceeding*, 2004.

[2] E. Trakhtenberg, J. Collins, P. Den Hartog, and M. White, "Design of a Prototype Precision Positioning System for the Undulators of the Linac Coherent Light Source." PAC2005 Proceedings, 2005.

[3] G. Bowden, P. Holik, S.R. Wagner, G. Heimlinger, and R. Settles, "Precision Magnet Movers for the Final Focus Test Beam." SLAC-PUB-95-6132, 1995.

[4] J. Wu, P. Emma and R.C. Field, "Preliminary Study on Electron Signal Detection for the Beam Finder Wire of the LCLS Undulator." LCLS-TN-06-7, 2006.

[5] P. Emma, H.-D. Nuhn, and R. Carr, "Beam Based Alignment for the LCLS FEL Undulator." Nucl. Instrum. Meth. **A**429:407-413, 1999.

[6] J. Welch, "Estimate of Undulator Magnet Damage Due to Beam Finder Wire Measurements." LCLS-TN-06-6, 2006.

[7] J. Welch, "Air Temperature in the Undulator Hall." LCLS-TN-06-2, 2006.

[8] K. Hacker, Z. Wolf, "Earth's Magnetic Field Measurements for the LCLS Undulators." LCLS-TN-05-4 , 2005.

[9] Z. Wolf, "Introduction to LCLS Undulator Tuning." SLAC-TN-05-043, 2004.

[10] J. Welch, "Ground Motion Expectations for the LCLS Undulator Hall." SLAC-TN-05-013, LCLS-TN-04-14, 2004.

[11] F. Peters, G. Gassner, and R. Ruland, "First Measurements and Results With a Stretched Wire Test Setup." LCLS-TN-05-7, 2005.

[12] J. Welch, et al., these FEL’06 proceedings.

[13] E. Bong, P. Emma, C. LeCocq, T. Montagne, and J. Welch, "LCLS Undulator Coordinate System." SLAC-TN-05-021, LCLS TN-03-8, 2004.

[14] G. Gassner, "Proposal for the Alignment of the ‘Loose End’." LCLS-TN-06-11, 2006.

HOW TO OBTAIN HIGH QUALITY ELECTRON BUNCHES IN PRESENCE OF NORMAL CONDUCTING LINAC WAKEFIELDS

S. Di Mitri*, ELETTRA, Trieste, Italy

Abstract

The dynamics of electron beams involved in Free Electron Lasers (FELs) projects is an interplay between sources of 6-dimensional emittance dilution and methods of emittance preservation. Relatively long bunches are required for harmonic cascade seeded FELs in order to accommodate the timing jitter and the seed provided by the bunch itself at each stage of the cascade. A high quality is required from such electron beams (small transverse emittance and energy spread) together with a uniform distribution in time along the usable part of the bunch; non-linearity in the longitudinal phase space and in the transverse planes are also issues. A complex longitudinal phase space dynamics characterizes the study often in presence of by the Coherent Synchrotron Radiation (CSR) generated in magnetic compressors. This paper reviews specific problems related to the electron beam dynamics dominated by bunches of kA peak current and varying length (0.1 to 2 ps) in the presence of normal conducting linac wakefields. Methods implemented to minimize the 6-dimensonal phase space degradation are discussed. Results of high beam quality performance are illustrated with particles tracking codes.

INTRODUCTION

This paper describes the degrading effects on the electron beam performance of wake fields present in normal conducting linacs for single pass FELs; in particular: (i) geometrical wake fields in accelerating structures [1–4]; (ii) Coherent Synchrotron Radiation (CSR) [5–8]; (iii) Longitudinal Space Charge (LSC) [9–12]. Their impact on the electron beam quality is discussed in terms of the properties relevant for Spontaneous Emission Self Amplified (SASE) [13–15] and seeded [16–19] FELs.

All the mentioned wake fields couple the 6-dimensional particle dynamics by putting some conflicting constraints on the design of the beam delivery system dedicated to the formation of electron bunches. This paper reviews some strategies for the machine design to compensate the emittances growth and improve the beam quality. The conclusions demonstrate the validity of manipulation techniques to control the electrons 6-dimensional phase space to unprecedented levels.

WAKE FIELDS AFFECTING THE ELECTRON BEAM QUALITY

In order to make the FEL process more efficient and the undulators chain reasonably short, the electron beam quality has to be characterised by high peak current, small transverse emittance, small energy spread. Due to the cooperative FEL process, priority is given to the slice beam quality.

Longitudinal phase space

Short range longitudinal wake fields generated by relatively short bunches with $\sigma_z \ll a$, being σ_z the bunch length and *a* the beam pipe radius, travelling into periodical structures induce a maximum FWHM relative energy loss [20]:

$$\frac{\Delta\gamma}{\gamma} = \frac{eW_0QL}{E_f} \qquad (1)$$

which is valid in the approximation $(\sigma_z / s_0)^{1/2} \ll 1$ with s_0 the characteristic parameter of the structure.

Assuming a linear energy gain in the linac, (1) shows that the impact of very long accelerators can be comparable to that of smaller machines. For example, the energy loss in the LCLS Linac 3 relative to the final average energy is about 0.5% [21], while that in the FERMI Linac 4 is 1.4% [22]. Off-crest acceleration is then needed to reduce the induced energy chirp below the FEL threshold and to re-establish the linearity in the longitudinal phase space.

With an appropriate positioning of the magnetic chicanes, longitudinal wake fields acting in the last part of the linac work for free to cancel the linear energy chirp required by the compression. In this way the chicane momentum compaction can be relaxed, thus reducing the influence of CSR, while using larger energy chirps.

Even after cancellation of the linear contribution, residual higher order energy chirps affect the final beam quality. A quadratic chirp $D(2) = d^2E/d^2z$ increases the correlated energy spread, thus reducing the SASE FEL gain. It also enlarges the bandwidth of a High Gain Harmonic Generation (HGHG) FEL to unwanted levels, corrupting the goal of producing a Fourier transform limited signal with narrow bandwidth of the order of few meV [23–25]. Figures 1–4 illustrate this topic comparing two cases with different values of the quadratic energy chirp.

---

*simone.dimitri@elettra.trieste.it

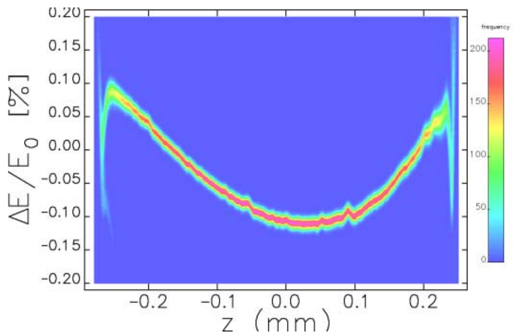

Figure 1. Longitudinal phase space affected by 0.9 MeV/ps^2 quadratic energy chirp.

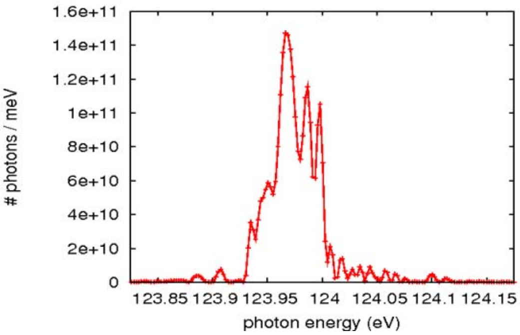

Figure 2. Spectral bandwidth of 40 meV FWHM generated by the electron bunch in Figure 1 through FERMI HGHG with fresh bunch technique at 10 nm.

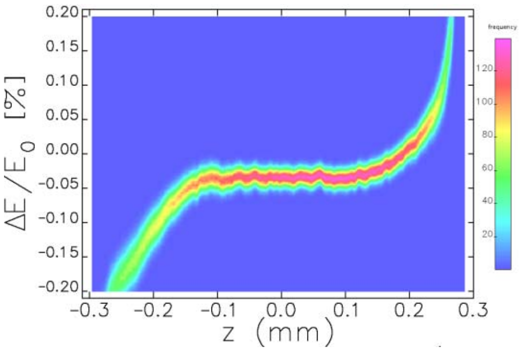

Figure 3. Longitudinal phase space affected by a reduced 0.5 MeV/ps^2 quadratic energy chirp.

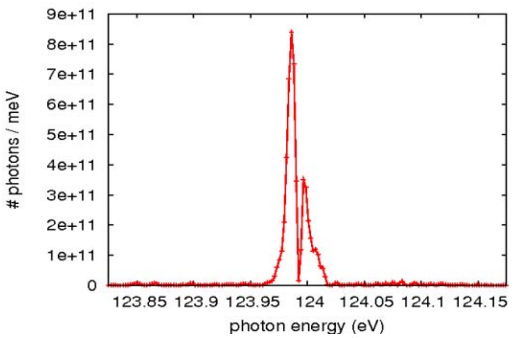

Figure 4. Spectral bandwidth of 10 meV FWHM generated by the electron bunch in Figure 3 through FERMI HGHG with fresh bunch technique at 10 nm.

Phase spaces and bandwidths were produced respectively by mean of Elegant [26] and Genesis [27].

The use of sextupoles [28] and of a high harmonic cavity [29–31] (also called "linearizer") to compensate the quadratic chirp is well-established. Nevertheless, it was also shown that a residual cubic chirp in the compression process can have a large impact on the final current profile [32].

Current profile

SASE FELs generally require a high peak current (kAs) in the bunch core, while HGHG FELs desire a uniform current distribution along the whole bunch, especially if based on fresh bunch injection technique. Even if with different purposes, both the first and the latter need a control of the final current distribution. A proper manipulation of the cubic energy chirp $D(3) = d^3E/d^3z$ is useful to maximize the current along the bunch and to avoid current spikes at the bunch edges. In fact, they are related to several dangerous effects: (i) introduce nonlinearity in the phase space (i.e., bifurcations); (ii) attract particles reducing the current in the bunch core; (iii) induce CSR instability at shorter wavelength than the bunch length; (iv) wake field excited by a leading edge spike may cause additional energy spread in the undulator vacuum chamber.

Transverse emittance

Apart from SC forces at low energy, slice emittance is directly affected by transverse CSR forces [6,33,34]. A coherent behaviour of the emitted radiation has been also observed at wavelength smaller than the bunch length [12,35]; due to the interplay of LSC and CSR on wavelengths which are a fraction of the bunch length, microbunching instability (μBI) [36–40] leads to phase space fragmentation and to slice emittance growth.

The projected emittance of high charge, short bunches is indirectly affected by CSR emitted on the scale of the bunch length [41–43]. Due to the absence of stochastic processes, the slices lateral offset can be cancelled through a *–I* transport matrix between two identical dispersive regions [44].

The transverse wake field contributes to the projected emittance growth by mean of the induced beam break up (BBU) instability [45,46]. The coupling between the electron bunch and the wake field at a given energy can be estimated by mean of the following dimensionless parameter [47]:

$$\varepsilon_r = \frac{4\pi\varepsilon_0 W_0 l_b L^2 I_{pk}}{\gamma_i I_A} \qquad (2)$$

It multiplies the resonant term acting on the transverse motion of the slices centroid, thus it should be made as small as possible.

CUBIC ENERGY CHIRP

The sign of the cubic energy chirp in the photo-injector (PI) is mainly determined by the SC force and, according to the present simulations, it is always negative for a flat-top charge distribution (bunch head on the left side of phase space) [48]. After the interaction with longitudinal wake fields, this sign is reversed at the entrance of the second compressor, enhancing the energy-position correlation of the bunch edges w.r.t the core. The edges are there over-compressed producing current spikes. On the contrary, a negative cubic chirp at the chicane provides under-compression of the edges. This mechanism is illustrated in Figure 5, where the longitudinal phase space and the corresponding current profile generated by LiTrack [49] are shown.

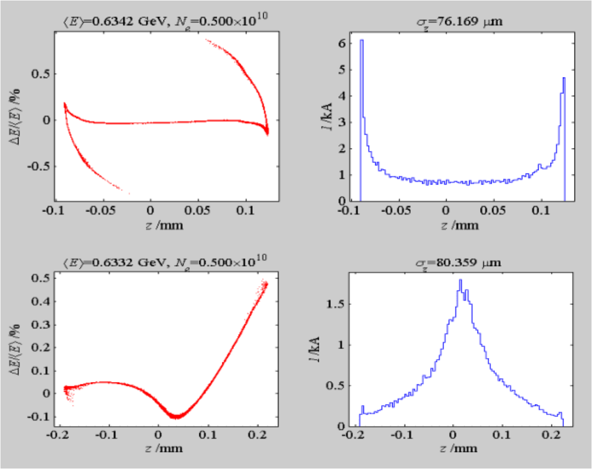

Figure 5. Longitudinal phase space (left) and current profile (right) at the end of the FERMI Linac. Cubic chirp at the PI is -3.9×10^{-4} mm^{-3} at top and 8.1×10^{-4} mm^{-3} at bottom.

Voltage and phase of the high harmonic cavity allow to control the cubic chirp in the following transport line that is the final current profile. For a 1-stage compression the following parameters are defined: $k=2\pi/\lambda_{rf}$ is the RF wave number and λ_{rf} is the RF wavelength; U_0 is the voltage amplitude of a first linac accelerating on-crest; U_1 is the amplitude of a second linac with off-crest acceleration at phase ϕ_1 (referred to the crest of the RF wave); U_4 and ϕ_4 are the amplitude and phase of the 4-th harmonic cavity. Thus, the third derivative of the energy gain is:

$$U'''_{(s=0)} = -k^2 U'_{(s=0)} + + \frac{15}{4} k^3 \left(U_0 + U_1 \cos(\phi_1)\right) \tan(\phi_4) \quad (3)$$

The quadratic chirp is cancelled if:

$$U_4 = -\frac{U_0 + U_1 \cos(\phi_1)}{16 \cos(\phi_4)} \quad (4)$$

(3) and (4) define the space where parameters of the harmonic cavity can be moved in order to linearize the longitudinal phase space up to the 3rd order.

REVERSE TRACKING

Due to the complexity of the interplay of SC, longitudinal wake fields and higher order energy chirps, it is not obvious to control simultaneously longitudinal phase space and current profile. In addition, it was demonstrated [50] that the linearizer can be used to relax until an order of magnitude the sensitivities of the final beam properties to the linac phase and voltage. Unfortunately, this technique assumes a negligible effect of the cubic chirp on the longitudinal beam dynamics and considers it a free parameter.

The reverse tracking [32] suggests how to improve the global quality of the longitudinal phase space for a given configuration of the wake potential, eventually leaving the linearizer free to be moved for jitter purposes. It applies to ultra-relativistic particles and is based on the assumptions of no stochastic processes in the beam transport and of negligible energy loss from CSR. CSR with wavelength in the range of the bunch length can be neglected in presence of an appropriate shielding [32,51,52] of the vacuum chamber. Moreover, the induced energy loss is relatively small for long bunches.

Within these approximations, the equations of motion can be reversed and a unique solution exists. The density distribution obtained at the beginning of the linac will automatically compensate all the effects perturbing the beam dynamics in the forward tracking, like RF curvature, wake fields and higher order optics.

It is clear this method calls the beam shaping at the photo-cathode to be a fundamental contribution to the final beam quality. For the FERMI specific case [32], a final beam with a flat current profile and a linear phase space corresponds to an initial beam with a ramped current profile (see, Figure 6).

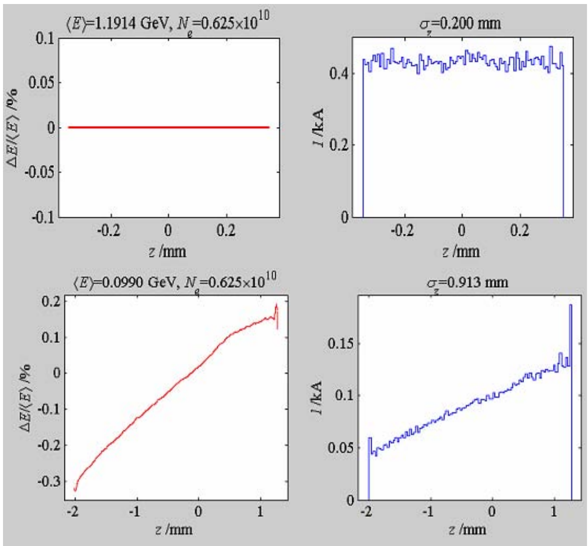

Figure 6. Top, electron beam desired at the undulators' entrance. Bottom, electron beam required at the PI end. LiTrack [49] output.

The approximate prediction of the reverse tracking was confirmed by the forward tracking, obtaining the phase space in Figure 3. In addition, it was proved that the convolution of the longitudinal wake function with a ramped particle distribution results in a mostly linear wake potential (see, Figure 7), while an initial parabolic current profile brings nonlinear contributions to the phase space.

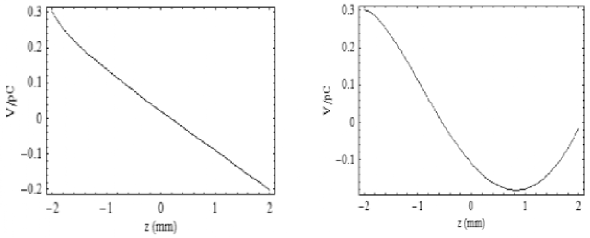

Figure 7. Longitudinal wake field generated in the FERMI Linac 4 resulting from the convolution of the wake function with a particles distribution characterized by a ramped current profile (left) and a parabolic one (right).

BEAM SHAPING AT THE PHOTO-INJECTOR

As discussed before, in presence of wake fields the initial electron density distribution plays an important role in formation of the electron bunches at the end of the accelerator [53–55]. As for the FERMI case, the LSC field at the cathode was investigated [56], since it is mainly responsible for blowing out the particles. Figure 8 shows the desired current profile at the cathode and the evolved charge distribution at the injector exit (at 100 MeV) for a 0.8 nC bunch.

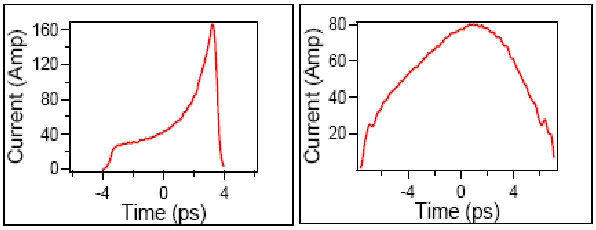

Figure 8. Ramped current distribution just after the cathode (left) and at the injector exit (right) for a 0.8 nC bunch.

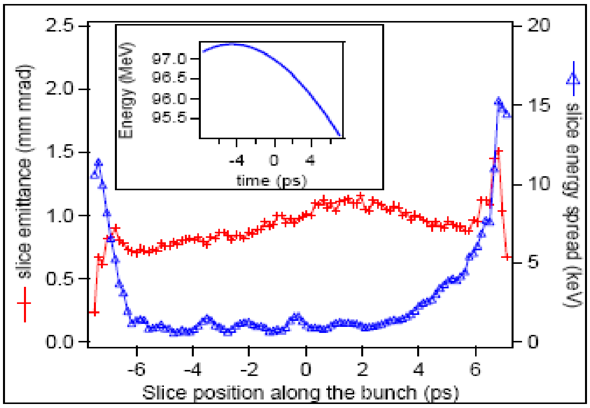

Figure 9. Slice emittance and slice energy spread along the bunch at the exit of the injector. $\varepsilon_{xn,80\%}$ = 1.2 mm mrad. Inside plot: longitudinal phase space including longitudinal wake fields. Head is on the left.

Since each longitudinal slice of the beam contains a differing amount of charge, each one evolves in a different way from the other. Thus, the so-called Ferrario's working point [57] can be only approximately adopted for the emittance compensation. Figure 9 shows the resulting slice emittance and the slice energy spread for the bunch in Figure 8 at the injector exit; results were produced through the GPT code [58].

BBU SUPPRESSION

BBU instability induces a lateral deviation of the bunch tail w.r.t. the head axis. The persistence of such oscillations tend to transform the temporal coordinate into the transversal one, thus inducing projected emittance dilution. A "banana" shape in the (t, x) and (t, y) plane is assumed by the electron bunch [59]; it makes a large part of the bunch travelling with a trajectory offset in the undulator. This fact reflects into an optical mismatch in the undulators and can also induce an effective K-value for the tailing particles different from the nominal one. The impact of a launching error of the bunch in an undulator for SASE FEL was studied and experimentally observed [60]. The off-axis motion in the device leads to power reduction and bandwidth enlargement because of the processes addressed above.

As for seeded FELs, if the bunch tail deviation is sufficiently larger than the beam size, it causes a missed overlap between the seeding laser and the bunch in the undulator, thus reducing the emitted photon pulse length and the peak power [61]. Figure 10 illustrates the horizontal banana shape exiting from the FERMI Linac (Elegant simulation) and a schematic of the seeding laser overlapping the beam.

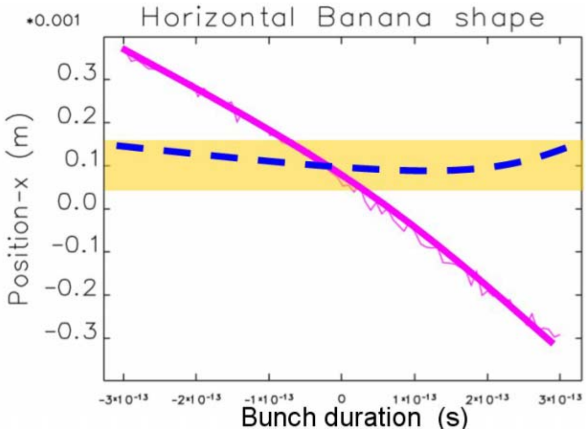

Figure 10. Horizontal banana shapes induced in the FERMI Linac. Bunch head is on the left. The solid curve shows a tail deviation 8 times larger than the 80 µm rms beam size. The dashed one corresponds to a different trajectory in the Linac for which the tail deviation is within the rms beam size. The super-imposed rectangle sketches the seeding laser and points out its overlap with the bunch in the two cases.

Figure 11 represents the dependence of peak power and phase shift for the FERMI FEL-1 scheme at 40 nm on the off-axis displacement error of the electron bunch at the undulator entrance [61].

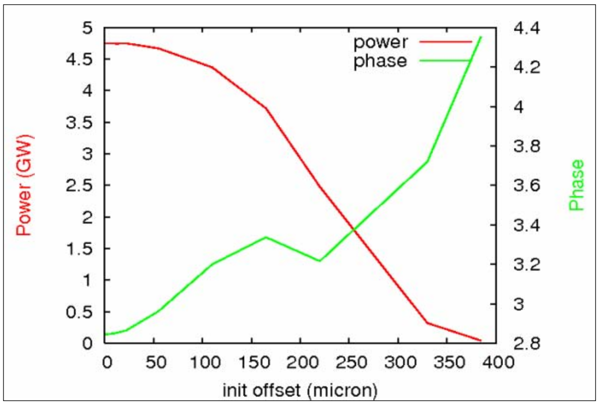

Figure 11. Effect of an off-axis displacement error of the electron bunch at the undulator entrance on peak power (decreasing with offset) and phase shift (increasing with offset) for FERMI FEL-1 HGHG scheme tuned at 40 nm. Seeding laser spot size is here assumed to be 210 μm.

In single pass FELs the BBU instability can be suppressed through trajectory bumps [59,62]. This technique looks for a “golden trajectory” for which all the kicks generated by the transverse wake field compensate each other and the banana shape is finally cancelled. Dashed curve in Figure 10 shows a compensated banana shape which maximizes the overlap with the seeding laser; the solid curve is the banana shape obtained in absence of bumps.

Since the bump is a local method of correction, it depends on the particular condition of operation at its location. For this reason, the sensitivity of the bump to the trajectory jitters has to be checked and made sufficiently small [59].

Reducing the average β-function along the linac is also useful since its square is proportional to the induced relative emittance growth [63]. On the other hand, in a FODO lattice the quadrupole strength $k \sim 1/\beta$ and the trajectory affected by errors $u_{err} \sim k\sqrt{\beta}$. Thus, lowering the β-function increases the sensitivity to the elements misalignment.

LOW CHARGE OPTION

The previous paragraphs describe techniques of electron beam manipulation in order to compensate the wake fields effects. Now a more general prescription of low charge beam production is exposed to minimize the wake fields once the compression factor, the final peak current and the final average energy are fixed.

The curves in Figure 12 represent the loss factor of a Gaussian charge distribution travelling in one accelerating structure of the FERMI Linac 4 vs. the rms bunch length; each curve is drawn for a given peak current (upper curve is at higher current), which is the parameter of interest for the FEL. Dots represent a 0.6 nC charged beam which is compressed twice (dots move from right to left) by a total factor of 15; triangles show the same dynamics for a 0.3 nC charged beam.

Due to the monotonic behaviour of the wake functions in the range of bunch length considered, a bunch with lower charge always suffers from a minor energy loss w.r.t. the higher charge option (look at the height of the yellow and orange bars). Obviously, for a fixed peak current a shorter bunch is required from the PI and will be provided at the end of the accelerator.

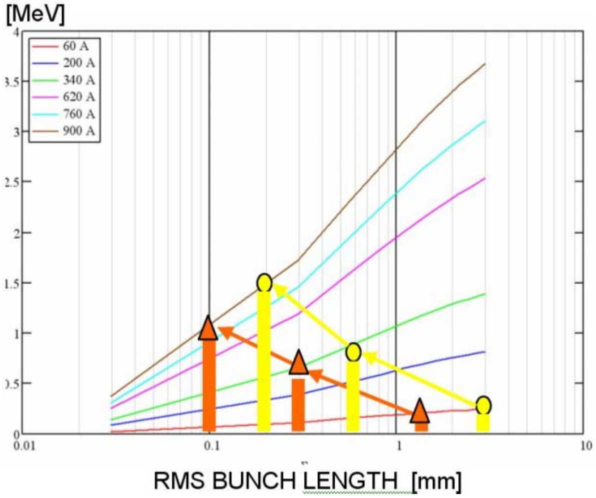

Figure 12. Loss factor in the FERMI Linac 4 accelerating structure vs. rms bunch length (a Gaussian charge distribution is assumed). Dots refer to the 0.6 nC electron bunch in a 2-stage linear compression (from right to left, the peak current increases as the bunch length decreases). Triangles refer to the 0.3 nC case.

Limitations to the shorter bunch length achievable are: (i) CSR instability; in the steady state approximation the induced rms energy spread $\sigma_{\delta,CSR} \sim I/\sigma_z^{1/3}$ [5]. This has an impact in terms of both energy modulation and brightness degradation [56]; (ii) timing jitter, especially for HGHG FELs with fresh bunch injection technique; the final bunch has to be sufficiently long in order to accommodate the timing jitter of the electron bunch w.r.t. the seeding laser.

A 0.2 nC low charge solution has been recently adopted by LCLS [64] instead of the 1.0 nC initially chosen; their dynamics is compared in Figure 13; there the low charge bunch shows an improvement in the longitudinal phase space linearity, a reduction of the current spikes at the bunch edges and a suppression of the BBU instability up to 10% of emittance growth. Reduction of the emittance from 1.2 to 0.85 mm mrad allows to obtain the same saturation length of the 1.0 nC case with a lower peak current (2.1 kA instead of 3.4 kA).

In some cases, a low charge option can also minimize the impact of CSR and SC forces on the transverse emittance. For the TESLA-XFEL, a low charge working point [65] of 0.25 nC was found with a good compromise between the slice emittance growth, due to stronger CSR transverse forces at shorter bunch length, and the preservation of the projected emittance, which is no longer affected by the optical mismatch generated by SC forces at low energies.

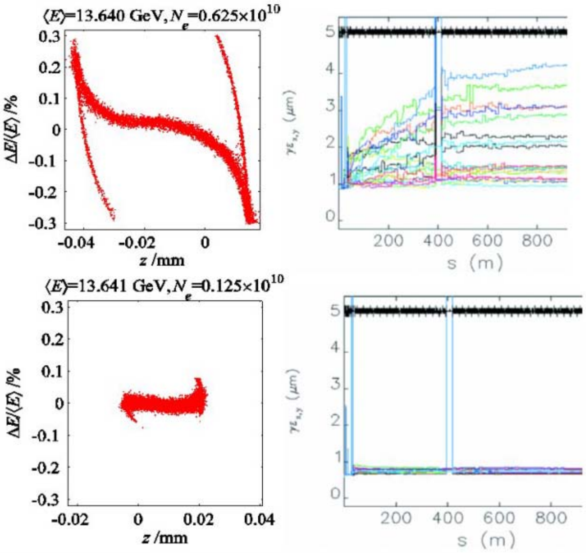

Figure 13. Longitudinal phase space (left plots) and transverse normalised projected emittance (right plots) in LCLS for the 1.0 nC charged bunch at top and for the 0.2 nC charged bunch at bottom.

LANDAU DAMPING

In the last 10 years microbunching instability (μBI) has been extensively studied and recently observed in experiments. The gain of the instability was calculated analytically in the 2-dimensional approximation [37,38]. Numerical solution was obtained including Landau damping from the beam finite emittance [39].

According to the linear theory, the longitudinal Landau damping can be made more effective by increasing the relative energy spread and the compression factor, like in a 1-stage compression. In fact, when adopting a 2-stage compression, analytical estimations confirmed by simulations demonstrate the fundamental role of the second compressor in the development of the μBI: it transforms all the LSC induced energy modulation accumulated in the upstream linac into density modulation; this effect sums to the enhancement of the density modulation already developed by the first compressor.

Figure 14 compares the spectral gain function of the 2-stage and of the 1-stage compression in the FERMI Linac [66]. The maximum of the instability gain is reduced by a factor 100 in the latter case.

The 1-stage compression is a pretty attractive solution but forces a very short bunch to travel along a large part of the linac; as a consequence, linearity of the longitudinal phase space is strongly affected by wake fields. This problem could be overcome by applying the reverse tracking to the single compression scheme [67].

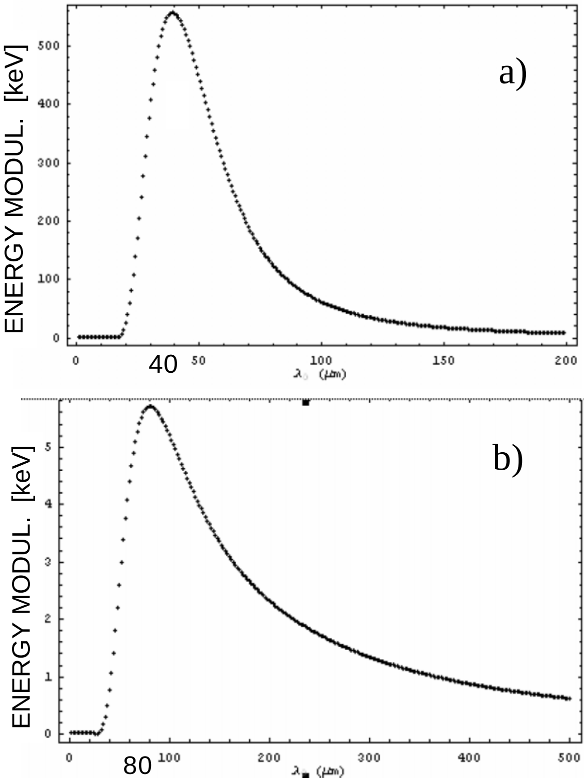

Figure 14. Spectral gain function of the microbunching instability in the FERMI Linac in case of double (a) and single (b) compression. Calculation is based on the 2-dimensional model for CSR and LSC in the linear approximation. μBI starts from realistic shot noise.

A 2-stage magnetic compression is generally associated with a laser heater at low energy for the reasons addressed above. This tool was proposed [9] to suppress the instability by increasing the relative energy spread just before the compression; on the other hand, its final value has to be still maintained below the FEL threshold. This is not obviously reached in low and medium energy machines and becomes more stringent for multi-stage harmonic cascade FELs.

Figure 15 shows the final slice energy spread as function of the energy spread induced by the laser heater in FERMI. μBI is supposed to start from shot noise in the initial density distribution. Figure 15 allows a comparison between the 2-dimensional analytical solution and the simulation of a Vlasov solver [68]. A Vlasov solver (see also [69]) avoids the problem of numerical noise in the simulation and automatically includes a nonlinear evolution of the instability which manifests itself in a folded phase space. This is not considered in the linear theory. Figure 15 shows a discrepancy in the results obtained with the two methods. Such studies, of general interest, are still in progress; the preliminary results indicate

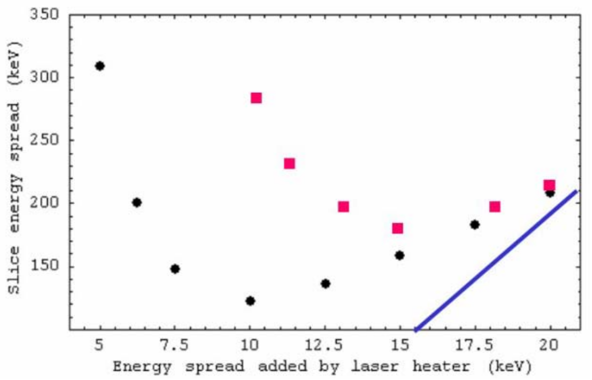

Figure 15. Rms slice energy spread in the final bunch for FERMI vs. the rms energy spread added by the laser heater at 100 MeV. Dots are the analytical prediction; squares are the results of the Vlasov solver. The solid line shows the expected energy spread in absence of any collective effect assuming a compression factor of 10 in linear approximation.

that the final prediction can often depend on details of the calculation.

CONCLUSIONS

The main effects on the electron beam quality by accelerating structures wake fields, CSR and LSC were reviewed in terms of the most relevant beam parameters for single pass FELs. This analysis points out the correlations between the 3 degrees of freedom of the electron dynamics in the accelerator generated by the wake fields.

A double magnetic compression results to be a suitable compromise to minimize instabilities induced by SC, longitudinal and transverse wake fields; at the same time, longitudinal wake field in the linac structures can be used to reduce the CSR effect in the second chicane.

Simultaneous control of the linearity in the longitudinal phase space and of the current profile can be achieved, under some approximations, by following the predictions of the reverse tracking. This technique forces the electron density distribution at the injector to cover an important role in formation of the electron bunches at the end of the accelerator. PI laser can be used to provide such suitable distribution for given wake potential; at the same time, special care has to be taken as for the emittance compensation scheme for unusual charge distributions exiting the photo-cathode.

A general prescription of low charge beam generation was investigated. Simulations demonstrate thatit brings several advantages in achieving a high beam quality; essentially, it reduces the effects of the accelerating structures wake fields, allows a compromise between slice and projected emittance growth, maximizes the current along the bunch.

Suppression of the microbunching instability was treated by mean of the single compression scheme, eventually joined with the reverse tracking, and of the laser heater. Implementation of the instability in 6-dimensional full s2e simulations is still work in progress. Nevertheless, recent results demonstrate the importance of shot noise as adriving term.

REFERENCES

[1] K. Bane, M. Sands, “Wakefields of very short bunches in an accelerating cavity”, SLAC-PUB-4441 (1987).

[2] K. Bane, “Short-range dipole wakefields in accelerating structures for the NLC”, SLAC-PUB-9663, LCC-0116 (2003).

[3] P. Craievich, T. Weiland, I. Zagorodnov, “The short-range wakefields in the BTW accelerating structure of the ELETTRA Linac, NIM A, **558**, 58 (2006).

[4] P. Craievich et al., “The accelerator design study for the FERMI FEL”, ST/F-TN-05/01 (2005).

[5] Y. Derbenev, J. Rossbach, E. Saldin, V. Shiltsev, “Microbunching radiative tail-head interaction”, TESLA-FEL 95-05 (1995).

[6] Y. Derbenev, V. Shiltsev, “Transverse effects of microbunch radiative interaction”, SLAC-PUB-7181 (1996).

[7] E. Saldin, E. Schneidmiller, M. Yurkov, “On the coherent radiation of an electron bunch moving in an arc of a circle”, NIM A, **398**, 373 (1997).

[8] M. Borland et al., NIM A, **483**, 268 (2002).

[9] E. L. Saldin, E. A. Schneidmiller, M. V. Yurkov, DESY Report No. TESLA_FEL-2003-02 (2003).

[10] T. Shaftan, Z. Huang, “Experimental characterization of a space charge induced modulation in high-brightness electron beam”, PRST-AB, **7**, 080702 (2004).

[11] K. Tian et al., “Experimental observation of longitudinal space-charge waves in intense electron beams”, PRST-AB, **9**, 014201 (2006).

[12] M. Huning, P. Piot, H. Schlarb, “Observation of longitudinal phase space fragmentation at the TESLA test facility free-electron laser”, NIM A, **475**, 348 (2001).

[13] S. Milton et al., Science **292**, 2307 (2001)

[14] C. Pellegrini, NIM A, **445**, 124 (2000).

[15] A. Tremaine et al., PRL **88**, 204801 (2002).

[16] R. Bonifacio, L. De Salvo Souza, E.T. Scharlemann, NIM A, **296**, 787 (1990).

[17] I. Ben-Zvi, K. M. Yang, L. H. Yu, NIM A, **318**, 726 (1992).

[18] L.H. Yu et al., Science, **289**, 932 (2000).

[19] G. Penn et al., Proc. of EPAC 2004, Lucern, Switzerland (2004).

[20] R. Gluckstern, PRD, **39**, 2780 (1989).

[21] “LCLS CDR”, SLAC-R-593 (2002).

[22] P. Craievich, S. Di Mitri, “Electron beam simulations for the FERMI project at Elettra”, Proc. of FEL 2004, Trieste, Italy.

[23] S. G. Biedron, S.V. Milton, and H.P. Freund, NIM A **475**, 401 (2001).

[24] T.Shaftan et al., Phys. Rev. E, **71**, 046501 (2005).
[25] W. Fawley, G. Penn, “Thoughts on Spectral Broadening Effects in FERMI and other FEL's Based upon Seeded Harmonic Generation”, ST/F-TN-06/07 (2006).
[26] M. Borland, APS LS-287 (2000).
[27] http://corona.physics.ucla.edu/~reiche/
[28] R. England et al., PRST-AB, **8**, 012801 (2005).
[29] P. Emma, “X-band RF harmonic compensation scheme for linear bunch compression in the LCLS”, LCLS-TN-01-1 (2001).
[30] K. Flottmann, T. Limberg, P. Piot, “Generation of ultrashort electron bunches by cancellation of nonlinear distorsions in the longitudinal phase space”, TESLA FEL 2001-06.
[31] P. McIntosh et al., “Realization of an x-band rf system for LCLS”, Proc. of PAC 2005, Knoxville, Tennessee
[32] A. Zholents et al., “Formation of electron bunches for harmonic cascade x-ray free electron lasers”, Proc. of EPAC 2004, Edinburgh, Scotland, UK.
[33] R. Talman, “Novel relativistic effect important in accelerators”, PRL, **56**, **14**, 1429 (1986).
[34] B. Carlsten, T. Raubenheimer, “Emittance growth of bunched beams in bends”, PRE, **51**, **2**, 1453 (1995).
[35] T. Limberg, P. Piot, E. Schneidmiller, “An analysis of longitudinal phase space fragmentation at the TESLA test facility”, NIM A, **475**, 353 (2001).
[36] M. Dohlus, A. Kabel, T. Limberg, “Uncorrelated emittance growth in the TTF-FEL bunch compression sections due to coherent synchrotron radiation and space charge forces”, Proc. EPAC 1998, Stockholm, Sweden.
[37] E. Saldin, E. Schneidmiller, M. Yurkov, “Klystron instability of a relativistic electron beam in a bunch compressor”, NIM A, **490**, 1 (2002).
[38] Z. Huang, K. Kim, “Formulas for coherent synchrotron radiation microbunching in a bunch compressor chicane”, PRST-AB, **5**, 074401 (2002).
[39] S. Heifets, S. Krinsky, G. Stupakov, “Coeherent synchrotron radiation instability in a bunch compressor”, PRST-AB, **5**, 064401 (2002).
[40] Z. Huang et al., “Suppression of microbunching instability in the linac coherent light source”, PRST-AB, **7**, 074401 (2004).
[41] M. Dohlus, T. Limberg, “Emittance growth due to wake fields on curved bunch trajectories”, NIM A, **393**, 494 (1997).
[42] P. Emma, R. Brinkmann, “Emittance dilution through coherent energy spread generation in bending systems”, SLAC-PUB-7554 (1997).
[43] P. Emma, “Issues and challenges for short pulse radiation production”, Proc. of EPAC 2004, Lucerne, Switzerland.
[44] D. Douglas, “Suppression and enhancement of CSR-driven emittance degradation in the IR-FEL driver”, JLAB-TN-98-012 (1998).
[45] J. Delayen, PRST-AB, **6**, 084402 (2003).
[46] J. Delayen, PRST-AB, **7**, 074402 (2004).
[47] P. Craievich, S. Di Mitri, “Emittance growth due to short-range transverse wakefields in the FERMI linac”, Proc. FEL 2005, SLAC, California, USA.
[48] G. Penco, private communications.
[49] K. Bane P. Emma, Proc. PAC 2005, Knoxville, Tennessee, (2005).
[50] M. Dohlus, T. Limberg, “Bunch compression stability dependence on RF parameters”, Proc. of FEL 2005, SLAC, California.
[51] J. Nodvick, D. Saxon, “Suppression of coherent radiation by electrons in a synchrotron”, PR, **96**, **1** (1954).
[52] R.Li, C.L. Bohn, J.J. Bisognano, Proc. Particle Accelerator Conference 1997, 1644 (1997).
[53] C. Limborg-Deprey, P. R. Bolton, LCLS-TN-04-16.
[54] C. Limborg-Deprey, Proc. of FEL 2005.
[55] H. Loos et al., Proc. of FEL 2005.
[56] S. Lidia, G. Penco, M. Trovo’, “Optimization studies of the FERMI@Elettra photoinjetor”, Proc. of EPAC 2006, Edinburgh, Scotland.
[57] M. Ferrario et al., SLAC-PUB-8400 (2000)
[58] S.B. Van der Geer et al., http://www.pulsar.nl/gpt/index/html.
[59] P. Craievich, S. Di Mitri, “Beam break-up instability in the FERMI@Elettra linac”, Proc. of EPAC 2006, Edinburgh, Scotland, UK.
[60] G. Andonian et al., “Observation of anomalously large spectral bandwidth ina high-gain self-amplified spontaneous emission free-electron laser”, PRL, **95**, 054801 (2005).
[61] G. De Ninno, W. Fawley, G. Penn, “Effect of Off-Axis Displacement Errors on FEL-1”, ST/F-TN-06/01 (2006).
[62] P. Tenenbaum, SLAC-TN-04-038 (2004).
[63] K. Bane, Proc. of EPAC 2004, Lucerne, Switzerland.
[64] P. Emma et al., “An optimized low-charge configuration of the linac coherent light source”, Proc. of PAC 2005, Knoxville, Tennessee.
[65] T. Limberg et al., “Optimized bunch compression system for the European xfel”, proc. Of PAC 2005, Knoxville, Tennessee, USA.
[66] A. Zholents, ST/F-TN-05/15
[67] A. Zholents, private communications
[68] M. Venturini, R. Warnock, and A. Zholents, “Development of a 2D Vlasov Solver for Longitudinal Beam Dynamics in Single-Pass Systems”, LBNL Report LBNL-60513.
[69] G. Bassi, J. A. Ellison, R. Warnock, “Progress on a Vlasov treatment of coherent synchrotron radiation from arbitrary planar orbits”, Proc. of PAC 2005.

STAIR-STEP TAPERED WIGGLER FOR HIGH-EFFICIENCY FEL *

D.C. Nguyen#, Los Alamos National Laboratory, Los Alamos, NM 87545, U.S.A.
H.P. Freund, Science Applications International Corp., McLean, VA 22102, U.S.A.

Abstract

A concept of a high-efficiency wiggler called the stair-step tapered wiggler is presented. The stair-step tapered wiggler consists of several uniform wiggler segments with decreasing wiggler periods (or decreasing a_w). The relatively large bucket in each wiggler segment enables a substantial fraction of the electrons to be captured, resulting in high extraction efficiencies. The stair-step tapered wiggler provides other advantages, such as ease of fabrication and flexibility in the taper rate. Numerical simulations using MEDUSA will be presented to show the high-efficiency performance of a representative FEL with a stair-step tapered wiggler.

INTRODUCTION

The FEL is known for its wavelength tunability and scalability to high power. However, the extraction efficiency, defined as the FEL power divided by the electron beam power, can be low, with typical values around 1%. The low extraction efficiency increases the requirements for the electron beam's average power and puts stringent demands on the high-power RF systems driving the accelerators. One way to increase the extraction efficiency is through the use of tapered wigglers. Most tapered wigglers are continuous, *i.e.* the periods (λ_w) or dimensionless field (a_w) decreases continuously to maintain the resonance condition,

$$\gamma_R = \sqrt{\frac{\lambda_w}{2\lambda}\left(1+a_w^2\right)}\,, \tag{1}$$

where γ_R is the resonance Lorentz factor; and λ is the wavelength.

Continuously tapered wigglers are only optimized for a narrow range of input radiation intensities and wavelengths. For an oscillator FEL, extraction efficiencies as high as 4.6% inside the resonator have been achieved but the efficiency outside the optical cavity is not significantly higher than that of a uniform wiggler [1].

In this paper, we discuss a different concept of tapering to achieve high extraction efficiency using a series of uniform wigglers. Our approach is an extension of the compound wiggler [2], also known as the step-tapered wiggler [3]. In our approach, a long uniform wiggler is used to bunch the electrons longitudinally and a number of short uniform segments with decreasing the wiggler periods (Fig. 1) or increasing the gaps between the magnets (Fig. 2) are used to extract the energy from the electrons as they execute synchrotron oscillations inside the ponderomotive potentials.

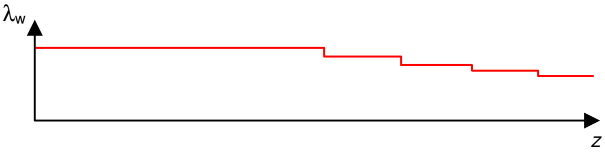

Figure 1: Plot of wiggler period versus z in a stair-step tapered wiggler with taper in wiggler period.

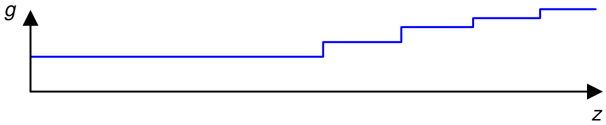

Figure 2: Plot of gaps between magnets versus z in a stair-step tapered wiggler with taper in magnetic field.

THEORY

In a uniform wiggler, the FEL extraction efficiency is the product of the capture efficiency (η_c) and the height of the bucket, as given by [4]

$$\eta = 2\eta_C\sqrt{\frac{a_w a_s}{1+a_w^2}}\quad , \tag{2}$$

where the term in the radical denotes the half-height of the bucket, and a_s the dimensionless optical field, is proportional to the square root of the optical intensity, I_s

$$a_s = \frac{e\lambda\sqrt{2Z_0 I_s}}{2\pi mc^2} \tag{3}$$

where e is electronic charge, Z_0 impedance of free space, m electron mass, and c speed of light.

As the electrons interact with the high optical intensity, they undergo synchrotron motion in the first uniform wiggler and, after becoming trapped, rotate to the bottom of the bucket. With a judicious combination of λ_w and a_w (see Eq. 1), the resonance energy of the next uniform wiggler segment can be lowered such that the electrons are at the top of the bucket of the new wiggler segment (Fig. 3). The electrons that are trapped in the bucket of the new segment now undergo synchrotron motion in this bucket to an even lower energy. The step-tapered wiggler efficiency is the sum of the first and second segments' efficiencies.

$$\eta = 2\eta_{C1}\sqrt{\frac{a_{w1}a_{s1}}{1+a_{w1}^2}} + 2\eta_{C2}\sqrt{\frac{a_{w2}a_{s2}}{1+a_{w2}^2}} \tag{4}$$

---

*Work supported by the Office of Naval Research and the High-Energy Laser Joint Technology Office. Author email: dcnguyen@lanl.gov

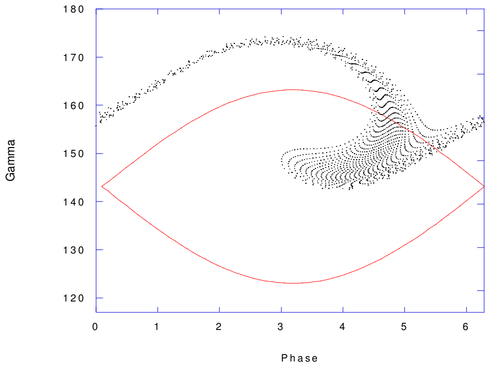

Figure 3: Longitudinal phase space of electrons at the transition between the first and second wiggler segment. The red line denotes the separatrix of the second wiggler.

The indices 1 and 2 in Eq. 4 correspond to the first two wigglers, respectively. The typical efficiency for a two-segment step tapered wiggler is twice that of a uniform wiggler, *i.e.* 2%. If there are n segments, then the efficiency can be increased n-fold. The limit in how far we can taper the wiggler is due to a steady reduction in the capture efficiency in each subsequent bucket, and in the induced energy spread. This is due to the non-adiabatic transitions from one segment to the next. However, since the bucket heights are large, it is possible to maintain high capture efficiency, and thus high extraction efficiency.

SIMULATION

We use the three-dimensional code MEDUSA [6,7] to model a seeded FEL amplifier with a stair-step tapered wiggler and a comparable linearly tapered wiggler. Table I summarizes the FEL and beam parameters used in the MEDUSA simulations. These parameters are chosen for a 1.05-micron wavelength where high-power seed lasers exist. Both wigglers are of a conventional permanent-magnet design with parabolic pole faces to provide equal two-plane, sextupole focusing. The first wiggler segment is the same for both linear and stair-step tapered wigglers. With an input power of 10^6 W (1 μJ pulse energy and 1 ps FWHM, for instance) the first wiggler saturates in 1.83 m. The subsequent wiggler segments are different for the two cases. For the linear taper, it has one 2.44-m long continuously tapered segment with a field taper rate of 0.48 kG per meter of wiggler length. For the stair-step taper, there are four short uniform wiggler segments, each with a smaller a_w. These wiggler segments can be short because the electrons are already bunched at the entrance of these segments. The pre-bunched electrons radiate power immediately and the electrons execute the synchrotron motion to the bottom of the bucket in each wiggler segment. For these simulations, the electron beam is matched in the wiggler. It is conceivable that a scalloped beam could be used to enhance the FEL interaction and/or to pinch the optical beam [5].

Table 1: MEDUSA simulation parameters and results.

Parameters	**Values**
Beam energy	80.8 MeV
Peak current	1000 A
Emittance	10 mm-mrad
Energy spread	0.25%
Wiggler period	2.18 cm
Wavelength	1.052 µ
First wiggler segment a_w	1.187
First wiggler segment length	1.831 m
Second wiggler segment a_w	1.159
Second wiggler segment length	0.698 m
Third wiggler segment a_w	1.116
Third wiggler segment length	0.567 m
Fourth wiggler segment a_w	1.058
Fourth wiggler segment length	0.523 m
Fifth wiggler segment a_w	1.007
Fifth wiggler segment length	0.654 m
Linear taper segment length	2.44 m
Linear taper rate	0.48 kG/m
Input power (peak)	1 MW
Stair-step taper output power (peak)	3.6 GW
Stair-step taper efficiency	4.5%
Linear taper output power (peak)	3.5 GW
Linear taper efficiency	4.4%

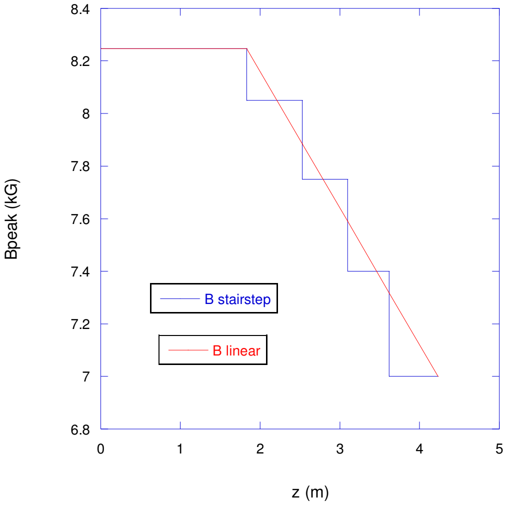

Figure 4: Plots of magnetic field versus distance along the wiggler for the linear (red) and stair-step (blue) tapered wigglers.

The MEDUSA simulation results are shown in Fig. 5. The stair-step and linear tapered wigglers achieve peak powers of 3.6 and 3.5 GW, respectively, corresponding to extraction efficiencies of 4.5% and 4.4%. While the FEL power grows continuously for the linear taper wiggler, the FEL power growth curve in the stair-step taper wiggler exhibit plateau regions in between segments. This is not due to a lack of wiggler magnets in the transition regions (there are no gaps in the stair-step wiggler). Rather, these plateaus are needed to rotate the electrons in the bucket so that they enter the next bucket in the correct phase of the synchrotron oscillation period. It is worth noting that the FEL peak power increase is approximately 0.7 GW per wiggler segment, and the extraction efficiency of the five-segment stair-step tapered wiggler is about 5 times that of the uniform wiggler.

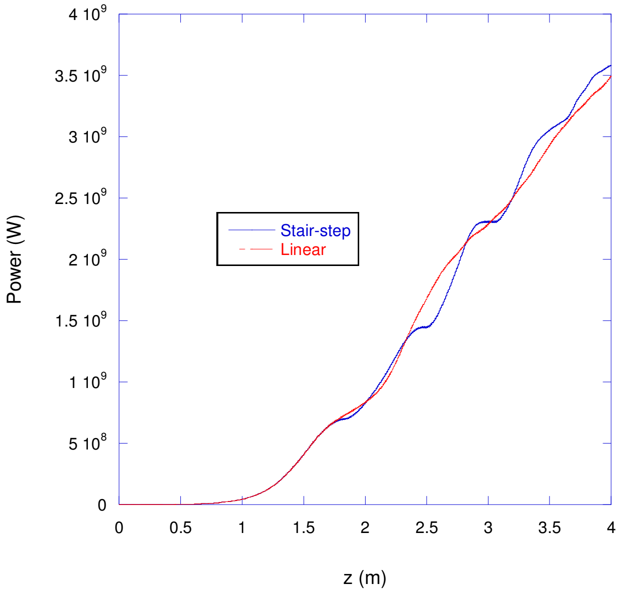

Figure 5: Plots of power versus distance for the linear (red) and stair-step (blue) tapered wigglers.

An important consideration in designing any high-efficiency wiggler is the energy spread in the electron beam exiting the wiggler. For energy recovery linac, it is necessary to minimize the energy spread of the spent electron beam so that one can transport the electron beam back through the linac for energy recovery. To this end, we plot the energy distributions of the electrons exiting the linear taper (red) and stair-step taper (blue) wigglers in Fig. 6. While the linear taper has a double-humped distribution with most electrons localized near the injected energy and maximum decelerated energy, the stair-step taper has electrons distributed in multiple peaks within the same energy bandwidth. The full energy spread for both tapered wigglers is 13%, three times the extraction efficiency of 4.5%. This energy spread is presently outside the 8% energy acceptance of the energy recovery linac [8]. However, we expect a reduction in electron energy spreads will be realized with further optimization of the stair-step tapered wiggler.

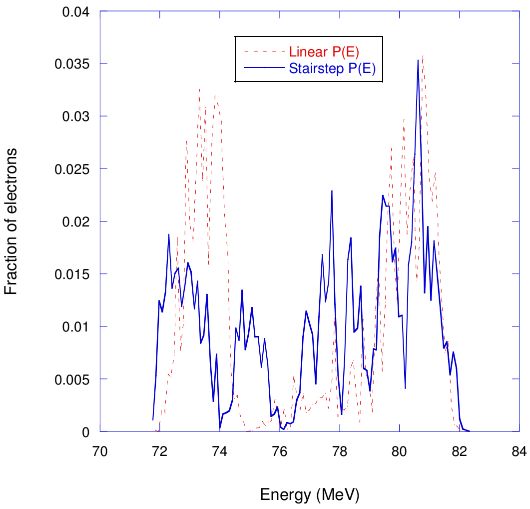

Figure 6: Energy distribution of electrons exiting the stair-step tapered wiggler.

SUMMARY

We have studied a different approach to high-efficiency wiggler called the stair-step tapered wiggler. The stair-step wiggler consists of uniform wigglers with decreasing magnetic fields (or wiggler periods) to extract power from a decelerated electron beam. MEDUSA simulations show the performance of the stair-step tapered wiggler is the same as that of a comparable linear tapered wiggler. For a representative example of an infrared FEL, the peak power (and extraction efficiency) that can achieved with a five-segment stair-step tapered wiggler is five times that of a uniform wiggler. The full energy spread of the electron beam exiting the stair-step wiggler is three times the extraction efficiency.

ACKNOWLEDGMENT

We thank Luca Giannessi for valuable assistance in programming a one-dimensional FEL code.

REFERENCES

[1] D. Feldman et al., Nucl. Instrum. Meth. A285 (1989) 11-16.

[2] R.W. Warren and D. Piovella, Nucl. Instrum. Meth. A304 (1991) 696.

[3] J. Blau *et al.*, Nucl. Instrum. Meth. A483 (2002) 148.

[4] C.A. Brau, Free Electron Lasers, Academic Press, Oxford (1990).

[5] D.C. Nguyen, H.P. Freund, and W. Colson, Phys. Rev. ST-AB 9 (2006) 050703.

[6] H.P. Freund, S.G. Biedron, and S.V. Milton, IEEE J. Quantum Electron. 36 (2000) 275.

[7] H.P. Freund, Phys. Rev. ST-AB 8 (2005) 110701.

[8] L. Merminga, D.R. Douglas and G.A. Krafft, Annu. Rev. Nucl. Part. Sci., 53 (2003) 387-429.

PRECISION MEASUREMENT OF THE UNDULATOR K PARAMETER USING SPONTANEOUS RADIATION [*]

J. Welch[†], J. Arthur, P. Emma, J. Hastings, Z. Huang, H.-D. Nuhn, P. Stefan,
SLAC, Stanford, CA 94309, USA
R. Dejus, B. Yang, ANL, Argonne, IL 60439, USA
R. Bionta, LLNL, Livermore, CA 94550, USA.

Abstract

Obtaining precise values of the undulator parameter, K, is critical for producing high-gain FEL radiation. At the LCLS [1], where the FEL wavelength reaches down to 1.5 Å, the relative precision of K must satisfy $(\Delta K/K)_{rms} \lesssim 0.015\%$ over the full length of the undulator. Transverse misalignments, construction errors, radiation damage, and temperature variations all contribute to errors in the mean K values among the undulator segments. It is therefore important to develop some means to measure relative K values, after installation and alignment. We propose a method using the angle-integrated spontaneous radiation spectrum of two nearby undulator segments, and the natural shot-to-shot energy jitter of the electron beam. Simulation of this scheme is presented using both ideal and measured undulator fields. By 'leap-frogging' to different pairs of segments with extended separations we hope to confirm or correct the values of K, including proper tapering, over the entire 130-m long LCLS undulator.

INTRODUCTION

Several methods have been proposed to measure *in situ* undulator K differences by alternately comparing spontaneous radiation spectra from two undulator segments [2]. We are looking into the possibilities of using the combined radiation spectrum produced by two nearby segments.

The first harmonic peak of the on-axis spontaneous radiation energy spectrum from a single undulator has a bandwidth equal to the inverse of the number of periods. The combined radiation from two such undulators has a bandwidth that is narrower by a factor of two. Compared with a single undulator, combined undulators produce twice the number of photons in half the bandwidth, so the spectrum has four times the peak height and therefore eight times steeper slopes. Integrating the spectrum over angles about the beam axis produces a complication, since the off-axis undulator spectral peak shifts to lower energy. Such integration causes the low-energy edge to extend lower by an amount depending on the integration angle, but the high-energy edge will remain stationary, though the slope becomes somewhat less steep. Based on a far-field undulator radiation formula, angle-integrated spectra are calculated for one, and two identical undulators without any phase error between them, and shown in Figure 1.

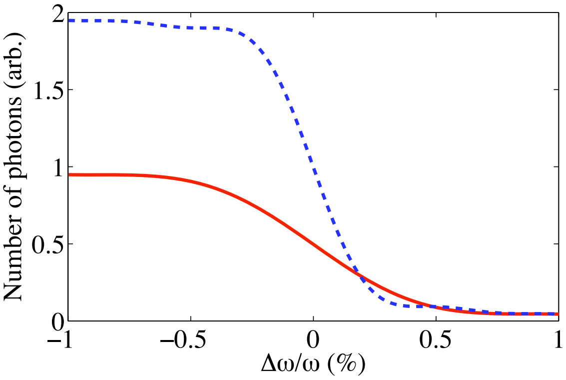

Figure 1: Angle-integrated spectra of a single undulator (solid-red) and two identical undulators (dashed-blue).

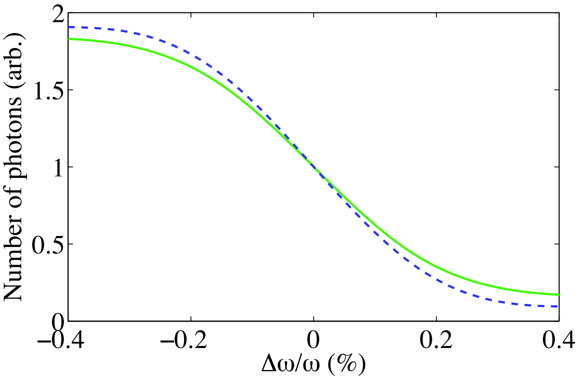

Figure 2: High-energy edge of spectrum for two cases: identical K (dashed-blue), and $\Delta K/K = +0.2\%$ (solid-green).

If the two undulators have different mean values of K, the slope of the high-energy spectrum edge will be reduced, depending on the relative difference, $\Delta K/K$. Figure 2 shows the high-energy edge of the angle-integrated spectrum of two undulators for two cases: identical K, and $\Delta K/K = +0.2\%$. As clearly shown, the slope of the high-energy edge of the spectrum is sensitive to the relative K differences of two adjacent undulators (phase errors will be addressed below). In this figure the left-right spectrum shift, $-\frac{K^2}{1+K^2/2}(\Delta K/K)$, has been subtracted off to allow

---

[*] This work is supported by the U.S. Department of Energy, contract DE-AC02-76SF00515, and was performed under the auspices of the U.S. Department of Energy, by University of California, Lawrence Livermore National Laboratory under Contract W-7405-Eng-48, in support of the LCLS project at SLAC.

[†] Welch@SLAC.Stanford.edu

more convenient comparison of the slopes at $\Delta\omega/\omega = 0$.

The LCLS undulator consists of 33 almost identical segments, each 3.4 m long. Each segment is provided with "roll-away" capability; and can be independently displaced up to 8 cm horizontally, effectively turning it 'off'. The segments are also constructed with a 4.5 mrad cant angle of the poles, which allows K-value adjustment by small horizontal displacements (about 1.5 mm per 0.1%), using the same "roll-away" mechanism. If the slope of the high-energy edge of the spectrum is measured with sufficient precision as a function of the horizontal displacement, (equivalent to scanning $\Delta K/K$), two undulator K values can be set equal within the required precision (0.015%), and this relative correction might be applied repetitively over the full 130-m undulator to adjacent, or nearly adjacent, segment pairs.

METHOD

The method proposed here requires retracting all but two adjacent, or nearly adjacent, undulator segments from the beamline so that all x-rays detected come only from the segments under test. The electron trajectory must then be brought to essentially beam-based alignment quality, so that the kinks in the trajectory between segments are less than 1μrad. Beam-based alignment is done by mechanically moving the quadrupoles to obtain a dispersion-free trajectory. The quadrupoles are mechanically tied to the undulator segments and both move together, so this step also insures that the undulator segments are brought vertically to within about 100 μm of the ideal position before starting.

On each machine pulse, a small portion of the x-ray spectrum is sampled in the region of the high-energy edge of the first harmonic, using a silicon crystal spectrometer, set for diffraction at a fixed Bragg angle from the (111) crystal planes. (The LCLS electron beam-angle jitter should be $< 1\mu$rad, which is small compared to the Darwin width of the crystal reflection.) As a result of the natural electron energy jitter ($\sim 0.1\%$ rms), the photon spectrum is randomly sampled. The electron energy jitter is measured on each pulse (see below) and the inferred photon energy shift is then associated with the detector data; the underlying spectrum is then reconstructed by plotting the detector data against the inferred photon spectrum shift.[1]

About 100 pulses will be needed to reconstruct a spectrum. After a spectrum is collected in this manner for a given arrangement of two adjacent undulator segments, the K value of the second undulator is changed by 0.05% by translating it $\Delta x = 0.75$ mm, and then a new spectrum is obtained. This process is repeated for 9 separate K values, ranging over about $\pm 0.2\%$.

The electron energy jitter is precisely measured by two beam position monitors (BPMs) located upstream of the undulator, at points of high horizontal momentum dispersion. The BPMs are separated in betatron phase advance by 2π and have opposite sign dispersion, such that the difference in their position readback values is proportional to the relative electron energy variation and completely insensitive to incoming betatron oscillations. With dispersion of ± 125 mm at each BPM, and a 5-μm rms single-pulse position resolution, the relative electron energy resolution is $(5\ \mu\text{m})/(125\ \text{mm})/\sqrt{2} \approx 3\times 10^{-5}$, and the corresponding photon energy resolution is twice this, or 6×10^{-5}.

Since the spectrum shifts towards $\Delta\omega/\omega > 0$ for $\Delta K/K < 0$ (see Fig. 3), the data tends to be poorly centered on the spectrum edge for $\Delta K/K \neq 0$. To improve resolution, we adjust the mean electron energy by $-\frac{K^2}{1+K^2/2}(\Delta K/K)$ for each new setting so that the energy always varies around the center of the edge. These small adjustments are possible using the BPM-based feedback loop, which maintains the desired average electron energy, but cannot remove the random pulse-to-pulse jitter.

The slope of each high-energy spectrum edge is found by fitting the data for each K value. The Δx at which the slope is steepest corresponds to equal K values in the two segments. At a 10 Hz machine rate, this process will require 90 seconds, plus the time required to translate the undulators nine times, for a total of about 4 minutes per undulator pair. A description of a simulation of this process, including realistic errors, follows.

SIMULATION

A simulation is performed using a computer-generated, two-undulator, spectrum integrated over all angles, at nine values of $\Delta K/K$: (-0.2% to $+0.2\%$ in steps of 0.05%). To simulate measured data, the perfect, computer-generated spectrum is sampled at random values of twice the electron energy error ($\Delta\omega/\omega = 2\Delta E/E$). The electron energy varies randomly in a Gaussian distribution with 0.1% rms. In practice, either the average electron beam energy or the Bragg angle can be adjusted to best center the data on the high-energy edge of the spectrum.

A cubic spline is used to interpolate the computer-generated spectrum for each randomly selected energy. An error of 6×10^{-5} rms is added to the photon energy to account for the BPM-based electron energy measurement resolution. An error is also added to the number of photons detected at that energy, assuming the bunch charge randomly varies from pulse to pulse, but a toroid charge monitor, capable of resolving the relative charge variation to within 0.5% rms, is used to normalize the data. In addition, the beam angle is assumed to vary by 0.5μrad rms (one-half the nominal rms beam divergence), adding another source of undetermined energy error based on small variations of the Bragg angle. Detector noise is also added assuming a noise level of 100 photons with respect to the the peak signal of 10^5 photons. And finally, a photon statistics error is included, which is proportional to the inverse square-root

---

[1] Electron energy loss from radiation is $\leq 0.005\%$ per segment and will be taken into account in setting the appropriate K values. Wakefield losses are expected to be even less. Both types of energy losses are ignored in the following discussion.

Table 1: Simulation parameters.

Parameter	**symbol**	**value**	**unit**
e^- energy	E_0	13.6	GeV
bunch charge	q	1.0	nC
undulator parameter	K_0	3.50	
fund. wavelength	λ_r	1.5	Å
Bragg spacing (111)	d	3.14	Å
Bragg angle (111)	θ	13.8	deg
rel. e^- energy jitter	$(\Delta E/E)_{rms}$	0.1	%
e^- energy meas. res.	$(\Delta E/E)_{res}$	0.003	%
bunch charge jitter	$(\Delta q/q)_{rms}$	2	%
charge meas. res.	$(\Delta q/q)_{res}$	0.5	%
e^- angle jitter	θ_{rms}	0.5	μrad
detector noise level	N_γ^{noise}	100	photons
peak signal	N_γ^{pk}	10^5	photons

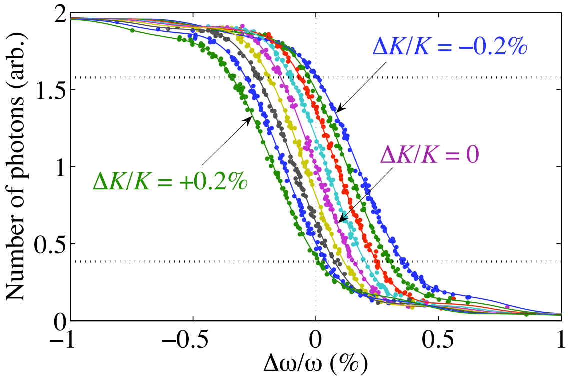

Figure 3: High-energy spectrum edge for each of nine values of $\Delta K/K$: (-0.2% to $+0.2\%$). Solid curves are perfect spectra and plot points are simulated noisy data.

of the number of photons detected in each pulse. Table 1 lists the simulation parameters.

Figure 3 shows the perfect, computer-generated spectrum for each of nine values of $\Delta K/K$ as solid curves, and the simulated, imperfect data as points randomly sampled on the frequency axis due to electron energy jitter. The scatter of the data points with respect to the curves is due to the various sources of error, such as BPM resolution, charge measurement resolution, unmeasured beam angle jitter, detector noise levels, and photon statistics, as described above.

The data shown in Fig. 3 must now be used to determine the slope of the high-energy spectrum edge for each value of $\Delta K/K$. The method used here is to fit the core of the data, which is between 15-20% below the signal peak and 15-20% above the signal minimum (see horizontal cut lines in Fig. 3), with a 3rd-order polynomial and solve for the steepest slope. The fitted polynomial form is

$$N = N_0 + a(\Delta\omega/\omega) + b(\Delta\omega/\omega)^2 + c(\Delta\omega/\omega)^3. \quad (1)$$

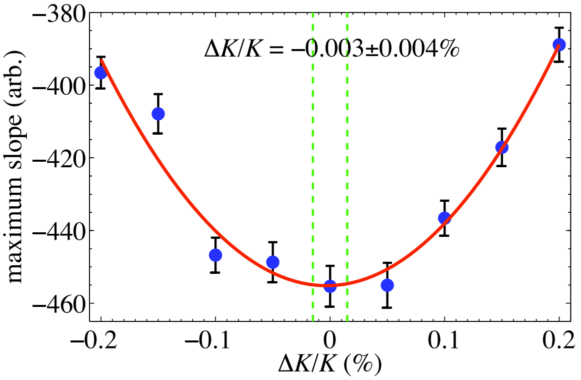

Figure 4: Maximum negative slope vs. $\Delta K/K$. Any $\Delta K/K$ error is resolved to within $\pm 0.004\%$. The goal of $|\Delta K/K| < 0.015\%$ is shown as vert. green lines.

This steepest slope (inflection point) on the cubic-fitted curve is then

$$\left(\frac{dN}{\Delta\omega/\omega}\right)_{max} = a - \frac{b^2}{3c}. \quad (2)$$

The nine determined steepest slopes of Eq. (2) are then plotted versus $\Delta K/K$, which is taken from the deliberate undulator displacements, Δx, and the known pole cant angle. The data is fitted to a simple parabolic curve in order to find the minimum. Figure 4 shows this plot where the steepest slope is found at $\Delta K/K = -0.003\%$, with a statistical error of $\pm 0.004\%$, well within the goal of 0.015%. The error bars are the propagated statistical errors, from the cubic fit, through each evaluation of Eq. (2).

Similar estimations are repeated for simulated radiation spectra using magnetic measurements from the real, imperfect prototype undulator. A systematic $\Delta K/K$ error of up to 0.008% is seen in this case, which is not fully understood, but is still within the required acceptance. It should be noted that the prototype is of lower magnetic quality than the first few production undulators.

In addition to statistical errors and imperfect undulators, the possibility also exists for a relative phase error between the two interfering undulators. Simulations were run for phase errors of 20 and 70 degrees. For reference, the maximum allowable net error within LCLS undulator specifications is 20 degrees. The 20 degree error has no significant impact on the result. The 70 degree error shown in Fig. 5, clearly affects the data, but the effect can be excluded from the fit if the lower data cut level is set no lower than 20%

DISCUSSION

Beam Angle and Alignment Systematics

There are two kinds of alignment errors that, when combined, can in principle lead to significant error in the measured $\Delta K/K$. One is a change in the electron beam angle

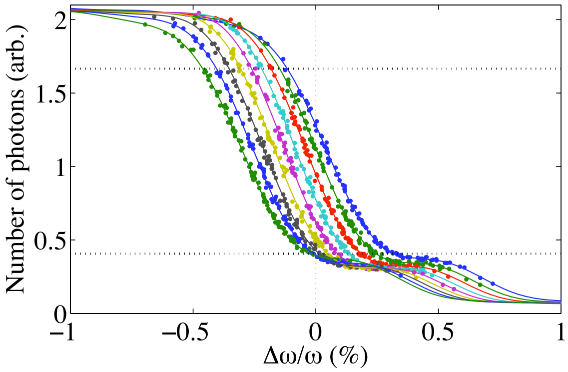

Figure 5: High-energy, two-undulator spectrum edge for 9 values of $\Delta K/K$ with a 70-degree relative phase error.

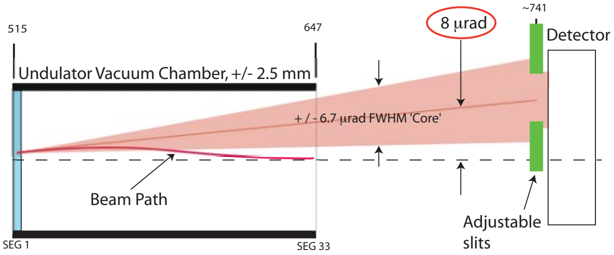

Figure 6: The 'core' synchrotron radiation will start to scrape off on the vacuum chamber if the central angle is greater than 8 μrad.

between segments (non-straightness). The other is a misalignment, with respect to the central ray of the beam, of the effective aperture (usually the vacuum chamber) which defines the angular distribution of photons detected.

Synchrotron radiation produced by undulator segments has a strong angle/energy correlation, whereby the spectrum is shifted to lower energy for finite angles between the central ray and the observation point. Theoretically, in the method presented above, the spectrum is integrated over all angles, so the measured spectrum should not change if there are alignment errors — all photons are collected. However, in practice the range of angular integration is limited by the vacuum chamber aperture, especially for the first segments, where there is only $\pm 20(32)$ μrad vertical(horizontal) acceptance, assuming a perfect chamber and a perfectly aligned beam.[2] The angle-energy correlation implies that, in part, the alignment of the aperture with respect to the central ray determines the spectrum of photons that pass through.

The FWHM angular spread for the resonant photon energy is $\pm 6.7\mu$rad. It is representative of the core angular size over which photons contribute to the high-energy edge of the spectrum. Figure 6 shows that beam angles of more than about ± 8 μrad will result in scraping ofthe core x-rays by the vacuum chamber. However, this situation will result in an error in the $\Delta K/K$ measurement only if there is also a change in beam angles between the segments being measured, because otherwise the effect would be the same for both segments.

We plan to avoid this error by using beam-based alignment, which will reduce the residual segment-to-segment angles to order 1μrad or less. In addition, we plan to check where the central ray is by scanning a 1 mm^2 'pinhole' aperture and finding the position that maximizes the average photon energy. If necessary, the beam orbit can be adjusted so that the central ray passes comfortably through the aperture so that no scraping of the core will occur.

Leap Frogging and Near Field Effects

The proposed method gives a measurement of the relative difference in K values between two nearby undulator segments. The complete undulator is composed of 33 segments and is 130 m long, with the last segment about 100 m from the detector. Simple pairwise measurement of adjacent segments builds up the expected error between the first and last segment by a factor of $\sqrt{33}$. By 'leap frogging' over two segments, only 11 measurements are needed to connect the first and last segments so the relative error between them would be $\sqrt{11}$ times more than the individual measurement error. If two segments are skipped, the phase difference that results from the missing segments can be adjusted using a closed orbit bump. Skipping more segments would tend to further reduce the error build-up. However, as the distance between the segments being measured increases, the possibility of significant electron trajectory angle errors increases as well. Also near-field effects can start to appear. The optimum strategy will become apparent during measurement.

In the theoretical model of the undulator segments, it is implicitly assumed that the observation angle from the beam to the detector is the same for the two segments, i.e., the detector is in the far-field of the spontaneous radiation. If the distance between segments is comparable with the distance to the detector, then the observation angles will be significantly different and the detector will see a red-shifted spectrum from the nearer segment. For the LCLS, segment spacing 10 m or less (roughly consistent with skipping over two segments) can be considered to be the far-field case.[3]

REFERENCES

[1] LCLS Conceptual Design Report, SLAC-R-593 (2002), http://www-ssrl.slac.stanford.edu/lcls/cdr/.

[2] www-ssrl.slac.stanford.edu/lcls/undulator/meetings/2005-11-14_bbkm_workshop/ The web page contains several relatively recent talks on the topic of *in situ* K measurement.

---

[2] The angular acceptance of the detector, when properly aligned, is assumed to be larger than the angular acceptance of the vacuum chamber.

[3] Differences in angle of less than 1μrad have negligible effect on the the measured spectrum. If the integration of radiation from one segment is over ± 15 μrad then a difference in the integration angle of 1μrad for the other segment corresponds to a segment spacing on the order of 10 m or three segments.

TEMPORAL ANALYSIS AND SHAPE CONTROL OF UV HIGH ENERGY LASER PULSES FOR PHOTOINJECTORS*

D. Garzella†, O. Gobert, Ph. Hollander, F. Lepetit, M. Perdrix
Commissariat à l´Energie Atomique (CEA-France)
T. Oksenhendler
FASTLITE, Ecole Polytechnique, Palaiseau (France).

Abstract

This work shows a survey of the studies conceived for obtaining Ultraviolet, high energy laser pulses, totally controlled and characterized in shape, on the kHz, Chirped Pulse Amplification (CPA)-based Ti:Sa laser system PLFA at CEA-Saclay. The pulse shaping deals with the amplitude and phase control of the stretched laser pulses issued from an amplifier before entering the compressor and the tripling unit. The work presents the theoretical background and the proposed experimental setup, before showing the preliminary promising results.

INTRODUCTION

In order to generate high power, subpicosecond XUV radiation by following the classical Self Amplified Spontaneous Emission (SASE) scheme [1, 2] and/or seeded FELs [3, 4, 5, 6, 7], tight specifications on the electron bunch are required, noteworthy in terms of highly reduced emittance, both for achieving very short wavelength or high average power, thus high duty cycle continuous electron beams (repetition rates ≥ 1 kHz). Even though emittance compensation schemes [8] are used, or ”RF-focusing” ones [9] for superconducting RF photo-injectors, for obtaining high brightness electron bunches, the laser pulses impinging onto the photocathode must meet special requirements not only in terms of wavelength and delivered energy per pulse. High repetition rate systems like the one retained for photo-injector operation at Arc-en-Ciel [10] will have to fulfil the following requirements:

- Up to $50\ \mu$J pulse energy in the UV (following the cathode material work function, between 240 and 300 nm), for a $1\ n$C electron bunch production on a photocathode with $\rho \approx 0.1 - 1$% quantum efficiency (QE) (as in the case of the most commonly used semiconductor Cs_2Te). This calls, before a very highly efficient third harmonic generation, for laser amplifiers delivering at least $1\ m$J in the IR ($800\ n$m), and, for high repetition rates, on Chirped Pulse Amplified (CPA), Ti:Sa based systems.

- A final duration in the UV, before the cathode, between 5 and $20\ p$s [10].

- A precise measurement and control of longitudinal and transverse features (dimensions and shape) in order to prevent non-linear contribution to the emittance increase.

Indeed, it has been shown [11, 12] that in order to minimize the bunch emittance at the issue of the electron gun, temporally and spatially shaped UV pulses are needed to prevent non linear space charge forces and then minimize the electron emittance. Shaping techniques for ultrashort laser pulses (in the sub-ps range) are well known. In transverse space an homogeneous energy distribution with a circular symmetry is needed. This can be obtained by use of mask filters or deformable mirrors and lenses. In longitudinal space, shaping techniques are mostly based on the utilisation of spatial masks, in some cases by using programmable liquid crystals structures at the fourier plane of a $4f$ zero-dispersion line [13], or by using an Acousto-Optic Programmable Dispersive Filter (AOPDF), or DAZZLER [14]. Both techniques have been already used in the framework of accelerator and FEL studies [15, 16]. In the EUROFEL program framework, our goal is to obtain a few picosecond, $100\ \mu$J laser pulses in the UV ($266\ n$m) with a totally controlled and characterized longitudinal and transversal shape. This work presents the experimental setup and the main diagnostics designed to obtain every desired pulse shape from the ”beer can” profile (corresponding to a cylindrical bunch in the 3D-space) to a parabolic one (”waterbag” bunch distribution) starting from the IR ultrashort pulse issued by the kHz, Chirped Pulse Amplification (CPA)-based Ti:Sa laser system PLFA (French acronym for Tunable Laser Femtosecond Platform) [17] at CEA-Saclay. The pulse manipulation is based on the amplitude and phase control of the stretched laser pulses issued from the amplifier, which is performed by the DAZZLER before entering the compressor and the tripling unit.

FEMTOSECOND LASER PULSES

Direct temporal manipulation of an ultrashort laser pulse is rather complicated. Thanks to Fourier Analysis, every temporal feature of a laser pulse has its corresponding one in the frequency domain. Thus, an ultrashort pulse in time space exhibits a very broadband spectrum (several tens of nm). The electric field $\widetilde{E}(\omega,\phi)$ can be described in terms of the spectral components of amplitude $E_0(\omega)$ and phase $\phi(\omega)$:

---

* This work has been supported by the EU Commission in the Sixth Framework Program, Contract No. 011935 - EUROFEL.

† david.garzella@cea.fr

$$\widetilde{E}(\omega, \phi) = E_0(\omega) \cdot e^{i(\omega_0 t + \phi(\omega))} \tag{1}$$

$$\phi(\omega) = \phi_0 + (\omega - \omega_0) \cdot \left.\frac{\delta\phi}{\delta\omega}\right|_{\omega_0} + \frac{(\omega - \omega_0)^2}{2} \cdot \left.\frac{\delta^2\phi}{\delta\omega^2}\right|_{\omega_0} \\ \ldots + \frac{(\omega - \omega_0)^n}{n!} \cdot \left.\frac{\delta^n\phi}{\delta\omega^n}\right|_{\omega_0} \tag{2}$$

In the polynomial approximation of the phase term (eq. 2), the constant and the first order term coefficient, called respectively the ”absolute” phase and the group delay, are not crucial for the propagation of the pulse, as they account respectively for the position of the peak amplitude of the field in the phase and the delay undertaken by the central frequency component $E_0(\omega_0)$ propagating between two reference planes [18]. The second-order term coefficient becomes extremely interesting for pulse manipulation as it accounts, for example, for the different response of the frequency components to the propagation of the pulse in a ”dispersive” medium. Thus, an original transform-limited laser pulse will be stretched by a factor $\propto \left.\frac{\delta^2\phi}{\delta\omega^2}\right|_{\omega_0}$. Higher order terms account for symetric and antisymetric distortion terms of the pulse shape.

EXPERIMENT

Pulse Shaping Technique

The principle of the AOPDF [14] is based on the coupling between the laser pulse and an acoustic wave in a birefringent crystal. For IR laser pulses, around $800\ n$m, a TeO_2 crystal is cut in such a way that the acoustic wave energy and the optical waves energy travel along the same axis. The incident optical pulse polarized on the ordinary axis is diffracted by the Bragg grating made by the acoustic wave onto the extraordinary axis. Shaping the pulse is equivalent to programmming the associated suite of acoustic grating, so that the spectral amplitude and phase of the laser pulse is directly linked to the acoustic wave ones.

Target, Filter and Correction Loop

Defining a ”target” pulse here means defining ”target” spectral amplitude and phase. As the DAZZLER is a linear filter, the output optical pulse is the product of the input pulse by the filter response in the spectral domain:

$$\widetilde{E}_{out}(\omega, \phi) = \widetilde{E}_{in}(\omega, \phi) \cdot \widetilde{S}(\omega, \phi) \tag{3}$$

where $\widetilde{S}(\omega, \phi)$ is the filter response.

Therefore, knowing the input pulse, the target pulse is directly obtained by fitting the filter response (see fig. 1). The spectral amplitude and phase shapings can be separated as they are independently measured and controlled.

In practice, amplitude loop preceeds phase loop because of bandwidth limitation. The complete procedure can be described as the following steps:

1. The user builds the target amplitude and phase terms.
2. Amplitude loop:
   - Initial filter amplitude.
   - spectrum measurement.
   - Modification of the filter by dividing the ”target” amplitude by the measured amplitude.
   - spectrum measurement ... loop until the measurement fits the ”target”.
3. Phase Loop: Analog process is made on the ”target” phase.
4. Experimental amplitude and phase are acquired and an initial check in the time domain is made by IFT on the experimental data, thus retrieving the temporal duration and shape (fig. 2).

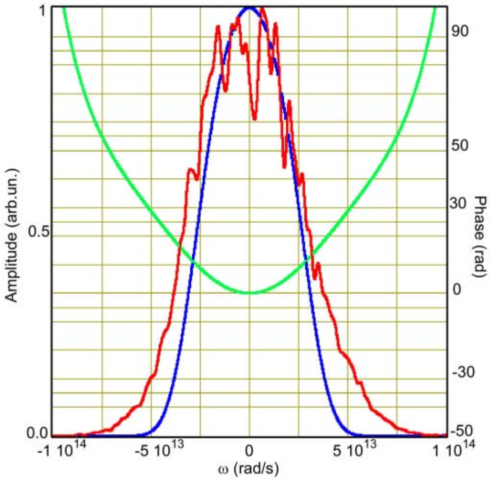

Figure 1: Blue curve : computed target spectral intensity; Red curve: experimental spectral intensity; Green curve: target spectral phase.

Spectral Interferometry

The crucial point in the laser pulse analysis is the retrieval of the spectral phase. Indeed, the spectrum intensity acquisition is not enough to characterise a non Fourier-limited pulse (i.e when its phase is not flat over all the spectral range). In our experiment, we want to measure the spectral phase on a single shot, simple, sensitive and extendable to UV range measurement. Spectral interferometry [21] between a reference pulse and the unknown pulse gives directly, through Fourier transform, access to the phase difference between these two pulses (cf. fig. 3). In our case, the reference pulse is the input pulse and the measurement confirms only the phase shaping. For complete phase shaping, the phase of the reference pulse is needed. As the reference pulse is close to Fourier transform pulse, any self-referenced measurement (SPIDER [19],

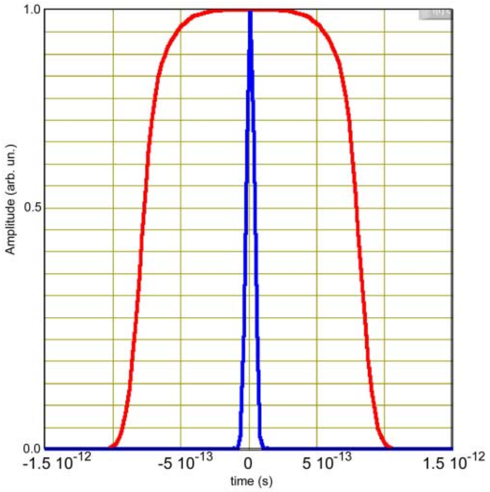

Figure 2: Blue curve : Fourier Limited laser pulse taking into account only the target spectral amplitude; Red curve: target temporal shape taking into account the target spectral phase.

FROG [20]...) is able to measure the residual phase of this pulse. This phase is then added to the measured one by spectral interferometry.

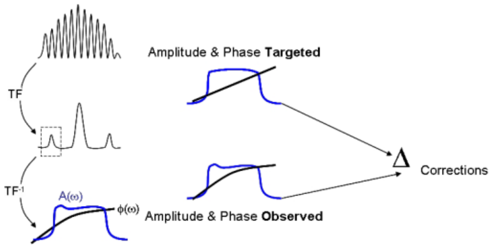

Figure 3: Layout of the Interferogram retrieving protocol.

Experimental Setup

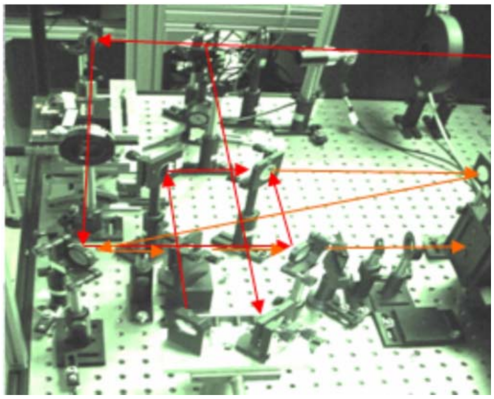

Figure 4: Experimental set-up for spectral interferometry. The red line shows the path for the two arms of the interferometer.

First studies are being performed on the laser facility LUCA (Tunable Ultra Short Laser) which delivers 50 fs long, 800 nm laser pulses, with an energy of up to 100 mJ, at a 20 Hz repetition rate. The pulse is split into the two arms of the interferometer (cf. fig. 4). On the first arm the laser passes through the acousto-optical device, thus undergoing a phase and/or amplitude manipulation. The second one travels through a delay line and it is then superposed on the first one. The two recombined beams enter the spectrometer where they interfere on the sensor. Single-shot interferograms are then collected on a personal computer. This latter also handles the transfer of the target or reference amplitude and phase files, as well as the associated reconstruction process. In practice the difficulty is to isolate the secondary lobe without information losses when the contrast is not very high. Also, to correctly recover the spectrum, a great care should be taken with the spectrometer calibration, and the signal processing to convert from the wavelength to the frequency space.

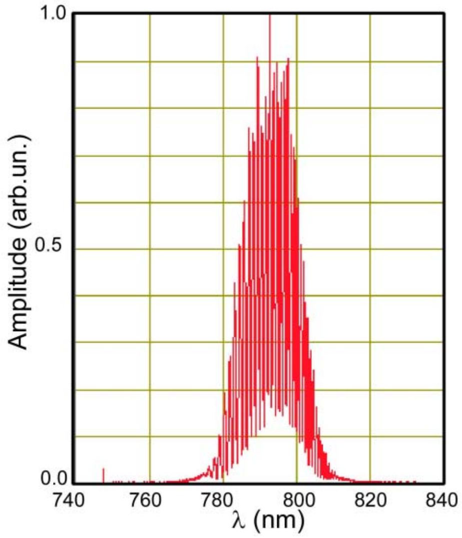

Figure 5: Typical interferogram acquired on the spectrometer.

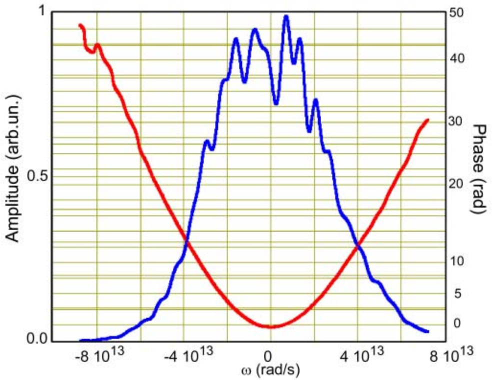

Figure 6: Retrieved Spectral Amplitude (blue curve) and Phase (red curve).

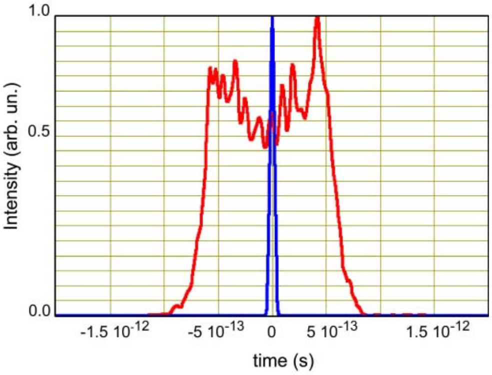

Figure 7: Temporal shape computed with IFT of the experimental data. Blue curve : Fourier Limited laser pulse taking into account only the target spectral amplitude; Red curve: with the target spectral phase.

PRELIMINARY RESULTS

The experiment has been implemented on the LUCA laser facility. Very low energy IR pulses ($\approx 10\ \mu$J) have been processed up to now. The few obtained preliminary results are very encouraging. A first example for a rectangular laser shape has been performed. Fig. 6 shows the retrieved amplitude and spectral phase behaviours, this latter without the constant and first order terms, whereas in fig. 7 the computed temporal shape, obtained with only one iteration, highlights the difference between the gaussian shape pulse which is obtained when only the spectral amplitude is taken into account, and the rectangular shape, when the spectral phase is inserted. The obtained pulse has a duration of 1.3 ps $FWHM$, with leading and trailing edges lasting around 170 fs. In order to get rid of the observed modulation on the top of the pulse, a higher signal-to-noise ratio should be achieved, always in a single shot configuration.

CONCLUSIONS

The spectral interferometry setup has been implemented on LUCA. Future steps will deal with the improvement of the laser beam spatial profile, the completion of the corrective loop for several different longitudinal shapes, a big increase of the pulse energy injected in the Dazzler, up to 1 mJ before compression. Afterwards the grating compressor will be installed on the beamline, together with a third harmonic generation stage and a further prisms stretcher, in order to obtain shaped pulse in the UV at 266 nm, with an energy of several tens of μJ.

REFERENCES

[1] C. Pellegrini, ”Design considerations for a SASE X-ray FEL”, *Nucl. Inst. Meth.*, A475, (2001) 1-12.

[2] S. G. Biedron, S.V. Milton, H.P. Freund, ”Modular approach to achieving the next-generation X-ray light source”, *Nucl. Inst. Meth.*, A475, (2001) 401-406.

[3] F. Ciocci et al., ”Design considerations on a high-power VUV FEL” *IEEE Jour. Quant. Elec.*,Vol. 31, No.7, July 1995, pp. 275-281.

[4] R. Bonifacio et al., ”Generation of XUV light by resonant frequency tripling in a two-wiggler FEL amplifier”*Nucl. Inst. Meth.*, A293, (1990) pp.627-629.

[5] L. H. Yu et al., ”High-Gain Harmonic-Generation Free-Electron Laser”,*Science*, Vol. 289, 11 August 2000, pp.932-934.

[6] D. Garzella et al., ”Using VUV high-order harmonics generated in gas as a seed for single pass FEL” *Nucl. Inst. Meth.* A528, August 2004, pp. 502-505.

[7] G. Lambert et al., ”Seeding the FEL of the SCSS Phase 1 facility with the 13th laser harmonic of a Ti:Sa laser produced in Xe gas”, *Proceedings FEL 2004*,Trieste, Italy, 29 August-3 September 2004, pp.155-158.

[8] L. Serafini and J.B. Rosenzweig, ”Envelope analysis of intense relativistic quasilaminar beams in rf photoinjectors: A theory of emittance compensation”, *Phys. Rev. E* 55 (1997) pp.7565-7590.

[9] M. Ferrario et al., An Ultra-High Brightness, High Duty Factor, Superconducting RF Photoinjector”, *Proceedings of EPAC 2004*, Lucerne, June 2004, pp. 402-404.

[10] M. E. Couprie et al., ”The ARC-EN-CIEL FEL proposal”, these Proceedings.

[11] M. Ferrario et al., ”Frontiers of RF Photoinjector”, *Proceedings of PAC 2005*, Knoxville, USA, May 2005.

[12] C. Limborg-Deprey and P. R. Bolton, “Optimum electron distribution for space charge dominated beams in photoinjectors”, *Nucl. Inst. Meth.* A557 (2006), p. 106-116.

[13] A. M. Weiner, ”Femtosecond pulse shaping using spatial light modulators”, *Rev.Scient. Inst.* Vol 71, No. 5, MAY 2000, pp. 1929-1960.

[14] F. Verluise et al., ” Arbitrary Dispersion Control of ultrashort optical pulses with acoustic waves ” *Jour. Opt. Soc. Am. B*, n 17 (2000), pp. 138-145.

[15] S. Cialdi and A. Boscolo,”A shaper for providing long laser target waveforms”, *Nucl. Inst. Meth.*, A538, (2005) pp.1-7.

[16] C. Vicario et al.,”Preliminary results using an acousticooptic dispersive filter for laser pulse shaping”, *SPARC Internal Note*, SPARC-LS-04/001, 15 January 2004.

[17] http://www-femtodrecam.cea.fr/

[18] I.A. Walmsley et al. ”The role of dispersion in Ultrafast optics”, *Rev.Scient. Inst.* Vol 72, No. 1, January 2001, pp. 1-29.

[19] C. Iaconis and I. A. Walmsley, Spectral phase Interferometry for direct electric-field reconstruction of ultrashort optical pulses, *Optics Letters* 23, pp. 792794 (1998).

[20] D.J. Kane and R. Trebino, ”Characterization of arbitrary femtosecond pulses using frequency-resolved optical gating” *IEEE Jour. Quant. Elec.* 29 (2), February 1993 pp. 571-579.

[21] L. Lepetit et al., ”Linear techniques of phase measurement by femtosecond spectral interferometry for applications in spectroscopy” *Opt. Lett.*, Vol. 12, No. 12, December 1995, pp. 2467-2474 and references therein.

CHARACTERISATION OF MICROPHONICS IN HOBICAT [*]

Oliver Kugeler, Wolfgang Anders, Jens Knobloch, Axel Neumann, Bessy GmbH, Berlin, Germany.

Abstract

The HoBiCaT test-facility at BESSY, which is designed for cryogenic testing of superconducting TESLA units has been equipped with a 9-cell TESLA-type cavity. Mechanical vibrations in the cryostat result in microphonic detuning of the cavity resonance. These microphonics have been characterized, and their sources analyzed, including the impact of operating conditions such as LHe pressure, cavity field and heater power. Furthermore, the mechanical transfer functions needed for the eventual compensation of the microphonics have been recorded.

INTRODUCTION

For CW operation of a superconducting, TESLA-type cavity microphonics represent the largest disturbance of the resonant frequency. In particular at a small bandwidth $\Delta f = \omega / Q_L$, according to the equation

$$\mathrm{P} \propto 1 + \frac{(\delta f)^2}{(\Delta f)^2} \qquad (1)$$

the microphonics δf lead to a significant increase of the generator power P, which is required to maintain a constant cavity field. Therefore it is highly desirable to minimize the microphonics. Measurements characterizing the microphonics and their impact on the cavity operation are presented below. The perspectives on possible countermeasures are described elsewhere [1].

MICROPHONICS MEASUREMENTS

Microphonics have been recorded in two different ways. In a first method, the RF-feedback signal, see Figure 1, is recorded over time. This is preferably done in open loop configuration, because obtaining a calibration factor is more straightforward here, than in closed loop configuration. A second method utilizes the sensor-actuator design of the piezo tuner to record the induced piezoelectric voltage over time. In this design, two high-voltage piezos are attached to the tuner, thus piezoelectric forces can be exercised on the cavity and measured simultaneously. The latter is only an indirect method, as the mechanical influence from cavity and tank on the frequency response does not necessarily lead to a linear relationship between cavity- and piezo position. The results presented here were solely obtained from the RF-feedback signal.

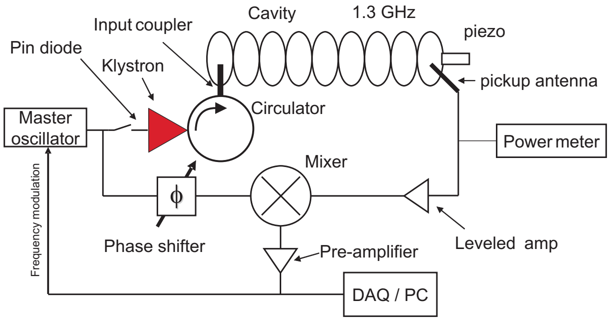

Figure 1: Phase-lock-loop used for cavity RF-measurements.

Calibration of RF-feedback signal

In order to interpret the voltage value from the RF-feedback in terms of a detuning frequency, a calibration factor has been determined. This was done by mechanically detuning the cavity with the piezo stack, which exhibited a detuning behavior of $\Delta \mathrm{f}/\Delta \mathrm{V}$ = 1.131 Hz/V. By varying the piezo voltage the cavity resonance was scanned open loop at a fixed master oscillator frequency over several bandwidths. The RF-feedback value varied by 0.84 V. Hence, all voltages could be easily interpreted as frequencies. This procedure is only possible because a leveled amplification is applied to the cavity pickup-signal. This ensures that the mixer output signal is solely dependent on the phase difference between master oscillator and cavity. Note that the frequency stability of the Rohde & Schwartz master oscillator at 1.3 GHz is better than 0.1 Hz.

Measurements at cryogenic temperatures

Microphonics have been measured at cryogenic temperatures. In Figure 2 the Fourier transform of a 30 second long measurement of the RF-feedback signal sampled at 5 kHz is depicted. An immediately identifiable feature is the constant signal of a turbo vacuum pump (18000 rpm) at 300 Hz. Furthermore, prominent features occur at 41 Hz, 90 Hz, and 170 Hz and are resonances of the cavity-tank-tuner system. The feature at 30 Hz is a so far unidentified source not related to any of the mechanical cavity resonances. It was further investigated whether the measured microphonics would change with the quality factor, or the bandwidth, respectively. For that purpose, the quality factor was varied over a wide range (a) by changing the coupler position and (b) by using a three stub tuner.

In Figure 3 the integrated microphonics frequency spectra taken at different values of $\mathrm{Q_L}$ are plotted. It can be seen that in general the RMS value of the microphonics in-

---

[*] Work funded by the European Commission in the Sixth Framework Program, contract No. 011935 EUROFEL.

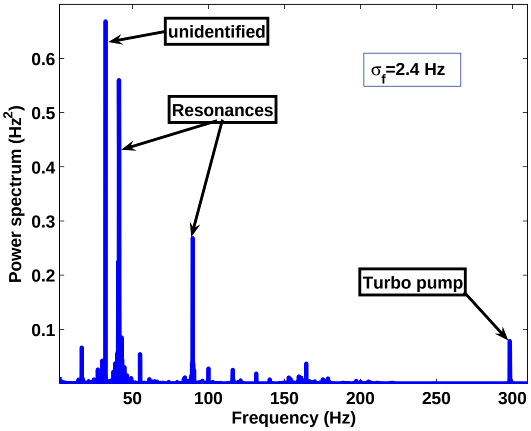

Figure 2: Microphonics in cavity measured open loop at 1.8 K.

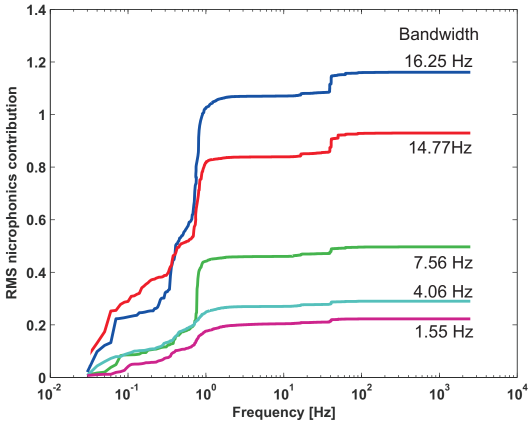

Figure 3: Integrated microphonics frequency spectra at different cavity bandwidths. The main contributions to the overall RMS value of the microphonics come from low microphonics frequencies (< 1 Hz). Microphonics increase with higher cavity bandwiths.

creases with the bandwidth, or in other words the cavity becomes less susceptible towards microphonics with increasing $\mathrm{Q_L}$. It can also be seen that the largest contributions to the RMS-microphonics are at low frequencies.

Influence of cryogenics on the microphonics

The heavy machinery in our cryogenic system consists of a Sogevac SV200 Leybold pump and two pairs of Leybold SV1200 and RA7001 SO pumps. They operate at 24 Hz, 11.66 Hz, and 50 Hz, respectively. Note that these mechanical vibrations can not be found in the microphonics spectra which was also confirmed by slightly varying the pumping frequencies. This observation suggests that the decoupling of the pumps from the HoBiCaT facility is sufficient.

The main contribution to the microphonics was found to be from within the cooling medium itself. A change in Helium pressure (measured with a Rosemount sensor) was measured to lead to a detuning of the resonant frequency of 55 Hz/mbar. Figure 4 shows the microphonics recorded over a period of 30 seconds in correlation with the He-bath pressure. In Figure 5 the Pearson correlation between the two signals is plotted. The maximum correlation occurs at an offset of 400 ms, which is due to the sampling time of the pressure sensor. This observation suggests, that a significant portion of the microphonics can be compensated with a feed forward system, provided fast and accurate pressure sensors are used. The microphonics created by the Helium heater, which is part of the cryogenic system and supports the Joule-Thomsen expansion of the cooling medium, were also investigated. In Figure 6 microphonics have been recorded as a direct fft from the RF feedback signal at different values of the heater power. It can be seen that different heater powers create significantly different microphonics spectra, suggesting that the heater itself is a source of microphonics.

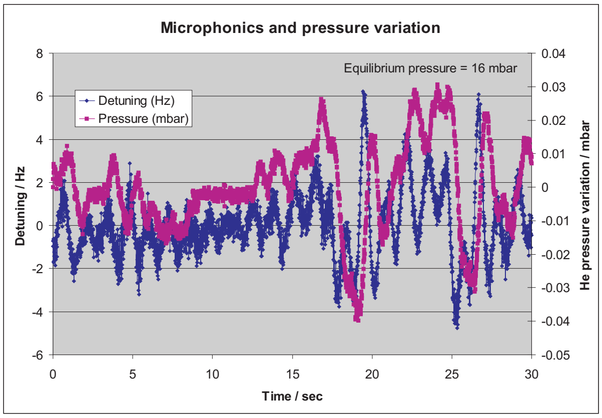

Figure 4: Microphonics and He-pressure difference.

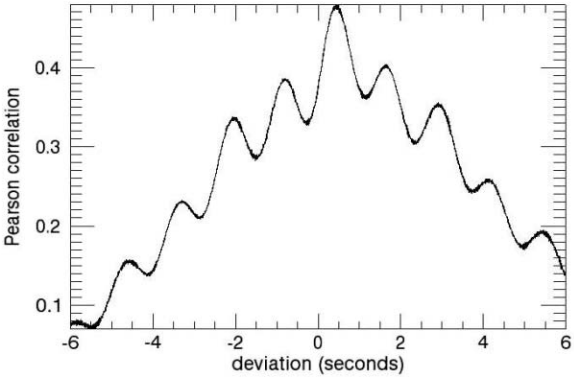

Figure 5: Pearson correlation between Helium bath pressure and microphonic detuning The 0.4 seconds offset is due to the preset sampling time of the pressure sensor. The occurrence of side maxima suggests, that there is some periodicity within the microphonics.

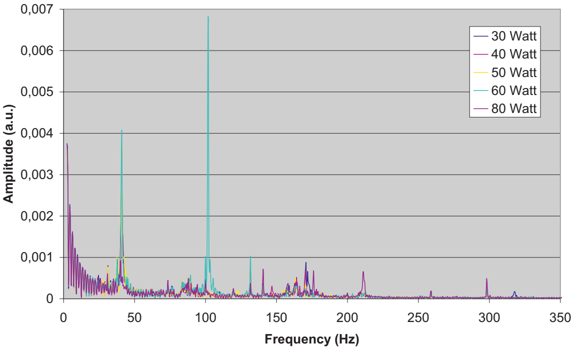

Figure 6: Influence of the heater power on the microphonics spectra

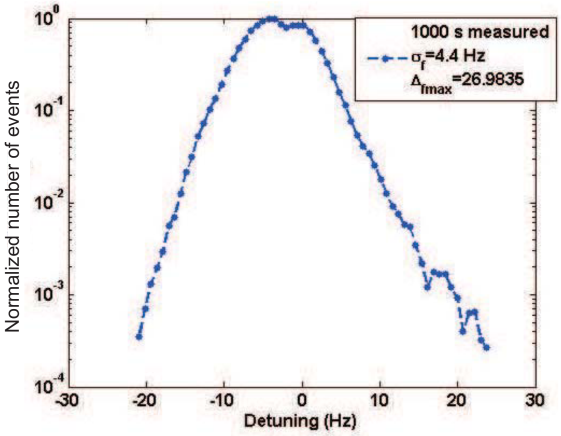

Figure 7: Long-time microphonics measurement.

Long-time measurements of microphonics

As the RF-system has to be laid out to deal with the maximum possible microphonics detuning, several long-time microphonics measurements have been performed. From these measurements the probability for a certain detuning within a given time period could be determined. The measurement presented in Figure 7 is a histogram of measured detuning values. It was taken over 1000 seconds and gives a maximum detuning frequency of 26.8 Hz and a rms detuning of 4.4 Hz. A 24 hours+ measurement is planned, but has so far been postponed due to long time stability issues of the klystron.

Lorentz force detuning

The static response of our setup to Lorentz force detuning has also been measured. We have obtained a value of $\mathrm{k_{LF}} = 1.42\ \mathrm{Hz/(MV/m)^2}$, see Figure 8, which is within the range of values of 1–2 $\mathrm{Hz/(MV/m)^2}$ gained at DESY [2].

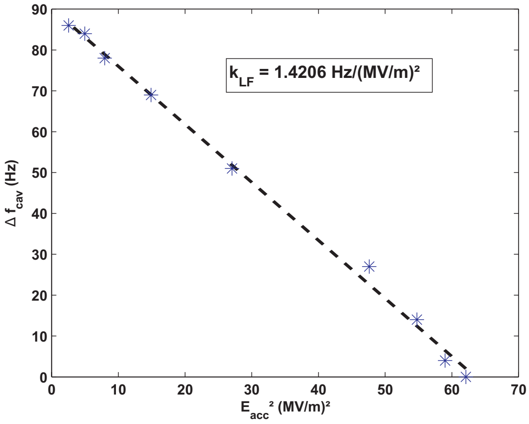

Figure 8: Lorentz Force Detuning vs. field gradient

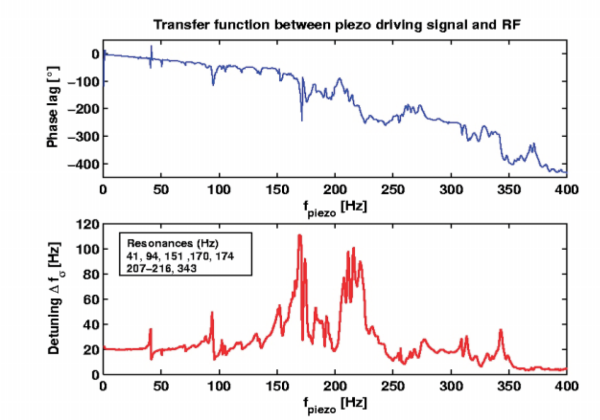

Figure 9: Transfer function of the cavity-tank-tuner system recorded over a frequency range of 0-400 Hz.

Transfer function

The reaction of the cavity resonance frequency on microphonic vibrations is determined by the mechanical eigenmodes of the tank-tuner-cavity system. Such Q-modes are measured via the transfer function. Here, the piezos are used to create sinusoidal vibration at distinct frequencies over a certain frequency range. The RF-feedback signal is recorded over time, yielding amplitude and phase information of the mechanical response, see Figure 9. Such modes arouse from transverse and longitudinal vibrations with respect to the cavity axis. Note, that only longitudinal symmetric stretch modes can be excited with the present piezo setup and thus only such modes can eventually be compensated. Numerical simulations by Luong et al. [3] suggest that these modes make up for the largest contribution to the detuning of the cavity.

Influence of passive cavity stabilizers

Titanium fixtures that can be attached between the cavity's stiffening rings and the helium tank have been developed by FZ Rossendorf and manufactured at AC-

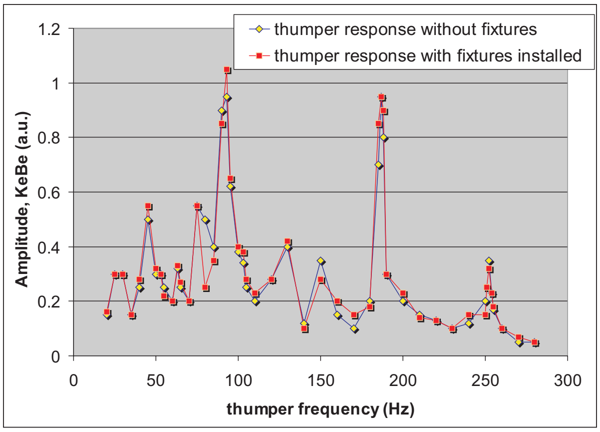

Figure 10: Integrated frequency response signal of cavity mounted in a He-tank (a) with and (b) without fixtures attached.

CEL. While they were originally intended for earthquake-protection, we have investigated to what extent they can dampen mechanical vibrations or shift resonances towards higher frequencies, and thus reduce the impact of microphonics. Room-temperature measurements were done at ACCEL with such a cavity. For the experiment, an acoustic thumper, operating between 30 Hz and 300 Hz, was attached to one end of the cavity (perpendicular to the cavity axis). The response was measured with KeBe inductive velocity meters attached at different positions of the tank. It was found that the fixtures contributed only marginally to a decrease of the microphonics response signal. As can be seen from Figure 10 the response function with and without fixtures is practically identical. The only significant deviation occurs at 80 Hz, but no significant microphonics were measured in HoBiCaT at this frequency.

OUTLOOK

The next step after characterization of microphonics is to take countermeasures to compensate them. Such a compensation does not have to be complete as even small improvements lower the required RF-power significantly. The correlation between He-pressure and low frequency microphonics suggests, that a feed-forward algorithm might be feasible. Such work is underway and will be presented soon. Also we are investigating adaptive feed forward compensation of higher frequency microphonics.

REFERENCES

[1] A. Neumann, et al., “Characterization of a Piezo-based Microphonics Compensation System at HoBiCaT”, EPAC’06, Edinburgh.

[2] H. Gassot, “Mechanical Stability Of The RF Superconducting Cavities”, Proceedings of EPAC 2002, Paris, 2002.

[3] M. Luong, et al., “Analysis of microphonic disturbances and simulation for feedback compensation”, Proceedings of EPAC’06, Edinburgh.

A HIGH AVERAGE POWER RF PHOTOINJECTOR GUN CAVITY DEVELOPED FOR THE BESSY SOFT X-RAY FEL*

F. Marhauser#, M. Dirsat, A. Meseck, D. Richter, V. Dürr, E. Weihreter,
BESSY, 12489 Berlin, Germany
G. Asova, J. Bähr, H.J. Grabosch, S. Khodyachykh, S. Korepanov, M. Krasilnikov, A. Oppelt,
B. Petrosyan, L. Staykov, F. Stephan, F. Tonisch, DESY, 15738 Zeuthen, Germany
O. Kalekin, Humboldt University, 12489 Berlin, Germany
J. Roensch, University of Hamburg, 22761 Hamburg, Germany.

Abstract

Based on the 1.3 GHz normal conducting RF photogun installed at the Free Electron Laser in Hamburg (FLASH) a new RF gun prototype with an optimized cooling layout has been developed at BESSY with the objective to operate in the 100 kW average power regime. This would significantly enhance the capability of present L-Band guns towards operation at higher accelerating fields or/and duty factors. High power RF-conditioning at the Photo Injector Test Facility at DESY in Zeuthen (PITZ) has recently been performed achieving 47 kW average power and an electric peak field of 53 MV/m in maximum respectively, so far only limited by power constraints of the RF-system. In this paper the RF-conditioning results and relevant simulation results are discussed. Tracking studies for the photoinjector including two linac modules and a subharmonic cavity section are presented.

INTRODUCTION

RF photoinjectors bear the potential to generate electron pulses of extraordinary high peak brightness suitable for future FELs and linear colliders. For the proposed BESSY Soft X-Ray FEL (“BESSY FEL”) [1] with its superconducting CW driver linac a superconducting RF (SRF) gun would be the ideal electron source to deliver most flexible pulse pattern considering the manifold demands of experimental users. Superconducting guns are therefore a very active research area. For example, FZR, DESY, MBI and BESSY are collaborating to commission an SRF 1.3 GHz 3½-cell photoinjector gun cavity at FZR in 2007. Initially, this gun will accelerate 1 nC, but schemes have been identified and investigated that are capable of achieving slice emittances in the order of 1.5 π mm mrad at 2.5 nC bunch charge [2].

At present, though, normal conducting (NC) photoguns are more established and will therefore be used to commission the BESSY FEL. Still, a very high rep rate (1 kHz) is planned to approach CW operation. Later this NC gun can be replaced by an SRF gun. In particular much progress has been made by the PITZ collaboration which has developed a series of 1.3 GHz NC guns (1 ½ cells) characterized at the PITZ facility [3]. So far a minimum projected emittance of 1.6 π mm mrad (geometrical average of horizontal and vertical emittance) for a bunch charge of 1 nC could be demonstrated [4]. This system has also been operational at FLASH. Improvements at PITZ are expected by further optimizing the transverse and temporal profile of the photocathode laser, increasing the electric field at the photocathode to E_c = 60 MV/m and by utilizing a booster cavity, whereby the emittance conversation principle will be studied [5]. Beam operation hitherto was performed typically with E_c = 40-45 MV/m and a duty factor of 0.9 % (10 Hz RF pulse repetition rate) corresponding to an average power in the range of 30 kW. The European XFEL [6] and the proposed BESSY FEL however require even higher values to be achieved as listed in Table 1.

Table 1: Target parameters of NC RF guns as proposed for the European XFEL and the BESSY FEL at commissioning phase

Parameter	**European XFEL**	**BESSY FEL**
Frequency / GHz	1.3	
Number of cells (copper)	1½	
Bunch charge / nC	1	2.5
Single bunch rep. rate / MHz	5	1/3
RF pulse rep. rate / Hz	10	1000
Peak field / (MV/m)	60	40
Peak power* / MW	~6.5	~3
Beam pulse length** / µs	650 (max.)	6
Duty factor / %	~0.67	~2.5
Average power / kW	~44	~75
Beam parameters at undulator		
Trans. norm. slice emittance / π mm mrad	1.4	1.5
Max. beam energy / GeV	20	2.3

* depending on Q_0 (~23000), ** excluding RF rise/fall time (~20 µs)

Gun cavity thermal drifts as a source of severe phase and amplitude jitters may then become more apparent. Despite the progress of RF field stability control [7], one challenging task remains the mitigation of these drifts. Thus elaborate cooling concepts for the gun have to be

---

* This work has partly been supported by the European Community, contract numbers RII3-CT-2004-506008 (IA-SFS) and 011935 (EUROFEL) and by the “Impuls- und Venetzungsfonds” of the Helmholtz Association, contract number VH-FZ-005

corresponding author: marhauser@bessy.de

considered. With respect to this issue a high average power 1 ½-cell RF gun cavity with an optimized cooling layout has been developed at BESSY ("BESSY Gun") as described below. A prototype of the cavity has been produced and thermal tests without photoemitted electrons were performed at PITZ. This gun also served as the basis for new beam dynamics simulations.

BESSY NC RF GUN CAVITY

A picture of the BESSY Gun and its outer water connections is shown in Fig. 1 (left), whereas the CAD model (right) reveals the inner cooling circuits. To provide sufficient water to the cavity a total number of 43 water inlets and outlets have been implemented with each water circuit separately addressable. Thus a sufficiently high water volume flow can be delivered to the cavity body and the water temperature rise within each meander can be kept rather low. Still emphasis has been placed on a simple conceptual design using drilled water holes of same dimensions throughout except in the iris aperture. Further details on the technical layout and cooling scheme can be found in [8].

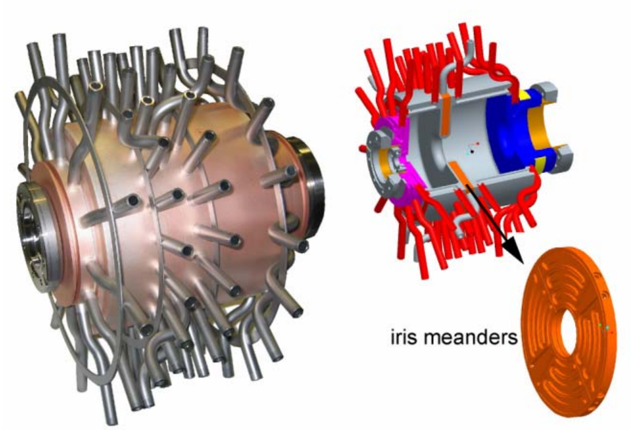

Figure 1: The copper 1 ½-cell BESSY Gun (photo left) with the outer water connections and the corresponding CAD model (right) revealing the inner water circuits.

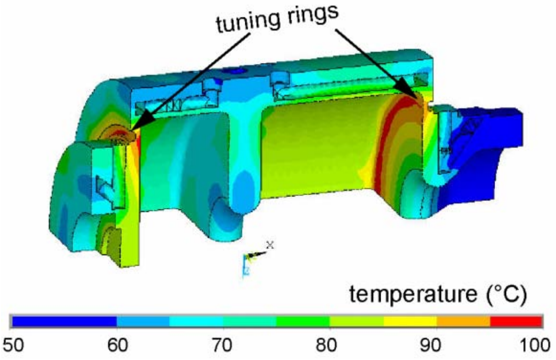

Figure 2: Temperature distribution in the BESSY Gun calculated at $P_{ave} = 75$ kW with $T_{in} = 42$°C for a quarter symmetric ANSYS model.

The cooling scheme was optimized with the help of thermal simulations using the FEA Code ANSYS [10]. Hence the BESSY Gun exhibits moderate temperatures (< 100°C) at an average power of $P_{ave} = 75$ kW, i.e. the nominal operation power for the BESSY FEL. As illustrated in Fig. 2 this has been achieved for a reasonable water inlet temperature of $T_{in} = 42$°C. Circular notches at each endplate ('tuning rings') have been implemented to ease a possible tuning effort. The reduced cooling efficiency at the tuning rings is taken into account for this prototype yielding the maximum local temperatures. Mechanical stresses however are not an issue [10].

As a feature the BESSY Gun was equipped with a small pickup port (Ø = 8mm) in the full cell implementing an antenna, loosely coupled to produce only a negligible field distortion. The antenna amplitude and phase information is beneficial for RF field stability control, critical for the overall jitter stability of the electron beam. Else - as practised at FLASH - the cavity field has to be artificially determined from the forward and reflected power signals of a directional waveguide coupler [7].

RF CONDITIONING

The first pulsed high power RF-conditioning tests of the BESSY Gun have been completed in May 2006 in the frame of the PITZ-collaboration. The conditioning test stand at PITZ is shown in Fig. 3. A 10 MW multi-beam klystron (MBK) was used to feed in the RF power to the gun via a standard DESY axially symmetric coupler. Due to the limited power capability of state-of-the-art RF vacuum windows the MBK output power is distributed into two separate WR650 waveguide arms. A T-combiner with two RF windows was flanged to the input coupler to add both RF-waves.

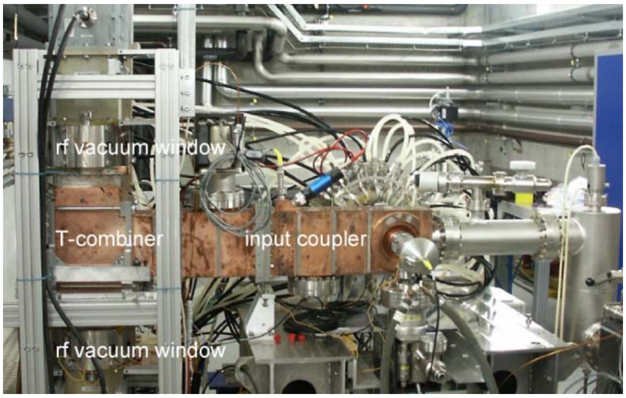

Figure 3: BESSY Gun on the conditioning test stand at PITZ. For conditioning no solenoids were installed.

After only 90 hours conditioning time -with a cavity vacuum interlock threshold of 10^{-7} mbar- a peak power of $P_{peak} = 2.9$ MW at $t_{RF} = 100$ µs was reached ($P_{ave} = 2.9$ kW) corresponding to a peak field of $E_c = 40$ MV/m as required for the BESSY FEL. It should be noted, that prior to the installation at PITZ the integrity of the gun was checked at BESSY operating several days in CW mode at 10 kW, which might have been beneficial to achieve this rather rapid progress. Since the repetition rate of the low level RF-system at PITZ is limited to f_{rep} = 10 Hz, the average power could only be increased by operating with both the peak power and the pulse length far beyond the desired BESSY FEL specifications (see Table 1). This "thermal" conditioning was time consuming, particularly because of sparking in the waveguide arms of the klystron at peak power levels above 3 MW. Despite the constraints of the RF-system, conditioning could be carried out successfully to a maximum operable peak power of P_{peak} = 5 MW with t_{RF} = 540 µs corresponding to an electric field of E_c = 53 MV/m. The maximum average power of P_{ave} = 47 kW was reached at the maximum pulse length of t_{RF} = 1 ms with P_{peak} = 4.7 MW (E_c = 51 MV/m). Higher power levels and longer pulse lengths could not be reached because of operational limitations of the RF-system. However up to 47 kW average power no thermal or technical limitations attributable to the gun were encountered. The main RF-conditioning results are listed in Table 2.

Table 2: BESSY Gun RF-conditioning results at PITZ

Parameter	Achieved at limit of RF system	Desired	Unit
P_{ave}	47	75	kW
P_{peak}	4.7^*	3	MW
E_c	51^*	40	MV/m
t_{RF}	1000	25	µs
f_{rep}	10	1000	Hz
d.f.	1	2.5	%

* max. P_{peak} = 5 MW corresponding to E_c = 53 MV/m at t_{RF} = 540 µs

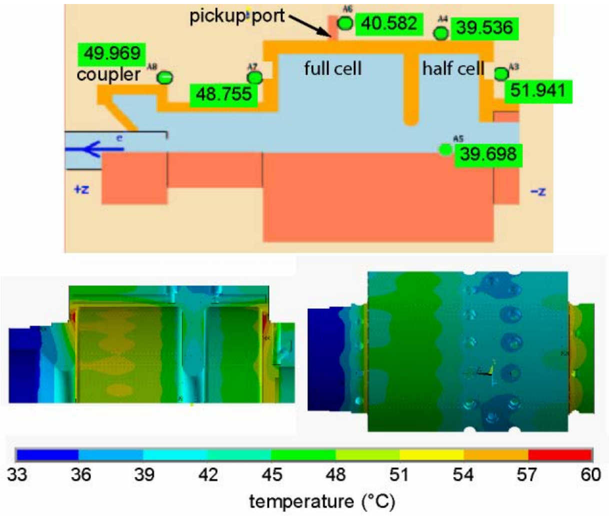

Figure 4: Measured (top) and simulated (bottom) gun temperatures when operating at P_{ave} = 40 kW and T_{in} = 27°C (P_{peak} = 4 MW, f_{rep} = 10 Hz, t_{RF} = 1 ms).

Fig. 4 (top) depicts a screen shot of the measured gun cavity temperatures using external PT100 sensors at distinctive locations (green dots). Here the temperatures are shown when operating at a thermal load of P_{ave} = 40 kW with an inlet water temperature of T_{in} = 27°C. At the bottom corresponding numerical results using ANSYS are plotted in good agreement with the monitored data. This is also true for the hot spots located at the tuning rings. At the antenna port no significant heat enhancement has been produced. The antenna port has been omitted in the calculation due to mesh size constraints.

To further check the reliability of numerical data, the frequency shift Δf caused by thermal deformation of the gun cavity has been measured at a constant inlet water temperature of 27°C when increasing the average power. Hereby the resonance was kept adjusting the master oscillator frequency to gain a reflected power below 1%. To evaluate Δf the resonance frequency at room temperature is taken as reference. In Fig. 5 the measured data are plotted as compared with numerical results. The latter have been computed by transferring the thermally deformed cavity profile given by ANSYS to Superfish [11]. This method has been extensively described in [12]. A linear drift in the order of Δf ~ -10 kHz/kW over the observed power regime at T_{in} = 27°C was obtained, consistent with the simulations.

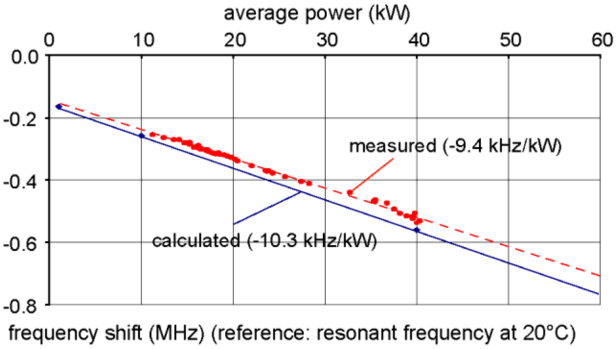

Figure 5: Thermal frequency drift in dependence on the average power as measured (red dots, f_{rep} = 10 Hz, t_{RF} = 1 ms) and calculated (blue line) both at T_{in} = 27°C.

BEAM DYNAMICS

Former beam dynamical studies using the accelerating field of the BESSY Gun as an input revealed that the photoinjector is able to deliver the required transverse slice emittances [10]. Further studies employing a multiparameter optimization with ASTRA [13] have been performed, the results being depicted in Figs. 6 and 7. Here 100000 macro particles have been tracked through the first two cryogenic linac modules comprising eight standard 1.3 GHz 9-cell TESLA-cavities. An intermediate section with quadrupoles as well as eight 9-cell 3.9 GHz cavities (under investigation at FERMILAB [14]) have been implemented to linearize the longitudinal phase space serving the needs of the subsequent first bunch compressor. A thermal energy of 0.55 eV for electrons emitted from a Cs_2Te photocathode illuminated by a UV laser (262 nm) has been taken into account. For the laser a temporal profile of 38 ps (flat top) with 4 ps rise/fall time and a spot size of 3.3 mm have been chosen. Furthermore a peak field of $E_c = 40$ MV/m has been presumed, which already has been exceeded by the BESSY Gun during the high power tests. As mentioned above this value however is rather constrained by thermal considerations.

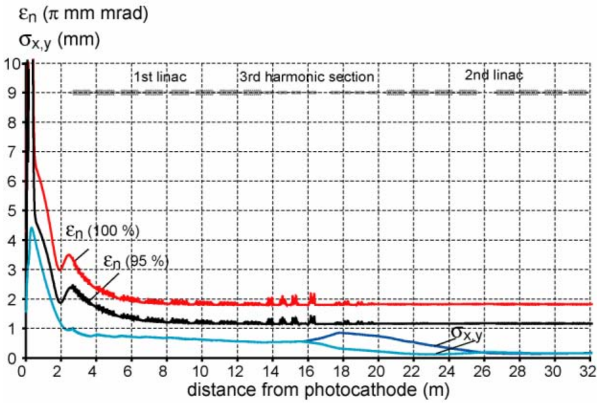

Figure 6: Evolution of the normalized transverse rms emittance ε_n (100% and 95% core emittance) and beam size $\sigma_{x,y}$ for a bunch charge of 2.5 nC up to the exit of the 2nd linac module.

For a bunch charge of 2.5 nC the normalized projected transverse emittance "frozen" at the exit of the second linac module ($E_{kin} = 223$ MeV) is 1.8 π mm mrad (1.2 π mm mrad for the 95% core emittance). At this point the slice emittance averaged over the whole bunch amounts to 1.5 π mm mrad fulfilling the design goal of the BESSY FEL.

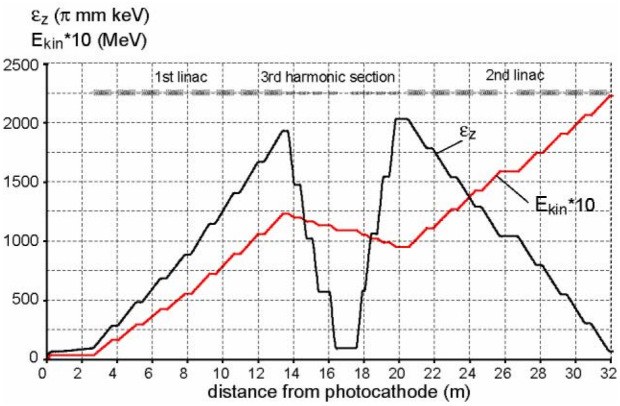

Figure 7: Evolution of the longitudinal rms emittance ε_z and average beam energy E_{kin} for a bunch charge of 2.5 nC up to the exit of the 2nd linac module.

The rms bunch length is 3.5 mm and a projected longitudinal rms emittance of 65 π keV mm has been obtained due to phase space linearization with the subharmonic cavity section (Fig. 7).

CONCLUSION

A high average power RF gun prototype developed at BESSY has been high power conditioned at the Photo Injector Test Facility at DESY in Zeuthen. The gun was tested up to an average power of 47 kW so far only limited by the maximum operable power of the RF-system. Similarly, the maximum electric field achieved at the cathode was 53 MV/m so far. All observations at present indicate that the gun is thermally stable at the desired power level of 75 kW or beyond. This is confirmed by corresponding thermal calculations. Operation of this prototype with photoemitted beams was not planned. However, new numerical tracking studies demonstrate that the gun is capable of producing the beam quality required for the BESSY FEL.

REFERENCES

[1] D. Krämer et al. (editors), "The BESSY Soft X-Ray Free Electron Laser", Technical Design Report, ISBN 3-9809534-0-8, BESSY, Berlin, 2004.

[2] D. Janssen at. al., "Progress of the Rossendorf SRF Gun Project", Proc. of the 2006 Europ. Acc. Conf., Edinburgh, Scotland, 2469.

[3] A. Oppelt et. al., "Tuning, Conditioning, and Dark Current Measurements of a New Gun Cavity at PITZ", these proceedings.

[4] F. Stephan, "Status and Perspectives of Photo Injector Developments for High Brightness Beams", Conf. on the Physics and Applications of High Brightness Beams, Erice, Italy, 2005.

[5] A. Oppelt et. al.,"Status of the PITZ Facility Upgrade", Proc. of the 2006 Lin. Acc. Conf., Knoxville, USA.

[6] M. Altarelli et al. (editors.), "The European X-Ray Free Electron Laser", Technical Design Report, ISBN 3-935702-17-5, DESY, Hamburg, July 2006.

[7] E. Vogel at. al.," FPGA Based RF Field Control at the Photo Cathode RF Gun of the DESY Vacuum Ultraviolet Free Electron Laser", Proc. of the 2006 Europ. Acc. Conf., Edinburgh, Scotland, 1456.

[8] F. Marhauser, "High Power Tests of a High Duty Cycle, High Repetition Rate RF Photoinjector Gun for the BESSY FEL", Proc. of the 2006 Europ. Acc. Conf., Edinburgh, Scotland, 68.

[9] www.ansys.com.

[10] F. Marhauser, "Photoinjector Studies for the BESSY Soft X-Ray FEL", Proc. of the 2004 Europ. Acc. Conf., Lucerne, Switzerland, 315.

[11] K. Halbach, R.F. Holsinger, Poisson Superfish, Particle Accelerators 7 (1976), page 213, distributed by the Los Alamos Accelerator Code Group (LAACG).

[12] F. Marhauser, "Finite Element Analyses for Photoinjector Gun Cavities", DESY Hamburg, January 2006, TESLA FEL-Report 2006-02.

[13] K. Flöttmann, http://www.desy.de/~mpyflo/.

[14] N. Solyak et. al, „The Progress in Developing Superconducting Third Harmonic Cavities", Proc. of the 2006 Europ. Acc. Conf., Edinburgh, Scotland, 804.

PHOTOCATHODE LASER FOR THE SUPERCONDUCTING PHOTO INJECTOR AT THE FORSCHUNGSZENTRUM ROSSENDORF

Ingo Will[#], Guido Klemz, Max-Born-Institute Berlin, Germany
Friedrich Staufenbiel, Jochen Teichert, Forschungszentrum Rossendorf, Germany.

Abstract

We report on the design of the photocathode laser for a superconducting RF gun, which is presently under development at the Forschungszentrum (FZ) Rossendorf. This laser is foreseen to drive the RF gun in CW mode with up to 1 nC bunch charge. It generates pulses of 12...14 ps duration with 500 kHz repetition rate and 0.8 µJ pulse energy at 263 nm wavelength. This should provide sufficient pulse energy for generation of bunches with 1 nC charge using caesium telluride photocathodes. Due to two active modelockers in the laser oscillator, the latter operates in tight synchronism to the RF master oscillator of the linac.

The laser consists of a short-pulse oscillator, a pulse picking Pockels cell, a regenerative amplifier and a wavelength conversion unit. The latter converts the infrared laser radiation to the ultra-violet (UV). This unit turns out to be a particularly critical element of such a photocathode laser driving a RF gun in CW mode.

INTRODUCTION

Photo injectors within RF guns are important for FELs, since they provide an efficient means for generating high-density electron bunches with low emittance. Most of the existing photo injectors are operated in pulsed or in burst mode.

At the FZ Rossendorf a superconducting RF gun is being developed [1], which needs an appropriate laser for illumination of the caesium telluride photocathode. This laser should deliver pulses of 500 kHz repetition rate at a wavelength within the range of 260 to 270 nm. The desired bunch charge of 1 nC demands a UV pulse energy in the order of 0.5 to 1 µJ. The present paper describes a first setup for a suitable laser system.

LAYOUT OF THE LASER

Fig. 1 shows the general scheme of the laser system, which consists of the following main building blocks:

- the laser oscillator,
- a pulse picker,
- a regenerative amplifier,
- a wavelength conversion stage.

The laser oscillator generates the initial picosecond seed pulses. Its Nd:YLF laser rod is pumped by two fiber-coupled laser diodes of 805 nm wavelength. Modelocking for generation of short picosecond pulses is accomplished by two active modelockers. One of them is a standard acousto-optic modelocker driven with a 27.08 MHz RF signal, while the second one is an electro-optical phase modulator for 1300 MHz. A detailed description how to operate several modelockers in a single cavity can be found in [2] and the references therein.

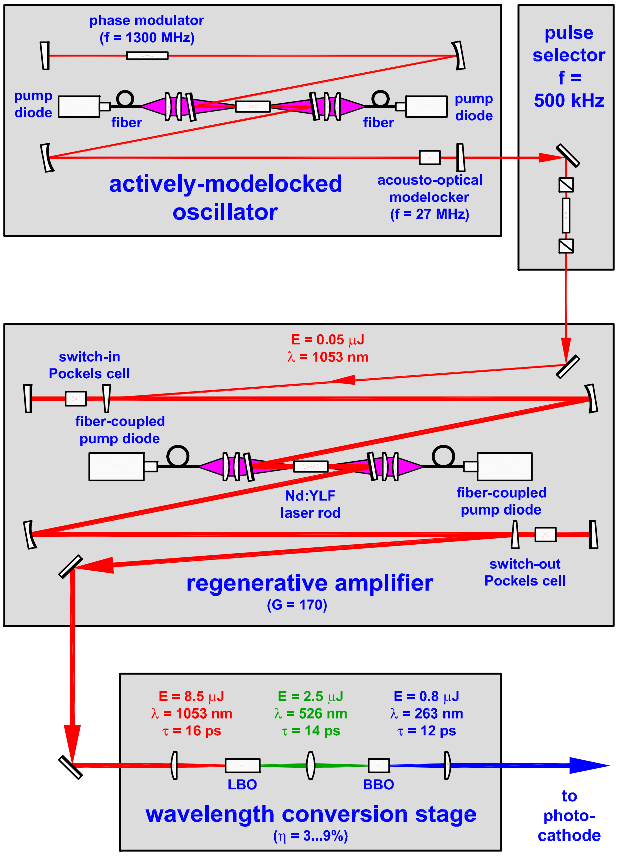

Figure 1: Optical scheme of the present photocathode laser.

The oscillator generates a CW pulse train of 54.16 MHz repetition rate and provides a single-pulse energy of 0.05 µJ. Since the signals for the active modelockers are derived from the electronic RF master oscillator of the gun, the laser pulses are synchronized with an accuracy of about 1 ps.

A subsequent electro-optic pulse selector reduces the high repetition rate of the pulses from the oscillator to the desired value of 500 kHz. This pulse train is further amplified by a regenerative amplifier (regen). The regen is based on a folded resonator with 25 ns round-trip time.

[#] will@mbi-berlin.de

In addition to the diode-pumped Nd:YLF laser rod, it contains two BBO Pockels cells. The first one switches the laser pulse from the oscillator into the cavity of the regen. Subsequently, this pulse performs 14 round trips in the resonator and is thereby amplified to an energy of 8.5 µJ.

THE WAVELENGTH CONVERTER

After switching the amplified pulses out of the resonator with the second Pockels cell, they are directed towards the wavelength conversion stage. This stage contains two consecutive nonlinear frequency doubling crystals that convert the infrared laser pulses of 1053 nm wavelength to the ultra-violet (263 nm wavelength).

The general scheme of this conversion unit is similar to the one used in the photocathode lasers of FLASH and PITZ. At first, a 12 mm long LBO crystal converts the pulses to green light. A further 8 mm long BBO crystal generates from this the UV output pulses

It turns out that both, the energy of the generated UV pulses as well as the profile of the UV beam depend in a highly sensitive way on the size of the beam waist in the BBO crystal. Tab. 1 as well as Fig. 1 show the results of appropriate measurements done for four different diameters of the beam in this crystal. Although the highest output energy of 0.83 µJ is achieved for the strongest focusing down to a diameter of 260 µm, this leads to a non-circular beam profile.

On the other hand, the most homogeneous output beam that largely maintains the original circular cross section is obtained when the beam diameter in the BBO crystal is larger. The optimum in this respect amounts to 703 µm. Unfortunately, this is accompanied by a drop of the laser intensity in that crystals by a factor of two, and only a smaller portion of the green light is converted to the UV. Since the conversion process is now operated far from saturation, the energy stability becomes much worse and we typically obtain a pulse energy between 2 and 4 µJ.

Table 1: Dependence of the resulting UV pulse energy on the focussing condition at the BBO crystal

Diameter of the beam waist [µm] in the BBO crystal	Measured output energy [µJ] of the UV pulses
260	0.83
352	0.71
527	0.49
703	0.45

Although the average power of the CW laser in comparison to the pulsed lasers at FLASH and SHARP (table 2) is significantly larger, its peak power is at least one order of magnitude less. This is reflected by the measured peak intensity in the UV. So, the above measurements show, that the present design of the wavelength converter cannot be used together with the photocathode laser for a CW gun without substantial modification.

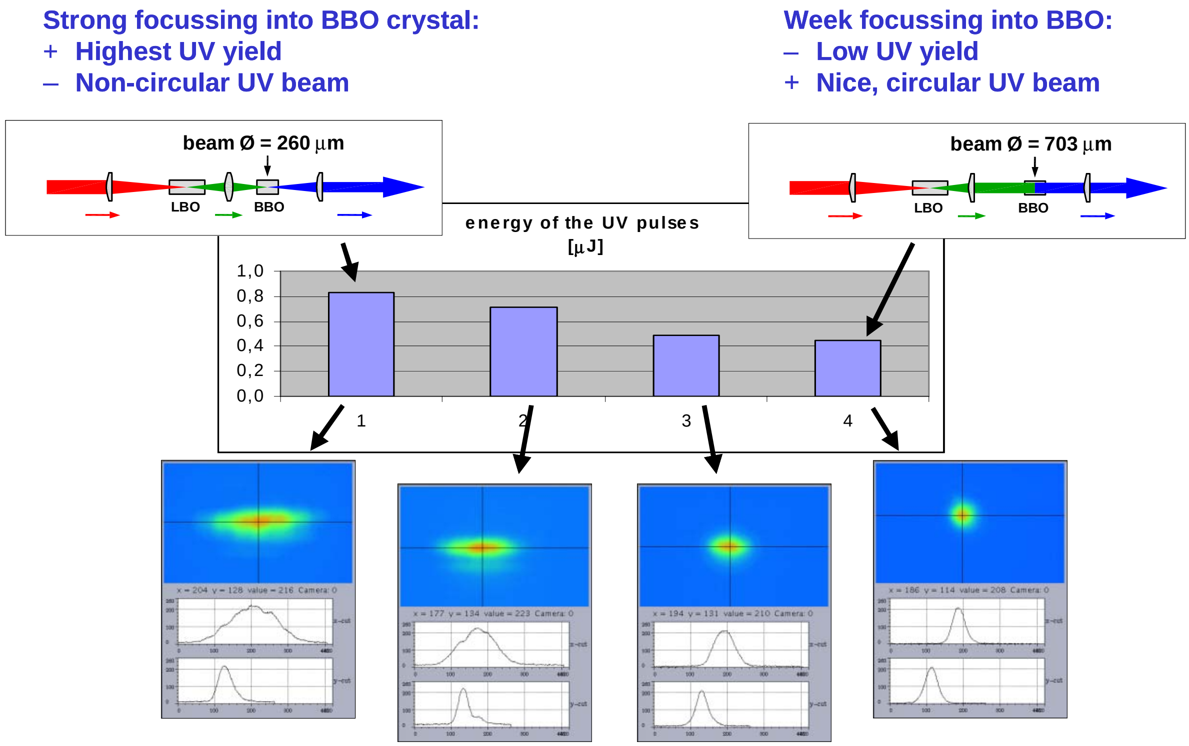

Figure 2: Intensity profile of the UV output at four different sizes of the focussed beam diameter in the BBO crystal (from left to right: 260, 352, 527 and 703 µm).

In order to still reach a reasonable conversion efficiency, the laser radiation must be stronger focused into the conversion crystals. This, in turn leads to a significant perturbation of the beam profile due to the limited acceptance angle as well as due to the walk-off between green and UV light in the BBO crystal.

Table 2: Comparison of the pulse parameters of the photocathode lasers at FLASH/PITZ and at the FZ Rossendorf

	FLASH, PITZ	**ELBE (f = 0.5 MHz)**	**ELBE (f = 13 MHz)**
pulses per s	$0.008 \cdot 10^6$	$0.5 \cdot 10^6$	$13 \cdot 10^6$
pulse energy (UV)	20 µJ	1 µJ	0.08 µJ
pulse duration	20 ps	20 ps	4 ps
average UV power	0.16 W	0.5 W	1 W
peak intensity (UV)	1	0.05	0.02

CONCLUSION AND OUTLOOK

From the above described measurements follows, that the photocathode lasers for RF guns in CW mode should be set up for the shortest pulse duration possible. This would yield better conversion efficiency to the UV at the same laser pulse energy. Since even sub-picosecond lasers with an average power larger than 10 W exist, the lower limit for the pulse duration is determined by space charge effects in the RF gun. Too short pulses however, will lead to an increased longitudinal emittance of the electron beam.

Further work is mainly required to develop an improved wavelength conversion unit to end up with reasonable conversion efficiency and simultaneously a nearly circular profile of the UV laser beam. A possible solution that is presently investigated at the MBI might be based on cylindrical lenses for focusing the beam differently in horizontal and vertical direction. Compensation of the walk-off between fundamental and harmonic wave that occurs in the crystals is another option.

ACKNOWLEDGEMENT

This work was supported by the German Ministry for Edjucation and Science, contract no. 05 ES4BM1/1 and 05ES4 BR1/8.

REFERENCES

[1] http://www.fz-rossendorf.de/pls/rois/Cms?pNid=604

[2] I. Will, G. Koss, I. Templin, The upgraded photocathode laser of the TESLA Test Facility, Nuclear Instruments and Methods in Physics research A 541 (2005), pp. 467-477.

1ST RF-MEASUREMENTS @ 3.5-CELL SRF-PHOTO-GUN CAVITY IN ROSSENDORF

A. Arnold#, H. Buettig, D. Jannsen, U. Lehnert, P. Michel, K. Moeller, P. Murcek, Ch. Schneider,
R. Schurig, F. Staufenbiel, J. Teichert, R. Xiang, FZR, Dresden, Germany
A. Matheisen, B. v. d. Horst, DESY, Germany
J. Stephan, IKS, Dresden, Germany
W.-D. Lehmann, IfE, Dresden, Germany
T. Kamps, D. Lipka, F. Marhauser, BESSY, Berlin, Germany
V. Volkov, BINP, Novosibirsk, Russia

Abstract

At the Forschungszentrum Rossendorf the development and the setup of the 2nd superconducting radio frequency photo electron injector (SRF-Photo-Gun) is nearly completed. In this report we present the results of the cavity treatment. The warm tuning was carried out considering pre-stressing and the tuning range of both tuners (half cell and full cells). The optimal antenna length of the main coupler and both fundamental pickups were determined by practical external Q studies. Furthermore the characteristic tuning curves of the choke filter and both HOM filters were simulated, measured and tuned at the pi-mode frequency. The preparation (etching and rinsing) and the vertical cold test were done at DESY.

INTRODUCTION

For future FEL light sources and high energy linear accelerators a high current electron gun with high brilliance is absolutely essential. Thus, an innovative superconducting RF photo injector (SRF gun) is under development at the Forschungszentrum Rossendorf (ELBE), which is a collaboration of BESSY, DESY, MBI and FZR and supported by the European Community.

Table 1: rf cavity parameters calculated with MWS© normalized to 50MV/m peak axis field

stored energy U	***32.5 J***
quality factor Q_0	***$1x10^{10}$***
dissipated power P_c	***25.8 W***
geometry factor G	***241.9 Ω***
acceleration voltage V_{acc}	***9.4 MV***
acceleration gradient E_{acc}	***18.8 MV/m***
shunt impedance $R_a = V_{acc}^2 / 2P_c$	***$1.72x10^{12}$ Ω***
R_a/Q_0	***166.6 Ω***
E_{peak}/E_{acc}	***2.66***
B_{peak}/E_{acc}	***6.1 mT/(MV/m)***

This gun allows continuous wave operation at an energy of 9.4 MeV and an average current of 1 mA. It can generate short pulses and high-brightness electron beams, as known from the conventional photo-injectors. Moreover, the use of the superconducting cavity allows cw-mode operation and thus high average currents. Table 1 shows some simulated rf cavity parameters.

The current progress of this project is presented in [1]. This paper deals with the treatment of the cavity itself, one of the main parts of the SRF-Gun. Fig. 1 shows a schematic of its design which is described more in detail in [2].

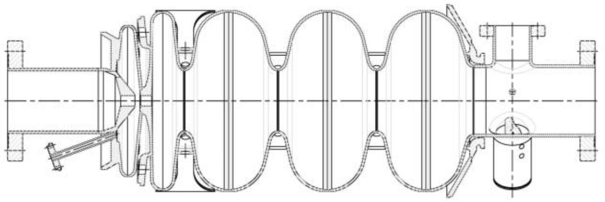

Fig. 1: cross section of the cavity design.

CAVITY WARM TUNING

In order to get the right field distribution and the accurate frequency at operation inside the cryostat, one has to consider different tuning parameters.

Table 2: evaluation of the estimated frequency @ 300K

operating frequency @ 2K	***1300.0 MHz***
cool down shrinking (measured @ ELBE)	*- 1.97 MHz*
50µm BCP @ DESY (simulated)	*+ 0.55 MHz*
pre-stressing half cell (measured)	*+ 0.10 MHz*
pre-stressing three TESLA cells (measured)	*+ 0.22 MHz*
required frequency @ 300K	***1298.9 MHz***

The correct frequency at room temperature mainly depends on cool down shrinking, additional chemical treatment and pre-stressing of both cavity tuners. These tuners permit an axial deformation of ±400µm and ±500µm for the half cell and the three TESLA cells, respectively. The induced frequency shifts have been taken into account. Thus, the estimated tuning frequency follows from Table 2.

Table 3: field detuning caused by pre-stressing half cell

	Gun Cell	TESLA1	TESLA2	End Cell
detuning axis field	***-7.3%***	***-1.8%***	***+1.4%***	***+3.1%***

#a.arnold@fz-rossendorf.de

A non-negligible detuning of the π-mode field, as shown in Table 3, is caused by pre-stressing of the half cell. This measurement has to be considered inversely by pre-tuning to obtain the right field profile in the cryostat.

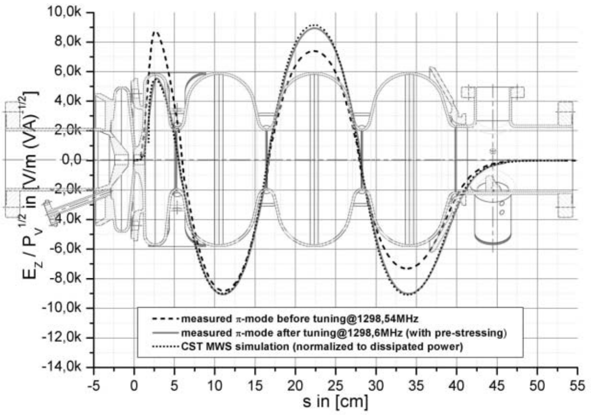

Fig. 2: measured vs. simulated π-mode field profiles before and after tuning.

Based on these target values, the tuning process was realized as presented in [3]. It succeeded in the measured field profile shown in Fig. 2 and met the calculated requirements.

EXT. Q STUDY MAIN-COUPLER

In order to maximize the rf power transfer from klystron to the electron beam, it is absolutely necessary to match the coupling. The applied Rossendorf main coupler is not adjustable, thus the antenna is optimized for maximum beam power with an external quality factor of:

$$Q_{ext} = \frac{Q_0}{1 + P_{beam}/P_C} = 2.7 \bullet 10^7 \qquad (1)$$

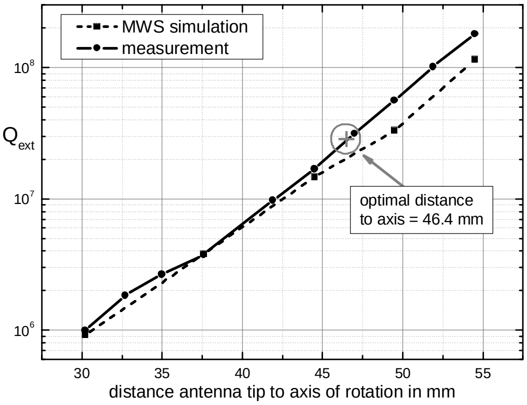

Fig. 3: external quality factor vs. antenna length.

The determination of the suitable distance between antenna tip and axis of rotation is done by an additional probe antenna added at the opposite side of the cavity at room temperature. As shown in equation 2 one has to measure incident and reflected power at the input port, the transmitted power at the main coupler as well as the unloaded quality factor of the cavity.

$$Q_{ext} = \frac{Q_0}{\beta_{ext}} \quad with \quad \beta_{ext} = \frac{P_t}{P_i - P_r - P_t} \qquad (2)$$

The results presented in Fig. 3, point to the best coupling at a distance of 46.4 mm from axis. An additional calculation, using the results of MWS©-simulations with different boundary conditions as shown in [4], gives a similar performance.

TUNING HOM-COUPLER

We use the welded DESY TTF II HOM-couplers. Due to the asymmetric design caused by the cathode and its cooling support, both couplers are welded to the coupler section at the end of the beam tube. To estimate the precision achieved by trap circuit tuning, we measured the external quality factor at the π-mode frequency versus tuning displacement and frequency shift. To prevent crosstalk it is necessary to place the input antenna probe at the opposite side of the HOM couplers. The result is presented in Fig. 4. It is obviously hard to get a better external quality factor than $Q_{ext}=10^{11}$. In that case less than 10% of the dissipated power is transmitted out of each HOM-coupler.

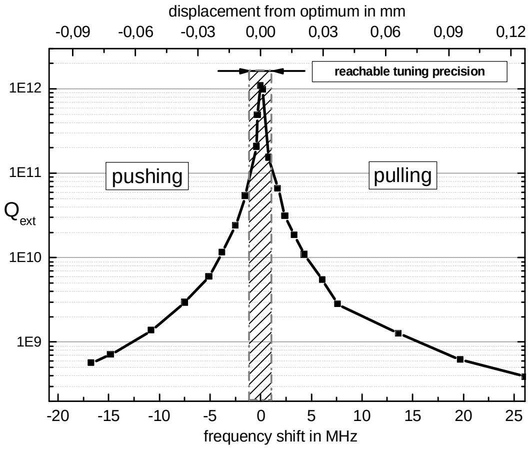

Fig. 4: external quality factor vs. detuning from best π-mode suppression.

TUNING CHOKEFILTER

The choke filter is situated next to the first gun cell and described more in detail in [5]. It prevents the leakage of RF power through the coaxial line out of the cavity which is caused by the cathode and its coupling to the gun cell. The filter is designed as a coaxial trap filter. Its band pass frequency will be adjusted during the assembling of the cryostat. To estimate the transmitted power, we measured the external quality factor versus detuning of the choke cavity by crushing and stretching. For this purpose an antenna probe with the same diameter as the original cathode was used. Thus the power behind the choke filter depending on the dissipated power through the walls can be measured (Fig. 5).

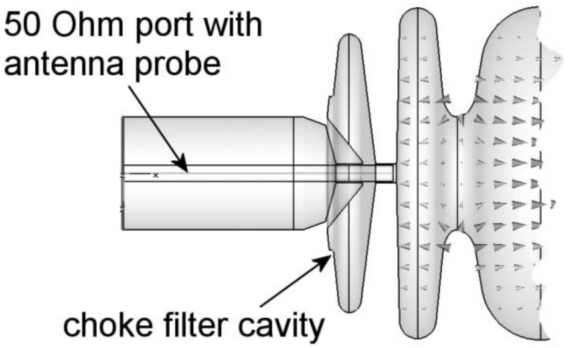

Fig. 5: assembly to measure π-mode suppression.

As a result one gets a tuning curve shown in Fig. 6. Because of mechanical tolerances during the assembling of the cryostat, it is hard to improve the accuracy better than ±100 microns. Within this range, the external quality factor is better than $Q_{ext}=10^{12}$ and the transmitted power behind the choke is less than 1% of the dissipated power. An additional MWS simulation yielded comparable results.

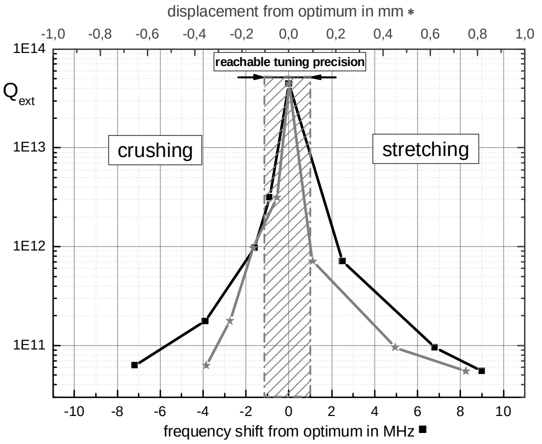

Fig. 6: external quality factor vs. choke filter detuning measured by frequency shift and deformation.

1^{ST} VERTICAL COLD TEST

Following the tuning procedures the cavity was prepared at DESY Hamburg by buffered chemical polishing (40μm BCP) and high pressure rinsing (HPR). Afterwards the cavity was tested in a vertical cold test, as described in [6]. During the cool down from 4.4K to 1.6K the unloaded quality factor was measured at low rf power (Fig. 7). The illustrated surface resistance follows from eq. 3 and the numerical calculated geometry factor G.

$$R_S = \frac{G}{Q_0} \qquad with \qquad G = 241.9\Omega \tag{3}$$

$$R_S = A_S \cdot \omega^2 \cdot \frac{1}{T} e^{-\frac{\Delta}{k\cdot T}} + R_{res} \qquad \text{für} \qquad T < T_C/2 \tag{4}$$

Based on the BCS-theory the surface resistance can also be calculated analytically. Fitting the measured data points by using eq. 4 leads to the following material parameters:

$$A_S = 2.42\cdot 10^{-15}\frac{\Omega\cdot{}^\circ K}{Hz^2} \quad ; \quad \Delta = 1.53meV \quad ; \quad \underline{R_{res} = 3.43n\Omega}$$

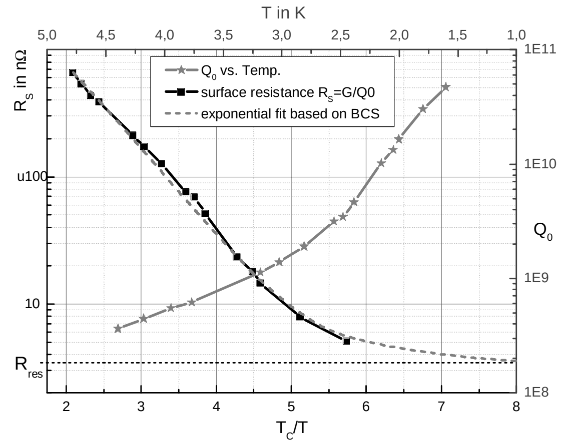

Fig. 7: surface resistance and unloaded quality factor versus temperature.

In view of the measured, unloaded high quality factor $Q_0(@1.8K)=3x10^{10}$ and the calculated low residual resistance of $R_{res}=3.4n\Omega$ the preparation of the cavity proceeded well.

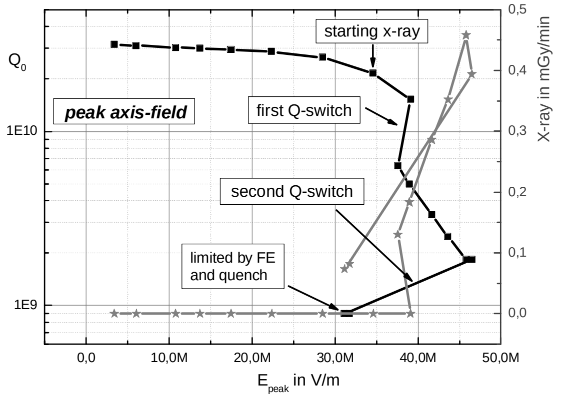

Fig. 8: Q_0 vs. peak axis field E_{peak} @1.8K.

Another matter of substantial interest is the Q vs. E chart. The corresponding measurement also takes place at DESY. In order to get comparable values, Q_0 is plotted versus peak axis field in the TESLA cells (design value

E_{peak}=50MV/m). Furthermore the radiation caused by field emitters is included into the same chart. As shown in Fig. 8 field emission started early and the quality factor decreases. Further increasing of rf power results in strong field emission and two Q-switches, which are probably caused by thermal breakdown at activated field emitters. After the second Q-switch the field was limited by quench. Especially the behaviour the Q-switches are most likely due to defects in the bulk niobium or to surface pollution. This might be induced by the hardly cleanable choke filter. Because of the narrow cathode feed through between choke filter and gun cell, direct cleaning of the filter cell wasn't feasible. Furthermore contaminated water runs out of it into the cavity which leads into polluted surface.

CONCLUSION

So far all measurements and tuning procedures yield acceptable results. In the next steps an improved HPR and BCP treatment will be established to achieve the designed peak field. Nevertheless the reached field of E_{peak}=39MV/m and the high quality factor of Q_0=1.5x10^{10} demonstrates first of all the proper design of the gun cavity.

ACKNOWLEDGEMENT

This work is supported by the European Commission within the framework of the CARE project, EU contract number RII3-CT-2003-506395.

REFERENCES

[1] D. Janssen , et al., “progress of the Rossendorf SRF Gun project”, proc. of EPAC 2006, Edinburgh, UK.
[2] J. Teichert, et al., “a superconducting photo-injector with a 3.5-cell cavity for the ELBE linac”, proc. of EPAC 2004, Lucerne, Switzerland.
[3] A. Arnold, et al., “field profile measurements of the 3½ cell SRF Gun”, proc. SRF Workshop, Ithaca, USA, 2005.
[4] P. Balleyguier: “External Q studies for APTT SC-Cavity Couplers”, CEA/DPTA, Bruyères-le-Châtel, France.
[5] P. v. Stein, internal report, FZR-227, Forschungszentrum Rossendorf, 1998.
[6] Jens Knobloch: Basic Concepts of Measurements Made on Superconducting RF Cavities, Laboratory of Nuclear Studies, Cornell University, August 1991.

HIGH PEAK CURRENT DESIGN OF A SUPERCONDUCTING CAVITY FOR A SRF PHOTOINJECTOR

D. Janssen, FZ-Rossendorf, Dresden, Germany, F. Marhauser, BESSY, Berlin, Germany
V. Volkov, BINP, Novosibirsk, Russia.

Abstract

A 1.5-cell cavity for a superconducting RF gun has been designed and a magnetic RF mode for emittance compensation is applied. For a peak current of 125A a transverse emittance of 1.8 mm mrad has been obtained.

INTRODUCTION

In collaboration between BESSY, DESY, FZR, MBI and BINP a 3½-cell superconducting RF electron gun is under development. The status of the project and the progress obtained is reported on this conference. The motivation for the design of a new gun cavity is the proposed FEL project at BESSY. This FEL requires a bunch charge of 2.5 nC with transverse slice emittances around 1.5 π mm mrad. In the following we will discuss the design of a 1½-cell cavity with a frequency of 520 MHz for the accelerating mode (TM mode) and 1560 MHz for the magnetic mode (TE mode). The design of a 1½ cell superconducting cavity with a frequency of 1.3 GHz has been also reported in [5].

DESIGN CONSIDERATION USING THE PILLBOX MODEL

In order to find some general rules for the cavity design, we will discuss a simple pillbox model, where the frequencies and RF fields are known analytically.

Figures of merit

In order to avoid a quench of the cavity, the maximum magnetic field on the cavity surface should be clear below 180 mT. Otherwise an optimal beam dynamics needs large electric and magnetic fields on the cavity axis. So the expressions

$$F_{nml}^{TM} = \left| \frac{Ez_{nml}^{\max}(r=0)}{Bs_{nml}^{\max}} \right|, \quad F_{0ml}^{TE} = \left| \frac{Bz_{0ml}^{\max}(r=0)}{Bs_{0ml}^{\max}} \right|$$

are essential parameters for the quality of the cavity. For a pillbox with length L and radius R one obtains:

Table 1: Figures of merit of the TM mode for R = L

$F_{0ml}^{TM}\ [\frac{MV/m}{mT}]$	m = 1	m = 2	m = 3
l = 0	0.587	0.587	0.587
l = 1	0.351	0.502	0.543

From the first table follows, that at the surface limit of 180 mT the pillbox has an accelerating field of 105 MV/m! Therefore our cavity design should be as close as possible to the pillbox geometry. The main difference between a pillbox and a realistic cavity cell is the beam tube. In order to minimize the influence of the beam tube on the RF field of the cavity cell, the ratio of the cell to the tube radius should be large. The lower limit of the beam tube radius is fixed by wake field effects of the bunch charge. Therefore the cell radius should be as large as possible. This radius is inversely proportional to the cell frequency, so we fix the frequency of the TM mode to 520 MHz, which is the TESLA frequency divided by 2.5.

Table 2: Figures of merit of the TE mode for
R/L $\geq J_1^{\max}\pi l / \left(J_0\left(q_m\right)q_m\right),\ J_1\left(q_m\right) = 0$

F_{0ml}^{TE}	m = 1	m = 2	m = 3
l = 1	2.48	3.33	4.00

The second table shows that the axial magnetic field is enhanced when increasing the radial node number for a given surface field. Therefore a high frequency TE mode should be preferred.

Third order effects

The power expansion of radial RF field components with respect to the radius r starts with a linear term and is followed by third order terms. These third order terms produce an increase of the transverse beam emittance. In the pillbox cavity for the TM modes with l = 0 the third order terms are zero. For the magnetic TE modes the ratio of the third order term divided by the first order term is given by

$$\frac{(Bz''' + \frac{\omega^2}{c^2} Bz')}{Bz'} = \left(\frac{q_m}{R}\right)^2 \qquad (1)$$

Therefore the nonlinear effects increase quadratic with increasing node number m of the TE mode and decreasing radius R of the cavity cell. From this point of view the gun should work at the lowest TE mode frequency.

Comparison of the TE mode with a static magnetic field

Neglecting terms in r^2 in the equation of motion for an electron in the RF field of the TE mode the following equations are obtained:

$$\varphi' = -\frac{eB_z}{2m\gamma}, \quad r'' = -\frac{e^2}{4\gamma^2} B_z^2 r \qquad (2)$$

These are the same equations as in the static magnetic field. Assuming $\beta \approx 1$ we can replace the time dependence in the RF field by z/c and calculate the focal distance of the corresponding magnetic lenses.

$$\frac{1}{f}=\frac{e^2}{4m^2c^2\gamma^2}\int_{-\infty}^{\infty}B_z^{\,2}dz\,,\quad B_z=b(z)\sin(\omega\frac{z}{c}+\varphi_0) \qquad (3)$$

In this case the focal distance is a function of the phase φ_0 of the TE mode. For the case of a pillbox cavity we obtain:

$$\frac{1}{f}=\frac{e^2}{4m^2c^2\beta^2\gamma^2}\frac{L}{\pi}B_0^2\left(\frac{\pi}{4}+\sin(\alpha\pi)\frac{\cos(\alpha\pi+2\varphi_0)}{4\alpha(\alpha^2-1)}\right)$$

$$\alpha=\sqrt{\left(\frac{q_m L}{\pi R}\right)^2+1} \qquad (4)$$

For α = 2,3, … the focal distance is independent of φ_o and for α =1/2 , 3/2, …. we have the maximal phase dependence. These limiting cases can be realized numerically also for realistic cell geometry.

The emittance compensation in a RF gun is based on the focussing of electrons inside a magnetic field. Therefore the quotient of cell radius and cell length defines the phase dependence of the focal distance and the phase dependence of the emittance.

CAVITY DESIGN AND RF FIELDS

As mentioned in the first section, the TM mode frequency of our gun cavity is 520 MHz. At this frequency the beam energy of a 1½-cell cavity with E_{peak} = 30MV/m is already greater 10 MeV. The cell radii are determined by the TM frequency and the field amplitudes on the cavity axis. We place the TE mode in the second cell. After this the phase slippage of the TM mode and the TE mode frequency define the width of the cells. As discussed in the previous section, the TE frequency can be defined by different arguments. In this calculation the frequency of 1560 MHz is used. This mode has the radial node number m = 2 and the field ratio $Bz_{max}(r=0)/Bs_{max}$ is 2.69. Furthermore, the integer value of the TE/TM frequency ratio allows the operation of the RF gun with the same TE - phase φ_o for each bunch. In this case it is meaningful to minimize the emittance with respect to this phase. The cell geometry and the field distribution of the gun are given in Fig.1 and Fig. 2 respectively.

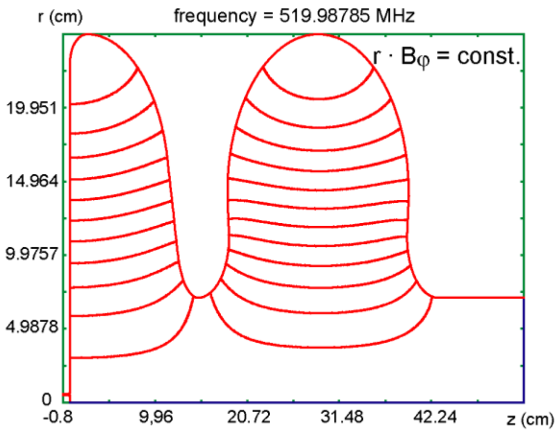

Figure 1: Cavity shape and electric field distribution of the TM mode.

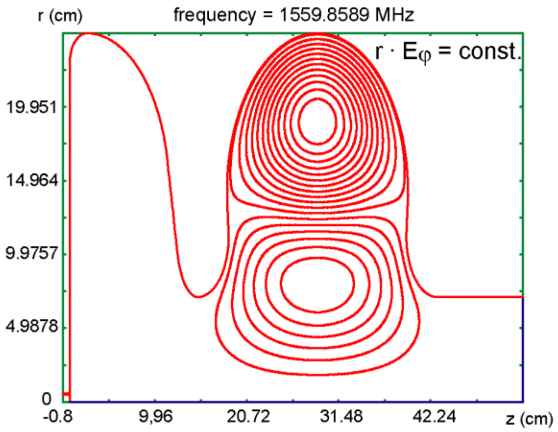

Figure 2: Cavity shape and magnetic field distribution of the TE mode.

Fig. 3 shows the fields on the cavity axis.

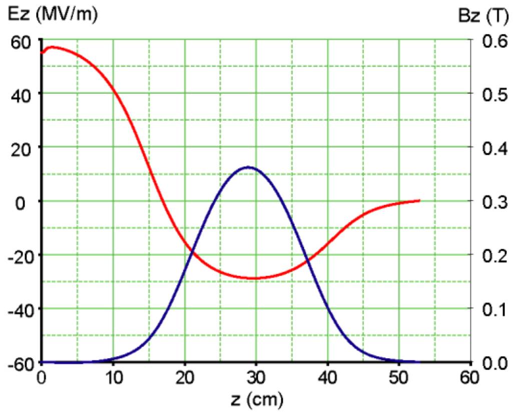

Figure 3: Axis fields of the cavity.

FIELD AMPLITUDES

The magnetic surface fields of the TM and the TE mode are perpendicular to each other. Therefore we have to evaluate the vector sum of both surface fields to compute the limiting field. Table 3 lists the maximal field limits used in the calculations. They are clearly below the critical limit. In Fig.4 the two surface fields and the sum of both fields are shown.

Table 3: Maximum axial and surface field values

field	unit	value
Ez_{max}	MV/m	57
Bz_{max}	mT	363
Bs_{max}(TM)	mT	130
Bs_{max}(TE)	mT	118
Bs_{max}	mT	130

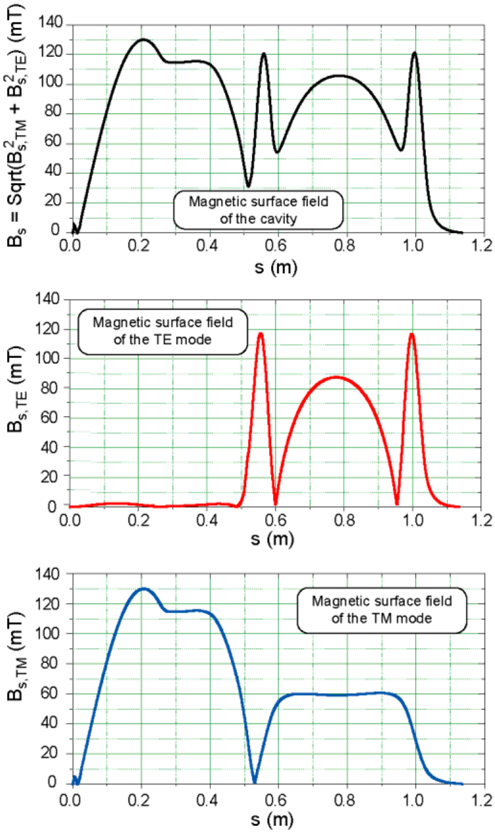

Figure 4: Magnetic surface fields in dependence on the surface coordinate s, $Bs = \sqrt{(Bs\_TM)^2 + (Bs\_TE)^2}$.

LASER PULSE SHAPE AND THERMAL EMITTANCE

In a RF photo cathode gun the laser pulse determines the bunch shape at the cathode. In the present calculations a temporal flat top laser pulse profile up to L_t = 40 ps and a rise and fall time of 2 ps have been used. The radial distribution is uniform. At a laser wavelength of 260 nm the electrons leave the cathode with a thermal energy of 1 eV isotropically in the whole space. This seems to be a set of realistic parameters [1].

RESULTS OF TRACKING CALCULATIONS

Tracking studies using ASTRA [2] have been performed for the gun cavity followed by a drift space and a booster linac section comprising 3 x 4 1.3 GHz standard 9-cell TESLA cavities to investigate emittance conservation. A Simplex routine has been utilized for a multi-parameter optimization. Hereby the transverse emittance at the linac exit has been minimized by varying the laser spot size at a given laser pulse length L_t and the operational parameters of the RF gun (TM and TE mode) and booster cavities with E_{acc} = 20 MV/m in maximum for the latter. To reduce the computation time four TESLA-cavities have been combined to one section. Typically for 1 nC bunch charge the reasonable laser pulse length is in the order of L_t =20 ps regarding space charge effects arising just at the cathode. To mitigate the enhanced space charge at 2.5 nC the laser pulse length could be further increased sacrificing some longitudinal emittance. First without the booster linac we have studied the behaviour for L_t = 20 ps resulting in a minimum transverse emittance of ~1.8 π mm mrad at a distance of ~5.3 m behind the photocathode for Bz_{max} = 363 mT as shown in Fig. 5.

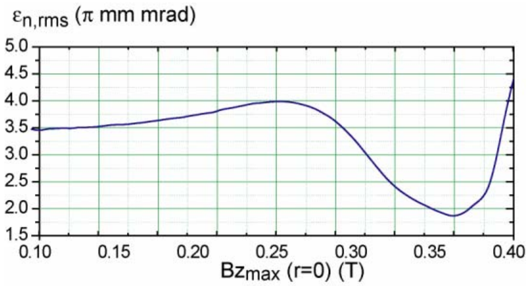

Figure 5: Dependence of the projected transverse emittance on the axial TE mode amplitude (position behind cathode z = 5.3 m, laser spot radius 1.25mm).

With these settings however one operates apart from the usual emittance compensation in the drift. Thus when including the booster we observed that the beam can not be matched according to the so-called invariant envelope (I.E.) [3]. Instead the beam is strongly focussed within the linac due to RF-focussing and without measures tends to extend behind the focal point.

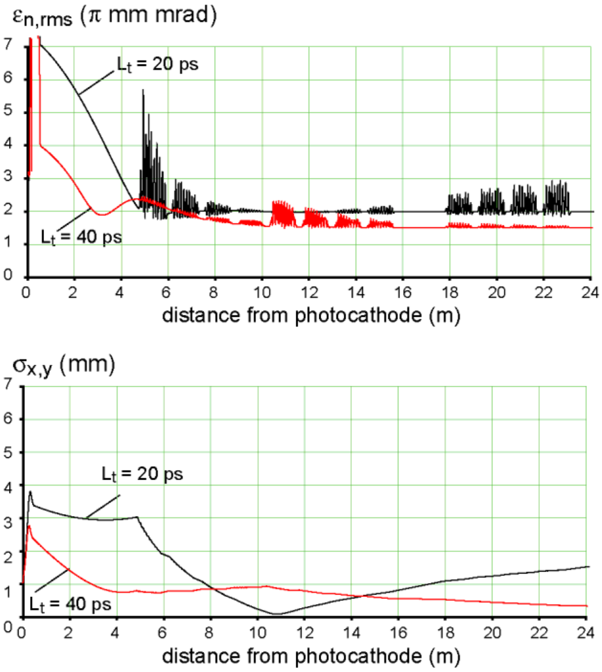

Figure 6: Evolution of the projected transverse rms emittance (top) and rms beam size (bottom) through the linac for L_t = 20 and 40 ps respectively (30000 particles).

The projected emittance can not be further minimized but rather stays constant. This is illustrated in Fig. 6 showing the evolution of the projected transverse rms emittance (top) and rms beam size (bottom) for L_t = 20. However the projected emittance is largely deluted by mismatched fringe particles which are responsible for the oscillations of the projected emittance within the linac cavities. Actually the slice emittance as the figure of merit amounts to only 1.1 π mm mrad in average.

We then tried to match the beam to the booster by following more closely the I.E.. This necessitates to adjust the electric field of the gun according to Bz_{max} to balance the repelling and focussing forces. Thus a typical emittance compensation accompanied by an emittance oscillation with a double emittance minimum in the drift [4] can be produced. Holding the I.E. criterion in this mode of operation the minimum projected emittance obtained for L_t =20 ps however is rather large (~4 π mm mrad). Moreover the accelerating fields in the first TESLA-cavities would be in the order of E_{acc} = 40 MV/m. However, the situation relaxes once the pulse length is further increased. This has been done using L_t =40 ps in a next step as shown in Fig. 6 as well. Here a projected transverse emittance of only 1.5 π mm mrad is achieved. As more particles follow the I.E., the average slice emittance is ~1.4 π mm mrad only marginally below the projected emittance.

Table 4 and 5 summarizes the optimized parameter settings and achieved results at the booster exit (z = 24m) for L_t = 20ps and L_t = 40ps respectively. Albeit the results are not regarded as an overall optimum yet, the required specifications of the BESSY FEL can be well fulfilled.

Table 4: Parameter settings for the photocathode laser, RF gun (TM and TE mode) and booster cavities respectively

parameter settings	unit	value	
laser			
flat top	ps	20	40
rise/fall time	ps	2	2
spot radius	mm	1.2	1.35
thermal energy	eV	1	1
thermal emittance	π mm mrad	0.69	0.77
RF gun			
gun TM field (max.)	MV/m	54.8	54.6
beam energy	MeV	9.8	9.7
magnetic TE field (max.)	mT	354	360
peak surface field	mT	128	127
booster cavities			
acc. field (cavities #1-4)	MV/m	10.5	7.5
acc. field (cavities #5-8)	MV/m	19.9	20
acc. field (cavities #9-12)	MV/m	17.6	17.4

Table 5: Achieved beam parameters with a bunch charge of 2.5 nC at the exit of the booster linac (z = 24m)

achieved parameters	unit	value	
laser pulse length (z = 0)	**ps**	**20**	**40**
normalized transverse projected rms emitttance	π mm mrad	2	1.5
average slice emittance	**π mm mrad**	**1.1**	**1.35**
trans. rms beam size	mm	1.45	0.37
long. rms beam size	mm	2.7	3.6
average kinetic energy	MeV	218	204
long. rms emittance	keV mm	1438	3250
correlated energy spread	keV	129	305

DISCUSSION AND SUMMARY

For two different lengths of the laser pulse it has been shown, that the design parameter of the injector for the BESSY FEL can be obtained, using a 1½-cell superconducting RF gun. In the calculation a maximal surface field of 130 mT has been assumed. This value corresponds to accelerating field strength of ~28MV/m in a TESLA cavity. For cavity frequencies in the order of 1.3 GHz this value is standard, but the frequency of the accelerating mode in the gun cavity is 520 MHz. For this frequency the maximal surface field, which can be obtained, is an open question.

In the present calculation the cathode has a flat surface, which is inside of the back wall of the cavity. In this simple arrangement we have near the cathode no focussing RF forces and possible wake fields from the cavity surface are absent.

In analogy to [6] we plan to place a Cs_2Te cathode into the superconducting cavity. For this material and λ_{laser} = 260 nm a quantum efficiency of 5% is realistic. In this case the bunch charge of 2.5 nC demands a laser pulse energy of 0.24 μJ.

ACKNOWLEDGMENT

The authors thanks Dirk Lipka (BESSY), Klaus Floettmann (DESY) and the members of the SRF gun project group for many helpful discussions.

REFERENCES

[1] I. Will, MBI Berlin, private communication.
[2] K. Flöttmann, http://www.desy.de/~mpyflo/.
[3] L. Serafini, J. B. Rosenzweig, Phys. Rev. E, Vol. 55, June 1996, 7565.
[4] M. Ferrario et. al., SLAC-PUB 8400, March 2000.
[5] J.Sekutowicz et al., Phys. Rev. ST Accel. Beams 8, 010701 (2005).
[6] D.Janssen et al., Nucl. Instr. and Meth. A507 (2003) 34.

CRYOMODULE AND TUNING SYSTEM OF THE SUPERCONDUCTING RF PHOTO-INJECTOR*

J. Teichert#, A. Arnold, H. Buettig , R. Hempel, D. Janssen, U. Lehnert, P. Michel, K. Moeller, P. Murcek, C. Schneider, R. Schurig, F. Staufenbiel, R. Xiang, FZ Rossendorf, Dresden, Germany,
T. Kamps, D. Lipka, BESSY, Berlin, Germany, J. Stephan, IKS, Dresden, Germany,
W.-D. Lehmann, SGE, Dresden, Germany, G. Klemz, I. Will, MBI, Berlin, Germany.

Abstract

The designs and a report on the progress in construction and testing of the cryomodule and the tuning system for the SRF gun are presented. The SRF gun project, a collaboration of BESSY, DESY, MBI and FZR, aims at the installation of a CW photo injector at the ELBE linac. The cryostat consists of a stainless steel vacuum vessel, a warm magnetic shield, a liquid N cooled thermal shield, and a He tank with two-phase supply tube. A heater pot in the He input port will be used for He level control. The 10 kW power coupler is adopted from the ELBE module. A cooling and support system for the NC photo cathode has been developed and tested. It allows the adjustment of the cathode with respect to the cavity from outside. The cryomodule will be connected with the 220 W He refrigerator of ELBE and will operate at 1.8 to 2 K. The static thermal loss is expected to be less than 20 W.

Two tuners will be installed for separate tuning of the three TESLA cells and the half-cell. The tuners are dual spindle-lever systems with step motors and low-vibration gears outside the cryostat. Functionality, tuning range and accuracy have been tested in cryogenic environment.

INTRODUCTION

Superconducting radio frequency (SRF) acceleration technology is well established for electron linacs with considerable progress in acceleration gradient during the last years [1]. The adequate SRF photo-injector was already proposed in 1988 [2], but up to now such an injector has not been operated at an accelerator. As electron sources for SRF electron linacs, DC photo-injectors or thermionic injectors are in use for CW operation or normal-conducting RF photoinjectors in pulsed mode. The RF photo-injectors deliver electron beams of highest quality (short bunch length and low transverse emittance at high bunch charge). Its combination with a superconducting cavity would further allow CW operation. After a successful proof-of-principle experiment with a half-cell cavity [3] a project for a SRF photo injector has been launched in 2004. The goal of this project, carried out in a collaboration of BESSY, DESY, MBI and FZR, is to build a fully functioning SRF photo-injector for the ELBE accelerator. Beside the significant beam quality improvement, the operation at ELBE will allow long term studies of important issues of SRF injectors like low-temperature operation and lifetime of photo cathodes, or cavity quality degradation.

The design parameters of the SRF gun are presented in Table 1. The gun will be operated in three modes: the standard ELBE FEL mode with 77 pC and 13 MHz pulse repetition, the high charge mode for neutron physics at ELBE and ERL studies (1 nC, 1 MHz), and the BESSY FEL mode (2.5 nC, 1 kHz). A UV driver laser system for these three operation modes is under development [4]. Beam parameter studies will be performed with a new diagnostic beam line [5]. The ELBE mode is determined by the two existing far infrared FELs which need 13 MHz bunch repetition rate, as well as the maximum average current of the ELBE accelerator. The high charge mode is essential for neutron physics experiments planned at ELBE where time-of-flight measurements require 1 µs pulse spacing without average current reduction. At the same time, 1 nC is a typical bunch charge for new FEL projects and state-of-the-art normal conducting RF photo injectors (e.g. FLASH at DESY) where the beam parameter should be measured and compared. It is planned to study and optimize different emittance compensation methods proposed for SRF guns, like a downstream magnetic solenoid, RF focusing with a backtracked and properly shaped photocathode, and RF focusing with an additional TE mode [6] in a future upgrade. For the soft x-ray BESSY FEL project [7] a bunch charge of 2.5 nC is envisaged and the SRF gun will be evaluated with respect to future application.

CRYOMODULE

The basic design for the SRF gun cryomodule was adopted from the ELBE cryomodule [8] which contains two 1.3 GHz TESLA cavities and is developed for CW operation with 10 MeV per cavity at a beam current up to 1 mA. ELBE modules are in routine operation since 2001 at FZ Rossendorf and wide experience has gained for these modules. The SRF gun cryomodule contains one 3½ cell cavity which consists of a half-cell with the normal-conducting cathode in it and three acceleration cells with TESLA shape [9]. The envisaged acceleration gradient of this cavity is 18.8 MV/m which corresponds to a

---

* We acknowledge the support of the European Community-Research Infrastructure Activity under the FP6 “Structuring the European Research Area” programme (CARE, contract number RII3-CT-2003-506395) and the support of the German Federal Ministry of Education and Research grant 05 ES4BR1/8.

#j.teichert@fz-rossendorf.de

maximum axial peak field of 50 MV/m in the TESLA cells. The geometry constant is 240 Ω and R/Q is 165 Ω. For $Q_0 = 1x10^{10}$ and the gradient mentioned above a RF power dissipation of 26 W is expected.

Table 1: Gun design parameters and expected beam values for the planned operation modes

	ELBE mode	**high charge mode**	**BESSY-FEL**
RF frequency	1.3 GHz		
beam energy	9.5 MeV		
Operation	CW		
drive laser	262 nm		
Photocathode	Cs_2Te		
quantum efficiency	>1 %		>2.5 %
average current	1 mA		2.5 µA
pulse length	5 ps	20 ps	50 ps
Repetition rate	13 MHz	[1MHz	1 kHz
bunch charge	77 pC	1 nC	2.5 nC
transverse emittance	1.5 µm	2.5 µm	3.0 µm

Fig. 1 shows a section view of the SRF gun cryomodule. The stainless steel vacuum vessel has a cylindrical shape with 1.3 m length and 0.75 m diameter. The vessel has flat plates on both sides and is designed as short as possible in order to get a minimum length of the transfer rod for cathode exchange, and on the beam line side it is planned to install a solenoid magnet for emittance compensation as close as possible. The He port and the N_2 port are on top on the right hand side. The refrigerator delivers 4.5 K helium to the valve box, about 5 m before the cryomodule. There is the Joule-Thompson valve for expansion. From the port the He flows through a heater pot and the two-phase supply tube into the chimney of the He tank. For the cooling of the thermal shield, liquid nitrogen is used. The 70 K shield consists of a cylindrical Al sheet welded to two circular tubes filled with N_2. The liquid N_2 tank in the upper part of the module must be refilled after about 5 h from an outside dewar. The liquid N_2 is also used for the cooling of the photo cathode stem. The photo emission layer, which is Cs_2Te, and the Cu cathode stem are normal conducting. The heat load from the RF field into these parts, estimated to be between 10 and 20 W, burdens the liquid N_2 bath.

The cavity is passively protected against ambient magnetic fields by means of a µ-metal shield, placed between the 80 K shield and the vacuum vessel. The shield is fabricated and its suppression of the earth magnetic field was measured. The results are shown in Fig. 2. In the region where the Nb cavitiy will be placed, the residual magnetic field is below 1 µT which is the limit during the cool-down [9].

The He tank is made of titanium. Three stainless steel bellows are integrated for the two tuning systems and for the manually tuned choke filter cell. The ten thin titanium spokes support the He tank and allow the adjustment of the cavity position. The spokes end in micrometer drives and vibration dampers attached to the vacuum vessel. The main power coupler is the 10 kW CW coupler of the ELBE module. It contains a conical cold ceramic window at 70 K in its coaxial part. The warm REXOLITE window is in the waveguide.

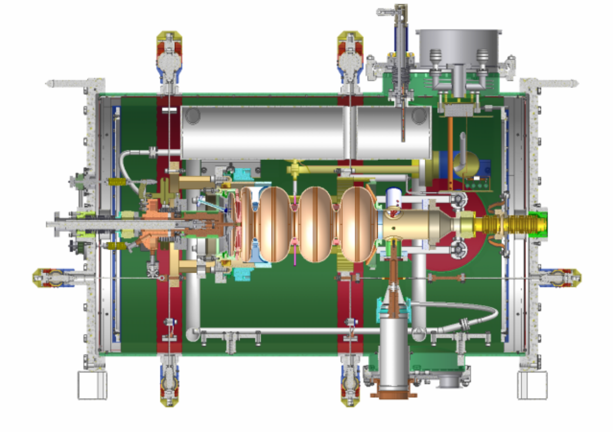

Figure 1: Cut drawing of the SRF gun cryostat.

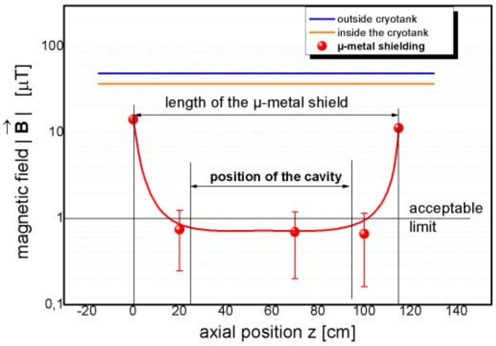

Figure 2: Measurement of the earth magnet field suppression by the µ-metal shield.

From outside it is also possible to move the cathode support and cooling system which allows the adjustment of the photo cathode with respect to the cavity. For that reason, three rotation feed-throughs exist in the backside plate of the vacuum vessel. Fig. 3 shows the design of that system.

The main sources for the static heat leak are the coaxial tube of the power coupler, the beamline vacuum tube and the vacuum tube for the cathode exchange system (both DN40), and the rotational drives of the two tuners. For all these subsystems the design is similar to the ELBE cryostat. Thus nearly the same static heat leak of less than 20 W can be expected.

The SRF gun will be installed in parallel to the existing thermionic injector of the ELBE accelerator. The cryostat will be connected with the existing 220 W He refrigerator. A new helium transfer line with valve box was assembled and tested in January 2006. Its design allows the connection of the SRF gun cryostat without warming up the other two ELBE cryomodules. The cryostat can be operated down to 1.8 K but the standard operation temperature at ELBE is 2 K (31 mbar). In the ELBE helium cooling system, the pressure stabilization is performed with cold compressors located in the cool box of the helium refrigerator. It will be performed for all three cryostats together based on a pressure value in one module. During operation of the two ELBE modules, it turned out that the common pressure stabilization worked well for constant liquid helium flux to the modules. In order to realize that, the total heat power from the electrical heater in the module and the RF power dissipation was hold constant by means of a feed-forward control.

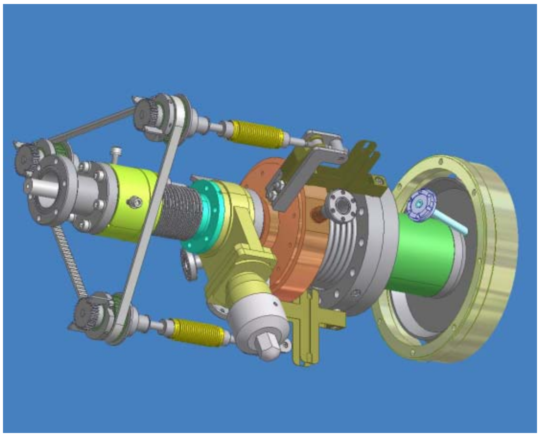

Figure 3: The cathode alignment system.

TUNING SYSTEMS

For the SRF gun cavity a frequency tuning is needed for the choke filter, the half-cell and the three TESLA cells. The bandwidth of choke filter is comparably large. Therefore a tuning during assembling in the warm stage is sufficient. For the accelerating cells tuning is required during operation. The half-cell on one hand and the three TESLA cells on the other essentially differ in their mechanical properties, especially in their stiffness. Therefore it was decided to use two separate tuning systems, one for the half-cell and one for the three TESLA cells in common.

The tuner design is adopted from the ELBE cryomodule dual spindle-lever tuning system [8]. Main objectives are a sufficiently large tuning range, high resolution, a hysteresis-free and linear operation, long life time and low cryogenic loss. But the requirements are less restrictive than for tuners in high-energy SRF linacs: Due to CW operation a fast tuning for the compensation of Lorentz force detuning (LFD) with piezoelectric actuators is not needed. This applies to active microphonics compensation too, since for a bandwidth of about 100 Hz and a moderate acceleration gradient up to about 20 MV/m, passive methods for microphonics reduction are sufficient. Costs per unit and compactness are less important too. On the other hand, the two tuners for the SRF gun cavity have required a sophisticated mechanical design due to many mechanical and cryogenic constraints and the insufficient clearance at cathode side of the cavity and the He tank. At the end, the ELBE tuner design was modified essentially.

The tuner mechanism consists of a spindle with partly left-hand thread and right-hand thread and two levers. Via the threads and the lever system the rotational motion is transformed into a longitudinal motion performing the length variation of the half-cell and the TESLA cells, respectively. The use of two levers ensures that no axial force is present on the spindle. The bearing point of the leverage system has no rotational parts. It consists of two flexible links as it is shown in Fig. 4. The advantage is the lack of any hysteresis due to friction effects and bearing clearance. The third flexible link is connected with a moving bolt which transfers the force to the parts of the He tank joint to the end plates of the half-cell or the TESLA cells. To allow the movement the He tank has two bellows.

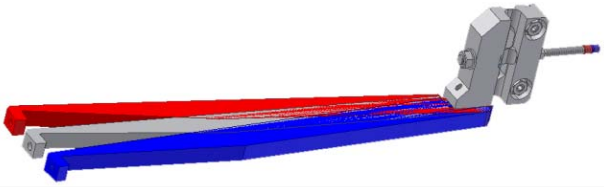

Figure 4: Lever and flexible link of the tuner.

The step motor driving the tuner spindle is outside the vacuum vessel. The fixed point is between the half-cell and the first full cell where the star-like arranged plates of the cavity are welded with the He tank. The motor motion is transmitted by rotation feed-throughs and a two-stage bellows coupling (the 70 K point is in between) to the spindle of the tuning system. The bellows compensate the shrinking offset and reduce the heat conduction. Both tuning systems have the same design. They differ in the lever lengths only.

The frequency constants Δf/dL of the SRF gun cavity were measured with the help of the warm tuning machine developed at FZR [10]. The measurement results are 254 kHz/mm for the half-cell and 449 kHz/mm for the three TESLA cells. These values belong to the change of the π mode frequency of the whole cavity, where the three TESLA cells were unchanged in the first case, and the half-cell in the second. Simple numerical estimations with SUPERFISH assuming a smoothly and homogeneous change of the surface contour give 674 kHz/mm for the half-cell and 625 kHz/mm for the TESLA cell tuning. The large difference for the half-cell seems to be an effect of the low stiffness of the end disk or of other weak areas having low influence on the frequency.

For operating tests and parameter measurements a test bench for the designed tuning system was built up. This test bench consists of the liquid nitrogen dewar, the leverage of the tuner, a spring packet to simulate the cavity, and the equipment to produce the tuning force, to perform force and length measurements. The spring packet was variable in order to simulate the half-cell and the three TESLA cells, as well as to measure with preload. For the three TESLA cells a spring constant of 9 kN/mm was taken [11]. The spring constant for the half-cell was assumed to be about three times higher. The preloads were varied between zero and 9 kN. In comparison to the final tuning systems the levers were made of aluminium instead of titanium and the tests were carried out with one lever only.

The results of the tuner test bench are summarized in Table 2. As expected, the tuning range became smaller with 5 kN preload due do the elastic behaviour of the flexible link of the tuner. The hysteresis measured is caused by the test bench mechanics itself. Fatigue effects were not found.

Table 2: Measurements of the tuning ranges in the tuner test bench

tuning range for 2° Lever range	half-cell tuner	TESLA cell tuner
without preload D = 0 N/mm	436 µm 416 kHz	450 µm 247 kHz
with 5000 N preload D = 9000 N/mm	218 µm 208 kHz	223 µm 122 kHz

Table 3 presents the properties of the two tuners for the SRF gun including the test bench results. The limit in the tuning range is given by the maximum bending of the flexible links of ± 1.5°. The expected tuning ranges are sufficient. By comparison, the tuning range in the ELBE modules is 230 kHz [8]. The overall tuner resolution given in the table are estimations taken from the ELBE system. A complete 3D view of the SRF gun tuners with parts of the He tank and the cavity is given in Fig. 5.

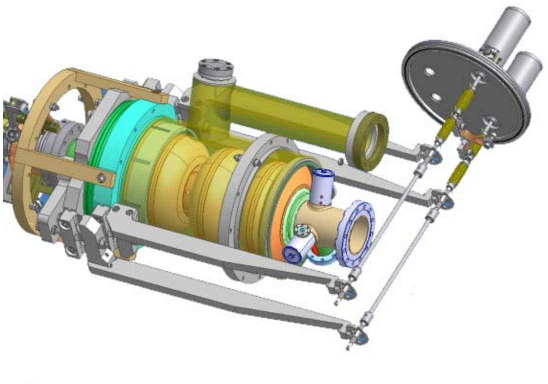

Fig. 5: The two tuners of the SRF gun.

SUMMARY AND OUTLOOK

In the paper the design and the parameters of the cryostat and the cavity tuning systems for the 3½ cell SRF gun are presented. Tests and parameter measurements of the tuners were carried out in a cryogenic test bench with sufficient results. At present, the different subsystems of the cryostat are being assembled und checked. In autumn, first vacuum and cryogenic test are planned. In parallel the treatment and measurement of the niobium cavity is carried out, following by the He tank welding. The commissioning is envisaged with the cool-down and RF tests beginning of 2007.

We would like to acknowledge the permanent support of the ELBE crew (FWL) and the staff of the technical departments (FWF) at FZ Rossendorf.

Table 3: Parameters of the SRF gun tuners

	half-cell tuner	TESLA cell tuner
lever length	630.6 mm	570.2 mm
leverage	50.4	44.2
lever range	33 mm 3.0°	30 mm 3.0°
tuning range	0.7 mm 204 kHz	0.7 mm 404 kHz
cavity frequency constants Δf/dL	178 kHz/mm	283 kHz/mm
mechanical drive step	0.70 nm/step	0.62 nm/step
frequency drive step	0.23 Hz/step	0.28 Hz/step
mechanical resolution	3 nm	
frequency resolution	1 Hz	
position of step-motors	warm, outside	

REFERENCES

[1] L. Lilje, et al., “High-Gradient Superconducting Radiofrequency Cavities for Particle Acceleration”, Proc. of EPAC 2006, Edinburgh, UK, 2006, p. 2752.

[2] H. Piel, et al., FEL 1988, Jerusalem, Isreal, 1988.

[3] D. Janssen, et al., “First Operation of a Superconducting RF Gun”, Nucl. Instr. and Meth. A 507 (2003) 314.

[4] I. Will, et al.,” Photocathode Laser and its Beamline for the Superconducting Photoinjector at the Forschungszentrum Rossendorf”, this conference.

[5] T. Kamps, et al.,”Diagnostics Beamline for the SRF Gun Project”, Proc. of FEL 2005, Stanford, USA, 2005, p. 530.

[6] K. Floettmann, D. Janssen, V. Volkov, “Emittance Compensation in a Superconducting RF Gun with a Magnetic Mode”, Phys. Rev. Special Topics, AB 7 (2004) 090702.

[7] “The BESSY Soft X-ray Free Electron Laser”, TDR BESSY March 2004, eds.: D.Krämer, E. Jaeschke, W. Eberhardt, ISBN 3-9809534-0-8, Berlin (2004).

[8] J. Teichert, et al., “RF Status of Superconducting Module Development Suitable for CW Operation: ELBE Cryostats”, Nucl. Instr. and Meth. A 557 (2006) 239.

[9] B. Aune, et al., “Superconducting TESLA Cavities”, Phys. Rev. Special Topics, 3(2000) 092001.

[10] J. Teichert, et al., “.Progress of the Rossendorf SRF Gun Project“, Proc. of FEL 2005, Stanford, USA, 2005, p. 534.

[11] C. Pagani et al., “Improvement of the Blade Tuner Design for Superconducting RF Cavities”, Proc. of PAC 2005, Knoxville, USA, p. 3456.

DARK CURRENT COLLIMATION AND MODIFIED GUN GEOMETRY FOR THE EUROPEAN X-RAY FEL PROJECT

Jang-Hui Han* and Klaus Flöttmann, DESY, Hamburg, Germany

Abstract

An rf field of 60 MV/m will be applied at the L-band gun of the European X-ray FEL project. Such high rf gradient will allow to achieve a transverse emittance below 1 mm mrad for 1 nC electron bunches but will also produce a high dark current. The dark current generated in the gun shows a comparable dynamics as the electron beams because the same acceleration will be provided from the gun to the last acceleration module. The dark current from the gun might generate high radiation doses in the undulator and limit the long pulse operation of the SASE. To minimize dark current before the first acceleration module, a modified design of a gun cavity and collimator is investigated. The beam dynamics for minimal transverse emittance is optimized with the present and the new designed gun cavity and the resultant machine parameters are used to understand the dark current behavior.

INTRODUCTION

The Free Electron Laser in Hamburg (FLASH) gun operates with a max rf field of about 44 MV/m at cathode. The L-band Cu cavity with cylindrical symmetry is fed through the coaxial rf input coupler [1]. The photocathode is composed of a Mo cathode plug and a Cs_2Te film on the plug. The plug is a cylindrical rod with 16 mm diameter and the emissive film has typically 30 nm thickness and 5 mm diameter. The cathode has a high quantum efficiency (QE) of the order of 1%. Such high QE relaxes the requirement for the drive-laser producing photoelectrons from the cathode.

In August 2006, a long rf pulse of 800 μs has been applied into the gun cavity to produce 600 electron bunches per rf pulse. The number of bunches was limited only by the flat range of the rf pulse in the accelerator modules. In the near future, the bunch train will be expanded to fill out the rf pulse of the gun [2]. At the same time of the long rf pulse operation, the SASE lasing was also successfully achieved with the 600 bunches.

One critical factor limiting the long bunch train operation is the dark current generated in the gun cavity. At the exit of the gun, the dark current is 0.2 $\sim$ 0.3 mA. Simulations of dark current trajectories show that only the dark current emitted at the cathode area can escape from the gun cavity and flow downstream. The dark current starting at the cathode area is mostly released at an rf phase around 90°, i.e. when the rf field is maximum. At the FLASH gun, dark current starting at the cathode has a similar size as the election beams at the collimator position, 1.27 m downstream from the cathode (see Fig. 1). The inner ring-shape dark current seems to come from the boarder of the Cs_2Te film on the cathode plug [3]. The dark current has a larger radius at the emission position and obtains a lower kinetic energy through the gun than the beams. However, 1 nC beams are focused over a longer distance due to the space charge force and the higher momentum than the dark cur-

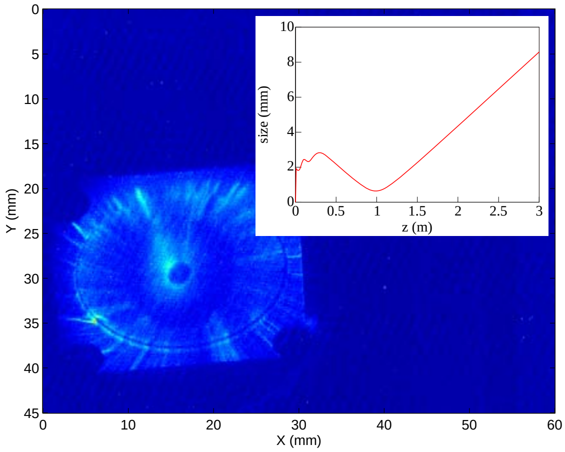

(a) Dark current image and simulation for the dark current from the cathode.

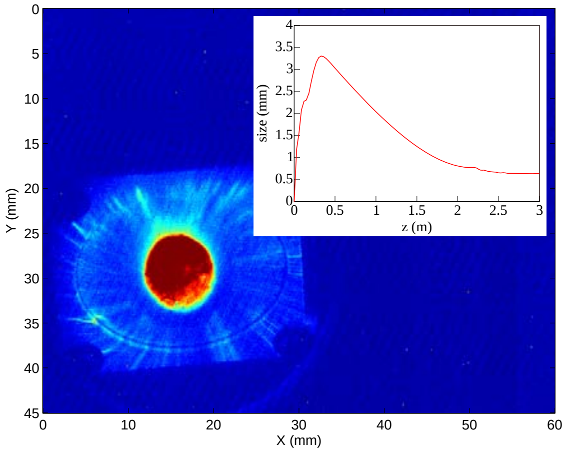

(b) Dark current and 1 nC beam image and beam simulation.

Figure 1: Dark current and beam images taken at the screen 1.27 m downstream from the cathode. Machine parameters for the nominal SASE operation are used. The simulations in the small boxes have been made with ASTRA [4]. A collimator is located at the same position as the screen. The dark current from the cathode has a similar size as the 1 nC bunch. Therefore, the dark current cannot be chopped with the collimator efficiently.

---

* jang.hui.han@desy.de

rent. With the influence of the focusing solenoid, the size of the dark current and the beams are similar at the collimator (see the simulations in Fig. 1).

For a better efficiency, the collimator should be located more downstream because the dark current is strongly overfocused. But, the collimator position is limited by the cryo tank of the first acceleration module. The dark current gets larger than beams as propagating downstream because the dark current has a lower momentum than the beams. This spreading dark current generates radiation doses at the accelerator modules, the bunch compressor and the other beamlines. After the first acceleration module, the dark current can get a kinetic energy of several tens MeV and possibly produce neutrons and γ rays especially at the first bunch compressor. Therefore, it is desirable to collimate the dark current before the first module. This situation is, however, significantly improved at the XFEL design parameters.

XFEL GUN

The XFEL gun will operate with 60 MV/m max rf field for a lower beam emittance and 700 μs rf pulse length for a long bunch train [5]. The dark current generated in the gun is an issue because the dark current might be very high due to the high rf field. Extrapolating the measured dark current level to gradients of 60 MV/m by means of the Fowler-Nordheim equation yields dark current levels in the mA range. This ignores conditioning effects. Moreover is a reduction of the dark current by improved cleaning techniques as dry-ice cleaning expected.

At FLASH a fraction of the dark current has a momentum as high as the electron beam [3]. As increasing the rf field in the gun cavity, the optimum emission phase for the highest momentum gain and the smallest transverse emittance is shifted toward 90° of the rf phase. At FLASH the optimum emission phase is about 38°. When 60 MV/m max field is applied to the FLASH gun cavity (type #1), the optimum emission phase will be shifted to 45°. This means that a larger fraction of the dark current emitted around 90° rf phase will overlap with the electron beam in the momentum spectrum.

In order to separate the momentum distribution of the dark current from the beam, the half cell of the gun cavity is elongated by 10 mm (type #2). The on-axis rf field profiles of the two cavity types are shown in Fig. 2. The rf field profile is calculated with SUPERFISH [6]. When the half cell is longer, the electrons have to start at an earlier rf phase to gain the most effective acceleration through the cavity. The dark current starting around 90° will be too late to be efficiently accelerated.

Beam dynamics

Machine parameters of the injector, including the gun and the first acceleration module, are optimized for a minimum emittance (Fig. 3 and Table 1). When the half cell is elongated, the optimum emission phase is shifted toward 0°. For cavity type #1, the optimum emission phase is 45°, resulting in an rf field of 42 MV/m at cathode during emission. For cavity type #2, optimum emission phase is 31° and the rf field during emission is 31 MV/m.

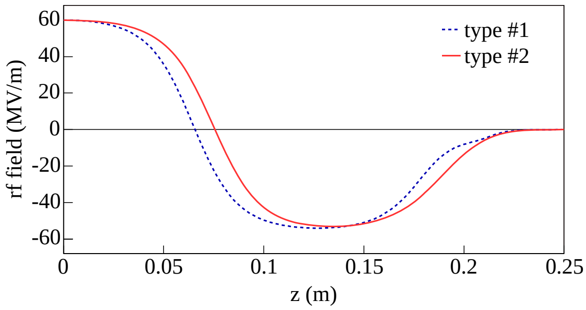

Figure 2: On-axis rf field profile for two gun types.

In photocathode rf guns, a strong rf field suppresses the beam expansion due to the space charge forces during the emission of high charge density electron beams. Because the emission field is lower in gun type #2, the initial beam size at cathode need to be larger in order to reduce the space charge force.

The kinetic energy of the emitted electrons is assumed to be 0.55 keV and an isotropic emission is assumed according to Ref. [7]. The kinetic energy of electrons emitted from Cs_2Te cathode has been measured in laboratory condition with a very low electric field at cathode [8].

In a high rf field, a Cs_2Te cathode changes its surface properties and the kinetic energy of the emitted electrons increases with the field strength [9]. For the case of gun type #1, the kinetic energy of the emitted elec-

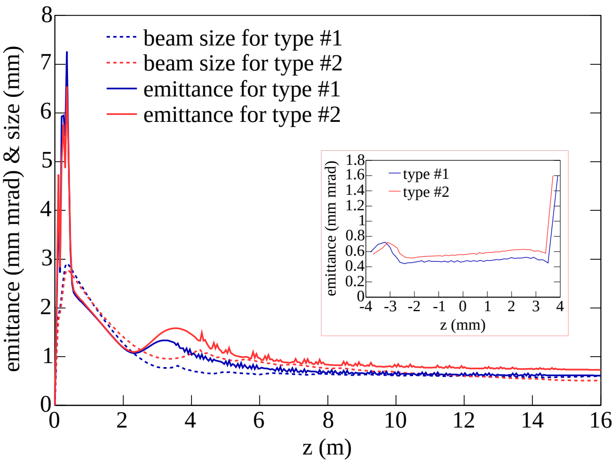

Figure 3: Rms beam size and normalized emittance evolution simulated with ASTRA. The simulation parameters are summarized in Table 1. The transverse slice emittances at z = 30 m are shown in the small box. The temporal profile of the electron bunches at z = 30 m is a hat-shape similar to the initial distribution of the bunch, i.e. the temporal profile of the drive-laser.

Table 1: Simulation parameters for two gun types.

Parameter	Type #1	Type #2
Initial distributions of electrons[a]		
transverse[b]	0.45 mm rms	0.55 mm rms
temporal (flat-top)	2 ps rise/fall and 20 ps fwhm	
thermal ε [c]	0.37 mm mrad	0.47 mm mrad
Gun		
max rf field		
at cathode	60 MV/m	60 MV/m
at full cell	54 MV/m	53 MV/m
emission phase	45°	31°
rf field at emission	42 MV/m	31 MV/m
max solenoid field	0.222 T at 0.28 m	0.226 T at 0.29 m
Accelerator[d]		
max rf field	20 MV/m	20 MV/m
start of 1st module	3.43 m	4.05 m
Simulation result[e]		
bunch charge	1 nC	1 nC
trans. projected ε	0.60 mm mrad	0.64 mm mrad
trans. slice ε [f]	0.47 mm mrad	0.56 mm mrad
bunch length	2.05 mm	1.95 mm
mean energy	90.1 MeV	90.4 MeV
energy spread	1.19 MeV rms	1.12 MeV rms
long. emittance	302 mm keV	262 mm keV

a This initial distribution is determined by controlling the three dimensional shape of the drive-laser at the cathode.

b Homogeneous distribution.

c Assuming the kinetic energy of emitted electrons to be 0.55 eV.

d Simulations include the acceleration with 8 × 9 cell TESLA type cavities.

e 200 000 macro particles are used for the tracking simulation with ASTRA.

f At the center of bunch.

trons is 0.738 eV according to the emission model in Ref. [9]. This kinetic energy rise and the field enhancement for photoemission increases the thermal emittance up to 0.59 mm mrad. For the case of gun type #2, the kinetic energy of the emitted electrons is 0.675 eV and the thermal emittance is estimated to 0.69 mm mrad.

Dark current

With the machine parameters obtained with the beam optimizations, dark current has been simulated (Fig. 4). For the two gun types, the same amount of dark current from the cathode is tracked with ASTRA. The inner structure of the cavities and beam pipe with 35 mm diameter is considered as aperture.

When machine parameters for the beam optimization are used, the amount of the surviving dark current to the entrance of the first acceleration module is below 40% for gun type #2 compared to the gun type #1 case. The overlapping of the momentum distribution with the beam is significantly reduced, which is of great benefit for the dark current collimator.

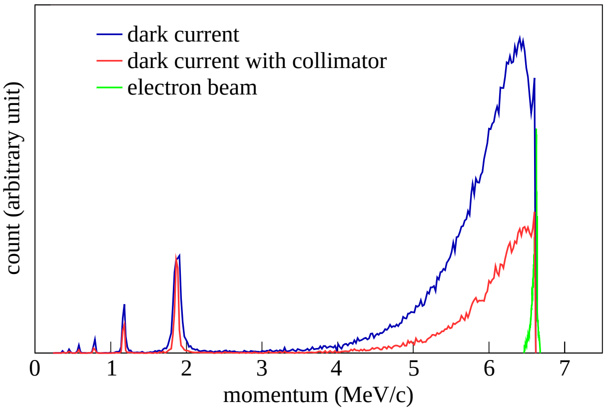

(a) Gun type #1.

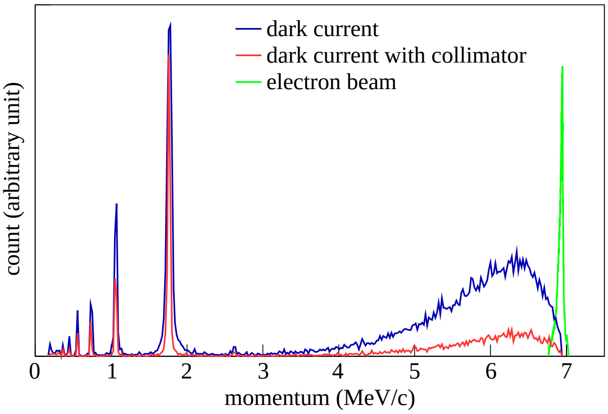

(b) Gun type #2.

Figure 4: Simulated momentum spectra of dark current and 1 nC beam. The machine parameters for the beam optimization are used. The dark current surviving to the entrance of the first acceleration module is shown. Because the emission phase of dark current is higher that the optimum emission phase, some part of the dark current stays in the gun cavity for several rf cycles. When the dark current finally escape from the gun cavity, the dark current can have certain definite momentum, appeared as spikes. The dark current reduction by the geometrical collimator is shown as well.

COLLIMATION IN THE GUN SECTION

In the gun section, two kinds of collimators can be used. The first one is a geometrical collimator for different transverse sizes (Fig. 5). Dark current with lower momentum is strongly overfocused by the solenoid field which is optimized for the beam focusing. The overfocused dark current is lost at the beam pipe. If a circular collimator is inserted inside the pipe, the dark current with larger transverse size can be cut out. Due to the cryo tank, a possible last position

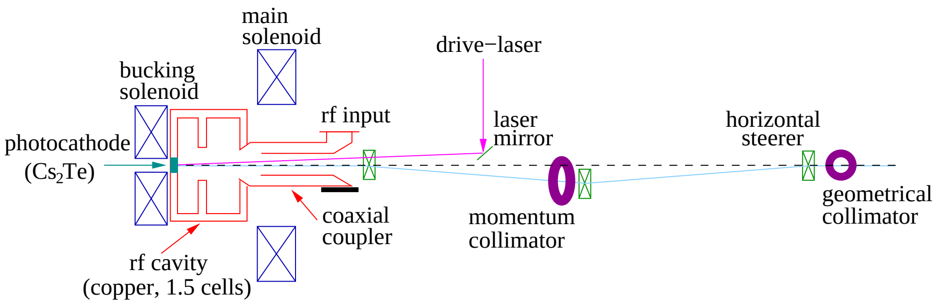

Figure 5: Schematic of gun section. The light blue line shows the reference path of beams. The circular shape collimator chops the dark current with larger transverse size. The elliptical shape collimator uses a difference in the momentum distributions of beams and dark current. The first horizontal steerer projects the momentum distributions of beams and dark current to the horizontal axis.

of the collimators is 1.2 m upstream from the entrance of the first acceleration module. For gun type #1, the position for the collimator is at 2.2 m. At that position, the electron beam size is 1.13 mm rms (Fig. 3) and a collimator with 10 mm diameter can be applied. With this collimator, the dark current from the gun can be reduced by 66%. For gun type #2, the position for the collimator is 2.8 m. The electron beam size will be 1.03 mm rms and a collimator with 10 mm diameter can be applied. With this collimator, the dark current current from the gun can be reduced by more than 70%. Taking into account the high losses at the beam pipe for gun type #2, the dark current behind the circular collimator is only 30% for type #2 compared to type #1.

The second possibility is a momentum collimator. This collimator is combined with a series of steerers and possibly has an elliptical shape with the major axis in the horizontal direction. If the first steerer kicks the beam and the dark current, the dark current with lower momentum is deflected more and can be chopped with a collimator. The minor axis length of the inner ellipsoid is determined by the beam size and the major axis length is determined by the beam size and the momentum distribution at the collimator position. When the dark current lower than 6.2 MeV/c, i.e. 10% lower than the mean momentum of the beam, is cut out with the elliptical collimator, again 75% of the dark current is possibly reduced for gun type #2. For gun type #1, 35% of the dark current is possibly reduced when the dark current lower than 5.9 MeV/c, again 10% of the mean momentum of the beam, is cut out.

The momentum collimator can be used to block the dark current from the acceleration modules which might have a momentum of several tens or even hundreds MeV/c. When the high energy dark current hits the Cs_2Te cathode, the emissive film might be seriously damaged.

CONCLUSION

The XFEL gun requires an rf field as high as 60 MV/m for 1 nC bunches with an transverse emittance below 1 mm mrad. But, such high rf field might generate very high dark current. With elonging the half cell length of the gun cavity, the dark current can be separated from the beam in the momentum spectrum. Collimators can be efficiently used to chop the dark current with lower momentum before the first acceleration module.

ACKNOWLEDGMENTS

The authors thank M. Krasilnikov and F. Stephan for helpful discussions.

REFERENCES

[1] B. Dwersteg, K. Flöttmann, J. Sekutowicz and Ch. Stolzenburg, “RF gun design for the TESLA VUV Free Electron Laser”, Nucl. Instr. and Meth. A **393** (1997) p. 93.

[2] S. Schreiber, private communication.

[3] J.-H. Han *et al.*, “Dark current and multipacting in the photocathode rf gun at PITZ”, in *Proceedings of the 2005 PAC*, p. 895.

[4] `http://www.desy.de/~mpyflo/`.

[5] `http://xfel.desy.de/`.

[6] J. H. Billen and L. M. Young, Poisson Superfish, LA-UR-96-1834.

[7] K. Flöttmann, “Note on the thermal emittance of electrons emitted by cesium telluride photo cathodes”, TESLA FEL Reports 1997-01, 1997.

[8] D. Sertore *et al.*, “Cesium telluride and metals photoelectron thermal emittance measurements using a time-of-flight spectrometer”, in *Proceedings of the 2004 EPAC*, p. 408.

[9] J.-H. Han, “Dynamics of Electron Beam and Dark Current in Photocathode RF Guns”, PhD thesis, University Hamburg, 2005.

IMPACT OF THE CATHODE ROUGHNESS ON THE EMITTANCE OF AN ELECTRON BEAM

M. Krasilnikov*, DESY, Zeuthen, Germany.

Abstract

An RF photo injector for the European XFEL should produce electron beams with normalized transverse emittance under 1 mm mrad. In order to achieve this high performance of the electron source the electric field at the photo cathode has to be increased up to 60 MV/m. The emittance budget of the optimized XFEL photo injector contains a significant part of thermal (intrinsic) emittance. A roughness of the cathode could lead to an additional uncorrelated divergence of the emitted electrons and therefore to an increased thermal emittance. The cathode roughness has been modelled using an analytical approximation and numerical simulations. The influence of the roughness parameters and the increase of the electric field have been studied.

INTRODUCTION

The main goal of the Photo Injector Test facility in Zeuthen (PITZ, [1]) is to optimize electron sources for FEL injectors, including already existing (FLASH) and future (XFEL) facilities. Increasing the maximum gradient at the photo cathode in the rf gun from 40 MV/m to 60 MV/m is one of the main improvements towards XFEL requirements. This implies (with taking into account an optimum launch rf phase) an increasing of the electric field at the photo cathode at the moment of the emission from 24 MV/m to 42 MV/m. The improved normalized beam emittance in the injector is expected to be under 1 mm mrad. Besides earlier suppressing of the space charge effect in the rf gun the gradient increase also leads to a significant increase of the contribution of initial (thermal) emittance in the total emittance budget.

The cathode roughness increases the intrinsic divergence of the emitted electron bunch. A model with a periodical roughness of the cathode is applied to study the geometrical emission effect in dependence on roughness parameters. A single bump model is used to study the impact of the applied electric field on the initial emittance.

THE MODEL OF THE PERIODIC SURFACE ROUGHNESS

2D model, normal emission only

Consider a cathode surface given by the formula

$$z = h\cos(kx) \quad , \tag{1}$$

where $2h$ is the roughness depth and $\lambda = 2\pi / k$ is the roughness period along the cathode surface. Let's consider first the case of the emission normal to the cathode surface, so $\varphi = 0$ (Figure 1a), what implies zero thermal emittance from the non-perturbed (no roughness) cathode.

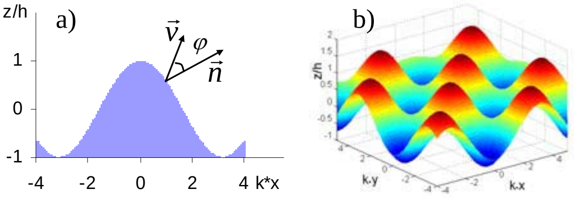

Figure 1: Periodic roughness, 2D (a) and 3D (b) models.

Transverse component of the electron velocity is

$$v_x = v_0 \frac{\xi \sin(kx)}{\sqrt{1+\xi^2 \sin^2(kx)}} , \tag{2}$$

where $\xi = kh$, v_0 is velocity of the emitted electron. After corresponding integration over the roughness period one can obtain an expression for the emittance induced by the rough cathode surface

$$\varepsilon_x^{2D} = \sigma_x \cdot \sqrt{\left\langle p_x^2 \right\rangle} \approx 2\sigma_x \sqrt{\frac{eE_0}{mc^2} h \cdot \left(1 - \frac{1}{\sqrt{1+\xi^2}} \right)} , \tag{3}$$

where σ_x is an rms electron beam size at the cathode, $p_x = \dfrac{v_x / c}{\sqrt{1 - v_0^2 / c^2}}$ is the normalized transverse momentum and E_0 is the electric field at the cathode at the moment of the emission.

3D model, normal emission only

A cathode surface with periodic roughness is given

$$z = h\cos(kx)\cos(ky) , \tag{4}$$

where $x - y$ isotropy is assumed (Figure 1b). Transverse component of the electron emission velocity:

$$v_x = v_0 \frac{\xi \sin(kx)\cos(ky)}{\sqrt{1+\xi^2 \left(\sin^2(kx)\cos^2(ky) + \cos^2(kx)\sin^2(ky) \right)}} . \tag{5}$$

Transverse emittance induced by 3D rough cathode surface (4) is

$$\varepsilon_x^{3D} = \sigma_x \cdot \sqrt{\left\langle p_x^2 \right\rangle} \approx 2\sigma_x \sqrt{\frac{eE_0}{mc^2} h \cdot I(\xi)} ,$$

where (6)

$$I(\xi) = \frac{\xi^2}{4\pi^2} \int_{-\pi}^{\pi} dX \int_{-\pi}^{\pi} \frac{\sin^2 X \cos^2 Y}{1+\xi^2 \left(\sin^2 X \cos^2 Y + \cos^2 X \sin^2 Y \right)} dY .$$

One can show, that for the for same roughness parameters the emittance ε_x^{3D} is in a factor $\sim \sqrt{2}$ smaller than 2D one, because the effective roughness depth ($\sim hI(\xi)$) in

---

*mikhail.krasilnikov@desy.de

the 3D case is smaller. A ratio $\varepsilon_x^{3D} / \varepsilon_x^{2D}$ is shown in Figure 2 as a function of the roughness parameter ξ.

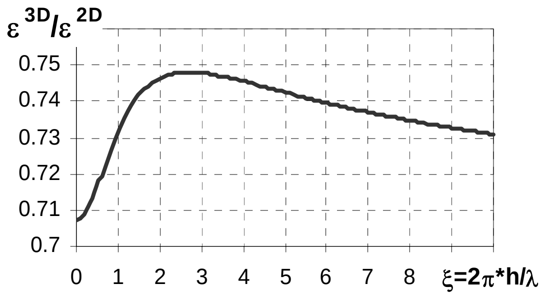

Figure 2: Emittance from 3D surface (4) compared to 2D case (1) vs. roughness parameter $\xi = 2\pi h/\lambda$.

2D model with emission distribution

In the case of nonzero non-perturbed thermal emittance there is an emission in a finite angle φ, as it happens i.e. by emission from the Cs2Te photo cathode. Using approach described in [2], one assumes that electrons are emitted isotropically in a cone with an angle $\varphi_m = \arccos\sqrt{E_A/E_k}$ with respect to the local surface normal, where E_A is the electron affinity of the emitting material and E_k is the electron kinetic energy. For the Cs2Te photo cathode $E_A \approx 0.2eV$, by a applying driving laser with 262 nm wavelength $E_k \approx 0.75eV$. This model yields a formula for the thermal emittance of the smooth cathode (no roughness assumed) [2]:

$$\varepsilon_x^{th,0} = \sigma_x \sqrt{\frac{2E_k}{mc^2}} \cdot \sqrt{\frac{2+\cos^3\varphi_m - 3\cos\varphi_m}{6(1-\cos\varphi_m)}}\,. \qquad (7)$$

Within an applied roughness model (1) a transverse momentum of the electron emitted at angle φ to the local normal is given

$$p_x = \sqrt{\frac{2E_k}{mc^2}} \cdot (\sin\varphi\cos\theta\cos\alpha + \cos\varphi\sin\alpha), \qquad (8)$$

where θ is a local azimuth angle, $\alpha(x)$ is a rough surface slope obtained from (1):

$$\tan\alpha = -\xi\sin kx\,. \qquad (9)$$

Applying triple integration to p_x^2 over $\varphi \in [0;\varphi_m]$, $\theta \in [0;\pi]$ and over the roughness period [3] yields a formula for the thermal emittance from the periodic rough surface:

$$\varepsilon_x^{th,rough} = \sigma_x \sqrt{\frac{2E_k}{mc^2}} \times \qquad (10)$$

$$\times \sqrt{\frac{(2+\cos^3\varphi_m - 3\cos\varphi_m)\cos\alpha_m + 2(1-\cos^3\varphi_m)(1-\cos\alpha_m)}{6(1-\cos\varphi_m)}},$$

where $\cos\alpha_m = 1\big/\sqrt{1+\xi^2}$. Obviously, that in the absence of the roughness ($\alpha_m = 0$) the formula (10) is reduced to the expression (7).

Thermal emittance growth $\left(\varepsilon_x^{th,rough} / \varepsilon_x^{th,0} - 1\right)$ due to the cathode roughness is shown in Figure 3. From this plot thermal emittance growth <30% corresponds to the cathode roughness with $\lambda > 5h$, for 10% growth $\lambda > 12h$ is required. Preliminary cathode plug roughness measurements performed at INFN LASA (Milano) [4] showed that photo cathodes presently used at PITZ have roughness with $\sigma \sim 10nm$. In order to keep the thermal emittance growth under 10% it is necessary to provide a roughness period over 100 nm.

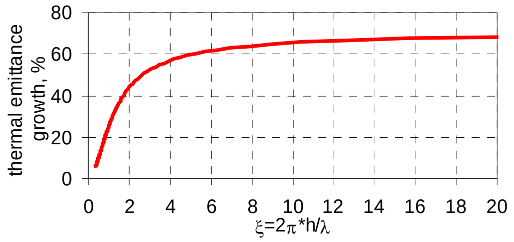

Figure 3: Thermal emittance growth vs. roughness parameter $\xi = 2\pi h/\lambda$. Ideal Cs2Te cathode parameters $E_A = 0.2eV$, $E_k = 0.75eV$ have been assumed [2].

In practical case the electron affinity is affected by many factors. It is well known that the quantum efficiency (QE) of the photo cathodes decreases with operation time; electron affinity increase due to the change of the cathode surface status is one of the possible mechanisms explaining QE degradation. On the other hand an applied rf field lowers the electron affinity due to the Schottky effect [5]. The electron affinity can be modelled as [6]:

$$E_A = \kappa E_{A,0} - \sqrt{\frac{e^3}{4\pi\varepsilon_0}\beta_{ph}E_0}\,, \qquad (11)$$

where κ is responsible for the increase with a time of the initial affinity $E_{A,0}$, β_{ph} is a field enhancement factor for photoemission, which partially can include also a surface roughness effect. A thermal emittance growth as a function of roughness period and electron affinity is shown in Figure 4 with a contour plot.

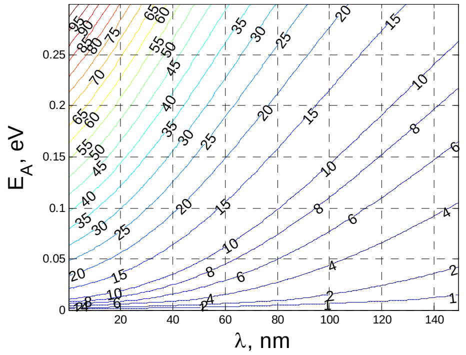

Figure 4: Thermal emittance growth $\left(\varepsilon_x^{th,rough} / \varepsilon_x^{th,0} - 1\right)$ given in % as a function of roughness period and electron affinity. For this plot $h = 10nm$, $E_k = 0.75eV$ is assumed.

DEPENDENCE ON ELECTRIC FIELD

In order to study the dependence of the initial emittance on the electric field during emission a model of single bump can be used. A two-dimensional model of the bump is described in [7]:

$$\frac{z}{b} = \sqrt{1+\frac{a^2}{b^2+x^2}}-1, \qquad (12)$$

where parameters a and b are constants depending on roughness depth and width. Typical bump shapes are shown in Figure 5.

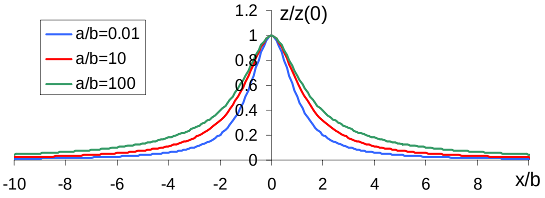

Figure 5: Rough cathode surface: single bump model (10). Upper curve corresponds to $a/b=100$.

The choice of equation (12) for the rough cathode surface is motivated by the simple conformal transformation

$$\zeta = u + iw = \sqrt{(x+iz+ib)^2+a^2}-ib, \qquad (13)$$

which maps the electric field of a plane capacitor onto the field of the surface (12). An analytical expression for the electric field can be obtained from the corresponding conformal transformation

$$E_x + iE_z = \frac{-iE_o\cdot[x-i(y+b)]}{\sqrt{[x-i(y+b)]^2+a^2}}. \qquad (14)$$

The electric field lines are shown in Figure 6.

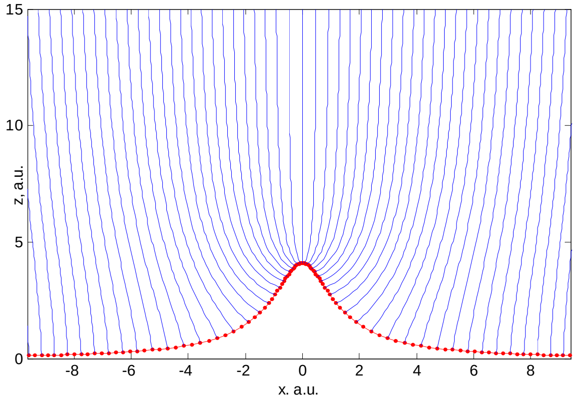

Figure 6: Electric field lines of the bump (10).

Once the electric field magnitude E_o and the bump parameters a and b are specified, the field profile is determined from (14) and particle position (x,z) and momentum (p_x,p_z) can be numerically integrated in time according to

$$\frac{d}{d(ct)}\begin{pmatrix} p_x/(mc) \\ p_z/(mc)\end{pmatrix} = \frac{e}{mc^2}\begin{pmatrix} E_x \\ E_z\end{pmatrix}$$
$$\frac{d}{d(ct)}\begin{pmatrix} x \\ z\end{pmatrix} = \frac{1}{\sqrt{1+p_x^2+p_z^2}}\begin{pmatrix} p_x \\ p_z\end{pmatrix}, \qquad (15)$$

with initial conditions:

$$x_n(t=0)=x_{n0}; \quad z_n(t=0)=z_{n0};$$
$$p_{xn}(t=0)=0; \quad p_{zn}(t=0)=0. \qquad (16)$$

Parameter u from (13) characterizes the location on the surface from which an electron is emitted ($w=0$):

$$x_{n0} = \frac{u_n b}{z_n+b}; \quad u_n = n\cdot u_N/N; \quad n=1...N$$
$$z_{n0} = -b+\sqrt{\frac{a^2+b^2-u_n^2+\sqrt{(u_n^2-a^2-b^2)+4u_n^2a^2}}{2}}. \qquad (17)$$

The last emission location u_N can be defined from the condition:

$$z_N = 0.01\cdot z(0) = 0.01\cdot\left(\sqrt{a^2+b^2}-b\right) \qquad (18)$$

It should be noticed that within this approach the space charge effect is neglected.

Shown in Figure 7 are typical numerical results of the local electron divergence $p_x/(mc)$ as a function of the emission parameter u/u_N at the moment in time when electrons reach the region of homogeneous field. At this z-position the electric field varies along x-axis not more than by 1%, it means that the field at this distance from the cathode does not "feel" the rough surface.

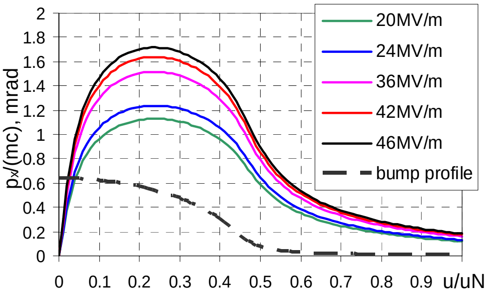

Figure 7: Local divergence as a function of u/u_N for various E_0. Roughness parameters: depth $h\approx 20nm$, width $\lambda = 10nm$ ($a=21.52nm; b=1.57nm$).

An estimation of the emittance growth due to the increase of the applied electric field could be done based on the analysis of the electron divergence for various roughness parameters. Emittance growth as a function of the applied electric field in comparison to the case of $E_0 = 24MV/m$ is shown in Figure 8. Relative emittance growth for various bump widths λ has a slope of about $2\%/(MV/m)$, so field increase up to $42MV/m$ results in a ~30% emittance growth.

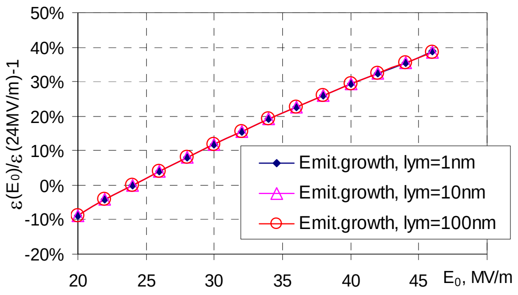

Figure 8: Emittance growth as a function of the electric field, compared to the emittance at $E_0 = 24MV/m$.

Simulations based on the assumption of the neglecting the space charge effect have been performed. Modelling the space charge limited emission from the bumpy cathode surface in the steady state regime [7] showed that the space charge may reduce the deterioration effect of the surface roughness. But from the other hand the cathode roughness may result also in additional density non-homogeneity of the emitted electron beam, which could lead to degradation of the beam quality.

CONCLUSIONS AND OUTLOOK

The photo cathode roughness contributes to the initial emittance of the electron beam. Several models of the cathode rough surface have been used to estimate the effect of the thermal emittance growth. Thermal emittance growth induced by the cathode roughness has been studied for different roughness parameters, including photo emission issues from a Cs2Te photo cathode.

Since one of the main improvement steps toward XFEL requirements is an increase of the maximum rf gun gradient from 40 to 60 MV/m, the impact of increasing the field at the cathode has been studied. The model of single bump has demonstrated that the increase of the electric field at the cathode could result in a ~30% growth of the roughness contribution to the initial thermal emittance.

Studies on the role of the space charge effect during emission from rough cathode as well as more detailed measurements of the cathode roughness have to be performed in order to improve the understanding of the thermal emittance features.

ACKNOWLEDGMENTS

I would like to thank K.Floettmann, F.Stephan and PITZ members for helpful discussions.

REFERENCES

[1] A. Oppelt et al., “Status and first results from the upgraded PITZ facility”, FEL 2005, Stanford, Aug.2005.
[2] K. Floettmann, “Note on the thermal emittance of electrons emitted by Cesium Telluride photo cathodes”, TESLA FEL Reports 1997-01, 1997.
[3] J. Schmerge, private communication.
[4] D. Sertore, private communication.
[5] R.Gomer, “Field emission and field ionization”, American Institute of Physics, New York, 1993.
[6] J.-H. Han, “Dynamics of electron beam and dark current in phototcathode rf guns”, PhD thesis, Hamburg University, 2005.
[7] Y. Lau, “Effects of cathode roughness on the quality of electron beams”, J. Appl. Phys 61(1), Jan. 1987.

FIRST EXPERIENCE WITH THE MACHINE PROTECTION SYSTEM OF FLASH

L. Fröhlich*, University of Hamburg and DESY, Hamburg, Germany
A. Hamdi, M. Luong, J. Novo, CEA-Saclay, Gif-sur-Yvette, France
M. Görler, P. Göttlicher, D. Nölle, D. Pugachov, H. Schlarb, S. Schreiber,
M. Staack, M. Werner, DESY, Hamburg, Germany

Abstract

The linac-based free electron laser facility FLASH[1] at DESY Hamburg is designed to transport electron beams with high average power of more than 50 kW. To protect the machine from serious damage passive and active systems have been installed. This paper concentrates on the fast active machine protection system (MPS), that stops the production of new bunches if hazardous machine conditions are detected. Furthermore, the results from the commissioning of the fast beam interlock system are presented that has for the first time allowed to operate the accelerator with macropulses of up to 600 bunches.

INTRODUCTION

The FLASH linac currently employs 40 superconducting 9-cell cavities distributed over five cryogenic modules to accelerate an electron beam to an energy of up to 700 MeV. The beam is guided through an undulator of approximately 30 m length to initiate a free electron laser (FEL) process based on the SASE principle. The facility is now alternating between blocks of accelerator development and user operation, supplying experimentators with pulsed radiation of high brilliance in the XUV wavelength range between 13 and 50 nm. [1]

As typical for superconducting linacs, the transported bunches are grouped in macropulses or bunch trains. The viable rf pulse length limits the length of a bunch train to 800 µs. With the standard bunch frequency of 1 MHz and a macropulse repetition rate of 5 Hz, the power delivered to the beam dump amounts to ∼3 kW. If the future option for high duty cycle operation with 9 MHz/10 Hz is realized, this figure increases above 50 kW. Even on partial loss of the beam along the linac, the induced heat load and radiation can cause substantial damage to accelerator components. Therefore, an active protection system is required to ensure safe operation of the machine.

MPS ORGANIZATION

The machine protection system of the FLASH linac is a substantially enhanced version of the system used in phase 1 of the TESLA Test Facility [2]. Since the description of the basic design in [3], the operational experience gained during the commissioning of FLASH has led to a number of changes that will be discussed in the following.

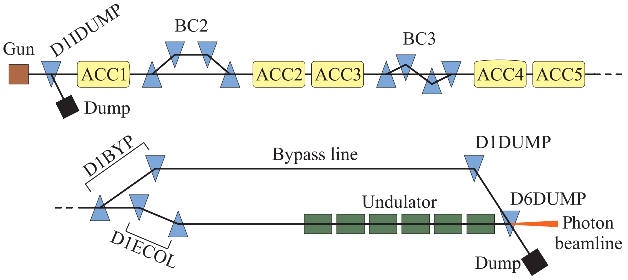

Figure 1: Schematic of the FLASH linac. The depicted elements include the five acceleration modules *ACCn*, the two bunch compressors *BCn*, and the main dipole magnets.

Detection Schemes

The detection of beam and darkcurrent losses in the linac is based on two independent approaches. The FPGA-controlled *Toroid Protection System* [4] measures the transmission by comparing the readings from charge monitors (toroids) in the injector and dump part of the machine, and generates alarms within less than 110 ns if one of several configurable thresholds is exceeded.

The second system for fault detection is constituted by a set of 51 photomultipliers and 18 secondary emission multipliers distributed along the machine. These *beam loss monitors* (BLMs) provide a bunch-resolved online display of electromagnetic shower intensities (Fig. 2). VME-based alarm generators with a reaction time far below 1 µs check whether user-defined thresholds for one or multiple bunches, or for the integrated signal are exceeded. They also generate an alarm on failure of the high voltage supply, or if a misconfiguration has been detected.

As the permanent magnets of the undulator are susceptiple to radiation, close monitoring of beam losses is required to avoid degradation of the field quality. Therefore, the undulator section features the highest concentration of BLMs in the whole machine, with 26 monitors currently in place and another 12 to be installed until the end of the year.

Response to alarms

The purpose of any MPS is to detect situations which may lead to damage of components, and to take appro-

---

* lars.froehlich@desy.de

[1] Since April 2006, FLASH—Free Electron Laser in Hamburg—is the new name for the VUV-FEL, part of the TESLA Test Facility TTF.

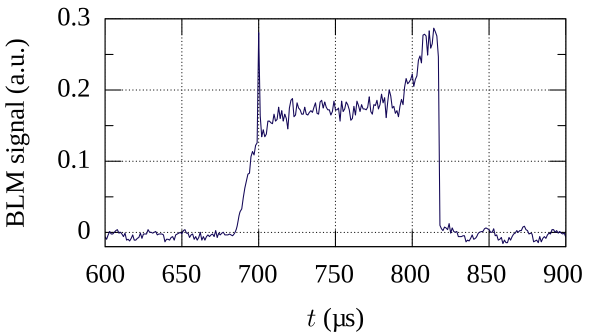

Figure 2: Signal from a beam loss monitor behind the collimation section. At $t = 700$ µs, a part of one single bunch is lost. The losses visible from 690–820 µs are caused by darkcurrent from the gun.

priate counter-measures. These potentially harmful conditions can be classified into three main categories:

Fast Since the loss of a complete macropulse may already present a substantial hazard, a fast system must stop the production of bunches within the train, i.e. on a time scale of few µs.

Intermediate For the major part of potential dangers, a reaction between two macropulses is sufficient. Since the time constants of all magnets employed at FLASH are of the order of tens of milliseconds or more, the failure of power supplies falls into this category.

Slow Even if moderate losses of darkcurrent or of few bunches do not pose an immediate threat, they contribute to the deposited radiation dose, and may thus cause damage over time scales of minutes or days. This issue is of special importance for the undulator.

To guarantee an appropriate response to events on any of these timescales, the FLASH MPS uses two independent subsystems: A network of *Beam Interlock Concentrators* for fast events, and a programmable logic control—the *Beam Interlock System*—for intermediate and slow events.

Beam Interlock Concentrators (BICs)

The function of the BIC modules is simply a fast logical OR concentrating 16 alarm inputs to two outputs within a processing time of ∼50 ns, with a configurable mask that allows to suppress any of the input channels. Ten modules are currently in use, connected in a tree-like fashion as illustrated in Fig. 3. Most of the input channels are used by the 69 BLM alarm signals, but also the TPS, the cavity quench detection, and a fast vacuum shutter are connected. When any of the inputs show an alarm, the top-level BICs will switch off the injector laser to suppress the production of new bunches in the gun, and cut the first acceleration module off from rf power as a precaution against further transport of darkcurrent.

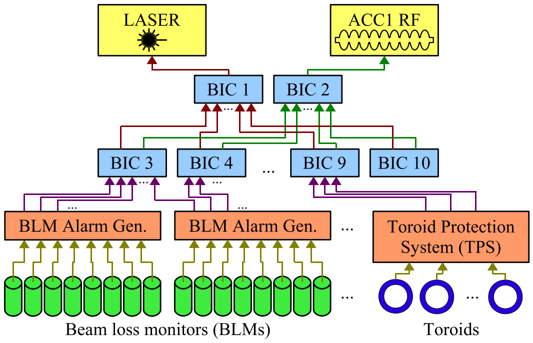

Figure 3: Organization of *beam interlock concentrators*. BIC 3–10 collect alarms from various alarm generators and relay them to BIC 1–2, which switch off the photoinjector laser and the rf power of the first acceleration module.

Measurements have confirmed that the reaction time of the BIC system to beam losses is below 4 µs. This time is dominated by cable delays, and it means that up to three more bunches enter the machine after detection of the loss at the standard bunch frequency of 1 MHz.

Beam Interlock System (BIS)

While the BIC system has been designed to guarantee minimum response time to fast events, the emphasis for the *Beam Interlock System* has been placed on flexibility. The programmable logic control continuously monitors the status of critical components like magnet power supplies, screens, collimators, and valves. It also checks the flow of cooling water, and the compliance to temperature limits.

From the status of the main dipole magnets and of several valves, the BIS deduces an *operation mode* defining the basic beam path through the machine according to Tab. 1. As a simple protective measure, no beam is allowed if there is no valid operation mode.

Furthermore, the BIS selects one of three *beam modes* as shown in Tab. 2. Besides defining the maximum allowed number of bunches per macropulse, the beam mode also determines whether the fast protection via the BIC system is active. This policy allows the operation under charge loss as long as only few bunches per macropulse are needed, which is necessary for tuning and for experiments using the beam. While the operator can choose between short and long mode, the BIS will automatically reduce to short or single mode if obstacles like screens are moved into the beam path, or if other conditions are met.

Apart from these general safety features, attempts have been made to limit the radiation dose deposited in the undulator with a special BIS routine. Due to the dense placement of BLMs in the undulator section, there is considerable overlap in their geometrical acceptances, and electromagnetic showers are usually observed on more than one monitor. The *BIS-BLM protection* takes advantage of this by counting the number of simultaneous BLM alarms in

Table 1: List of *operation modes* with the required valve and dipole magnet settings, and the maximum allowed beam mode.

operation mode	*conditions*	*beam mode*
Gun	gun valve open, ACC1 valve closed, D1IDUMP off	short
Analysis	gun valve open, ACC1 valve closed, D1IDUMP on	long
Bypass	all valves open, D1BYP on, D1DUMP on, D6DUMP off	long
FEL	all valves open, D1BYP off, D1ECOL on, D6DUMP on	long

Table 2: List of *beam modes* with the maximum allowed number of bunches per macropulse.

beam mode	*nr. of bunches*	*BIC system*
Single	2	disabled
Short	30	disabled
Long	no limit	active

the section. If 2 alarms are pending over 120 s, 4 over 30 s, or 8 over 5 s, the beam is stopped and has to be restarted manually via the control system. To allow tuning, the tolerances of this routine can be increased for 30 minutes.

Figure 4 shows the average dose rates in the first two undulator segments measured with thermoluminescence dosimeters [5]. Since the activation of the BIS-BLM protection in September 2005, the dose rates have been predominantly below 10 Gy/day, indicating that—together with an overall improved understanding of orbit and optics—the requirement of avoiding beam stops has led to a reduction of losses.

OPERATION WITH LONG MACROPULSES

The commissioning of MPS components relevant for long pulse operation has been completed in August 2006. The increase of the gun rf pulse length from 70 to 800 μs led to the expected rise of darkcurrent losses in the bunch compressors and in the collimation section by about an order of magnitude. By successive optimization of orbit and optics, the beam losses could be reduced to a minimum, and operation of the FEL with 600 bunches per macropulse was possible with minimal interference of the BIC system. At an average energy of 20 μJ per photon pulse, the output power during the test run has reached about 60 mW.

Imperfections of the rf regulation constitute the main problem in setting up a stable transmission of long macropulses. Due to poorly compensated beam loading or transient behavior at the beginning of the rf pulse, the bunches at the head of the macropulse can experience amplitudes and phases of the accelerating field that deviate significantly from the designated values. For the first bunch, an energy deviation of 0.6 % with respect to the last bunches of a 300 μs long macropulse has been measured after the first acceleration module. This effectively enlarges the total phase space occupied by the macropulse and thus reduces the tolerance for jitter and drifts.

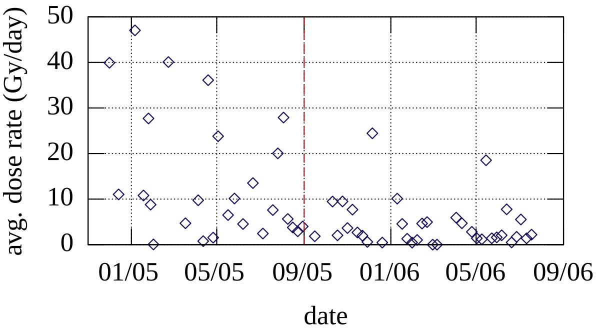

Figure 4: Average dose rates measured in the first two undulator segments.

CONCLUSION AND OUTLOOK

The FLASH machine protection system reliably prevents damage of the accelerator due to beam losses, with the total downtime of the linac caused by MPS failures and misconfigurations amounting to only few hours. It is also successful in limiting the slow accumulation of radiation dose in the undulator.

While the number of bunches per macropulse has been limited to 30 during past accelerator runs, the recent commissioning of the beam interlock concentrator system with reaction times in the microsecond range now allows to operate the machine with bunch trains of up to 800 pulses. We expect that future user experiments will benefit highly from the improved duty cycle.

ACKNOWLEDGEMENTS

We wish to thank all members of the operation crew for their outstanding commitment and support. The assistance of the controls and low-level rf groups is greatly appreciated.

REFERENCES

[1] V. Ayvazyan, et al., “First operation of a free-electron laser generating GW power radiation at 32 nm wavelength”. Eur. Phys. J. D, 37:297–303, November 2006.

[2] H. Schlarb, et al., “Expansion of the fast linac protection system for high duty cycle operation at the TESLA Test Facility”. EPAC’02, pp. 1966–1968. Paris, France, June 2002.

[3] D. Nölle, et al., “The beam inhibit system for TTF II”. DIPAC’03, pp. 62–64. Mainz, Germany, 2003.

[4] A. Hamdi, et al., “VHDL design and simulation of a fast beam loss interlock for TTF2”. EPAC’04, pp. 2020–2022. Lucerne, Switzerland, 2004.

[5] T. Vielitz, Hasylab, Hamburg, private communication.

EXPERIENCE WITH THE PHOTOINJECTOR LASER AT FLASH

S. Schreiber,[*], M. Görler, K. Klose, M. Staack, L. Fröhlich, DESY, Hamburg, Germany
I. Will, I. Templin, MBI, Berlin, Germany

Abstract

The photoinjector laser system of FLASH is a key element for the generation of high quality electron beams required for a stable and reliable operation of the facility. FLASH is the VUV and soft X-ray FEL user facility at DESY. FLASH is based on superconducting accelerating structures allowing to accelerate electron bunch trains of a length of up to 800 μs with a repetition rate of 10 Hz. Based on the standard 1 MHz pattern, the laser provides to some extend a flexible bunch train structure. We report on operational issues and on the performance of the laser system and its integration into the machine protection system.

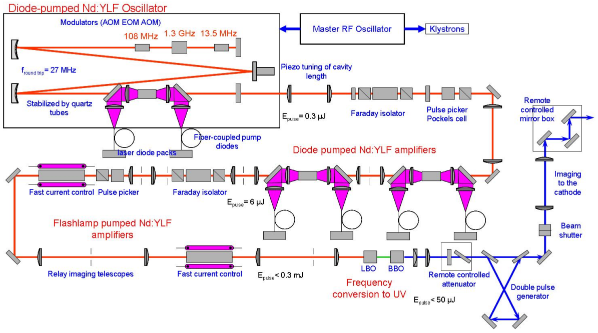

Figure 1: Schematic overview of the laser system.

INTRODUCTION

FLASH is a free electron laser user facility at DESY providing laser-like radiation from the VUV to the soft X-ray wavelength regime.[1, 2] SASE free electron lasers require an excellent beam quality, which is achieved with an injector based on a laser driven rf gun.[3] The electron beam is accelerated with TESLA superconducting modules.

A high quantum efficiency photocathode [4] together with a synchronized mode-locked laser system is used to generate the electron beam structure typical for superconducting accelerators: some thousand bunches in a millisecond long rf pulse. High quantum efficiency cathodes allow to use a laser system with moderate average power in the Watt range.

The user facility FLASH has been realized by upgrading the TESLA Test Facility (TTF) phase 1 FEL to phase 2.[5] The TTF phase 1 laser system [6] has also been upgraded to a partially diode pumped system as described in [7].

In this report we describe the running experience with the laser system and its integration into the machine protection system of FLASH.

OVERVIEW OF THE LASER BASED ELECTRON SOURCE

The FLASH electron source is based on a laser driven L-band 1+1/2-cell rf gun operated with a 5 MW 1.3 GHz klystron. The rf pulse length is up to 900 μs, the repetition rate 5 Hz, up to 10 Hz are possible.

The electron beam is generated by photoemission with a Cs_2Te photocathode. With a forward rf power of 3.2 MW a gradient of 42 MV/m on the cathode surface is achieved on crest. High gradient on the cathode surface is required to preserve excellent beam quality. The cathode exhibit a high quantum efficiency in the range between 1 and 5 % for UV laser light. The charge per bunch required is 1 nC which translates into a laser pulse energy of not more then 0.5 μJ per pulse. The design of the laser accounted for a QE of 0.5 % only, a bunch frequency of 9 MHz within the train and an overhead by a factor of 4. With a conversion efficiency of 15 % from the IR to UV this asks for an average power of 2 W in the infrared.

THE LASER SYSTEM

The laser design is based on a pulsed master oscillator with subsequent amplification stages. Details of the system layout are described in [7], a schematic overview shows Fig. 1.

The laser material chosen is Nd:YLF, lasing at a wavelength of 1047 nm. The material has together with a high gain a long upper-state lifetime of 480 μs, and exhibits only a weak thermal lensing. This makes it suitable to produce pulse trains with milliseconds length. The oscillator and preamplifers are end-pumped with laser diodes emitting at 805 nm with a maximum power of 32 W. The two main amplifiers are flashlamp pumped.

The Pulse Train Oscillator

The pulse train oscillator (PTO) runs at 27 MHz synchronized to the master rf of the accelerator. It is a pulsed osciallator with the advantage of a much higher single pulse energy of 300 nJ as compared to typical cw oscillators. The master provides reference rf signals in the frequency of the accelerator of 1.3 GHz and its harmonics 108, 27, and 9 MHz. The synchronization to the rf is achieved using two

---

[*] siegfried.schreiber@desy.de

Figure 2: As an example, the air temperature measured at the laser over a period of 3 days. The temperature reading is within ±0.02°C.

acousto-optic modulators running at $27/2 = 13.5$ MHz and 108 MHz resp., and an additional electro-optic modulator powered with the amplified 1.3 GHz reference. The latter provides synchronization to the required 1 ps level. The oscillator length is stabilized against temperature drifts with two quartz rods. Quartz has a low temperature coefficient of expansion of $0.6{\cdot}10^{-6}$ m/°C. At the same time, the temperature of the laser room is stabilized to ±0.02 °C (Fig. 2). Both measures provide the bases for an excellent phase stabilization of the laser pulses with respect to the rf. An active fast feedback loop could be omitted, only a slow feedback acting on the resonator length is implemented.

The phase jitter of the laser pulses in respect to the rf can be estimated using the phase scan technique. The phase stability measured with this technique depends also on the performance of the gun rf amplitude and phase regulation system and therefore only gives an upper limit. The measurement results an rms phase jitter of 0.14 °in respect to 1.3 GHz rf.[8] This translates in an timing stability of the laser pulses of better than 300 fs rms.

Amplification

Selected pulses of the 27 MHz output of the PTO is amplified with a chain of linear amplifiers, also based on Nd:YLF, diode and flashlamp pumped.

A Pockels cell based pulse picker before amplification runs at 1 MHz forming a pulse train with a length of 1.5 ms. With the present high voltage driver (4 kV), up to 3 MHz is possible. The train is amplified by two diode pumped single pass amplifiers from 0.3 to 6 μJ per micro pulse.

A second pulse picker before the last amplification stage has two functions. The diode pumped amplifiers produce a transient at the beginning of the pulse train. The second pulse picker choses the flat part of the train. The second aim is to give the operator or user of the laser the possibility to remote control the number of pulses and to a certain extend the bunch pattern. Details will be described later in this report.

The final amplification to 300 μJ per pulse is performed by two flashlamp pumped amplifiers. They have already been used at the phase 1 laser system. They provide a power over the pulse train of about 300 W or an average power of up to 3 W for 10 Hz repetition rate.

The pump diode lasers are running since their installation for more than 20.000 h without any visible degradation. The flashlamp life time is between 1 to $5{\cdot}10^7$ shots and are routinely replaced every 40 days.

The infrared radiation (1047 nm) is doubled twice with an LBO and a BBO crystal to the UV (262 nm). The energy stability of a single micro pulse is between 1 and 2 % rms. However, to maintain this stability, a frequent fine tuning of the BBO phase matching angle is required.

Transport Beamline

A variable attenuator consisting out of a Brewster angle polarizer together with a remotely rotatable half wave plate. It allows to adjust the laser pulse energy according to the electron beam charge required. It is also used for a slow charge feedback to compensate slow drifts in electron charge.

Spent beams at various locations (PTO, Pockels cell, LBO, attenuator) are measured with fast photodiodes and recorded with a 1 MHz ADC giving additional information to the operator.

A double pulse generator can be switched into the beamline doubling each micro pulse with a variable distance of some nanoseconds in order to accelerate double bunches in close-by rf buckets. Refer to [9] for details.

In addition, the laser beam can be directed remotely to a joulemeter to measure its energy. It is frequently used for quantum efficiency measurements. The laser pulse can also be directed to a fast streak camera (Hamamatsu FESCA 200) to measure its longitudinal pulse structure. The pulse length in the UV is measured frequently and is stable at 4.4±0.1 ps sigma.

The UV beam is transported from the laser hut to the rf gun. The beamline has a length of 10 m. It is protected with tubes against dust and air turbulences. The beamline needs five dielectric mirrors with a coating optimized for 262 nm. A remote controlled mirror box allows true linear steering of the beam along the cathode. The last mirror in the vacuum chamber guides the beam to the cathode. It is manufactured of solid aluminum. Its surface is diamond turned and has a good optical flatness and a reasonable reflectivity of 90 %. We have chosen a solid metal mirror for two reasons. Dielectric mirrors charge up when hit by darkcurrent. Charging and discharging leads to cracks on the mirror surface and influences the electron beam trajectory. Secondly, experiments supported by simulations have shown, that the beam emittance is also effected.[10]

The laser beam transport is based on the relay imaging technique together with spatial filtering. A hard edge aperture downstream of the diode pumped amplifiers is consecutively imaged to the flashlamp pumped laser heads, to the doubling crystals and finally to the cathode. This results in a quasi flat laser pulse on the cathode which is further sharpened by a hard edge iris aperture close to the gun. The magnification of the telescope system is about 10 re-

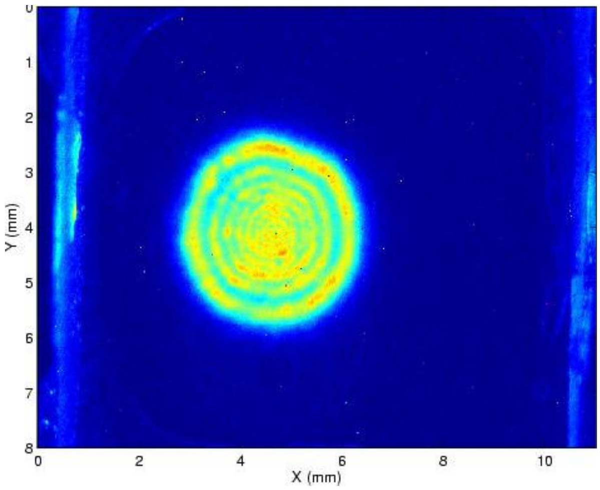

Figure 3: Laser beam profile measured with a Ce:YAG crystal at the 'virtual cathode'. A large laser spot (diameter 1 to 1.5 cm) is seen through an iris of 3 mm in diameter. Although interference fringes show up, the pointing stability is much improved.

Table 1: Laser parameters. Most parameters are adjustable and are set according to the requirements for the specific experiment.

parameter	value
laser material	Nd:YLF
wavelength after conversion	262 nm
output structure	pulsed trains
train repetition rate	5 or 10 Hz
train length	up to 800 μs *
micro pulse spacing	0.33 us to 800 μs *
micro pulse longitudinal shape	gaussian
micro pulse length	4.4±0.1 ps (sigma)
transverse profile	flat, with fringes
transverse size on cathode	3 mm diam.*
	*adjustable

sulting in a large beam size of about 1 cm in diameter. The iris is remote controlled and is usually adjusted to a diameter of 3 mm cutting a large portion of the laser beam. This results in a roughly flat transverse profile. In addition and most important, these measures reduce the pointing jitter by a large amount and contributes to the stability of the electron source. However, interference fringes created by the hard edge aperture could not been completely avoided. The modulation is about 20 %. An upgrade is foreseen to reduce the modulation (see [11]).

A so called virtual cathode is used to set-up and control the transverse laser beam shape. A remote controlled mirror directs the laser beam onto a Ce:YAG crystal mounted at a distance identical to the cathode position. Figure 3 shows an image of the laser beam on the virtual cathode.

Table 1 summarizes the main laser parameters.

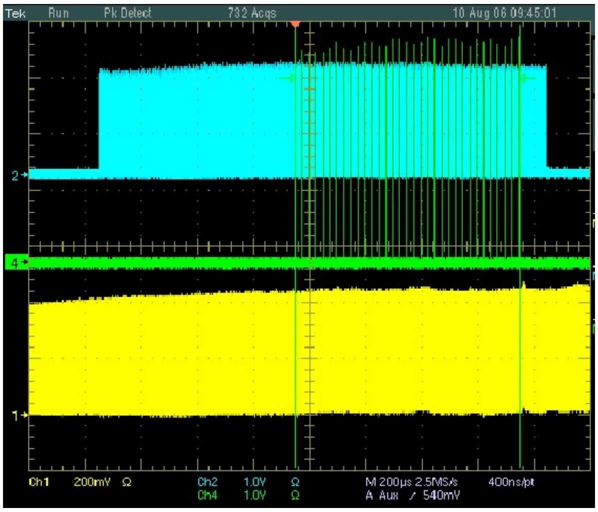

Figure 4: Scope screen shot of a 40 kHz pulse train (green trace, Nb. 4). In addition, the central part of the 27 MHz train of the oscillator (PTO) (yellow, nb 1), and the 1 MHz pulse train after the diode pumped preamplifiers (cyan, nb. 2) are shown.

BUNCH TRAIN PATTERN AND MACHINE PROTECTION

Experiments with FEL radiation often require different electron bunch train pattern. The laser can provide to a certain extend a flexible bunch train pattern chosen by the operator.

We use the Pockels cell based pulse pickers to vary the pattern of the laser pulse train. The Pockels cells may run for 1.5 ms with a rate of up to 3 MHz, pulsed with up to 10 Hz.

An FPGA based controller has been developed. It takes as an input the 9 MHz rf signal from the master oscillator and the 5 Hz or 10 Hz trigger from the control system. The controller produces the trigger gates which go to the Pockels cell drivers. The FPGA allows a flexible control on the number of pulses and the repetition rate, for example in addition to the standard 1 MHz, 250 kHz, 100 kHz, 10 kHz, and others are possible. As an example, Fig. 4 shows a scope screen shot of a 40 kHz pulse train.

The controller also serves as an interface to the machine protection system (MPS).[12] Three beam modes are defined: a single pulse, short pulse, and a long pulse mode. These modes are a machine safety measure, for instance only single bunches are allowed when screens are inserted in the high energy part of the accelerator. Depending on the mode, the controller limits the number of laser pulses picked by the second Pockels cell, independent of the operator request. It also receives a fast beam stop signal from the MPS, for instance when losses grow within a pulse train. The stop signal suppresses further triggers to the pulse pickers. The reaction is immediate within some tens of nanoseconds.

For a safe operation of the laser, important operating conditions are surveyed by an SPS based system. For instance, the system issues warnings and interlocks on overtemperature, water flow interruptions and so on. The overall system is controlled with a VME-crate based cpu integrated into the FLASH control system providing an interface to the operators. The cpu reads important laser parameters and drives for instance flashlamps, slow feedbacks on a shot to shot bases.

CONCLUSION

The photoinjector laser system has been upgraded by partially replacing flashlamp pumped laser heads by diode pumped heads. The upgraded system has been put into operation at FLASH in February 2004 and providing beam since then (for more than 20.000 h). The stability and reliability of the system is satisfactory, maintenance a routine task. An FPGA based controller allows to drive the pulse pickers with a variable pulse pattern and serves at the same time as an interface to the machine protection system. The laser is integrated into the FLASH control system providing informations about the status of the system and various remote control options.

ACKNOWLEDGMENT

We like to thank our colleagues from the FLASH controls group for their support, mainly B. Petrosyan for the interface to the doocs control system, J. Thomas and O. Hensler for the motor drivers. We also thank M. Werner for many fruitful discussions and his valuable help on the implementing of the FPGA controller, and O. Grimm for his kind help with the streak camera.

REFERENCES

[1] V. Ayvazian *et al.*, Eur. Phys. J. **D 37**, 297 (2006).

[2] S. Schreiber, “First lasing at 32-nm of the VUV-FEL at DESY,” eConf **C0508213**, MOOB002 (2005), *Presented at the 27th International Free Electron Laser Conference (FEL 2005), Stanford, California, 22-26 August 2005.*

[3] S. Schreiber, eConf **C0508213** (2005) THPP038 [arXiv:/] *Presented at the 27th International Free Electron Laser Conference (FEL 2005), Stanford, California, 22-26 August 2005.*

[4] D. Sertore, P. Michelato, L. Monaco, A. Bonucci, J. H. Han and S. Schreiber, PAC-2005-MOPB009 *Prepared for Particle Accelerator Conference (PAC 05), Knoxville, Tennessee, 16-20 May 2005.*

[5] “SASE FEL at the TESLA Facility, Phase 2,” DESY-TESLA-FEL-2002-01.

[6] S. Schreiber, D. Sertore, I. Will, A. Liero and W. Sandner, Nucl. Instrum. Meth. A **445** (2000) 427.

[7] I. Will, G. Koss and I. Templin, Nucl. Instrum. Meth. A **541** (2005) 467.

[8] E. Vogel, W. Koprek, P. Pucyk, EPAC-2006-TUPCH189, Proceedings of EPAC 2006, Edinburgh, UK, 26-30 June 2006.

[9] O. Grimm, K. Klose and S. Schreiber, EPAC-2006-THPCH150, Proceedings of EPAC 2006, Edinburgh, UK, 26-30 June 2006.

[10] M. Krasilnikov *et al.*, DESY-M-04-03U *Prepared for 9th European Particle Accelerator Conference (EPAC 2004), Lucerne, Switzerland, 5-9 Jul 2004.*

[11] M. V. Hartrott *et al.*, eConf **C0508213** (2005) MOPP034 [arXiv:/] *Presented at the 27th International Free Electron Laser Conference (FEL 2005), Stanford, California, 22-26 August 2005.*

[12] L. Fröhlich *et al.*, ”First Experience with the Machine Protections System of FLASH”, FEL-2006-THPPH016, these proceedings.

SINGLE-SHOT LONGITUDINAL DIAGNOSTICS WITH THZ RADIATION AT THE FREE-ELECTRON LASER FLASH

H. Delsim-Hashemi, J. Rossbach, P. Schmüser , Univ. Hamburg, Germany
O. Grimm, H. Schlarb , B. Schmidt, DESY, Hamburg, Germany
A.F.G. van der Meer, FOM, Nieuwegein, The Netherlands.

Abstract

The longitudinal charge distribution in the electron bunches has a strong impact on the lasing process in a Free-Electron Laser based on the principle of Self Amplified Spontaneous Emission of radiation. For the ultraviolet and soft X ray FEL FLASH at DESY, structures in the range of ten to hundred micrometers play a crucial role. The investigation of the longitudinal charge distribution in the electron bunches on a bunch-by-bunch basis is an important issue for optimizing the bunch compression and improving the performance of the machine. This paper introduces a new tool for longitudinal diagnostics based on THz spectroscopy of coherent radiation. A novel spectrometer has been designed which permits to analyze the radiation of single electron bunches in a broad spectral range and with high resolution. Preliminary measurements with this spectrometer are presented.

INTRODUCTION

FEL facilities in the VUV and X-ray regime require kA peak currents which are usually achieved by several stages of bunch compression. The longitudinal charge distribution of the compressed bunches has to be measured with high precision in order to fine-tune the off-crest phase in the accelerating section preceding the magnetic bunch compressor chicanes and to optimize the SASE performance. The existing interferometers operate in the scanning mode and determine the average pulse shape of many thousand bunches. They are intrinsically unable to yield information on single bunches. The new single-shot spectrometer uses diffraction gratings as dispersive elements and an array of pyro-electric detectors with multi-channel readout. Exploratory measurements with the first stage, containing thirty channels will be presented.

GRATING SPECTROMETER

The coherent radiation of the compressed bunches subjected to a radiation process in the FLASH linac covers a wide wavelength spectrum from the millimeter range down to a few micrometers. Diffraction gratings are well suited to disperse broad-band radiation to different detection channels. The principles of grating based spectrometers as tools for longitudinal diagnostic are described in reference [1]. These principles are applied in several devices that are described in [2] and [3] or will be explained in this paper.

Advanced bunch compression monitor

As it is described in reference [3], a multi stage reflectance blazed grating spectrometer is used to study bunch compression versus machine parameters. In the following comes an example. It is known that the off-crest phase φ in the first acceleration module ACC1 has a strong influence on the longitudinal bunch profile that is obtained when the bunches have passed the two magnetic chicanes. Empirically it is found that the SASE efficiency depends very critically on φ and reaches its maximum at $\varphi \approx -5^\circ$ to -6°. A phase scan around this value is shown in Fig.1. The signal of the gas monitor detector (GMD), measuring the pulse energy of the FEL light, exhibits a pronounced maximum at $\varphi = -5.7^\circ$ with a width of $\pm 0.2^\circ$. The coherent transition radiation intensities in various wavelength channels are also plotted in Fig.1. The remarkable observation is that the intensity for short wavelengths (20 to 75 μm) exhibits a strong peak in the region of maximum SASE intensity while the intensity of long wavelengths has a monotonic increase towards more negative phase.

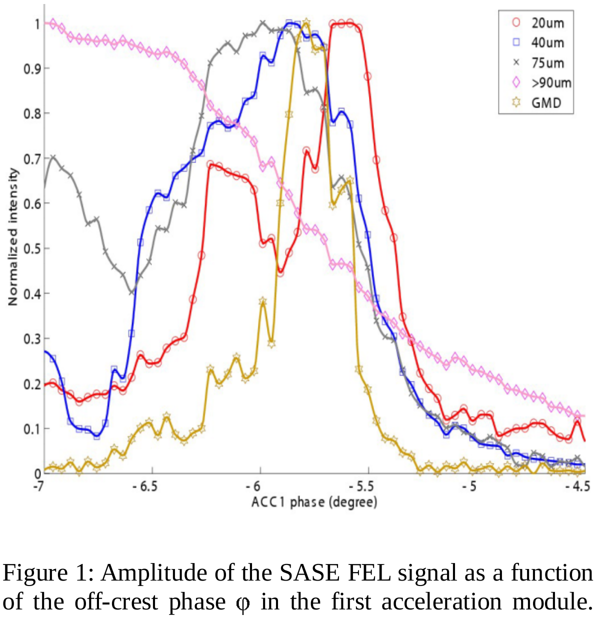

Figure 1: Amplitude of the SASE FEL signal as a function of the off-crest phase φ in the first acceleration module. Also the intensity of coherent transition radiation for wavelengths of $20 \pm 1\mu m$, $40 \pm 2\mu m$, $75 \pm 4\mu m$ and for $\lambda > 90\mu m$ is shown. Distributions are individually normalized to a maximum value of 1.

Spectrograph

Here a single shot spectrometer that gives the ultra broadband spectra of coherent radiation on a shot to shot basis is called spectrograph. As it was described in [1] a spectrograph is composed of three main components, one that disperses the polychromatic radiation, one that focuses the dispersed radiation to spatially different coordinates dependent on wavelength without mix-up and the detector system. The first two issues were covered and explored in [2] and [3]. The most new achievement is the development of a fast 30 channel detection system based on pyro-electric sensors, Fig. 2.

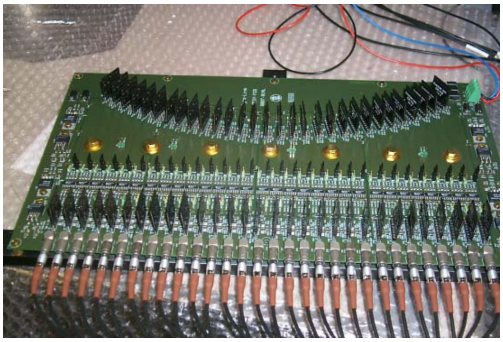

Figure 2: The 30 channel pyro line detector is equipped with fast read out electronics and pyro sensors with broadband smooth response function. The sensitivity is about 300 pJ (5 times noise level) for 1μm < λ < 1mm, [4].

Two types of single stage spectrographs based on Transmission Grating (TG) and Reflectance Blazed Grating (RBG) have been successfully tested.

A TG base spectrograph can cover a rather large range of wavelengths in a single stage. It should be noticed that with a single stage TG spectrograph we will cover the entire interesting wavelength range from 50 to 300 μm, with only two stages the spectra up to 1.8 mm could be derived, Fig. 3. Fig. 4 shows a sequence of 600 subsequent single shot spectra.

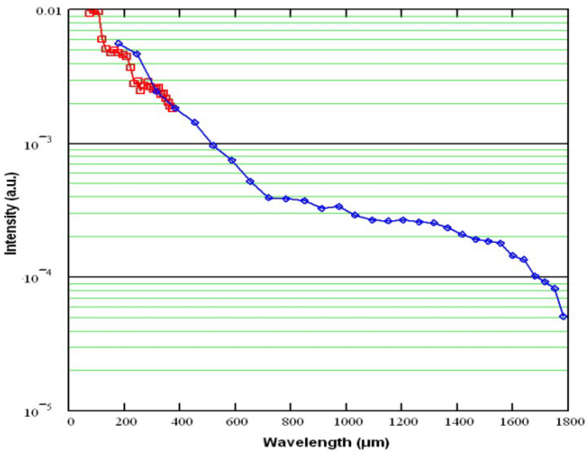

Figure 3: The averaged combined spectra recorded by stages with 2.5 and 0.5 line per mm.

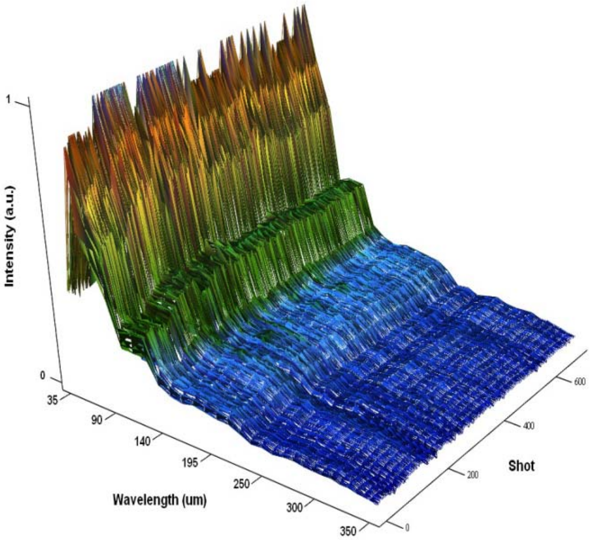

Figure 4: Recorded spectra by using a transmission grating with 2.5 lines per mm.

Reflectance blazed grating have a limited free spectral range of about a factor of two but offer much better resolution and efficiency and can be staged [1]. From the previous studies it is clear that the most relevant part of the spectra for the FLASH machine operation in SASE mode is about 10 to 100 μm. One of the measured spectra in this regime is shown in Fig.5. A combined plot of measured spectra on different regions, averaged over many shots, is shown in Fig. 6.

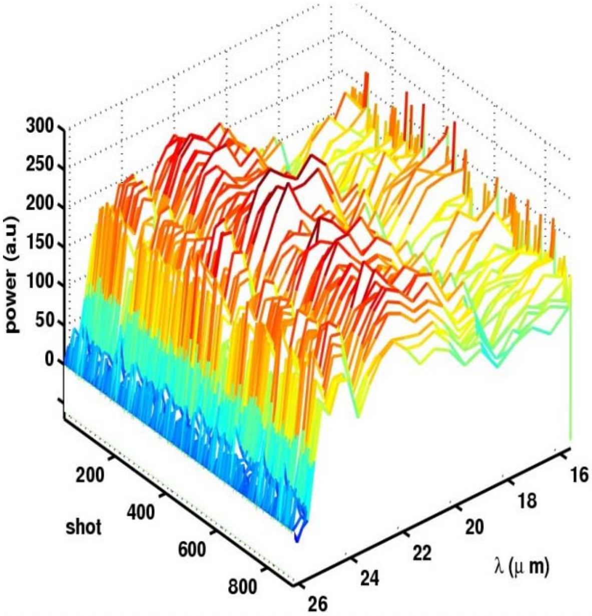

Figure 5: About 900 subsequent shots measured with reflectance grating of 50 lines per mm during SASE operation.

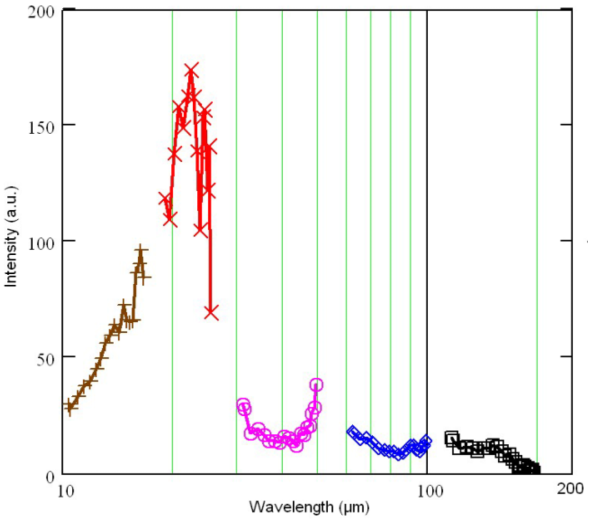

Figure 6: The averaged combined spectra recorded by different RBGs. Full coverage of interesting range of the spectra for FLASH electron bunches requires 5 stages of RBG base spectrograph.

Fig. 7 shows a series of single shot spectra in the wavelength range from 30 to 50 μm recorded while the phase of first accelerating module was changed by ~10 degrees. The spectra shows a very pronounced peak at the phase of operation for optimum SASE.

CONCLUSION

We have demonstrated that single-shot wavelength-selective spectroscopy of coherent radiation is possible. The described spectrograph can give, on a shot to shot basis, information on very short structures of the electron bunches which is not possible by other techniques and can be used for fast feedback systems.

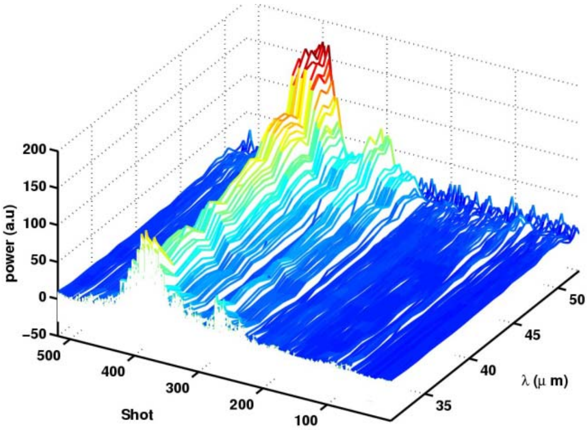

Figure 7: Plotted is the variation of the spectra in one of the stages of reflectance blazed grating spectrograph (with 25 lines per mm) when phase of the first accelerating module changed over ~10 degrees. The peak coherent radiation intensity corresponds to operational condition for optimum SASE.

REFERENCES

[1] H. Delsim-Hashemi et. al., Broadband single shot spectrometer, Proceedings FEL2005.
[2] H. Delsim-Hashemi et. al., Single-shot longitudinal diagnostics with THz radiation, Proceedings FLS2006.
[3] H. Delsim-Hashemi et. al., Bunch compression monitor, Proceedings EPAC2006.
[4] B. Schmidt and H. Delsim-Hashemi, to be published.

INVESTIGATIONS OF THE LONGITUDINAL BEAM PROPERTIES AT THE PHOTOINJECTOR TEST FACILITY IN ZEUTHEN*

J. Rönsch†, J. Rossbach, Hamburg University, 22761 Hamburg, Germany
G. Asova, J. Bähr, H.-J. Grabosch, S. Khodyachykh, S. Korepanov, M. Krasilnikov,
A. Oppelt, B. Petrosyan, S. Riemann, L. Staykov, F. Stephan, DESY, 15738 Zeuthen, Germany
D. Lipka, D. Richter, F. Marhauser BESSY, 12489 Berlin, Germany
A. Onuchin, Budker Institut of Nuclear Physics, Novosibirsk 630090, Russia.

Abstract

The goal of the Photoinjector Test Facility at DESY in Zeuthen (PITZ) is to test and optimise electron guns for FELs like FLASH and X-FEL at DESY in Hamburg. In 2005 the setup was extended by a booster cavity. In order to measure longitudinal and transverse properties of the beam with a momentum in the range between 4 to 40 MeV/c, a viewport after the booster cavity has been developed. It contains several radiators. One of them is Silica aerogel used as Cherenkov radiator for the measurement of the longitudinal electron distribution with a streak camera. Design considerations are presented in this paper.

INTRODUCTION

The main goal of PITZ is the test and optimization of L-Band RF photo injectors for Free-Electron Lasers (FELs). The demands on this photo injector are long bunch trains with short bunches, a charge of about 1 nC and small emittances. The linac based FEL at FLASH incorporates a 1.5 cell RF gun capable of producing a high charge density, followed by an acceleration section and a magnetic bunch compressor. For an effective bunch compression detailed studies of the longitudinal phase space after the gun and its evolution behind the booster cavity have to be performed. The new screen station (HIGH1.Scr2) is planed to be placed about 5 m downstream of the photocathode and about 1.5 m downstream of the exit of the booster cavity in the PITZ2 setup [1] as shown in Figure1.

In the past, PITZ made good experience by using the full cone of a Cherenkov radiator for bunch length measurements after the gun [2]. It will be discussed whether a copy of screen station LOW.Scr3 can be used and which modifications are necessary.

SCREEN STATION FOR BUNCH LENGTH MEASUREMENTS

Screen station LOW.Scr3 was designed for an electron energy of about 5 MeV. It contains a YAG screen to determine transverse properties using a TV camera, three radiators (aerogel, an optical transition radiator (OTR), quartz), whose light is transported to the streak camera [3] and a tapered empty tube, for beam passage without wakefield production. The Silica aerogel (refractive index $n = 1.03$, thickness $th = 2$ mm) is used as a Cherenkov radiator and the pulse length is measured using an optical transmission line [4] and a streak camera.

The new screen station (HIGH1.Scr2) and its elements should be designed for electron energies in the range of 4 up to 40 MeV, so it can be used even if the booster cavity is off. Planed elements are: a YAG-screen and an OTR for the determination of the transverse beam size and position of the electron beam using a TV camera, Silica aerogel and a further OTR for bunch length measurements as well as an empty tube.

Screen Dimensions

For higher energies the beam size becomes smaller, but when the booster cavity is turned off the beam size increases. Simulations of transverse beam size at the position of HIGH1.Scr2 were made to clarify the needed dimensions. Figure 2 (a) shows the simulated transverse beam size at a gun and booster phase with maximum energy gain for different solenoid currents, when the booster is turned on. The smallest transverse beam size could be reached for about 260 A. In Figure 2 (b) the simulated transverse beam distribution are shown for 260 A and a gun and booster phase with maximum energy gain.

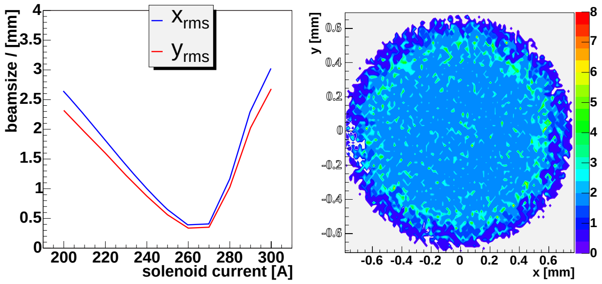

(a) (b)

Figure 2: Simulations of the electron beam size as a function of the solenoid current (a) and transverse beam properties at the screen station (b) for a gun and booster phase with maximum energy gain and a flat-top longitudinal laser distribution at 1 nC.

---

* This work has partly been supported by the European Community, contract numbers RII3-CT-2004-506008 and 011935, and by the 'Impuls- und Vernetzungsfonds' of the Helmholtz Association, contract number VH-FZ-005.

† jroensch@ifh.de

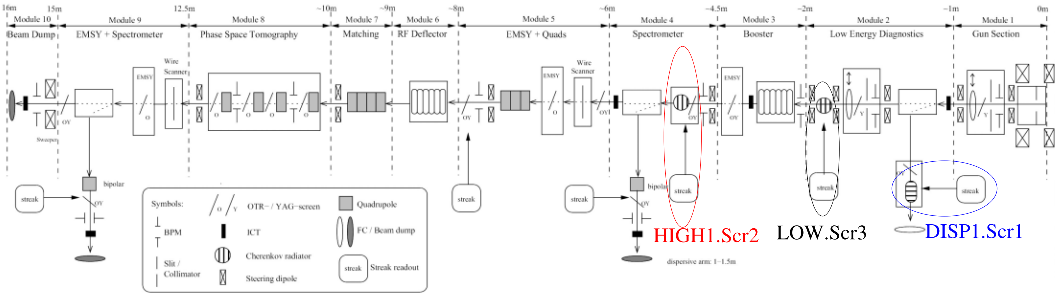

Figure 1: Planed setup of PITZ2. The screen station HIGH1.Scr2, LOW.Scr3 and DISP1.Scr1 are marked.

Results of simulations of the beam dynamics, when the booster is off are shown in Figure 3. In this case the beam size is almost 10 times higher than with the booster cavity turned on.

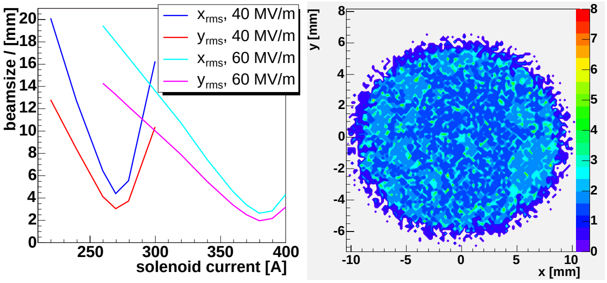

(a) (b)

Figure 3: Simulated transverse electron beam size as a function of the solenoid current for 40MV/m and 60MV/m gradient (a) and transverse beam properties at the screen station (b) for a gradient of 40MV/m in the gun and a phase with maximum energy gain, a flat-top longitudinal laser distribution at 1 nC, when the booster is turned off.

For measurements using the booster the beam size could be very small, therefore both OTRs will have an effective size of 20 mm × 20 mm. Using an OTR at an angle of 45° with respect to the beam direction, backward radiation is emitted at 90° regarding the beam direction. A thin plate (about 300 μm) will be used as OTR, because of its better optical quality and resistance compared to a thin foil. Two different types of OTR screens are in use at FLASH [5]:

- 350 um thick polished silicon (Si)
- 350 um thick Si with an aluminium (Al) coating

The Si has a better thermal resistance than Al, and therefore the pure Si screen stands a higher charge density (i.e small beam with high charge) than Si coated with Al. On the other hand the Al emits about 2-3 times more photons than polished Si, i.e. the light yield is much better. That is why we decided to use the Al coated Si plates.

Since there are no quadrupoles planed before this screen station there is no possibility to reduce the beam size in the case the booster is off. To catch the whole beam even when the booster is off the effective size of the YAG screen should have the dimension size as the beam tube (diameter = 35 mm).

Bunch Length Measurement

The temporal resolution of the Silica aerogel used at LOW.Scr3 was calculated to be 0.12 ps at a beam momentum of 4.5 MeV/c [6]. This value is very small compared to the resolution of the optical transmission line. The temporal resolution of the optical transmission line was determined with 1.15 ps when using an optical transmission filter of 550 nm with a bandwidth of 10 nm [7]. The bunch length measurements were typically done for a streak camera slit width of 100 μm. The temporal resolution of a 100 μm slit was determined with about 1.75 ps for the streak camera used at PITZ [2]. The resolution of the streak camera C5680 is denoted by the producer with 2 ps FWHM [3]. Therefore it is useful to increase the thickness of the Silica aerogel in order to increase the number of photons, so one could reduce the slit width or the number of pulses used for a measurement. The initial idea was to use Silica aerogel with an index of refraction $n = 1.03$ and a thickness of 5 mm. Cherenkov light is emitted under a certain angle depending on the average refractive index of the radiator (n) and the electron energy. It leaves the radiator following Snells law. Figure 4(a) shows the emission angle of Cherenkov radiators with three different indices of refraction. For low energies the angle changes strongly with the energy, but at higher energies it stays constant. Aerogel with $n = 1.03$ has an emission angle of up to $14.3°$ at an electron beam momentum of 40 MeV/c, but the acceptance angle of the optical system from the screen station to the streak camera is only $\pm 11.8°$. Using an aerogel with $n = 1.03$ it is impossible to collected the whole Cherenkov cone.

In contrast to Cherenkov radiator the optical transition radiator emits the light within a certain angular distribution. The angular distribution of transition radiation depends on the particle energy and the angle of incident [8]. In Figure 4,(b) the angular distribution for a beam momentum of 40 MeV/c and 5 MeV/c electrons are shown. At 40 MeV/c beam momentum most of the light is emitted within a small angle. At smaller energies it becomes impossible to collect

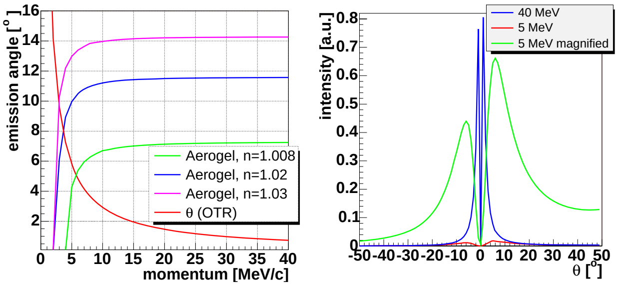

(a) (b)

Figure 4: The emission angle of OTR and the Silica aerogel radiators with different reflective indices as a function of the electron momentum (a) and the angular distribution of optical transition radiation produced by 40 MeV and 5 MeV electrons (b).

all the light by the used optical system. The red curve in Figure 4 (a) shows the angle with the highest number of emitted photons.

An aerogel with $n = 1.02$ and $th = 7$ mm (as well as $n = 1.008$ and $th = 15$ mm) would lead to about the same temporal resolution as an aerogel with $n = 1.03$ and a thickness of $th = 5$mm, but the number of photons is lower, as shown in Figure 5.

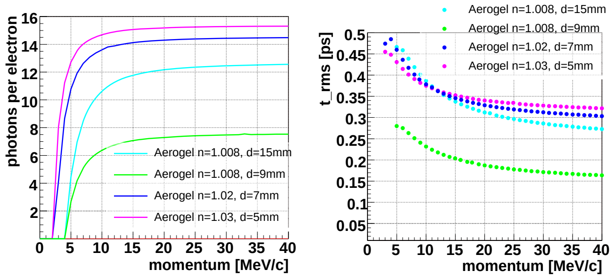

(a) (b)

Figure 5: Number of photons (a) and resolution (b) of Silica aerogels with different indices of refraction and thickness's as a function of the energy.

By mechanical reason the maximum usable thickness is 9 mm. The Budker Institut of Nuclear Physics (Novosibirsk) is producing Silica aerogel for PITZ, but only Silica aerogel with $n = 1.008$, 1.03 and 1.05 are produced by default. A production of Silica aerogel with $n = 1.02$ would take a lot of effort. So we will start to use aerogel with n = 1.008 and 9 mm, which can be replaced later. The main disadvantage of the refractive index $n = 1.008$ is that the lower limit for the production of Cherenkov light is at about 4 MeV/c and the photon yield changes strongly within the beam momentum range from 4 to 6 MeV/c. The advantage is that the Cherenkov light of bigger transverse distributions can be transported and small misalignments of the optical transmission line does not lead to losses. The number of photons produced by aerogel at 40 MeV/c is still a factor of a few hundred higher compared to OTR.

LONGITUDINAL PHASE SPACE MEASUREMENTS

The longitudinal phase space after the gun at DISP1.Scr1 (shown in Figure1) and its projection were measured for different phases of the gun. In order to compare simulated (Fig.6 second row) and measured (Fig.6 first row) longitudinal phase space the simulated one was tracked through the dipole using matrix formalism. The vertical scale was converted into momentum scale after the correction of M_{56} [9] by shearing the distribution (Fig.6 third row). Matrix element M_{56} describes the influence of the dipole on the longitudinal distribution due to different particle momenta. The measured momentum distribution fits very well with the distribution traced through the dipole (Fig.6 fourth row). Also the longitudinal distribution (Fig.6 fifth row) shows a rather good agreement. It is difficult to find similarities with in the longitudinal phase space. The longitudinal phase space changes completely after tracing the particle though the dipole. In [10] it will be shown, how to design a dipole magnet in order to minimize this problem. Beside the influence of the dipole magnet the optical transmission line and the streak camera itself have an influence onto the resolution as described in [7].

CONCLUSION

A screen station to measure longitudinal and transverse beam properties in the momentum range from 4 to 40 MeV/c was designed. One of the radiator is Silica aerogel used as Cherenkov radiator for the measurement of the longitudinal electron distribution with a streak camera. Even at 40 MeV/c Silica aerogel produces a higher photon yield than OTR. Longitudinal phase space studies and improvements of the system are ongoing.

ACKNOWLEDGMENT

We would like to thank Lap Van Vu (DESY Zeuthen) for the technical design and J. Kolbe for useful discussions and hints concerning the design and construction.

REFERENCES

[1] A. Oppelt, PITZ2 Elements and Coordinates, http://www-zeuthen.desy.de/~apohl/pitz2/PITZ2-Schema.jpg (11.08.2006).

[2] D. Lipka, “Investigations about the longitudinal phase space at a photo injector for minimized emittance”, PhD Thesis 2004 Humboldt University Berlin.

[3] Hamamatsu, “Test report C5680-21, Serial No. 040168”.

[4] J. Bähr, D. Lipka, H. Lüdecke, “Optical transmission line for streak camera measurement at PITZ”, Dipac Mainz 2003.

[5] K.Honkavaara private communication.

[6] D. Lipka et al, “Silica aerogel radiators for bunch length measurements”, Nuclear Instruments and Methods in Physics Research A 538 (2005) 597?607.

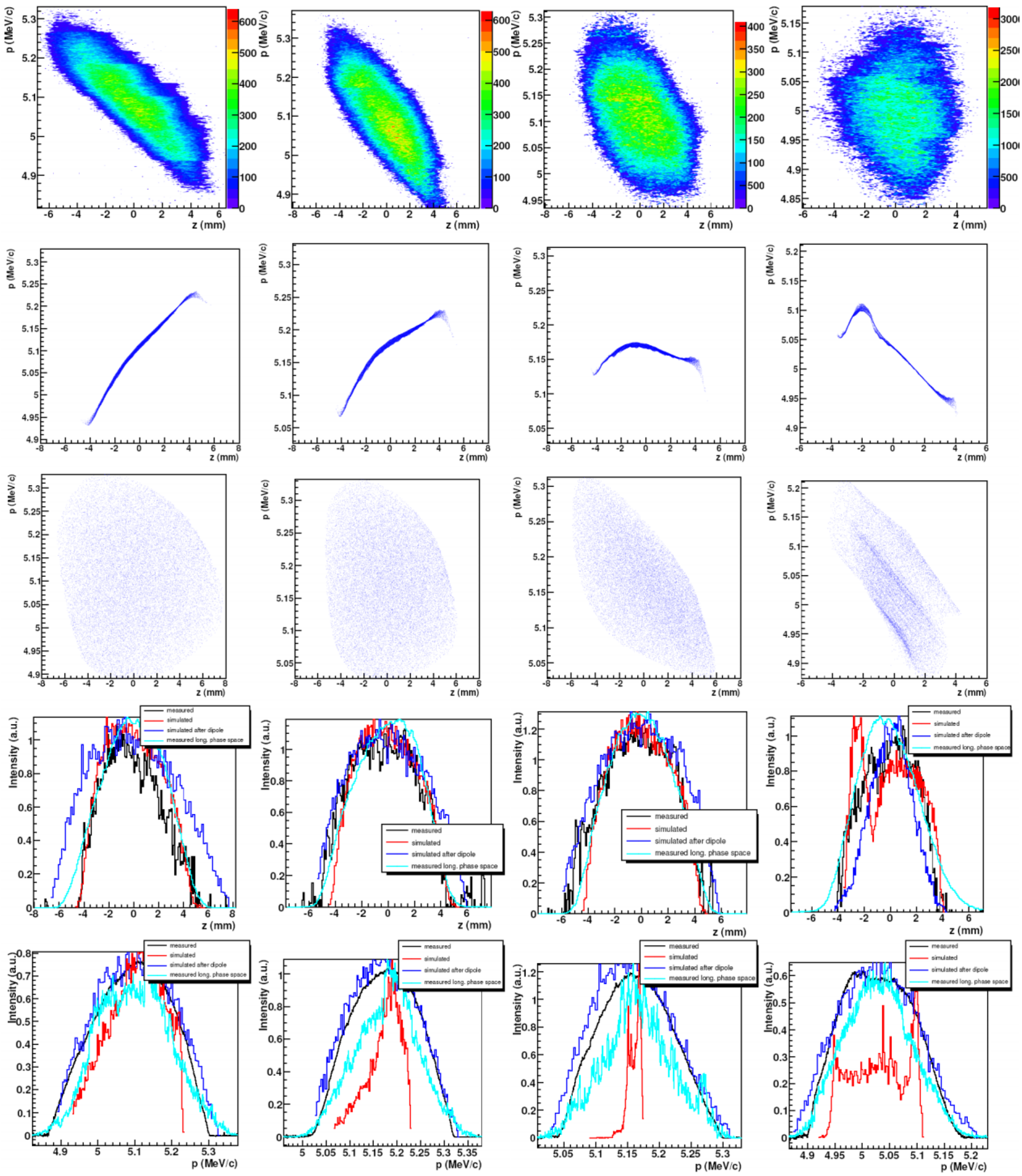

Figure 6: Measurement (1st row) and simulation (2nd row) of the longitudinal phase space. The simulation was traced through the dipole to show the expected distribution. The projections of the three distributions were compared to the direct bunch length measurement (4th row) and momentum measurement (5th row). Black line is direct measurement, red simulation, cyan projection of the phase space measurement and blue projection of the traced distribution. The results were shown for gun phase with maximum energy gain +10 °, +0°, -10° and -25° (from left to right).

[7] J. Rönsch et al, “Investigations of the longitudinal phase space at PITZ”, EPAC Edinburgh 2006.

[8] K.Honkavaara, “Considerations of streak camera measurements for Photoinjector Test Facility (PITZ) in DESY Zeuthen”, note, July 2000.

[9] D. C. Carey, K. L. Brown, F. Rothacker, “Third-Order TRANSPORT with MAD Input”, FERMILAB-PUB-98/310.

[10] S. Khodyachykh et al., Design of the Multipurpose Dispersive Section at PITZ, contribution THPPH020, FEL 2006.

DESIGN OF MULTIPURPOSE DISPERSIVE SECTION AT PITZ*

S. Khodyachykh†, J. Bähr, M. Krasilnikov, A. Oppelt, L. Staykov, F. Stephan,
DESY, Zeuthen, Germany,
T. Garvey, LAL, Orsay, France, D. Lipk, BESSY GmbH, Berlin, Germany,
J. Rönsch, University of Hamburg, Hamburg, Germany.

Abstract

A detailed knowledge of the parameters of a high-brightness electron beam is of major importance for evaluating the performance of a free electron laser using the beam. Therefore, a full characterization of the beam parameters is required during the commissioning of RF photo injectors. As one important contribution to fulfill this task, a multi-purpose high energy dispersive arm (HEDA1) for electron energies up to 40 MeV is presently under construction at the Photo Injector Test Facility at DESY in Zeuthen (PITZ). The dispersive section is designed such that it will combine the functionality of 1) an electron spectrometer, 2) a device for characterization of the longitudinal phase space, and 3) a transverse slice emittance measuring system. The HEDA1 consists of a 180° dipole magnet (C-Bend), followed by removable slit, a quadrupole magnet, and a screen station with a read-out for the streak camera. Design considerations and the detailed lay out of the high-energy dispersive section are presented.

INTRODUCTION

The Photo-Injector Test Facility at DESY in Zeuthen (PITZ) is an electron accelerator which was built by Deutsches Elektronen-Synchrotron (DESY) in collaboration with international partners with the goal to develop and to optimize high brightness electron sources suitable for SASE FEL operation.

The PITZ facility consists of a 1.5 cell L-band RF gun, a photo-cathode laser system, a normal-conducting booster cavity and a diagnostic section. Being an operational machine showing pioneering results in achieving of high-charge low-emittance electron beams for electron bunch trains [1], PITZ is still under development. The beam line which has a present length of about 13 meters will be extended up to about 21 meters within the next two years. Many additional diagnostics components will be added to the present layout. Together with the deflecting cavity [2], the phase space tomography module [3] and the second high-energy dispersive arm (HEDA2), HEDA1 will extend the existing diagnostics system of the photo injector. The scope of the present paper is the multi-purpose high energy dispersive arm (HEDA1). The dispersive section is designed to combine the functionality of (i) an electron spectrometer, (ii) a device for characterization of the longitudinal phase space, and (iii) a transverse slice emittance measuring system.

SETUP

The layout of the dispersive section HEDA1 is schematically shown in Fig 1.

The heart of the dispersive section is a 180° dipole magnet having the bending radius of 300 mm. The bending radius has been chosen as a compromise between the space requirements and momentum resolution on the one hand and the ability of the spectrometer to operate within the large range of gun and booster parameters. Being deflected in vertical plane, the electron beam enters the dispersive arm which goes below the main beam line parallel to it. The dispersive arm includes a pumping port combined with a removable slit mask, a quadrupole magnet Q_1 for the slice emittance measurements, a drift space of 600 mm followed by two screen stations (for simplicity only one is shown) and by a beam dump. For measuring of the bunch charge an integrating current transformer (ICT) is foreseen between the two screen stations (not shown).

For the reasons described in the following sections additional components which contribute to the measurements at HEDA are located in the main beam line. These are the quadrupole magnet Q_2 and the screen station S_2 placed up- and downstream to the dipole magnet D, respectively.

The main advantage of the 180-degree spectrometer is the simplicity to reconstruct the momentum distribution [4]. One uses the screen S_2 in the straight section and measures the contribution from the transverse beam size and divergence, which can be de-convoluted with the measured spectrum to obtain the pure momentum distribution. This can be illustrated by comparing of the transport matrix M_D (describing the transport of the electron beam between the position of the quadrupole magnet Q_2 and the screen S_1) with the matrix M_S which corresponds to the drift between Q_2 and the screen S_2. The matrices in thin lens approximation have the form

$$M_D = \begin{pmatrix} -1 & -l_1 - l_2 & 2\rho \\ 0 & -1 & 0 \\ 0 & 0 & 1 \end{pmatrix}$$

$$M_S = \begin{pmatrix} 1 & l_1 + l_2 & 0 \\ 0 & 1 & 0 \\ 0 & 0 & 1 \end{pmatrix} \qquad (1)$$

---

* This work has partly been supported by the European Community, contracts RII3-CT-2004-506008 and 011935, and by the 'Impuls- und Vernetzungsfonds' of the Helmholtz Association, contract VH-FZ-005.

† sergiy.khodyachykh@desy.de

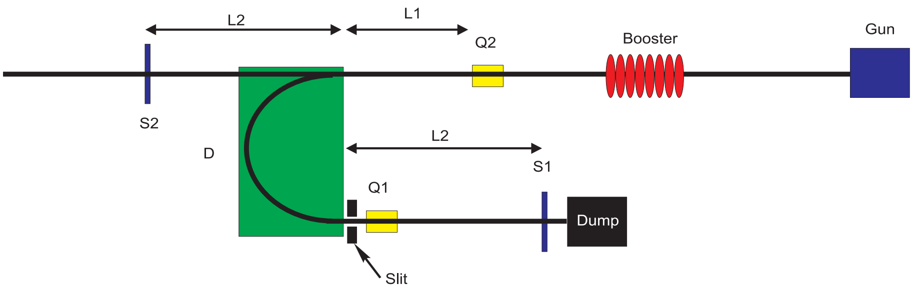

Figure 1: Simplified layout of PITZ with the first high energy dispersive section.

where ρ is the bending radius of the dipole magnet and lengths l_1 and l_2 are defined in Fig 1.

The transverse coordinates of the i-th electron can be described by a vector $\vec{y}_i = (y_i, y'_i, p_i/\langle p\rangle)^T$, where y_i is the transverse position, y'_i is the divergency and $p_i/\langle p\rangle$ is the relative momentum. Assuming the electron with the coordinate y_0 is transported through the spectrometer it will get the transverse coordinate on the screen S_1 which is described by the first component of vector $\vec{y}_1 = M_D\vec{y}_0$. The shift of the particle with respect to the reference trajectory is thus defined not only by the relative momentum of the particle, but also by it initial transverse offset and divergency. To exclude these two contributions one uses the measurements on the screen S_2 where only initial coordinate and initial divergency define the position of the particle (compare M_{11} and M_{12} elements of matrices in Eq.1). Moreover, by focusing the beam on the screen S_2 with the help of the quadrupole magnet Q_2 one can control the resolution of the momentum measurement.

Beam momentum and momentum spread depends strongly on the machine parameters. It is very sensitive to the RF phases of the gun and of the booster. Because of the large dispersion of the dipole magnet the spot sizes on the screen S_1 are expected to be very large, especially in cases of far off-crest RF phases. Figure 2 shows the dependence of the vertical beam size on the screen S_1 as a two dimensional function of the gun and booster phases. The aperture of the quadrupole magnet Q_1 (80 mm) defines the transversal acceptance of the dispersive section. Thus, using HEDA1 measurements within the range of $-35 ... 35°$ of booster phases will be possible in single shot. For larger off-crest phases a scan of dipole current will be used.

LONGITUDINAL PHASE SPACE

Very important information for the understanding of the photo-injector can be gained by studying the electron distribution in the longitudinal phase space, when the electron momentum is measured as a function of its longitudinal position within the bunch. For this purpose one of the screen stations will be equipped with an aerogel screen used as a Cherenkov radiator and a read-out for the streak-camera.

Figure 3 (a) shows the results of numerical simulation of the longitudinal phase space using the code ASTRA [7] at the entrance of the dipole magnet. The particles were tracked through the dipole using the matrix formalism, similar to that described in previous section, but using 6×6 transport matrix. The longitudinal phase space reconstructed on the screen S_1 of the dispersive section after the drift having the length of a 1 m is shown in Fig. 3 (b). A correction of the influence from the matrix element M_{56} [6] was applied in Fig. 3 (c). Figure 3 (d) shows the momentum distribution as a projection of Fig. 3 (a) in red and 3 (c) in blue.

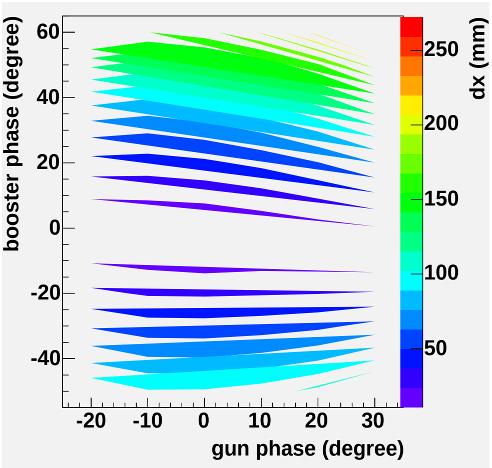

Figure 2: The total beam size in dispersive plane on screen S_1 as a function of gun and booster phases.

A comparison of the initial and the reconstructed values of mean momentum $\langle p\rangle$, momentum spread p_{rms} and longitudinal emittance ϵ_l are shownin table 1. The results in Fig. 3 and table 1 were done without quadrupole. These results could be improved by applying deconvolution with known beam size at S_2. However, this procedure unnecessary complicates data analysis comparing to the method discussed below.

Table 1:Initial and reconstructed values of mean momentum, momentum spread and longitudinal emittance.

	$< p >$ (MeV)	p_{rms} (keV)	ϵ_l (π keV mm)
(a)	18.3111	36.6	75.99
(c)	18.3109	49.0	105.08
$(a-c)/a$	-0.0009%	33.8%	38.3%

The simulations were repeated using a quadrupole triplet 4.5 m downstream the photocathode in order to focus the

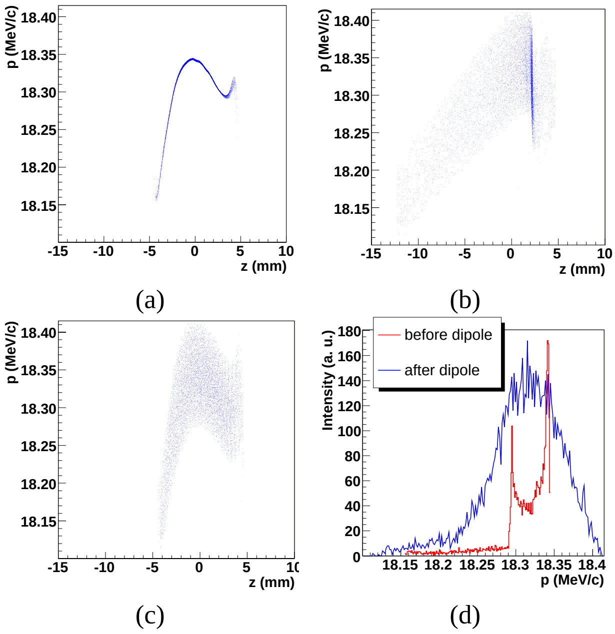

(a) (b)

(c) (d)

Figure 3: Longitudinal phase space obtained with the quadrupole magnet Q_2 being off: longitudinal phase space (a), reconstructed longitudinal phase space at S_1 (b), reconstructed longitudinal phase space at S_1 after correction of M_{56} (c), momentum distribution (d).

beam onto screen S_1 (at position 6.5 m). The results are shown in figure 4 and table 2.

Table 2: Initial and reconstructed values using a quadrupole triplett

	p_{mean} (MeV)	p_{rms} (keV)	ϵ_l (π keV mm)
(a)	18.3105	36.54	75.72
(c)	18.3104	36.59	76.11
$(a-c)/a$	-0.0005%	0.16%	0.5%

The use of a quadrupole triplet brings a remarkable improvement to the measurements of the longitudinal phase space. Both, the longitudinal phase space and the momentum distribution are reproduced with very good agreement. The differences between the simulated and reconstructed values of the momentum spread and longitudinal emittance reduces by using of the triplet from about 35% down to less than one per cent.

In order to save some space in the main beamline, we studied the possibility to exchange the quadrupole triplet with a single quadrupole magnet. Indeed such replacement almost does not decrease the accuracy of the longitudinal phase-space reconstruction. Figure 5 shows a comparison of the momentum measurements. The differences between the simulated and reconstructed mean momentum, momentum spread and longitudinal phase space are still within 1 %.

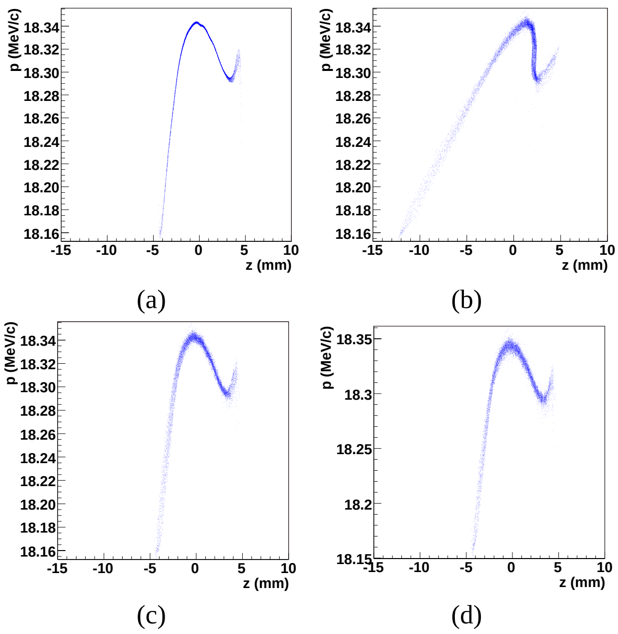

(a) (b)

(c) (d)

Figure 4: Longitudinal phase space obtained with the quadrupole triplet placed on the position of Q_2 being on: longitudinal phase space (a), reconstructed longitudinal phase space at S_1 (b), reconstructed longitudinal phase space at S_1 after correction of M_{56} (c). For a comparison reconstructed longitudinal phase space at S_1 [as (c)] but with a single quadrupole instead of a triplet.

TRANSVERSE SLICE EMITTANCE MEASUREMENTS

The functionality of the HEDA can be enhanced with a setup that allows us to measure the transverse emittance of the electron beam at different longitudinal positions along the bunch. The so called slice emittance is providing better understanding of the physics of a photoinjector, particulary the emittance compensation and conservation principles. It is also an important parameter for the SASE FELs since the slice emittance and slice peak current define the gain of the SASE FEL process. Using proper phasing of the booster cavity we can obtain linear correlation between the momentum and longitudinal distribution of the electrons in

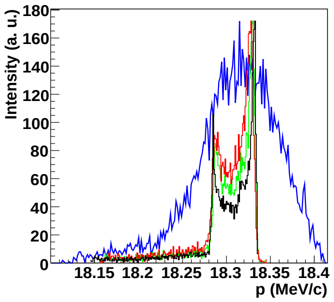

Figure 5: Simulated momentum distribution (black) compared to its reconstruction in the dispersive arm with the single quadrupole Q_2 (red), quadrupole triplet (green) and without quadrupole (blue).

the bunch. Afterwards one applies the standard quadrupole scan technique and measures the emittance for different momentum/time slices of the bunch.

A setup similar to that in [8] will be implemented. A slit at the dipole exit selects the necessary slice from the energy chirped beam. This slice is scanned with the quadrupole Q_1 focusing in a plane orthogonal to the dispersion plane of the dipole, the beam distribution will be observed on screen S_1. Due to the short distance between the quadrupole and the screen the beam size tends to become very small during the scan. For the correction of this the quadrupole magnet Q_2 with fixed strength placed before the dipole will be used (see Fig.1). The experimental setup was simulated with ASTRA [7] in attempt to verify the technique and to optimize the setup. For the simulations presented here, a gun gradient of 60 MV/m and a phase of maximum acceleration in the gun, the current in the main solenoid was 385 A, and a booster phase of +70 degrees were chosen. This corresponds to a projected emittance of $1.6\ mm \cdot mrad$ (see Fig. 6), a mean momentum of 17 MeV/c and an RMS momentum spread of 1.4 MeV/c.

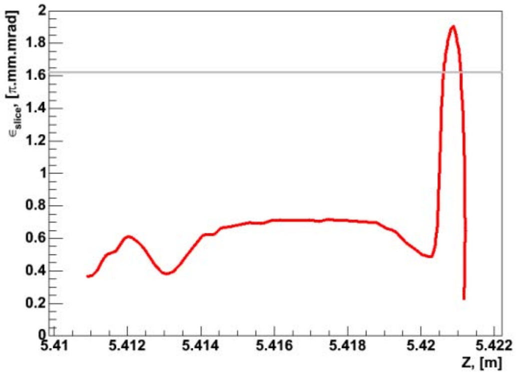

Figure 6: Slice emittance distribution at the dipole entrance. The solid line gives the value for the projected emittance.

The electron bunch was separated in ten longitudinal slices which were scanned with ten different quadrupole strengths. The distribution is fited to a quadratic equation (2) where the corresponding beam parameters are obtained.

$$\langle x_s^2\rangle = M_{11}^2\cdot\langle x_0^2\rangle + 2\cdot M_{11}M_{12}\langle x_0\cdot x_0'\rangle + M_{22}^2\cdot\langle x_0'^2\rangle \qquad (2)$$

Here $\langle x_s^2\rangle$ is the beam size coresponding to the particular strength of the quadrupole magnet, M_{11}, M_{12} and M_{22} are the elements of the transport matrix, functions of the quadrupole strength, $\langle x_0^2\rangle$, $\langle x_0\cdot x_0'\rangle$ and $\langle x_0'^2\rangle$ are the initial beam parameters that need to be found. The corresponding value for the emittance then is calculated using Eq. 3.

$$\varepsilon_n = \beta\gamma\cdot\sqrt{\langle x_0^2\rangle\cdot\langle x_0'^2\rangle - \langle x_0\cdot x_0'\rangle^2}. \qquad (3)$$

Here $\langle x_0^2\rangle$ and $\langle x_0'^2\rangle$ are the rms dimensions of the beam in the so-called trace phase space and $\langle x_0\cdot x_0'\rangle$ is the correlation between both.

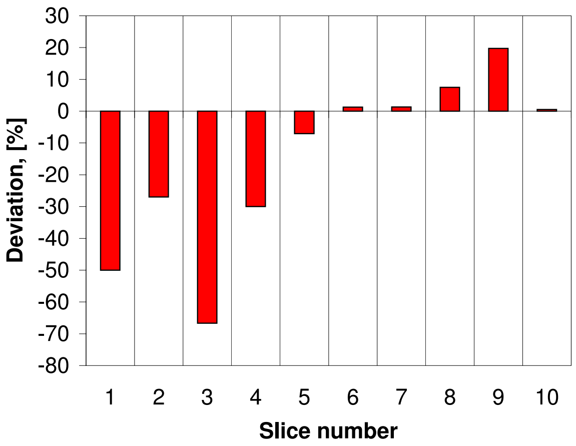

Figure 7: Deviation between the result from the simulated measurement and the slice emittance distribution obtained with ASTRA.

Figure 7 shows the deviation between the result from the simulated measurement and the slice emittance distribution obtained with ASTRA. The average deviation is 21 % but for some slices it can reach up to 66 %. Further improvement of the measuring accuracy can be reached by taking into account the space charge during the reconstruction.

ACKNOWLEDGEMENTS

Besides the funding agencies mentioned on the first page of the present paper the authors would like to thank S. Riemann, H.-J. Grabosch (both DESY) for valuable discussions. Without brilliant ideas of our engineers the realization of this work would not be thinkable.

REFERENCES

[1] F. Stephan, Status and perspectives of photo injector developments for high brightness beams, proceedings of teh workshop on the Physics and Applications of High Brightness Electron Beams. Erice, Italy, 2005.

[2] S. Korepanov et al., Design Consideration of the RF Deflector to Optimize the Photo Injector for PITZ, Proceedings of the FEL2006, Contribution THPPH021.

[3] D.J. Holder et al., A phase space tomography diagnostic for PITZ, Proceedings of EPAC 2006.

[4] D. Lipka, Spectrometer design for the SRF Gun, BESSY Note SRFgun-BESSY-003-12-2004, 2005.

[5] D. Lipka et al, Silica aerogel radiators for bunch length measurements, Nucl. Instr. Meth. A 538 (2005) 597.

[6] J. Rönsch et al., Measurement of the longitudinal phase space at the photo injector test facility at DESY in Zeuthen (PITZ), Proceedings of DIPAC 2005, Lyon.

[7] K.Floetmann, ASTRA, http://www.desy.de/ mpyflo.

[8] X. Qiu et al., Demonstration of emittance compensation through the measurement of the slice emittance of a 10 picosecond electron bunch, Phys. Rev. Let. 76 No. 20 (1996) 3723.

DESIGN CONSIDERATION OF THE RF DEFLECTOR TO OPTIMIZE THE PHOTO INJECTOR AT PITZ*

S. Korepanov#, S. Khodyachykh, M. Krasilnikov, A. Oppelt, F. Stephan, DESY-Zeuthen, Germany
V. Paramonov, INR, Moscow, Russia.

Abstract

In order to optimize photo injector for Free Electron Laser (FEL) applications, a detailed characterization of the longitudinal and transverse phase space of the electron beam provided by the Photo Injector Test Facility at DESY in Zeuthen (PITZ) is required. In the paper we present design considerations of the RF deflecting cavity for transverse slice emittance and longitudinal phase space measurements.

INTRODUCTION

The main research goal of PITZ is the development of electron sources with minimized transverse emittance [1]. The current setup at PITZ permits us to measure transverse emittance averaged along a bunch using the Emittance Measurement System (EMSY) [2]. With the use of an RF deflector it is possible to analyse the slice transverse emittance. Adding a dispersive arm the longitudinal beam phase space can be completely re-constructed.

At PITZ2 the application of an RF deflector is planned. The deflector position is about 9 m from the gun. The next 3.5 m space is taken by a tomography module, which will be used for transverse phase space measurements. At about 15.5 m a spectrometer based on dipole magnet is positioned.

In Fig. 1 the effect of the RF deflector is illustrated: the RF deflector voltage is null in the longitudinal centre of the bunch and gives a linear transverse deflection to the bunch itself. The maximum displacement of the edge slice Y_B can be estimated by the expression

$$Y_b = \frac{\pi \cdot f_{RF} \cdot L \cdot L_B \cdot V_\perp}{c \cdot E / e} , \qquad (1)$$

where f_{RF} is the frequency of the deflecting voltage, $V_\perp$ is the peak transverse voltage, L – drift space after the deflector, and E is the beam energy in eV units [3].

The resolution length L_{res} can be estimated as the bunch length L_B divided by the number of slices N_{slices} which can be resolved at the screen. And the number of the slices is Y_B divided to transverse beam size σ_B.

$$L_{res} = \frac{L_B}{N_{slices}} = \frac{L_B \cdot \sigma_B}{Y_B} = \frac{\sigma_B \cdot c \cdot E / e}{\pi \cdot f_{RF} \cdot L \cdot V_\perp} \qquad (2)$$

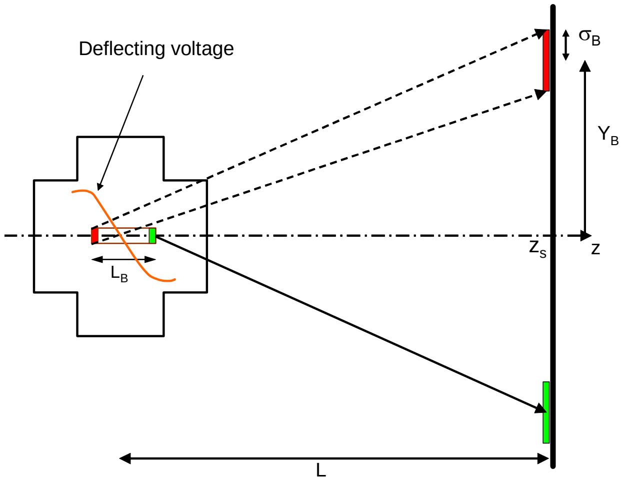

Figure 1. The principle of the RF deflector work.

For the prospect beam parameters at PITZ2 (Table 1) the possible resolution length is limited by the transverse size of the screen (< 36 mm) and minimum transverse beam size (σ_B ~ 1.6 mm). That gives the maximum number of the slices about 20 and the longitudinal resolution length about 0.4 mm (1.3 ps).

Table 1. PITZ2 beam parameters.

bunch charge	1 nC
max. long. momentum	32 MeV/c
min. norm. emittance (rms)	< 1 π mm mrad
transverse beam size on screen in tomography module, rms (full)	< 0.4 (1.6) mm
full longitudinal beam size	8 mm (27 ps)
pulse frequency	1-9 MHz
repetition rate	10 Hz

RF DEFLECTORS

For PITZ2 diagnostics we have reviewed three kinds of RF deflectors. Two of them are steady wave resonators and one is a travelling wave cavity. We analyzed electron beam parameters after passing the cavity and compared the results for the different deflectors.

Steady wave cavities

We have chosen the well known cavity which is a disk loaded waveguide [3]. It has five cylindrical cells. We scaled it to the frequency 1.3 GHz, Fig.2a. This cavity

---

* This work has been partly supported by the European Community, contracts RII3-CT-2004-506008 and 011935, and by the ‘Impuls- und Vernetzungsfonds’ of the Helmholtz Association, contract VH-FZ-005
# sergey.korepanov@desy.de

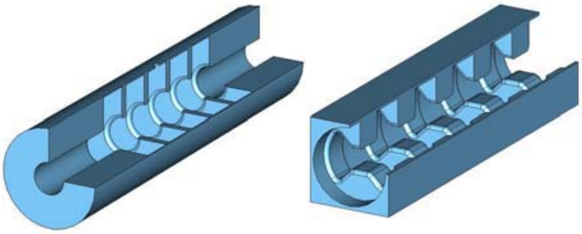

Figure 2. General view of “classical” cavity (a) and “Paramonov” cavity (b).

operates with TM11 mode. Another steady wave cavity is a new one designed by V. Paramonov. The shape of the structure is shown in Fig.2b. It operates in TE11 mode. More details about this cavity are given in [4].

Travelling wave cavity

The third cavity is based on LOLA-IV - transverse deflecting cavity [5], Fig.3. We have adapted it for our beam: scaled it from 2.856 GHZ to 1.3 GHZ and changed length from 3.6 m to 0.7 m. It has 9 cells and two additional cells for coupler and load.

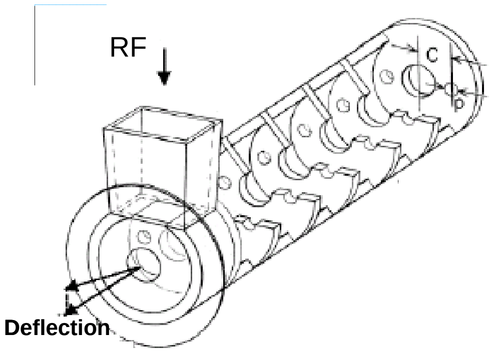

Figure 3. Travelling wave cavity based on LOLA-IV.

In the Table 2 we compare the deflector parameters for two operations regimes - to analyse the longitudinal phase space at a distance of about 6 m from the deflector in the dispersive arm and – to observe the beam at the first screen in tomography module at a distance of ~ 2 m from the deflector. In the table Q is unloaded quality factor, “Field build up” is the time which field needs to reaches about 99% of there maximum value [5].

Table 2. Deflector parameters.

	Classic cavity		“Paramonov” cavity		Travelling wave cavity	
Frequency GHz	1.3	1.3	1.3	1.3	1.3	1.3
Distance, m	2	6	2	6	2	6
$V_{\perp}$, MV	1.8	0.6	1.8	0.6	1.8	0.6
Q	21000	21000	15000	15000	19000	19000
P_{RF}, MW	2	0.12	0.17	0.02	9.1	1.01
Field build up, μs	~20	~20	~20	~20	~0.2	~0.2

BEAM DYNAMICS

Beam dynamics simulations have been performed for comparing the cavities presented above. For our simulations we use a beam with the parameters: average energy 32 MeV, energy dispersion 140 keV, transverse beam size about 0.7 mm, transverse emittance - 0.9 π mm mrad. The beam is passing through the deflector and is observed at the points of screens positions in the tomography module and in the dispersive section after the dipole.

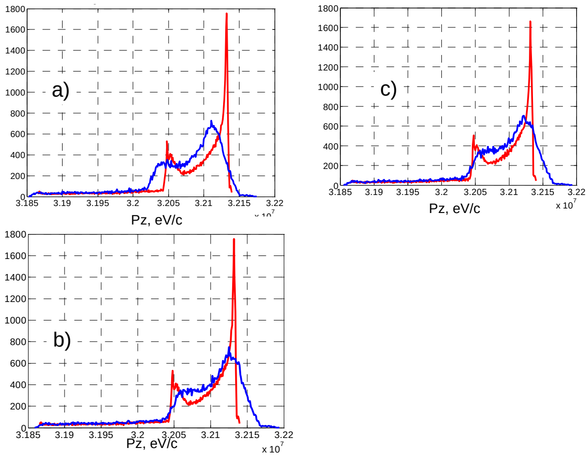

Figure 4. Longitudinal momentum distribution.
Red line corresponds to the initial distribution (before deflector).Blue line is the distribution for the beam passed through a)“classic” cavity, b) “Paramonov” cavity, c) traveling wave cavity.

For correct longitudinal phase space measurements in the dispersive arm we have to minimize distortion of the longitudinal momentum distribution during passing the deflector. We compared the longitudinal momentum distribution on the dispersive arm screen for the different deflectors. In Fig.4 momentum distributions for the three variants of the deflectors are compared with the initial momentum distribution (before deflector). One can not see large difference between these three cases. The estimated resolution of the method is about 25keV/c. This value we can roughly resolve from the presented distributions. The rise or fall edge in the initial momentum distribution is about a few keV. They are transformed to the edges with the width of about 25 keV.

The transverse slice emittance measurements require high similarity of the initial longitudinal charge distribution to the transverse charge distribution (along deflecting direction) after deflector. This requires a lineal dependence of the deflecting voltage to the position inside the bunch. The requirement is provided by a quite large RF wave length (230 mm) in the cavities in comparison with the bunch length (8 mm). Beside that the cavity has to generate a minimum distortion in the transverse

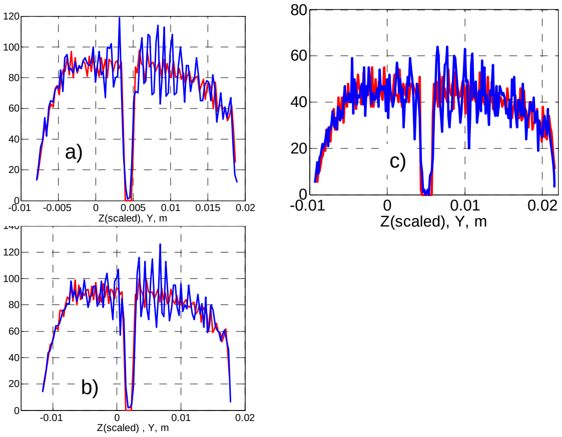

Figure 5. Charge distributions.
Red line corresponds to the initial longitudinal distribution (before deflector). Blue line is the transverse distribution in the deflected direction for the beam passed through a) "classic" cavity, b) "Paramonov" cavity, c) traveling wave cavity.

direction (perpendicular to deflected direction). This is necessary for correct emittance measurements. In Fig.5 we compare the longitudinal charge distribution of the initial beam and transverse charge distribution for the beam passed through deflecting cavity. We add a special gap (0.4mm) in the initial distribution in our simulations. That helps us to estimate the resolution length by observing the gap in the transverse distribution of the deflected bunch. One can see that all cavities provide transverse bunch charge profile (corresponds to deflected direction) similar to the initial longitudinal charge profile. Because of the 100 % degree of the modulation in the final distribution we can estimate that the resolution length for these measurements is about the gap width (0.4 mm). The transverse momentum distributions (perpendicular to deflection direction) practically are not changed in the deflector. An example of the transverse momentum distribution before and after the deflector is shown on Fig.6 for the travelling wave cavity. The simulations show minimal influence from the deflectors to transverse beam parameters (perpendicular to deflection direction).

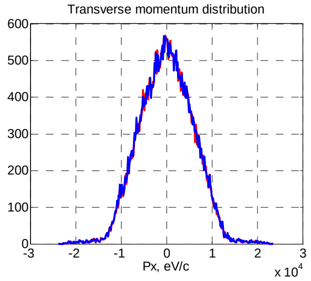

Figure 6. Transverse momentum distribution (perpendicular to deflect direction). Red line – initial distribution (before deflector), blue line – distribution for the beam passed through traveling wave cavity

DISSCUSION OF THE RESULTS

All presented cavities can be used for the beam phase space analysis. We have considered their advantages and disadvantages. The main differences are between steady wave and travelling wave cavities. The first one request less RF power (see Table 2) and is easy in control. But the travelling wave cavity gives us a possibility to analyse a single bunch in a bunch train. We plan to work with the beam bunch repetition frequency up to 9 MHz (period ~0.11 μs). Because of short filling time in travelling wave cavity (0.2 μs) we can "take" a single bunch and direct it to a screen and distort 1-2 other pulses in the train only. This possibility is important for the analysis of the beam parameters fluctuation in the train from bunch to bunch. Also we can make the beam monitoring during tuning the beam. We decided to use the travelling wave cavity in combination with the tomography module for the possibility to analyse single bunches.

DIAGNOSTIC COMPLEX FOR LONGITUDINAL SLICE TRANSVERSE EMITTANCE MEASUREMENTS

The layout of the prospect system for slice emittance measurements is shown in Fig.7. It contains a deflecting cavity, a tomography module and four kickers. The beam is matched by quadrupoles on the entrance of the tomography section so that α and β functions are periodically repeated from screen to screen [6]. That permits us to analyse the beam more easily. The bunch deflected in the RF cavity in vertical direction is deflected by the kicker in horizontal direction to the screens. The screens are located off axis. The kicker pulse duration is less 100 ns with rise(fall) time about 10 ns. That permits to observe deflected bunches only. The few bunches which are distorted in deflecting cavity by the rising or falling RF field don't hit the screens and are lost in the beam line. All other bunches are passing through the tomography module and accepted at the beam dump.

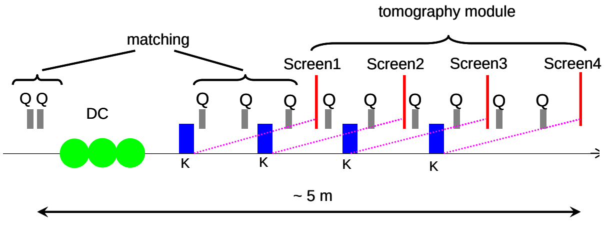

Figure 7. Prospect diagnostic for longitudinal slice emittance measurements.
Q – quadruple; K – kicker; DC – deflecting cavity

The layout of diagnostics for longitudinal beam phase space measurements is shown in Fig.8. After tomography module downstream we plan to set dispersive section. The distance between the deflector and the screen in the dispersive arm is about 6 m. Bunches are deflected by a dipole magnet and are analysed on the screen. During the dispersive arm operation the magnets in the tomography module will be off.

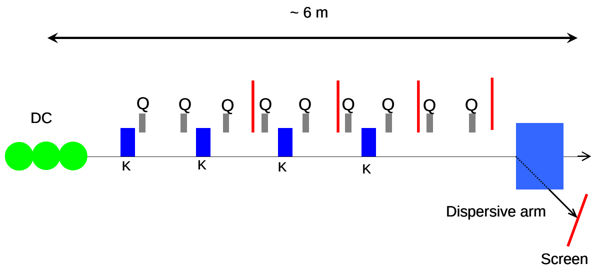

Figure 8. Prospect diagnostics for longitudinal beam phase space measurements.

CONCLUSION

The deflectors reviewed in this paper satisfy the requirements for the beam diagnostic at PITZ2. We consider to use the travelling deflecting cavity due to its additional possibility to analyse single bunches in a bunch train. We expect the possibility to measure transverse slice emittance with ~20 slices in the tomography module. For longitudinal phase space measurements in the dispersive arm we estimate the resolution as ~25 keV/c.

The authors would like to thank D.J. Holder and B.D. Muratori for their work under the tomography module analysing.

REFERENCES

[1] F.Stephan, D.Kraemer, I.Will and A.Novokhatski, Proc. FEL2k, Durham, USA, August 2000
[2] V.Miltchev et al., “Transverse Emittance Measurements at the Photo Injector Test Facility at DESY Zeuthen (PITZ)”, DIPAC, 2003
[3] D.Alesini, C.Vaccarezza, “Longitudinal and transverse phase space characterization”, SPARC-RF-03/003, INFN/LNF, Frascati, 2003
[4] V.Paramonov, et. al. “Effrctive standing-wave RF structure for charged-particle deflector”, LINAC, 2006, (to be published)
[5] O.H.Altenmueller, et.al., “Investigations of traveling – wave separator s for the Stanford two-mile linear accelerator”, The rev. of Sci. instr., Vol.35(4), 1964
[6] D.J.Holder, et. al., “A phase space tomography diagnostic for PITZ”, EPAC2006, Edinburgh, UK

TUNING, CONDITIONING, AND DARK CURRENT MEASUREMENTS OF A NEW GUN CAVITY AT PITZ*

A.Oppelt[†], K.Abrahamyan, O.Aldrian, G.Asova, J.Bähr, G.Dimitrov, H.-J.Grabosch,
L.Hakobyan, J.Ivanisenko, S.Khodyachykh, S.Korepanov, M.Krasilnikov, B.Petrosyan,
R.Spesyvtsev, L.Staykov, F.Stephan, F.Tonisch, DESY, 15738 Zeuthen, Germany
F.Marhauser, D.Richter, E.Weihreter, BESSY, 12487 Berlin, Germany
K.Flöttmann, J.H.Han, C.Martens, R.Meyer, V.Miltchev, DESY, 22603 Hamburg, Germany
O.Kalekin, Humboldt University, 12489 Berlin, Germany
P.Michelato, L.Monaco, D.Sertore, INFN Milano, 20090 Segrate, Italy
J.Rönsch, University of Hamburg, 22761 Hamburg, Germany.

Abstract

In December 2005, a new gun cavity for the Photo Injector Test Facility at DESY in Zeuthen (PITZ) was tuned with the help of a specially designed tuning device. The tuning procedure and its results as well as RF measurements will be presented. Meanwhile, the cavity was installed in the PITZ facility and conditioned. Dark current measurements with different cathodes were performed and are described. Comparisons to former measurements are made.

INTRODUCTION

The photo injector test facility at DESY in Zeuthen (PITZ) was built in order to test and optimize electron sources for Free Electron Lasers and Linear Colliders. One of the main tasks is to prepare gun cavities for subsequent use at FLASH and XFEL. Up to now, three gun cavities have been built by DESY and another one is in production. They are designed for a peak power of 4.5 MW and an average heat load of 50 kW [1]. In order to reach higher power levels, two further guns with improved cooling will be built towards the end of 2006.

After the production of the first gun cavity, prototype No.1, a water-to-vacuum leak was found. It was figured out that the used copper did not fulfill the specifications. The leak was repaired with a kind of glue, but an installation at FLASH was not recommended. Therefore, this gun was used for high power tests at PITZ after the commissioning of a 10 MW multi beam klystron in June 2005 [2]. The conditioning towards higher peak and average power ended suddenly with the break-up of the old water-to-vacuum leak which appeared at a gradient of about 57 MV/m [3]. Meanwhile, the cavity was again repaired and is available for further tests.

Frequency measurements after the gun production showed a frequency difference from the goal frequency of 1.3 GHz (detuning) of 615 kHz, see Table 1. This detuning is caused by the brazing and cannot be calculated. Thus, the gun was mechanically tuned and the dimensions of the cells have been corrected in the design of the next gun cavity.

Gun cavity prototype No.2 was nevertheless showing a large detuning, probably due to the different copper quality. The gun was used in the PITZ1 phase until Nov.2003 and was installed at FLASH after a complete characterization at PITZ [4] where it is in operation since February 2004.

Table 1: RF measurements results of all three existing DESY cavities before tuning. The detuning was calculated for an operation temperature of 43°C under vacuum (measurement at 23°C in air).

Gun cavity prototype No.	1	2	3.1
Frequency detuning (kHz)	616	1207	632
Field flatness E_{half}/E_{full}	0.90	0.97	0.94
Mode spacing 0-π-mode (MHz)	5.3	5.2	5.2

The third gun cavity (prototype No.3.1) has been built in 2003. In order to avoid the complicated tuning procedure that was necessary for the previous guns, the cell's dimensions have been corrected again. In addition, the gun has special tuning knobs that allow modifying the resonance

Figure 1: Photograph of gun cavity prototype No.3.1.

---

* This work has partly been supported by the European Community, contract numbers RII3-CT-2004-506008 (IA-SFS) and 011935 (EURO-FEL), and by the 'Impuls- und Vernetzungsfonds' of the Helmholtz Association, contract number VH-FZ-005.

[†] presenting author: anne.oppelt@desy.de

frequency by up to 300 kHz. However, after some first rf measurements of the resonance frequency in September 2004, it became clear that the tuning knobs cannot be used: the measured detuning was too large (Table 1).

TUNING OF THE NEW GUN CAVITY

In order to shift the frequency and to correct the field profile, a new tuning device has been developed. It consists of a stable girder on which the gun is placed, and two tools for deforming the cavity walls: a tuning stamp for pushing the cathode wall at the cathode plane, and a tuning clamp for pulling the coupler-facing wall of the full cell. For frequency measurements a small tapered coupler has been built by BESSY. Thus the system became much easier to handle compared to the large and heavy coaxial coupler used in the beamline installation. A bead pull setup for field profil measurements can be easily mounted to the tuning device. Figure 2 shows a photograph of the complete setup.

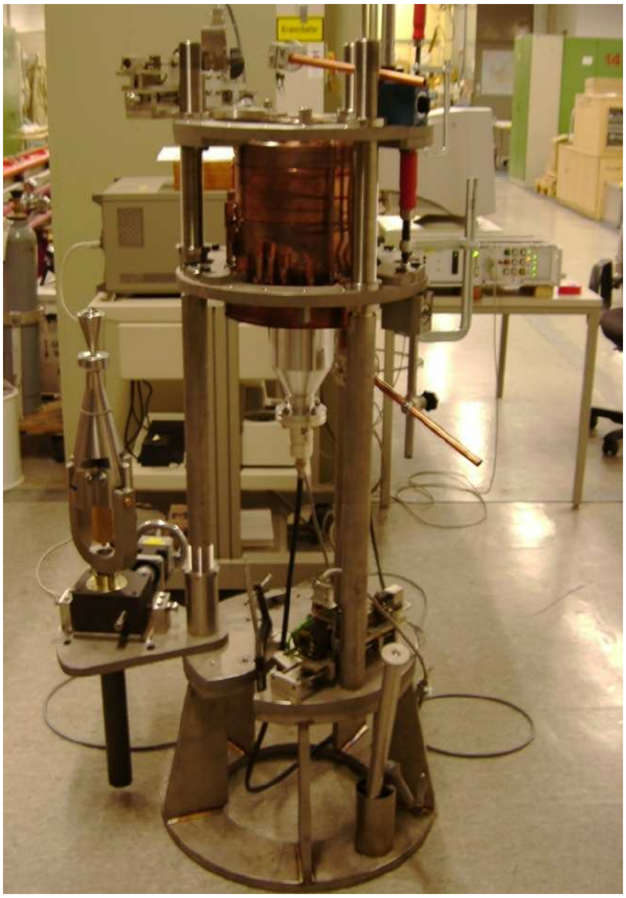

Figure 2: Photograph of the tuning device with the gun cavity, the BESSY test coupler, the bead pull setup, and the tuning tools: the clamp (mounted) and the stamp.

In November 2005, the new tuning device was used for the first time. Gun cavity No.3.1 was tuned in several consequent steps. Each time the cavity walls were pushed or pulled some ten microns and the deformation was surveyed. The use of the tuning tools left partly visible signatures in the material, but mostly not to recognize when touching. Figure 3 shows an example of the marks from both tuning tools.

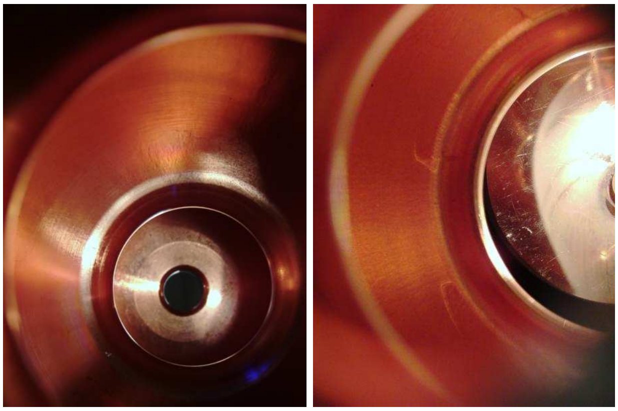

Figure 3: Marks in the copper material from the tuning stamp (left; a circular mark around the cathode hole) and from the tuning clamp (right; two imprints in the coupler-side wall).

As result of the tuning, the resonance frequency is reached at the design operation temperature of $54°C$, while the field flatness E_{half}/E_{full} was measured to be about 1.06, see Figure 4. This means, the field at the cathode is 6% higher than in the full cell. According to simulations, this is a good compromise between high average accelerating

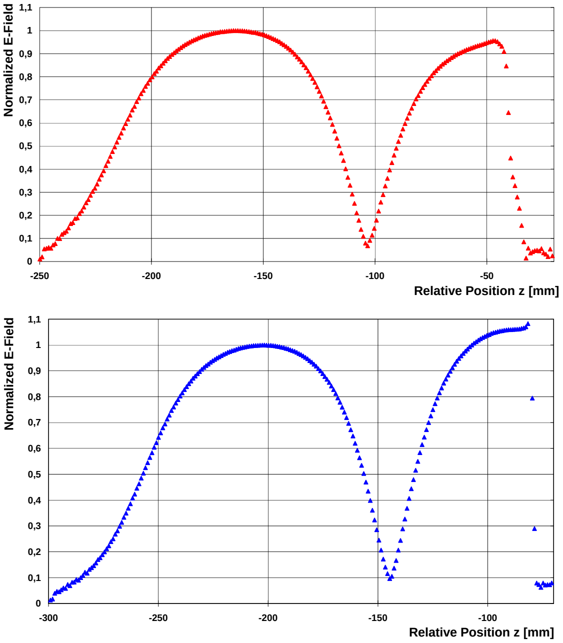

Figure 4: Field distribution in the gun before (top) and after (bottom) tuning. The cathode field is finally 6% higher than the field in the full cell.

gradient and maximum gradient at the cathode for space charge compensation. The quality factor of the cavity was also determined: Q_0= 24200.

Using the new tuning device, the tuning procedure was very smooth and comfortable. Therefore, it was decided to do a re-tuning of cavity No.1 which was tuned in 2001 for an operation temperature of 35°C. But during the high power tests in 2005 it was found that the lower temperature limit of the cooling water system limits the reachable average power at such a low operation temperature. The goal of the tuning was thus to increase the operation temperature. As a result of the re-tuning, an operation temperature of 50°C was obtained while keeping the field flatness constant at a value of about 1.05.

DARK CURRENT STUDIES

After the tuning, the new gun cavity was installed in the PITZ beamline and conditioned up to the full FLASH specifications: 3.5 MW peak power, 900 μs pulse duration, and 10 Hz repetition rate, corresponding to an average power of 31.5 kW [3].

Extensive dark current studies started in April 2006 and continued during the summer. The measurements were done for one Cs_2Te cathode (used for beam operation in 2005 and 2006), and for four Mo cathodes (with optical polished surface, used for gun conditioning). One of the Mo cathodes (cathode 80.1) has a hole pattern on its surface [5]. It was foreseen to serve for dark current generation studies but the corresponding pattern was not found in the dark current images. An example of such an image is displayed in Figure 5: it shows the YAG screen signal of dark current emitted by this specially prepared cathode 80.1.

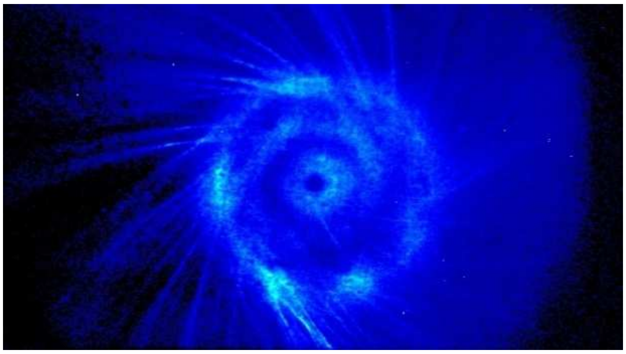

Figure 5: Dark current from cathode 80.1 on a YAG screen.

Figure 6 displays a photograph of the cathode 80.1 as well as a picture of cathode 58.1 (Cs_2Te).

Figure 7 shows the measured dark current level without solenoid magnets ($I_{main} = I_{bucking} = 0$ A) as function of the gradient at the cathode for two different guns: cavity prototype No.2 (data from 2002) and cavity prototype No.3.1 (data from 2006). For each gun, one distribution is shown for Mo and one for Cs_2Te. The dark current level produced 2002 without magnets is higher than the currently measured level. In order to understand the origin of this difference - the cavity or the photo cathodes or both - more detailed studies are necessary. One possible reason is a difference in the emitted dark current spectrum, as presented in [3]. At fixed magnet settings it can lead to a different effective aperture (due to the gun itself, the coupler, and the following beamline) and thus to a different detected dark current level downstream the gun.

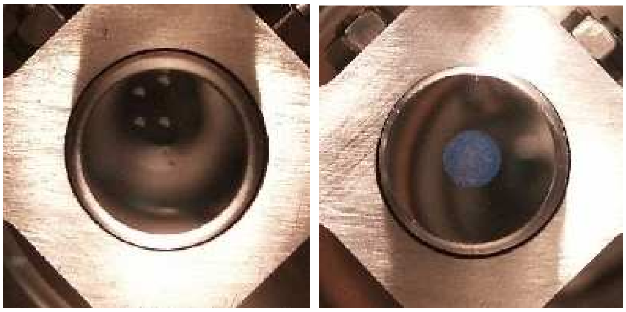

Figure 6: Topview of two of cathodes in the cathode chamber: Mo cathode 80.1 with the special hole pattern (left) and Cs_2Te cathode 58.1 (right).

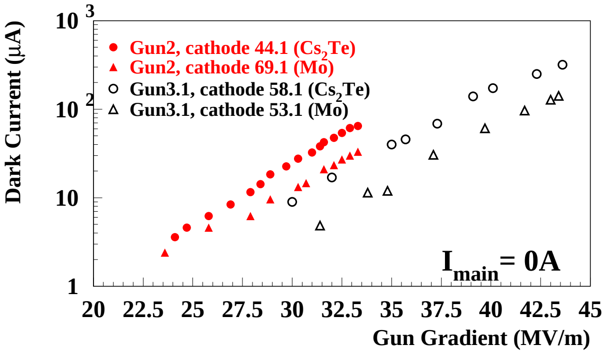

Figure 7: Dark current without solenoids produced with two gun cavities for different cathodes at PITZ.

Dark current measurements at different gradients have been performed as function of the currents in the main and the bucking solenoids. Examples for such 2D dark current measurements are shown in Figure 8: the dark current emitted by cathode 75.1 (Mo) was recorded for all combinations of I_{main} and $I_{bucking}$ at three different gradients.

Taking the maximum entry in such a 2D dark current distribution, one obtains the maximum dark current level emitted by a certain cathode at a defined gradient. Figure 9 shows the resulting distribution for gun cavity No.3.1 with cathode 53.1 (Mo) and cathode 58.1 (Cs_2Te). In addition to the data from 2006, an old result from the PITZ1 phase (spring 2003) when using gun cavity No.2 is drawn for comparison. The level of the emitted dark current is approximately equal, at least for the Cs_2Te cathode.

Finally, the maximum dark current of all Mo cathodes used in gun cavity No.3.1 is shown in Figure 10. The maxi-

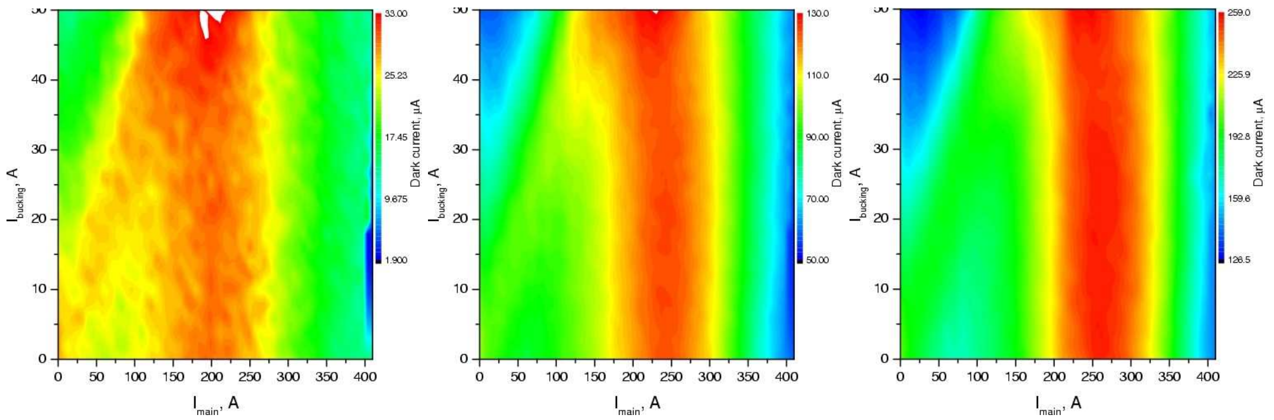

Figure 8: 2D scans of dark current emitted by Mo cathode 75.1 for all combinations of I_{main} and $I_{bucking}$ at different gradients: 35 MV/m, 40 MV/m, and 3543 MV/m (from left to right). Note the different color coded scale.

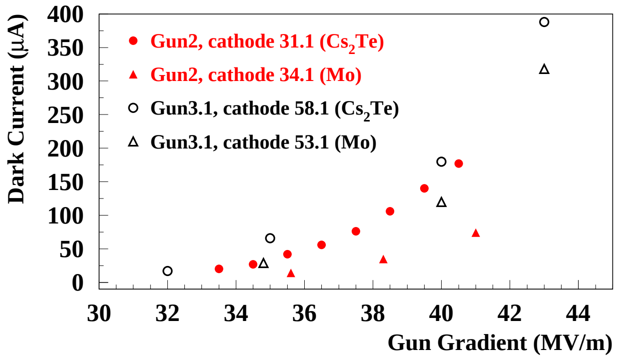

Figure 9: Maximum emitted dark current with two gun cavities for different cathodes.

mum amount of dark current is comparable for the analyzed cathodes, even if the emitted spectrum was different, as reported in [3].

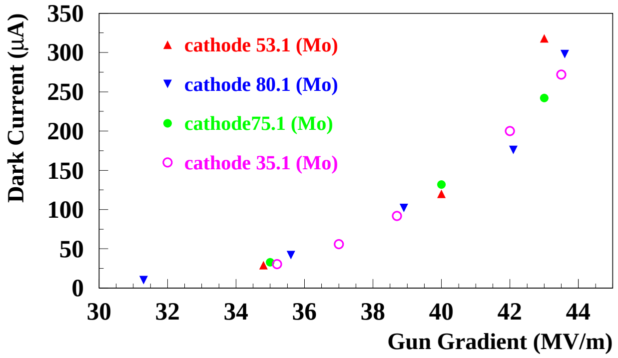

Figure 10: Maximum emitted dark current from the Mo cathodes used in gun cavity No.3.1.

From all dark current studies done with the new gun cavity it can be concluded that this cavity produces about the same amount of dark current as the former used cavity (prototype No.2). This means that there is no influence on the dark current from the tuning marks which have been produced by using the new tuning device. Therefore, the device can be also used for the tuning of further new cavities which are planned to be used at PITZ.

Nevertheless, the dark current level produced by the cathodes needs to be further decreased. In order to do so, more detailed studies of the dark current emission are necessary as well as improvements on the photo cathodes themselves.

SUMMARY AND OUTLOOK

A new gun cavity (prototype No.3.1) has been built, tuned, and commissioned at PITZ. The results of the tuning and extensive dark current measurements have been presented in this paper. Comparisons with formerly taken data was done. The gun is currently used for beam measurements at PITZ. After its full characterization, it will be dismounted from the beamline in autumn 2006 in order to be available as spare gun for the FLASH user facility. For PITZ, a new gun is currently in preparation (prototype No.3.2).

REFERENCES

[1] K.Flöttmann et al., RF gun design for the TESLA VUV Free Electron Laser, NIM A 393 (1997) 93-95.

[2] A.Oppelt et al., Status and first results from the upgraded PITZ facility, FEL 2005, Stanford, Aug.2005.

[3] A.Oppelt et al., Status of the PITZ facility upgrade, LINAC 2006, Knoxville, Aug.2006.

[4] F.Stephan et al., Recent results and perspectives of the low emittance photo injector at PITZ, FEL 2004, Trieste, Sept.2004.

[5] L.Monaco et al., dark current investigations of FLASH and PITZ RF guns, EPAC 2006, Edinburgh, June 2006.

DESIGN OF THE CAVITY BPM FOR FERMI@ELETTRA

P. Craievich*, D. Castronovo, M. Ferianis, ELETTRA, Trieste, Italy
M. Poggi, Laboratori Nazionali di Legnaro, INFN, Legnaro, Italy

Abstract

High resolution Beam Position Monitors (BPM) are fundamental diagnostics for a seeded FEL, like FERMI@ELETTRA, as they allow to measure the electron beam trajectory non destructively and on a shot-by shot basis. Cavity BPMs provide the required sub-micrometer resolution relying on the excitation of the TM_{110} dipole mode when the beam passes through the cavity off axis. For the seeded FEL FERMI, we adopted a pair of cavity BPMs located upstream the modulating undulator to measure the electron beam trajectory at the sub-micrometer level. In this paper we first discuss the requirements for such a cavity BPM including those for the beam based alignment. The scaling from an X-band design to the final C-band design is presented. The resolution to stay below one micrometer has been cross-checked, both analytically and numerically. The losses of the common mode TM_{010} have been also checked, leading to the final dimensions which keep the losses at the level of the X-band cavity BPM.

INTRODUCTION

An accurate measurement of the transverse beam position is an important issue throughout all the machine; in the undulator sections, the position and angle of the electron beam at the entrance is a fundamental parameter to be measured in order to match it to the seed laser trajectory to maximise the interaction, laser to beam. In order to provide the required single shot resolution for the position measurement two cavity BPMs have been adopted in front of the modulator. According to the FERMI layout based on two undulator sections (FEL-1 and FEL-2), two pairs of cavity BPMs will be located in front of each FEL. The design of this cavity BPM is based on a previous development [1, 2]. It is a resonant pill-box cavity where the information on beam position is encoded in the amplitude and phase variations of the dipole mode (TM_{110}) with beam transverse position, as measured on the two ports located on opposite sides of the cavity. A scaling from X-band to C-band of cavity BPM has been performed. We evaluated by means of analytical and numerical models that the resolution at C-band remains below 1 micron. In the scaling process we paid attention at the losses in the common mode: the new dimensions have been set to get same losses as for the X-band common mode. Using previous analysis we have fixed geometrical dimensions for a 3-D model of the cavity BPM and coupling waveguide used to extract the signals excited by electron bunch. Here we present results of the simulations obtained by means of Microwave Studio 3-D code [3].

BACKGROUND

The cavity BPM is essentially a pill-box cavity; the analytical formulas for a cylindrical cavity with circular section without beam pipe are an upper limit to estimate beam losses and RF parameters. From a theoretical point of view the energy losses experienced by a charge q when passing through a cavity are: $\Delta U_{110} = q^2 k_{110} x^2$ and $\Delta U_{010} = q^2 k_{010}$ for TM_{110} and TM_{010} modes respectively. The loss factors are defined as $k_{110} = (\omega_{110}/2)(R/Q)_{110}$ and $k_{010} = (\omega_{010}/2)(R/Q)_{010}$. ω_{110} and ω_{010} are the resonant frequencies of dipole and monopole modes. The ratio R over Q is defined for the two modes as:

$$\left(\frac{R}{Q}\right)_{110} = \frac{|V_z(x)|^2_{110}}{x^2 2\omega_{110} U_{110}} \tag{1}$$

$$\left(\frac{R}{Q}\right)_{010} = \frac{|V_z(x)|^2_{010}}{2\omega_{010} U_{010}} \tag{2}$$

where $|V_z(x)|^2_{110}$ and $|V_z(x)|^2_{010}$ are the squared voltages for each mode seen by a charge particle when it flies along the longitudinal axis at some offset x (x=0 for monopole). U_{110} and U_{010} are stored energy in cavity for the TM_{110} and TM_{010} modes respectively. The ratio R over Q of a given mode can be also theoretically computed for a cavity without beam pipe.

Dipole mode TM_{110}

$$\left(\frac{R}{Q}\right)_{110} = \frac{2LJ_1(\frac{a_{11}}{b}x)^2 T^2}{\pi\epsilon_0\omega_{110} b^2 J_0(a_{11})^2 x^2} \tag{3}$$

where L is cavity gap, b is the cavity radius, ϵ_0 is the permeability of the vacuum, J_0 is the 0^{th} order Bessel function of the 1^{st} kind, J_1 is the 1^{st} order Bessel function of the 1^{st} kind, with its first zero $a_{11} = 3.832$ and T is the transit time factor defined by:

$$T = \frac{sin\left(\frac{\omega_{110}L}{2c_0}\right)}{\frac{\omega_{110}L}{2c_0}} \tag{4}$$

being c_0 the speed of light. It is worthwhile to mention that for small x, $J_1(\frac{a_{11}}{b}x) \approx \frac{a_{11}}{2b}x$; furthermore R over Q and also k_{110} become independent from x. The loss factor k_{110}, as a function of the cavity gap L and of the resonant frequency of TM_{110}, is plotted in figure 1. In general for a small cavity gap, the transit time factor T is almost equal to 1, but from figure 1 we can see that in the X-band range

---

* paolo.craievich@elettra.trieste.it

and with a cavity gap longer than 15mm, approximately, there is a reduction of the loss factor due to influence of T.

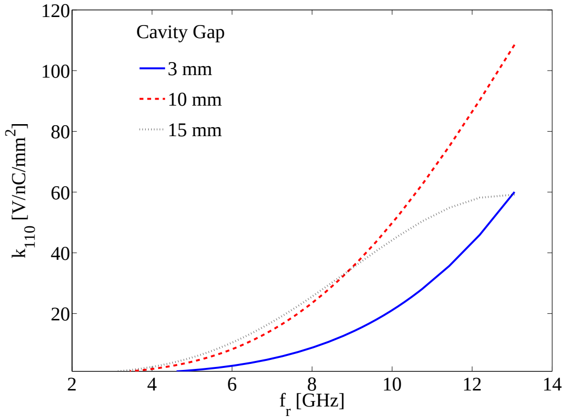

Figure 1: Loss factor of the dipole mode TM_{110} versus cavity gap L and resonant frequency.

Monopole mode TM_{010}

$$\left(\frac{R}{Q}\right)_{010} = \frac{LJ_0(\frac{a_{01}}{b}x)^2T^2}{\pi\epsilon_0\omega_{010}b^2J_1(a_{01})^2} \qquad (5)$$

where $a_{01} = 2.405$ is the first zero of the Bessel function J_0 and T defined as above. For the monopole mode the R over Q is calculated on longitudinal axis (x=0) where $J_0(\frac{a_{01}}{b}x) = 1$. The loss factor k_{010} as a function of cavity gap L and resonant frequency of TM_{010} is shown in figure 2. The energy lost in the TM_{010} mode produces undesirable wake fields and has to be minimized in the design. We can see from figure 2 that, using a lower resonant frequency, we can increase cavity gap L without increasing the value of the loss factor.

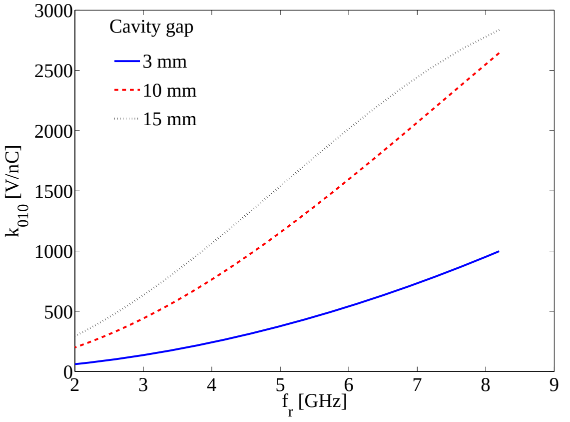

Figure 2: Loss factor of the monopole mode TM_{010} versus cavity gap L and resonant frequency.

BPM RESOLUTION

As presented in [1, 2] it is possible to design the coupling waveguide to selectively couple out to the TM_{110} mode but not the TM_{010} mode. Without the contamination of the monopole mode, the intrinsic BPM resolution is limited by the signal to thermal noise ratio of the system. For a given coupling coefficient, the external signal voltage on matched impedance Z_0 for a charge q is:

$$V_{ext} = q\sqrt{Z_0\frac{\omega_{110}}{Q_{ext}}k_{110}}\,x \qquad (6)$$

The thermal noise voltage of the BPM is given by $N = \sqrt{Z_0kT_k\Delta f}$ where k is the Boltzmann's constant, T_k the temperature in Kelvin and $\Delta f = f_{110}/Q_{ext}$ is the bandwidth. The upper limit of resolution can be achieved when the external signal V_{ext} is equal to the thermal noise N for:

$$x_{min} = \frac{1}{q}\sqrt{\frac{kT_k}{2\pi k_{110}}} \qquad (7)$$

Assuming a charge $q = 0.8nC$ and $T_k = 300K$, in figure 3 we plot the BPM resolution with respect to the resolution at X-band as a function of resonant frequency of dipole mode TM_{110}. As a reference case for an X-band design we have assumed a pill-box cavity without beam pipe, with gap length $L = 3mm$ and cavity radius $b = 14.7mm$. In table 1 we report the parameters for the X-band cavity used as reference.

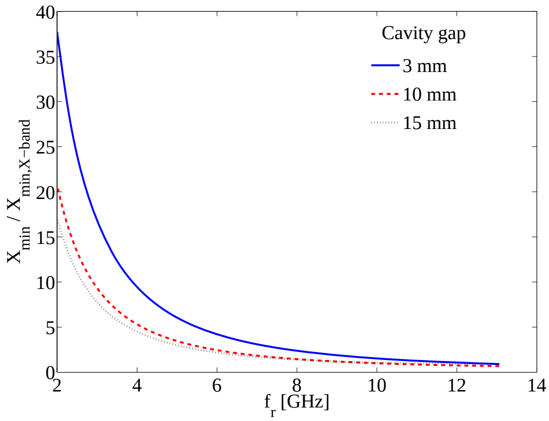

Figure 3: Resolution of the cavity BPM with respect to the resolution of an X-band cavity BPM versus its resonant frequency.

Table 1: Loss factors and resonant frequencies for X-band cavity BPM without beam pipe used as reference.

f_{110} $[GHz]$	k_{110} $[V/nC/mm^2]$	x_{min} $[nm]$	f_{010} $[GHz]$	k_{010} $[V/nC]$
12.4	49.7	0.14	7.8	907.6

SCALING OF THE CAVITY BPM

At X-band frequencies the mechanical tolerances are more stringent than at lower frequencies. Considering also the requirement on the minimum beam pipe radius, being equal to about $10mm$ in the undulator region, we have explored the achievable performance adopting a scaling at frequencies lower than X-band. In fact, dipole mode TM_{110} will be coupled away into the beam pipe if its resonant frequency is higher than the lowest cut-off frequency of the beam pipe. Assuming a beam pipe radius of $10mm$, the beam pipe cut-off frequencies are: $8.8GHz$ and $11.5GHz$, respectively for the TE_{11} and TM_{01} circular waveguide modes. Considering the available C-band hardware together with the above motivations, a resonant frequency of $6GHz$ (C-band) for the cavity BPM (radius cavity $b = 30.4mm$) has been selected. From figure 3, we can see that the resolution at C-band is still within an acceptable range. Looking at figures 2 we can increase the cavity gap up to about $L = 10mm$ without increasing losses in TM_{010} mode if compared to the losses in the X-band cavity. Assuming a charge $q = 0.8nC$, at room temperature, in table 2 are reported the parameters for C-band BPM cavity.

Table 2: Loss factors and resonant frequencies for C-band BPM cavity without beam pipe (cavity radius $b = 30.4mm$ and gap length $L = 10mm$).

f_{110} $[GHz]$	k_{110} $[V/nC/mm^2]$	x_{min} $[nm]$	f_{010} $[GHz]$	k_{010} $[V/nC]$
6.0	8.3	0.35	3.8	684.9

C-BAND CAVITY BPM

Preliminary numerical simulations by means of CST MWS[3] were done on a 3-D model with beam pipe to have a comparison with previous analytical treatments. For 3-D model we have adopted the following dimensions: $b = 30.4mm$, $L = 10mm$ and beam pipe radius $a = 10mm$. Table 3 shows results from analytical and numerical calculations and we can observe that the analytical one without beam pipe is a good estimation of cavity BPM with beam pipe for both dipole and monopole modes. We have adopted as waveguide the commercially available standard WR137 with internal dimensions of $34.85 \times 15.80 mm^2$. To couple this waveguide to the cavity we have left unchanged the width while we have used a transition to 6mm for the height. This standard works in the frequency range of 5.85-8.20 GHz thus we have fixed the resonant frequency at 6.5GHz decreasing the radius of the cavity to 26.4mm. Figure 4 shows the 3-D model of the C-band cavity BPM where we can observe the waveguide transition to the standard WR137.

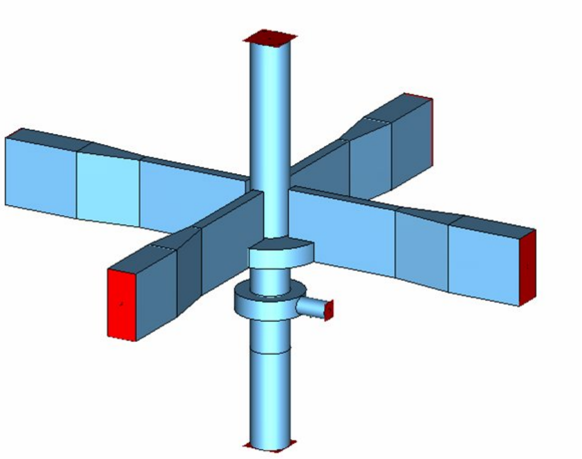

Figure 4: C-band cavity BPM with its four coupling waveguides and reference cavity.

Table 3: Comparison between numerical obtained by means of CST MWS and analytical results for C-band BPM.

	analytical	numerical	unit
f_{110}	6.0	5.7	$[GHz]$
$(R/Q)_{110}$	0.44	0.39	$[\Omega/mm^2]$
k_{110}	8.3	7.0	$[V/nC/mm^2]$
Q_0		8400	
f_{010}	3.8	4.0	$[GHz]$
k_{010}	685	523	$[V/nC]$

The external voltage in eq. 6 depends on $Q_{ext} = Q_0/\beta$ where β is the coupling coefficient and $Q_0 = 8530$ is the unloaded Q factor of the cavity with new dimensions. Figure 5 shows the dipole Q_{ext} as a function of the distance between beam axis and bottom of the waveguide.

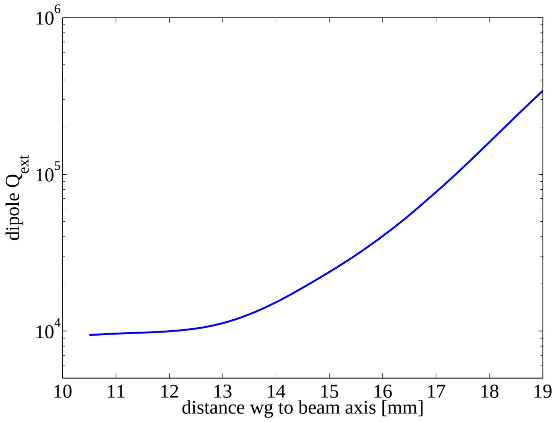

Figure 5: Q_{ext} of the dipole mode as a function of distance of the bottom of waveguide to beam axis.

The waveguide is always under coupled to the cavity and for distance below 13 mm the Q_{ext} remains about constant. We have fixed the distance between waveguide and beam axis at 12 mm thus $\beta = 0.1$ and $Q_{ext} = 10500$. In this situation we only have a loss of 0.9 dB in the external voltage with respect to a critical coupling $\beta = 1$. In figure 4 the reference cavity is also indicated. The cavity will be used to provide the reference signal in the RF electronics and is designed to resonate at 6.5 GHz approximately with TM_{010} mode. The external coupling is foreseen by means of an antenna placed on the cavity lateral side.

A prototype C-band cavity BPM is being designed and cold test are foreseen. Table 4 shows dimensional and RF parameters of the C-band and reference cavity prototypes. From the mechanical point of view, we are faced with some challenges. First of all the required machining tolerance was fixed to $\pm 10 \mu m$ for cavities, waveguides and their relative positioning. An important item is to decide how to build the BPM and reference cavities from bulk copper. One idea is to divide in two parts the whole geometry along the longitudinal symmetrical plane. The first part consists of half cavity together with waveguides, as shown in figure 6 [4], and second part consists of the other half cavity without waveguides. Both parts will be milled with the profile of the cavity and waveguides and subsequently the beam pipes, cavity and waveguides are brazed together. So the challenge concerns the brazing process and in particular to find the best brazing material. During the process it is important not to pollute the copper nor to deform the construct. This last item must be investigated through additional numerical simulations.

Table 4: Collections of the dimensional and RF parameters of the C-band cavity BPM and reference cavity.

C-band cavity BPM	
Cavity gap	$10mm$
Cavity radius	$26.4mm$
Beam pipe radius	$10mm$
Coupling WG	$34.85 \times 6mm^2$
Distance WG to beam axis	$12mm$
WG standard	WR137
Resonant frequency	$6.5GHz$
Unloaded Q factor	8530
External Q	10500
Coupling coefficient	0.1
Reference cavity	
Cavity gap	$10mm$
Cavity radius	$17.6mm$

CONCLUSION

In this paper we have explored a possible scaling of the cavity BPM presented in [1, 2]. For our considerations, we have used a model of a pill-box without beam pipe and have shown that a scaling from X-band to C-band frequencies is possible without loss of resolution. In addition, we have done simulations on a 3-D model to validate the analytical treatment and we have analyzed the position of the coupling waveguide to the cavity. These studies have allowed fixing dimensional parameters for a C-band prototype of the cavity BPM.

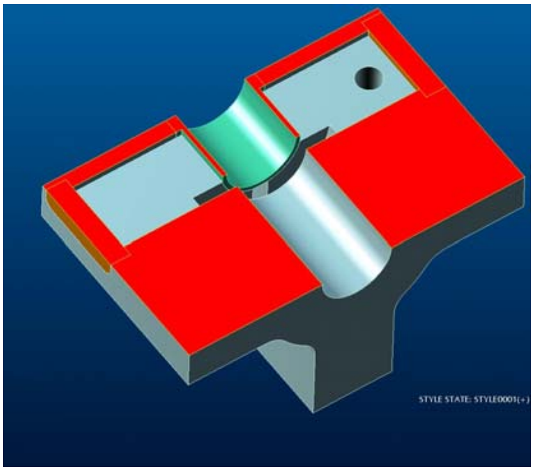

Figure 6: Preliminary technical drawing of the cavity BPM [4].

REFERENCES

[1] R. Johnson et al., “Cavity BPMs for NLC”, BIW 2002, Upton, NY, May 2002.

[2] Z. Li et al., “An X-band Cavity for a high precision beam position monitor”, DIPAC 2003, Mainz, Germany, May 2003.

[3] CST Microwave Studio, http://www.cst.de.

[4] Cinel Strumenti Scientifici, http://www.cinel.com.

DESIGN OF A TWO-STAGE LASER PULSE SHAPING SYSTEM FOR FEL PHOTOINJECTORS[*]

M. B. Danailov, A. Demidovich, R. Ivanov (ELETTRA, Basovizza, Trieste).

Abstract

This paper presents an approach for photoinjector laser pulse shaping which combines the two main pulse shaping techniques, namely acousto-optic dispersive filter (DAZZLER) and Fourier-based 4-f system. The DAZZLER is inserted between the seed mode-locked oscillator and the amplifier and is used for preliminary shaping in the infrared, while the final pulse shape and duration are determined by a 4-f dispersive system positioned after the harmonic conversion to UV.

INTRODUCTION

Temporal pulse shaping is one of the most important requirements to photoinjector lasers needed in the majority of FEL projects. The laser pulses commonly requested for excitation of the photocathode are in the UV (around 260 nm) and have flat-top shape of duration in the 5-10 ps range. Recently, more complex pulse shapes like ramps have been shown to be advantageous and proposed for implementation [1,3], indicating that the pulse shaping scheme must offer flexibility in generating different shapes. In principle, there are two main ultrashort pulse shaping techniques, namely 4-f type Fourie shaping [4] and acousto-optic dispersive modulator (DAZZLER) based [5] shaping. As it will be shown below, the use of one of these only is unlikely to allow reaching the required performance. The main complication comes from the fact, that the pulse shape is needed in the UV, and the required pulse energy is quite high, while pulse shaping is easy to do at low pulse energy in the IR. In the paper we describe a hybrid scheme proposed for the FERMI photoinjector, which utilizes both methods, one in the infrared and the other in UV. The paper starts with brief introduction to the ultrashort pulse shaping basics and notation, which is important for understanding the analysis and results presented later on. The specific problems related to photoinjector laser pulse shaping and the proposed optical scheme are discussed in the next section, followed by simulations and preliminary experimental results of flat-top and increasing ramp pulse generation.

PULSE SHAPING BASICS

As mentioned above, there are different laser pulse shapes that can be used to optimize the photoinjector (and overall FEL) performance. Here we will mostly refer to two of them, namely flat-top and increasing ramp, however the techniques used allow in principle to generate any desired pulse shape. To make the discussion of the pulse shaping schemes clearer, we will very briefly introduce some basics of the pulse shaping theory.

Assuming that the light field can be factorized into spatial and time dependent part, the electric field of the latter can be written as:

$$E(t)=1/2\,[I(t)]^{1/2}\,exp\{i[\omega_0 t-\varphi(t)]\}+\text{c.c.}\,, \qquad (1)$$

where ω_0 is the central frequency , $I(t)^{1/2}$ and φ (t) are the time dependent temporal amplitude and phase. For simplicity in the following equations the c.c. part will be omitted. The quantity

$$E(t)= I(t)^{1/2}\,exp[-i\varphi(t)] \qquad (2)$$

is referred to as the complex amplitude in the time domain. In the frequency domain, the pulse field can be represented in a similar manner:

$$E(\omega)=1/2\,[S(\omega)]^{1/2}\,exp[-i\psi(\omega)]\,, \qquad (3)$$

where $S(\omega)$ is the spectral intensity of the light pulse. As it is known, the time and frequency domain field representations are linked by a Fourier transform relation:

$$E(t)=(1/2\pi)\int_{-\infty}^{\infty} E(\omega)exp\,(i\omega t)\,d\omega \qquad (4).$$

Most of the known methods for shaping of ultrashort pulses are based on this relation, they implement manipulation of the spectral amplitude or phase (or both) of the pulse, which in turn leads to the required modulation in the time domain. The output pulse shape is given by the convolution of the input pulse and the impulse response function of the modulating function:

$$E_{out}(t)=\int_{-\infty}^{\infty} E_{in}(t`)h(t-t`)\,dt`\,, \qquad (5)$$

where h(t) can be calculated from its complex frequency transfer function by:

$$h(t)=(1/2\pi)\int_{-\infty}^{\infty} M(\omega)exp\,(i\omega t)\,d\omega. \qquad (6)$$

The complex transmission function $M(\omega)$ can be presented as:

$$M(\omega)=[M_I(\omega)]^{1/2}\,exp[-i\Phi(\omega)]\quad , \qquad (7)$$

and the phase transmission is commonly expanded in Taylor series :

$$\Phi(\omega)=\Phi(\omega_0)+\Phi^{(1)}\Delta\omega+(1/2!)\Phi^{(2)}\Delta\omega^2+ +(1/3!)\Phi^{(3)}\Delta\omega^3+\ldots \qquad (8)$$

---

[*] This work has been partially supported by the EU Commission in the Sixth Framework Program, Contract No. 011935 EUROFEL

where $\Phi^{(i)}$ is the i-th derivative of the phase evaluated at ω_0 and are usually called i-th order dispersion. While the first and second terms in (9) represent only a constant and an overall time shift of the pulse, the third and higher order terms may lead to significant pulse shape changes even if the spectral amplitude $[M_I(\omega)]^{1/2}$ remains constant. In principle, if one could design a frequency filter with a prescribed optical frequency transmission function, any desired pulse shape (with temporal resolution limited by the inverse bandwidth of the input pulse $E_{in}(t)$) can be generated. In reality, it is quite difficult to produce optical filters with complex frequency transmission functions defined with high precision. As will be shown later, some specific shapes, like flat-tops, however, can be produced by use of interference filter.

The first technique which solves in a general way the pulse shaping has been known for more than a decade [4] : the spectral components of the input pulse are spatially separated by a dispersive element (e.g. diffraction grating) , and then manipulated in the spatial domain by using a modulator with spatially dependent transmission, placed in the Fourier (focal) plane of a lens, as shown on Fig.1. A second lens and grating recollimated the pulse spectral components, so the output pulse has again a spatially independent pulse shape that can be calculated using Eq.6. By proper choice of the modulator the technique allows to use both amplitude and phase modulation. It is worth noting that large second order phase terms (i.e large linear chirp) can be produced even without the use of modulator in this scheme, by just shifting the grating with respect to the focal plane of the lens.

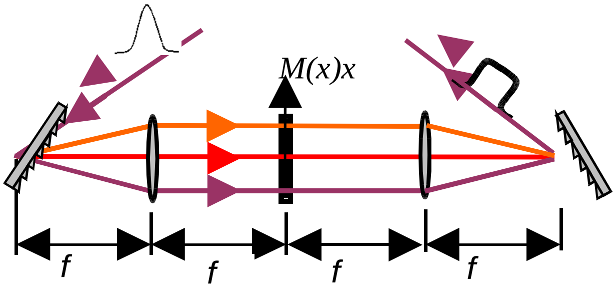

Figure 1: 4-f Fourier shaping system

A newer and very powerful technique for pulse shaping is the so called DAZZLER introduced by P.Tournois [5] and commercially available from Fastlite (France). In this method, also based on Eq.6, the spectral components are not separated spatially, the optical pulse travels in an acousto-optic modulator where a longitudinal acoustic wave is present. By shaping the acoustic wave frequency and amplitude, the spectral components of the optical pulse are diffracted out of the crystal at different positions (and therefore with different delay) and with different efficiency. In this way, the deviated part of the incoming pulse can be time modulated with very good precision.

DISCUSSION

The basic gun laser specs in the case of Copper photocathode are relatively well agreed. It is usually accepted that about 0.5 mJ of pulse energy in the UV (wavelength around 260 nm) has to be provided in order to obtain about 1 nC of charge.

Both techniques presented above allow in principle to obtain pulses with the required shape for the photoinjector. When flat-top is concerned, some experimental results with Dazzler have been presented in [6].The Dazzler has the obvious advantage of flexibility and compactness. It is provided with computer control allowing both amplitude and phase modulation. However, it has the following limitations:

- wavelength resolution of the high resolution model is about 0.3 nm. For this reason the bandwidth of the input pulse should be about 10 nm or higher in order to obtain high fidelity amplitude shaping;
- if a single pass is used, the maximum second order dispersion that can be provided by the Dazzler allows to generate pulses of up to 4 ps, which is not enough in most cases. A two pass geometry can be used for having ~10 ps long pulses, however in this case the insertion loss , even at maximum diffraction efficiency, is above 90% which does not seem to be practical;
- the Dazzler can be used only in IR. Fastlite announced recently a UV version, however it is not suitable for the task considered here (allowed power levels and wavelength resolution can not be met)
- maximum peak power limitation in the IR does not allow to use the Dazzler after the amplifier. For this reason it has to be placed between the seed oscillator and laser amplifier.

On the other hand, the 4-f based shaping can be used directly in UV, if a proper modulator is found. At present, the only available option is a piezo-deformable mirror [7] with a dielectric coating. Liquid crystal modulators like are only available down to 350 nm, which is not enough for our photoinjector case. There are two main limitations to be taken into account:

- the use of deformable mirror allows to obtain only phase modulation
- the obtainable phase curvature is limited by the limit of about 8 micron for maximum mirror deformation, so the deformable mirror alone will not be enough for obtaining large phase gradients, it can rather be used as a tool for compensating slow phase curvature errors.

PROPOSED LAYOUT

Fig.2 presents a layout of the hybrid shaping setup proposed for the FERMI photoinjector. Input seed pulses with a bandwidth of about 12 nm at 780 nm are generated by a mode-locked Ti:Sapphire laser. The IR pulse shaping is done by a DAZZLER inserted before the amplifier stages. The Dazzler is implemented primarily for producing the desired spectral amplitude shape (e.g. super-gaussian like) , and in addition for compensation of

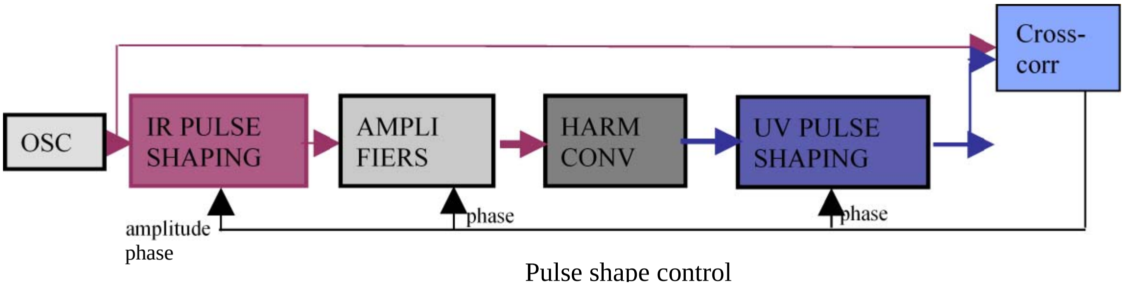

Figure 2: Proposed two-step shaping setup

third-order phase distortions due to the grating compressor of the amplifier. Usually this compressor is used for exact compensation of the chirp introduced by the stretcher. In our scheme it is also used for adding a second order dispersion by detuning with respect to maximum compression point. In this way, the pulse duration at the entrance at the harmonic generation crystals can be adjusted to an optimum value which allows to have high enough harmonic efficiency while still keeping high order nonlinear effects (e.g. self-phase modulation) at low. Such a safe peak power level is reported to be in the order of 10-20 GW/cm^2 for BBO. We note that our approach gives an additional degree of freedom for adjusting this level.

The final pulse duration and shape is then controlled by a dispersion based system working in the UV. Two version of this system are under consideration. The simpler one is just a two-pass grating stretcher used for adding a second-order phase needed to obtain the exact pulse duration (see the simulation later on). This version will be used in case the DAZZLER alone allows good enough compensation of all phase distortions. If it appears that an additional high order spectral phase compensation is needed after the harmonic generation, the UV shaping will include also a deformable mirror in a modified 4-f arrangement.

In order to illustrate better the described scheme, on Figs.3 and 4 we present the results of a simple simulation of pulseshaping which generates the pulse shape (increasing ramp) requested for the FERMI 'long bunch case' [3].

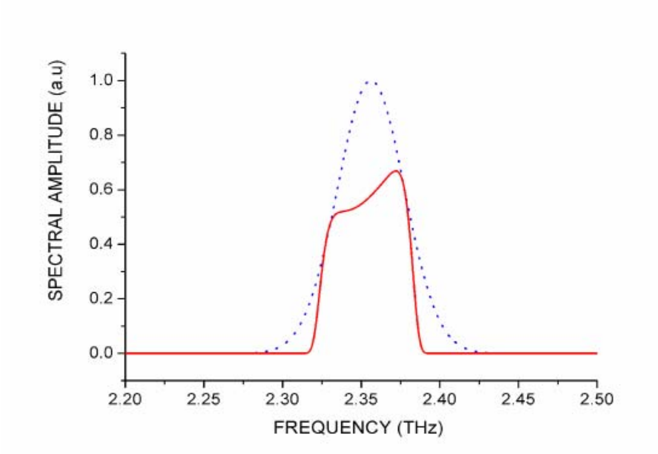

Figure 3: Input spectrum for the simulation (blue dots) and modulated spectrum after Dazzler (red solid line).

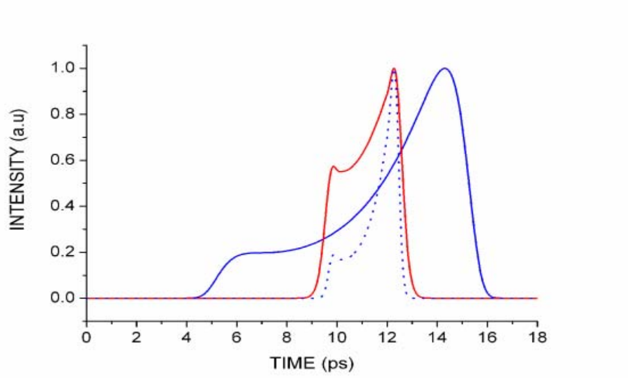

Figure 4: Pulse profiles after compressor in the IR(red solid line), after THG (blue dots), after UV stretcher (blue solid).

The simulation is done starting with a transform-limited Gaussian pulse at 800 nm having 12 nm of FWHM bandwidth (dashed blue line on Fig.3). The spectrum shown in red line is obtained after amplitude filtering by the Dazzler. In addition, it is assumed that the latter completely compensates the residual third-order dispersion of the system. The pulse shape shown by blue line on Fig.4 corresponds to the amplifier output, where a second order dispersion of about 60000 fs^2 has been introduced by detuning the compressor. Assuming that the third harmonic generation is performed in sufficiently thin BBO crystals , so GVM and spectral acceptance effects can be neglected, the UV pulse shape (dashed blue line) is proportional to the third power of the IR one. The final shape and duration, shown by solid blue line are obtained by adding only an additional second order dispersion from the UV grating stretcher. We note that this stretcher will inevitably add also a third order dispersion term on the order of 100 000 fs^3 , which is in principle possible to compensate in advance by the Dazzler, so it has not been taken into account into the above presented simulation. As mentioned above, in case the DAZZLER compensation is not sufficient the odd dispersion terms will be cancelled by the use of deformable mirror.

PRELIMINARY EXPERIMENTAL RESULTS

Most of the components of the above presented setup have already been tested at Elettra. Here we will briefly summarise some of the results. The DAZZLER has been installed and tested using a femtosecond Ti:Sapphire oscillator at 780 nm. On Figure 5, two typical flattop pulse shapes are presented: phase only polynomial modulation (blue line) and amplitude super-gaussian modulation. In both cases, the pulses were additionally stretched by the use of grating stretcher. The pulse measurement is done by cross-correlating the shaped pulse with a part of the input 100 fs long pulse.

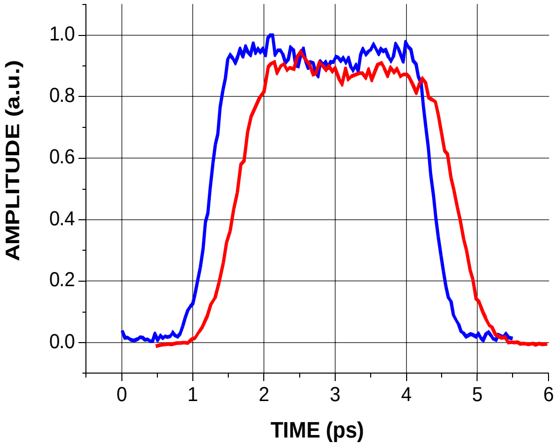

Figure 5: Flat-top pulses generated by the Dazzler; blue line: phase modulation, red line: amplitude modulation

It is important to mention here that the fact that amplitude filtering plus stretcher added second order dispersion works well indicates a simpler method. The amplitude filtering can be performed by the use of an interference filter. Indeed, we demonstrated this by the use of a commercial filter (Spectrogon), centered at 780 nm. There is some freedom to detune the filter transmission curve position and shape by tilting and to obtain a nearly perfect super-Gaussian spectrum. As a result, after stretching , a flat-top pulse can also be obtained, as shown on Fig.6.The price to pay for the simplicity is that there is no control on phase, this might not be a problem if the UV part contains the deformable mirror.

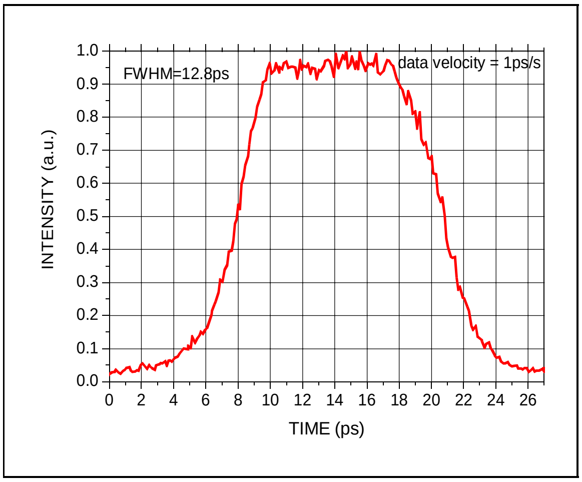

Figure 6: Flat-top pulse generated by the use of interference filter as an amplitude filter.

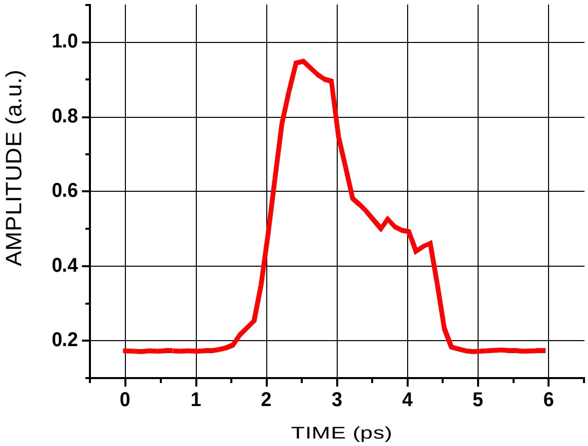

Figure 7: Increasing ramp generated by the Dazzler with pure amplitude modulation

On Fig. 7 we show a ramp type pulse profile [3] obtained on the same setup by using the Dazzler in amplitude modulation mode. We note that the cross-correlator scanning in this setup was starting from the back of the pulse, so the pulse front is on the right of graph and the ramp is increasing, as requested.

CONCLUSIONS

The setup described above is in principle capable of producing arbitrary pulse shapes in UV, especially in the version containing deformable mirror. The two basic techniques have been already tested at low power at Elettra, and a high energy version including the UV part is to be completed and tested in a few months time. There is still some freedom to choose the exact system and laser pulse parameters in order to obtain the required shapes with high fidelity.

REFERENCES

[1] C. Limborg-Deprey, Proc.27th FEL Conf.(2005), 418.
[2] O.J. Luiten, M.J. Van der Wiel, 27th FEL Conf.(2005) ,paper WEOB003.
[3] G.Penco et al, Proc.EPAC 2006, to be published
[4] A. M. Weiner, J. P. Heritage, E. M. Kirschner, J. Opt. Soc. Am. B **5**, (1988). 1563
[5] P. Tournois, Opt. Comm. 140 (1997), p.245 .
[6] C.Vicario et al, Proc.EPAC 2004, p.1300
[7] J.Gardino-Mejia et al, JOSA B 21 (2004), 833.

RAMPING LONGITUDINAL DISTRIBUTION STUDIES FOR THE FERMI@ELETTRA INJECTOR

G. Penco*, M.Trovò, Sincrotrone Trieste, Trieste, Italy
Steven M. Lidia, LBNL, Berkeley, California, USA.

Abstract

In the FERMI Linac optimization studies it comes out the request to have at the exit of the photoinjector a linear ramp in the current distribution along the bunch as alternative option with respect to the flat-top. This requirement is translated in the photoinjector optimization in a big issue. In fact the longitudinal bunch profile at the exit of the photoinjector is affected by the strong non linearity of the space charge fields at the cathode and in the drift between the gun and the first booster. The knowledge of the space charge fields at the cathode plays in important role in finding the optimum driven laser pulse shape. At this purpose an analytical description of the space charge fields produced by a bunch with an arbitrary current distribution at the cathode is provided. Space charge codes (GPT [1] and ASTRA [2]) have been used to evaluate the evolution of several ramping profiles from the cathode to the entrance of the first booster and the results are presented in this paper.

INTRODUCTION

In the optimization of the high brightness RF photoinjector a great effort is usually spent to produce an electron bunch as much as possible uniformly charged distributed. This is a precise requirement coming from the optimization of the emittance compensation in the injector and in the bunch transport through the linac, especially in presence of bunch compressors. By the other hand it has been demonstrated that the strong non-linearity of the linac sections longitudinal wakefields can be compensated by providing at the exit of the photoinjector a linear ramping electrons distribution instead of a flat top [3]. This requirement translates to the photoinjector optimization as a large perturbation due to the strong nonlinearity of the space charge fields at the cathode and in the drift between the gun and the first booster. To produce a ramped current bunch, a special initial profile has to be found that evolves along the injector to produce the final desired shape.

LONGITUDINAL SPACE CHARGE FIELD ON AXIS

In order to solve this problem, the longitudinal space charge fields on axis at the cathode was investigated, since it is mainly responsible for blowing out the particles, especially in case of high peak current. In case of a uniformly charged bunch the longitudinal space charge field on axis, inside and outside the bunch, at a distance z from the bunch tail is given by the following equation [4]:

$$E_z^{SC}(z) = \frac{Q}{2\pi\epsilon_0 R^2} H(z) \tag{1}$$

where H(z) is

$$\begin{aligned} H(z) = \; & \sqrt{\left(1-\frac{z}{L}\right)^2 + \left(\frac{R}{\gamma L}\right)^2} - \\ & \sqrt{\left(\frac{z}{L}\right)^2 + \left(\frac{R}{\gamma L}\right)^2} - \left|1-\frac{z}{L}\right| + \left|\frac{z}{L}\right| \end{aligned} \tag{2}$$

and Q is the total bunch charge, L the bunch length, R the bunch radius. For simplicity $\gamma = 1$ is assumed.
As example the figure 1 shows the field $E_z^{SC}(z)$ versus z (normalized with respect to the bunch length L) for a nominal 1nC bunch, with a radius of 1mm and a bunch length of 3mm. The flat-top current distribution at the cathode is deformed by this space charge field into a parabolic distribution after several centimeters, suggesting that a linear current distribution would suffer a strong degradation before entering into the relativistic regime. Thus the drive laser pulse should be shaped according to a non-linear distribution pattern. Eq.(1) has been generalized for an arbitrary longitudinal current density distribution $\rho(z)$ at the cathode [5], obtaining:

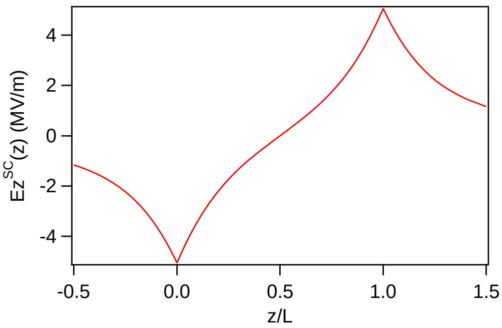

Figure 1: Longitudinal space charge field on axis of a bunch just extracted from the cathode; Q=1nC, R=1mm, L=3mm

$$\begin{aligned} E_z^{SC}(z) = \; & \int_0^L dz' \frac{\rho(z')}{2\epsilon_0} \left[\frac{z'-z}{\sqrt{(z'-z)^2+R^2}} - \right. \\ & \left. \frac{|z'-z|}{z'-z} \right] \end{aligned} \tag{3}$$

---

[*] giuseppe.penco@elettra.trieste.it

Eq.(3) represents a useful analytical instrument to quickly predict the evolution and distortion of an arbitrary current profile. For example figure 2 shows the longitudinal space charge field on axis inside a bunch with respectively a linear and a quadratic ramping in the current distribution (image charge not included). Electrons in the high charge density region are pushed backwards during the bunch propagation because of the strong repulsive electric field and this modifies the starting bunch profile.

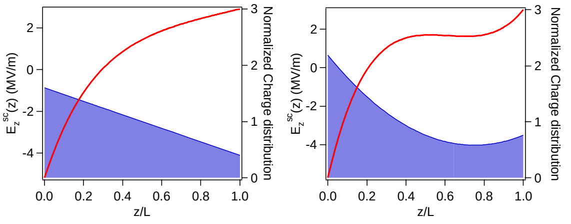

(a) (b)

Figure 2: Longitudinal space charge field on axis of a linear (a) and parabolic (b) ramping charged bunch just extracted from the cathode having different radius; Q=1nC, L=3mm. Cathode plate is in z=0.

Figure 2a shows that a linear ramp charge distribution samples an almost quadratic longitudinal space charge field (Figure 2a). Thus one can easily expect a large deterioration of the initial ramping current profile while propagating through the injector. Multiparticles codes trackings of linear ramp profiles similar to figure 2a have confirmed the expectation and figure 3 shows the bunch current profile at the exit of the injector: the initial linear ramp has been destroyed and the bunch presents a parabolic-like charge distribution.

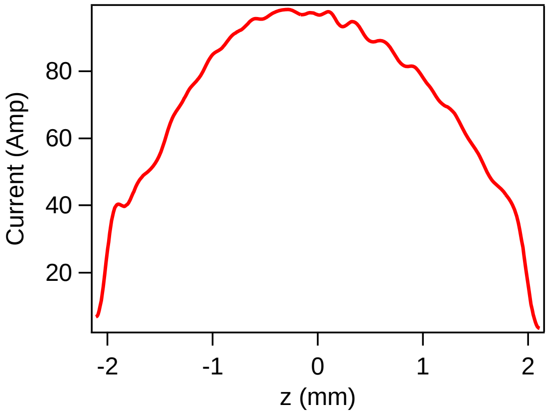

Figure 3: Resulting profile at the exit of the injector in case of an 800pC-bunch with a linear ramp at the cathode.

Also a quadratic ramp, like Figure 2b, is strongly modified during the transport between the cathode and the first booster section, but the linearity of the space charge field at least in the middle of the bunch helps in preserving the linear ramp in about 70% of the bunch (see Figure 4).

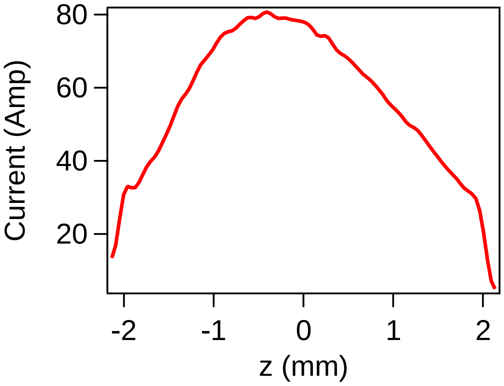

Figure 4: Resulting profile at the exit of the injector in case of an 800pC-bunch with a quadratic ramp at the cathode as Figure 2b.

Several initial current distributions have been studied in order to find the best one which linearizes as much as possible the space charge field experienced by electrons within the bunch and which evolves into the desired longitudinal profile. A fourth-degree polynomial distribution (see Figure 5) has been found to be an interesting solution that offers flexibility in compensating the high orders contributions of the space charge field and that increases the bunch fraction sampling a linear space charge field.

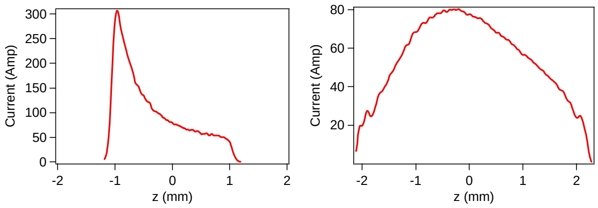

(a) (b)

Figure 5: A fourth-degree polynomial distribution at the cathode (a) and at the end of the photoinjector (b).

The current distribution plotted in Figure 5a has been considered as the baseline ramping distribution for the medium bunch case assuming a large efficiency in the laser pulse shaping process [6]. However in a conservative scenario even a quadratic distribution could be used without severe drawbacks.

A large charge density close to the cathode surface increases the image charge field and this should be considered in the generation of a ramping charge distribution. The effect of the image charge at the cathode can be easily included by adding the field $E_z^{SC}(-z)$ to the formula 3.
As example the space charge field with and without the image charges effects in case of a parabolic ramping charged bunch is shown in figure 6: the electrons close to the cathode sample a space charge field two times the value obtained without considering the image charges. In the optimization process and in the multiparticles trackings the

image charge effects have been included.

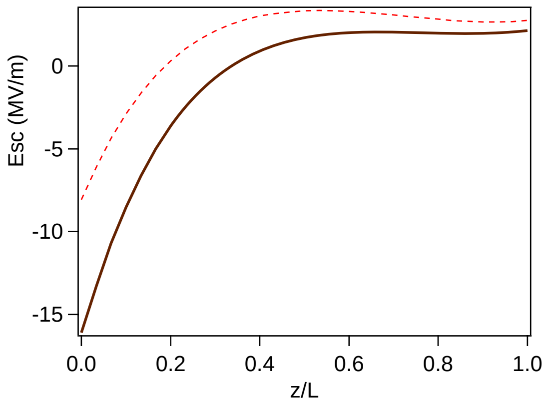

Figure 6: Comparison between the Longitudinal space charge field on axis with (continuous line) and without (dashed line) the image charges effects; Q=1nC, L=3mm

EMITTANCE COMPENSATION AND OPTICS MATCHING ISSUES

Because of the non-uniform charge distribution of the ramping regime, it is very difficult to find an injector parameter set-up that completely satisfies the invariant envelope equation, performing perfect emittance compensation for all slices. Since each slice contains a different amount of charge, each slice evolves in a particular and unique way in the gun-booster drift when the injector parameters are fixed. In order to minimize the projected emittance at the end of the injector an average parameters setting should be found, taking in account also the slice parameters behavior along the bunch. Studies were carried on by tracking several initial laser shapes with GPT and ASTRA. A crucial role has been played by the coefficients of the quadratic ramp chosen at the cathode. For example an attractive solution is to consider a quadratic profile with “double peaks”, as showed in figure 7a. The small peak electrons are pushed forwards by the space charge field and this partially compensates the backwards spreading of the high peak electrons, increasing the linearity and the width of the ramping fraction of the bunch (figure 7b). In addition the head of the bunch presents a hard edge, instead of a smoothing falling edge. By the other hand, finding the optimum focusing condition is an issue in this case. In fact in order to compensate the emittance contribution of the high charge fraction of the bunch, the solenoid strength has been increased, leading to an overfocusing of the bunch core and head, as showed in the top view of figure 8.

Figure 9 shows the slice analysis concerning the emittance and the Twiss parameters for this case. The overfocused electrons in the middle of the bunch have even a higher slice emittance, around 1.4mm mrad. This ovefocusing has consequences also in the optics parameters: Twiss parameters suffer a very large oscillation slice by slice. These modulations in α and β affect not only the matching with the linac optics, but they can be even sources of microbunching instabilities when the bunch propagates through the chicanes, leading finally to enlarge the bandwidth of the FEL output radiation [7]. A different result is obtained starting with a profile similar to figure 5a, which presents at the end of the injector a trasversal distribution showed in figure 10. The slice analysis have been performed as well and the results are reported in figure 11. In this case the slice emittance has a ramping behavior very similar to the ramp in the charge distribution, and no bunch

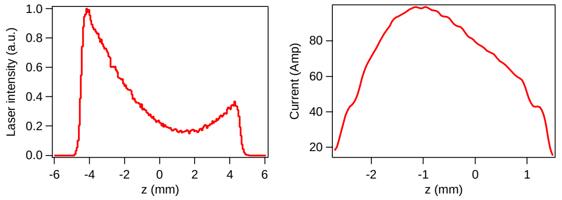

(a) (b)

Figure 7: The “double peaks” charge distribution at the cathode (a) and at the end of the potoinjector (b).

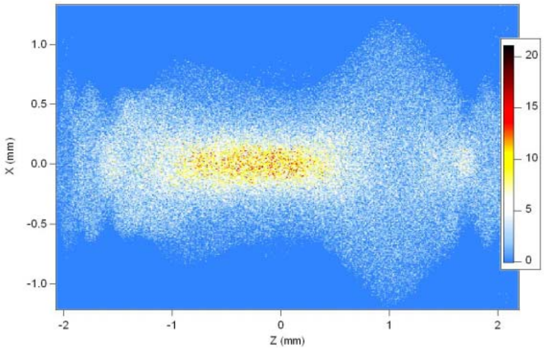

Figure 8: Top view of the evolved “double peaks” option. The initial charge distribution is translated into a transversal charge density.

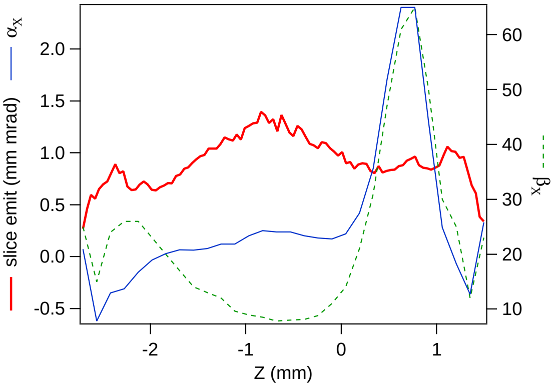

Figure 9: Slice analysis of the emittance, α_X and β_X parameters for the double peaks solution.

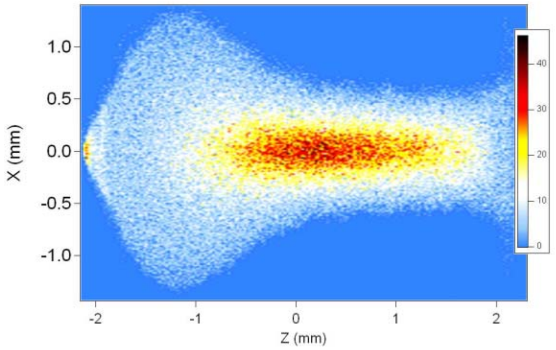

Figure 10: Top view of the evolved profile of figure 5a.

fraction is overfocused. By the way in correspondence of the high charge density the space charge field leads to increase the transversal dimension, as showed in the plot inside of figure 11. Also the slice β and α functions are very high in correspondence to the high charge density, but they are quite constant in the remainder bunch fraction and this constitutes a great improvement for the linac matching

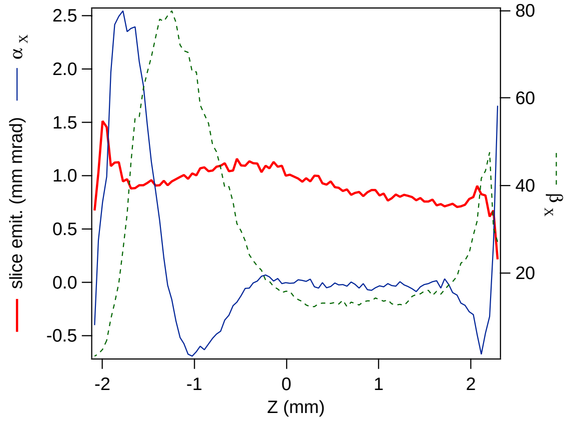

Figure 11: Slice analysis of the emittance, α_X and β_X parameters for the propagated bunch of figure 5a.

CONCLUSION

The linac requirement to have a bunch with a linear current ramp at the injector exit has been translated in studying the best current distribution at the cathode that evolves in the desired profile. An analytical description of the longitudinal space charge field on axis helps in predicting the evolution of an arbitrary current ramp before running the multiparticles space-charge codes. A quadratic current ramp at the cathode constitutes a good option to have at the end of the injector a reasonable large ramping bunch fraction.

Emittance compensation scheme has been showed to be an issue since each slice evolves in an unique way. Optimization of the injector parameters has to aim not only to minimize the projected emittance, but also to avoid overfocusing and slice emittance blowing-up, paying attention also to the behavior of the slice optics parameters. In fact tracking results have revealed that large modulation of the slice α and β functions can be an issue in the bunch propagation through the linac chicanes. Finally great attention has to be paid in the choice of the coefficients of the quadratic ramp, in order to reach the best compromise between the achievement of the linear ramp at the end of the injector and emittance and optics functions slice behavior.

REFERENCES

[1] S.B. Van der Geer et al.,“General Particle tracer Overview”, http://www.pulsar.nl/gpt/index/html.

[2] K. Flöttman, ASTRA User’s Manual, *https://www.desy.de/˜mpyflo/Astra_dokumentation*.

[3] A.Zholents at al., “Study of the electron beam dynamics in the FERMI@ELETTRA linac”, Proc. of the EPAC 2006 Conf., Edimburgh (GB).

[4] M.Ferrario et alter, “HOMDYN Study for the LCLS RF Photo-Injector”, LCLS-TN-00-04.

[5] G. Penco, “Longitudinal Space Charge Field at the Cathode In Case of a Non Uniform Bunch”, ST/F-TN-06/03 (2006).

[6] M.Trovò, G.Penco, S.Lidia, “Further Studies in the FERMI@elettra photoinjector optimization”, this conference.

[7] S. di Mitri and E. Allaria, private communication.

FURTHER STUDIES IN THE FERMI@ELETTRA PHOTOINJECTOR OPTIMIZATION

M. Trovò*, G. Penco, Sincrotrone Trieste, Trieste, Italy
S. M. Lidia, LBNL, Berkeley, California

Abstract

In the framework of the FERMI@elettra project we are presently studying an electron beam configuration satisfying the bunch energy distribution requirements coming from the FEL photon production system. The multi-particle tracking results concerning the photoinjector, which include the RF gun and the first two accelerating sections, are presented in this paper. We describe two possible electron bunch configurations which satisfy the FEL operation modes. Both injector configurations match the linac requirements for a 'ramped' current profile at the exit of the photoinjector. Sensitivity studies and time and energy jitter estimations are presented for both cases.

INTRODUCTION

Several configurations of the electron bunch delivered to the undulator chain by the linac accelerator have been considered in the optimization study process for the FERMI@elettra project. After considerations of performance optimization in the remainder of the FERMI linac [1], a new type of laser excitation at the photocathode, consisting in a ramped current distribution, is proposed. In particular, the linac studies show that the accelerating structure wakefield and chicane CSR effects require an initial electron beam distribution with a quasi-linear head-tail ramp in the instantaneous current in order to produce a 'flat-flat' beam profile (i.e. uniform in current and energy) at the entrance of the FEL undulators. This linac requirement translates to photoinjector in the problem of finding a special laser shape that extracts from the cathode a bunch that evolves along the gun machine section (mainly a drift at low energy), producing the desired output profile. In this paper two possible 'ramped' bunch solutions are presented. These two FERMI photoinjector configurations are suitable for the machine operation in the so called medium and long bunch modes [2].

PHOTOINJECTOR CONFIGURATIONS

For the FERMI@elettra project two machine operating modes are proposed that provide at the undulator entrance two different bunches in term of length and peak current [3]. These two mode require the gun to provide two different beams, presented in Table 1. To produce a quasi-linear head-tail current ramp in the bunch an unconventional shape of the laser pulse has to be introduced. In the simulations performed so far a transverse cylindrical distribution (top hat with 1mm edge radius) has been used while a time-varying intensity is used to produce the variation in instantaneous current along the bunch. This particular shaping is achievable with the appropriate design of the drive laser optical system [4].

Table 1: Main beam parameters required at the exit of injector in the two studied configurations.

Parameters	Medium	Long
E	95 MeV	95 MeV
Q	800 pC	1 nC
I_{peak} A	80 A	100 A
L_b (FWHM)	8 ps	10 ps
$\epsilon_{proj.}$	<1.5 μ m	1.5 μm
ϵ_{slice}	<1.0 μm	<1.0 μm
σ_E (uncorr.)	<2 keV	<2 keV

Medium bunch case

The first case (so called medium bunch case) requires from the photoinjector a bunch charge of 800pC and a current profile, in the ramped part, with a length of about 8ps.

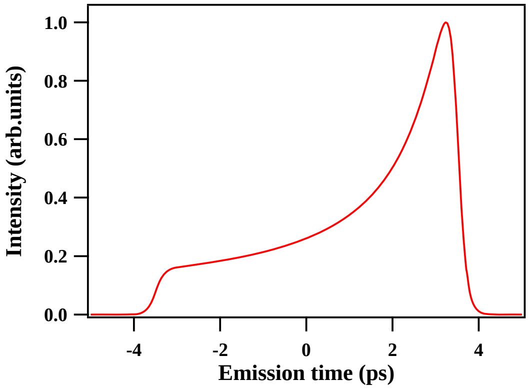

Figure 1: Longitudinal laser pulse shape: temporal intensity modulation.

Figure 1 shows the shape chosen for laser pulse intensity [2]. The curve is a Fermi-edge (with 7ps FWHM, 0.5ps of rise/fall time) multiplied by a polynomial $(0.26 + 0.05 \cdot t + 0.012 \cdot t^2 + 0.008 \cdot t^3 + 0.0019 \cdot t^4)$. A bunch generated

---

* mauro.trovo@elettra.trieste.it

by such a laser pulse propagates in the FERMI Gun machine section producing the output current profile shown in Figure 2.

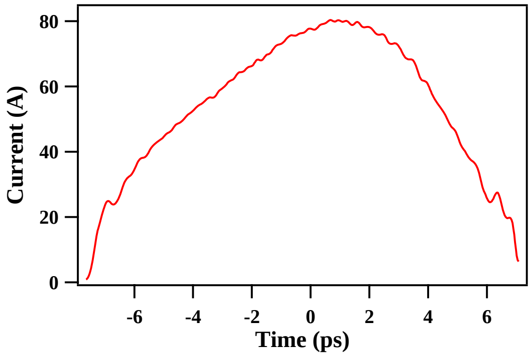

Figure 2: Current profile of the output bunch (head on the left).

Because of the highly non-linear charge distribution of the ramped profile, it is difficult to find an injector parameter configuration that completely satisfies the invariant envelope equation, performing perfect emittance compensation for all slices. Since each slice contains a different amount of charge, it evolves in a particular and unique way in the gun drift. Thus an average setting has been found that minimizes the projected emittance at the exit of the photoinjector (see Figure 3), which reaches 1.39 mm mrad. In the core 80% of the bunch particles the emittance is reduced to 1.21 mm mrad.

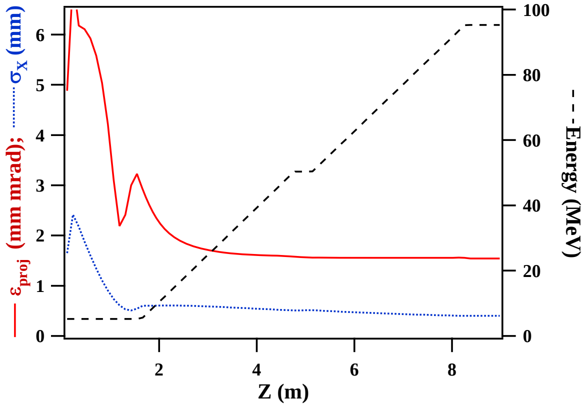

Figure 3: Transverse normalized emittance, radial spot dimension and energy along the photoinjector beamline for the medium bunch regime.

The slice analysis of the bunch at the injector exit, see Figure 4, shows that the slice emittance is affected by the current ramp and presents an head-tail increase from 0.7 up to 1.1 mm mrad.

Long bunch case

The second, or “long bunch”, case represents the configuration with higher bunch charge (1 nC) and longer drive laser pulse. Figure 5 shows the laser shape chosen for the long case. The curve has FWHM of 10ps and the slope is driven by polynomial as $35 + 10 \cdot t + 1.5 \cdot t^2$. The output current profile is also shown and it reaches a peak current of 100 A. The useful bunch part (from head to the current drop) is about 10ps and this satisfies the linac requirements (Table 1).

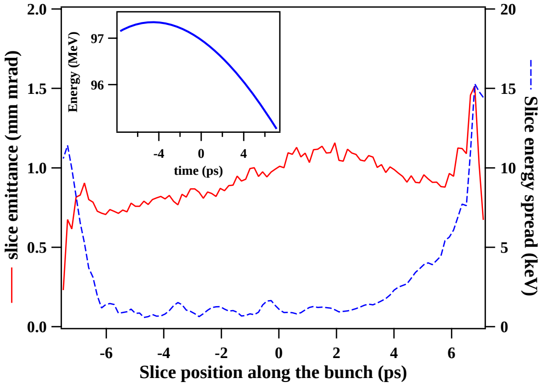

Figure 4: Slice emittance and slice energy spread at the injector exit for the medium bunch case calculated at the exit of the photoinjector machine section. Plot inside: Longitudinal phase space. Bunch head is to the left.

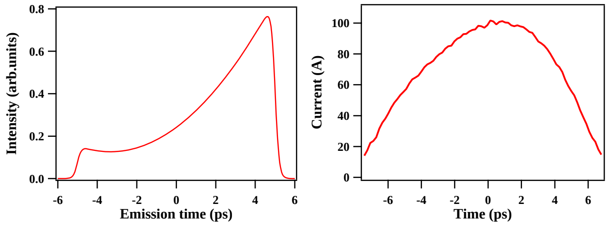

Figure 5: Longitudinal laser pulse shape: temporal intensity modulation on the left. Output current profile on the right.

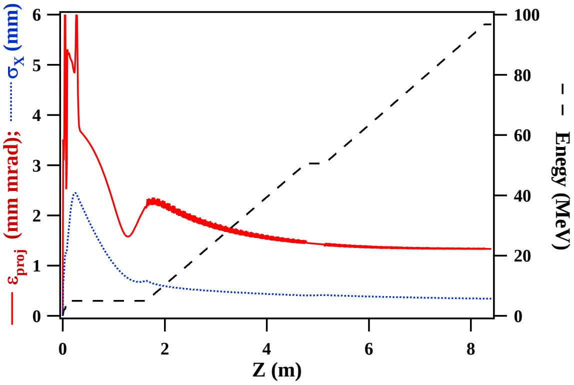

Figure 6: Transverse normalized emittance, radial spot dimension and energy along the photoinjector beamline for the long bunch regime.

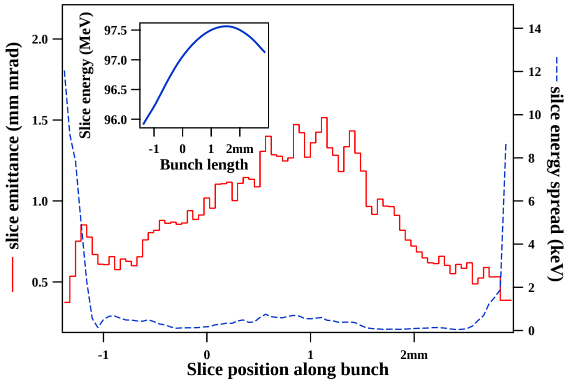

Figure 7: Slice emittance and slice energy spread at the injector exit for the long bunch case calculated at the exit of the photoinjector machine section. Plot inside: Longitudinal phase space. Bunch head is to the left.

Figure 6 shows the evolution of the transverse beam emittance, spot size and beam energy in this case. A final projected emittance of 1.33 mm mrad is achieved. Similarly to the medium bunch case The slice emittance also presents an head-tail ramp (see Figure 7).

SENSITIVITY AND JITTER STUDIES

The time of flight, the energy, the energy spread and the emittance at the end of the injector have been identified as the main output parameters whose shot to shot variation should be quantified, as well the slice properties of the bunch. To identify the main sources of variation for each of these, a single-parameter sensitivity study has been performed for the two cases, with results shown in Table 2. The time of flight is sensitive to gun parameters, while the emittance is more effected by a solenoid variation.

By randomly sampling each injector parameter within a specified tolerance range fixed by present technology (see Table 3), one thousand injector cases have been tracked (with 50000 particles), obtaining a statistical evaluation of the expected jitter. Results are presented in Table 4. Figures 8 and 9 show the jitter distributions for the emittance and the time of flight and their histograms. The gun solenoid has been neglected in this analysis due to the high stability (10^{-5}) provided by DC power supplies. The bunch time of flight jitter is about 300 fs at the injector exit and, linked to the energy jitter, it is propagated through the whole machine [5]. This effect becames an issue in the synchronization in the undulators between bunch and a short seed laser.

In order to consider the optical matching between the injector and the linac, an analysis of the jitter in the Twiss parameters has been also carried out on the same ensemble of bunches. The results are reported in Table 4. The average α_x and β_x are respectively -0.09 and 18m for the medium case (0.77 and 21m for the long), but the jittered outputs are spread out with a standard deviation respectively of 0.15 and 2.1m (0.26 and 6.3m for the long case). This should be taken into account for the finalization of the optics matching.

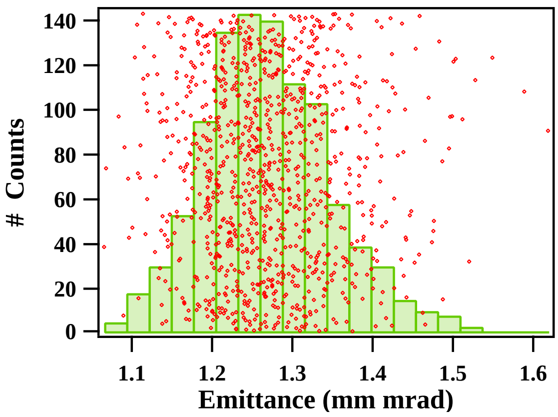

Figure 8: Projected transverse emittance jitter at the injector exit obtained by randomly sampling input injector parameters.

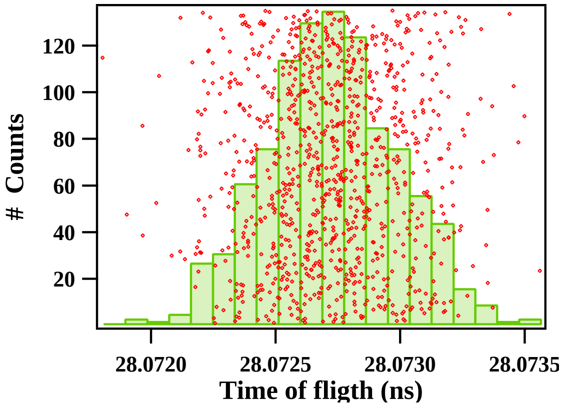

Figure 9: Electron bunch time of flight jitter at the injector exit obtained by randomly sampling input injector parameters.

Parameters	Tolerances
RF injection phase	0.1 deg
Laser time jitter	200 fs
Gun Eacc	0.25%
SOA Eacc	0.25 %
SOA RF phase	0.1 deg
Charge	4%
Laser spot size	4%
Laser pulse length (FWHM)	5%

Table 3: Tolerance budget for the injector parameters.

Further analysis

A further analysis of the injector output bunches from the jitter simulations has been implemented. Polynomial fittings of the longitudinal phase space and current bunch

Table 2: Minimum parameters variation, for the medium bunch and long bunch (in parentheses) cases, providing a fixed variation of the outputs, indicated in brackets in the first row. The average slice emittance $< \epsilon_{slice} >$ is calculated over all the slices. n/s = not sensitive.

Parameters (variation)	ΔI **(1%)**	ΔT **(100fs)**	σ_E**(10keV)**	$\Delta E/E$ **(0.1%)**	ϵ_{proj} **(10%)**	$< \epsilon_{slice} >$ **(10%)**
$Gun\ B_{sol}$ (%)	1.5 (2.2)	$>$ 10 (10)	1.1 (5)	n/s (n/s)	0.2 (0.8)	2 (1.2)
$Gun\ E_{acc}$ (%)	0.47 (0.6)	0.13 (0.15)	0.12 (0.17)	0.96 (1.6)	0.33 (0.5)	4.3 (0.9)
$Gun\ RFphase$ (deg)	0.65 (1.0)	2.8 (0.3)	0.8 (0.28)	3.8 (1.8)	0.5 (2.9)	4.8 (4.6)
$SOA\ E_{acc}$ (%)	20 (n/s)	2.0 (2.0)	3.9 (1.1)	0.21 (0.2)	n/s (n/s)	n/s (n/s)
$SOA\ RFphase$ (deg)	6.2 (n/s)	n/s (n/s)	0.1 (0.22)	1.9 (0.7)	n/s (n/s)	n/s (n/s)

Table 4: Simulation results of the output jitter for the medium and long bunch cases.

Output parameter	**RMS jitter medium**	**RMS jitter long**
Arrival Time (fs)	351	266
Peak Current (%)	2.4	3.3
Energy (%)	0.17	0.17
σ_E (keV)	42	24
Emittance$_x$ (%)	13.1	6.3
α_x	0.15	0.26
β_x (m)	2.1	6.3

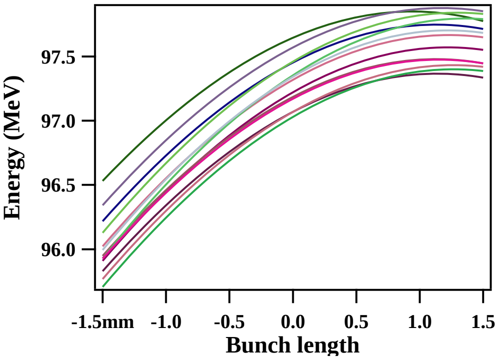

Figure 10: Twelve polynomial curve fits (fourth order), randomly sampled in the thousands performed, of the longitudinal phase spaces of bunches simulated for the long case. Bunch head is on the left.

profile have been performed for each simulated case. Figure 10 shows twelve fourth order polynomial curve fits of the longitudinal phase spaces of the bunches simulated for the long case, while Figure 11 shows the current profile cases. The curves show the synchronous bunch core (3mm) while the bunch tails are neglected.

After fitting all simulation results, a statistical analysis of the fit coefficients has been performed [6]. These statistical characterization can be used to reconstruct analytically the injector output particle distribution with respect to the jitter.

CONCLUSION

Injector optimization of the medium and long bunch ramped cases have been described. The ramped current distributions have been presented as possible interesting solutions for the FERMI@elettra FEL operation with respect to the “standard” flat-top distribution despite the slight projected emittance increase. The jitter studies have shown that time jitter remains a critical parameter for seeded machine FELs and it will drive the future improvements in the performance of the laser and RF systems.

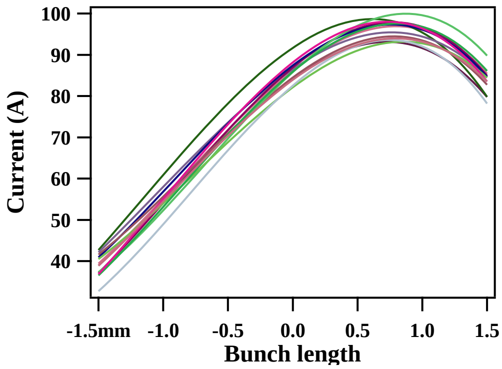

Figure 11: Twelve polynomial curve fits (fourth order), randomly sampled in the thousands performed, of the current profile of bunches simulated for the long ramped case. Bunch head is on the left.

REFERENCES

[1] A. Zholents et al., “Study of the electron beam dynamics in the FERMI@ELETTRA linac”, Proc. EPAC 2006, Edinburgh, UK.

[2] G. Penco et al., “Optimization Studies of the FERMI@ELETTRA Photoinjector”, Proc. EPAC 2006, Edinburgh, UK.

[3] S. D. Mitri, “How to obtain high quality electron bunches in presence of normal conductiong Linac Wakefields”, Proc. this conferece.

[4] M. B. Danailov et al., “Design of a Two-Stage Laser Pulse Shaping System for FEL Photoinjectors”, Proc. this conferece.

[5] P. Craievich et al., “Jitter Studies for the FERMI@ELETTRA Linac”, Proc. EPAC 2006, Edinburgh, UK.

[6] G. Penco, M. Trovò and S. Lidia, *Technical Note* ST/F-TN-06/11.

THE DIAGNOSTICS OF THE FERMI@ELETTRA BUNCH COMPRESSORS

M. Veronese*, S. Di Mitri, M. Ferianis, Sincrotrone Trieste, Trieste, Italy

Abstract

Bunch compressors (BC) are key components of the seeded FEL FERMI@ELETTRA. A complete set up of non destructive diagnostics is foreseen to provide the required stability for the production of sub-psec electron bunches. Main task of these diagnostics is to provide the error signals to the feedback systems used to stabilize the energy and the peak current of the electron bunch which are crucial parameters for optimum FEL operation. The different operation regimes foreseen for FERMI [1] call for a flexible set-up, for both the bunch compressors and the associated diagnostics. In this paper we present the adopted diagnostics for the measurement of position, energy and energy spread; both "energy" BPM, in between bunch compressors (BC), and optical transition radiation (OTR) screen plus wire scanner have been adopted. The design of a relative bunch length monitor needed for the determination of the optimal compression and for peak current stabilization is presented as well. The scheme is based on non-invasive techniques, namely the detection of the coherent synchrotron radiation (CSR) from the last bending of the BC plus the coherent diffraction radiation (CDR) from a downstream slit. Finally, a technique for the bunch phase measurement is presented.

INTRODUCTION

The FERMI FEL, presently under construction at the Elettra Laboratory, is based on a seeded HGHG scheme. Two FEL undulator chains FEL1 and FEL2 are foreseen according to the needs of the FERMI scientific community, to lase in two adiacent UV spectral regions (100-40nm and 40-10nm) with different pulse lengths. The FERMI layout has been described in detail in [1], its main parameters are presented in Table 1. High charge (~nC) electron bunches are produced in a RF photo-injector, with bunch length (L_B) of about 10psec$_{FWHM}$. The acceleration is provided by normal conducting S-band RF structures and the bunch compression is achieved by two magnetic chicanes. Up to now, two main bunch regimes have been studied: the "medium bunch" (L_B=600fs$_{FWHM}$) optimized for the FEL1 operation and the "long bunch" (L_B=1.4ps$_{FWHM}$) which is best suited for FEL2. High quality beams (low emittance, low energy spread, high current stability and high energy stability) are needed to obtain high quality FEL output radiation. Non-standard diagnostics and instrumentation suitable to fully characterize and monitor the beam during the machine operation have to be developed according to the specific beam parameters and machine requirements.

Table 1: Fermi@Elettra parameters

Parameter	**FEL 1 (medium bunch)**	**FEL 2 (long bunch)**
Wavelength	100-40 nm	40-10 nm
Electron Beam Energy	1.2 GeV	1.2 GeV
Bunch Charge	0.8 nC	1 nC
Peak Current	800 A	500 A
Bunch Length (FWHM)	600 fs	1400 fs
Energy Spread (slice)	100 KeV	100 KeV
Norm. emittance (slice)	1.5 mm mrad	1.5 mm mrad
Repetition Rate	10-50 Hz	50 Hz
Photon Pulse Length (FWHM)	≤ 100fs	~ 1000 fs

BUNCH COMPRESSORS

Bunch compressors are used to produce high peak current electron bunches needed to obtain GW peak power FEL radiation generation. Several aspects have to be considered to avoid beam quality degradation (e.g. CSR induced emittance dilution). In particular, the stabilisation of the peak current and the energy in the chicane are needed to guarantee the long term stability of the FEL output [2]. The bunch compression is obtained with two magnetic chicanes located at the nominal energies of 220 MeV (BC1) and 600 MeV (BC2) respectively. This design allows for both single and double compression schemes, with a total compression factor ranging from 2 up to about 100 [3].

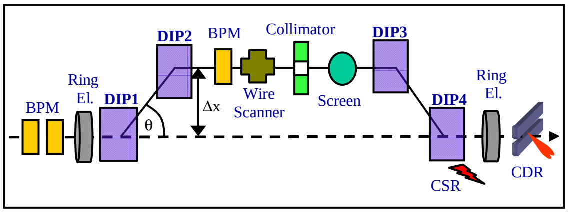

Figure 1: Bunch Compressor Diagnostics layout.

The conceptual scheme is the same for BC1 and BC2, but some components are adapted according to the different bunch parameters. In Fig. 1 the bunch compressor scheme is sketched together with the foreseen diagnostics. The main parameters of BCs for a double compression scheme are summarized in Table 2.

---

*E-mail: marco.veronese@elettra.trieste.it

Table 2: Fermi bunch compressors parameters.

Parameter	BC1	BC2
Number of magnets	4	4
Magnetic length	0.5 m	0.5 m
Distance DIP1-DIP2	2.5 m	2.5 m
Distance DIP2-DIP3	1 m	1 m
Distance DIP3-DIP4	2.5 m	2.5 m
Nominal DIP angular range	66.8 :77.2 mrad	53.1:77.5 mrad
Commis. DIP angular range	50 : 80 mrad	50 : 80 mrad
Linac phases ranges	L1=-42° : -20°	L1=-42° : -20° L2,3=-20° : -10°

From Table 2 it can be seen that even if the bending angles are quite small they span over a wide relative range [3]. This fact, together with the dispersion and the energy spread, has a deep impact on the electron beam parameters in the chicanes (see Table 3) and on their measurement.

Table 3: Main beam parameters at BC1 and BC2.

Parameter	BC1	BC2
Energy Range	220 : 260 MeV	580 : 615 MeV
Rel. En. Spread	2.3 : 2.7 %	0.97 : 1.05 %
Beta (β_x)	16 m (z=31 m)	23 m (z=98 m)
Dispersion (D_x)	0.165 : 0.255 m	0.155 : 0.24 m
Transverse displacement (Δx)	0.165 : 0.255 m	0.155 : 0.24 m
Energy Spread Beam size ±3σ	28 : 44 mm	10 : 15 mm
Betatron Beam size ±3σ	1.4 mm	2.0 mm

In particular, in the area between DIP2 and DIP3, where all diagnostics will be located, the beam size is expected to be dominated by the dispersion.

DIAGNOSTICS

We will now discuss the diagnostics according to the measured parameter: energy, energy spread, bunch arrival time, relative bunch length.

Energy Measurement

The transverse displacement of the beam centroid (Δx of Fig.1) spans, for the BC1 and BC2 ranges, over approximately 100mm. If we consider building the BCs with a wide vacuum chamber, then for that chamber a width of at least 150mm is needed to allocate the wide electron beam (±3σ beam size of 35mm) and its displacements. Taking in account a beam transversely centred at Δx=200 mm, the rms energy stability required by the FEL (ΔE/E=0.1%) will translate in terms of rm displacement variations to 200 μm (at nominal BC1 operating conditions). To correctly operate the feedback system, the resolution of the position measurement has to be at least four times better than the value we want to stabilize within, which means that a single shot resolution of 50 μm is needed. This is a very tough value to be met on a 150mm chamber width and with a beam size of 35mm. Therefore, we plan to put the second and the third dipoles of the chicanes and all the related diagnostics on a transverse high precision translator stage. This will allow us to reduce the vacuum chamber transverse size to about 60 mm and thus to use an "energy BPM". Another possible approach to the problem has been proposed at DESY; it is based on the measurement of the relative time difference between two pulses generated in a transverse strip-line arrangement [4]. Its applicability to Fermi will be evaluated in the near future.

Energy Spread Measurement

The energy spread is a crucial parameter for the machine operation and it has to be carefully monitored. It will be measured by means of a wire-scanner on multi shot basis and by an OTR screen plus a CCD camera, shot by shot. Both techniques are destructive and the measurements will be performed during the commissioning and, periodically, during the operation to check the long term stability of the energy spread. As depicted in Fig. 1, in between the wire-scanner and the OTR screen, we plan to install a collimator. With this geometry the energy spread of the beam can be measured upstream and downstream of the collimator and its effect can be followed step by step. The energy spread can be directly extracted from the measurement of the transverse size of the beam since the dispersion in the middle of the chicane is known and dominates the beam size. The needed resolution is different for the two bunch compressors. For BC1 the minimum δE/E is 2.3% which will reflect in a 28 mm beam size (±3σ beam). The needed relative resolution is estimated to be 2%, which means 0.56 mm, in terms of spatial resolution. For BC2 the energy spread will be smaller and it will have a small operation range. Then for a 0.95% δE/E will reflect in a ±3σ beam size of 10 mm and to appreciate the changes in energy spread we will need to have a 1% relative resolution which means 100 microns spatial resolution. This resolution level can be achieved with an OTR screen plus a CCD detector, higher resolutions will be achieved by the wire-scanners [5].

Bunch Arrival Time Measurement

The bunch arrival time measurement will be provided by a new kind of diagnostics. The concept has been proposed at DESY [6] and will make use of the optical pulses from the ultra stable timing distribution system [7] to measure the bunch arrival time relative to the optical clock pulse. This technique is non-destructive and it has shown so far a resolution better than 100fs. Two devices, one at the entrance and one at the exit of each chicane, will be installed. The signal from the device at the entrance of BC1 will provide a direct measure of the total initial jitter from the injector.

$$\Sigma_f^2 = \left(\frac{r_{56}}{c_0}\frac{\sigma_A}{A}\right)^2 + \left(\frac{C-1}{C}\right)^2\left(\frac{\sigma_\phi}{c_0 k_{RF}}\right)^2 + \left(\frac{1}{C}\right)^2 \Sigma_i^2 \qquad (1)$$

As can be seen from Eq. 1 the coupled measurement of the jitter at the entrance and at the exit of the chicane initial will give us the RF contribution of the timing jitter.

Relative Bunch Length Measurement

The needs for peak current stabilisation push to develop a non-destructive relative bunch length monitor, so that its signal can be fed to the feedbacks systems that will keep the peak current stability acting on the phases of the RF accelerating sections. For this purpose we will develop power monitors based on the detection of coherent synchrotron radiation (CSR) [8] and coherent diffraction radiation (CDR) [9]. We plan to implement a redundant system based on the detection of the CSR emitted from the last dipole of the chicanes and on the detection of the CDR emitted from a slit placed downstream the chicane.

Coherent radiation is emitted from short electron bunches, in the case of a Gaussian bunch where σ_z is the sigma of the distribution, it is emitted at wavelengths longer than roughly $2\pi\sigma_z$. For electron bunches with psec and sub-psec duration the coherent emission is in the mm/sub-mm wavelength spectral range. An overview of the related physics can be found in [10]. The CSR spectral angular distribution of a N-electrons bunch can be related to the spectral angular distribution of a single electron as shown in Eq. 2.

$$\left.\frac{d^2 I}{d\nu d\Omega}\right|_{N-el.} = \left[N + N(N-1)\left|F(\rho(t))\right|^2\right]\left.\frac{d^2 I}{d\nu d\Omega}\right|_{1-el.} \qquad (2)$$

Where $F(\rho(z))$ is the Fourier transform of the longitudinal normalized bunch distribution $\rho(t)$. From Eq. 2 we can see that the total N-electron CSR angular distribution is the sum of the incoherent synchrotron radiation of N electrons ($\propto$ N) and a coherently enhanced term ($\propto N^2$). The frequency behaviour of the coherently enhanced term depends on the square of the Fourier Transform of $\rho(t)$. As the bunch gets shorter the $F(\rho)$ get spectrally broader and the emitted power increases. To evaluate the emission properties (spectral distribution and intensity) we have computed the CSR spectra angular distribution in two steps. In the first we have calculated $F(\rho)$, by means of the FFT of the bunch profile coming from Elegant simulations (shown in Fig. 2). In the second, to calculate the single electron spectral-angular distribution, since the circular motion approximation is not sufficient in our case, we have used a numerical code written by O.Grimm at DESY.

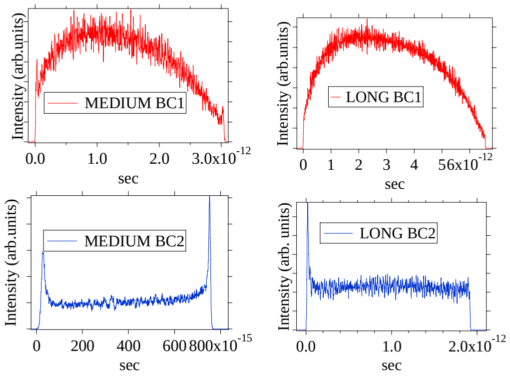

Figure 2: Longitudinal electron distributions at BC1 exit (red) and BC2 exit (blue) for the “medium bunch” (left) and the “long bunch” (right).

The code implements a full Liénardt-Wiechert potential formalism, and makes a tracking of a single electron through an arbitrary magnetic field. In the calculation both velocity and acceleration terms are included as well as the finite dimensions of the dipoles, the contributions of both 3rd and 4th bending magnets and the shielding effects of the vacuum chamber walls (in a parallel perfectly conducting planes approximation). Some results of these simulations are shown in Fig.3 for the CSR emission from the last bending magnet of BC1 for the “medium bunch” and in Fig.4 for the “long bunch” case. Plotted are the angle integrated spectral intensity distributions, for a detector (30x30 mm) placed 150 mm downstream the last bending of BC1 and normal to the edge radiation direction centred 25 mm away from the straight beam path.

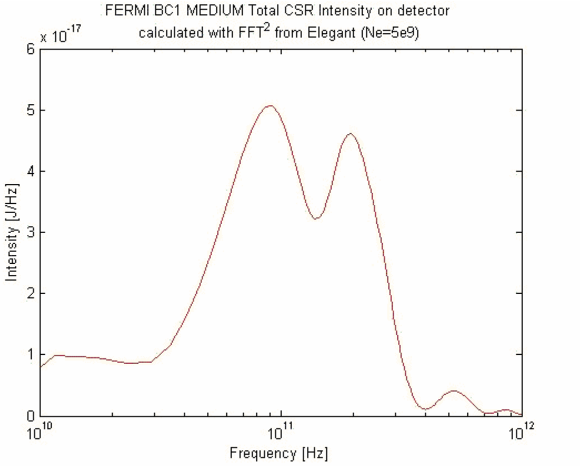

Figure 3: Expected spectral distribution of the radiation extracted from the 4th dipole of BC1 for the “medium bunch.

These results suggest that, for the CSR emitted from the bunch compressors of FERMI the Gaussian bunch plus circular motion approximations [8] might not be sufficient. They also indicated that the choice of the frequency range for the detectors has to be done with special care for narrowband detectors. Moreover considering both BC1 and BC2 the core of CSR emission is in a critical spectral region (between 10GHz and 1THz) for the detectors.

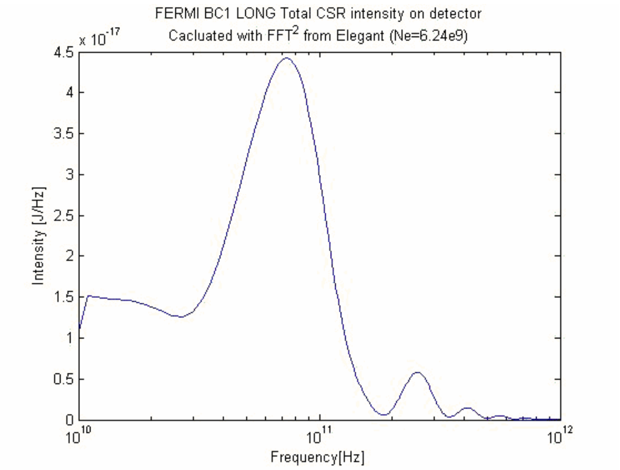

Figure 4: Expected spectral distribution of the radiation extracted from the 4th dipole of BC1 for the “long bunch”.

In this region the detection of CSR can be done by RF diodes or pyrodetectors. The diodes have higher sensitivity in the sub-THz range, but are limited at about 600GHz while pyrodetectors offer a wider operation range starting from about 150GHz. We plan to use the pyrodetectors for their flexibility and ease of use, but RF diodes may be employed especially for the case of “long” bunch in BC1. The total energy per pulse emitted in the spectral range from 10 GHz to 1THz is of about 10μJ for the “medium bunch” and of about 4μJ for the “long bunch”. In the spectral range of the pyrodetector (e.g. Coherent/Molectron P4-42) the energy per pulse is respectively of 1.5μJ and 0.3μJ. In this case a simple estimate gives us a sensitivity of 0.04% sufficient to fulfil the 2% of the feedback requirements (to obtain 10% current stability). Other factors should also be considered: the efficiency of the radiation collection, the absorption and reflection from air and from the vacuum window.

A second coherent radiation source, a CDR source (e.g. an OTR screen with a small aperture) will be installed immediately downstream the bunch compressors. It is meant to add redundancy to the CSR system. We have performed some calculations to evaluate its application to FERMI diagnostics. Our calculation started from the CDR description given in [11] for a relativistic electron beam. Here γ is the Lorentz factor of the electrons passing through a hole of radius “b” in a circular screen of radius “a”. It is worth saying that the infinite screen approximation is satisfied if $a > \lambda\gamma$. For FERMI BC1 “medium” bunch we can consider: λ=3 mm and γ=430 then the condition becomes a > 1.3 m. This shows that a large screen and a large detector angular acceptance are desirable to avoid low frequency intensity suppression. On the other hand a compromise has to be found to meet space requirements. This led us to choose a screen radius “a” of 60 mm and an angular acceptance of 0.2 rad. The effect of the hole radius has to be considered, for CDR emission, the smaller the hole radius is, the better. On the other side the higher is the radius, the smaller is the impact of the CDR emitter on the beam dynamics. CDR Spectral distributions calculated with a rectangular distribution approximation of the longitudinal bunch profile are shown in Fig. 5 for two extreme cases: BC1 “long bunch” and of BC2 medium bunch for different values of the hole radius.

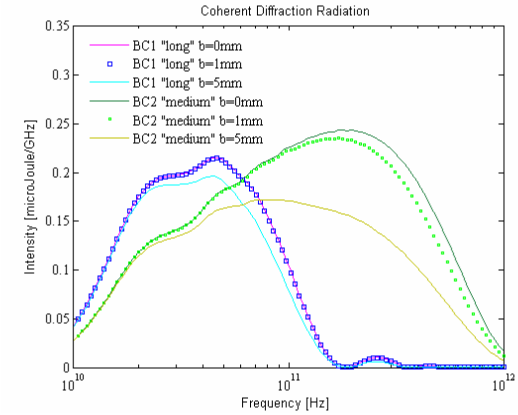

Figure 5: CDR spectral distributions for “medium bunch” at the exit of BC2 and the “long bunch” at the exit of BC1 for values of b=0, 1, 5 mm.

The calculation indicates that, for the “long” bunch at BC1 a quite large hole can be used without loosing too much in intensity, while the hole size effect is more important in the case of the “medium” bunch in BC2.

ACKNOWLEDGMENTS

We would like to thank O.Grimm for providing his code, P. Craievich, M. Cornacchia, M. Dunnig, J. Travish, J. Wu and P. Krejcik for fruitful discussions. And F. Rossi for his help with Matlab simulations. This work has been partially supported by the EU Commission in the Sixth Framework Program, Contract No. 011935 – EUROFEL.

REFERENCES

[1] M. Cornacchia, *et al.* EPAC 06, 145, (2006).
[2] J. Wu, *et al.* PAC 05, 1156, (2005).
[3] S. Di Mitri, ELETTRA, ST/F-TN-06/09, (2006).
[4] K. Hacker, *et al.* EPAC 06, 1043, (2006).
[5] K. Wittenburg, Tesla Report 2000-18 (2000).
[6] F. Loehl, *et al.* EPAC 06, 2781, (2006).
[7] M. Ferianis, *et al.* FEL 05, 134, (2005).
[8] J. Wu, *et al.* PAC 05, 428, (2005).
[9] E.Chiadroni, *et al.* EPAC 06, 1127, (2006).
[10] O. Grimm, EPAC 06, 1040, (2006).
[11] S. Casalbuoni, *et al.* TESLA Report 2005-15 (2005).

MAIN HIGH VOLTAGE SOLID STATE GYROTRON POWER SUPPLY 60kV / 80A *

G. Taddia, M. Pretelli[#], L. Rinaldi, V. Rossi, L. Sita, O.C.E.M. SpA, San Giorgio di Piano, Italy
T. Bonicelli, P.L. Mondino, EFDA CSU Garching, Germany
D. Fasel, EPFL/CRPP Lausanne, Switzerland
R. Claesen, M. Santinelli, ENEA Frascati, Italy.

Abstract

This paper will describe the preliminary design of a 4.8 MW Main High Voltage Power Supply, rated 60kV/80A, especially conceived to supply the voltage between Cathode and Collector of a Gyrotron. A full solid state technology, named SWM (Stair-Way Modulation) for the full scale Electron Cyclotron (EC) Test Facility at CRPP, Lausanne. The ITER EC system may also make use of a similar system, in alternative to the present baseline design based on naturally commutated thyristor converters and series high voltages solid state switches. The 60kV output is reached by adding more than 120 high voltage modules in series connection, with ad hoc control criteria to allow a regulation at full performances in the range of 45kV-60kV, a square wave modulation and a fast switch-off in less than 10us.Components choices and simulations of the system will be highlighted in order to demonstrate the fulfilments of the technical specification before the manufacturing stage. This solution can be extended to several applications in the High Voltage domain and is aimed to enhance the reliability, decrease costs, provide redundancy, plug-in modularity, component de-rating and component standardization.

INTRODUCTION

The ITER Heating and Current Drive (H&CD) system, includes the installation of an Electron Cyclotron system based on CPD type Gyrotrons (170GHz). This type of RF sources requires two power supplies, one Main High Voltage Power Supply (MHVPS) between cathode and collector (typically V = 50 ÷ 60kV, 80A) and an Acceleration Power Supply, which, with the MHVPS, establishes the voltage between body and cathode, typically 80 ÷ 100 kV. The modulation frequency specified in the ITER reference design is 1 kHz but in the developments on-going in Europe, 5 kHz are considered for the stabilization of Neoclassical Tearing Modes (NTM). The continuous developments of solid state devices, available for both higher voltages and higher switching frequencies, have highlighted several advantages of the fully static solutions which could conveniently replace the more traditional systems based on vacuum tubes (e.g. tetrodes). On the basis of the above considerations, OCEM has performed a conceptual study of a Solid State Body Power Supply (BPS) [1] for ENEA Frascati, with support from EFDA. The first fully solid state BPS has now been completed [2] and installed at ENEA Frascati. For the new EC Test Facility in Lausanne, EFDA is now procuring, on behalf of European Commission, both power supplies (MHVPS and BPS). The results of a competitive tendering showed that the above described modular topology was economically convenient beside yielding some important technical advantages.

OUTLINE SPECIFICATIONS

The performance specifications are listed in Table 1:

Table 1: Main Performance Specifications

Description	**Value**
Duty Cycle	8 / 24 hours
AC input Voltage	20kV / 50Hz (±10%)
Nominal Output Voltage	-60 kV DC
Output Voltage range	-1 kVDC < V_{DC} < -60kVDC regulation at full performances -45kV to –60kV
Nominal Output Current	80 A
Modulation freq.(ON/OFF)	5kHz
Output Voltage Accuracy: Static Reproducibility Dynamic transient Ripple	 <± 1% of V_{DC} nominal <± 0.5% of V_{DC} nominal <± 1500V <± 2%@600Hz, <±0.5% for higher frequencies
Voltage Settling time	<15us
Shutdown time	<10us
Max Energy delivered to the load in case of arc	10J
Protection Transm. delay	<1us
Measurement Accuracy Voltage Current	 +/-0.1% in DC +/-0.2% at 10kHz +/-0.3% at 50kHz <± 1% of nom. value
Measurement Bandwidth	≥500kHz

---

*Work supported by European Fusion Development Agreement
[#] physics@ocem.com

MHVPS TOPOLOGY

The preliminary design of the MHVPS is based on a series connection of elementary power modules which do not require direct series connection of semiconductors. Each module, is provided with its own DC power supply so that the voltage is evenly shared during normal operation. The total output voltage is hence controlled by the number of switched-on modules in quantization steps of voltage. This topology, together with an ad hoc control strategy developed by OCEM, the Multi Pulse Width Modulation (MPWM), has been named Stair-Way Modulation (SWM). This type of modulation has the advantage of an averaged power distribution among all the modules, with a consequent minor stress of the main transformers. Also the achievement of a high bandwidth is not related to the increasing of the switching frequency of only a few modules. In a SWM system the maximum switching frequency of each module remains equal to all the modules. This leads to reach a very high value of bandwidth, according to the constraints due to the particular specifications. The overall system also foresees a level of modularity in a redundant and fault tolerant configuration. Hence, in case of fault of a single module, the faulty module can be easily excluded from the main circuit, ensuring continuous operation.

The MHVPS consists mainly of the following blocks:

- **Input circuit breaker** with a protection relay, to connect the P.S. to the medium voltage grid (20kV, 50Hz, three-phase) through a soft start equipment.
- **Multi Secondary Transformer system**, to adapt the input voltage from the grid to the voltage required by the downstream parts, with the proper insulation level.
- **Power modules** in series connection, to transform the 50 Hz supply voltage from the transformer system in a regulated DC voltage.
- **Control electronics**, to provide regulation, protection and interface.

The main parts of the MHVPS are described in the following subsections.

Multi Secondary Transformer System

Due to the design constraints (mainly the 120kVdc insulation voltage, the reduced available space on the installation site and the requested very low harmonic content in the input current) the transformer system is based on two cast-resin transformers, made of several secondary, each feeding one power module.

The secondary coupling of these two transformers is either of the star type or of the delta type, in order to obtain an overall primary current from the grid with low harmonics. Finally, soft-start devices are integrated between the transformers and the main grid.

Power Modules

The general scheme diagram of the power module is shown in Figure 1.

The switched-on power modules, controlled by a modulation index, determine the total output voltage. By using this technique and a proper switching strategy, the modulation can be performed in order to obtain the desired value of output voltage within the specification requirements. The Module is ON when the switch Q2 is closed and Q1 is open; a voltage step of -Vdc is added to the total output voltage. The Module is OFF when the switch Q2 is open and Q1 is closed; the module is bypassed. The two switches Q1 and Q2 must be never ON simultaneously. Using this structure it is relatively simple to perform a fast switch-off: there is enough time to simultaneously open the series switches (Q2) of each module, and then to close all the parallel switches (Q1); this operation can be very fast, in the order of 2-3 us.

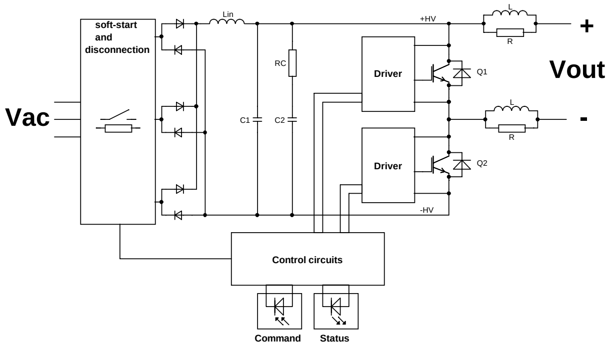

Figure 1: General schematic of a Power Module.

Each module has an output L-R filter, which is a portion of the total output filter seen by the load. The filter has been conceived for:

- smoothing the output voltage ripple;
- limiting the di/dt and the peak current during the arc;
- obtaining a correctly damped overall system;

Calculations show that in order to minimize the energy delivered to the system it is necessary to consider an additional resistor of some ohms (4 ohms) in series with the load; this will permit to dissipate a portion of the energy before that this energy is delivered to the Gyrotron. The module is designed for an output voltage of 560V. This leads to a series connection of more than 120 modules with the consequence of a relatively high complexity of transformer and cabling. However the components mounted on each module can be low voltage devices, with an advantage in terms of cost and availability. Moreover, each stair of voltage is lower than the allowable peak to peak ripple, leading to have an additional degree of freedom in the dimensioning of the output filter.

Control Electronics

The control electronics has been designed to perform the following functions:

- measurement of the output voltage and current;
- regulation: to keep the output voltage at the desired value and within the allowed fluctuations;

- protection: to guarantee an effective protection in case of internal faults or external overloads;
- interface: to communicate with the main control system and to allow the local or remote command of the power supply.

The user interface, data log and Ethernet connections are based on commercially available electronics, with custom designed software. The regulation system (fully digital, based on an high performance FPGA card) determines the number of modules that must be ON in each time interval, providing a proper "rotation" in the module sequence. This allows to equally share the stresses among the modules. During commutations, with a proper modulation strategy for the semiconductor switches, the switching frequency seen by the load is equal to the frequency of the single module multiplied by the number of modules. This allows an high output switching frequency (seen by the load) with the advantage of a relatively low switching frequency seen by the components of the modules.

In steady state, when the output voltage is between an acceptable range around the set value, the algorithm foresees a lock modulation input that stops the switching of the modules and the rotation. This prevents an unnecessary power dissipation.

Components Choice

After a careful market inspection, the main standard components have been chosen. The IGBTs is a V_{CES}=1200V / I_C=140A @80°C (I_C=200A @25°C) device based on the SPT technology which offers a good compromise between the V_{CE_ON} and the switching speed (switching losses). The size of the IGBT was chosen also looking at its overload behaviour: it has a short circuit capability of 1000 pulses at ten times I_C and self limiting current capability to 6•I_C. The IGBT driver choice was made looking firstly to its delays which are extremely small. The input DC filter topology is an LC-parallel damped filter. The damping is chosen to avoid excessive over-voltages during power connection or load disconnection and to limit the filter peak output impedance to less then 0.5 Ohm.

PRELIMINARY SIMULATIONS RESULTS

The preliminary simulations for the MHVPS have been performed by considering the overall system which will be installed in Lausanne and which include the CPD Gyrotron, the BPS and MHVPS in order to verify the adequate compatibility of the MHVPS to the already designed BPS now under construction.

The model of the whole system has been developed using Pspice and Matlab/Simulink. Figure 2 shows the step up of the whole system simulation (with Simulink): the ramp up of the MHVPS current and voltage are shown in the first and third rows respectively. In the second row the switch-on of the BPS is simulated. This leads to the increase of the Body to Cathode Voltage up to the maximum value 100kV, as shown in the fourth row.

In Figure 3 it is sketched how the MHVPS and the overall system behave during the required 5kHz modulation. The first two rows show the commands given to the BPS and MHVPS for starting the modulation; both power supplies start modulating as specified, and the voltage patterns can be observed in rows 3 (BPS) and 4 (MHVPS). The total output voltage between Body and Cathode is the result shown in row 5 (100kV peak). Last row is the MHVPS current which shows a promising behaviour of the overall system during the 5kHz modulation.

Finally, Figure 4 reports a simulation of the overall system in case of an arc between Cathode and Collector. The arc is simulated by adding in the Simulink model a voltage generator of 100V. At 200 us the arc occurs and Body to Cathode voltage collapses by leading to an increase of the amount of charge in the Gyrotron (fifth row). The 0,1 limit value depicted in the fifth row, represents the amount of charge delivered to the load and, considering an arc voltage of 100V, corresponds to the maximum value of energy that could be delivered as per technical specification (10 Joules). However it can be

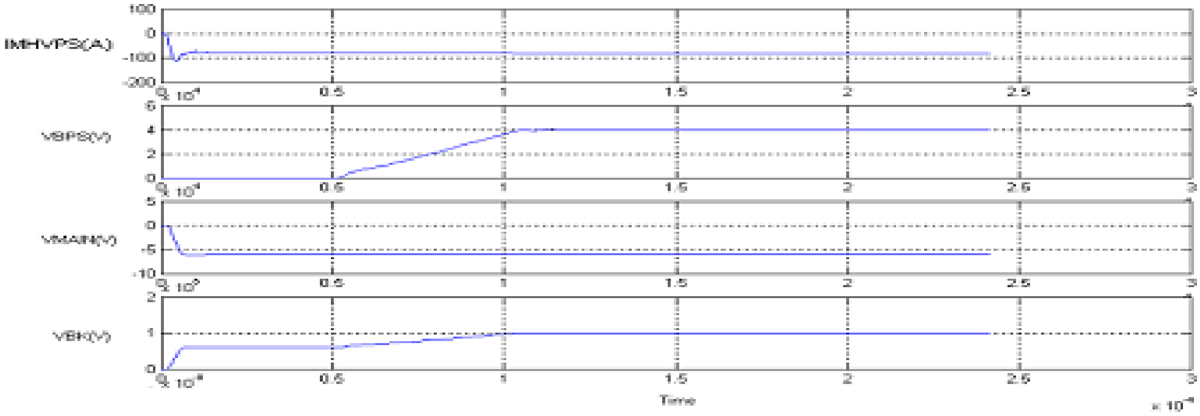

Figure 2: Simulation of the Step up of the whole system (MHVPS+BPS+Gyrotron)

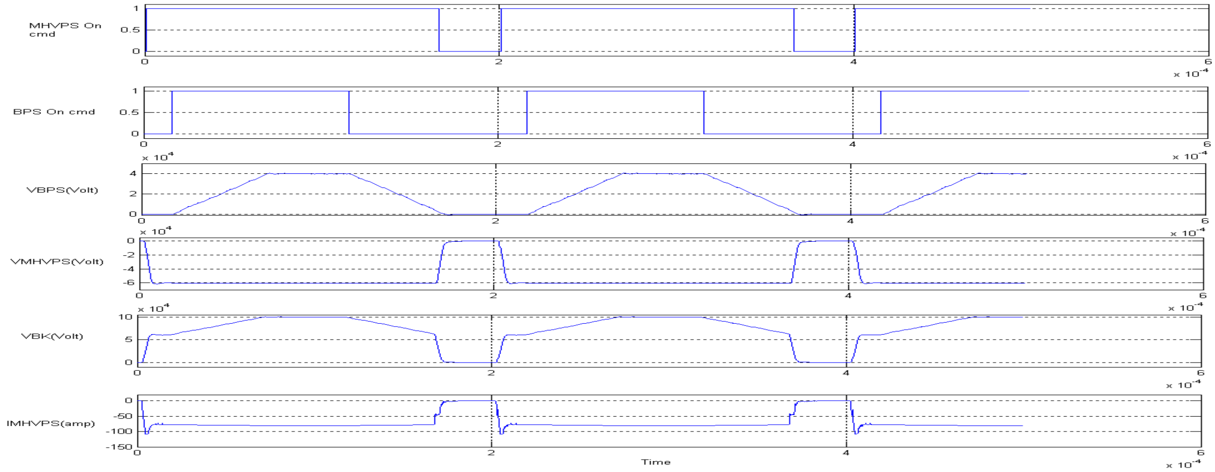

Figure 3: Simulation of the 5kHz Modulation

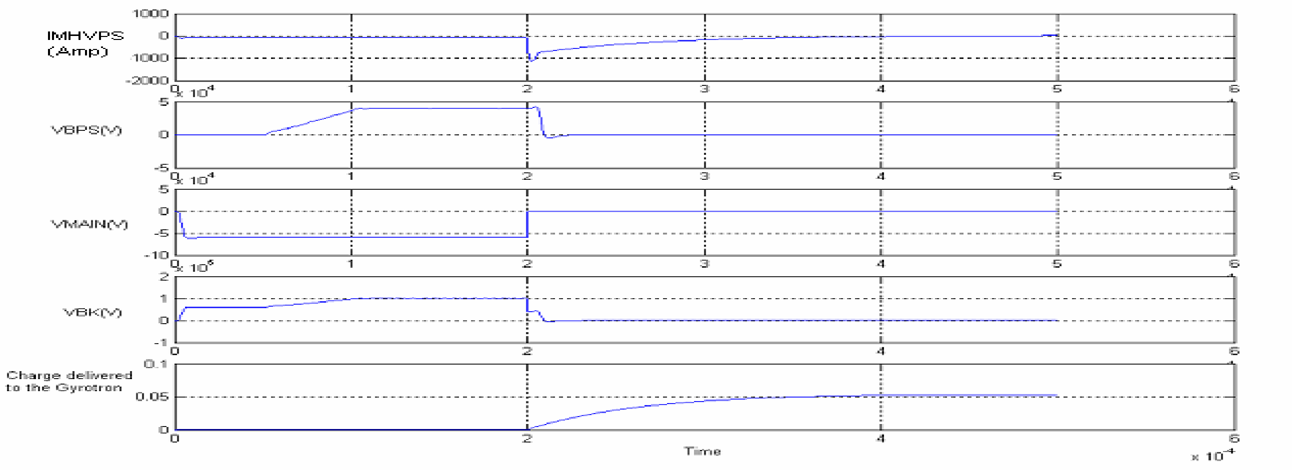

Figure 4: Simulation of the Step up of the whole system with an arc between K-C at 200us

CONCLUSIONS

This paper has described the preliminary design of a 4.8 MW Main High Voltage Power Supply, rated 60kV/80A, especially conceived to supply the voltage between Cathode and Collector of a Gyrotron. This topology has been chosen for the EC Test Facility at CRPP, Lausanne (CH). Similar systems could be adopted for ITER, which includes the installation of an Electron Cyclotron system based on CPD type Gyrotrons (170GHz) in alternative to the present baseline design.

The first simulations have demonstrated the correct behaviour of the MHVPS not only as a stand alone modulator but as part of a complete system which will be installed in Lausanne, and which include the MHVPS, the BPS and the CPD Gyrotron. Three main situations have been depicted in the simulation sketches: the step-up and the steady state, the 5kHz ON/OFF modulation and the behaviour of the system in case of an arc between Cathode and Collector. The first results are very encouraging and the design phase can enter into a further final detail before entering the manufacturing stage. The installation of the overall system in Lausanne is foreseen to be starting by September 2007.

REFERENCES

[1] T. Bonicelli et alia, “High Frequency/High Voltage Solid State Body Power Supplies for CPD Gyrotrons”, SOFT’02, Helsinki, September 2002, p. 543-548.

[2] G. Taddia et alia, “High Voltage Solid State Gyrotron Body Power Supply”, 14th Joint Workshop on Electron Cyclotron Resonance Heating, Santorini, May 2006, p 95.

COMMISSIONING OF THE SPARC PHOTO-INJECTOR*

M. Bellaveglia, D. Alesini, S. Bertolucci, M. E. Biagini, R. Boni, M. Boscolo,
M. Castellano, E. Chiadroni, A. Clozza, L. Cultrera, G. Di Pirro, A. Drago, A. Esposito,
M. Ferrario, L. Ficcadenti, D. Filippetto, V. Fusco, G. Gatti, A. Gallo, A. Ghigo,
S. Guiducci, M. Incurvati, C. Ligi, M. Migliorati, A. Mostacci, L. Palumbo,
L. Pellegrino, M. Preger, R. Ricci, C. Sanelli, F. Sgamma, B. Spataro,
F. Tazzioli, C. Vaccarezza, M. Vescovi, C. Vicario (INFN/LNF);
A. Bacci, I. Boscolo, F. Broggi, S. Cialdi, D. Giove, M. Mauri,
A. Rossi, L. Serafini (INFN/Milano);
M. Mattioli, P. Musumeci, M. Petrarca (INFN/Roma1);
L. Catani, A. Cianchi, S. Tazzari (INFN/Roma2);
A. Perrone (INFN /Lecce);
L. Giannessi, M. Quattromini, A. Renieri, C. Ronsivalle (ENEA/FIS);
J. Rosenzweig (UCLA)

Abstract

The SPARC project [1] is born to perform R&D activity headed to realize SASE-FEL experiments at $500nm$ and higher harmonic generation. The project foresees the realization of a high brightness photo-injector able to produce a $150 \div 200MeV$ electron beam to drive FEL process inside a dedicated $12m$ long undulator. The machine is going to be assembled at LNF and its final configuration is made up of an RF gun, driven by a Ti:Sa laser, injecting into three SLAC type accelerating sections. Nowadays we are working in a photo-injector test phase, aiming to characterize the main hardware components and to investigate the behavior of the e-beam dynamics in the first meters of drift. To do this we utilize the emittance-meter, a home designed diagnostic device placed just after the RF gun, able to move 1.2 meters along the longitudinal axis to measure beam parameters. In this paper we report a more accurate description of the project, the status of the single systems constituting the machine and the most important results we obtained in the e-meter phase.

INTRODUCTION

The commissioning of the SPARC photo-injector is started at Frascati INFN laboratories and we are operating in a gun test phase, before installing the accelerating sections. In this phase, laser, radiofrequency, timing, control system and beam diagnostics are installed and working in the SPARC bunker. We performed a characterization of the beam at the gun exit with the home-designed movable emittance-meter [2] and a spectrometer. A picture of the hardware installed in the bunker is reported in figure 1. The most significant results are reported in table 1 that shows the two investigated main beam configurations.

Table 1: Main beam configurations

	Low charge	**High charge**
Charge	$200pC$	$900pC$
Emittance	$0.8mm\ mrad$	$2.2mm\ mrad$
Energy	$5.65MeV$	$5.55MeV$
Energy spread	1%	2.6%
Pulse length	$8ps$	$12ps$

PHOTO-INJECTOR STATUS

In the following paragraphs we will give a short description of the main systems constituting the machine.

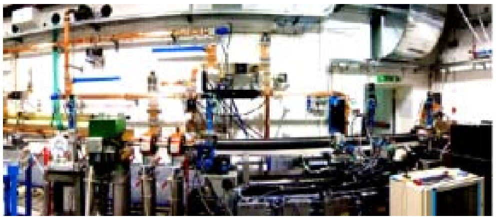

Figure 1: Picture taken in the SPARC bunker

RF and timing system

The SPARC RF system is mainly constituted by two RF chains and its scheme is reported in figure 2 together with the synchronization system layout [3]. The power sources, shown in figure 3(a), are the 45 MW peak, 2856 MHz klystrons TH2128C. The klystron n.1 presently feeds only the RF gun with $3\mu sec$ pulses and it is designed to feed also one accelerating section via a $3dB$ waveguide coupler and an RF deflecting cavity for beam diagnostic purposes.

The RF gun, reported in figure 3(b), was successfully conditioned without relevant problems and we fed into it more than $10MW$ of RF power that corresponds to an

---

* Work supported by the EU Commission in the 6th FP, contract no. 011935 EUROFEL and contract no. RII3-CT-2003-506395 CARE.

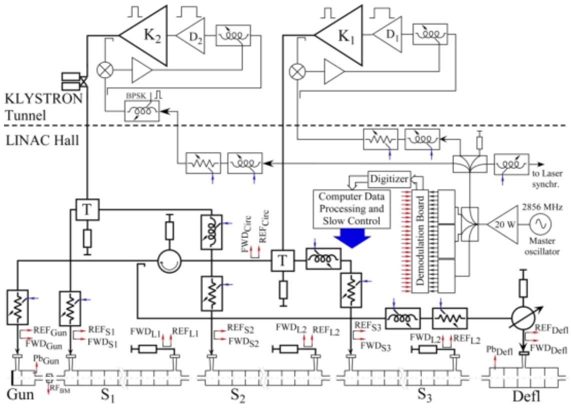

Figure 2: RF system layout

(a) (b)

Figure 3: Installed RF hardware: (a) modulators and klystrons and (b) RF gun

accelerating electric field of about $120 MV/m$. Klystron n. 2 and its waveguide distribution lines are now under test and they will feed two high gradient accelerating sections through an energy compressor that allows to obtain a $60MW$ - $0.8\mu sec$ RF pulse.

The timing distribution system is installed and it provides the $79.33MHz$ reference to lock the laser system to the RF oscillator using a home-designed frequency divider board. It also furnish the $10Hz$ repetition rate signal to the machine, synchronous with the external line and to the $2856MHz$ internal distribution.

The synchronization diagnostic is working with good and stable performances and the time jitter from each location of the machine (relative to the main oscillator) is displayed in the control room monitors. Also an RF phase feedback system was implemented to correct slow drifts due to temperature. The observed time jitter of the accelerating field inside the gun is $250fs_{RMS}$ and the laser oscillator time jitter is $350fs_{RMS}$.

Laser system

Beam dynamics simulations defined the SPARC laser system [4] specs in order to obtain $2mm\ mrad$ emittance at $100A$. The laser is a $10Hz$ CPA Ti:SA, TW system produced by Coherent. At the laser exit a THG and an UV stretcher produce the required wavelength ($266nm$) and pulse duration ($2 \div 10ps$). To manipulate the time profile an acousto-optic programmable dispersive filter is installed before the amplifier.

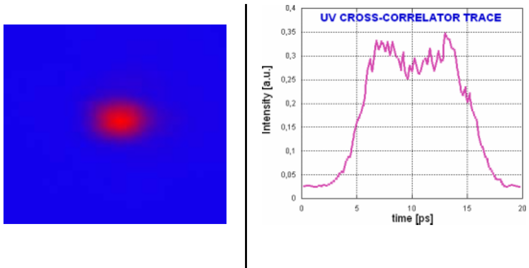

(a) (b)

Figure 4: (a) transverse laser spot on the cathode and (b) UV pulse longitudinal shape

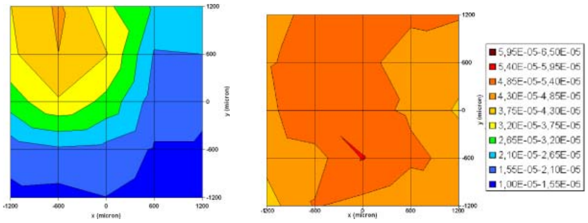

Figure 5: Cathode QE before (left) and after (right) laser cleaning

The pulse profile is flat in time and gaussian in transverse plane (with $1mm$ spot size) and an image of the spot is shown in figure 4(a). We are using a cross-correlator to investigate the longitudinal behavior of the UV pulse and a typical observed shape is reported in figure 4(b). The optical transfer line is designed to increase the pointing stability, to easily change the spot dimension and to compensate the $72°$ incidence distortions.

A laser cleaning on the cathode was performed and it has given good results, increasing the quantum efficiency from $3.75 \cdot 10^{-5}$ to $6 \cdot 10^-5$ and improving the emission uniformity as can be seen in figure 5.

Control system

The control system is perfectly working and it is ready to be extended to the SPARC full configuration. The SPARC main server with a RHEL3 operating system, is in a LTSP configuration so that the consoles are identical diskless workstations. The photo-injector device drivers are installed in industrial PCs placed in the bunker. The layout of figure 6 report the SPARC protected $1Gbit/s$ LAN architecture. Two machines form a connecting bridge from the front-end industrial PCs to the control room consoles:

- the data server: it accepts a request of information from the consoles and send them the data read from the proper industrial PC. The data can be software variables (that identify the controlled devices), sampled signals, images or information about the status of the computer itself;

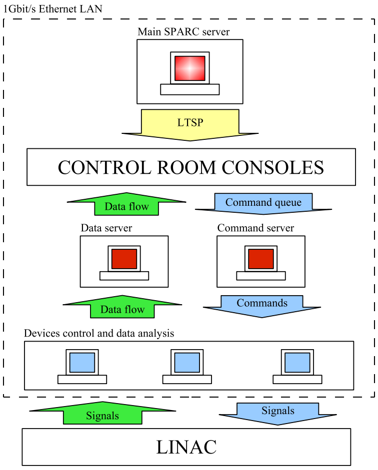

Figure 6: Control system architecture

- the command server: it elaborates the queue coming from the consoles and, once identified legal commands, it delivers them to the front-end PCs to control the photo-injector devices.

Diagnostics

Beam diagnostic devices are placed along the photo-injector as shown in figure 7 and reported in table 2. The main diagnostic tool is the home-designed emittance-meter, able to move $1.2m$ along the longitudinal axis and to study the first meters of beam propagation, where space charge effects and plasma oscillations dominate the electron dynamics.

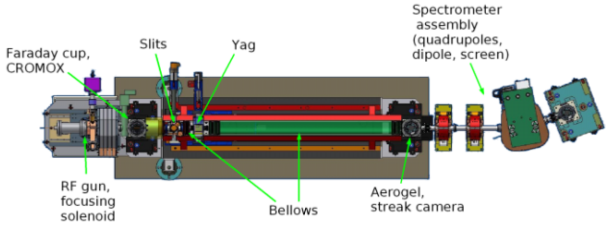

Figure 7: Photo-injector actual layout

Table 2: Diagnostic elements

Distance from cathode [cm]	Device	Measurement
60	Faraday cup, CROMOX screen	charge, beam centering
85 ÷ 200	E-meter (slits, YAG screen, CCD)	emittance, beam envelope and parameters
220	aerogel + streak camera	beam duration
250 ÷ 300	FODO cell, dipole	beam conditioning before spectrometer
250 ÷ 300	spectrometer (Yag + CCD)	energy and energy spread
350	BCM	beam charge

An exhaustive description of the measurements taken using these items is given in the next section.

BEAM MEASUREMENTS

Charge vs phase

First of all we report the charge relative to the gun RF phase measurement (phase scan) that allow us to choose day by day the optimal phase for the electron extraction and to collect information about the accelerating gradient and the quantum efficiency. Moreover this kind of measurement permit us to obtain a rough estimation of the beam duration. Picture 8 report some phase scans performed in different photo-injector working points.

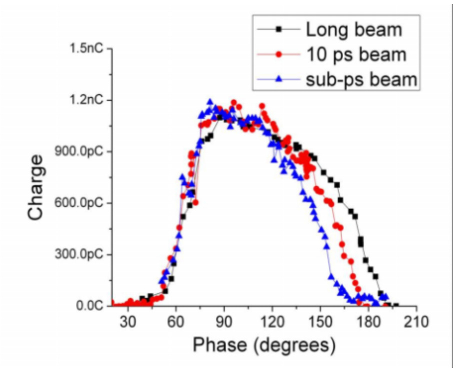

Figure 8: Charge vs phase in three different beam configurations

Energy and energy spread

A spectrometer and its transport line (constituted by a FODO cell) are placed at the end of the diagnostics chain to measure energy and energy spread. We performed these measurements in low and high charge configurations as function of the launching phase as shown in figure 9. The difference both in maximum energy and energy spread between the low and high charge case are due to longitudinal space charge effects (including the image charge at the cathode) and to the wakefield effects in the long bellows.

The presence of the emittance-meter allowed us to perform some special energy spread measurements inserting a slit in the bunch orbit and selecting a beam slice in different longitudinal locations. In fact, as shown in picture 10, we ‘froze’ the beam evolution under the longitudinal space charge and wakefield effects at different points along the beamline.

Bunch length

A longitudinal diagnostic, based on Cherenkov radiation produced by the beam passing through a $5mm$ thick aerogel slab with index of refraction $n = 1.017$, was installed with the main purpose of studying the photo-injector response to hundreds femtosecond long laser pulses created

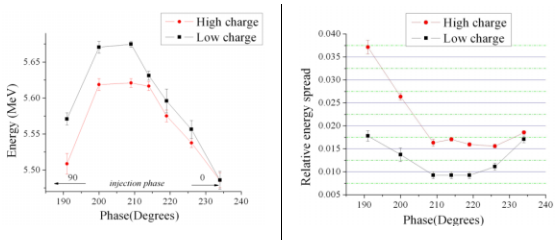

(a) (b)

Figure 9: Energy (a) and energy spread (b) for low and high bunch charge

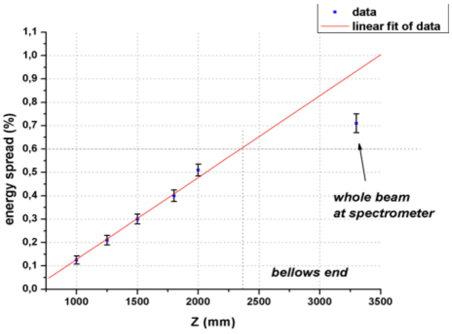

Figure 10: 'Slit' energy spread

by the Ti:Sa laser system [5]. A field-lens narrow band filtering optical system delivers the Cherenkov light to the entrance slit of a $2ps$ resolution Hamamatsu streak camera enabling pulse length measurements (see figure 11).

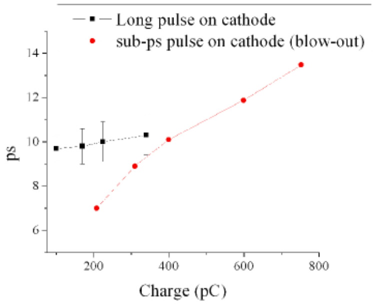

Figure 11: Bunch length measurements with streak camera

Transverse dynamics

Using the emittance-meter we were able to characterize the emittance as function of the longitudinal coordinate and to observe clear indications of emittance oscillations driven by space charge forces in the drift downstream of the RF gun, in agreement to what expected from our theoretical model and numerical simulations. Figure 12 reports two set of measurements compared with numerical simulation. The algorithm used to calculate the emittance was designed also to reconstruct the phase space and good results were achieved (see figure 13).

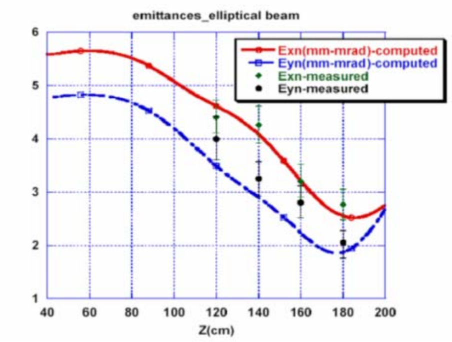

Figure 12: Emittance measurement with relative simulated curves

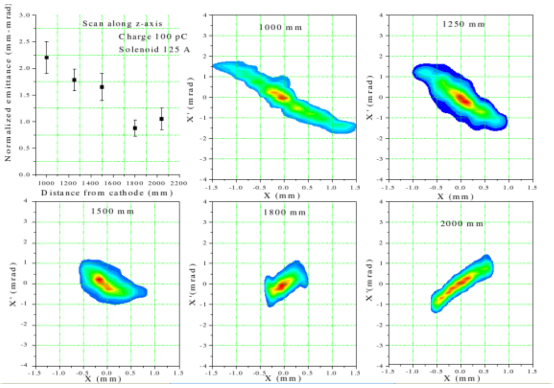

Figure 13: Phase space reconstruction

CONCLUSIONS

The SPARC photo-injector commissioning was started and a good characterization of the electron beam at the exit of the gun has been performed with the emittance-meter. In particular measurements show that the beam brightness required to drive a SASE-FEL experiment was achieved. The linac installation phase will begin at the end of this summer with the commissioning of the accelerating sections and the second RF power line. Moreover it is planned to use a SPARC-like system as photo-injector for the future SPARX X-ray FEL experiment [6].

REFERENCES

[1] D.Alesini et al., IEEE Cat. N. 05CH37623C, (2005) 1327.

[2] L. Catani et al., 'Operational experience with the emittance-meter at SPARC', these proceedings.

[3] A. Gallo et al., 'The SPARC RF Synchronization System', PAC'05 proceedings, Knoxville, May 2005, p. 1024.

[4] C. Vicario et al., 'Commissioning of the Laser System for SPARC Photoinjector', EPAC'06 proceedings, Edinburgh, June 2006.

[5] M. P. Dunning et al., 'Optimum beam creation in photoinjectors using space-charge expansion', these proceedings.

[6] D. Alesini et al., 'Status of the SPARX FEL project', EPAC'06 proceedings, Edinburgh, June 2006.

FREE ELECTRON LASER TRIGGERED PHOTO-CATHODE

E. Sabia, A. Dipace, ENEA, C.R. Portici (Napoli), Italy
G. Dattoli, ENEA, C.R. Frascati (Roma), Italy.

Abstract

The possibility of realizing a FEL triggered photocathode has been proposed long time ago and the advantages have been pointed out. In these devices the FEL can be exploited to extract electrons from a photocathode to provide a high quality e-beam. The device becomes even more appealing if photo-thermoionic cathodes can be exploited in two different phases. In the first the electrons are extracted from the cathode working as thermoionic and are used to drive a FEL oscillator, the FEL light is then used to flash the cathode which operates as a photo thermal assisted device. We comment on the possibility of using FEL triggered photocathodes to produce high quality e-beams for SASE or oscillator FEL devices. The use of the same e-beam driving the photocathode and the FEL makes the system naturally free of any synchronization problem arising when an external laser is used. Examples of interplay between the generation of electron and optical bursts are also investigated.

INTRODUCTION

In previous investigations it has been shown that FEL radiation can be exploited to trigger a photocathode gun [1], [2]. In this paper an extension to an "hybrid device" has been considered: in such a device, sketched in Fig. 1,2 a thermoionic gun produces an e-beam driving a FEL oscillator, the FEL radiation can be backward sent to illuminate the thermoionic cathode in order to exploit a different operating regime, i.e., a thermally assisted photoemission. Such a feedback mechanism, with a proper choice of the parameters, can enhance the e-beam brightness despite a modest increase of the transverse emittance.

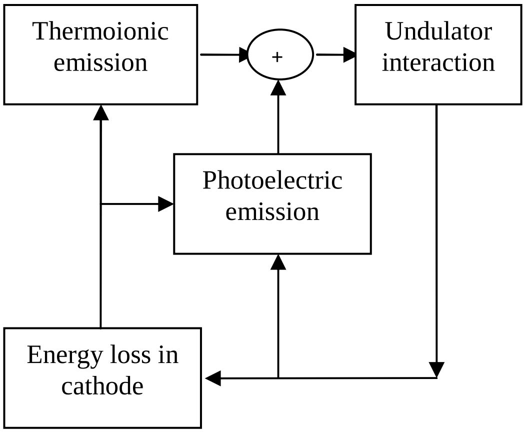

Fig. 1: Block diagram of "hybrid FEL oscillator".

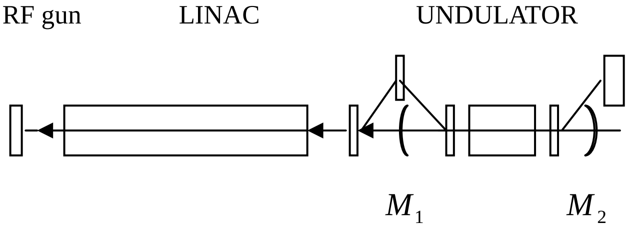

Fig.2: Layout of the "hybrid FEL oscillator".

In this paper we will consider a thermal dispenser cathode [3], with good photoelectric quantum efficiency, initially operating in the thermoionic mode and heated at a sufficient temperature in order to have enough e-beam current to allow FEL operation, radiation is then feed back to the cathode to switch it on the photo-assisted mode.

THEORETICAL MODEL

Under a number of assumptions and proper approximations that will be explained in the following, a semi-analytical model has been developed to take into account the interplay among the oscillator intra-cavity radiation growth, the temperature rise due the photonic incident energy loss in the cathode material and the electron current extracted. It has already been shown that the round-trip evolution of a FEL oscillator can be written as [4]:

$$I_n = I_0 \frac{[(1-\eta_{cl})(1+G)]^n}{1+\frac{I_0}{I_E}[[(1-\eta_{cl})(1+G)]^n-1]} \qquad (1)$$

where n is the round trip number, G the maximum small signal gain, η_{cl} the total cavity losses, I_0 the initial seed and I_E the intra-cavity equilibrium intensity given by

$$I_E = \left(\sqrt{2}+1\right)\left(\sqrt{\frac{1-\eta_{cl}}{\eta_{cl}}G}-1\right)\frac{1}{2Ng_0}P_e \qquad (2)$$

with N being the number of undulator periods, g_0 the small gain coefficient and P_e the e-beam power.

In the previous relations (1) and (2), the quantities I_0, g_0, G, P_e are no longer constant but, due to the feed-back mechanism, they are updated at each round trip.

The temperature rise due to the photonic incident energy loss in the cathode can be evaluated using the Anisimov heat equations [5], [6] which relate the electron to the lattice temperature. As suggested in [3], for time scale characteristic of laser pulse in the range 1ps-1ns, a steady state approximation of the Anisimov equation can be considered, which implies that the electron and lattice temperature are equal. Moreover, under the assumption of a laser pulse with a uniform spatial profile and a constant power of duration τ (microbunch duration) [7], at a power level such that neither melting nor vaporization occure, and by considering the heat to be generated at the surface of the cathode, we get:

$$\Delta T = \frac{(1-\eta-R)I_\lambda \tau}{\sqrt{2\kappa\rho c_v \tau}} \tag{3}$$

where η is the photoelectric quantum efficiency, κ, ρ, c_v are the thermal conductivity, the density and the specific heat of the cathode material respectively, R the cathode reflectance, τ the laser micro-pulse duration, I_λ the power laser density to the cathode.

The electron current density extracted from the cathode, using the Richardson approximation, can be obtained as a sum of 2 contributions: one proportional to the laser intensity, the other to the Richardson-Laue-Dushmann current density for thermoionic emission [3]:

$$J = (1-R)\left(\frac{e}{h\nu}\right) I_\lambda \left(\frac{U((h\nu-\phi)/kT)}{U(\mu/kT)}\right) + J_{RLD} \tag{4}$$

$$J_{RLD} = AT^2 e^{-\phi/kT} \tag{5}$$

where A is the Richardson constant, R the cathode reflectance, $h\nu$ the incident photon energy, k the Boltzmann constant, T the electrons temperature, μ the chemical potential, $\phi = \Phi - \sqrt{4QF}$ the barrier height, Φ the cathode work function, $\sqrt{4QF}$ the Schottky barrier lowering due to the image charge Q , F the product of the electric field gradient between cathode and anode and the electron charge and finally U is the Fowler-DuBridge function [8], [9].

It may be argued that since the cathode is operated as thermoionic and photocathode there is a detrimental effect due to the increase of beam emittance (both transverse and longitudinal). The emittance increase can be estimated following the recent analysis by Bazarov and Sinclair [10]. In their scaling law the transverse emittance is related to the extracted charge and bunch length :

$$\varepsilon\,[\text{mm mrad}] = q\,[\text{nC}] \cdot \left(0.73 + \frac{0.15}{\sigma_z^{2.3}[mm]}\right) \tag{6}$$

where q is the photoelectric extracted charge and σ_z is the length of the bunch.

We can estimate the amount of emittance increase by relating it to the illuminating power. An example of the relevant behaviour is given in Fig. 3.

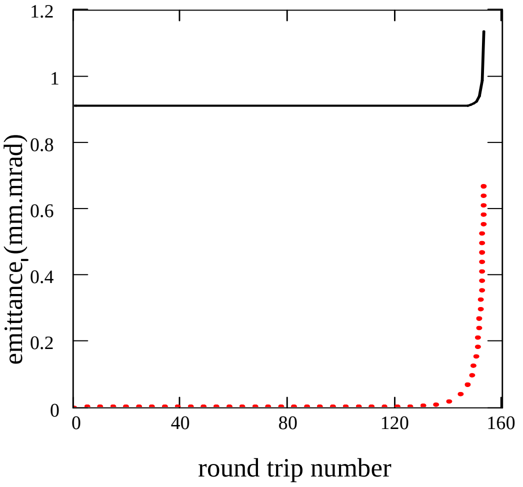

Fig.3: Emittance increase vs. round trip number (in red the photoelectric contribution, see Eq. 6, in black the total emittance) [mm mrad].

It is evident that with increasing number of reflections the emittance grows (we have assumed quadratic composition for the different emittance contributions) but the increase of current is larger and the net effect is an increase of the e-beam brightness. We must however not exceed the reflections to avoid effects of power overloading which may create a too large emittance degradation as shown in Fig. 4. It may also be argued that the Bazarov-Sinclair scaling holds for an optimized system and therefore the previous estimation may be optimistic.

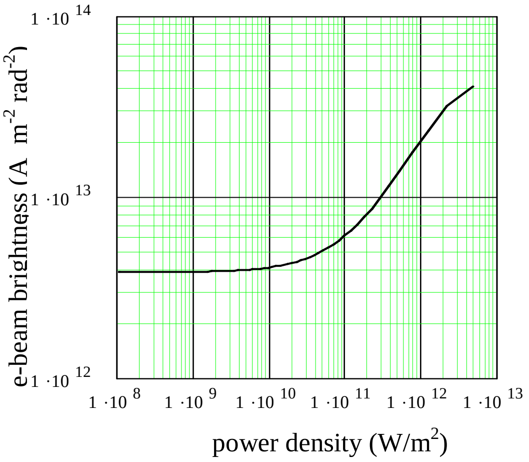

Fig. 4: e-beam brightness [A m^{-2} rad^{-2}] vs. power density [W m^{-2}]

RESULTS AND DISCUSSION

A preliminary analysis of the device has been developed using the parameters listed in Table 1 and 2

Table 1: FEL oscillator

λ	laser wavelength	500 nm
λ_u	undulator wavelength	2.8 cm
N	number of undulator periods	100
γ	e-beam energy	305.8
σ_ε	relative energy spread	10^{-3}
r	e-beam radius	$8.9\ 10^{-3}$ m
I_0	Input seed	1 W/cm^2
τ	e-beam micropulse duration	3 ps
τ_M	e-beam macropulse duration	10 μs
n	round trip number	153
δ	distance between RF gun and mirror M_1 (see Fig. 2)	20 m
L_c	resonator cavity length	10 m
η_{cl}	total cavity losses	4%
T_1	mirror M_1 transmissivity	2%

Table 2: Dispenser cathode characteristics

Sc_2O_3 in matrix of W		
Φ_w	work function	1.8 eV
ϕ	effective barrier height	1.68 eV
d	inter-electrode distance	1 cm
κ	thermal conductivity	1.78 W/cm°K
ρ	density	19.3 g/cm^3
c_v	specific heat	0.13 J/g°K
T_{in}	temperature operation before first illumination	1300 °K

The example we have considered is a FEL oscillator in which the distance between the cathode and the first semitransparent mirror M_1 (see Fig. 2) is 2 times the length L_c of the resonator cavity. The system is designed in such a way that for the first 3 round trips the intra-cavity radiation grows according to the Eq. 1 with constant parameters (I_0, g_0, G, P_e), then Eqs. 1, 2, 3, 4 and 5 are fully coupled.

In our example we have considered 153 round trips which ensure, as already remarked

- Increase of the bunch current.
- Increase of the e-beam brightness despite a modest increase of the transverse emittance (this last point deserves however a dedicate analysis including the contributions from the longitudinal and transverse shapes of the optical bunch).

In Fig. 5, 6 and 7 the time evolution of cathode temperature, e-beam current density and laser intensity are shown respectively.

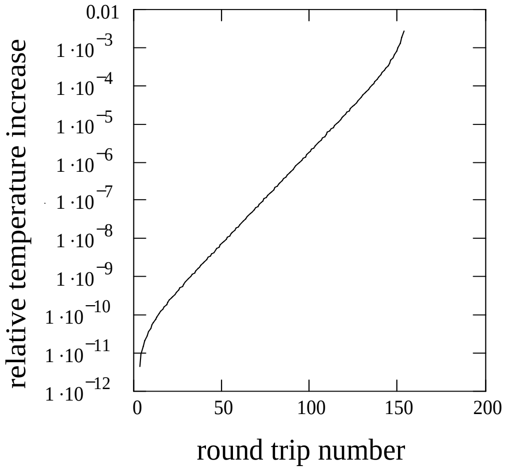

Fig. 5: Relative temperature increase vs. round trip number.

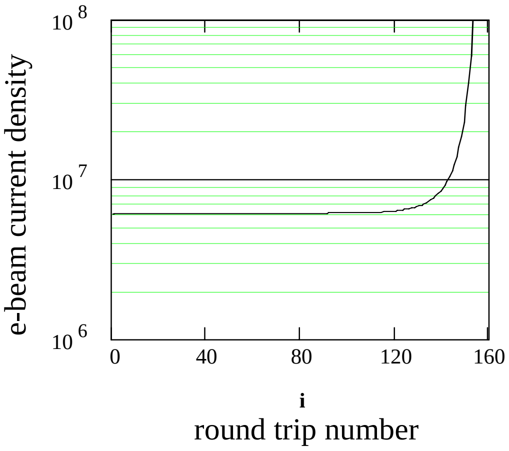

Fig. 6: E-beam current density [A m^{-2}] vs. round trip number.

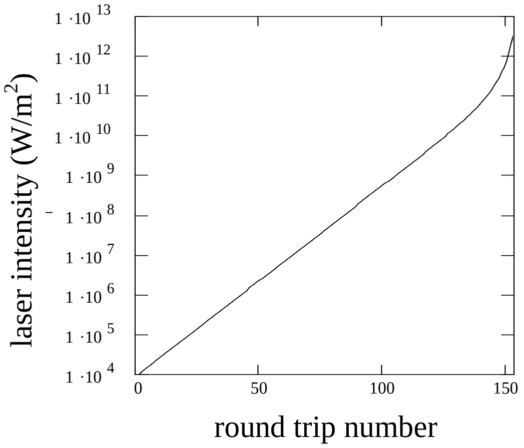

Fig. 7: Laser intensity [W m^{-2}] vs. round trip number.

CONCLUSIONS

A different possibility has been discussed in a previous paper [11] in which a hybrid SASE FEL has been considered: the radiation inside the undulator may be collected with a mirror (if we consider radiation in the visible) and sent back to the cathode. This has not a feed back on the radiation and it is just an external passive device. We must underline that for this device the radiation grows from the noise and the optical spectrum may be dominated by spikes and energy fluctuations, thus inducing dangerous effects which may strongly affect the quality of the e-beam itself. On the contrary, the use of the resonator cavity, acting as an active feed back on the optical field, may eliminate all the problems due to the shot noise, and the length of the optical pulse can also be easily controlled as well as other problems due to the transverse distribution.

It is worth noting that the technique we have considered can be exploited for higher harmonics of the radiation. It is indeed well known that along with the fundamental higher order harmonics are generated in the optical cavity. The harmonic power is not stored in the cavity but it is emitted shot after shot. The harmonic radiation too can be exploited to irradiate the cathode. This different operation will be more deeply examined in a forthcoming investigation.

REFERENCES

[1] G. Dattoli, L. Giannessi, and L. Serafini, J. Appl. Phys., 93,1 (2003).
[2] G. Dattoli, L. Giannessi, A. Renieri, A. Marino, and L. Serafini, Appl. Phys. B: Photophys. Laser Chem. B55, 446 (1992).
[3] K.L. Jensen, D.W. Feldman, M. Virgo, P.G. O’Shea, Phys. Rev. Special Topics, 6, 083501 (2003).
[4] G. Dattoli and P.L. Ottaviani, Opt. Commun. 204, 283 (2002).
[5] S.I. Anisimov, B.L. Kapeliovich, T.L. Perelman, Zh. Eksp. Teor. Fiz., 66,776 (1974) (Engl. Transl. 1974 Sov. Phys.-JETP,39,375).
[6] N.A. Papadogiannis, S.D. Moustaizis, J.P. Girardeau-Montaut, J. Phys. D: Appl. Phys. 30,2389 (1997).
[7] J.H. Bechtel, J. Appl. Phys., 46, 1585 (1975).
[8] R.H. Fowler, Phys. Rev. 38,45 (1931).
[9] L.E. DuBridge, Phys. Rev., 43,727 (1933).
[10] I.V. Bazarov and C.K. Sinclair, Phys. Rev. Special Topics-Accelerators and Beams 8, 03402-1 (2005).
[11] E. Sabia, G. Dattoli, A. Dipace and G. Messina, submitted to J. Appl. Phys.

SUB-PICO-SECOND TRIGGER SYSTEM FOR THE SCSS PROTOTYPE ACCELERATOR

Yuji Otake[A)], Hirokazu Maesaka [A)], Takashi Ohshima [B)], Naoyasu Hosoda[B)],
Toru Fukui [B)], Toru Ohata [B)], Tumoru Shintake [A)]

[A)] RIKEN, Harima Institute 1-1-1 Kouto, Sayo-tyou, Sayo-gun, Hyogo, 679-5148, Japan
[B)] Japan Synchrotron Radiation Research Institute (JASRI/SPring-8)
1-1-1 Kouto, Sayo-tyou, Sayo-gun, Hyogo, 679-5198, Japan.

Abstract

To verify the feasibility of X-FEL using an 8 GeV linac, the 250 MeV SCSS prototype accelerator was built at SPring-8. A sub-pico-second time jitter was set as a development target for the timing system of the prototype accelerator, because of its beam pulse width of several pico-seconds. This jitter value had a possibility to be achieved by the present technology. In accordance with the target, we developed a very low-noise reference signal source that generates 238 MHz and 5712 MHz RF signals for acceleration, a master trigger VME module having output pulses synchronized to 238 MHz, and a trigger delay VME module synchronized to 5712 MHz. The time jitters of the delay module are less than 700 fs, and the SSB noise of the 5712 MHz reference signal source is less than -120 dBc at 1 kHz offset. These values are sufficient for our present requirement. A beam energy variation of 0.06% was achieved by the timing system. The beam stability based on AM noise theory in the FEL linac is discussed based on the above data.

INTRODUCTION

The SASE (Self Amplified Spontaneous Emission) X-FEL project at RIKEN HARIMA Institute is now under way.[1] The important component of the project is an accelerator, having an energy of 8 GeV, which comprises a 500 kV thermonic electron gun, a 238 MHz sub-harmonic buncher, a 476 MHz booster, a 2856 MHz booster and 2856 MHz accelerating structures, 5712 MHz accelerating structures with an accelerator field of 32 MV/m, and in-vacuum undulators. To evaluate the feasibility of X-FEL, a 250 MeV prototype accelerator, including the main key elements of the above-mentioned linac (not a full number of the elements), at SPring-8 was constructed by November, 2005, and is under beam testing to generate SASE VUV-FEL.

To generate a stable VUV laser in the prototype linac, an accelerated electron beam with a pulse width of less than 1 ps should pass through an orbit within one hundred micrometers for the undulator section having a length of 12 m.[2] The energy stability of the beam is in the order of 10^{-4}, and the timing jitter of the trigger pulses to accelerator instruments is less than 1 ps were required to archive the orbit and the stable beam pulse width in a bunch compressor, which means the constant peak current of the beam to generate stable laser light. Therefore, we employed a timing jitter and a drift of less than 1ps, as development targets. This is because the beam energy variation of 10^{-4} corresponded to a phase change of about 1 deg. (about 500 fs) in 5712 MHz RF acceleration at the crest point. For the present, in the case of the prototype accelerator, these targets are sufficient for generating and amplifying 60 nm light with about a 1 ps pulse width. In accordance with the targets, we have developed the timing system of the prototype accelerator as shown in Fig. 1. In this system, the final time jitters and drift of the accelerated electron beams, which are directly connected to the energy variation, are decided by the synchronization accuracy of the trigger delay, and the SSB noise of RF instruments, such as a signal source. The long-term drift of the timing is reduced by a feedback control. Therefore, to decrease the SSB noise and to realize a less than 1ps time jitter were set as the main purposes of our instrument development to make the system. This paper describes how to realize these purposes.

TIMMING CONTROL SYSTEM

System Configuration

The configuration of the timing system of the SCSS prototype accelerator is shown in Fig. 1. The timing system comprises a master trigger VME module synchronized to a 238 MHz RF signal and also synchronized to a commercial AC of 60 Hz, a very low-noise signal oscillator to generate 238 and 5712 MHz RF signals as a time reference, a 10 W RF amplifier to amplify the RF signals for signal transmissions, RF signal distributors, a trigger transmission system using 100 Ω differential cables with LVDS (Low Voltage Differential Signaling), and trigger delay VME modules synchronized to both acceleration RF signals of 238 MHz and 5712 MHz.

Master Trigger VME Module

The circuit configuration of the master trigger VME module is shown in Fig. 1. The module comprises a FPGA including 24-bit counters of eight channels, which are driven by a 238 MHz clock signal. The output pulse is also resynchronized by a fast flip/flop working by the 238 MHz clock to reduce the time jitters. The main function of the modules is to generate a trigger pulse train from 1 Hz to 60 Hz for activating the accelerator components, such as the klystron modulators. The pulses are also synchronized to a commercial AC line, and distributed to the components.

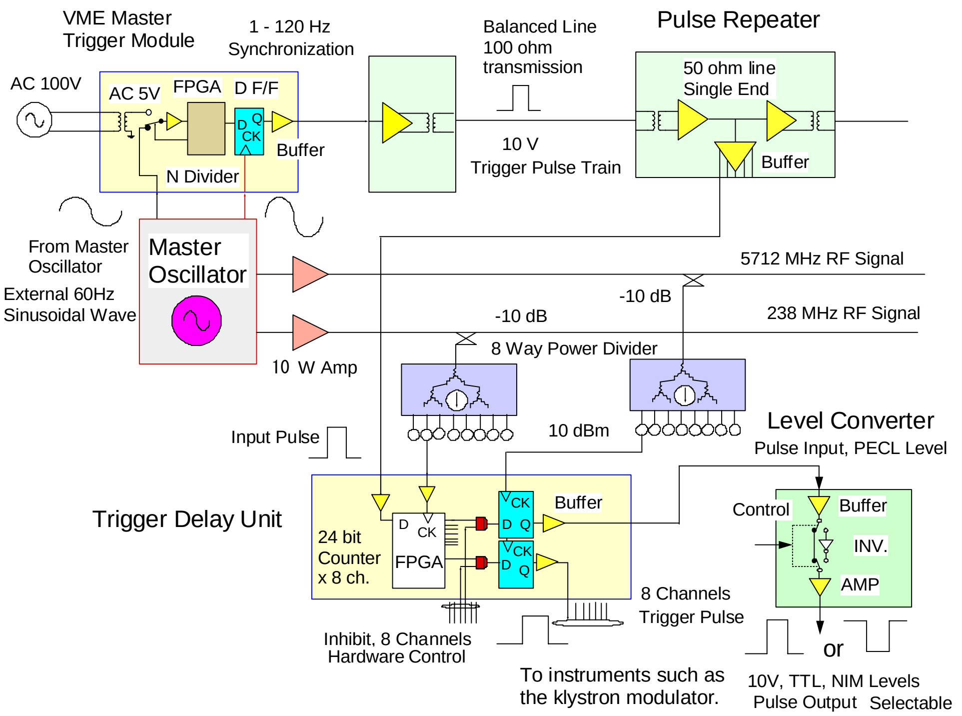

Fig. 1. Trigger system of the SCSS prototype accelerator.

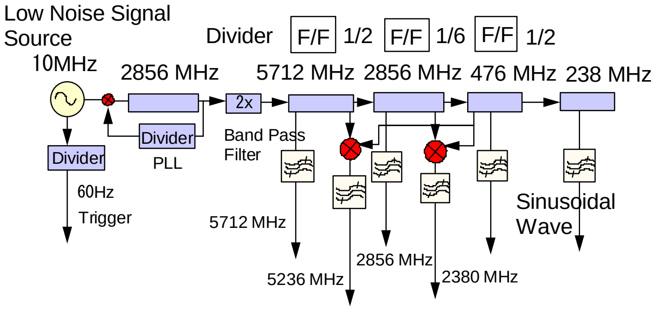

Fig. 2. Circuit diagram of the master oscillator. The signal source uses frequency dividing, a very low-noise power supply and the PLL connection between the 10 MHz and 2856 MHz sources to achieve a low noise.

Master Oscillator

The master oscillator, which generates 238, 476, 2380, 2856, 5236, and 5712 MHz stable RF signals, is a time reference source. The circuit configuration of the oscillator is shown in Fig. 2. It comprises a very stable reference generator (stability of 10^{-11}) of 10 MHz, which has a low-noise characteristic in the frequency region below 1 kHz measured from 10 MHz, a 2856 MHz signal generator having a low noise characteristic in the frequency region over 1 kHz measured from 2856 MHz, a frequency doubler instrument to make 5712 MHz from 2856 MHz, and frequency dividers to generate the above-mentioned frequency signals. Both low-noise signal generators are connected by a PLL (Phase Locked Loop) circuit to make the very low SSB (Single Side Band) power noise over the whole frequency range, as shown in Fig. 3. The noise level is -140 dBc at 1 MHz measured from 2856 MHz. The most important feature is that the signal source uses the frequency-dividing method, a very low-noise power supply (-150 dBV), and the above-mentioned PLL connection. The other important function is to decrease the effect of the environmental temperature around the master oscillator. For achieving this function, a temperature controller using a heater to eliminate the temperature variation within +/- 0.1 °K was employed.

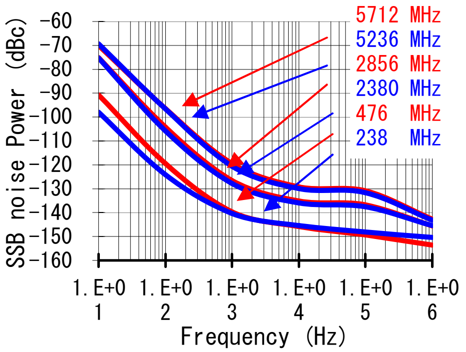

Fig. 3. SSB noise power spectrum of the master oscillator. The decreasing noise level at individual frequencies is proportional to the dividing ratio.

Differential trigger pulse transmission system

Our trigger system employs a trigger-pulse repeater including the function of a differential trigger pulse transmission of LVDS to reduce the influence of noise. The twisted-pair cable to transmit LVDS has a characteristic impedance of 100 Ω to easily adapt to the usual 50 Ω circuit without any signal reflection. The temperature dependence of its electrical length is about 100 ppm, which does not exceed quarter wavelengths of

238 MHz under the conditions of the usual temperature variation for a day and a length of several ten meters used in the prototype accelerator. The repeater, as shown in Fig. 1, can interconnect between the other two repeaters separated by more than 10 m. One port of the repeater is input from the previous repeater, and the other port is output to the following repeater. The repeater also has a function to distribute 8 trigger pulses of LVPECL (Low Voltage Positive Emitter Couple Logic) from the master trigger module to the trigger delay VME modules.

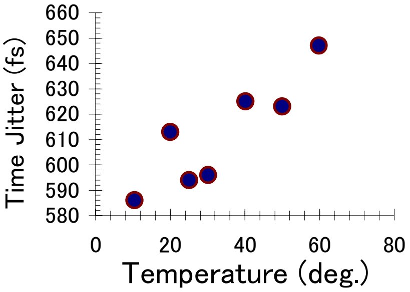

Fig. 4. Measurement result of the time jitters of the trigger delay unit. The jitters (rms) are less than 1ps, which satisfies our requirement. The temperature dependence of the jitter is very low.

Trigger delay unit

The trigger delay unit is the main instrument of our trigger system, and the VME module, as shown in Fig. 1. The circuit of the module comprises a FPGA having 8 counters with 24 bits driven by the 238 MHz RF signal, fast flip/flops, and a temperature controller using a heater to stabilize the temperature of the flip/flips circuit within +/- 0.1 ^{o}K. The output pulses of the FPGA are resynchronized by fast flip/flops working by the 5712 MHz signal to realize sub-picosecond time jitters referred to the acceleration RF. The outputs of the delay unit have a voltage level of LVPECL to decrease jitters. A jitters measurement used to evaluate the module was carried out; Fig. 4 shows the result of the measurement to a 5712 MHz signal dependent on the temperatures. The result shows that the jitters are about 700 fs (rms). In addition, a delay time change of the unit dependent on the temperature was about 400 fs/ ^{o}K (rms).

Level converter

The accelerator comprises many instruments, equipping such various trigger voltage levels as TTL, NIM, and 10V, for historical reasons. However, the output of the delay unit is LVPECL. Therefore we developed an eight-channel level converter to change from the output voltage level of the delay unit to the input levels of the instruments (Fig. 1).

RF distribution and 10 W RF amplifier

To drive the VME modules related to the trigger system (Fig. 1), the RF signals generated with the master oscillator must be transmitted. This signal transmission guarantees synchronization of the whole accelerator system to achieve the stable generation of FEL light. Phase-stabilized RF cables having an electrical length variation of 5 ppm/^{o}K were employed to transmit such signals as 5712 MHz for about more than 20 m. By considering the RF loss of the cables, RF amplifiers, having PLL, ALC and 10 W outputs were used. The amplifier was cooled by water to stabilize the temperature within +/- 0.5 ^{o}K. For distributing many RF signals of about 1 mW to drive the trigger instruments, RF distributors handling the 238 MHz and 5712 MHz signals were developed. The phase variation of the distributor dependent on the temperature was decreased by such design work as choosing an RF divider with a low thermal effect. The thermal phase variation of the amplifier and the distributor were 0.8 deg./^{o}K and 0.28 deg./^{o}K at 5712 MHz without PLL.

SUMMARY AND DISCUSSION

In the SCSS prototype accelerator, we finally obtained a fruitful result: a beam energy stability of less than 0.06 % at the exit of the S-band accelerating structure (at 50 MeV). This accelerated beam almost stably drove a SASE of 53 nm in the undulator section. The measured time jitter of the accelerated beams to the acceleration RF, which was directly connected to the energy variation, was less than 340 fs (rms). The measured jitter of the delay unit was about 700 fs (rms). These jitter values satisfied our requirement.

These jitters were mainly determined by the rise time of a pulse of the synchronization clock for the delay unit and the SSB noise of the RF signal. To realize the sub-pico-second jitters, we employed a clock signal of 5712 MHz, and very low-noise signal sources of 238 MHz and 5712 MHz.

The influence of the SSB noise on the beam energy variation and the time jitters of the beams is not very clear. Therefore, we want to discuss the verification of the SSB noise effect to the beam energy stability in the prototype accelerator. The effect, that is the time-domain voltage variations, of the SSB noise to an RF pulse in an accelerating structure is calculated by integrating the SSB noise amplitude for a certain frequency band width.[5] In general, a carrier signal including SSB noise is expressed, as shown in Fig. 5-A, and as the rotating vector of the noise at the top end of the carrier wave vector. The AM and FM modulations generated by the SSB noise are an equivalent. To calculate the energy variation of the beam caused by the amplitude and phase variation on a CW RF signal, the integration span on the frequency axis of the SSB noise graph is from less than 1 Hz to several more figures of the frequency corresponding the filling time of an accelerating cavity. If this integration span is applied to the calculation in the case of our accelerator with the 5712 MHz RF pulse of 2 μs (f_p = 0.5 MHz) width, the time-domain noise level on the pulse increases by more about 7 digits compared to the noise level of -140 dB at f_p in Fig. 3. In this calculation, the voltage variation on the pulse is near 0.1%. This value should be over estimated, if the other noises generated by the accelerator components are taken into account of. We can not explain the present beam energy stability of 0.06%. For these reasons, the frequency span of the integration should be limited to the case of pulsed RF acceleration.

In this paper, we do not consider a beam energy variation below a reputation frequency of 60 Hz in our accelerator, because it can be eliminated by feedback control. Here, we consider the SSB noise components around f_p, which do not change the base level of the RF pulse, and only change the amplitude of the pulse. This SSB noise effect to the beam energy change is assumed as shown in Fig. 5. In the case of the frequency components over f_p, (Fig. 5-C), the effects of the noise, which is expressed as odd functions (f_{h2} ---) mixed on the RF pulse, are cancelled by integration of the accelerating force, when the beam passes through in the accelerating structure. However, the even components ($f_{h1,}$, f_{h3} --- f_{hn}), like Fig. 5-C, are not cancelled, and have an influence on the energy variation, which is inversely proportional to the frequency. In the lower frequency components, measured from the RF pulse frequency, f_p, the effect of the noise components to the pulse decreases in proportion to the frequency, because of a constant pulse width. The slope of the amplitude variation of individual frequency components ($f_{l1,}$, f_{l3} ---- f_{ln}) of the noise within the pulse width decreases in proportion to the frequency, as shown in Fig. 5-B.

The integration of the SSB noise to estimate the effect, $N(t)$, to the beam energy variation could have a factor of 1/2, which corresponds to the influence of the even functions, and the weight functions reflecting the above mentioned frequency dependence. By an assumption based on the above-mentioned discussion, we can consider the flowing equations. In the case of a higher frequency, f, than f_p, the equation is

$$N(t) = \int \frac{1}{2} w(f) N_{SSB}(f)df \qquad f \geq f_p . \qquad 1)$$

At a frequency lower than f_p, the equation is

$$N(t) = \int w(1/f) N_{SSB}(f)df \qquad f < f_p . \qquad 2)$$

The equations are integrating the SSB noise, $N_{SSB}(f)$, times the weight functions, $w(f$ or $1/f)$, having a linear peak shape like Fig. 5-D. For describing the above-mentioned method by another way, we can also consider applying the square window function (RF pulse) in a time-domain to the SSB noise, to calculate FFT.[6]

The RF amplitude and phase variations in the accelerating structure of the prototype accelerator were estimated by integrating the 5712 MHz noise spectrum of Fig. 3 with the weigh functions described in Fig. 5-D. The result of the integration for a frequency span between 1 Hz and 1 MHz was that the amplitude variation was 0.01% and the phase variation was 0.06 deg (about 30 fs). These values were ten-times smaller than the values that were integrated without the weight functions. From these results, we can explain the 0.06% energy variation of the prototype accelerator with the noise caused by the other components by using the above-mentioned method. The 30 fs time variation is enough for our requirement.

REFERENCES

[1] SCSS X-FEL Conceptual Design Report, 2005.

[2] Dr. T. Tanaka, private communications.

[3] M. Cohlus et al., Bunch Compression Stability Dependence on RF Parameters, Proc. The 27th FEL conf., 250-253, USA, 2005.

[4] SCSS X-FEL Conceptual Design Report, pp 81-89,2005.

[5] S. Goldman, Frequency Analysis, Modulation and Noise, DOVER, pp 211-215, 1967.

[6] T. Koshikawa, Introduction of Signal Analysis, Kindai Kagakusya pp25-30, 2001, in Japanese.

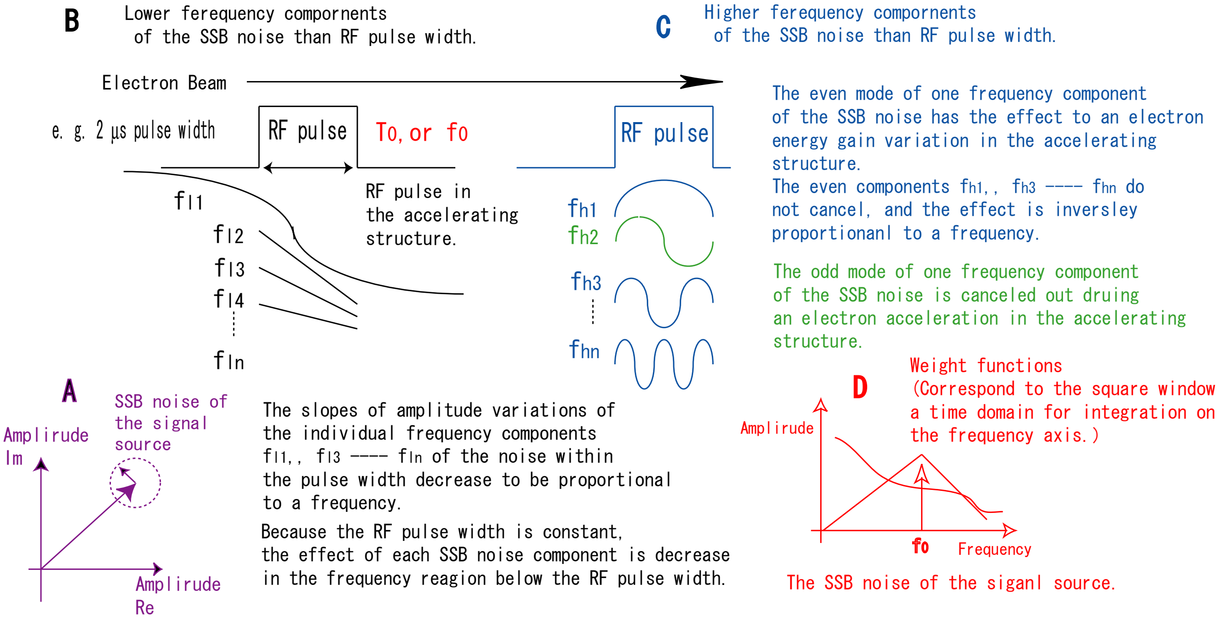

Lower ferequency compornents of the SSB noise than RF pulse width.

Higher ferequency compornents of the SSB noise than RF pulse width.

The even mode of one frequency component of the SSB noise has the effect to an electron energy gain variation in the accelerating structure.
The even components fh1,, fh3 ---- fhn do not cancel, and the effect is inversley proportionanl to a frequency.

The odd mode of one frequency component of the SSB noise is canceled out druing an electron acceleration in the accelerating structure.

The slopes of amplitude variations of the individual frequency components fl1,, fl3 ---- fln of the noise within the pulse width decrease to be proportional to a frequency.

Because the RF pulse width is constant, the effect of each SSB noise component is decrease in the frequency reagion below the RF pulse width.

Weight functions (Correspond to the square window in a time domain for integration on the frequency axis.)

The SSB noise of the siganl source.

Fig. 5. SSB noise effect on the RF pulse in the accelerating structure.

LASER PULSE LENGTH DEPENDENCE OF BEAM EMITTANCE OF PHOTOCATHODE RFGUN

H. Dewa, T. Asaka, H. Hanaki, T. Kobayashi, A. Mizuno, S. Suzuki, T. Taniuchi, H. Tomizawa, and K. Yanagida, SPring-8, 1-1-1 Kouto, Sayo-cho, Sayo-gun, Hyogo-ken 679-5198, Japan

Abstract

Laser pulse length and laser shape should be optimized to minimize the beam emittance of photo-cathode RF-gun. A 3-D particle tracking simulation predicted the smallest beam emittance could be obtained with the square laser pulse length of about 20 ps. To examine the effect of the laser pulse length to beam emittance, the square laser pulse of 10 and 20 ps was generated with laser pulse stacking of 2.5-ps micro pulses and each beam emittance was measured at the low beam charge of 0.4 nC/pulse. The measured beam emittance was not significantly different each other.

Then beam emittance was measured at the higher beam charge of 1.0 nC/pulse. The minimum beam emittance with 20-ps laser pulse was 2.3 πmmmrad with 0.8mm x 1.0 mm elliptical laser profile. Although we also tried to measure the beam emittance with 10-ps laser pulse, the beam charge of 1.0 nC could not be generated at the same laser spot size due to probably space charge limit. The measured beam emittance for 20-ps laser pulse was smaller than the minimum beam emittance 3.0 πmmmrad for 10-ps laser pulse measured under different laser condition, especially micro pulse of 1.0 ps and laser spot diameter of ø 1.0 mm.

Although we could not compare the laser pulse 10 ps and 20 ps at the equivalent conditions in high charge region, these experimental results would indicate at least the possibility of using long laser pulse about 20 ps to minimize the beam emittance for beam charge around 1.0 nC.

INTRODUCTION

The electron source for several XFEL projects [1-3] requires very low emittance beam as low as 1 πmmmrad. To minimize the beam emittance of a photocathode RF-gun, the laser pulse shape should be optimized three-dimensionally. The transverse shape could be modified with a microlens array [4] or a deformable mirror (DM) [5]. As well as the transverse shape, the longitudinal shape can be also modified with a spatial light modulator [5,6] or pulse stacker described in this paper. Beam emittance of 1.2 πmmmrad for 1 nC/pulse has already realized by J. Yang et. al. with square 9-ps laser pulse [6].

So far, we demonstrated transverse shape optimization and low emittance beam generation of 1.7 πmmmrad at the electron charge of 0.1 nC [5]. The beam emittance at high charge was, however, much larger, because the laser pulse length is too short (5 ps) and the diameter was 1mm (top hat) and therefore the charge density was too high.

In this paper, we tested longer laser pulse of 10-ps and 20-ps square generated with laser pulse stacker to get low emittance in high charge region. Three stages of pulse stacking generated 20-ps pulse from eight micro pulses. The purpose introducing longer laser pulse is to keep the laser beam size small but decrease the charge density. The small beam size contributes to decreasing the initial emittance, and small charge density to the space charge effect. Therefore, long laser pulse is effective especially in high charge region. A 3-D particle tracking simulation predicted smaller beam emittance could be obtained with the laser pulse length of about 20 ps at 1nC/pulse as shown in Fig. 1. It also predicted electron bunch length can keep around 10 ps with both 10 and 20-ps laser pulse length due to bunch length compression in the RF cavity.

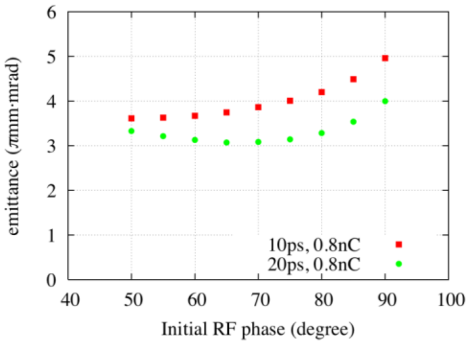

Figure 1: Beam emittance of the photo cathode RF gun for 10 and 20-ps laser square pulse length calculated with a 3-D particle tracking simulation. In the calculation, the laser spot diameter was 1.6 mm (top hat) and the maximum electric field on the cathode was 135 MV/m.

LASER PULSE STACKING

Pulse stacker is composed of sets of half-wave plates and polarizing beam splitter cubes. The fully s-polarised pulse laser is rotated to 45 degrees polarised pulse with a half-wave plate. It is divided into an s-polarized pulse and p-polarised one with a polarizing beam splitter. The p-polarized pulse is delayed with an optical delay line and then combined with the s-polarized pulse after another polarized beam splitter. Finally, as shown in Fig. 2, the laser pulse of 2.5 ps was stacked with optical delay at each stage to generate longer square pulse. With three stages, we can obtain 20-ps square pulse.

The polarizing beam splitter cubes used in the first and second stage is optical contact type (produced by Showa Optronics) considering the high power density of the UV laser. The polarizing beam splitter used in the third stage is bonded with optical cement, because the power density

---

#dewa@spring8.or.jp

is lower at the stage. The diagram of the optical system is shown in Fig. 3.

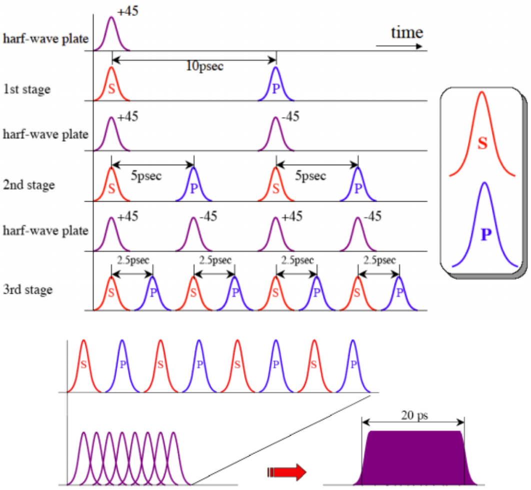

Figure 2: Timing chart of pulse stacking

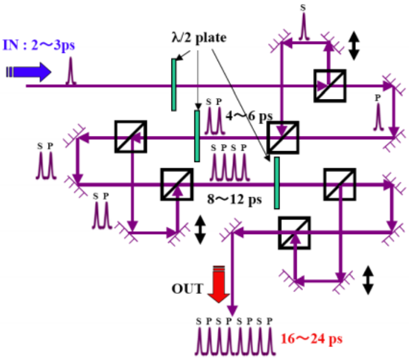

Figure 3: Optical system of laser pulse stacker (three stages)

PULSE LENGTH CONTROL

Finding the origins of optical delay lines

To generate long pulse without any timing gap or overlap, origins of the optical delay lines must determined with a precision less than 1 ps. The origin is defined here as the position of micrometer in the delay line such that the s-polarization and p-polarization pulses reach the cathode at the same time. The way that determines the origin is as follows. The energy of the electron pulse was measured for two laser pulses divided by each stage of the pulse stacker. The energy of the electron beam is measured as beam position on a profile monitor after a bending magnet downstream the RF-gun cavity. To eliminate the positioning jitter and short time drift, the beam positions were measured for 5000 times. The micrometer for p-polarized pulse was tuned as these two electron beam pulses come to the same position on the profile monitor after 3-5 times iterations. The timing precision of the origin was about 0.5 ps estimated from the position jitter distribution.

Setting of optical delay lines

After setting the origins of three micrometers, the position of these micrometers are determined by simple calculation. For example, if the pulse length is 20 ps, the micrometer positions are set as follows,

Position for 1st stage: origin - 1.5mm
Position for 2nd stage: origin - 0.75mm
Position for 3rd stage: origin - 0.375mm.

The stacked laser pulse was finally checked by the beam energy distribution on the profile monitor with illuminating all eight micro pulses. The energy distribution of the beam is shown in Fig. 4. At an optimum phase (85 degree), the beam focuses on the profile monitor. When RF phase is 44 degree, the energy dispersion was made purposely larger to evaluate stacking pulse structure. The uniformity is not ideal but there are not any gaps and strong hot spot in the distribution. Therefore, the eight micro pulses are thought to be stacked properly. The incomplete uniformity mainly comes from the insufficient flatness of energy among the laser micro pulses.

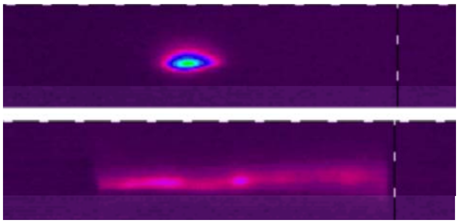

Figure 4: The energy distribution on the profile monitor for the 20-ps laser square pulse at different RF phase. Top: RF phase at 85 degree (3.52 MeV @center), Bottom: RF phase at 44 deg (3.29MeV @center)

The information of the pulse length of the micro pulse can be also obtained from this measurement. When the micro pulse was around 1.5 - 2.0 ps, five strong spots were observed on the profile monitor as shown in Fig. 5. These spots come from overlapping on the edges of two micro pulses. Not all energy spots are seen on the profile monitor, because of small screen. The number of the spot was found to be totally seven when the RF phase was moved.

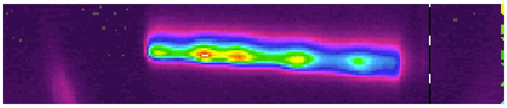

Figure 5: The energy distribution on the profile monitor for the 20-ps laser pulse, when the micro pulse is around 1.5 -2.0 ps.

Simulation results of the energy distribution for micro pulse lengths of 1.5 ps and 2.5 ps are shown in Fig. 6.

There are seven spots for the case of 1.5 ps, while there is not any strong spot for the case of 2.5 ps.

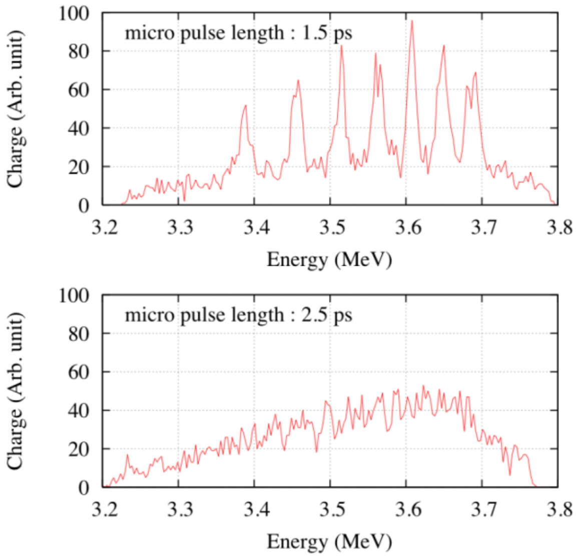

Figure 6: Simulated of the energy distribution for micro pulse length of 1.5 ps (Top) and 2.5 ps (Bottom).

BEAM EXPERIMENTS

Laser distribution and electron beam charge

The laser pulse energy of eight (20 ps) and four (10 ps) micro pulses was tuned by the angle of half-wave plates to get the beam charge of 0.4 nC and energy flatness. The results are shown in Fig. 7.

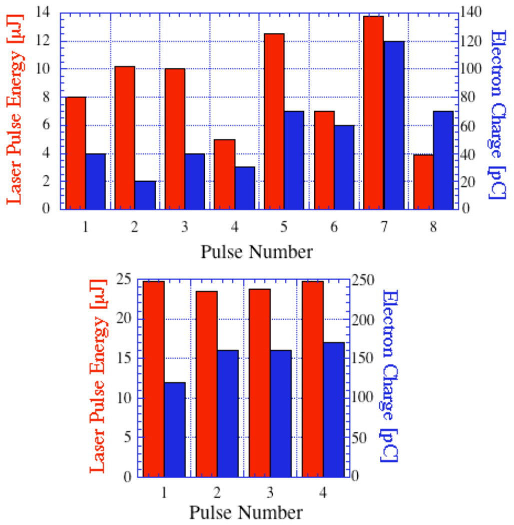

Figure 7: The laser pulse energy and electron beam charge of micro pulse for 20-ps (Top), and 10-ps pulse structure (Bottom).

The 20-ps pulse was generated with pulse stacker of three stages, and 10 ps with first two stages. The energy flatness for 20 ps is worse than 10 ps. The polarizing beam splitter of the third stage could not divide the two pulses ideally because it is bonded with optical cement and the energy loss of p-polarization pulse is larger at higher intensity.

There is a difference in total pulse energy to get the same charge of 0.4 nC; 70.4 μJ for 20 ps and 96.6 μJ for 10 ps. This is due to both of the Schottky effect and space charge limit. These effects is not theoretically calculated but can be understand from the facts that four micro pulses in 10-ps pulse individually generate increasing charge of 0.12, 0.16, 0.16, 0.17 nC, but generate only 0.4 nC with all four pulse at the same time.

Setup of Beam emittance measurements

The electron beam generated from the RF gun was accelerated to 26 MeV with a 3m-long accelerating structure. The beam emittance was measured with quad scan downstream the accelerating structure [7].

When we operate quad scan to measure the beam emittance, the beam size must be measured at the resolution of the order of 10 μm. To realize the fine resolution, we adopted a profile monitor with a thin screen and high resolution CCD camera. The screen is an alumina fluorescence sheet (Desmarquest AF995) with the thickness of 0.05 mm. The CCD camera is 1.3-mega pixels camera (SONY XCD-SX910). It has a 1/2-inch CCD chip with 1280(H) x 960 (V) pixels, and each pixel size is 4.65 x 4.65 μm^2. To get a large depth of field, we used a telecentric lens of 1/4 magnification. The estimated resolution of the image is about 20-30 μm. Only center quadrupole magnet of the triplet quadruple magnet was used to focus the beam on the screen with quad scan. The setup of the quad scan measurement is shown in Fig. 8.

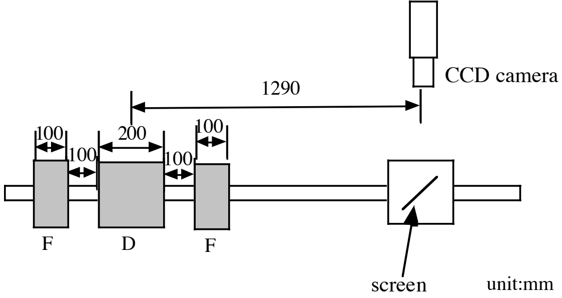

Figure 8: Setup of quad-scan measurement.

The emittance measurement was automatically executed in about 5 minutes if the measurement points were less than 15. The automatic measurement system was programmed with Labview 7.1 and Vision developing module (National Instruments Co.).

Beam emittance measurements

Beam emittance for 10 and 20-ps laser pulse was measured in low charge region of 0.4 nC/pulse. The current of solenoid coils were optimized to get minimum beam emittance. The laser shape was elliptical (0.8 mm (H) x 1.0 mm (V)). In this experiment, the optimization of DM could not executed because the CCD of laser profiler was damaged. The results of the quad scan are shown in Fig. 9. The emittance of both beam were almost same, 3.2 πmmmrad for 20 ps and 3.3 πmmmrad for 10 ps.

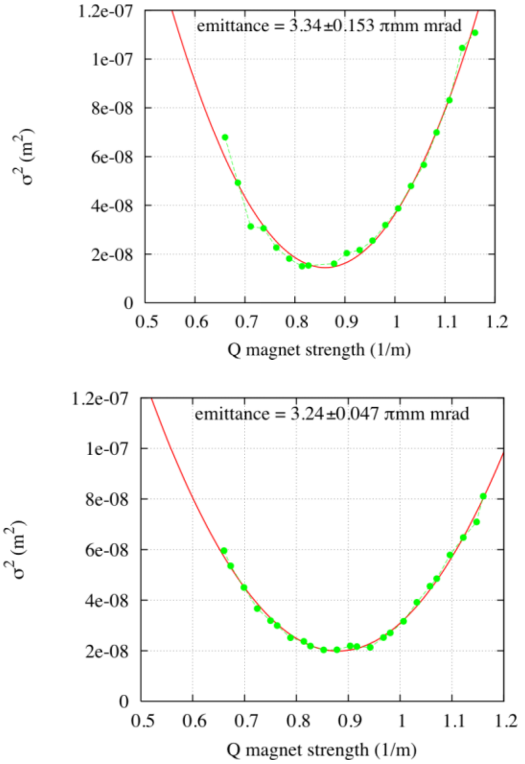

Figure 9: Measured beam emittance for 10-ps and 20-ps laser pulse at the beam charge of 0.4 nC/pulse.

Next, the beam emittance was measured in case of high current beam. The beam current of 1.0 nC was generated for 20-ps pulse but only 0.6 nC beam current could be generated for 10-ps pulse at the same laser spot size, though the laser power was high enough. It may be due to space charge limit. After further optimizing parameters such as solenoid current, RF phase and half-wave plates, the measured minimum emittance of the beam for 20-ps laser pulse was 2.3 πmmmrad as shown in Fig.10.

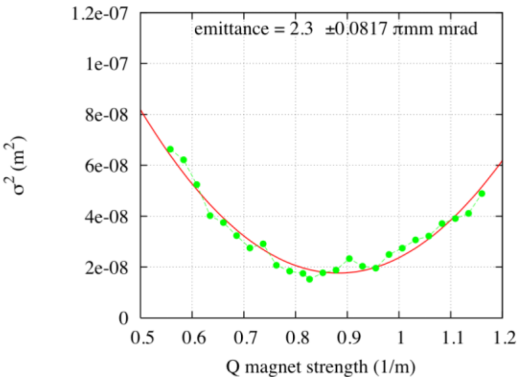

Figure 10: Measured beam emittance for 20-ps laser pulse at the beam charge of 1.0 nC/pulse.

DISCUSSION

Long laser pulse of 20 ps generated with a pulse stacker was tested, and low emittance beam of 2.3 πmmmrad was generated successfully without optimization of laser transverse profile with DM. No large difference was found between 10 ps and 20 ps in the low charge region. It is very important that the beam current for 10 ps could not reach 0.7 nC if the laser beam size was small even if the laser pulse energy was increased high. This effect may limit the initial emittance of the beam in high charge region. Long laser pulse of 20 ps is thought to have an advantage in generating high charge with small initial beam size.

Of course, the pulse charge of 1nC could be generated if the laser spot size was large enough. However, the measured beam emittance for 20-ps laser pulse was smaller than the minimum beam emittance 3.0 πmmmrad for 10-ps laser pulse at 1.0 nC/pulse measured under different conditions of micro pulse length at 1 ps and laser profile modified with DM to a flat circle of ø1.0 mm [8].

The possibility of 20-ps laser pulse to get low emittance has been confirmed by these results. Next, the splitter cube of the third stage in pulse stacker will be exchanged to that bonded with optical contact. Then micro laser pulses should be tuned to get flat longitudinal distribution of electron beam. Further experiments to pursue smaller beam emittance will be planed with simultaneous transverse and longitudinal laser profile optimization.

REFERENCES

[1] “Linac Coherent Light Source (LCLS) Conceptual Design Report”, SLAC-R-593, April 2002.

[2] “TESLA Technical Design Report, PART V, The X-Ray Free Electron Laser”, ed. G. Materlik and Th.Tschentscher, March 2001.

[3] “SCSS X-FEL Conceptual Design Report, RIKEN, May 2005.

[4] H. Tomizawa et. al., “Reduction of electron-beam emittance with shaping both spatial and temporal profiles of UV laser light source for photo-cathode RF gun“, Proceedings of EPAC 2002, Paris, June 2002, pp. 1819-1821.

[5] H. Tomizawa et. al., “Status of SPring-8 photocathode RF gun for future light sources“, Proceedings FEL2005, Stanford, August 2005, pp138-141.

[6] J. Yang et. al., “Low-emittance electron-beam generation with laser pulse shaping in photocathode radio-frequency gun“, J. Appl. Phys. Vol 92, pp. 1608-1612.

[7] H. Dewa et. al., "Photocathode RF gun designed a single cell cavity", Proceedings of EPAC 2004, Lucern, July 2004, pp. 411-413.

[8] H. Tomizawa et. al., “Automatic minimization of electron beam emittance with three-dimensionally shaping laser pulse for a light source of rf gun“, Proc. of the 2nd Annual Meeting of Particle Accelerator Society of Japan, Sendai, Japan, 2-4 August 2006, (2006) pp. 16, (in Japanese).

DESIGN STUDY ON HIGH- TC SUPERCONDUCTING MICRO-UNDULATOR

T. Kii, H. Zen, N. Okawachi, M. Nakano, K. Masuda, H. Ohgaki, K. Yoshikawa, T. Yamazaki.
Institute of Advanced Energy, Kyoto University, Uji, Japan.

Abstract

Design study on a new type of high critical temperature (T_C) superconducting micro-undulator was carried out. In this work, we introduce staggered array type micro-undulator using high T_C superconducting material. Transverse magnetic field was measured with $YBa_2Cu_3O_7$ bulk superconductors at 77 K. The maximum transverse magnetic field strength was about 0.5 mT, when longitudinal magnetic field of the strength in the range of 2 mT to 15 mT was applied.

INTRODUCTION

A micro-undulator or short period undulator will be a useful device for a compact FEL device and/or a short wavelength FEL.

When a high energy electron beam moves in the periodic magnetic field, resonant wavelength emitted from the undulator λ_R is written by following well-known equations.

$$\lambda_R \cong \frac{\lambda_u}{2\gamma^2}\left(1+\frac{K^2}{2}\right) \tag{1}$$

$$K = \frac{e \cdot B_0 \cdot \lambda_u}{2\pi \cdot m_0 c} \approx 93.36 B_0 \cdot \lambda_u \tag{2}$$

Here, λ_u is the undulator period and γ is Lorentz factor, K is the undulator parameter, e is the charge of the electron, B_0 is the maximum transverse magnetic field strength of the undulator, m_0 is the electron mass and c is the speed of light. To obtain shorter wavelength radiation, undulator period should be short or electron energy should be high. Thus, if the λ_u is limited, high energy electron beam is required for short wavelength FEL such as X-FEL. In other word, if a short period undulator realizes, high energy electron is not required. Moreover since the FEL gain increases as the number of period of undulator increases, the short period undulator will have advantage.

However, if we need K=1 for short period undulator of 5 mm, B_0 should be almost 2 T. Thus, to realize micro undulator or short period undulator, strong transverse magnetic field is required.

HIGH TC SUPERCONDUCTING UNDULATOR

Design of high T_C superconducting undulator

To obtain transverse periodic magnetic field in a short period, we introduce following micro-undulator as shown in Fig. 1.

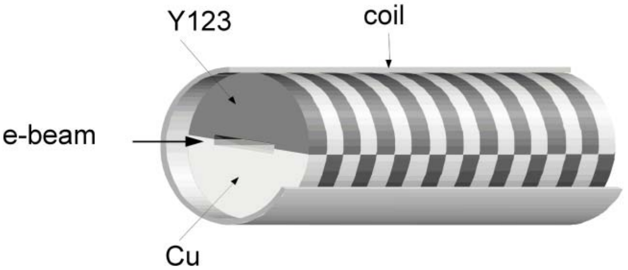

Fig. 1. Conceptual drawing of the high T_C SC undulator.

High Tc bulk superconducting materials are stacked in the solenoid. First, these superconducting pieces are cooled down below the critical temperature T_C. Then, a solenoid field is applied. As a result, density modulation of the magnetic field is produced, and thus the periodic transverse magnetic field is generated on the electron beam axis. To realize shorter period, in vacuum structure is planned. If we can control the magnetic field precisely, extreme good electron beam confinement can be realized [1].

If a perfect Meissner state is kept in a high magnetic field strength of several T, excellent performance will be realized. Unfortunately, Meissner region is typically limited below the lower critical field of several hundred mT, but superconductivity is left up to the higher critical field of 100 T. Thus we tried to measure the transverse magnetic field above lower critical field.

Expected performance

We have estimated performance of the undulator for following applications.

1) Compact IR device
2) Ultra short wavelength FEL
3) THz device

If such short period undulator with high transverse magnetic field is applied for 1) compact IR FEL device, required electron energy will be less than 15 MeV as shown in Fig. 2. Therefore a very compact IR system can be designed.

#kii@iae.kyoto-u.ac.jp

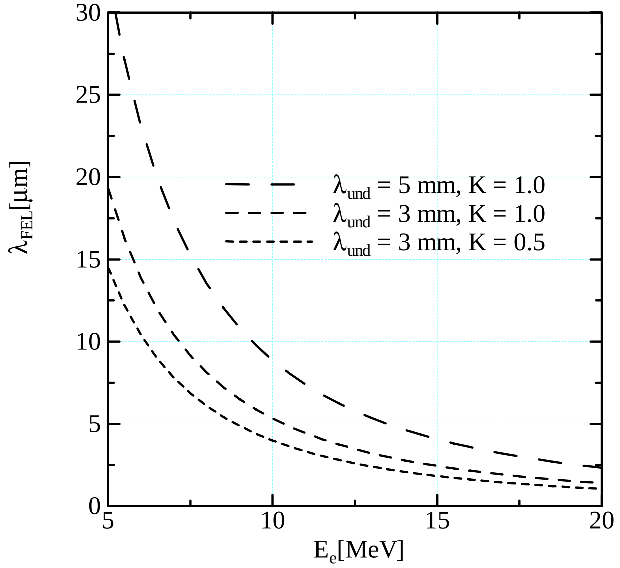

Fig. 2. Expected wavelength for short period undulator with several tenth MeV electron beam.

For application to 2) ultra short wavelength FEL, the device is also fascinating as shown in Fig. 3. The FEL wavelength of 1 Å will be achieved with 3 GeV electron beam. It is expected that the whole system could be compact, because the length of the undulator and the accelerator will be shortened compared to present configurations of such X-FEL systems.

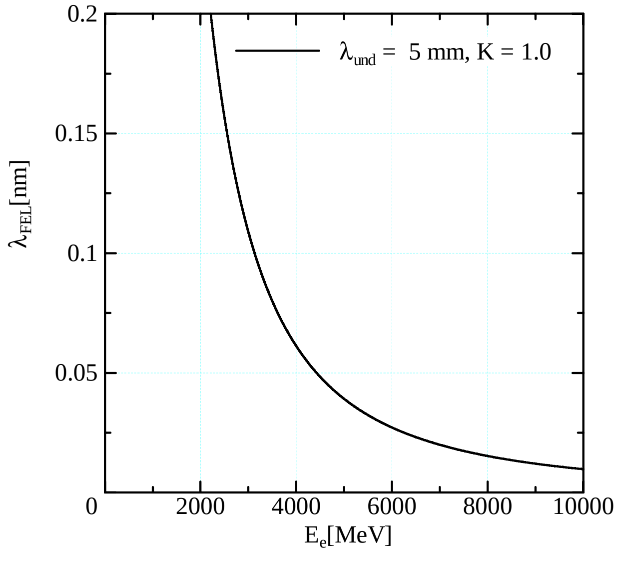

Fig.3. Expected wavelength for GeV class electron beam.

A simple configuration consisted of an electron injector and the proposed micro-undulator will provide 3) the THz radiation as shown in Fig. 4. This system could generate an intense THz radiation with a variety of operation mode, in CW, because we can use a CW electron injector.

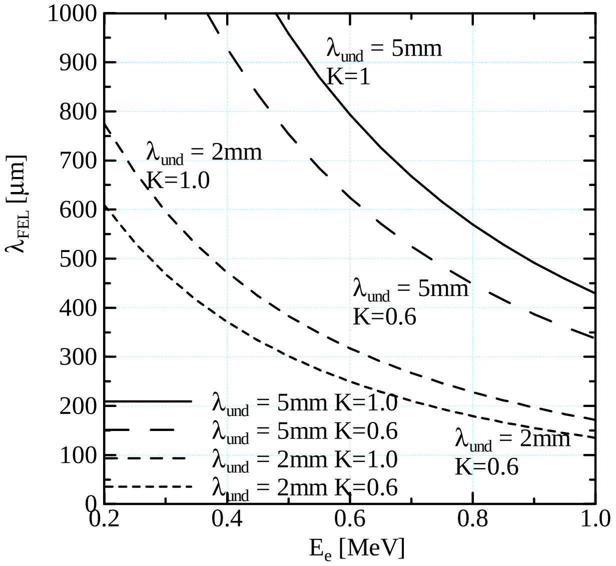

Fig. 4. Expected wavelength for THz device.

EXPERIMENT

To confirm the proposed micro-undulator, a preliminary experiment has been performed. In this work, $YBa_2Cu_3O_7$ (YBCO) ceramic was selected as the high T_C superconducting materials, because it is easy to obtain, and Tc is higher than the boiling point of liquid nitrogen. Presintered YBCO powder made by Furuuchi Chemical Corporation was used for sample fabrication. Test peaces were made as following. The powder was pressed into disks and sintered in an oxygen-containing atmosphere for 12 hours at a temperature of 900° C, and annealed for 48 hours at a temperature of 500° C. Diameter of the test pieces was 27 mm and thickness was 2.5 mm. Superconductivity of the test pieces were checked by the Meisner effect and pinning effect using small permanent magnet on the cooled test material. Schematic drawing of the superconducting test piece is shown in Fig. 6.

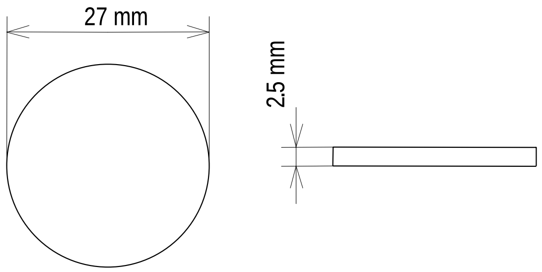

Fig. 5 Schematic drawing of the YBCO test piece.

Transverse magnetic field produced by the cooled ceramics was measured with a dipole magnet and a 3-Channel Gaussmeter Model 460, manufactured by Lake Shore Cryotronics, inc. Experimental setup is shown in Fig. 6.

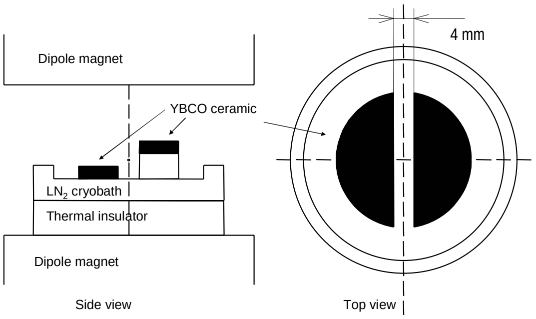

Fig. 6 Experimental setup.

Test piece was cut into two ‘D shapes’ for the transverse magnetic field measurement. The test pieces were cooled down to 77 K in a LN_2 cryobath. After cooled down below the critical temperature, they were moved into the gap of the dipole magnet. Longitudinal magnetic field of the strength in the range of 2 mT to 15 mT was applied. The magnetic field strength was measured using a Hall probe. The measured strength was about 0.5 mT, and did not depend on the amplitude of the longitudinal magnetic field.

DISCUSSION

Transverse magnetic field was successfully generated with YBCO test pieces, but the magnitude was very small. Let us discuss on the small transverse magnetic field strength. Although the upper critical field strength for the YBCO is high, the lower critical field is about 1 mT. Thus, the magnetic vortex lines penetrate into the superconductors. As a result the enough transverse magnetic field was not produced.

To overcome this problem, strong pinning center should be introduced. Then the penetration of the vortex lines would be suppressed. Doping of Praseodymd[2] is planned to introduce pinning center and increase critical current density.

Although, zero-field cooling is introduced in this work, filed cooling is also considerable to produce transverse magnetic field. If the each superconducting pieces with strong pinning center are cooled in the strong solenoid field, each pieces work as strong permanent magnet of several T after the solenoid field is turned off. Such strong permanent magnet would increase the performance of hybrid staggered undulator [3]. Although the peak field depends on the trapped magnetic field by the superconducting pieces, recently typical trapped field is greater than 2T [4], thus the peak field of greater than 1T is expected.

ACKNOWLEDGEMENT

This work was supported by the Grant-in-Aid for Young Scientists (A) by the Ministry of Education, Culture, Sports, Science and Technology of Japan.

REFERENCES

[1] J. Kitagaki, et al, “A design study on electron beam confinement in a staggered array undulator based on a 3D code”, Nucl. Instr. Meth. A475 (2001) 613-616.

[2] T. Harada; K. Yoshida, “The effects of Pr-doping on the critical current density in $YBa_2Cu_3O_{7-\delta}$”, Physica C: Superconductivity and Its Applications 383 (2002) 48-54.

[3] S. Sasaki, “The possibility for a short-period hybrid staggered undulator”, Proceedings of 2005 Particle Accelerator Conference, Knoxville, Tennessee (2005) 982-984.

[4] M. Morita, et al, “Development of Oxide Superconductors - High T_c Bulk Superconductor, QMG, and Its Magnetic Applications -”, Nippon Steel Technical Report No. 93 January 2006 (2006) 18-23.

DESIGN STUDY OF RF TRIODE STRUCTURE FOR THE KU-FEL THERMIONIC RF GUN

K. Masuda#, K. Kusukame, T. Shiiyama, H. Zen, T. Kii, H. Ohgaki, K. Yoshikawa, T. Yamazaki,
Institute of Advanced Energy, Kyoto Univ., Gokasho, Uji, Kyoto 611-0011, Japan

Abstract

A coaxial rf cavity with a thermionic cathode on its inner rod has been designed to be adopted in a 4.5-cell rf gun in order to minimize the inherent back-bombardment of electrons onto the cathode. Dependences of the back-bombardment power and the output beam properties on the axial mounting position of the coaxial cavity have been studied using a 2-dimensional simulation code. With an optimal mounting position and phase of ~90 kW rf input fed into the coaxial cavity have shown significant reduction of back-bombardment power of over 80 %. It has also shown a lower longitudinal emittance and a higher peak current of the output beam than the conventional rf gun, while the transverse emittance degradation is reasonably acceptable.

INTRODUCTION

Thermionic rf guns have advantages against photocathode ones, such as low cost, high micropulse repetition rate (high averaged current), and easy operation, which make them well suited for FELs. They however suffer from back-bombardment of electrons onto the thermionic cathode which eventually leads to an output beam energy drop and limits the macropulse duration [1-3]. The back-bombardment effect is seen significant in the 4.5-cell rf gun (Fig. 1 and Table 1) for the KU-FEL linac because of its original design, i.e. a high coupling coefficient, large number of cells, small aperture between the cells. Some countermeasures are applied, such as the use of transverse magnetic fields [4,5] and the temporal control of the rf input for compensating time-varying beam-loading [6-8] with limited successes. The macropulse duration achieved so far is 4 μsec at most for a limited beam output of ~80 mA [8], while a longer duration and a higher current would be desired for the FEL operation.

Numerical studies so far have suggested that the rf triode structure could potentially reduce the back-bombardment power drastically (~80 - 99%) [9,10].

Especially the use of a metal grid for the rf cutoff has shown numerically over 99% reductions of the back-bombardment power without degradation in the output beam properties, by simulations on neglect of the beam scattering by the grid [10,11]. In this work, we investigated an rf triode without a grid for comparison, since the use of a grid is practically undesirable unless it is necessary in terms of the back-bombardment reduction and/or the output beam characteristics.

Also, though the beam properties at the 1.6-cell [9] and the half-cell [10] exits have shown reasonably acceptable degradations or rather enhancements, the beam extraction phase from the rf triode should be considered in adopting it to the 4.5-cell gun, because an off-crest beam injection to the successive cells would lead to a degradation in the output beam transverse emittance due to an increased rf contribution to the emittance growth. In this work, we investigated both the input rf phase and axial mounting position of the coaxial cavity with respect to the main accelerating cells.

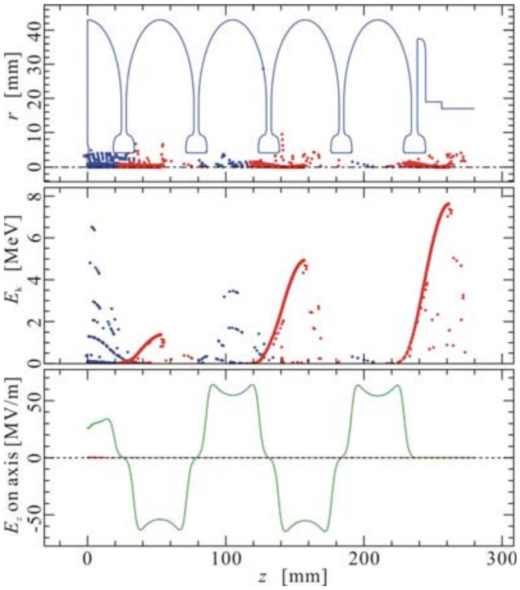

Figure 1: A simulation snapshot showing electrons' radial positions and energies along the longitudinal position, and the on-axis cavity field. The blue dots indicate back-streaming electrons. A 2mm ϕ thermionic cathode with a 30 A/cm^2 current density is located at $z = 0$, and the cavity voltage is 10 MV to yield 7.6 MeV output.

Table 1: Beam properties by the simulation on neglect of the back-bombardment effect. Only the electrons within an output beam energy spread of $\Delta E_k/E_{k,max}$ = 3 % are taken into account.

at the gun exit	
charge, ΔQ	29.00 pC
peak current, I_{peak}	10.00 A
normalized rms emittance, $\varepsilon_{r,n}$	1.20 π mm mrad
longitudinal rms emittance, ε_z	37.00 psec keV
at the 1st cell exit	
energy spread, $\Delta E_{k1}/E_{k1,max}$	6.60 %
charge, ΔQ_1	29.00 pC
peak current, $I_{1,peak}$	10.40 A
normalized rms emittance, $\varepsilon_{r1,n}$	0.53 π mm mrad
longitudinal rms emittance, ε_{z1}	1.80 psec keV

[#] masuda@iae.kyoto-u.ac.jp

COAXIAL CAVITY DESIGN

Figure 2 shows the coaxial cavity geometry to be installed in the rf gun instead of the conventional cathode, and the fundamental (2856 MHz) eigenmode pattern by a 2-dimensinal eigenmode solver [12]. The outer radius is limited up to ~15 mm due to the cathode mount geometry in the rf gun. We set it as the maximum, 15 mm to minimize the coupling coefficient, β, between the coaxial cavity and the backside coaxial waveguide from which an rf power is to be fed. The rf cutoff is ensured by a drift tube of 4 mm in diameter and 5 mm in length between the coaxial cavity and the successive half cell.

Figure 3 shows particles' snapshots by a 2-dimensional particle-in-cell simulation code [13] for three different coaxial inner rod geometries on which the same thermionic cathode (2 mmϕ, 30 A/cm^2) as is used in the conventional diode rf gun shown in Fig. 1. The code can reproduce the required rf input, P_{in}, for a given rf voltage, V_o, taking into account the beam-loading effect [3,13].

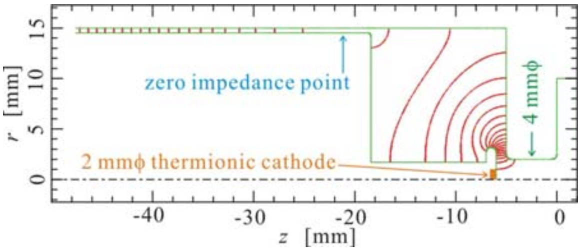

Figure 2: An eigenmode pattern in a coaxial cavity with a thermionic cathode on its inner rod, to replace the cathode in the conventional diode rf gun.

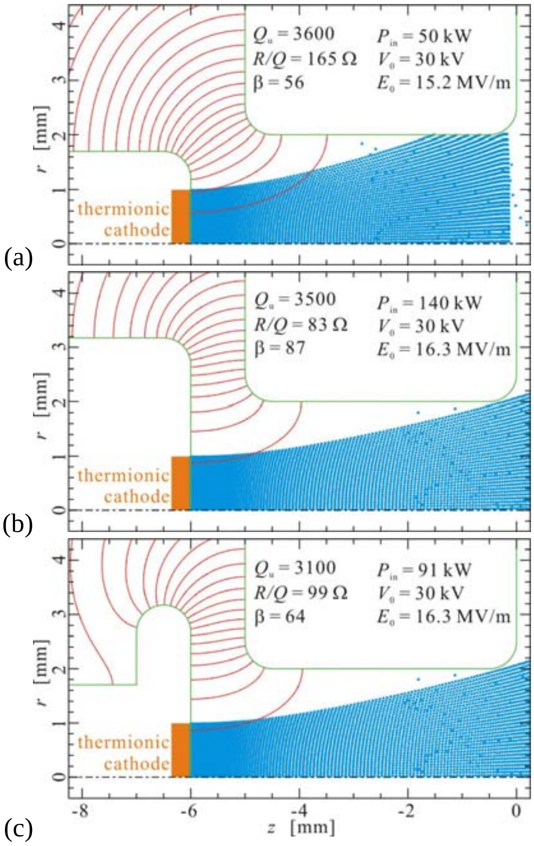

Figure 3: Eigenmode patterns and particle snapshots in the coaxial cavity, comparing three different geometrical designs of the coaxial inner rod. Peak electric field strengths on the cathode (E_0), and required rf input (P_{in}) are shown for a fixed peak cavity voltage, $V_0 = 30$ kV.

In the design (a), the beam tends to hit the drift tube due to radial forces by both the rf and the space charge. The geometry (b) shows a good beam transport because of a reduced radial rf field, while at the same time the larger inner rod diameter increases β, leading to a higher P_{in} requirement for a fixed V_0. Finally, the design refinement in (c) meets both the requirements, showing a good beam transport and an acceptably high field with a moderate P_{in} below 100 kW, the maximum available power in our experiments scheduled in the near futere.

BACKBOMBARDMENT AND BEAM PROPETIES BY THE TRIODE RF GUN

In the simulations in the triode rf gun, we varied the axial mounting position, z_0, of the coaxial cavity with respect to the main accelerating cells in the 4.5-cell rf gun (see Fig. 4), as well as the rf voltage, V_0, and phase, $\Delta\phi_{01}$, in the coaxial cavity. The cavity voltage in the main accelerating 4.5 cells is fixed as 10 MV throughout.

As seen in Fig. 4, the 1st half cell geometry is slightly changed as the z_0 varies, so that its resonant frequency, quality factor and shunt impedance remain unchanged.

The back-bombardment effect is neglected, i.e. the cavity voltages and the cathode current density are kept constant until periodically steady-state solutions.

Back-Bombardment Power and Beam Properties at the First Cell Exit

Figure 5 and 6 show back-bombardment power onto the 2 mmϕ cathode, P_{back}, bunch charge, ΔQ_1, and transverse normalized rms emittance $\varepsilon_{r1,\mathrm{n}}$ at the 1st half cell exit. For comparisons, they are normalized by those in the conventional diode rf gun listed in Table 1. Electrons

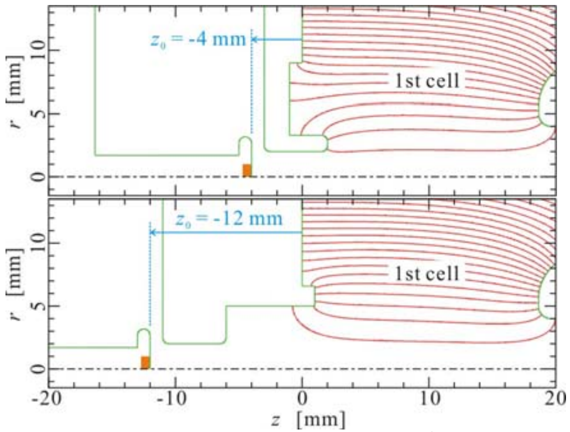

Figure 4: Eigenmode patterns of the 1st cell for two different mounting positions (z_0) of the coaxial cavity. In the conventional diode rf gun (see Fig. 1 and Table 1) the cathode is located at $z = 0$.

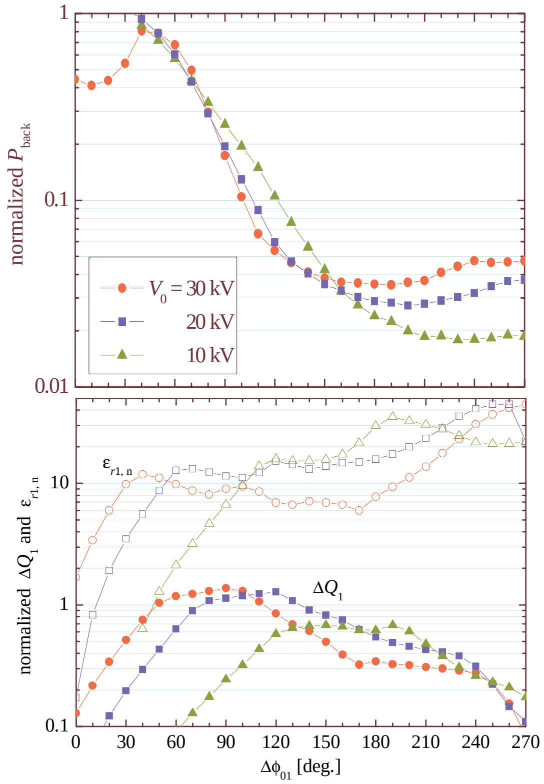

Figure 5: Back-bombardment power (P_{back}), bunch charge and transverse normalized rms emittance at the 1st cell exit (ΔQ_1 and $\varepsilon_{r1,n}$) divided by those in the conventional diode rf gun (see Table 1), as functions of $\Delta\phi_{01}$ and V_0 for z_0 = -4 mm.

within an energy spread of $\Delta E_{k1}/E_{k1,max}$ = 6.6 % are taken in account in the ΔQ_1 and $\varepsilon_{r1,n}$, since they are found contribute to an acceptable output beam energy spread of $\Delta E_k/E_{k,max}$ = 3 % for the case of the conventional diode rf gun shown in Fig. 1 and Table 1.

As seen in Fig. 5, a lower V_0 results in a lower ΔQ_1 and larger $\varepsilon_{r1,n}$ without significant reduction of P_{back}. Thus V_0 is fixed as the maximum, 30 kV hereafter.

In comparison with the use of a metal grid instead for the rf cutoff [10], the existence of zero-field region in between the cathode and the 1st half cell is found result in higher P_{back}, while the reduction of P_{back} by the present rf triode is still significant.

In Fig. 6, regardless of the phase control by z_0, $\phi_{1,head}$ is found far ahead of the crest for $\Delta\phi_{01}$'s where the P_{back} reduction is over 90 % (called operational mode (I) hereafter).

At a lower $\Delta\phi_{01}$, however, a local minimum of P_{back} is found, which is seen to reach 80 % reduction for z_0 = –6, –8 and –10, and is also seen to shift in terms of $\Delta\phi_{01}$ as z_0 decreases. Thus P_{back} at $\phi_{1,head}$ = 1 π rad (crest) decreases with decreasing z_0 as shown in Fig. 7. This operational mode (II) is not seen in the grid-based rf triode [10], which corresponds virtually to z_0 = ~ –1 mm.

Note that, in the conventional rf gun, $\phi_{1,head}$ is 0.94 π rad, slightly ahead of the crest as shown in Fig. 6, because the rf voltage and corresponding output energy of 7.6 MeV is higher than the nominal value of 5 MeV. Nevertheless we usually operate the gun at a higher energy, since it results in a lower beam emittance.

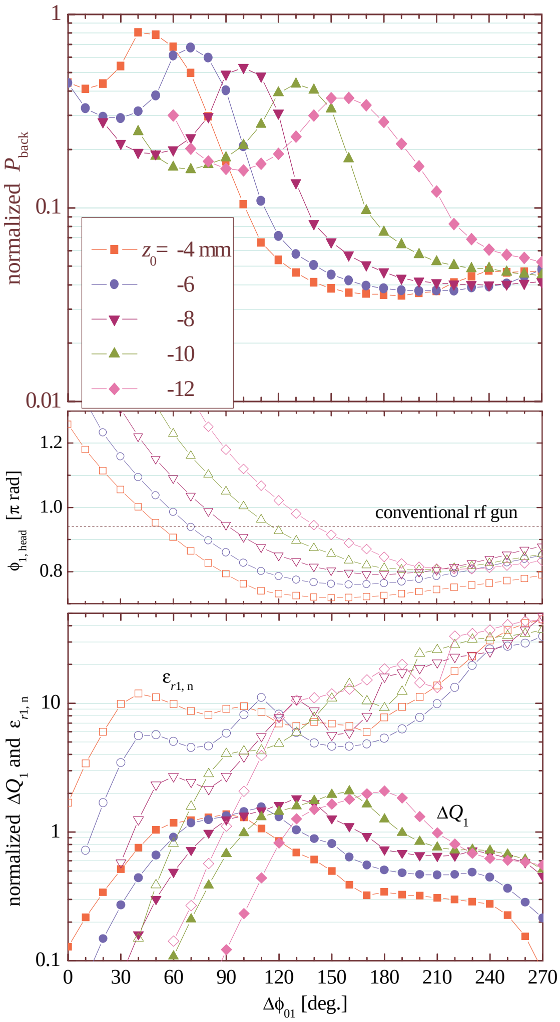

Figure 6: P_{back}, ΔQ_1 and $\varepsilon_{r1,n}$ divided by those in the conventional diode rf gun, and bunch head phase through the 1st cell exit ($\phi_{1,head}$), as functions of $\Delta\phi_{01}$ and z_0 for V_0 = 30 kV.

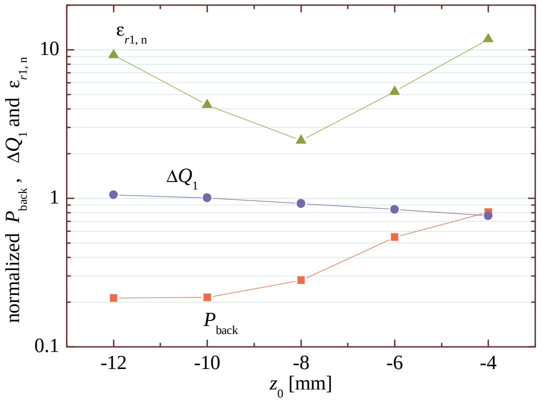

Figure 7: P_{back}, ΔQ_1 and $\varepsilon_{r1,n}$ divided by those in the conventional diode rf gun for $\Delta\phi_{01}$ where $\phi_{1,head}$ = 1 π rad, as functions of z_0 for V_0 = 30 kV.

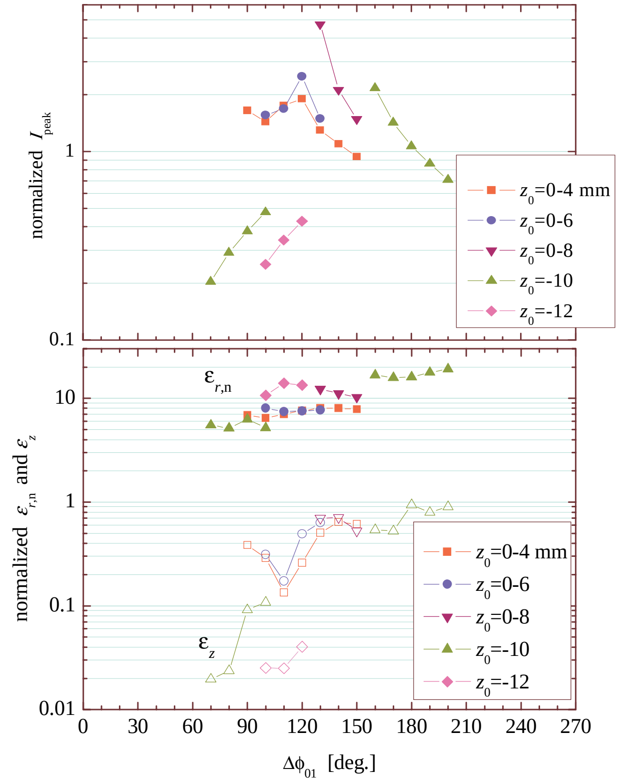

Figure 8: Dependences of the output beam properties on $\Delta\phi_{01}$ and z_0.

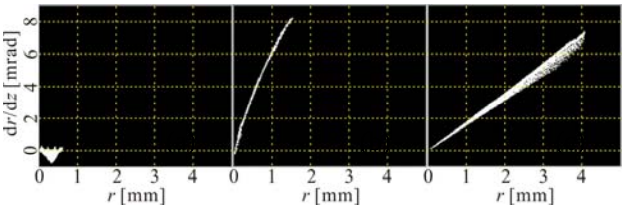

Figure 9: Transverse phase space distributions of the output beams by (a) the conventional diode gun, the triode gun with (b) z_0 = –10 mm, $\Delta\phi_{01}$ = 100 deg. (mode (II)), and (c) z_0 = –6 mm, $\Delta\phi_{01}$ = 120 deg (mode(I)).

Table 2: Comparisons of back-bombardment powers and output beams' properties between the conventional diode and the triode rf guns.

	P_{back} [kW]	I_{peak} [A]	$\varepsilon_{r,n}$ [π mm mrad]	ε_z [psec keV]
conventional diode rf gun	21.0	10.0	1.2	37.0
z_0 = –10 mm, $\Delta\phi_{01}$ = 100 deg.	04.3	04.9	6.3	04.0
z_0 = 0–6 mm, $\Delta\phi_{01}$ = 120 deg.	01.6	26.0	9.1	18.0

Output Beam Properties

Figure 8 shows output beam properties for $\Delta\phi_{01}$'s and z_0's where the reduction of P_{back} is found over 80 % in Fig. 6, in both modes (I) and (II). Figure 9 and Table 2 show the output beams at optimal $\Delta\phi_{01}$'s and z_0's in terms of $I_{peak}/e_{r,n}^2$ for the modes (I) and (II), together with the output by the conventional diode rf gun.

The off-crest beam injection in the mode (I) is found to result in larger emittances than the mode (II) in exchange of higher peak currents. It should be noted that the mode (I) greatly reduces the rf contribution to the transverse emittance growth, i.e. the beam is obviously seen narrow in the phase space in Fig. 9(b), because of the optimal beam injection phase into the 2nd full cell. In comparison with the conventional rf gun, though the rf contribution is seen much reduced in the mode (II), transverse emittance is rather degraded by the radial rf field nonlinear to the radial position, i.e. the phase space distribution is seen bent much in Fig. 9(b). In the longitudinal emittance, improvements are seen in both modes (I) and (II).

CONCLUSIONS

The present rf triode structure has shown significant reductions of the back-bombardment power, and reduced longitudinal emittances and enhanced peak currents of the output beam. The optimal axial position of the coaxial cavity with respect to the main cells has shown a greatly reduced rf contribution to the transverse emittance growth by controlling the beam longitudinally with respect to the rf. Transversely, however, the present design yields a larger beam radius, eventually leading to a transverse emittance growth due to the contribution by the nonlinear radial rf fields. Though the transverse emittance degradation is reasonably acceptable, the wehnelt configuration and/or optimal control of the rf voltages should be considered in order to induce radial beam focusing to minimize the output transverse emittance.

REFERENCES

[1] C.B. McKee, et al., Nuclear Instruments and Methods in Physics Research A **304** (1991) 386.
[2] T. Kii, et al., Nuclear Instruments and Methods in Physics Research A **475** (2001) 588.
[3] K.Masuda, et al., Nuclear Instruments and Methods in Physics Research A **483** (2002) 315.
[4] T. Kii, et al., Proc. 9th Intnl. Conf. Synchrotron Radiation Instrumentation, May 2006, in press.
[5] C.B. McKee, et al., Nuclear Instruments and Methods in Physics Research A **296** (1990) 716.
[6] T. Kii, et al., Nuclear Instruments and Methods in Physics Research A **507** (2003) 340.
[7] F. Li, et al., Nuclear Instruments and Methods in Physics Research A **407** (1998) 332.
[8] T. Kii, et al., Proc. FEL2005 (2006) 584.
[9] K. Kanno, et al., Japanese Journal of Applied Physics **41**-1 （2002） 62.
[10] K. Masuda, et al., Proc. FEL2005 (2006) 588.
[11] K. Kusukame, master thesis Kyoto Univ., 2006 (in Japanese).
[12] K. Masuda, et al., IEEE Transaction on Microwave Theory and Techniques **46**-8 (1998) 1180.
[13] K.Masuda, Ph,D. thesis Kyoto Univ, 1997.

MAGNETIC FIELD MEASUREMENT OF UNDULATOR IN KU-FEL

M. Nakano, N. Okawachi, H. Zen, T. Kii, K. Masuda, H. Ohgaki[#], K. Yoshikawa, T. Yamazaki
Institute of Advanced Energy, Kyoto University, Gokasyo, Uji, 611-011, Japan.

Abstract

An FEL system (KU-FEL) covering wavelengths from 4 to 13 μm is under construction at Institute of Advanced Energy, Kyoto University. The magnetic field of the undulator in KU-FEL has been measured. Measured magnetic field showed demagnetization in the downstream part of the undulator. By using the measured data, we have estimated the optimal parameters of both the electron beam and the optical cavity to enhance the FEL gains for the first lasing. In this optimized condition, though FEL gains decreased by a few % but, FEL powers were not much decreased, compared with those for the design field. Saturated FEL in 6-12 μm is expected from the recent studies in the macropulse width of the electron beam from the RF gun.

INTRODUCTION

KU-FEL system for bio/chemical researches in 4-13μm is under construction [1]. Figure 1 shows a schematic view of the system. The system consists of a 4.5 cell thermionic RF gun, a 3-m accelerator tube, a Halbach type undulator and an optical cavity. The RF gun and the accelerator tube have been installed and accelerated an electron beam up to 40 MeV. The undulator and the optical cavity will be installed within this year.

In parallel with the construction, in order to estimate the high FEL gains for the first lasing, we have optimized parameters of electron beam and optical cavity based on original design parameters of our undulator (shown in Table 1) [2]. However, demagnetization was anticipated since the undulator had been used for lasing experiments under the cooperation of FELI and University of Tokyo [3]. Then, we measured the magnetic field of the undulator. By using the date, we have optimized parameters of electron beams and the optical cavity and calculated realistic FEL gains and powers.

MEASUREMENT OF MAGNETIC FIELD

The magnetic field of the undulator was measured in vertical and horizontal direction, using a Hall probe manufactured by F. W. BELL. The probe was driven by moving stage that run on a stepping motor (Fig. 2) and was moved on the central axis of the undulator by 1 mm step. Specification of the measurement device is shown in Table 2. Figure 3 shows the measured magnetic field of the undulator. The undulator error (shown in Fig. 4) is defined by following : *Error* = 1- $B_{p,exp}/B_{p,ideal}$, where $B_{p,exp}$ is the peak magnetic induction from fitting the measured date to sinusoidal function and $B_{p,ideal}$ is the peak value of the design magnetic field. Thus, the error is positive when there is demagnetization. The initial and end peak of the measured magnetic field of the undulator

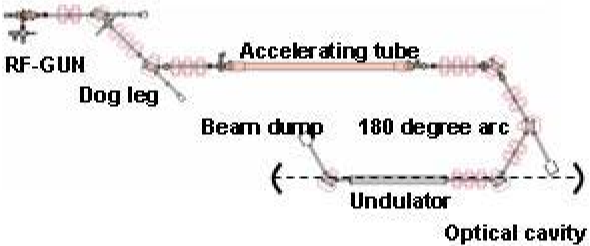

Fig. 1 . Schematic view of KU-FEL.

Table 1: Parameters of the original designed undulator of KU-FEL

Length	1.6 m
Period	40 mm
Number of period	40
Gap	26 - 45 mm
Maximum magnetic field	0.25 - 0.045 T
K-value	0.95 - 0.17

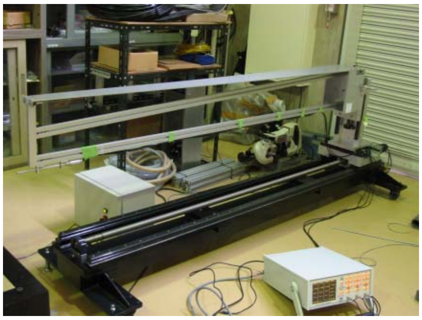

Fig. 2: Measurement device for magnetic field.

Table 2: Specification of measurement device

Moving stage

Motor	Stepping motor
Resolution	0.01 mm
Operation range	2 m

Gauss meter

Resolution	0.10%
Stability of temperature	0.040 %/K

[#] ohgaki@iae.kyoto-u.ac.jp

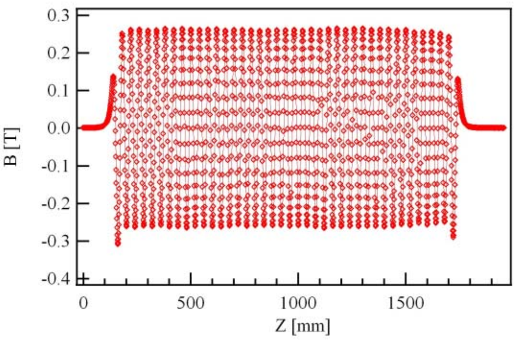

Fig. 3: Measured magnetic field of the along the central undulator axis.

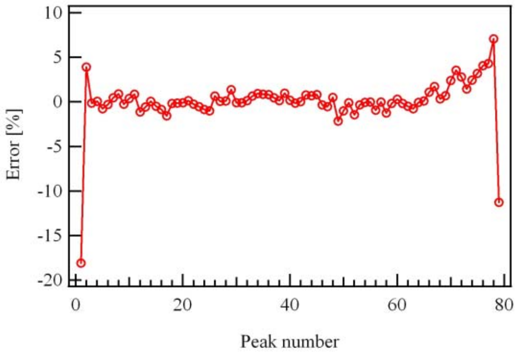

Fig. 4: Undulator error as a function of peak number.

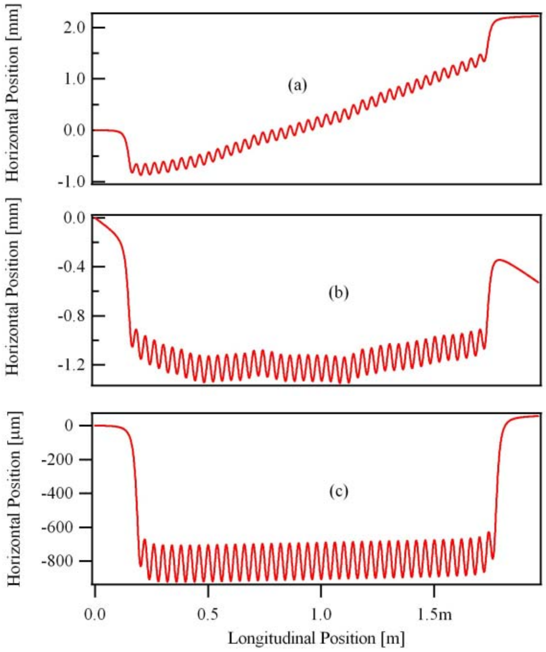

Fig. 5: (a) and (b) is horizontal trajectories calculated from the measurement without and with deflection at the entrance of the undulator, respectively. (c) is a horizontal trajectory calculated from the design.

is not considered as peak number: the number of peak field is 79. Figure 3 and Fig. 4 clearly show a demagnetization in the downstream part, peak number 70-78 in Fig.4. The gap is narrower (25.5 mm) than the original design, because we have modified the undulator in order to make the gap variable. Thus, the maximum value of peak magnetic field and K-value are 0.26 T and 0.99, respectively.

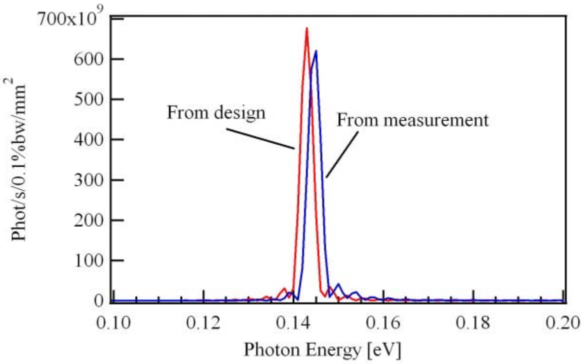

Fig. 6: Calculated spectrum of spontaneous radiation.

BEAM TRAJECTORY AND SPONTANEOUS RADIATION

Evaluation of beam trajectory and spontaneous radiation is an effective method to verify the measurement of the magnetic field. At first, We calculated electron beam trajectories at 30 MeV with the measured magnetic field and the designed field by using SRW [4]. Vertical displacement of the electron beam in the undulator shown in Fig. 5 (a) is 2 mm so that overlap between electron beam and laser is too poor. In order to compensate this, we are going to set a steering magnet before the undulator. The beam trajectory thus deflected at an angle of 1.4 mrad is shown Fig. 5 (b). Figure 5 (c) shows a beam trajectory calculated from the designed field. Fig 6 shows calculated spectra of spontaneous radiations. The radiation intensity calculated from the measured magnetic field is reduced by 9 %, and the spectrum is shifted to longer wavelength and shows asymmetric distribution, compared with that from the design field.

FEL GAIN CALCULATION

We previously reported on FEL gains based on designed magnetic field of undulator (Table 1) [2]. On the other hand, by using the measured magnetic field instead of the designed one, FEL gains have been recalculated to estimate realistic gains, which will be compared in the following.

The axial symmetric 3D code TDA3D [5] was used to calculate FEL gain and saturation. In addition, the undulator period was forced to be 39. This is because the number of peak magnetic field for TDA3D is defined as double of the undulator period while the undulator period in KU-FEL is 39.5.

At the 180-degree arc between the accelerator tube and the undulator shown Fig. 1, we can control the electron beam parameters for the optimization. Among the

Table 3: Fixed parameters of electron beam

Peak current	40 A
Normalized emmitance in x	11 πmm-mrad
Normalized emmitance in y	10 πmm-mrad
Energy spread	0.50%

Table 4: The optimized beam parameters

Beam energy (MeV)	25	30	35
Beam size in x (mm)	0.65	0.60	0.55
Beam size in y (mm)	0.33	0.36	0.36
Twiss parameter α_x	1.9	2.0	1.9
Twiss parameter α_y	0	0	0

Table 5: Optimized optical parameters

Beam energy (MeV)	25	30	35
Rayleigh range	0.40 m		
Beam waist position	0.60 m		
Wavelength (mm)	12.3	8.6	6.3
Out coupling (%)	4.0	2.5	0.8
Diffraction loss (%)	5.6	6.0	7.0
Total loss (%)	9.6	8.5	7.8

electron beam parameters, a peak current, a transverse emittance, and an energy spread, which are evaluated by PARMELA [6], are fixed (Table 3) during the calculation. The other electron beam parameters, electron beam sizes and Twiss parameters, are optimized to obtain the maximum FEL gains in three electron beam energies, 25, 30, 35 MeV. Electron beam sizes are RMS values. Twiss parameter α_y is set to zero due to the natural focusing of the undulator field. Table 4 shows the beam parameters optimized to the measured magnetic field of the undulator.

Optimization of the parameters of the optical cavity is also essential to enhance the FEL gains. We also optimized the optical parameters, Rayleigh range and beam waist position, for three electron beam energies. Table 5 shows the optimized optical parameters. The optical cavity of the KU-FEL system has been designed taking into account the diffraction loss and the out coupling. The laser field is assumed to be the Gaussian in the calculation optical loss. The out coupling hole is 1 mmϕ located at the upstream mirror. As the result, the curvature of upstream mirror is calculated to be 2.58 m and that of downstream mirror is 1.92 m. Table 5 also shows the diffraction loss and out coupling of the designed optical cavity. From the setup condition of the optical cavity, shown in Fig. 7, the beam waist position is not at the center of the undulator but is shifted to upstream in order to reduce the diffraction loss at upstream chamber (30 mmϕ). FEL gains with optimization of both of electron beam and of optical cavity are shown in Table 6. The realistic FEL gains are lower by a few % than those based on the design magnetic field distribution.

By using the above optimized conditions, we have estimated the evolution of the FEL power with the TDA3D modified to take into account the successive development of the laser power after round-trip. The optical loss is subtracted from the FEL gain in each pass. Figure 8 shows that FEL power from the measured magnetic field decreases by about 5 %.Then the numbers of round-trips necessary for saturation increase by about round-trips to reach gain saturation by 0.2 µm, compared with those from the design ones.

The injector in KU-FEL is a thermionic RF gun which have a disadvantage of back bombardment, so that macropulse duration has been restricted to 4 µs. However, since we have estimated macropulse duration is up to 8 µs [7], FEL saturation in each energy is expected.

Table 6: Comparison of the optimized FEL gains of the measurement with those of the design

Beam energy (MeV)	25	30	35
Gain of design undulator (%)	89	65	49
Gain of real undulator (%)	87	64	49

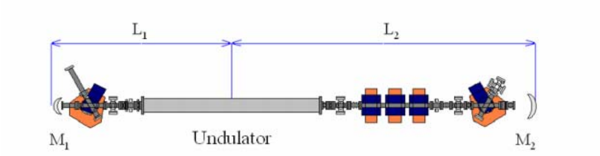

Fig. 7: Undulator and optical cavity in KU-FEL. L_1 is 1.605 m, L_2 is 2.70 m, R_1 (the curvature of M_1) is 1.92 m, and R_2 is 2.58 m.

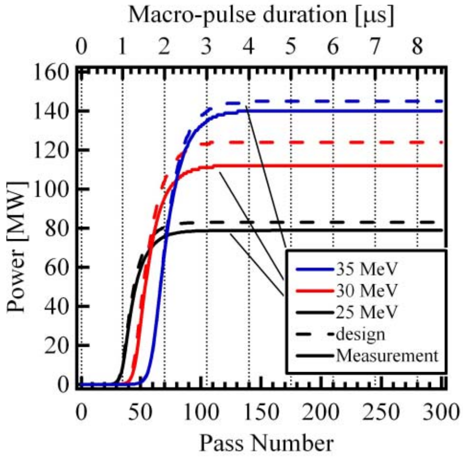

Fig. 8: FEL power as a function of pass number in each beam energy.

SUMMARY

The measurement of the magnetic field of the KU-FEL undulator has been carried out. The electron beam trajectory in the undulator and the spontaneous radiation have been evaluated with measured magnetic field. The beam displacement is about 2 mm for 30 MeV electron beam. However, it can be reduced to 0.2 mm with a steering magnet placed just before the undulator. By using the measured magnetic field, the beam parameters and the optical parameters were optimized to obtain the maximum FEL gain. Calculation of FEL gain and FEL gain saturation have been performed. Although FEL gains show a few % decrease and thus the times to reach FEL saturations with the measured magnetic field are slightly longer than these with the design field, FEL saturation is expected in the wavelength region of from 6 to 12 μm.

REFERENCES

[1] T. Yamazaki, et al., Proc. Free Electron Laser Conf. 2001 (2002) II–13.

[2] T. Fukui, et al, Proc. Free Electron Laser 2005 (2006).

[3] E. Nishimura, et al., Nucl. Instrum. Methods, A341(1994) 39.

[4] O. Chubar, et al., Proc. of EPAC98, p.1177, 1998.

[5] J.S. Wurtele T.M. Tran. Computer Physics Comm., Vol.54, p.263, 1989.

[6] L. M. Young, James H. Billen : LA-UR-96-1835 (2002).

[7] N. Ohkawachi, et al., “Production of electron beam with constant energy by controlling input power into a thermionic RF gun”, in these proceedings.

PRODUCTION OF ELECTRON BEAM WITH CONSTANT ENERGY BY CONTROLLING INPUT POWER INTO A THERMIONIC RF GUN

N. Okawachi, M. Nakano, H. Zen, T. Kii#, K. Masuda, H. Ohgaki, K. Yoshikawa, T. Yamazaki,
Institute of Advanced Energy, Kyoto University, Uji, Japan

Abstract

A thermionic RF gun is compact and economical, but it is difficult to produce electron beam of pulse width longer than a few μsec with constant energy owing to inherent back-bombardment effect. In this work we tried to keep beam energy constant in macro pulse duration by feeding modulated RF power. We also tried to perform transient analysis with equivalent circuit taking into account the back-bombardment effect in macro pulse duration in the cases of the W cathode and the LaB_6 cathode. We found that the degradation of the peak energy could be kept below 100 keV in the macro pulse duration of 8.0 μsec and 8.2 μsec, respectively.

INTRODUCTION

It is necessary for the development of an FEL to improve the source of electron beam, and a thermionic RF gun is suitable for a compact and economical FEL system. However a back-bombardment effect degrades the beam energy during the macro pulse. In a previous work, we reported the preliminary result of improvement of a thermionic RF gun [1]. In this work we tried to reduce beam energy degradation due to the back-bombardment effect by feeding modulated RF power into a thermionic RF gun. In addition, we have performed a self-consistent transient analysis which took into account the back-bombardment effect during macro pulse duration by using an equivalent circuit model and a thermal conduction.

EXPERIMENTAL SETUP

Fig.1 shows the experimental setup. The cathode is of 6-mm diameter made of porous tungsten impregnated with barium. RF power fed into the RF gun is controlled by remotely adjusting the reactors in the pulse forming network (PFN) with stepping motors. This experiment was performed varying the beam current drawn from the RF gun and input RF power in both the cases a flat input RF and a modulated RF waveform power.

The profiles of the electron beam current were measured with current transformer (CT) and Faraday cup (FC). The energy spectrum of the electron beam was analyzed with a bending magnet, beam slit and CT.

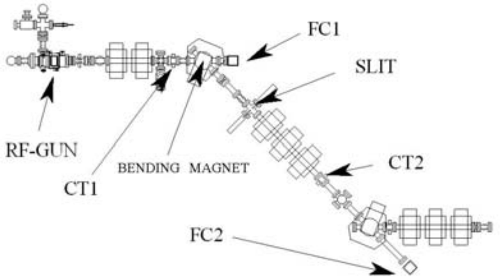

Figure 1: Experimental setup.

METHOD OF ANALYSIS

Back-bombardment effect depends on both the cavity voltage in the RF gun and the cathode current density. We performed a transient analysis in the RF gun taking into account the time evolution of the beam loading depending on the cavity voltage and the cathode current density by using an equivalent circuit model and a thermal conduction model. The beam loading was calculated from the cavity voltage and the cathode current density which was calculated from the thermal conduction in the cathode taking into account the stopping power of the back streaming electron in the cathode.

Analysis of the cathode current density

The energy distribution of the back-streaming electrons was calculated by using the results of the particle simulation code PARMELA [2]. From this result the heat quantity given to the cathode by the back streaming electron with various energy was calculated. In this calculation we assumed that the cathode consisted of thin 2000 disks.

In order to evaluate the effect of the back streaming electrons on the time evolution of the cathode temperature, we used following quasi empirical formula of the TIO [3]:

$$R = \frac{a_1}{\rho}\left\{\frac{\ln\left[1+a_2(\gamma-1)\right]}{a_2} - \frac{a_3(\gamma-1)}{1+a_4(\gamma-1)^{a5}}\right\} \quad (1)$$

$$a_1 = 2.335A/Z^{1.209} \qquad a_2 = 1.78\times10^{-4}Z$$

$$a_3 = 0.9891-(3.01\times10^{-4}Z)$$

$$a_4 = 1.468-(1.180\times10^{-2}Z)$$

#kii@iae.kyoto-u.ac.jp

$$a_5 = 1.232 / Z^{0.109} \qquad \gamma = (E + \mathrm{m}_0\mathrm{c}^2)/m_0c^2$$

where, R is the stopping range of the electron in m, A is the mass number of the absorber material, Z is the atomic number of it, E is the kinetic energy of electrons in MeV, ρ is the density of the absorber material in kg/m^3. Equation (1) is applicable to the 0.3 keV – 30 MeV electrons. With this equation, stopping power dE_b/dz was obtained. Here, we used the values of ρ = 19250 kg/m^3, A = 183.85, Z = 74 assuming that the cathode material was made of W alone..

The time evolution of the temperature was calculated in each disks of the cathode, and the time evolution of the cathode temperature was calculated by using the equation below,

$$\mathrm{c\rho V}\frac{\partial T}{\partial t} = \lambda\frac{\partial^2 T}{\partial z^2} + Q_b(z,t) \tag{2}$$

where, c is the specific heat, ρ is the density, V is the volume, T is the temperature, λ is the thermal conductivity of the cathode, z is the distance from the cathode surface, $Q_b(z, t)$ is the heat quantity from the back streaming electrons. Here, we used the values of c = 130 J/kg/K, λ = 174 W/m/K.

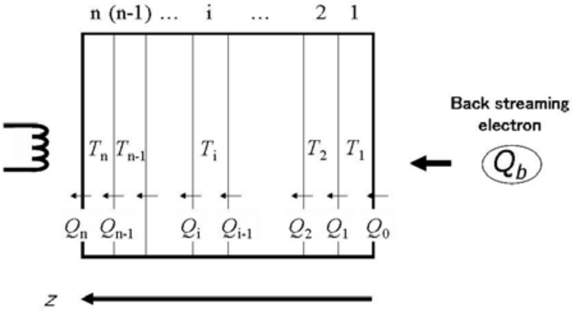

Figure 2: Thermal conduction model.

The cathode current density was obtained from the time evolution of the cathode temperature calculated above. The relationship between the cathode temperature and the cathode current density used in this analysis was obtained by the results of the cathode performance test of Heat Wave Labs, Inc.

Analysis of the cavity voltage in the RF gun

The cavity voltage in the RF gun and the reflecting RF power were calculated with the equivalent circuit model shown in Fig. 3. In this circuit, the RF power source was expressed by a source i_g, the RF gun was expressed by LCG resonant circuit, and the beam loading was expressed by an admittance Y_b. The conductance and the susceptance of the electron beam were calculated from the cavity voltage and the cathode current density by using the particle simulation code KUBLAI [4]. Thus the beam loading was calculated.

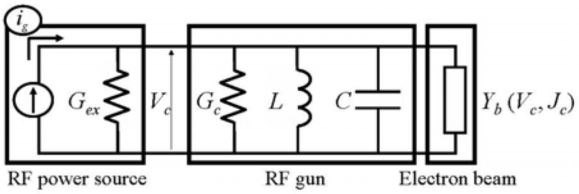

Figure 3: Equivalent circuit model.

RESULT

Experimental result

We have succeeded to keep the peak energy of the electron beam constant in 4 μsec by feeding a modulated RF power into a RF gun. Fig. 4 shows the flat RF power waveform and the modulated RF power waveform fed into a RF gun. Fig. 5 shows the beam current waveform whose peak energy is 8.6 MeV at CT2. Fig. 6 shows the time evolution of the peak energy in macro pulse duration.

As shown in Fig. 5 feeding modulated RF power into a RF gun was an effective way to extend the macro pulse duration and to increase the beam current. As shown in Fig. 6 the beam energy which had been degraded in the latter part of the macro pulse duration was kept constant by feeding modulated RF power.

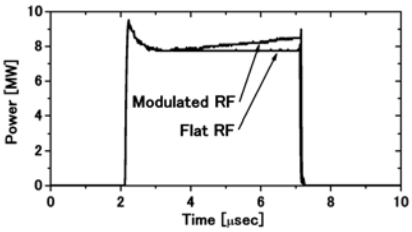

Figure 4: Input RF power waveform.

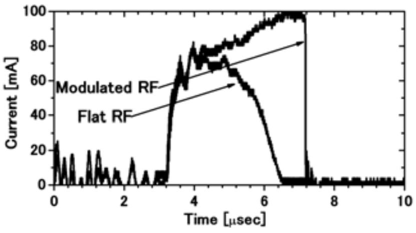

Figure 5: Beam current waveform.

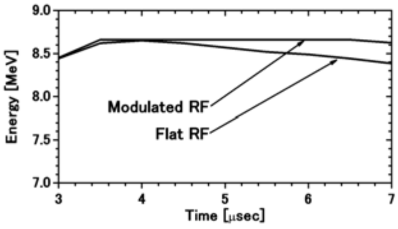

Figure 6: Peak energy @ CT2.

Result of calculation

In order to confirm the validity of calculation model, experimental and calculated reflecting RF power waveforms were compared. Fig.7 shows the measured and reproduced reflecting RF power waveform when a flat RF power was fed. Fig. 8 shows them when a modulated RF power was fed. Experimental and calculation results agree very well.

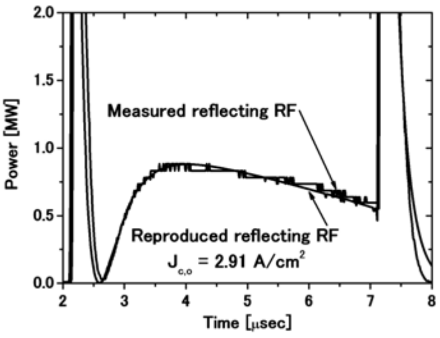

Figure 7: Reflecting RF power waveform.

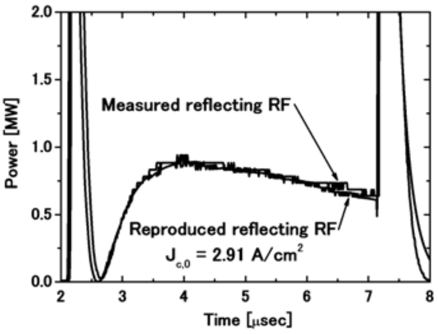

Figure 8: Reflecting RF power waveform.

As shown in Fig. 9, there was a relationship between the cavity voltage (V_c) and the peak energy of the electron beam (E), and the peak energy could be kept constant by keeping the cavity voltage constant.

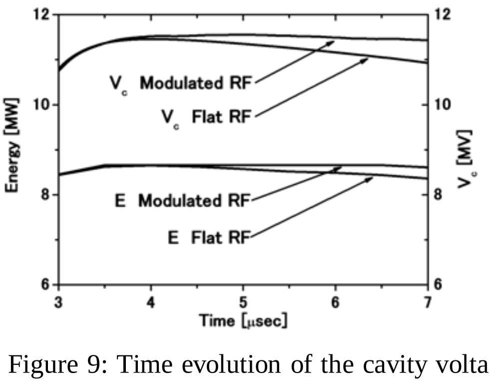

Figure 9: Time evolution of the cavity voltage and the peak energy.

We estimated how long time the peak energy of the electron beam could be kept constant by using our KU-FEL 4.5 cell RF gun. The calculation was performed in both cases of W cathode and LaB_6 cathode. We used the value of ρ = 4700 kg/m^3, A = 94.75, Z = 40, c = 122 J/kg/K, λ = 147 W/m/K and the relationship between the cathode temperature and the cathode current density was obtained by the results of the cathode performance test of KIMBALL PHYSICS INC, in the case of LaB_6 cathode.

Fig. 10 shows the time evolution of the cavity voltage of W and LaB_6 when a flat RF power was fed, respectively. The degradation of the cavity voltage of LaB_6 was a little smaller than that of W.

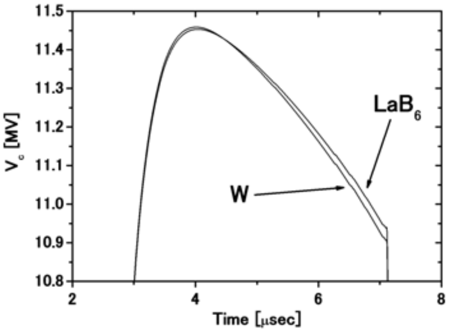

Figure 10: Comparison of W with LaB_6.

Fig. 11 and Fig. 12 show the time evolutions of the cavity voltage when an optimized modulated RF power was fed. The input RF power was 8 MW at the beginning of the macro pulse and the controlled range was 1.6 MW and the initial current density was 2.28 A/cm^2 in each calculations. We found that the degradation of the peak energy could be kept below 100 keV in the macro pulse duration of 8.0 μsec when the cathode was W, 8.2 μsec when the cathode was LaB_6.

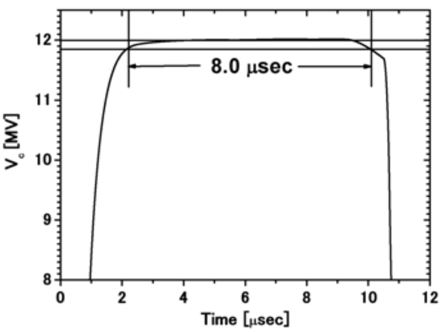

Figure 11: Expected time evolution of the cavity voltage (W).

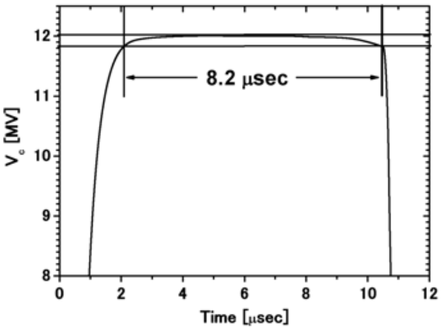

Figure 12: Expected time evolution of the cavity voltage (LaB_6).

SUMMARY

It was confirmed in experiment that feeding modulated RF power into a RF gun was effective on the reduction of the degradation of the beam energy.

By the calculation in this work, the experimental results were reproduced well. Moreover, the degradation of the peak energy of the electron beam could be kept below 100 keV in the macro pulse duration of 8.0 μsec when the cathode was W, 8.2 μsec when the cathode was LaB_6.

REFERENCES

[1] T. Kii, et al, Proceedings of the 27th International Free Electron Laser conference, (2005) pp584-587.

[2] L. M. Young, James H. Billen : LA-UR-96-1835 (2002).

[3] M. J. Berger and S. M. Seltzer, STOPPING POWER AND RANGES OF ELECTRONS AND POSITRONS (2nd Ed.),NBSIR (1982).

[4] K. Masuda, Development of numerical simulation code and application to Klystron efficiency enhancement, Ph. D Thesis, Kyoto University, (1998).

EXPERIMENTAL STUDY ON EFFECT OF ENERGY DISTRIBUTION ON TRANSVERSE PHASE SPACE TOMOGRAPHY

H. Zen[#], H. Ohgaki, K. Masuda, T. Kii, T. Shiiyama, S. Sasaki, N. Okawachi, M. Nakano,
K. Yoshikawa, T. Yamazaki
Institute of Advanced Energy, Kyoto University, Gokasho, Uji, Kyoto, 611-0011, Japan.

Abstract

Effect of energy distribution of electron beam on transverse phase space distroiion obtained by the use of tomographic method is described. Experimental phase space distribution of electron beam with low energy-tail has weak and scattered halo, which does not appear in the case of the beam without the tail. The result is consistent with the result of previous simulations. An iterative elliptical analysis is proposed to extract the beam parameters of main component from distorted phase space image. It was shown in simulation that the method could extract the beam parameters of main component from distorted image. And then, the method was applied to experimental results. As the results, the vertical and horizontal emittances at the upstream and downstream of energy filter are agreed well.

INTRODUCTION

It is indispensable to measure not only emittances but also phase space distributions of electron beams to evaluate and optimize the performance of electron guns. Transverse phase space tomography [1] is powerful method especially for non-Gaussian beam, because the method directly reconstructs the phase space distribution of electron beams. However, the assumption of mono-energy is essential for the method. Thermionic rf guns inherently produce electron beams which have large energy spread (about 10 to 15 percent) and low energy tail, and the energy distribution distorts measured phase space distribution obtained by tomographic method.

We have evaluated the effect of energy distribution on the tomographic method by numerical simulations [2]. It was found that the signals of low energetic electrons are reconstructed as weak and scattered signals on wide region of reconstructed phase spaces, and those signals lead to large errors in beam parameters. On the other hand, it was also found that the energy spread of main component have no large effect on the method even if the energy spread is 15 percent.

The effect was evaluated by comparison of the reconstructed image from the upstream and that from the downstream of an energy filtering section. Furthermore for the beam just after the gun, we introduced an elliptical analysis to remove the effect of low energy tail in order to obtain correct beam parameters at the gun exit by the tomographic method.

EXPERIMENTAL SETUP

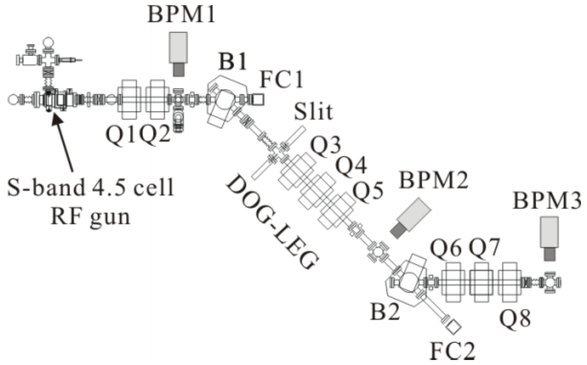

Figure 1: Experimental arrangement.

Figure 1 shows the experimental setup. A dispenser cathode of disk shape with 6 mm diameter is mounted in the first half cell of our 4.5 cell RF gun. To reduce back-streaming electrons [3], transverse magnetic field was applied with a dipole magnet located just before the rf gun [4]. The beam profile monitor (BPM) consist of a fluorescence screen (Cr doped Al_2O_3) and a CCD camera, and its spatial resolution is 0.05 mm.

Dog-leg section in Fig. 1, which consisted of two dipole magnets, a slit, and a quadrupole triplet, worked as an energy filter and its energy resolution is about 5 percent.

The quadrupole magnet 1 (Q1) and the BPM1 are used to measure the phase space distributions at the upstream of the energy filter, and the Q6 and BPM3 are used to measure them at the downstream.

Beam parameters in the experiments are shown in Table 1, and the energy distribution obtained with bending magnet 1 (B1) and Faraday cup 2 (FC2) is shown in Fig. 2. Unfortunately signals of FC2 of low energy tail (less than 7 MeV) were too weak to be separated from the electric noise. However, the existence of low energy tail has been predicted in the previous simulation for our rf gun [2].

For tomographic reconstruction, we used ordered-subset expectation maximization algorithm [5] whose advantage is that there is no artefact on reconstructed images.

[#] heishun@iae.kyoto-u.ac.jp

Table 1: Beam parameters in experiments

	@ BPM1	@ BPM3
Macro pulse duration	1.6 μ sec	1 μ sec
Total charge	300 nC	100 nC
Charge per bunch	66 pC	35 pC
Peak Energy	9.2 MeV	

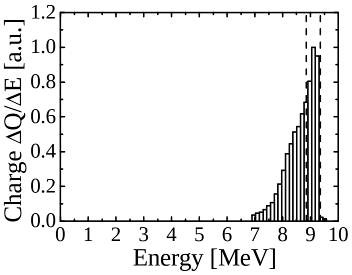

Figure 2: Measured energy spectrum of the electron beam at the exit of gun (dashed lines indicate the energy acceptance of dog-leg section).

RESULTS OF EXPERIMENT

The results of experiments are shown in Fig. 3 and 4. Before reconstruct the Q1 result, background signals were subtracted. At the Q1 entrance horizontal and vertical normalized emittances are evaluated as 82 and 44 π mm mrad, respectively, while those are 12 and 6.9 π mm mrad at the Q6 entrance.

There are weak and scattered signals in Fig. 3 where the electron beam had a low energy tail, while such signals are not seen in Fig. 4. It is consistent with previous numerical studies that the phase space distributions for the beam with low energy tail are severely distorted.

In Fig. 3, the region between dashed lines indicates where electrons can exist and the region is calculated from aperture of the gun exit (4 mm in diameter) and the distance between the gun exit and Q1 (27.5 cm). The signals in outside of the region are miss-reconstructed signals due to difference from assumed energy at least.

Therefore, it was shown in experiment that the signals from low energy tail are reconstructed as weak and scattered signals. We can not obtain correct phase space distributions by using tomographic method if low energy tail is contained in an electron beam.

REMOVAL OF LOW ENERGY SIGNALS

Amount of low energy electrons produced by a thermionic rf gun is much fewer than amount of electrons included in main component, and low energy electrons are reconstructed wider and weaker than true distribution. So intensity of low energy electrons on reconstructed phase space is much weaker than intensity of electrons included in main component. However, the emittance calculation is strongly affected by the tail. Therefore, we need to remove the weak signals which are originated from low energy electrons to obtain correct beam parameters by the tomographic method.

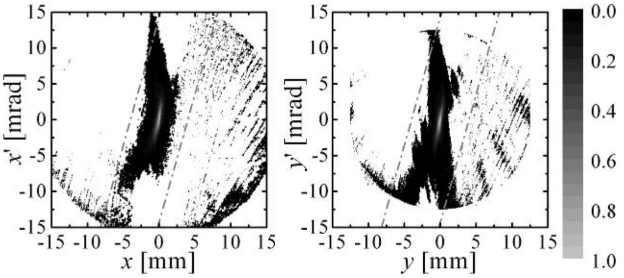

(a) (b)

Figure 3: Phase space distributions at the entrance of Q1 (dashed lines indicate the regions where electrons can exist and are calculated from experimental geometry). (a) Horizontal and, (b) vertical.

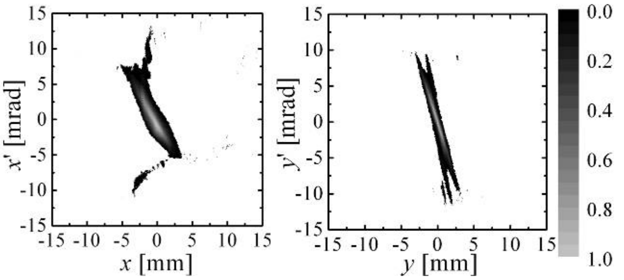

(a) (b)

Figure 4: Phase space distributions at the entrance of Q6 measured by tomographic method, (a) Horizontal and (b) vertical.

Procedure of Iterative Elliptical Analysis

To remove the weak signals produced by low energy electrons automatically, we introduced an iterative elliptical analysis (IEA) [6]. The procedure is:

I : Calculate $<x^2>$, $<x'^2>$ and $<xx'>$ from reconstructed phase space distribution.

II : Draw ellipse defined by Eq. 1 on reconstructed phase space.

$$\left\langle x'^2 \right\rangle x^2 + 2\left\langle xx' \right\rangle xx' + \left\langle x^2 \right\rangle x'^2 = 9\varepsilon^2 \qquad (1)$$

Eq. (1) represents the 99 percent ellipse of Gaussian distributions.

III: Calculate $<x^2>$, $<x'^2>$ and $<xx'>$ from reconstructed phase space distribution only in the ellipse.

IV : In the same way with step II and III, draw ellipse using newly calculated $<x^2>$, $<x'^2>$ and $<xx'>$ in step

V : Repeat step III and IV until $<x^2>$, $<x'^2>$ and $<xx'>$ sufficiently converge.

Simulation of Iterative Elliptical Analysis

Reliability of IEA was examined by using numerical simulation. We gave the Gaussian-shaped phase space distribution with the energy distribution shown in Fig. 5 as original distribution and simulated the experiment of tomographic method. In this simulation, space charge effect was neglected, since it was not significant for our thermionic rf gun. As the result of the simulation, a distorted phase space distribution was reconstructed (Fig. 6). Although weak and scattered signals exist in the figure, strong signals in the center are looked similar to the original phase space distribution (Fig.5).

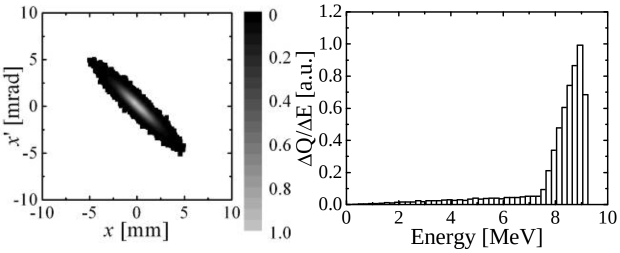

(a) (b)

Figure 5: Original distribution of numerical simulation, (a) phase space distribution (normalized emittance = 3.3 π mm mrad, α = 2.9 and β = 3.1 m), (b) energy spectrum.

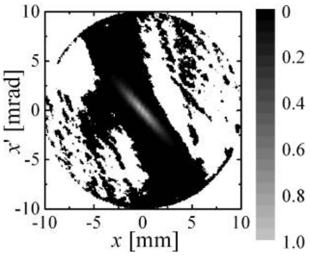

Figure 6: A result of numerical simulation (normalized emittance = 10 π mm mrad, α = 1.5 and β = 1.4 m).

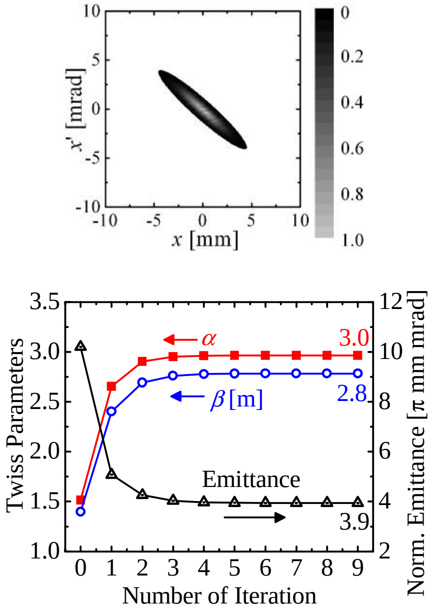

(a)

(b)

Figure 7: Result of IEA applied to simulation result, (a) phase space distribution (normalized emittance = 3.9 π mm mrad, α = 3.0 and β = 2.8 m), (b) convergence of emittance and Twiss parameters.

The result of IEA applied to the Fig.6 is shown in Fig. 7. The normalized emittance and Twiss parameters gradually converged to 3.9 π mm mrad, α = 3.0 and β = 2.8 m, respectively as iteration number increased. The beam parameters of original distribution were normalized emittance = 3.3π mm mrad, α = 2.9 and β = 2.8 m. Since each error in beam parameters is less than 20 percent, this method is reliable.

Application of IEA to Experimental Result

IEA was applied to experimental results at the entrance of Q1 and the results are shown in Fig. 8. A center core of reconstructed phase space distribution was successfully obtained and beam parameters sufficiently converged. As results of application of IEA, measured horizontal and vertical emittances were 5.4 and 4.7 π mm mrad, respectively.

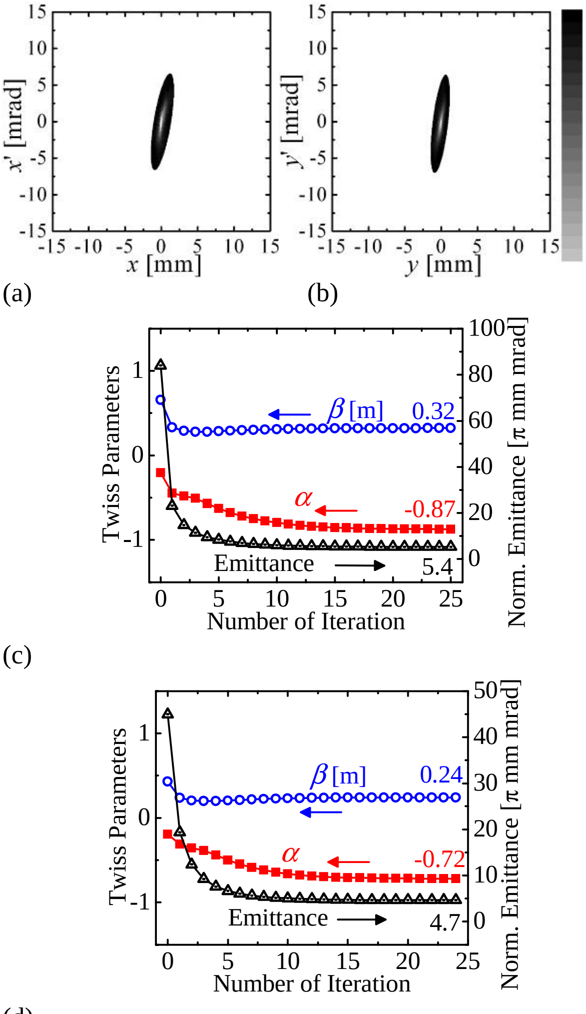

(a) (b)

(c)

(d)

Figure 8: Results of IEA applied to experimental results. (a) Horizontal phase space distribution of horizontal direction. (b) Vertical phase space distribution. (c) and (d) convergence of horizontal and vertical beam parameters, respectively.

The IEA was also applied to experimental results at the Q6 entrance and measured emittances of horizontal and vertical directions at the Q6 entrance were 7.4 and 4.3 π mm mrad, respectively. Measured emittances of vertical direction at the Q1 and Q6 entrance agreed well. However, emittances of horizontal direction did not agree well. The reason of this disagreement was the non-zero horizontal dispersion in the Dog-leg section.

Reliability and an ability of IEA were confirmed both in simulation and experiment. We are now planning to do more experiments under various conditions of the gun in order to evaluate the accuracy of IEA quantitatively. Comparison of transverse phase space distribution with the slit methods will be useful, since the methods are not suffered from energy distribution.

SUMMARY

To study the effect of energy distribution to transverse phase space tomography, experimental results at the upstream and downstream of the energy filter were compared. As the result, the low energy electrons are reconstructed as weak and scattered signals, which are predicted by previous numerical investigation.

To remove the signals from low energy electrons, IEA was introduced and examined. By a numerical simulation, the validity of the analysis was shown. IEA was applied to experimental results at the upstream of energy filter and compared with the experimental results at the downstream of the filter. The emittances of vertical direction at the upstream and downstream of energy filter agreed well, although horizontal ones were not due to non zero horizontal dispersion in the Dog-leg section. Consequently, reliability and an ability of IEA were shown both in simulation and in experiment.

REFERENCES

[1] C.B.McKee, et al., NIM A358, 1995, p.264.

[2] H.Zen, et al., Proc. of FEL2005, 2006, p.592.

[3] T.Kii, et al., Proc. of FEL2005, 2006, p.584.

[4] T.Kii, et al., NIM A507, 2003, p.340.

[5] H.M. Hudson, et al., *IEEE. Trans. Med. Imaging,* **13**, 1994, p.601.

[6] H.Zen, et al, “Transverse phase space measurement using tomographic method”, conference proceedings of SRI2006, in press.

STUDY ON FOCUSING PROPERTY OF NEW TYPE WIGGLER AND SASE-FEL EXPERIMENT AT THE ISIR, OSAKA UNIVERSITY

S. Kashiwagi#, R. Kato, Y. Kon, T. Igo, G. Isoyama,
Institute of Scientific and Industrial Research, Osaka University, Ibaraki, Osaka 567-0047, Japan
S. Yamamoto*, K. Tsuchiya and H. Sasaki
Institute of Materials Structure Science, KEK, Tsukuba, Ibaraki 305-0801, Japan
*School of Advanced Sciences, The Graduate University for Advanced Studies,
Tsukuba, Ibaraki 305-0801, Japan.

Abstract

We have developed a new type of wiggler based on the edge-focusing wiggler for free electron laser (FEL) and self-amplified spontaneous emission (SASE) in the infrared region at the Institute of Scientific and Industrial Research (ISIR), Osaka University. The strong focusing (SF) scheme is adopted for the new wiggler in order to keep the beam size small along whole the wiggler. The wiggler consists of four FODO cells for double focusing. A gain length and SASE output power for the strong focusing wiggler were numerically estimated using the 1D FEL model and Genesis code. Measuring the electron beam size in the wiggler at different wiggler gaps performed the experimental study on focusing property of the new type wiggler. We are conducting experiments to generate SASE in the infrared region and to measure its characteristics, using the strong focusing wiggler and a high intensity single bunch electron beam. We have measured the wavelength spectrum of SASE in the wavelength region between 220 and 50 μm using a grating monochromator and a Ge:Ga detector. The second harmonic and the third harmonic peaks of SASE were also observed in the spectrum measurement.

INTRODUCTION

We are conducting experiments of FEL and SASE with a high intensity electron beam in the infrared region at ISIR L-band linear accelerator, Osaka University. While the beam experiment are performing, we have developed a new type wiggler, named the edge-focusing (EF) wiggler, which produces the strong transverse focusing field incorporated with the normal wiggler field [1]. To demonstrate its principle and evaluate the performance, the first model wiggler has been fabricated. It is experimentally confirmed that a field gradient of 1.0 T/m is realized along the beam axis in the EF wiggler. The details of the model wiggler were reported in previous conference [2-3]. The EF scheme has been applied to the wiggler being used for FEL and SASE in the far-infrared region at the ISIR L-band linear accelerator, to make the gain length of SASE shorter by keeping the beam size small along whole the wiggler. Before replacing of the wiggler, the wiggler was a conventional Halbach-type wiggler and we changed its magnet parts with new ones. We, therefore, hold the wiggler parameters same as before. In order to meet a wide range of the electron beam energy and the wiggler gap, we adopt the strong focusing scheme using the EF wiggler. Focusing and defocusing elements are composed of permanent magnet blocks with the edge angle and they are alternately inserted in magnet arrays of the wiggler. The strong focusing wiggler has been fabricated and the magnetic field has been measured at KEK. In June 2005, the strong focusing wiggler installed to the FEL system at ISIR L-band linear accelerator [4].

After the installation of the strong focusing wiggler, we resumed to conduct the experiment to generate SASE in the far-infrared region. In the beam experiments, a focusing property of the strong focusing wiggler is also studied by measuring the beam sizes using screen monitors in the wiggler at different gaps.

STRONG FOCUSING WIGGLER

In this section, the developed strong focusing wiggler is described shortly. The edge-focusing wiggler is basically a Halbach type wiggler made only of permanent magnet blocks, but their shapes are not rectangular parallelepipeds. The field gradient on the permanent magnet with edge is approximately proportional to the edge angle ϕ and hence the focusing force can be easily adjusted with the edge angle. A polarity of the field gradient can be decided by choosing positive or negative angle of edge against to beam trajectory. In the strong focusing scheme, the electron beam is focused alternatively in the vertical and the horizontal directions to obtain focusing in the both directions using a sequence of focusing and defocusing elements separated by drift spaces, which is called the FODO lattice. Parameters of the FODO lattice were optimized to meet the requirements of our experiment and the parameters of the strong focusing wiggler are listed in Table 1. The permanent magnet used is NdFeB (NEOMAX-38VH, NEOMAX Co.) with Br = 1.22 T and the peak magnetic field of the EF wiggler is 0.39 T at the minimum gap of 30 mm. The number of FODO cells in the wiggler is four and the cell length is 0.48 m. The number of cells is a factor of the number of wiggler periods, 32. Focusing elements are single wiggler periods with the edge angle of +5° and defocusing ones are those with –5°, and they are

---

#shigeruk@sanken.osaka-u.ac.jp

Table 1: Main parameters of the SF wiggler

Block sizes	90x20x15 mm^3
Magnet materials (Coating)	Nd-Fe-B (TiN)
Period length	60 mm
Number of periods	32 periods
Total length	1.938 m
Peak magnetic field	0.39 T (gap 30mm)
Number of FODO cells	4 cells
Length of FODO cell	0.48 m
Edge angle	±5 °
Field gradient	±3.2 T/m

separated by 3 normal wiggler periods. Longitudinally magnetized blocks are added at both ends of the strong focusing wiggler in order to compensate for the horizontal shift of the oscillatory beam orbit due to the fringing magnetic field at the ends. Thus the total length of the SF wiggler is 1.938 m.

In the field measurement, the peak magnetic field was 0.392 T and peak magnitude of field gradient at focusing and defocusing elements was about 3.2 T/m at the wiggler gap of 30 mm. The results of measurements were good agreement with the numerical calculations.

NUMERICAL ESTIMATION

Beam focusing of the strong focusing wiggler

The envelope of beam sizes in horizontal and vertical direction for the strong focusing wiggler and a planar wiggler were calculated with an electron beam of 10 MeV, a normalized emittance of 150π mm mrad in transverse directions and a peak wiggler field of 0.392 T. Figure 1 shows the calculated beam envelopes and the solid line and dashed line show the strong focusing wiggler and the planer wiggler, respectively. In the horizontal direction, the beam envelope of the strong focusing wiggler alternatively changes along the wiggler and the average beam size (σ) in the wiggler much smaller than that of the planar wiggler. On the other hand, the vertical beam sizes for the both type of wigglers are almost same. The FODO lattice of the strong focusing wiggler slightly distorted due to the natural focusing of the wiggler. The average beam size for the strong focusing wiggler (σ_{SF}) and the planar wiggler (σ_{PL}) are 1.41 mm and 1.69 mm respectively, when the average beam size in the wiggler assumed to be $\sqrt{\sigma_{horizontal}\cdot\sigma_{vertical}}$. Transverse charge density of the beam, which is a square of the average beam size, in that of the strong focusing is about 30% higher than that of the planar wiggler. The gain length (L_g) for each wiggler is estimated from the above average beam sizes by 1D FEL model using Eq. 1.

$$L_g = \frac{\lambda_u}{4\sqrt{3}\pi\cdot\rho} \qquad (1)$$

where λ_u and ρ are period length of the wiggler and FEL parameter. Here, the bunch charge and the length of the electron beam are assumed to 30 nC and 30 ps (FWHM), corresponds to the peak current of 1.0 kA. The derived the gain length of the strong focusing wiggler and the planar wiggler are 0.152 m and 0.163 m respectively, therefore the gain length of the strong focusing wiggler is about 7% shorter than that of the planar wiggler. From the difference of the gain length, it can expect 2 times large gain of FEL can be obtained by using the strong focusing wiggler.

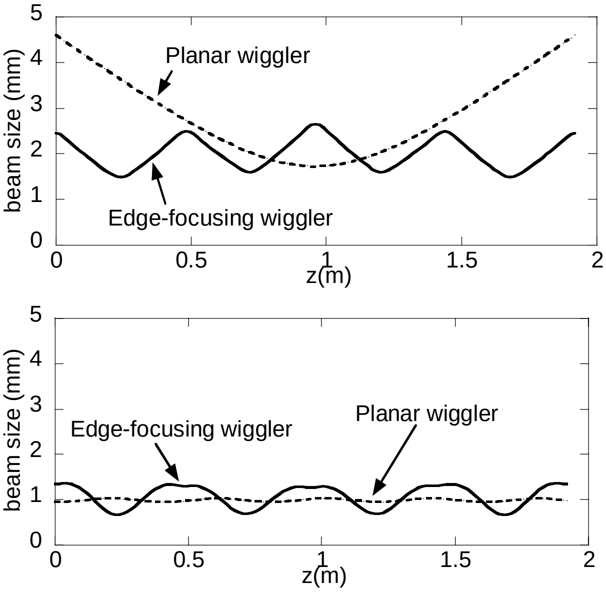

Figure 1: The envelopes of beam size in horizontal (upper) and vertical (down) directions for the strong focusing wiggler and a planar wiggler.

SASE output power

SASE output power of the strong focusing wiggler and the planar wiggler are estimated using Genesis code [5]. The beam parameters of electron beam are same in above calculations. Figure 2 shows SASE radiation power along the wigglers. In this figure, the red and the blue lines are SASE radiation power of the strong focusing wiggler and the planar wiggler, respectively. At 10MeV, the beam size is kept small in the strong-focus wiggler and the SASE power of strong focusing wiggler is 5~6 times higher than that of planar wiggler.

BEAM EXPERIMENT

The beam experiment was conducting using the L-band linear accelerator at ISIR, Osaka University. ISIR L-band linac consists of an electron gun, three-stage sub-harmonic buncher (SHB) system, pre-buncher, buncher, 3m-long accelerating structure and the experimental beam lines. The electron beam with peak current of 17 A and a pulse duration of 5 ns was produced with a thermionic gun. The electron beam was injected into the SHB system composed of two 1/12 and one 1/6 SHB cavities for the accelerating frequency of 1.3 GHz to generate a high intensity single bunch beam, and then it was accelerated to 10.3 MeV in the linac. The electron beam was

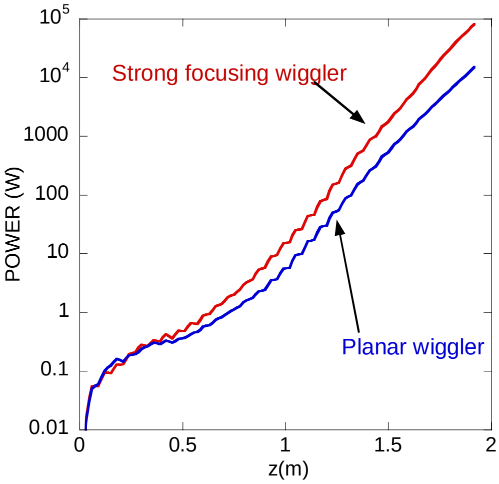

Figure 2: SASE radiation power along the wiggler. (Red line: Strong focusing wiggler, Blue line: Planar wiggler).

transported to the strong focusing wiggler via the achromatic beam transport line as shown in Fig. 3. The peak magnetic field and K-value of the strong focusing wiggler were 0.353 T and 1.4 at the wiggler gap of 32 mm. Twiss parameter and the emittance were measured using a quadrupole scan technique with a 100 μm thickness phosphor screen monitor at the exit of the accelerating structure. The normalized transverse beam emittance was ~170π mm mrad with a bunch charge of 30 nC and an energy spread of 3.0 % (FWHM). The beam injection condition and an orbit of electron beam were tuned using quadrupole magnets and steering coils at the beam transport line for FEL experiment. The unnecessary energy part of the electron beam was collimated by an energy-slit located at the dispersion section of the transport line and the energy width of the slit was about 2 %. Therefore, the net charge per bunch passing through the wiggler was about 20 nC. The experimental arrangement is shown schematically in Fig. 3. SASE radiation by the single bunch beam passing through the wiggler was reflected with a mirror (MP1) at downstream, and led to a far-infrared monochromator in the measurement room via an optical transport line. The optical transport line and the monochromator were evacuated together with a rotary vacuum pump. The low vacuum in the optical transport line and the high vacuum in the beam transport line were separated by a 0.2 mm thick, 20 mm in diameter synthetic diamond window, denoted by W1 in Fig. 3. The monochromator is a cross Czerny-Tuner type with a plane reflective grating, whose braze wavelength is 112.5 μm. The monochromator can be used in the wavelength region from 50 to over 240 μm. The wevelength resolution of the monochromator is almost constant over the range and approximately 1.5 μm for a slit width of 6 mm. The monochromatized light was detected with a Ge:Ga photo-conductive detector cooled with liquid-helium.

EXPERIMENTAL RESULT

Beam size measurement in the wiggler

We measured the transverse beam size in the wiggler using three screen monitors, denoted by F3, F4 and F5 in Fig. 3, at different wiggler gap with 10.3 MeV electron beam. In Fig. 4, the solid circles with the solid lines show horizontal beam size and the open circles with the dashed lines show vertical beam on each screen monitors at different wiggler gap from 30 to 50 mm. The horizontal beam sizes on the all screens slightly change; but they were almost constant at different wiggler gap. The vertical beam size on the F4 and F5 periodically change at different wiggler gap. It seems that the variation of the vertical beam sizes come from the changing of the natural focusing, which is strongly depend on the magnetic field strength of the wiggler. The strength of natural focusing is proportional to the square of the peak magnetic field and

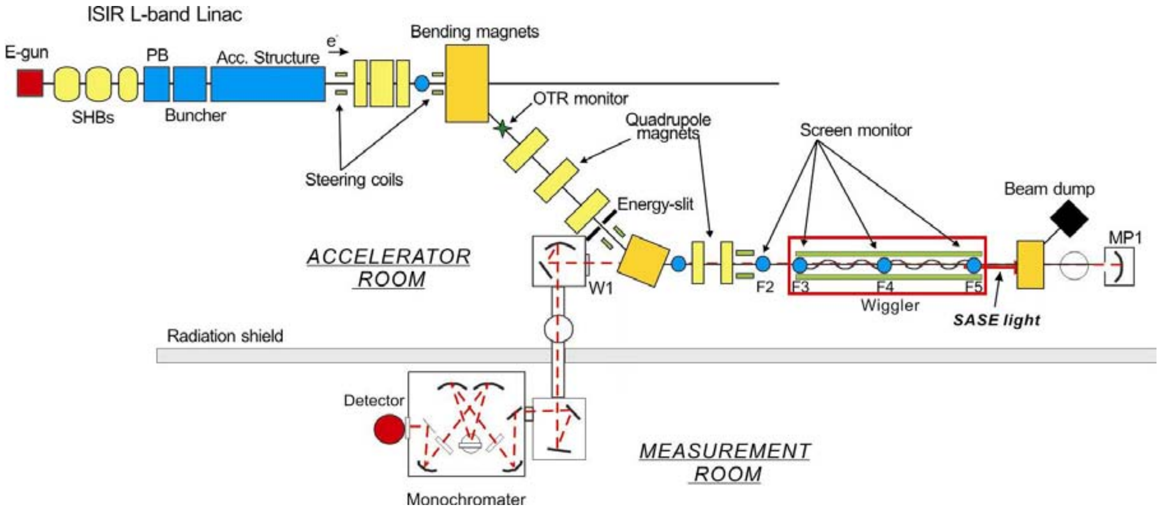

Figure 3: Schematic layout of the ISIR L-band linac and the FEL system. SASE radiation is deriver to the grating monochromator and Ge:Ga detector using optical mirrors.

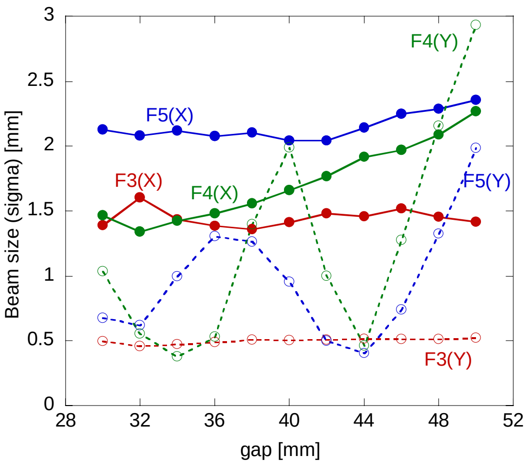

Figure 4: Measured horizontal (X) and vertical (Y) beam size using three screen monitors, denoted by F3, F4 and F5 in Fig. 3.

the strength of the edge focusing is only proportional to the peak magnetic field in the simple model of the wiggler composed of alternating bending magnets with the edge angle. Furthermore, as reported previous FEL conference [4], we have observed the peak field decreases to one-third with wiggler gap from 30 to 50 mm, whereas the field gradient decreases only by 56 % in the magnetic field measurement. The field gradient of the edge-focusing wiggler is kept at different wiggler gap. At this condition of electron beam, the natural focusing is strong and the edge focusing effect cannot be observed clearly. The measurement results were compared with the calculated beam size in the wiggler. In vertical direction, the periodically variation of beam sizes are large different, since the electron beam was injected into wiggler with not matching conditions. We will continue the study on the focusing property of the strong focusing wiggler at different condition of electron beam energy using the beam profile monitors.

Result of SASE spectrum measurement

Figure 5 shows a wavelength spectrum of SASE in the wavelength range from 50 to 240 μm with 1μm step. The closed dots and the error bar show the average values of intensities and a standard deviation, respectively, of five highest intensities in thirty successive optical pulses for each wavelength. As reported in Ref. [6], the total sensitivity of the measurement system, including the sensitivity of the detector, the efficiency of the monochromator, the transmission efficiency of the optical transport line, was calibrated over the wavelength range from 50 to 200 μm using a blackbody radiator. We have not measured the sensitivity of the measurement system above 200 μm. In Fig.5, the plotted intensities are, therefore, signal intensities from the detector and the intensities at different wavelengths are not calibrated. Although the second and the third harmonic peaks are comparable in signal intensity to the fundamental one due to the higher sensitivity of the measurement system around 100 μm wavelength, the fundamental peak is actually strongest. The intensity ratios of the second and the third harmonic peak to the fundamental one are roughly estimated from the extrapolation from the previous calibration data to be 1/35 and 1/10, respectively.

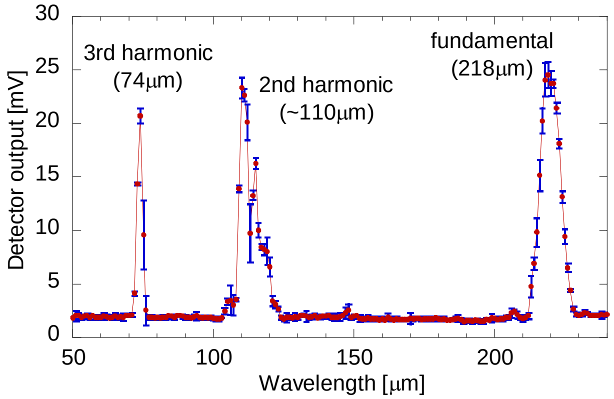

Figure 5: Wavelength spectrum of SASE in the wavelength range from 50 to 220 μm.

The measured spectral width of the fundamental peak was about 1.75 %, which is slightly smaller than those predicted value (1.9 %) by the 1D FEL model (Eq. 2).

$$dw = \sqrt{\frac{9\rho}{2\pi\sqrt{3}\cdot N_w}} \tag{2}$$

We can expect that the FEL parameter (ρ) in the actual experiment is smaller than the predicted one due to that the Twiss parameter of the electron beam are different with matching condition at the entrance of the wiggler and the beam size is larger than optimum one. We will conduct to study on SASE about the spectral width and the angular distribution of the higher-harmonics and the statistically fluctuation of SASE output power.

ACKNOWLEDGEMENTS

The authors would like to thank Messrs. S. Suemine and T. Yamamoto for the help of accelerator operation. This research was partly supported by the Joint Development Research at the High Energy Accelerator Research Organization (KEK), 2006-15, 2006 and The Ministry of Education, Culture, Sports, Science and Technology (MEXT), Grant-in-Aid and for Young Scientists (B), 17740144, 2005-2006.

REFERENCES

[1] G. Isoyama et al., Nucl. Instr. and Meth. A 507 (2003) 234
[2] S. Kashiwagi et al., Nucl. Instr. and Meth. A 528 (2004) 203
[3] S. Kashiwagi et al., Proceedings of the 2004 FEL Conference (2004) pp458-461.
[4] S. Kashiwagi et al., Proceedings of 27th International FEL Conference (2005) pp199-202
[5] http://pbpl.physics.ucla.edu/~reiche/index.html
[6] R. Kato et al., Nucl. Instr. and Meth. A 507 (2003) 409-412.

LONGITUDINAL PHASE-SPACE MEASUREMENTS OF A HIGH-BRIGHTNESS SINGLE-BUNCH BEAM

R. Kato[#], S. Kashiwagi, T. Igo, Y. Kon, G. Isoyama
ISIR, Osaka University, Ibaraki, Osaka 567-0047, Japan

Abstract

A measurement system of the longitudinal phase-space distribution of electrons using the combination of an optical transition radiation profile monitor and a streak camera are currently under development at ISIR, Osaka University. The energy spectrum is measured using transition radiation in a preliminary experiment. It is found that the OTR monitor has a higher momentum resolution than the momentum analyzer system usually used.

INTRODUCTION

We are conducting experimental studies on Self-Amplified Spontaneous Emission (SASE) in the infrared region using the L-band linac at the Institute of Scientific and Industrial Research (ISIR), Osaka University [1-3]. The performance of SASE-FEL strongly depends on beam parameters, such as a longitudinal beam profile, bunch charge, the transverse emittance and an energy profile. A correlation between longitudinal positions of electrons in a bunch and their energies has a crucial effect on the temporal evolution of the optical pulse of SASE. Several types of methods are extensively under study to evaluate the longitudinal phase-space profile of the electron beam [4-7]. Among them, a combination of Cherenkov radiation and a streak camera was used in Ref. 5 and a combination of synchrotron radiation and a streak camera in Ref. 7.

In order to measure the electron distribution in the longitudinal phase-space, we use a combination of an optical transition radiation (OTR) monitor and a streak camera together with a bending magnet. Since the bending magnet produces momentum dispersion in the electron beam, electrons diverge in the horizontal direction. The OTR radiator is placed in the lower course of the beam line from the bending magnet and it works as a converter from electrons to photons. The horizontal intensity distribution of photons is proportional to the momentum distribution of electrons, provided that the beam size of the electron beam due to the transverse emittance is negligibly small compared with the momentum distribution. By means of an appropriate optical system, the intensity distribution of photons on the OTR radiator can be focused on the horizontal slit of the streak camera. When the temporal sweep of the camera is turned on, a streak image reproduces the electron distribution on the longitudinal phase-space.

Advantages of using OTR are as follows: (1) the radiator is a simple metallic plate or foil, which produce no vacuum degradation by irradiation, (2) since the emission process is a very rapid phenomenon at a flat surface, the temporal resolution is expected to be high, (3) the number of photons is proportional to the incident electron number without intensity saturation. Furthermore, if a very thin organic film vapour-deposited with metal is used as an OTR radiator, a quasi-non-destructive monitor will be realized [8].

Compared with Cherenkov radiation or synchrotron radiation, on the other hand, the intensity of transition radiation is lower and the photon yield in the visible region is of the order of 10^{-2} photons per incident electron [9]. The L-band linac, however, can produce a high-intensity single-bunch beam typically with charge of 30 nC, so that a detectable number of photons is expected.

We recently began the feasibility study of the longitudinal phase-space monitor with OTR. In this contribution, we will present preliminary experimental results of the energy spectrum measurements with OTR.

PROPERTIES OF TRANSITION RADIATION

Transition radiation is produced by relativistic charged particles when they traverse the boundary surface of two media with different dielectric constants. When a charged particle of the velocity βc, energy γ and charge e passes across a metallic surface in a vacuum, the radiation energy per unit solid angle dΩ and unit frequency dω is given by [10]:

$$\frac{d^2W}{d\omega d\Omega} = R\frac{e^2}{4\pi^2 c}\frac{\sin^2\theta}{\left(1-\beta\cos\theta\right)^2}, \tag{1}$$

where R is the reflection coefficient of the metal and θ the angle of emitted photons with respect to the electron

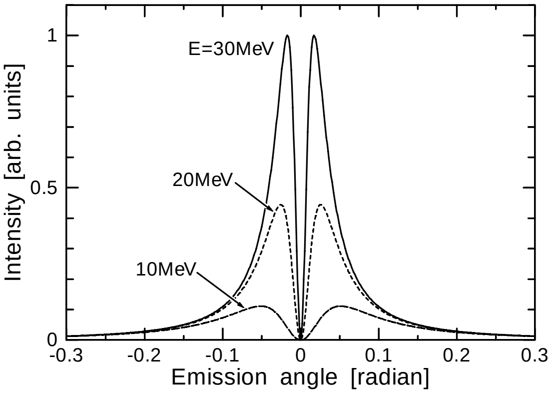

Figure 1: Angular distribution of the transition radiation.

[#] kato@sanken.osaka-u.ac.jp

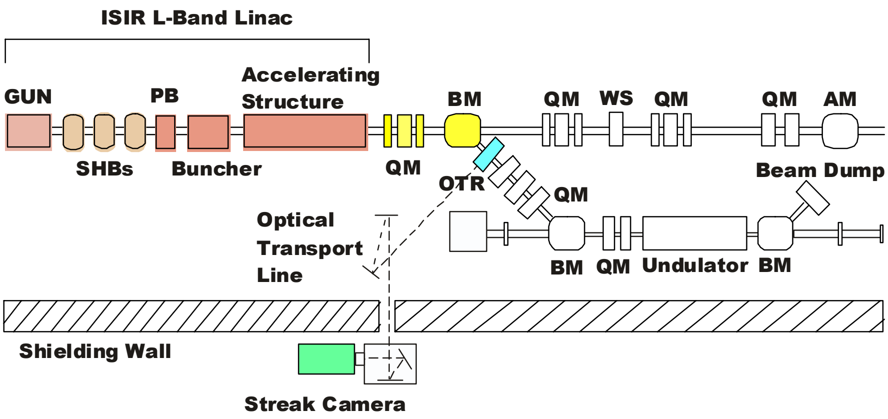

Figure 2: Schematic layout of the ISIR L-band Linac and FEL beam line. GUN: Electron gun, SHBs: Sub-harmonic Bunchers, BM: Bending magnet, QM: Q-magnet, AM: Analyser magnet, WS: Wire Scanner Monitor.

beam axis for the forward radiation and the direction of specular reflection for the backward. The angular distributions of the emitted radiation for electron energies obtained with our linac are shown in Figure 1. The emission angle of the maximum intensity is expressed by

$$\theta \cong \frac{1}{\gamma}. \qquad (2)$$

The peak intensity of transition radiation for 10 MeV energy is one-tenth of that for 30 MeV, and the emission angle for 10 MeV increases three times wider than that for 30 MeV. We, therefore, have to broaden the acceptance angle of the photon detection system in order to make use of the transition radiation as a longitudinal phase space monitor for lower energy electrons.

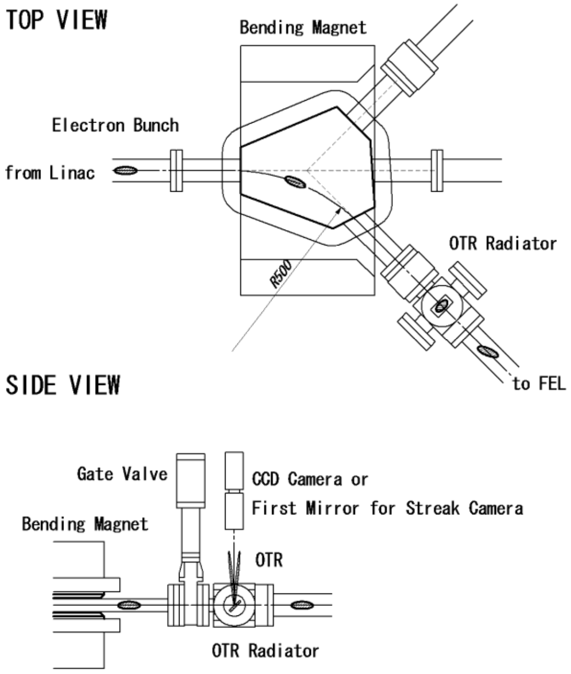

Figure 3: Configuration of the OTR radiator.

EXPERIMENTAL SETUP

Figure 2 shows a schematic layout of the L-band linac. The linac is equipped with a three-stage sub-harmonic buncher (SHB) system composed of two 1/12 and one 1/6 SHBs in order to produce an intense single-bunch beam with charge up to 91 nC/bunch. For single-bunch operation, the electron beam with a peak current up to 28 A (typically 18 A in our experiments) and a duration of 5 ns is injected from a thermionic gun (EIMAC, YU-156) into the SHB system. After being compressed to a single-bunch, the electron beam is accelerated to 10 – 30 MeV in the 1.3 GHz accelerating tube. The electron beam is transported via an achromatic beam transport line to the wiggler for the FEL system.

The OTR radiator, which converts electrons to photons, is placed at a position 320 mm downstream from the first bending magnet as shown in Figure 3. The screen is an aluminium plate having sizes of $55 \times 40 \times 1.6$ mm^3, and it is tilted vertically by an angle of 45° with respect to the

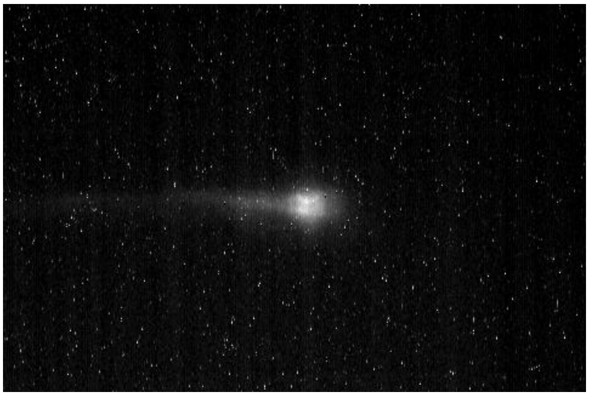

Figure 4: The OTR image of the beam profile measured using a CCD camera. The horizontal direction is the bending orbital plane of the electron beam. Left side of the image is lower momentum one.

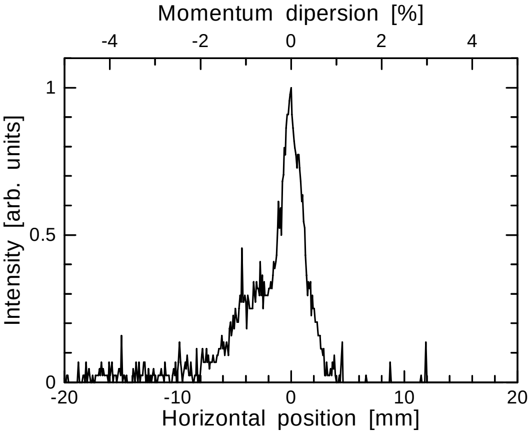

Figure 5: Momentum profile of the electron bunch obtained by integrating the OTR image in a vertical.

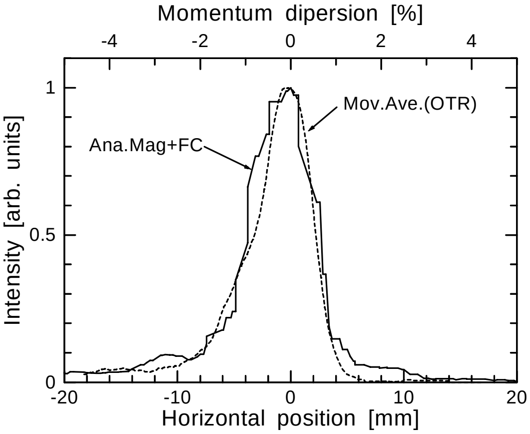

Figure 6: Momentum profiles of the electron bunch. The solid line is the momentum profile measured with an analyzer magnet and a faraday-cup current monitor. The dashed line is the profile obtained by moving average of the OTR profile within a ± 0.5 % width.

bending orbital plane, so that backward transition radiation is emitted in the vertical plane. The first mirror of the optical transport system is a concave mirror and it is placed the focal length away from center of the radiator, so that OTR image on the radiator, which diverges in the horizontal direction, is mostly included in the depth of field of the first mirror.

At first we have used a CCD camera, instead of the streak camera, for directly observing the OTR image. The camera (TAKEX, FC300M) is a progressive shutter camera and works with 659(H) × 494(V) pixels in 1/3 inch. A macro lens (Canon, J6X11) with a lens aperture of 40 mm was used for focusing. The camera was placed at a distance of 210 mm from the OTR radiator. In this configuration, an acceptance angle is approximately ± 0.1 radians, which is sufficient to capture the radiation emitted by the 20 – 30 MeV electrons.

EXPERIMENTAL RESULTS

An experiment is conducted with a single-bunch electron beam of 26.6 MeV energy. The normalized emittances are 165 π mm mrad in the horizontal direction and 160 π mm mrad in the vertical direction. A measured OTR image is shown in Figure 4. The horizontal and the vertical scales are 0.085 mm/pixel. Figure 5 shows the momentum profile of the electron bunch obtained by integrating the image in a vertical. Since dispersion function η is 0.4 m at the position of the OTR radiator, momentum resolution of the measurement system is estimated to be 0.02 %/pixel. Using the resolution, the momentum spread of the OTR profile was evaluated to be 0.4 % (full-width half-maximum). Figure 6 shows a momentum profile measured with a momentum analyzer magnet and a faraday-cup current monitor. The spectrum width of the profile is 1.6 %. The dashed line in Figure 6 shows the profile obtained by moving average of the OTR profile within a ± 0.5 % width. Since the both profiles have a similar width, the resolution of the analyzer magnet slit is estimated approximately to be 1 %. It turns out that the OTR monitor has a higher momentum resolution than the momentum analyzer system usually used.

SUMMARY

In order to measure the longitudinal phase-space profile of the electron beam, we are developing the measurement system consisted of an OTR radiator, a bending magnet and a streak camera. As a preliminary experiment, the momentum spectrum is obtained from the OTR profile, and the momentum resolution of the new system is evaluated. We are now preparing for the longitudinal phase-space measurement experiments.

ACKNOWLEDGEMENTS

The authors express their sincere thanks to Mr. T. Yamamoto for his technical contribution and Mr. S. Suemine for his support of linac operation. This research is partially supported by Japan Society for the Promotion of Science (JSPS), Grant-in-Aid for Scientific Research (C), 18540273, 2006.

REFERENCES

[1] R. Kato et al, Nucl. Instr. and Meth. in Phys. Res. A 445 (2000) 164.

[2] R. Kato et al, Nucl. Instr. and Meth. in Phys. Res. A 475 (2001) 334.

[3] R. Kato et al, Nucl. Instr. and Meth. in Phys. Res. A 483 (2002) 46.

[4] A. Doria et al., Nucl. Instr. and Meth. in Phys. Res. A 475, (2001) 296.

[5] J. Rönsch et al, “Longitudinal Phase Space Studies at PITZ”, FEL’05, Stanford, August 2005, p.552, http://www.jacow.org.

[6] H. Loos et al, “Experimental Studies of Temporal Electron Beam Shaping at the DUV-FEL Accelerator”, FEL’05, Stanford, August 2005, p.632, http://www.jacow.org.

[7] S. Zhang et al, “Temporal Characterization of Electron Beam Bunches with a Fast Streak Camera at the JLab FEL Facility”, FEL’05, Stanford, August 2005, p.640, http://www.jacow.org.

[8] T. Asaka et al, "Development of the quasi-non-destructive beam screen monitor", 27th Linear Accelerator Meeting in Japan, (2002).

[9] L. Wartski et al, IEEE. Trans. Nucl. Sci. NS-20 (1973) 544.

[10] M. Jablonka et al, “Beam Diagnostics Using Transition Radiation Produced By A 100 MeV Electron Beam”, PAC’91, San Francisco, May 1991, p.1534.

A COMPACT LOW EMITTANCE DC GUN EMPLOYING SINGLE CRYSTAL CATHODE OF LaB$_6$*

K. Kasamsook[#], K. Nanbu, M. Kawai ,K. Akiyama, F. Hinode, T. Muto , T. Tanaka, M. Yasuda, H. Hama
Laboratory of Nuclear Science, Tohoku University,
1-2-1 Mikamine, Taihaku-ku, Sendai 982-0826, Japan

Abstract

Development of an electron gun capable of producing low emittance is in the interests of further applications of high brightness electron beam such as Smith-Purcell FEL [1] for example. A prominent point of this DC gun is that operation high voltage is very low (50 kV). Since a higher beam current of the macropulse is required in general, a cathode should have higher current density, while the smaller size of the cathode is preferred for lower emittance. Consequently we have chosen single crystal LaB$_6$ as the cathode, which can provide higher current with good homogeneity emission. Some numerical calculations have also been performed. There are some good agreement in calculated results between them. Numerical calculations show a normalized rms emittance is expected to be less than 5 π mm mrad. A state-of-the-art electron source will possibly open new scientific opportunities in the many fields.

INTRODUCTION

Nowadays, the demand for high-brightness electron gun has increased dramatically to achieve many applications in the field of electron beam technolygy. The low emittance DC electron gun at LNS is one of the candidates. This DC electron gun has no grid which would degrade beam emittance. The cathode is made of materials with the low work function, and heated to 1700 - 1900 K for producing electrons. We have employed the cathode voltage of -50 kV with respect to grounded anode and variable pulse duration from 1 to 5 μsec. This low voltage choice can make the entire system to compact. The schematic diagram of DC gun power supply is shown in Fig.1. In spite of such low voltage, the emittance can be reduced to very small because of a very short distance between the cathode and the anode. In order to produce low emittance beam, the cathode size should be small, so that the higher current density is required. Such high current density can be realized by some cathode materials such as single crystal LaB$_6$ [2] or CeB$_6$ [3].The design parameters and the drawing of the low emittance DC electron gun are shown in Table 1 and Fig.2, respectively.

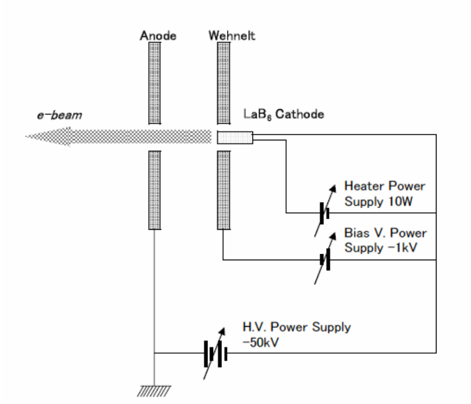

Figure 1: The schematic diagram of DC gun power supply.

Table 1: Design parameters of electron gun.

Beam energy	50 keV (Max.)
Peak current	>300 mA
Pulse width (FWHM)	1-5 μsec
Repetition rate	300 pps (Max.)
Normalized emittance	<10 π mm mrad.
Normalized thermal emittance	0.25 π mm mrad* *theoretical
Cathode diameter	1.75 mm.

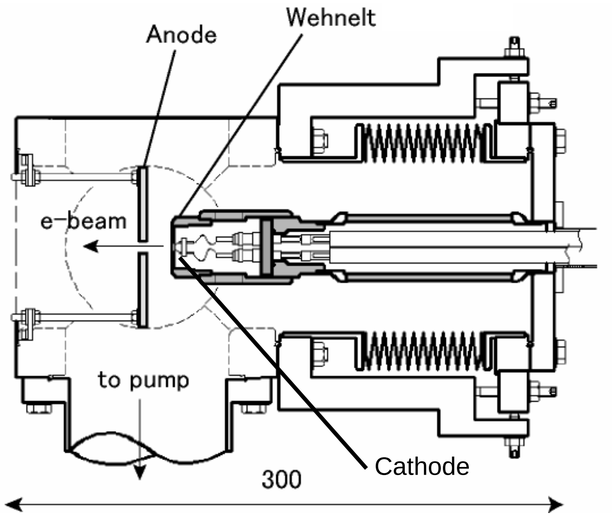

Figure 2: The low emittance DC electron gun.

---

*Work supported by KEK grant for accelerator science.

[#] kasam@lns.tohoku.ac.jp

THE LOW EMITTANCE DC GUN

LaB$_6$ cathode

The normalized rms thermal emittance of electrons emitted from a hot cathode is followed by equation (1):

$$\varepsilon_{\text{n,rms}} = \frac{r_c}{2}\sqrt{\frac{k_B T}{m_o c^2}} \quad , \tag{1}$$

where r_C is the cathode radius, k_B is Boltzman's constant, m_0 is electron rest mass and T is the cathode absolute temperature. From the above relation, in order to obtain the small emittance less than 1 π mm mrad required for an example, the X-ray FEL application, the diameter of the cathode must be in the range of a few mm. On the other hand, high emission density (~12 A/cm^2) is required to produce a several hundred miliampere peak current from the small surface. The LaB$_6$ or CeB$_6$ can emit such an intense current over long lifetimes. A single crystal is preferable for obtaining low emittance because of its extremely flat surface with low porosity after surface material evaporation. The emission density is more uniform because the crystal orientation is the same over the whole surface. In recent years, single crystal LaB$_6$ cathodes are widely used for scanning electron microscope (SEM) and superior stability has been demonstrated. So, we decided to use a single-crystal LaB$_6$ cathode with a flat crystal surface shown in Fig.3. The diameter of our LaB$_6$ cathode is 1.75 mm. The 300 mA peak current will be produced when the cathode is heated to ~1900 K at vacuum level of 10^{-8} torr or better. The theoretical thermal normalized emittance is 0.25 π mm mrad.

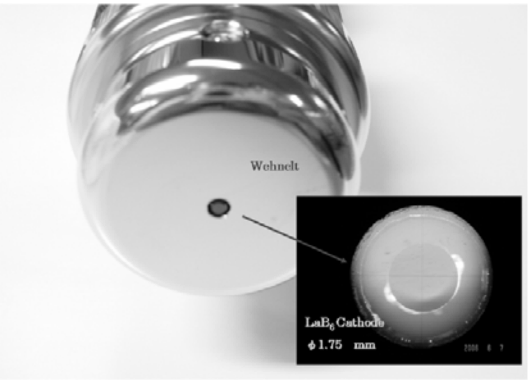

Figure 3: The assembly of single-crystal LaB$_6$ cathode.

High-voltage power supply

A high voltage DC thermionic gun uses a heated cathode to produce electrons, which are then initially accelerated with a DC pulse voltage. A low energy electron gun high-voltage power supply was developed for 0~-50 kV with 300 mA a peak current, a pulse width of 1-5 μsec, and pulse droop 0.1%, respectively. The wehnelt voltage can be adjusted from 0~-1 kV. In addition, a floating bias voltage can be applied between the cathode and the wehnelt to optimize the electric field for achieving the lowest emittance. In the case of the heater power supply, we use 1 V$_{dc}$ and 12 A maximum current to feed the LaB$_6$ cathode.

The high-voltage power supply was tested by loading at an electron gun system to generate an electron beam.The beam current was measured by the Faraday plate. The cathode was heated up to ~1800 K and the current, 200 mA, was measured in the test chamber by applying 10 W of heater power. So, one of reasons to achieve peak current, 300 mA, is that we have to increase the absolute temperature of the cathode. Up to now, the cathode has been operated for 1000 hours without failure. Fig. 4 shows the measurement waveform of the accelerating voltage and beam current.

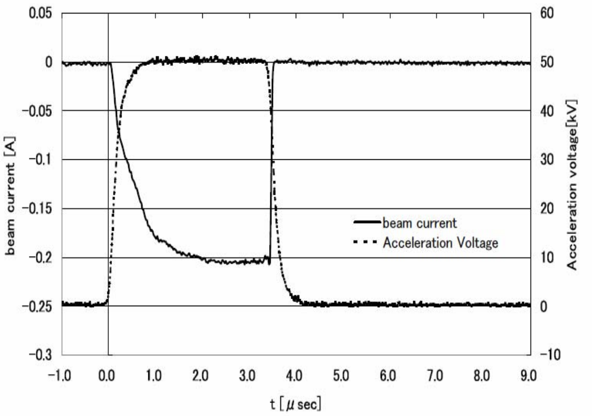

Figure 4: The measurement waveform of the accelerating voltage and beam current.

NUMERICAL CALCULATION RESULTS

We performed a computer simulation using 2 dimensional simulation code [KUAD2 v2.21] developed by Kyoto University [4,5] for 50 keV, 300 mA beam current and 15 mm cathode-anode distance in simple model. As shown in Fig.5, the beam trajectories diverge too much including the emittance growth due to space charge, which would result in a rapid increase in beam spot size. Nevertheless, the normalized emittance from the anode exit still has a small value (4 π mm mrad) at the longitudinal position far from the anode. Fig.6 shows the macro-particle distribution and the phase space distribution at the position 200 mm from the cathode. In addition, the simulation result shows electric field near the cathode surface is very sensitive to the emittance growth, which means the mechanical positioning of the cathode is very important. So we need special bias voltage between cathode and wehnelt to manipulate the electric field around cathode surface. On the other hand, we developed the 3 dimensional self-developed code 3-D FDTD [6] and compared with 2 dimensional simulation code. The trend of position dependence of the emittance is good agreement between them, and both of them still result in the small value of normalized emittance. The result of electron beam extraction and normalized emittance is shown in Fig.7, and the macro-particle distribution and phase space distribution at the end point are shown in Fig.8.

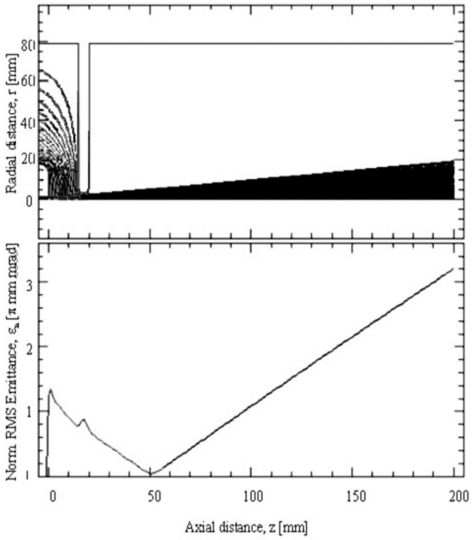

Figure 5: An electron beam extraction and normalized emittance of 300 mA in a DC gun according to a simulation with KUAD2.

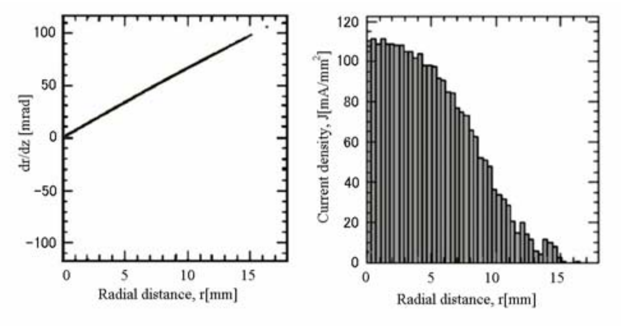

Figure 6: The macro-particle distribution and phase space distribution at the position 200 mm from cathode according to a simulation with KUAD2.

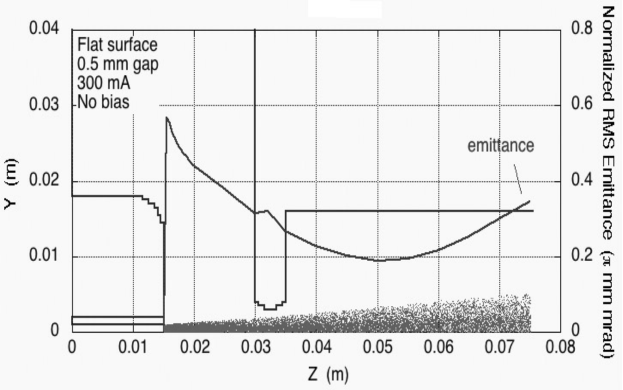

Figure 7: An electron beam extraction and normalized emittance of 300 mA in a DC gun according to a simulation with 3D FDTD.

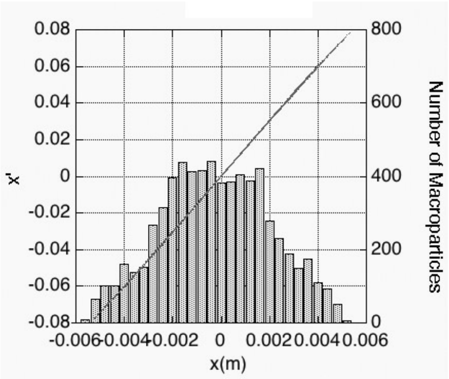

Figure 8: The macro-particle distribution and phase space distribution at the end point according to a simulation with 3D FDTD.

In another result of the 3D FDTD simulation, we applied bias voltage between wehnelt and cathode to manipulate the electric field around the cathode surface as shown in Fig.9. At the low bias voltage, a little focussing action, therefore, the emittance is gradually grow and become smoothly when the bias voltage was increased from 200 V to 400 V. The minimum point of emittance was shifted backward to cathode side by increasing of special bias voltage. At the high bias voltage, the negative field from wehnelt predominates and deflects the electron beam away from anode, so the 600 V case shows the over correction of emittance. This result shows that we can manipulate the equipotential line near the cathode surface by adjusting the special bias voltage to optimize the extracted beam emittance.

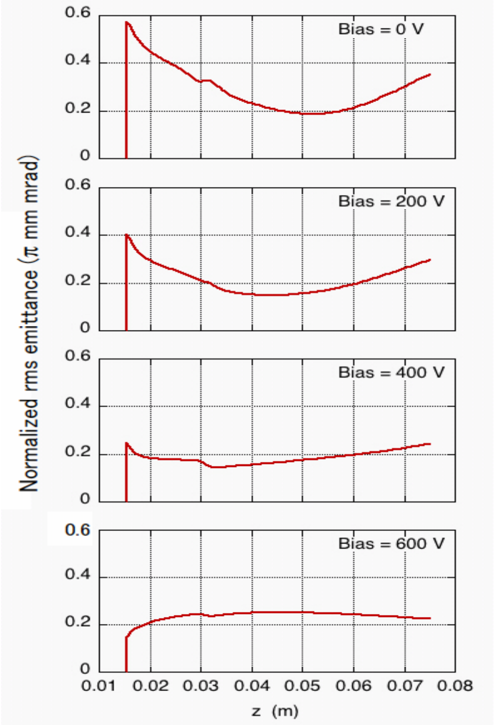

Figure 9: The bias voltage dependence of normalized emittance.

SUMMARY

Presently the DC gun has been examined on a test stand, and characteristics of the extracted beam from the gun are measured. Some numerical calculations have also been performed using 2 dimensional code and 3 dimensional self-developped code. There are some good agreement in calculated results between them. Moreover, both of them show the small value of normalized emittance. So that, the beam transportation after the gun should be carefully designed to keep such small emittance and utilize the beam. We can also apply special bias voltage to manipulate the electric field near the cathode surface.

ACKNOWLEDGEMENT

This work was supported by the KEK grant for related university accelerator science and the authors would like to thanks Prof. Kai Masuda for his 2 dimensional code calculation and the discussions.

REFERENCES

[1] K. Kim et al., Nucl. Instr. And Meth. A 475 (2001) 158.
[2] H. Kobayashi et al., Emittance Mearsurement for High-Brightness Electron Guns, 1992 Linear Accelerator Conf., Ottawa, Canada, August 1992.
[3] K. Togawa et al.,”CeB$_6$ Electron Gun for the Soft X-ray FEL Project at Spring-8”,FEL2003, Tsukuba, Japan, September 2003.
[4] K. Masuda, private communication.
[5] K. Masuda, Development of Numerical Simulation Codes and Application to Klystron Efficiency Enhancement ,Ph.D thesis , Kyoto University(1997).
[6] H. Hama, et al., Nucl. Instr. And Meth. A 528 (2004) 371.

STABLE RF PHASE INSENSITIVE TO THE MODULATOR VOLTAGE FLUCTUATION OF THE C-BAND MAIN LINAC FOR SCSS XFEL

Jong-Seok Oh[1, 2, #], Takahiro Inagaki[1], Katsutoshi Shirasawa[1], Toru Hara[1], Tsumoru Shintake[1]
[1]RIKEN Harima Institute, [2]PAL/POSTECH.

Abstract

The SCSS (SPring-8 Compact SASE Source) XFEL [1] requires extremely stable RF system in both amplitude and phase. The pulse-to-pulse fluctuation of RF output is mainly caused by modulation of the klystron beam-voltage pulse, which is directly governed by the charging stability of a klystron modulator. During R&D study on beam stability, we found a special operation point, where the beam energy gain is insensitive to the modulator voltage fluctuation. This phase can cancel out the both fluctuations and provide constant accelerating field. The stable phase depends on the klystron parameters such as the length of drift tube, operating voltage, efficiency. It is about +9° in case of the C-band main linac for SCSS XFEL. The bunch length after bunch compressor is so short that additional longitudinal energy spread due to the RF curvature is about 5% of the one caused by the longitudinal wake field. The particle energy is high enough so that longitudinal defocusing is negligible. The reduction of beam energy due to off-crest acceleration is less than 2%. This paper shows the analytical relation of the stable phase. ELEGANT [2] simulation shows no appreciable degradation of the slice parameters.

INTRODUCTION

The stability of the beam acceleration is determined by the fluctuation of both RF power and phase that are mainly caused by the modulation of a klystron voltage pulse, which is directly governed by the PFN (pulse forming network) charging stability of a modulator. Therefore, it is useful to define the sensitivities of the RF parameters such as klystron voltage, RF phase and RF power by its relative stabilities to the one of a charging voltage. This paper analyzes the sensitivities of RF parameters and beam energy, and shows a special operation point, where the beam energy gain is insensitive to the modulator voltage fluctuation.

In general, off-crest acceleration makes the beam energy more fluctuate. However, at certain phase, it is possible for this fluctuation to be same as the one due to power fluctuation with opposite polarity in the falling slope with respect to beam. This phase is preferable to get the stable beam energy even under the voltage fluctuation of the klystron. This paper shows the analytical relation of the stable phase and experimental verification.

The longitudinal profile of a bunch has to be managed to fit the SASE requirements. Energy spread, slice emittance and peak current are analytically evaluated and compared with numerical results obtained by ELEGANT simulation.

RF SENSITIVITY

The klystron voltage is directly determined by the PFN charging voltage in a modulator. The sensitivity of a klystron voltage defined by

$$s_V = \left(\frac{dV_K}{V_K}\right) / \left(\frac{dV_O}{V_O}\right) = \left(1 + \frac{Z_{PFN}}{Z_K}\right) / \left(1 + 1.5\frac{Z_{PFN}}{Z_K}\right) \qquad (1)$$

is obtained by using the Ohm's law

$$V_O = V_K + Z_{PFN} \times I_K \;, \qquad (2)$$

and the klystron beam current

$$I_K = k\, V_K^{1.5} \qquad (3)$$

where V_o is a PFN charging voltage, V_K is a klystron voltage, Z_{PFN} is PFN impedance, k is a klystron perveance, Z_k is klystron impedance. At the nominal klystron voltage where the impedance is matched, the typical sensitivity of a klystron voltage becomes 0.8.

The RF phase ϕ_{RF} from a klystron [3]

$$\phi_{RF} = \phi_o - 2\pi\, f\, t_{transit} = \phi_o - 2\pi\left(\frac{c}{\lambda_{RF}}\right)\left(\frac{L_{KLY}}{v}\right) \qquad (4)$$

is delayed from a driving input RF phase ϕ_o by the transit time $t_{transit}$ of a drift length L_{KLY} between the input cavity and the output cavity of the klystron with an electron velocity v where λ_{RF} is a wavelength in a free-space, c is the speed of light in vacuum. Therefore, the RF phase fluctuation of a klystron is

$$\left(\frac{d\phi_{RF}}{2\pi}\right) / \left(\frac{dV_K}{V_K}\right) = \left(\frac{L_{KLY}}{\lambda_{RF}}\right)\left(\gamma^2 - 1\right)^{-1.5}\left(\gamma - 1\right) \qquad (5)$$

where γ is the Lorentz factor of the electron. And the sensitivity of the RF phase is

$$s_\phi = \left(\frac{d\phi_{RF}}{2\pi}\right) / \left(\frac{dV_O}{V_O}\right) \approx \left(\frac{L_{KLY}}{\lambda_{RF}}\right)\left(\gamma^2 - 1\right)^{-1.5}\left(\gamma - 1\right) \times s_V \;. \qquad (6)$$

The typical sensitivity of the RF phase at 350 kV is 1.26 for a C-band klystron.

The RF power P_{RF} of a klystron is given by

$$P_{RF} = \eta\, I_K V_K = \eta\, k V_K^{2.5} \qquad (7)$$

where η is the RF conversion efficiency of a klystron. Therefore, the RF power fluctuation of a klystron is

$$\left(\frac{dP_{RF}}{P_{RF}}\right) / \left(\frac{dV_K}{V_K}\right) = \left(\frac{d\eta}{\eta}\right) / \left(\frac{dV_K}{V_K}\right) + \left(\frac{dk}{k}\right) / \left(\frac{dV_K}{V_K}\right) + 2.5 \;. \qquad (8)$$

[#] jsoh@postech.ac.kr

Figure 1 shows the calculated relative variation of RF power, efficiency and perveance due to the klystron voltage fluctuation of the C-band klystron (Toshiba E3746A). The perveance dependency is relatively so small that it is neglected in the sensitivity of the RF power

$$s_P = \left(\frac{dP_{RF}}{P_{RF}}\right) / \left(\frac{dV_O}{V_O}\right) \approx s_\eta + 2.5\, s_V \tag{9}$$

where s_η is the sensitivity of efficiency given by

$$s_\eta = (d\eta/\eta)/(dV_o/V_o) \quad . \tag{10}$$

The efficiency variation of a klystron at low voltage has large effect on the sensitivity of RF power. The typical sensitivity of the RF power at 350 kV is 2.4 for the C-band klystron.

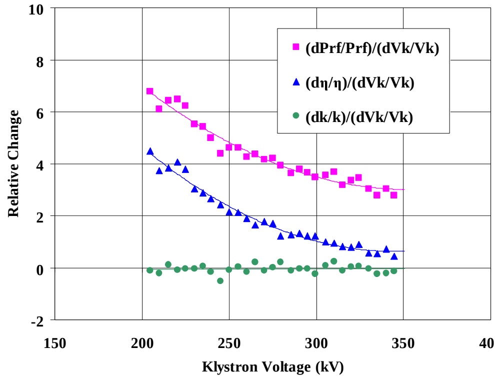

Figure 1: Relative variation of RF power (P_{rf}), efficiency (η), and perveance (k) of a C-band klystron.

ENERGY SENSITIVITY

The energy gain of an accelerating unit is

$$E \propto \sqrt{P_{RF}} \cos\phi_{RF} \quad . \tag{11}$$

Thus, its relative fluctuation by a klystron is

$$\frac{dE}{E} = 0.5 \times \left(\frac{dP_{RF}}{P_{RF}}\right) - (2\pi \times \tan\phi_{RF})\left(\frac{d\phi_{RF}}{2\pi}\right) \quad . \tag{12}$$

Using Egs. (6) and (9), the sensitivity of energy gain is

$$s_E = \left(\frac{dE}{E}\right) / \left(\frac{dV_O}{V_O}\right) = 0.5\, s_\eta + 1.25\, s_V - 2\pi \tan\phi_{RF}\ s_\phi \, . \tag{13}$$

Figure 2 shows the relative energy gain of C-band units as a function of operating RF phase with charging voltage variations at the klystron voltage of 350 kV. On a certain RF phase of the falling slope with respect to beam, which is marked by the circle in the figure, the amplitude is somewhat constant because the both fluctuations are cancelled out, which provides constant accelerating field. The energy gain is insensitive to the modulator voltage fluctuation around the stable phase satisfying following condition

$$\tan\phi_{RF} = \left(\frac{1}{2\pi\, s_\phi}\right)(0.5\, s_\eta + 1.25\, s_V) \quad . \tag{14}$$

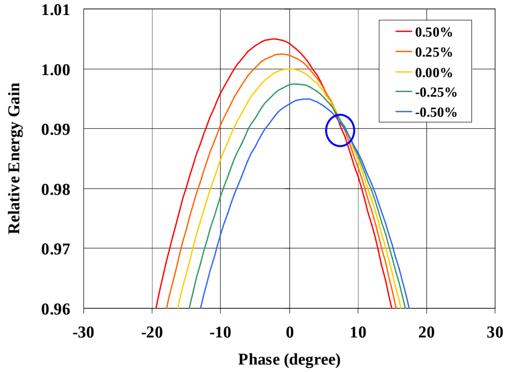

Figure 2: Relative energy gain vs. RF phase with charging voltage variations at the klystron voltage of 350 with a C-band klystron. The stable phase is +7.2° at 350 kV level.

Figure 3 shows the sensitivity of energy gain for the crest phase and the off-crest phase. The typical sensitivity of the energy gain at 350 kV is 1.2 for a C-band unit. The energy gain is insensitive over wide range of klystron voltage at the off-crest phase of +9°. A little large angle than +7.2° provides better sensitivity for wide operating range below 350 kV. The loss of energy gain by the off-crest acceleration is 1.2%.

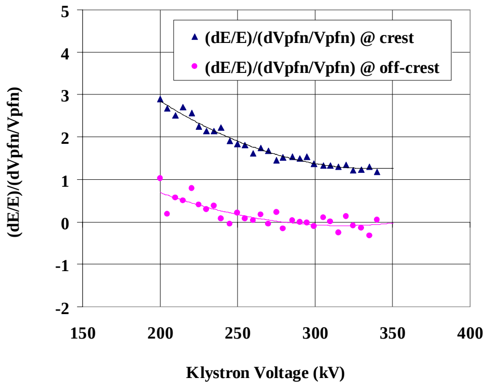

Figure 3: Relative variations of energy gain due to the fluctuation of the PFN charging voltage for crest phase and off-crest phase of +9°.

Including the effect of relative phase jitter σ_ϕ between injected beams and C-band RF at an arbitrary phase, the sensitivity of energy gain becomes

$$s_E^2 = (0.5\, s_\eta + 1.25\, s_V - 2\pi \tan\phi_{RF}\, s_\phi)^2 + (2\pi \tan\phi_{RF})^2 \left(\frac{\sigma_\phi}{2\pi}\right)^2 / \left(\frac{dV_o}{V_o}\right)^2 \quad . \tag{15}$$

EXPERIMENTS

The SCSS prototype accelerator has a C-band main linac after an S-band unit of an injector [4]. The main linac has two RF sources and increases the beam energy from 50 MeV to 250 MeV. The beam energy fluctuation is measured for different RF phases by the screen monitor located at the middle of a chicane having a dispersion of

150 mm. Figure 4 shows the measured beam energy fluctuation of the C-band main linac. The beam energy stability at crest for two C-band units is 0.34% (6σ); the stability of energy gain per unit is 0.59% (6σ). The energy fluctuation is sensitive to the operating phase and also is asymmetric with respect to the crest phase. The energy fluctuation at the off-crest phase of +10° is reduced to 50% level of the one at crest acceleration.

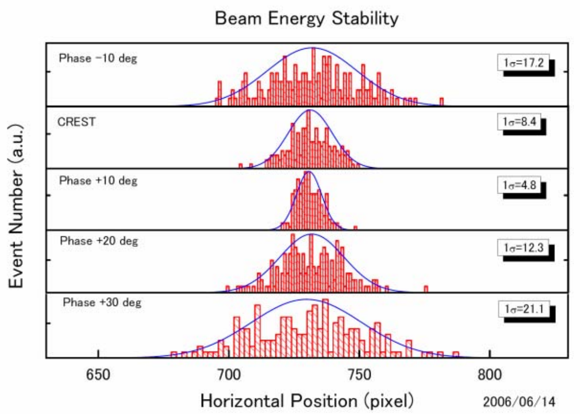

Figure 4: Beam energy fluctuation vs. RF phase of C-band main linac of SCSS prototype accelerator (0.01 mm/pixel).

Figure 5 shows the stability trend of energy gain per C-band unit normalized by the one at crest phase:

$$\left(\frac{dE}{E}\right)^2 / \left(\frac{dE}{E}\right)^2_{crest} = \left(1 - \frac{2\pi \tan\phi_{RF} s_\phi}{0.5 s_\eta + 1.25 s_V}\right)^2 + \left(2\pi \tan\phi_{RF}\right)^2 \left(\frac{\sigma_\phi}{2\pi}\right)^2 / \left(\frac{dE}{E}\right)^2_{crest} \quad . \tag{16}$$

Each curve has different relative phase jitter normalized by the energy stability at crest, $(\sigma_\phi/(2\pi))/(dE/E)_{crest}$. For example, with 0.2% energy stability at crest, 50% normalized phase jitter corresponds to 0.1% relative phase jitter that is equivalent to 0.36°. Measured data (C-band 060614) in Figure 5 agree to the case of 50% normalized relative phase jitter. It means that the phase jitter is about 1.1° that corresponds to the timing jitter of 0.52-ps at C-band frequency.

At the off-crest phase satisfying Eq. (14), the energy stability becomes

$$\left(\frac{dE}{E}\right) = \left(\frac{0.5 s_\eta + 1.25 s_V}{s_\phi}\right)\left(\frac{\sigma_\phi}{2\pi}\right) \quad . \tag{17}$$

Then, it becomes ~ $\sigma_\phi/(2\pi)$ at 350 kV. Therefore, the total energy stability is directly determined by the phase jitter.

Measured data (C-band 060614) indicate that the minimum fluctuation of the beam energy is located at about +8° from the crest as expected. The fluctuation at this phase is limited by the phase jitter. The different set of measured data (C-band 060711) shows that the normalized relative phase jitter is increased to 100%, which is identified later to be caused by the instability of a maser RF oscillator.

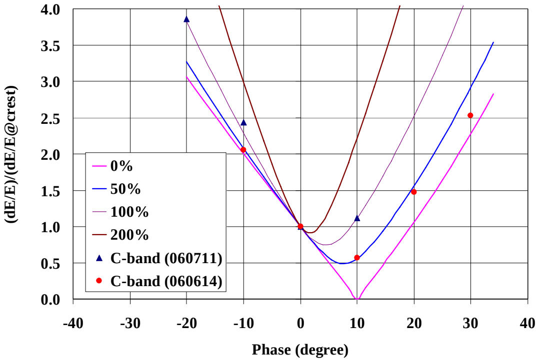

Figure 5: Stability of energy gain per C-band unit normalized by the one at crest phase for relative phase jitter of 0%, 50%, and 100%.

BEAM QUALITIES

The geometry of a C-band accelerating structure with iris radius *a*, cavity radius *b*, gap length *g*, and cavity period L_{cell} is shown in Figure 6. The short-range wakefield of the structure is evaluated by the K. Bane's formula [5]

$$W(s) = \frac{Z_o c}{\pi a^2} \exp(-\sqrt{s/s_{oo}}) \tag{18}$$

where

$$s_{oo} = \frac{g}{8}\left(\frac{a}{\alpha(g_{cell}/L_{cell}) L_{cell}}\right)^2 \quad , \tag{19}$$

and

$$\alpha(\gamma) = 1 - 0.4648\sqrt{\gamma} - 0.0704\gamma \quad , \tag{20}$$

and $Z_o = 120\pi$ [Ω].

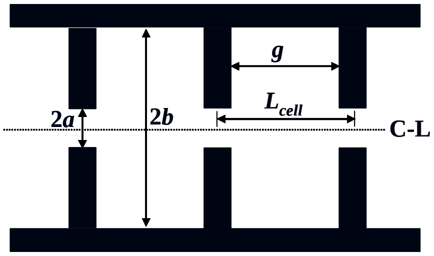

Figure 6: The geometry of a C-band accelerating structure: *a* = 7.6 mm, *b* = 21.2 mm, *g* = 15.2 mm, and L_{cell} = 19.682 mm.

With structure parameters of a C-band unit, s_{oo} = 982 μm, and *W*(0) = 0.623 kV/pC/m. This paper uses the beam parameters given in the "Optimization of Parameters" of the 6-GeV SCSS CDR [1] where the accelerating gradient is 34.0 MV/m after the second bunch compressor BC2. The compressed bunch length *s* after BC2 is 24 μm. It is so short that the wakefield over the bunch is close to *W*(0), then the longitudinal energy spread of a bunch due to the short-range wakefield with a bunch charge *Q* over a total accelerator length *L* is approximately

$$\Delta W \approx -eQW(0)L \quad . \tag{21}$$

There are 25 accelerator modules in the C-band main linac of the SCSS 6-GeV machine. Each module has 4 units of 1.8-m long structures. Therefore, total accelerating length is 180 and the longitudinal energy spread becomes -44.6 MeV. Considering the effect of finite bunch length, it is -40.1 MeV. The net change of head-tail energy spread through the C-band linac obtained by ELEGANT code is – 41.3 MeV as shown in Figure 7.

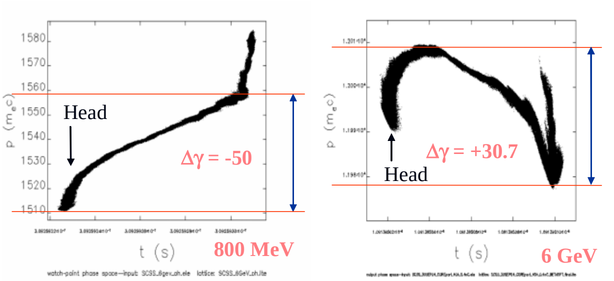

Figure 7: Structural wake effect on the longitudinal energy profile of a bunch (left: 800-MeV beam at the inlet of C-band main linac, right: 6-GeV beam after C-band main linac, bunch head at left side).

There is energy gain difference ΔW_{RF} between the head electron and the tail electron of a bunch, which is caused by the phase difference of RF fields along the bunch.

$$\Delta W_{RF} = \Delta[eEL\cos\phi] \cong -eEL\sin\phi_o \Delta\phi \tag{22}$$

where e is electronic charge, E is peak accelerating field. In case of 6-GeV SCSS design, eEL = 5200 MeV, and $\Delta\phi$ = 0.164° for s = 24 µm. Therefore, the energy spread due to the RF fields becomes -2.33 MeV for the off-crest phase of ϕ_o = +9°. This energy spread is 5.81% of the one caused by wakefield. The ELEGANT simulation shows the difference of -1.53 MeV as shown in Figure 8.

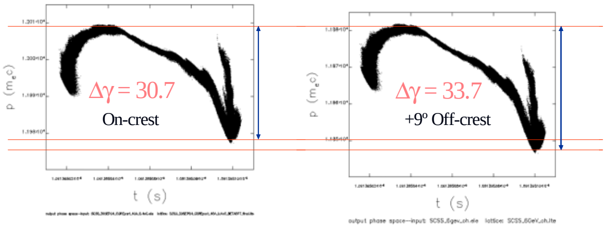

Figure 8: Comparison of longitudinal energy profile of a bunch for the on-crest acceleration (left) and +9° off-crest acceleration (right).

The slice parameters such as slice emittance and peak current are dominant governing parameters of SASE process. We have to keep the slice parameters as good as possible. It is confirmed that there is no appreciable degradation of slice parameters for off-crest acceleration as shown in Figure 9.

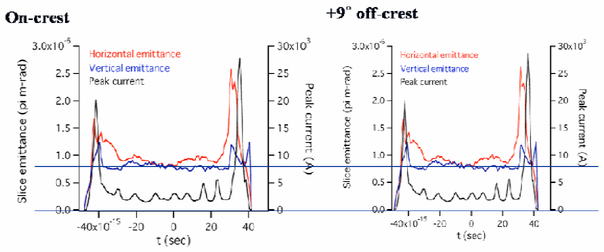

Figure 9: Horizontal slice emittance (top), vertical slice emittance (middle), and peak current (bottom) profile of a bunch (left: on-crest acceleration, right: +9° off-crest acceleration).

SUMMARY AND DISCUSSION

The SCSS XFEL is a challenging machine that requires extremely stable RF system. Therefore, it is critical issue to realize stable RF system for both phase and amplitude to provide stable XFEL. The phase-dependent stability characteristics are in detail analyzed and examined. It is confirmed that the off-crest phase of around +9° provides better stability in case of the C-band main linac for SCSS XFEL if phase jitter is small. The low-level RF control has to provide better stability than the one of a klystron modulator for this scheme to be effective. The reduction of beam energy due to off-crest acceleration is about 1%.

The additional longitudinal energy spread due to the RF curvature is about 5% of the one caused by the longitudinal wake field and there is no appreciable degradation of the slice parameters.

The RF unit for a velocity buncher or a bunch compressor is more sensitive to the RF fluctuation because of the off-crest operation to provide a necessary energy chirp. For example, the energy fluctuation is more than 4 times higher than the crest one at the typical off crest phase of -40° for SCSS accelerating units between BC1 and BC2.

REFERENCES

[1] http://www-xfel.spring8.or.jp

[2] M. Borland, “ELEGANT” LS-287, ANL, Argonne, IL 60439, USA.

[3] Linear Accelerators, P. M. Lapostolle and A. L. Septier, editors, North Holland Publishing Company, p322 (1970).

[4] T. Hara, “Electron Beam Simulations on the SCSS Accelerator,” the 26th International Free Electron Laser Conference, Italy, 2004.

[5] K. L. F. Bane, “Short-Range Dipole Wakefields in Accelerating Structures for the NLC,” SLAC-PUB-9663, LCC-0116, 2003.

ANALYSIS OF INVERTER CHARGING WAVEFORM FOR ULTRA STABLE SCSS MODULATOR

Jong-Seok Oh[1, 2, #], Takahiro Inagaki[1], Katsutoshi Shirasawa[1], Tsumoru Shintake[1]
[1]RIKEN Harima Institute, [2]PAL/POSTECH.

Abstract

The SCSS (SPring-8 Compact SASE Source) XFEL [1] requires ultra stable RF sources. The SCSS smart modulator driving a klystron RF source uses an inverter charging system. Therefore, the stability of RF sources is directly determined by the one of inverter power supplies. The regulation and the stability of an inverter depend on not only the structure of inverter topology but also the fidelity of a signal monitoring. For better stability, we need stable and adequate monitoring of a charging voltage. The charging waveform is composed of a net PFN (pulse forming network) voltage and ripple components that is related to the system-dependent circuit parameters. This ripple is proportional to the ratio of the PFN capacitance to the stray capacitance of a pulse transformer and a klystron load. We can manipulate the feedback signal with suitable filtering but it is shown that the charging stability depends on the way of signal conditioning also. The long-term drift has to be minimized by the temperature stabilization of the probe and feedback circuits.

INTRODUCTION

The SCSS XFEL uses normal conducting technology for beam acceleration, in which pulse-to-pulse power fluctuation in RF-system dominates beam stability. The RF output is mainly fluctuating due to the pulse-to-pulse variation of a klystron voltage that is determined by the PFN charging voltage of a modulator. The inverter is responsible to the RF stability because it charges the PFN capacitor. In order to stabilize the charging level, we need a clean and stable signal for the PFN voltage. There are not only pulse forming network capacitors but also protective series resistors and distributed reactive components of a pulse transformer and a klystron load in the charging path. Therefore, the charging waveform becomes somewhat complicated. The understanding of the charging waveform and the proper conditioning of feedback signal is necessary to realize an ultra stable charging performance. This paper shows the detail analysis of the charging waveform of SCSS modulators and the stability dependency on the signal conditioning.

SCSS MODULATOR

Figure 1 shows the circuit topology and its charging waveform for inverter charging scheme using a constant current source. This scheme is compared with the ones of the traditional resonant charging scheme using a constant voltage source. The inverter topology provides high reliability: a thyratron switch is safely turned off because next charging schedule is digitally controllable, it is inherently fail-safe system under short-circuit condition due to the current limit feature of a constant current power supply. In addition, it is naturally compact by using a high frequency inverter. Also it has other attractive features: expandability, easy maintenance, and flexible control interface [2]. These features are well matched to the next generation modulator for SCSS XFEL facility.

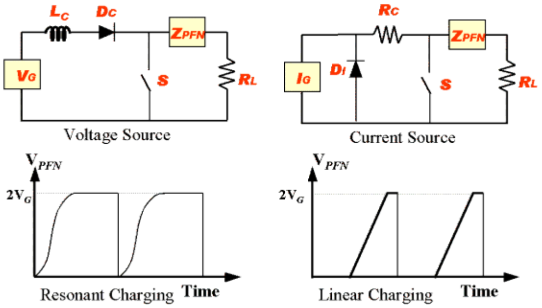

Figure 1: Basic circuits and charging waveforms of a voltage source and a current source power supply.

Figure 2 shows the simplified circuit diagram of SCSS modulator that consists of a PFN, a thyratron switch, a pulse transformer, and an inverter power supply as a PFN charging unit. The inverse voltage is limited by a tail circuit absorbing the magnetic energy stored in the pulse transformer. The main specifications are as follows; 114-MW peak power, 30-kW average power, 60-pulse per second, 3.8-µs pulse width, 1:16 step-up ratio, 350-kV peak voltage (secondary side) [3].

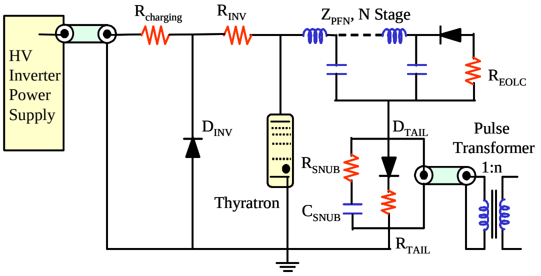

Figure 2: Simplified circuit diagram of SCSS modulator.

Figure 3 shows detailed charging waveforms of a C-band modulator (C_{PFN} = 0.4 µF) around the charging level of 38 kV. The average increment of charging step ΔV_{PFN} is about 100 V with a switching frequency f of 34.6 kHz; therefore, the average charging current I_{dc} is 1.38 A at this charging level according to the following equation.

$$I_{dc} = C_{PFN}\Delta V_{PFN} f \tag{1}$$

[#] jsoh@postech.ac.kr

The charging voltage is not rising smoothly and monotonically but includes high-frequency spikes. The magnitude of spikes is larger than the increment of charging level for each switching cycle. The voltage waveform at the pulse transformer secondary shown in the figure has similar oscillating pattern. Therefore, it is expected that the spike is made by the circuit components connected in parallel to the pulse transformer. The noisy spikes seem to be harmful for the feedback circuit to correctly compare the charging level with a reference level.

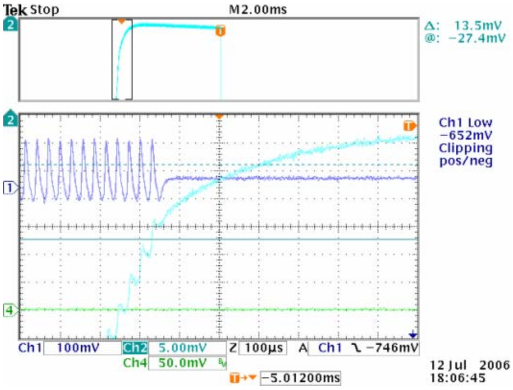

Figure 3: Waveforms of charging buckets (Upper box: charging voltage waveform, Lower box: expanded view of square box marked on the upper box for pulse transformer secondary voltage (upper curve, 1.18 kV/div) and PFN charging voltage (lower curve, 100 V/div), Horizontal: 100 µs/div)

ANALYSIS OF CHARGING WAVEFORM

In order to analyze the circuit response of charging current, it is useful to know the Fourier components of charging current. The inverter output is a full-wave rectified current as shown in Figure 4.

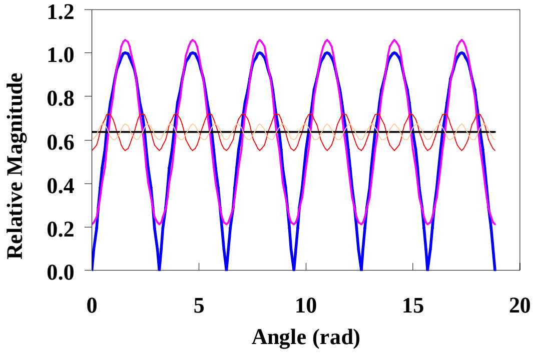

Figure 4: Full-wave rectified current (thick blue line) and Fourier series.

It has an average value of I_{dc} and higher frequency components I_{ac}. The average current is 2/π of a peak value I_{peak}. The second harmonic current is dominant and it is 4/(3π) of the peak value according to Eq. (2). Therefore, the magnitude of second harmonic current is 66.7% of the average charging current; $I_{ac} = (2/3)\, I_{dc}$.

$$\begin{aligned}\frac{I_{ac}}{I_{peak}} &= -\frac{4}{\pi}\sum_{n=2}^{\infty}\frac{\cos n\omega t}{(n+1)(n-1)} \quad (n = even\ only) \\ &= -\frac{4}{\pi}[\frac{1}{3}\cos 2\omega t + \frac{1}{15}\cos 4\omega t + \ldots] \approx -\frac{4}{3\pi}\cos 2\omega t \end{aligned} \tag{2}$$

The output current from an inverter power supply, *I*, has to flow through the series impedances of R_1, R_2, Z_{PFN}, and Z_L in the equivalent charging circuit shown in Figure 5. The charging current flows through the complicated load impedance network Z_L. The spike voltage is generated by oscillation caused by the total stray capacitance and the magnetizing inductance of a pulse transformer.

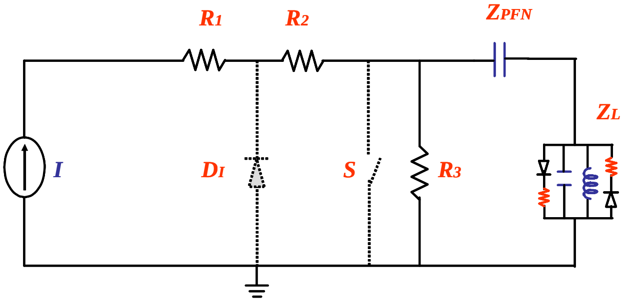

Figure 5: Equivalent charging circuit.

To improve the present stability of SCSS modulators, it is planed to use an ultra stable inverter power supply that is operating in parallel with a main inverter. The concept and design example is described in Ref. [4]. This inverter has small charge per switching with higher switching frequency. The frequency response of the charging network of a SCSS modulator measured because of the possibility of a resonance, which distorts the charging waveform. Figure 6 shows the measured data and the calculated frequency response by the circuit model. The phase transition occurs at 40 kHz that is caused by the parallel resonance driven by the magnetizing inductance L_{mag} of a pulse transformer and total stray capacitance C_{stray} of a pulse transformer and a klystron load. Series resonance at higher frequency of Figure 6-(b) is driven by C_{stay} and a series inductance in the charging path.

The second harmonic current of a SCSS modulator is capacitive-coupled because its frequency is higher that 40 kHz. There is no resonance till 250 kHz and the gain is monotonically decreasing. Therefore, higher frequency is able to be applied without serious waveform distortion for a high precision inverter up to 100 kHz.

The ripple voltage, V_{ac} introduced by the second harmonic current through a stray capacitive impedance X_c (=2πfC_{stray}) is given by

$$V_{ac} = I_{ac}X_c = I_{dc}/(6\pi fC_{stray}) \ . \tag{3}$$

The ripple factor defined by $2V_{ac}/\Delta V_{PFN}$ is the relative magnitude of the ripple voltage to the increment of a charging voltage per one cycle of an inverter switching. By using Eq. (1) and (3), the ripple factor is

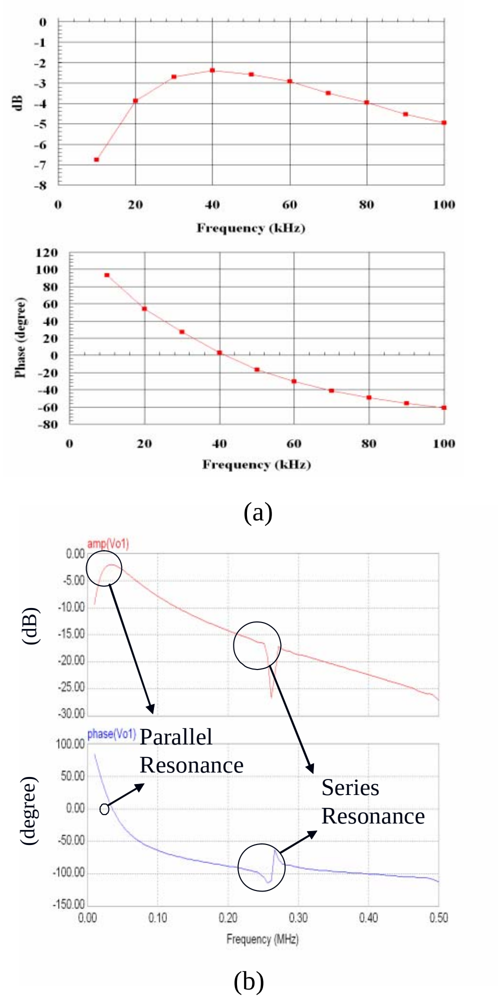

(a)

(b)

Figure 6: Frequency response of a charging network of a SCSS modulator: (a) measured data, (b) circuit simulation.

$$2V_{ac}/\Delta V_{PFN} = C_{PFN}/(3\pi C_{stray}) \quad . \tag{4}$$

Table 1 shows the summary of ripple voltage parameters for the SCSS modulator. In order to verify this evaluation, equivalent circuit analysis is performed.

Table 1: Ripple voltage parameters of charging waveform

PFN capacitance, C_{PFN}	0.4 μF
Average charging current, I_{dc}	1.58 A
Switching frequency, f	34.6 kHz
Increment of charging, ΔV_{PFN}	114.2 V
Stray capacitance, C_{stray}	25.9 nF
Ripple current, I_{ac}	1.05 A
Charging impedance, X_c	88.8 Ω
Ripple voltage, V_{ac}	93.2 V
Ripple factor, $2V_{ac}/\Delta V_{PFN}$	1.63

Figure 7 shows the simulated charging waveform with the conditions given in the Table 1. Figure 7(a) is the initial charging waveform. The net PFN voltage (VPFN-V_primary) is monotonically increasing but the PFN voltage (VPFN) has 100-V ripple with second harmonic frequency. It shows that the DC component I_{dc} is flowing through the magnetizing inductance of a pulse transformer (I_Lmag) and AC ripple current is mainly flowing through the stray capacitance (I_Cstray). Figure 7(b) is the charging waveform at the 38 kV level. The former half of the full-wave rectified current is gradually increasing to two-time large value than the initial one, and the latter half is gradually decreasing to zero. Accordingly, the diode in the tail circuit is turned on as the positive primary peak is increasing. At last, it becomes half-wave rectified waveform having a two times large peak current but the net average charging current is still same.

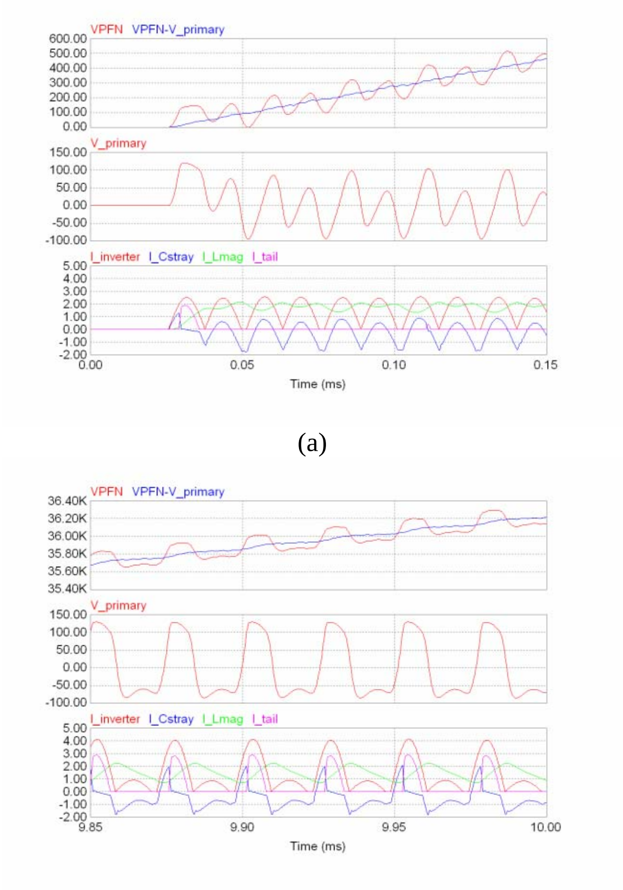

(a)

(b)

Figure 7: Simulated charging waveforms: "V_PFN" = PFN voltage from ground potential, "V_PFN - V_primary" = net PFN voltage: (a) initial charging waveform, (b) charging waveform around 36 kV.

The Fourier series of the higher harmonic for the half-wave rectified waveform depicted in Figure 8, is described by

$$\begin{aligned}\frac{I_{ac}}{I_{peak}} &= \frac{1}{2}\sin\omega t - \frac{2}{\pi}\sum_{n=2}^{\infty}\frac{\cos n\omega t}{(n+1)(n-1)} \qquad (n\ even\ only) \\ &= \frac{1}{2}\sin\omega t - \frac{2}{\pi}[\frac{1}{3}\cos 2\omega t + \frac{1}{15}\cos 4\omega t + \ldots] \quad .\end{aligned} \tag{5}$$

The dominant term now has same frequency as the switching one and its magnitude is 50% of the average charging current that is similar to the one of dominant term for the full-wave rectified waveform. Therefore, its ripple has same magnitude as the one of full-wave mode.

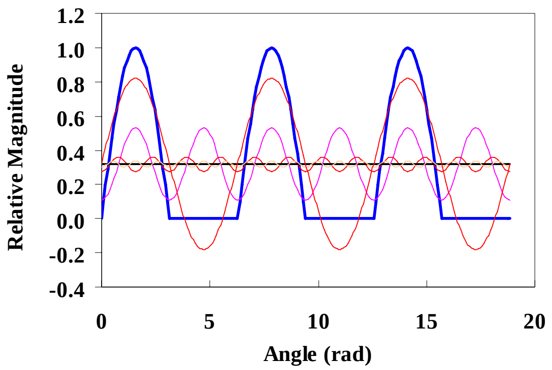

Figure 8: Half-wave rectified current (thick blue line) and Fourier series.

EFFECT OF SIGNAL FILTERING

The charging voltage is determined by the command reference. The reference level is compared with a feedback signal coming from a high voltage probe. Therefore, not only the reference level but also the feedback signal has to have high fidelity and stability. Figure 9 shows how improper conditioning of monitoring signal affect the charging stability under the reference level of 30 kV. The high frequency ripple on the rising slop of a feedback signal is well filtered out in the case (a); 1-kHz low pass filter. The charging voltage is regulated at the level higher than the reference one. Therefore, it is not able to correct the time dependent variation of the droop of top level. If the circuit has low frequency cut below 0.5 Hz, then, the actual PFN voltage is gradually rising even the comparator circuit is feeling the same level of feedback signal as shown in the case (b).

SUMMARY AND DISCUSSION

The SCSS modulator has many features fitting to the XFEL application, which are provided by adopting the inverter power supply that is one of governing factors for the stability of electron beams of SCSS linac. The ripple voltage superimposed on the PFN charging waveform is analyzed as a function of circuit parameters. It is found that the ripple factor is proportional to the ratio of the PFN capacitance to the stray capacitance. The conditioning of the feedback signal has large effect on the regulation of PFN voltage. The understanding of the charging waveform and the proper conditioning of feedback signal is essential to realize an ultra stable charging performance.

It is possible to measure the net differential voltage by using an additional probe that has equally calibrated and balanced for high frequency response.

The high voltage components of a probing system such as resistors and capacitors are temperature sensitive elements. The devices on the low level feedback circuits also have thermal drift. Therefore, it is essential to stabilize the temperature of the probe and feedback circuits to remove the long-term slow drift of beam energy.

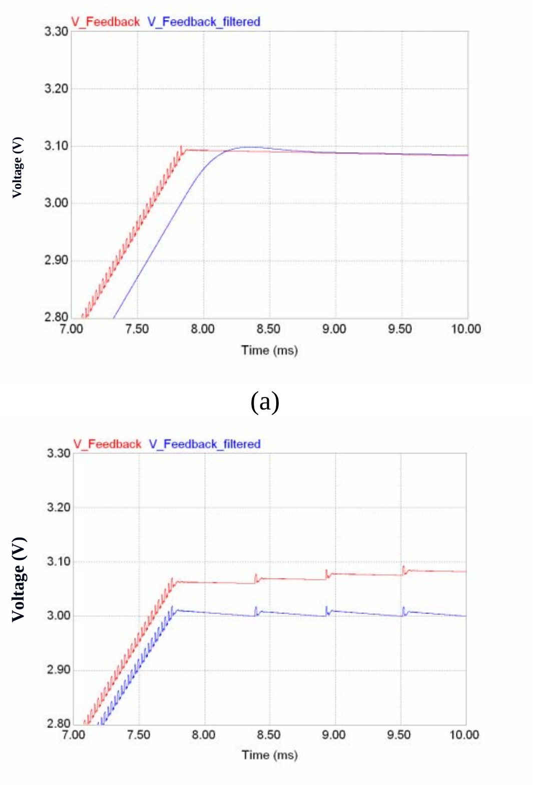

(a)

(b)

Figure 9: Regulation characteristic for different filtering of a feedback signal with high voltage probe attenuation of 1/10,000: (a) 1 kHz low pass filter, (b) 0.5 Hz high pass filter.

REFERENCES

[1] http://www-xfel.spring8.or.jp

[2] J. S. Oh, et. al., “Development and Application of an Inverter Charging Supply to a Pulse Modulator,” the XXI International LINAC Conference, Korea, 2002.

[3] T. Inagaki, et. al., “High Power Test of the Compact, Oil-Filled Modulator for C-band Klystron,” the third Asian Particle Accelerator Conference, Korea, 2004.

[4] J. S. Oh, et. al., “Development of an Ultra Stable Klystron-Modulator for PAL XFEL,” the 27th International Free Electron Laser Conference, USA, 2005.

ELECTRO-OPTIC SAMPLING METHOD USING HIGH DC VOLTAGE APPLYING SETUP*

Yong-Woon Parc#, Changbum Kim, Jung Yun Huang, Jangho Park, Sung-Ju Park, In Soo Ko,

PAL, Pohang, Korea

Xiang Dao,
Department of Engineering Physics, Tsinghua University, Beijing, China.

Abstract

A RF photo-cathode (RF PC) gun with 1.6 cell cavity is installed at GTS(Gun Test Stand) being built at the Pohang Accelerator Laboratory (PAL). The short, intense, and low emittance electron beams are produced by the RF PC gun. For the successful construction of PAL-XFEL, the timing jitter and bunch length of the beam at the exit of the gun should be measured accurately. EOS (Electro-Optic Sampling) is a very promising method to measure the jitter without any interference with the electron beam. The spatially resolved method will be used in this experiment, which is a single shot measurement using cooled CCD carmera due to very low energy. Before the measurement with the beam at the exit of the gun, the calibration experiment is done with DC high voltage applying setup with 1mm thick ZnTe crystal. The broadening of our laser pulse by the ZnTe crystal will be measured with auto-correlation method to know the resolution limit in this experiment and to do data analysis properly. In this presentation, the result of calibration experiment will be presented with a description of the experiment in detail and simulation result for low energy beam.

INTRODUCTION

EOS (Electro Optic Sampling) method to measure short, intense electron beam which is essential to construct XFEL light source is developed greatly in last few year [1,2,3,4]. For the successful construction of XFEL light source, the monitoring of timing jitter of electron beam is crucial in online condition. The method can be used for monitoring the timing jitter of all section of the light source for example injector, bunch compressor, undulator sections. We are now trying to measure the electron beam at the injector part of XFEL to be constructed in PAL. A 2 MeV electron beam with a tunable bunch length and 0.2nC bunch charge has recently been realized at PAL[5,6].

THEORY

The theory for the signal detection scheme of EOS is well described in ref[7], so we give only a short summary of it here.

Balanced detection scheme

The vertical and horizontal polarized part intensities of the incident laser to the ZnTe crystal is changed due to the birefringence of the crystal induced from the electron electric field. The analytic expression is in Eq.(1),(2)

$$\Gamma = \frac{\omega_0 d}{c}\left(n_h - n_v\right) = \frac{\pi d}{\lambda_0} n_0^3 r_{41} E_0 \qquad (1)$$

$$I_h - I_v = \left|\mathrm{E}_h\right|^2 - \left|\mathrm{E}_v\right|^2 = E_0^2 \sin\left(\Gamma\right) \qquad (2)$$

where the Γ is the relative phase shift between the two polarized parts of the laser field, and d is the crystal thickness.

Layout

In order to understand the theory for the signal detection scheme of EOS, the layout is described in detail in Fig. 1. The linearly polarzed laser experiences the birefringence in EO crystal due to electric field from the electron beam. The difference of the vertical and horizontal part of the laser field can be measured with quarter wave plate and Wollaston prism with sine function proportionality as mention in above section.

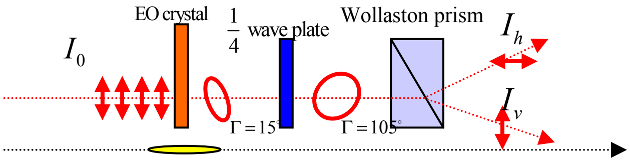

Figure 1: Layout of Electro-optic sampling

---

* This work is supported by the KOSEF under the contract number R01-2006-000-11309-0 and also by the Ministry of Science and Technology.

#young1@postech.ac.kr

DC SETUP EXPERIMENT

To test the EO crystal response to the electric field strength, we made a high DC voltage applying setup. The result is shown in Fig. 2.

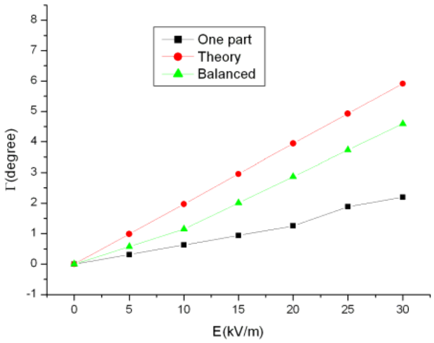

Figure 2: The response of the ZnTe crystal in DC electric field. The circle(red line) is theory, the triangle(green line) is balanced detected result and the square(black line) is measured result from the vertical part of the laser using single photodiode

The result showed that the crystal which thickness is 3.2 mm used in this experiment followed the theory well.

SIMULATION

Simulation method for Thz propagation

The ZnTe crystal showed frequency dependent refractive index which is propotional to the electric field called Pockel effect. The electric field profile due to the electron longitudinal profile is Fourier transformed to know the response of the electric field inside the crystal. We know the speed of each Fourier component in the crystal, which make us possible to reconstruct the field profile passing through the crystal. The field profile is shown in Fig. 3 with time domain representation.

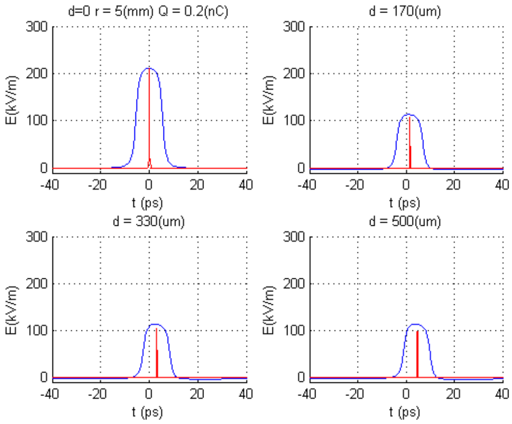

Figure 3: Electric field propagation in the crystal. The blue line showed the electric field strength, the red line showed the laser pulse. The r is the distance between the laser and electron beam and d is the thickness of the crystal.

Ring approximation of electron beam

The exact field profile of the electron beam is complicated to expressed in an analytic form. Instead of the exact field profile, we can use the ring approximation which has an exact solution which allowed the relativistic expression. The result showed that we can make almost exact field profile with only two terms, one is monopole term and the other is quadrupole term. The quadrupole term amplitude is very small compared to the monopole term. The Equation(3) showed the relativitic expression of the ring approximation.

$$E_r = \frac{q\gamma}{4\pi\varepsilon_0}\left[\begin{array}{l}\dfrac{r}{\left(\gamma^2v^2t^2+r^2\right)^{3/2}} \\ -\dfrac{a^2}{4}\left(\dfrac{2r}{\left(\gamma^2v^2t^2+r^2\right)^{5/2}}+\dfrac{5r\left(2\gamma^2v^2t^2-r^2\right)}{\left(\gamma^2v^2t^2+r^2\right)^{7/2}}\right)\end{array}\right] \qquad (3)$$

In the above equation, q is the charge of the electron beam and v is the velocity of the beam and r is the distance between the laser passing point and the electron beam. In Fig. 4, the green line shows the field profile in the free space and the blue line sowes it in the crystal which is smaller than free space case because of the reflection in the surface of the crystal due to the boundary condition of electro-magnetic theory.

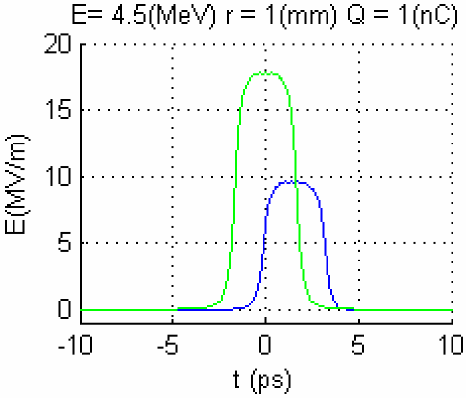

Figure 4: Electric field strength in free space (green) and in the crystal (blue).

Balanced signal

The laser pulse speed and the Thz radiation speed in the crystal is not same which makes the slippage between two pulse. In our simulation, we calculate the relative phase shift from the integral with 50 sections of the crystal.

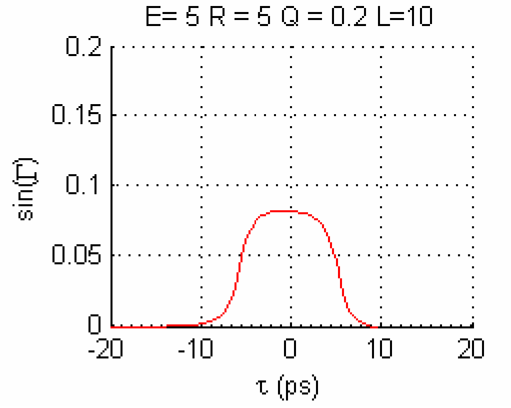

Figure 5: The simulated balanced signal of low energy beam which energy is 5MeV, beam charge is 0.2nC and the pulse length is 10ps uniform beam. R the distance between the laser and electron beam is 5mm. τ is the arrival time of the laser at the crystal compared to the electron beam.

The result showed that the low energy beam of the injector of XFEL can also be measured with EOS very successfully. The signal level is almost 1/10 of initial laser intensity incident in the crystal which is very easily detected using phtodiode or balanced detector.

LOW ENERGY BEAM DIAGNOSITICS

At present, we completely installed the EOS experiment setup in the GTS(Gun Test Stand) in PAL. The coarse timing of the arrival time of electron beam and laser beam at the crystal is solved with measurement of all path of the UV and IR laser and the distance between the gun cathode and electro optic crystal chamber. Belanced detector signal is observed easily in the oscillocope which is not saturated. We moved two mirrors in the path of 800nm laser beam to make time delay between electron beam and laser beam to find exact synchronization to see the change of the signal. The precision timing will be done very accurately with balanced detector. Sampling method is not appropiate to measure the bunchlength due to the electron arrival time jitter. Instead of the sampling method, the spatial method which is using the CCD carmera to take a picture of the laser gives a way to measure the bunch length and timing jitter simultaneously.

REFERENCES

[1] X. Yan et al., Phys. Rev. Lett. 85, p 3404 (2000).
[2] I. Wilke et al., Phys. Rev. Lett. 88, p 124801 (2002).
[3] G. Berden et al., phys. Rev.. Lett. 93, p 114802 (2003).
[4] A. L. Cavalieri et al., phys. Rev.. Lett. 94, p 114801 (2005).
[5] Jangho Park et al., to be appeared in FEL2006 (2006).
[6] Tae-Yeon Lee et al., to be appeared in FEL2006 (2006).
[7] M. Bruken et al., TESLS Report 2003-11, (2003).

PRELIMINARY MEASUREMENT OF EMITTANCE EVOLUTION USING EMITTANCE METER AT THE PAL*

Jangho Park#, Sung-Ju Park, Changbum Kim, Yong-Woon Parc, Jung Yun Huang, and In Soo Ko,
Pohang Accelerator Laboratory, POSTECH, Pohang 790-784, Korea
Xiang Dao, Department of Engineering Physics, Tsinghua University, Beijing 100084, China
X.J. Wang, NSLS, Brookhaven National Laboratory, Upton, NY 11973, USA.

Abstract

A high-brightness electron beam is emitted from a RF photocatoode gun with 1.6 cell cavity from October 2005 at the Pohang Accereator Laboratory (PAL). The project of 4th Generation Light Source (4GLS) with the Spontaneous Amplification Sponteneous Emission Free-electron Laser (SASE FEL) in the PAL is called Pohang Accereator Laboratory X-ray Free-electron Laser (PAL-XFEL). In order to success of the PAL-XFEL project, it is necessary to research the high-brightness electron beam at the injector. A emittance meter (E-Meter) is installed for the high-brightness research in GTS (Gun Test Stand). The measurement of transverse emittance and beam size profile along the longitudinal direction was done by the E-Meter. Precise measurement of the emittance profile will be provided with a powerful tool for the commissioning of the 4GLS injectors based on the emittance compensation principle. We are going to achieve this with the use of slit-based E-Meter that can be moved along the longitudinal direction. In this article, we present a preliminary measurement of the emittance evolution with the E-Meter for the commissioning of the photocathode RF gun.

INTRODUCTION

The Pohang Accelerator Laboratory X-ray Free Electron Laser (PAL X-FEL) is proposed with self amplifiered spontanous emision (SASE) lasging sheme that will use the final 3.7 GeV for the drive beam energy [1-2]. The performance of the PAL X-FEL in the 3.0 Angstrom regime is predicted on the capacity of 1 nC, 100 A beam at the end of the photoinjetor with transverse normalized rms emittance of 1.2 π mm mrad. For the low emittance beam, emittance compensation scheme is essential for the design and commitioning of the photoinjector.

In this paper, we review and report the emittance evolution in the beam drift region with emittance meter (E-Meter). This paper is composed of previous work on the subject of the emittance evolution measurements systems and the preliminary measuring of the beam emittance evolution of the photocathode rf gun. We then describe preliminary experimental result at the PAL where the slit based emittance measurement technique is used to measure the emittance evolution of the PC RF gun. The results of the experiment, which show that a possibility of the emittance evolution measurement found with the E-Meter, are compared with simulation.

EMITTANCE COMPENSATION

The emitance compensation is a technique used to reduce the normailzed rms emittance of the beam at the photoinjector. The emittance compensation typically involves two complementary stages: the rotation of phase space for each slice of the beam in the solenoid and the realignment of the slices and fast acceleration in the booster. Essentially, the principle of the emittance compensation by solenoid is the balance between the repulsive forces due to space-charge and external focusing forces. After the beam goes through the solenoid magnet region, the beam is blowed up by space-charge force if there is no booster linac [3-4]. Thus a booster is needed to fast accelrate the beam to a relatively high energy region at which the phase space is frozen and the beam is emittance dominated. To shift the second emittance minimum to the enterance of the booster where the beam is emittance dominated, Serafini and Ferrario suggested a matching condition [3-4] for properly matching the space-charge dominated beam from the gun to the booster,

$$\sigma' = 0\,, \qquad \gamma' = \frac{2}{\sigma}\sqrt{\frac{I_P}{2 I_A \gamma}}\,, \tag{1}$$

where σ is the rms transverse spot size, I_P is peak current of the beam, I_A = 17 kA is the Alfven current. The booster matching point will be investigated by our experiments for optimizing the emittance compensation process i.e., by the emittance characterizations for various longitudinal position which will be performed with the Emittance-Meter using a slit based emittance measument technique. We use the rms emitance and the normalized rms emitance, defined by [5]

$$\varepsilon_{rms} = \sqrt{\left\langle x^2 \right\rangle \left\langle x'^2 \right\rangle - \left\langle x x' \right\rangle^2}\,, \qquad \varepsilon_{n,rms} = \beta\gamma\varepsilon_{rms}\,, \tag{2}$$

where β and $\gamma = 1/\sqrt{1-\beta^2}$ are the relativistic factors, the bracket denotes an average over the beam distribution at each location, the primes refer to axial derivatives, and

---

*Work supported by the CHEP and the KOSEF (Project No.: R01-2006-000-11309-0) of Korea.

#wpjho@postech.ac.kr

$\left\langle x^2 \right\rangle, \left\langle x'^2 \right\rangle$ are the second monents of the beam distribution.

A BNL GUN-IV type rf photo-cathode gun for far infra-red radiation (FIR) project is installed in the PAL. A resonant frequency of the gun cavity is 2856.0 MHz with 3.4 MHz mode separation. The photoelectron beam is emitted from the PC RF gun at the PAL since October 2005. The beam parameters are achieved 2.5 MeV beam energy with 2.5 % relative energy spread and 400 pC beam cahrge at the 30° laser injection phase. The emittance, the beam size, and the beam energy are simulated by the PARMELA code for the PAL XFEL injector with fullfilled emittance matching condition and the emittance compensation as shown in Fig. 1.

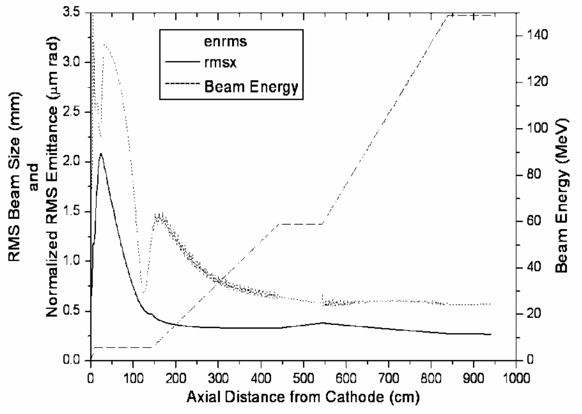

Figure 1. The beam size (solid line), the normalized rms emittance (dot line), and the beam energy (dash line) are simulated by PARMELA code for PAL-XFEL injector with fulfilled emittance matching condition.

EXPERIMENTAL SETUP

Our electron beam parameters are shown in Table1. The beam parameters depend on the laser parameters and rf power and phase.

Photocathode RF Gun and Basic Instruments

Figure. 2 shows the experimental setup with a 1.6 Cell photocathode S-band (2856 MHz) rf gun with 8 pancake-like solenoids. The PC rf gun was developed and constructed by collaboration of the BNL, KAIST, and PAL. The laser driven copper cathode rf gun consisted of 1.6 cell cavity with a half cell and a full cell. The half cell of the 1.6-cell rf gun is symmetrized by two laser ports which are rotated 45° from the waveguide, tuner, and pumping port in the full cell. The laser incident port, there is an angle of 67.5° between the laser propagation direction and the cathode normal vector, allows for ultra-violet (UV) laser to flash the cathode surface and to minimize the transmission loss. The gun is operated in pi-mode at S-band with multi-pole suppression achieved through cavity symmetrization. The coupling between the waveguide and the full cell is accomplished via the coupling slot on the full cell cavity. An electric coupling located between the half cell and full cell is utilized to couple rf power from the full cell to half cell. A home made klystron was proceeded to yield 80 MW at an rf pulse length of 1 μs of 2856 MHz. The klystron can be operated with maximum 60 Hz repetition rate at a 10MW rf power. The field gradient in the cavity was built by the rf power with 2856 MHz of 2 μs pulse width. The temperature of the cavity can be maintained by the precision cooling system for tuning the rf resonant condition. In order to reduce the space-charge induced emittance growth should be quickly accelerated in the gun. After the gun, a solenoid for the transverse emittance compensation is directly mounted with four ceramic key to prevent heat transmission. A steering magnet with maximum magnetic field of 80 Gauss is installed a space between inside the solenoid bore and outside the vacuum pipe. Immediately following the solenoid is an integrated current transformer (ICT) to measure the beam charge without beam dump.

After the ICT there was a screen to downstream for measurement and monitoring of the beam profile. The screen, which is about 15 μm layer of YAG:Ce doped on aluminium substrate of 100 μm thickness, is mounted on an aluminium holder at the 45° with respect to the beam axis. The position of the screen is 0.56 m from the cathode. A charged coupled device (CCD) camera to acquire of the electron beam image is synchronized to the electron beam for a shot-to-shot measurement. The spectrometer with a 60° sector dipole magnet for electron beam energy and the energy spread is located downstream of the screen.

Laser Systems

The laser system consists of an active mode-locked Ti:Sapphire oscillator, a regenerative amplifier, a second harmonic generator (SHG), a third harmonic generator (THG), and a custom designed UV stretcher system. The laser system for the rf PC gun is installed in a clean room which temperature stability is dynamically controlled within 0.5 °C for stable operation. The oscillator is operated at a frequency of 79.33 MHz by using a frequency divider (/36) with the master oscillator of 2856 MHz for the lock-to-clock between the master and laser oscillator. The oscillator output is phase-locked with a reference 79.33 MHz divided rf frequency by dynamically adjusting the cavity length of the oscillator with piezo mirror by lock-to-clock module. The timing jitter is measured to within an rms value of 130 fs using a phase detection method. The measured energy stability of the oscillator output using by infra-red (IR) power meter is 1 % peak to peak. From the oscillator, 105 fs width with a full width at half maximum (FWHM) value, 800 nm wavelength pulse is generated with 79.33 MHz repetition rate. These laser pulses come into the regenerative amplifier to amplify the pulse energy up to about 2.5 mJ with 1 kHz repetition rate. After the regenerative amplifier, the amplified laser pulse comes into the THG with a pair of frequency conversion non-linear crystals to obtain 266 nm UV light with maximum laser energy of 250 μJ. The UV laser pulse still has an ultra short pulse width. An UV pulse stretcher with a pair of prisms is installed in order to stretch the pulse width of the UV laser to 10 ps FWHM. In addition, the UV pulse stretcher has a capability to change the pulse duration of the UV laser from 1 ps (FWHM) to 10 ps (FWHM). A cross correlator with a BBO crystal is installed in order to measure the pulse width at the UV region using cross correlation method.

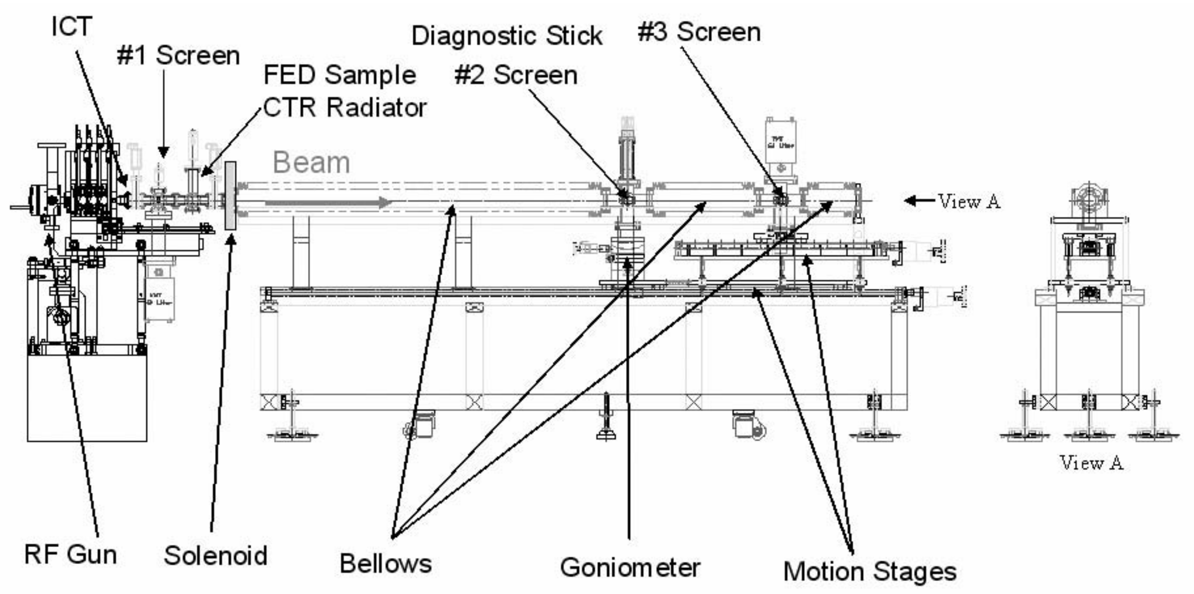

Figure 2: Schematic diagram of experimental setup of the gun test stand (GTS) for photo-injector developments of the PAL-XFEL.

Emittance Meter

We have designed the Emittance-Meter which has the movable slits chamber and screen chamber along the beam axis with bellows independently, which will be used to demonstrate the emittance evolution predicted by theory and simulation [3-4]. The transverse emittance evolution after solenoid magnet to compensate of the beam emittance along the beam axis can be measured by this Emittance-Meter. Designed Emittance-Meter was shown in Fig. 2, the left side part was the PC RF gun, and the right side part was the Emittance-Meter. The Emittance-Meter consisted of three long bellows, the slit plate chamber with the YAG screen to make beamlet and to measure the main beam size, at the downstream of the slit chamber YAG screen chamber to measure of the beamlet size. The long bellows is used for the transverse emittance measurement from 0.9 m to 2.1 m position measured from the cathode. The length of the bellows can be changed from 0.54 m to 1.54 m without vacuum breaking. The distance from pin-hole chamber to screen chamber can be moved along to the beam divergence. If the beam has a big divergence, the distance should be short and the other case it should be large to make an optimized image size at the screen. In the last part, we put another bellows to make the vacuum force balance in the front part bellows. We will check the position of the slit plate chamber and the screen chamber with CCD cameras and a long scale attached on the shelf. The slits are fabricated by high power Laser micro-drilling with 30 μm, 40 μm, and 50 μm silt widths in tungsten plate with 0.5 mm thickness. The plates in the Emittance-Meter are designed to be changeable at the specific experimental position with stepping motor. We can compare the emittance value to each slit width along to a space-charge dominance factor [6]. The sizes of the slit are determined by considering the signal to noise ratio (SNR) and the acceptance angle when the beam goes through the plate [7]. Also, very small size hole should be aligned on the beam axis for beam measurement, because if the hole is not aligned, the beam is dumped on the tungsten plate. We designed to realize an alignment technique with goniometric motion, rotary motion, and linear motion with high accuracy stepping motor. The single slit scanning method will be used in usually with x and y directional linear motion which method is needed precision moving control, however the analysis of the data files is easy [8].

.

THE PRELIMINARY MEASUREMENT OF TRANSVERSE EMITTANCE EVOLUTION

The transverse emittance evolution was measured by a pair of a singe slit with 30, 40, and 50 μm slit width and an YAG screen downstream of the slit. The beamlet.is created by the slit plate, which is made by 0.5 mm tungsten plate. The beamlet distribution is then imaged on the screen downstream of the slit plate at a distance of 71 cm from the slit. The width of the beamlet has a connection with a measure of the width of the transverse momentum distribution at the slit. The beamlet yield the correlated beam divergence and the rms transverse divergence,

$$x_c' = < x - w > / L,$$

$$\sigma' = \sqrt{\frac{\langle x^2 \rangle}{L^2} - \left(x_c'\right)^2},$$

where L is the distance between the slit and the YAG screen, x is the measured beamlet size on the screen, and w is the slit width. Here the average is performed over the distribution in the measured beamlet. The beamlet size is measured about 10 times larger than the slit width to reduce the space-charge effect in the emittance measurement In generally, quad technique for beam emittance measurement was reported over-estimated due to the purely space-charge dominated region [refer insert]. The position of the slit from the cathode can be changed with stepping motor without vacuum break which of the least position of the slit is 1.4 m from the cathode. The distance between the slit and the YAG screen can be changed for optimizing of the beamlet measuring on the YAG screen.

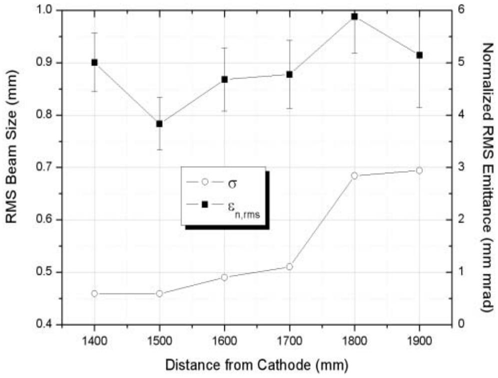

Figure 3: Preliminary measurement of the emittance evolution (solid circle) and the beam evolution (empty circle).

The distance is 0.71 m between the slit chamber with the screen and the screen chamber for measuring of a beamlet size. The main beam size on the #2 screen at the slit chamber and beamlet size on the #3 screen at the screen chamber are measured by the synchronized CCD camera. From measured the beam size and the beamlet size the beam gradient is calculated which for the beam emitance calculation. The evolution of the beam emitance and beam size is shown in Fig.3.This experiment is performed with the condition of 2.0 MeV beam energy and 350 pC beam charge with 30º laser injection phase.

SUMMARY

The experimental measurement by the E-Meter is to measure the emittance evolution in the drift region for many experimental conditions to find optimized operating condition for our injector. We measure the first measurement of the emittance evolution at the drift region of the photo-injector. For better results of the emittance evolution, we need to improve data analysis methodology, and to automate data acquisition processes. For advanced experiments, we need to improve high energy (more than 5 MeV at the gun) beam experiment or normal laser incidence.

REFERENCE

[1] 4th Generation Light Source: *Conceptual Design Report*, Pohang Accelerator Laboratory (Nov. 2004).
[2] T.-Y. Lee et al., J. Korea Phys. Soc. **48** pp. 791-795 (2006).
[3] M. Ferrario et al., SLAC-PUB-8400, March 2000.
[4] L. Serafini, J.B. Rosenzweig, Nucl. Instrum. and Meth. A 311 (1992), 437.
[5] J. D. Lawson, *The Physics of Charged-Particle Beams*, 2nd ed., Oxford University Press (1988).
[6] S. G. Anderson and J. B. Rosenzweig ed. al., PRST-AB Vol 5, 014201 (2002).
[7] K. Flottmann, TESLA-FEL 96-09, May 1996.
[8] A. Cianchi, et al., Proceedings of EPAC 2004, Lucerne, Switzerland (2004).

BEAT-WAVE LASER-DRIVEN PHOTOINJECTOR FOR SUPERRADIANCE FREE-ELECTRON LASER

Yen-Chieh Huang, Han-Lung Chang, and An-Chung Chiang, National Tsinghua University, Taiwan.

Abstract

A periodically bunched electron beam is useful for generating electron superradiance. This paper studies the generation and acceleration of density-modulated electron beams from a photocathode electron gun driven by a laser beat wave. Computer simulation shows feasibility of accelerating and preserving the density-modulated electron beam in an accelerator.

INTRODUCTION

Radiation from relativistic electrons is important for generating THz and *x*-ray wavelengths at which solid-state laser sources are not readily available. The spectral brightness of electron radiation is strongly influenced by the electron bunch length relative to the radiation wavelength. When the electron bunch length is significantly shorter than the radiation wavelength, the radiation fields from all electrons are coherent and can be summed to a large value.

In a conventional free-electron laser (FEL) the optical feedbacks from resonator mirrors can help the electron bunching process during laser buildup. At short wavelengths a single-pass, mirrorless FEL generating self-amplified spontaneous emission (SASE) is the preferred mode of operation due to the scarce of mirror materials at deep UV and *x*-ray wavelengths. However, it usually takes a long undulator for a high-quality electron beam to form micro-bunches and reach the onset of the SASE mode. It is therefore desirable to invent an accelerator that generates a periodically bunched electron beam with an arbitrarily tunable bunch length and bunch frequency. Perviously Neumann *et al.* [1] used a comb filter to induce a few temporal ripples to the driver laser of a photocathode gun and observed coherently enhanced radiation at THz. In the paper, a laser beat wave with a tunable beat frequency is employed to induce a density-modulated photocurrent from the photocathode cathode of an electron gun. We study in this paper the acceleration of the density-modulated electron beam and the implementation of such a beat-wave laser system.

SUPERRADIANCE

Superradiance from relativistic electrons has been studied theoretically and experimentally in numerous papers. To facilitate subsequent discussions, we briefly review a few key concepts of superradiance based on Gover's work [2].

Regardless of the nature of the radiation device or scheme, let $(dW/d\omega)_1$ denote the spectral energy emitted from a single electron, where W is the radiation energy, ω is the angular frequency of the radiation, and subscript 1 denotes "a single electron". When a long stream of N electrons traverses a radiation device, the electrons radiate with all possible phases between 0 and 2π and the radiation has a spectral energy expressed by

$$(dW/d\omega)_{inc} = N(dW/d\omega)_1 \,, \qquad (1)$$

Eq. (1) is linearly proportional to the total number of electrons participating in the radiation process, because not all the radiation fields from the electrons are added up constructively. However, if N_b electrons are distributed in an infinitesimal time period, all the radiation fields from the electrons are in phase and summed up constructively, resulting in a total spectral energy equal to $N_b^2(dW/d\omega)_1$. This radiation process is dubbed as superradiant emission or superradiance. To account for a finite electron bunch length τ_b the total energy spectral density from an electron bunch is expressed by

$$(dW/d\omega)_{SR} = N_b^2(dW/d\omega)_1 M_b^2(\omega) \,, \qquad (2)$$

where $M_b(\omega)$ is the Fourier transform of the electron pulse-shape function with a unitary peak amplitude. Usually $M_b^2(\omega)$ has a characteristic width ~$1/\tau_b$ in the frequency domain. If there are N_{pb} electron "micro-bunches" repeating at a rate $\omega_{pb}/2\pi$ and there are N_b electrons in each micro-bunch, the total spectral energy from such an electron beam becomes

$$(dW/d\omega)_{SR,pb} = N_b^2 N_{pb}^2 (dW/d\omega)_1 M_b^2(\omega) M_{pb}^2(\omega) \,, \qquad (3)$$

where

$$M_{pb}^2(\omega) = \frac{\sin^2(N_{pb}\pi\omega/\omega_{pb})}{N_{pb}^2 \sin^2(\pi\omega/\omega_{pb})} \qquad (4)$$

is the coherent sum of the radiation fields from all the micro-bunches and has a unitary amplitude at the resonance frequencies (m = 1, 2, 3…). At $\omega = \omega_{pb}$, the spectral energy, Eq. (3), is enhanced by a factor equal to the number of electrons compared with that from an unbunched beam. Superradiance power has a quadratic dependence on a beam current, as can be seen from Eq. (2, 3); whereas the incoherent radiation power from a long-bunch beam is linearly proportional to a beam current, according to Eq. (1).

In Eq. (1), the spectral linewidth of the radiation from a long electron bunch is determined by the radiation bandwidth of a radiation device or a radiation scheme.

The superradiance linewidth from a short electron bunch, according to Eq. (2), is further modulated by $M_b^2(\omega)$. For a short electron bunch, $M_b^2(\omega)$ is usually a broadband curve. The coherent sum Eq. (4), however, has narrow spectral peaks at the frequencies $\omega = m\omega_{pb}$. Each resonant peak has a linewidth of ω_{pb}/N_{pb}. The superradiance linewidth from periodically bunched electrons can be greatly reduced for a large N_{pb}.

GENERATION OF LASER BEAT-WAVE BUNCHED BEAM

We illustrate in Fig. 1 the schematic of the proposed beat-wave bunched beam technique for producing and accelerating periodically bunched electrons with a variable bunch frequency. The idea is to use a laser beat wave to induce periodically density-modulated photoemission from the photocathode of an electron gun. The density-modulated photocurrent is then accelerated to some energy for generating superradiance in a downstream radiation device. The beat-wave laser system consists of wavelength-tunable lasers for generating laser beat waves with a variable beat frequency. If the desired electron bunch frequency is higher than the beat frequency available from a laser beat wave, one could in principle first generate an energy-chirped, density-modulated beam and compress it in a magnetic compressor to obtain a beam with a higher bunch frequency.

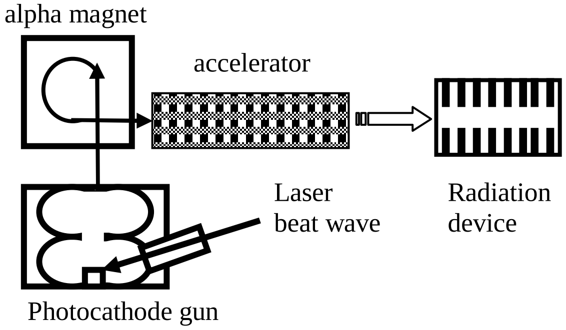

Figure 1: A laser beat wave excites a density-modulated photocurrent from a photocathode, which is subsequently accelerated to some energy for generating superradiance in a radiation device. An alpha magnetic could compress a density-modulated, energy-chirped beam to obtain a beam with a higher bunch frequency.

A laser beat wave can be generated from a superposition of two laser fields with a constant frequency offset. Assume that a beat-wave field is generated from the sum of two equal-amplitude laser fields with a frequency offset $\Delta\omega$. The instantaneous intensity of the beat wave is given by

$$I_{ins} = 4I_0 \cos^2[(\omega + \frac{\Delta\omega}{2})t] \cdot \cos^2(\frac{\Delta\omega}{2}t), \qquad (5)$$

where t is the time variable, I_0 is the average intensity of each laser component, and $\omega + \Delta\omega/2$ is the central frequency of the laser beat wave. A laser beat wave can also be generated from a superposition of several laser fields with a constant frequency shift $\Delta\omega$. For example, the coherent sum of the N_l equal-amplitude laser fields gives a time-averaged intensity

$$I_{avg} = N_l^2 I_0 \frac{\sin^2 \frac{N_l \Delta\omega}{2} t}{N_l^2 \sin^2 \frac{\Delta\omega}{2} t}. \qquad (6)$$

Eq. (6) shows laser beat pulses repeating at a frequency $\Delta\omega$ with a pulse width equal to $(2\pi/\Delta\omega)/N_l$. The beat pulses given in Eq. (6) are very useful for providing high-contrast density modulation to the photocurrent from a photocathode. By adjusting the number of interfering waves N_l one can adjust the beat-pulse width to optimize the modulation depth of the photocurrent emitted from a photocathode. In fact the locked-locked laser pulse commonly used for exciting a photocathode gun is a consequence of beating many longitudinal modes in a laser cavity with a beat frequency of ~100 MHz. To obtain a narrow beat pulse repeating at THz, one could, for example, use an intense laser to pump a Raman material with a THz Stokes shift and generate multiple Stokes waves beating at the Stoke shift. Of course, the shortest electron bunch that can be generated from photoemission depends on the temporal response of a specific cathode material. In view of the mechanism of a photoemission process, it is also preferred that all the beat-wave photons have photon energy higher than the work function of a cathode material.

ACCELERATION OF PERIODICALLY BUNCHED ELECTRONS

A major concern for the proposed bunching technology is whether particle acceleration following the density-modulated photoemission would smear out the periodic electron micro-bunches. In the following we conduct a feasibility study for accelerating ps and fs micro-bunches by using a space-charge tracking code ASTRA [3].

We first simulated the particle acceleration for the 1-1/2 cell SSRL electron gun [4] with twenty-five Gaussian electron bunches with 1-fs rms bunch length periodically emitted over 250-fs duration from the photocathode. The emitted charges have a uniform radial distribution on a 3-mm diameter cathode. Each micro-electron bunch contains 1 pC in a 10-fs time period. The total 25 pC charge was evenly divided into 12500 negatively charged macro-particles. The average current over the whole 250 fs duration is 100 A. With a peak acceleration field of 125 MV/m in the 2nd gun cell and an acceleration phase of 211.6°, Fig. 2 shows periodic density modulation of a 4-MeV beam with a characteristic period of 6 μm along the axial distance (z_e) at the gun exit. The output pulse duration is stretched to 500 fs and thus the average beam current is reduced to 50 A. Since the 250-fs emission time only occupies a very small RF acceleration phase, we confirm in the ASTRA simulation that the space charge field is responsible for the pulse-length increase. Although the shortest possible electron bunch is limited by a cathode material, the above computer stimulation is just an illustration of preserving periodic fs electron bunches during particle acceleration. Whether generation of fs electron bunches from a certain cathode mateiral is practical or not, it is another subject of study in the future.

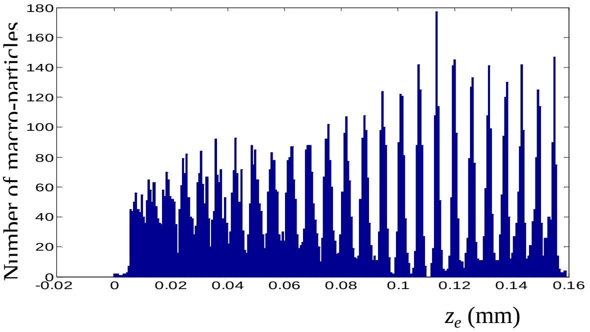

Figure 2: Histogram of the 4-MeV charges versus *z* at the exit of the SSRL gun with an input beam of twenty-five Gaussian bunches periodically emitted over 250 fs. The output beam distribution shows a good contrast in the density modulation.

A Smith-Purcell emitter driven by a keV, mA electron gun usually generates negligible radiation at THz. This proposed technique could be very useful for producing coherent radiation at THz frequencies from a miniature Smith-Purcell free-electron laser. Previously Ref. [5] reported Smith-Purcell superradiance, which was interpreted by Ref. [6] as coherent radiation from surface-mode induced electron bunching at the sub-harmonic of the Smith-Purcell radiation frequency. Up to date, no independent experiment can verify the superradiance claimed by Ref. [5]. A convenient approach is to produce electron bunches repeating at the radiation frequency directly from an electron source and generate wavelength tunable superradiance from a Smith-Purcell radiator. In our simulation, we emitted 50 Gaussian electron bunches each having a 0.2-ps rms bunch length from the photocathode of a 42 keV DC accelerator over a 50-ps time period. Each electron bunch contains 1 fC charge or 6.25×10^3 electrons, resulting 1 mA average current over the 50 ps macropulse. The electrons have a uniform radial distribution on the cathode with an rms radius of 0.3 mm. The electron gun has a length of 4.5 cm with 1-Tesla axial magnetic field for beam confinement. Figures 3(a) and (b) are the $M_b^2(\omega)M_{pb}^2(\omega)$ for the emitted electrons and the 42-keV output electrons, respectively. The accelerated electrons are slightly re-distributed due to the space charge force. Nonetheless the enhancement in the spectral power due to the periodic bunching is apparent at the harmonics of the bunching frequencies. For example, with 6.25×10^3 electrons/bunch and 1000 bunches over a 1 ns time, the spectral energy is coherently enhanced by almost 7 orders of magnitude at 1 THz.

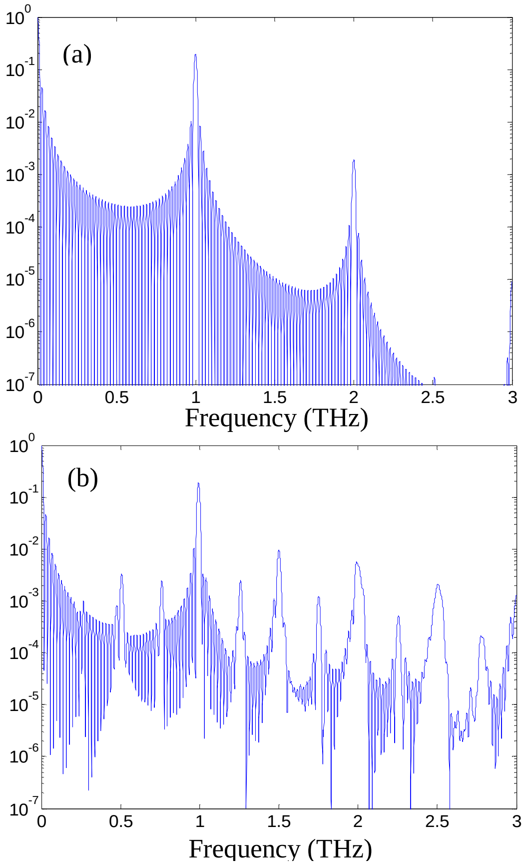

Figure 3: The $[M_b(\omega)M_{pb}(\omega)]^2$ of 50 electron bunches repeating at 1 THz (a) before and (b) after acceleration in a 40 keV DC electron gun. Spectral enhancement at the harmonics of 1 THz frequency is apparent.

FREQUENCY-TUNABLE BEAT-WAVE LASER SYSTEM

Although the laser beat wave can simply be obtained by overlapping two chirped pulses from the laser driver of a photocathode gun, the intensity contrast in the beat wave and the tunability in the beat frequency are not ideal [7]. We describe below one example of engineering a beat-wave UV laser system capable of generating mJ-level, 10-ps laser pulses near 260 nm with a tunable beat frequency range over 200 THz. Figure 4 shows the block diagram of the proposed beat-wave laser system, which consists of three major stages with a beat-wave seed source, a first-stage broadband pulsed amplifier and a second harmonic generator, and finally a frequency-tripled Ti:sapphire laser amplifier. The two seed lasers in the first stage are often used in optical communications. The Ti:sapphire laser amplifier and harmonic generators are commonly seen for driving a Cu photocathode gun. Specifically, one can starts with the beating of kHz-linewidth distributed-feedback (DFB) and frequency-tunable external-cavity diode lasers (ECDL) near the optical-communication wavelength 1.5 μm. An Erbium-doped fiber amplifier (EDFA) following the DFB diode laser and ECDL boosts the beat-note power to ~100 mW. The CW beat signal can be further amplified in a pulsed optical parametric amplifier (OPA) pumped by, say, a diode-pumped mode-locked Nd:YVO_4 laser to generate ~10-ps beat-wave pulses with nJ pulse energy. After frequency doubling the beat-wave pulses in a second harmonic generator (SHG), the wavelengths of the beat wave will fall into the bandwidth of a Ti:sapphire amplifier. Therefore, the rest of the laser system can be a replication of the UV laser amplifier for driving a Cu photocathode gun. The proposed beat-wave laser system spares a mode-locked Ti:sapphire laser oscillator from a typical photocathode-gun laser driver. Instead, a user-friendly, directly diode-pumped mode-locked Nd:YVO4 is proposed for pumping the OPA to generate beat-wave pulses near the optical-communication wavelengths.

To produce the proposed Smith-Purcell superradiance, the mode-locked Nd laser can be replaced by an economic Q-switched Nd laser, and harmonic generators can directly follow the OPA to generate long-pulse UV laser.

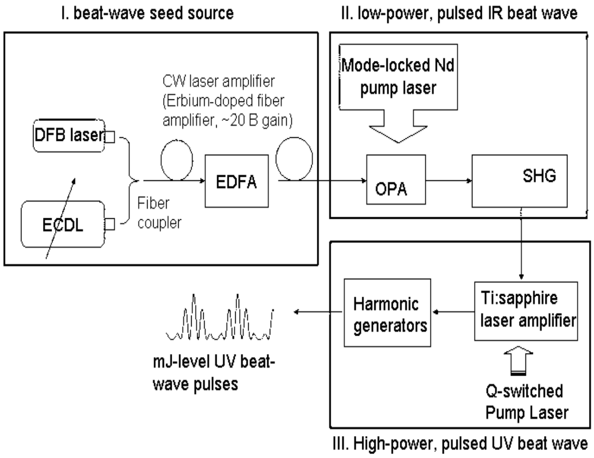

Figure 4: One example of a beat-wave laser system modified from a typical UV laser system for a Cu-photocathode gun.

The beat frequency of the laser system can be arbitrarily tuned by adjusting the wavelength of the ECDL or by plugging in assorted narrow-line telecommunication diode lasers with a wavelength range between 1.3 and 1.6 μm. Taking into account the successive harmonic generations leading to the 260 nm photons, one would expect a beat-frequency tuning range well over 240 THz.

SUMMARY

We have described a novel scheme for generating tunable periodic electron bunches for superradiance FEL. Specifically a laser beat wave is used to introduce density modulation to the photocurrent of a photocathode electron gun. The periodic electron bunches are subsequently accelerated to high energy in a particle accelerator. Computer simulations using the space-charge tracking code, ASTRA, showed feasibility of accelerating and preserving the density-modulated electron beam at both nonrelativistic and relativistic energies.

We have also described the implementation of a beat-wave laser system with a beat-frequency tuning range over 200 THz. The laser system adopts the state-of-the-art and yet economic photonics products often used in the optical-communication and laser industries. Real-time tuning on the beat frequency provides unprecedented flexibility to match the frequency of down-stream radiation devices.

The shortest electron-bunch length from the proposed beat-wave bunching technique could be limited by the beat-wave frequency or the response time of a cathode material. We proposed chirped-pulse compression in an alpha magnet to increase the bunch frequency. Knowing the potential problem of microbunching instability in the compression, we have planned a feasibility study in the near future.

The author is in debt to Michael Borland and Klaus Floettmann for advices on computer simulations. This work is supported by National Science Council under Contract 95-2112-M-007-027-MY2 and NTHU Frontier Research Initiatives under Project Code 95N2509E1.

REFERENCES

[1] J.G. Neumann, P.G. O'shea, D. Demske, W.S. Graves, B. Sheehy, H. Loos, and G.L. Carr, "Electron beam modulation by using a laser-driven photo-cathode" Nucl. Inst. Meth. Phys. Res. A **507**, 498 (2003).

[2] A. Gover, "Superradiance and stimulated-superradiant emission in prebunched electron-beam radiators. I. Formulation", Phys. Rev. ST AB, 8, 030701 (2005).

[3] K. Floettmann, ASTRA User Manual, http://www.desy.de/mpyflo/Astra_dokumentation.

[4] Y.C. Huang, H.C. Wang, R.H. Pantell, J. Feinstein, J.F. Schmerge, and J. Lewellen, "Electron Beam Characterization for a Far Infrared Free-electron Laser," IEEE J. Quantum Electronics, 31, 1637-41 (1995).

[5] J. Urata, M. Goldstein, M.F. Kimmitt, A. Naumov, C. Platt, and J.E. Walsh, "Superradiant Smith-Purcell Emission", Phy. Rev. **80**, 516 (1998).

[6] H.L. Andrews, C.H. Boulware, C.A. Brau, J.D. Jarvis, "Gain and coherent radiation from a Smith-Purcell free-electron laser," Proceedings FEL04, Trieste, Italy, p. 278 (http://www.JACoW.org).

[7] A.S. Weling, B.B. Hu, N.M. Froberg, D.H. Auston, "Generation of tunable narrow-band THz radiation from large aperture photoconducting antennas," Appl. Phys. Lett. 64, 137 (1994).

3-D LASER PULSE SHAPING FOR PHOTOINJECTOR DRIVE LASERS*

Yuelin Li#, ANL, Argonne, IL 60439, U.S.A.
Xiangyun Chang, BNL, Upton, NY 11973, U.S.A.

Abstract

In this paper we present a three-dimensional (3-D) laser pulse shaping scheme that can be applied for generating ellipsoidal electron bunches from a photoinjector. The 3-D shaping is realized through laser phase tailoring in combination with chromatic aberration in a focusing optics. Performance of an electron beam generated from such shaped laser pulses is compared with that of a uniforma ellipsoidal, a uniform cylindrical, and a Gaussian electron beam. PARMELA simulation shows the advantage of this shaped beam in both transverse and longitudinal performances.

INTRODUCTION

The emittance of an electron beam is governed by the emittance at its birth and the growth during its propagation. If the beam is only subjected to linear force, the latter can be fully recovered with proper beam compensation. It is well known that an ellipsoidal beam with uniform charge distribution has a linear space-charge force [1-3] and hence the most expected distribution for modern high-brightness beams. Recently, several researchers looked at practical ways of generating such ellipsoidal beams, including self-evolving [4], cold electron harvesting [5], and laser pulse manipulations including spectral masking, pulse stacking, and dynamic spatial filtering [6]. In-depth analysis shows that in practical situations, the ellipsoidal beams do generate beam with lower emittance than Gaussian and cylindrical beams [1, 6-8]. Applications for such high-brightness beams include next-generation light sources such as the Linac Coherent Light Source (LCLS), high-energy colliders such as the International Linear Collider, as well as energy-recovery linacs (ERLs).

LASER PULSE SHAPING

To generate an ellipsoidal beam directly from the photocathode, the laser pulse has to be shaped in 3-D. It is well known that the longitudinal laser pulse shape can be manipulated by controlling the phase space using techniques such as DAZZLER [9] or SLIM [10]. One essence of this phase modulation is to control the phase and amplitude at certain frequencies at the same time. In the meantime, we notice that the instant frequency of a laser pulse is related to the phase by $\omega(t) = \mathrm{d}\phi(t)/\mathrm{d}t$. This gives a way of actively controlling the focal size of the laser as a function of time using the chromatic aberration of a common lens, of which the focal length can be expressed as [11]

$$\frac{1}{f(\omega)} = \left[n(\omega)-1\right]\left(\frac{1}{R_1}-\frac{1}{R_1}\right), \tag{1}$$

where R_1 and R_2 are the radius of curvature of the first and second surface of the lens, respectively, and n is the frequency-dependent refractive index. Clearly, the time-dependent frequency can then be mapped onto a time-dependent focal length. For an observer at the focal plane at a nominal frequency ω_0, this is equivalent to a time-dependent defocusing of the beam of

$$\delta f(t) = -\frac{f_0}{n_0-1}\beta\delta\omega(t), \tag{2}$$

where we assume the frequency range is small and $\beta = dn/d\omega$ is constant. For a Gaussian beam this translates into a time-dependence of the beam size at the nominal focal plane,

$$w(t) = w_0\left[1+\left(\frac{\lambda_0\delta f(t)}{\pi w_0^2}\right)^2\right]^{1/2}. \tag{3}$$

Here, $w_0 = N\lambda_0/\pi$ is the beam waist at the nominal wavelength λ_0, and N is the numerical aperture. For $\delta f >> w_0$, we have asymptotically,

$$w(t) \cong \frac{\left|\delta f(t)\right|}{N}. \tag{3a}$$

To generate an ellipsoidal outline, the transverse beam size should be of the form:

$$w(t) = W\left[1-\left(\frac{t}{T}\right)^2\right]^{1/2}. \tag{4}$$

Here, W is the maximum transverse beam size at $t = 0$ and $2T$ is the laser pulse duration.

From Eqs. (3-4), we have

$$\left|\delta\omega(t)\right| = \Delta\omega\left[1-\left(\frac{t}{T}\right)^2\right]^{1/2}, \tag{5}$$

where $\Delta\omega = (n_0\text{-}1)NW/\beta f_0$ is the bandwidth of the pulse; hence the phase of the pulse is

$$\begin{aligned}\phi(t) &= \int\left[\omega(t)-\omega_0\right]dt \\ &= -\omega_0 t \pm \frac{\Delta\omega}{2}\left[t\left(1-\left(\frac{t}{T}\right)^2\right)+T\sin^{-1}\frac{t}{T}\right].\end{aligned} \tag{6}$$

To make the pulse intensity constant over time, i.e., $|A(t)|^2/w(t)^2 = \text{constant}$, the amplitude of the pulse is thus

$$A(t) = A_0\left[1-\left(\frac{t}{T}\right)^2\right]^{1/2}. \tag{7}$$

With a transverse top-hat spatial profile, the field $E(t) = A(t)\exp[\mathrm{i}\phi(t)]$ represents a 3-D ellipsoidal pulse at the nominal focal plane at λ_0. The time domain representation of the pulse and its spectrum are shown in Fig. 1.

---

* Work supported by U.S. Department of Energy, Office of Science, Office of Basic Energy Sciences under Contract No. W-31-109-ENG-38.

ylli@aps.anl.gov

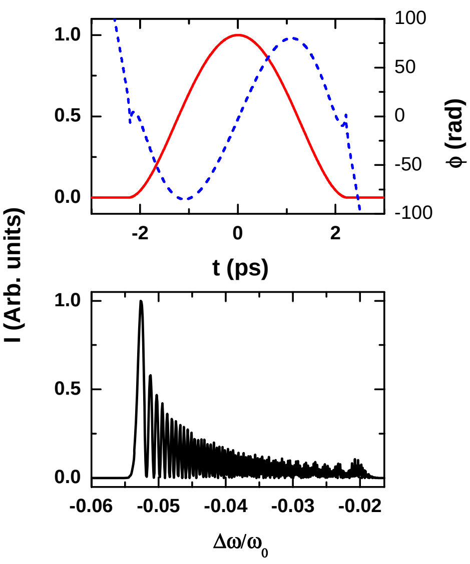

Figure 1: Laser pulse calculated using Eqs. (6) and (7). The intensity and phase in the time domain (top) and its spectrum (bottom).

Note that the above model used Gaussian beam geometrical optics, and the effects of group velocity delay (GVDE) and group velocity dispersion (GVDI) due to the varying thickness across the aperture of the lens are not included [11]. It does not take into account the wave property of the light. To evaluate the effects of GVDE and GVDI, we use the method elaborated by Kempe et al. [12] to calculate the temporal-spatial distribution of the pulse near the focus of a lens. The calculation assumes a collimated beam with top-hat intensity distribution for the input and was performed in the frequency domain. The final result was Fourier transformed into the time domain to give the laser intensity distribution at the focal plane as a function of time. Figure 2 shows one example of such a shaped pulse generate by sending a pulse in Fig. 1 though a zone plate (a zone plate has similar chromatic aberration as a lens).

Clearly, this shaped pulse differs from an ideal ellipsoid. It has substantial substructures. The deviation from an ideal ellipsoidal is not unexpected due to the group delay across the plate, which is the source for the distortion at the beginning and the end of the pulse. This has been studied theoretically and experimentally by a few authors and is an important effect in focusing short-duration, short-wavelength laser light [12].

The substructure is due to the fringes typical of the Fourier transform of a square waveform. As is shown below, those substructures seem to have minimum impact on the performance of the beam.

BEAM SIMULATION

To evaluate the performance of this shaped laser beam, preliminary simulations using PARMELA were performed and compared with other beam shapes for the following setting.

The simulation followed a setup for the design of the electron cooling ring injector for Relativistic Heavy Ion Collider [13]. The gun is a 1.5-cell rf gun at 703.75 MHz with maximum field on axis of 29.5 MV/m and maximum field on surface at 49.3 MV/m. The rf initial phase is set at 40 degrees. Beam distortion due to image charge is considered. The gun is followed with a drift space before entering a linac.

A series of simulations were performed using PARMELA. The simulations compared the performance of the 3-D laser pulse against three standard cases (see Table 1): c) a perfect ellipsoidal beam, d) a cylindrical beam, and e) a transversely uniform but longitudinally Gaussian beam. For the shaped beam, two cases were tested: a) without considering the substructures and b) with. The simulations use the parameters listed in Table 1. Both the longitudinal and the transverse emittances are compared at the exit of the gun. In total, 46,600 particles are used in each simulation, representing 0.15 nC of charge. The low charge is used due to the relatively low rf field in this setup.

The emittances as a function of the propagation distance are shown in Fig. 3. In general, the performances

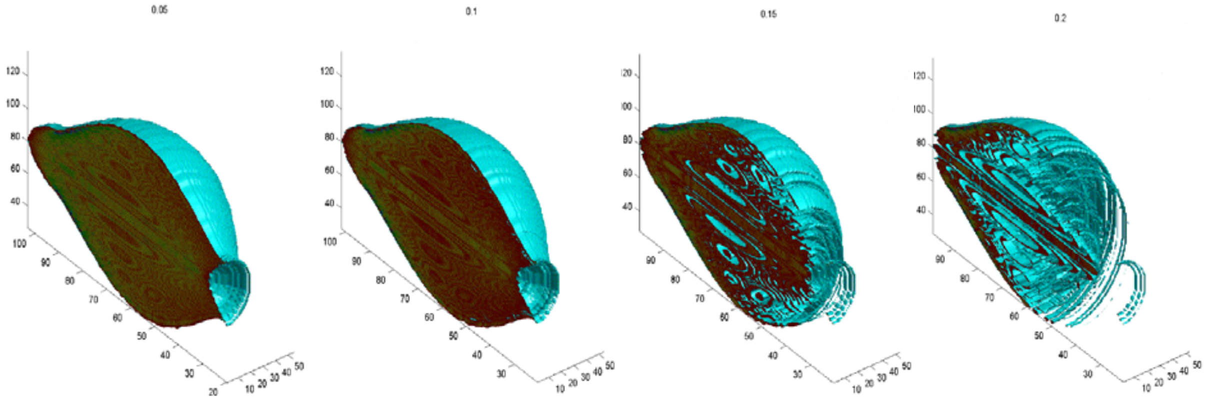

Figure 2: An ellipsoidal laser pulse. The isosurface plots show the structure at different laser intensities of 0.05, 0.1, 0.15, and 0.2. The pulse is generated using a zone plate with 20-mm diameter and 150-mm focal length at 249 nm. The pulse parameter is shown in Table 1, case b.

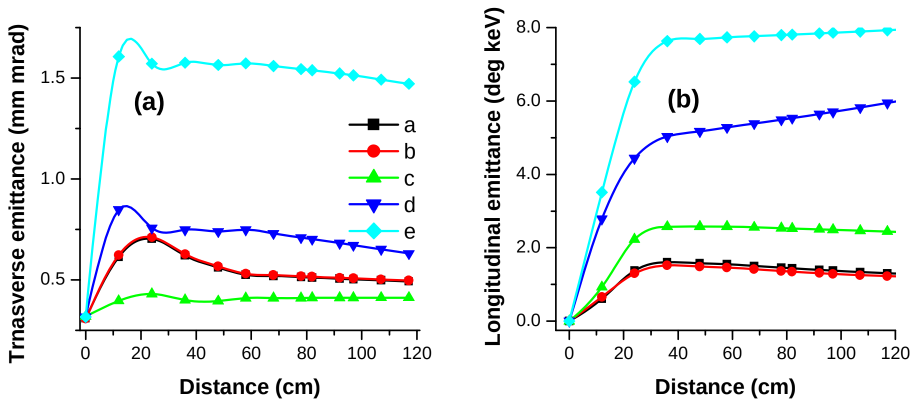

Figure 3: Transverse (a) and longitudinal (b) emittances as a function of propagation distance. The labels correspond to those in Table 1. Clearly, the shaped pulse has a better performance in comparison with those of the cylindrical and Gaussian form, even with the presence of the substructures shown in Fig. 2. The gun exit is located at 48 cm, followed a drift space.

Table 1. Initial Beam Conditions

	Length (ps)	Radius (mm)
a.Shaped, no substructure	17	1.28
b.Shaped, substructure	17	1.28
c. Ideal ellipsoid	18	1.28
d. Ideal cylinder	18	1.13
e. Ideal Gaussian	σ= 3.82, truncated at 9	1.13

of the shaped-pulse cases closely trail the performances of the ideal ellipsoidal beam in both longitudinal and transverse emittances. More remarkably, the substructure, as shown in Fig. 2, has almost no impact on the performance of the beam in this setup. It will be interesting to perform simulations with bending magnets, such as a chicane structure to evaluate the influence of coherence transition radiation, which is detrimental to cylindrical and Gaussian beams but has minimum impact on an ideal ellipsoidal beam. One simulation indicates that after accelerated to high beam energy, the ellipsoidal beam shape will be destroyed but the low emittance of the beam is preserved [8], making it favorable for application in free-electron lasers such as LCLS and ERLs.

SUMMARY

We described a scheme for generating an ellipsoidal laser pulse and performed preliminary simulations comparing the electron beam generated from this laser beam with an ideal ellipsoidal beam, a cylindrical beam, and a Gaussian beam. It is shown that although the beam generated still defers from an ideal ellipsoidal beam, it has clearly better performance than a cylindrical beam and a Gaussian beam in providing smaller transverse and longitudinal emittance. Further beam simulations are needed to investigate the coherent synchrotron radiation effect for setup relevant to LCLS and future ERLs.

REFERENCES

[1] F. Sacherer, IEEE Trans. Nucl. Sci. NS-**18**, 1105 (1971).
[2] I.M. Kapchinskij, V.V. Vladimirskij, Conference on High Energy Accelerators and Instrumentation, CERN, Geneva, 274 (1959).
[3] P.M. Lapostolle, IEEE Trans. Nucl. Sci. NS-**18**, 1101 (1971).
[4] O.J. Luiten, S.B. van der Geer, M.J. de Loos, F.B. Kiewiet, and M.J. van der Wiel, Phys. Rev. Lett **93**, 094802 (2004).
[5] B.J. Claessens, S.B. van der Geer, G.Taban, E.J.D. Vredenbregt, and O.J. Luiten, Phys. Rev. Lett **95**, 164801 (2005).
[6] C. Limborg-Deprey and P. Bolton, Nucl. Instrum. Methods A**557**, 106 (2006).
[7] J.B. Rosenzweig et al., Nucl. Instrum. Methods A**557**, 87 (2006).
[8] S.B. van der Geer, M.J. de Loos, T. van Oudheusden, W.P.E.M. op't Root, M.J. van der Wiel, and O.J. Luiten, Phys Rev. ST-AB **9**, 044203 (2006).
[9] P. Tournois, Opt. Commun. **140**, 245 (1997).
[10] A.M. Weiner, D.E. Leaird, J.S. Patel, and J.R. Wullert, Opt. Lett. **15**, 326 (1990).
[11] M. Born and E. Wolf, *Principles of Optics*, University Press, Cambridge, UK, 2003.
[12] M. Kempe, U. Stamm, B. Wilhelmi, and W. Rudolph, J. Opt. Soc. Am. B**9**, 1158 (1992).
[13] I. Ben-Zvi et al., Nucl. Instrum. Methods A**557**, 28 (2006).

LINAC COHERENT LIGHT SOURCE UNDULATOR RF BPM SYSTEM *

R. Lill, G. Waldschmidt, D. Walters, L. Morrison
Advanced Photon Source, Argonne National Laboratory, Argonne IL
S. Smith, T. Straumann, Z. Li, R. Johnson
Stanford Linear Accelerator Center, Sand Hill Road
Menlo Park, CA 94025 USA

Abstract

The Linac Coherent Light Source (LCLS) will be the world's first x-ray free-electron laser (FEL) when it becomes operational in 2009. The LCLS is currently in the construction phase. The beam position monitor (BPM) system planned for the LCLS undulator will incorporate a high-resolution X-band cavity BPM system described in this paper. The BPM system will provide high-resolution measurements of the electron beam trajectory on a pulse-to-pulse basis and over many shots. The X-band cavity BPM size, simple fabrication, and high resolution make it an ideal choice for LCLS beam position detection. We will discuss the system specifications, design, and prototype test results.

INTRODUCTION

The LCLS FEL will produce x-ray radiation over the 1.5-to 15-Angstrom wavelength range. To produce x-rays in this regime, the electron and photon beams within the 131-m-long undulator must be collinear to less than 10% of the transverse beam size (≈37 μm rms) over a minimum distance that is comparable to the FEL amplitude gain length (≈10 m) in order to achieve saturation [1,2]. To establish and maintain the electron beam trajectory, a high-resolution and stable BPM system has been designed. The requirements for the system are delineated in Table 1. The beam-position resolution and stability over 1-h and 24-h periods were the major design challenges for the BPM system. Other design considerations were physical size, centering accuracy, radiation hardness, and reproducibility.

The LCLS undulator hall will house 33 undulators. The BPMs will be located in the drift space between each undulator and at the upstream end of the first undulator for a total of 34 BPMs. There are also two BPMs placed in the Linac to Undulator (LTU) transport line. The BPM system must provide stable and repeatable beam position data for both planes on a pulse-to-pulse basis for up to a 120-Hz repetition rate. The BPMs are critical for beam-based alignment and operations.

Table 1. General system specifications.

Parameter	**Specification**	**Conditions**
Resolution	< 1 μm rms	0.2– 1.0 nC
Offset Stability	< +/- 1 μm rms	1 hour
Offset Stability	< +/- 3 μm rms	24 hours
Dynamic Range, Position	+/- 1mm	10mm diameter chamber
Dynamic Range, Intensity	0.2-1 nC	PC Gun (single bunch)
Gain Error	< +/- 10 %	+/- 1mm range

BPM SYSTEM OVERVEIW

The system proposed for the LCLS undulator features a high-resolution X-band cavity BPMs. Each BPM detector has a reference cavity and position cavity as shown in Fig. 1. The major sub-systems include the cavity BPM, receiver, and data acquisition components. The cavity BPM and downconverter will reside in the tunnel and the analog-to-digital converter (ADC) will be located in surface buildings.

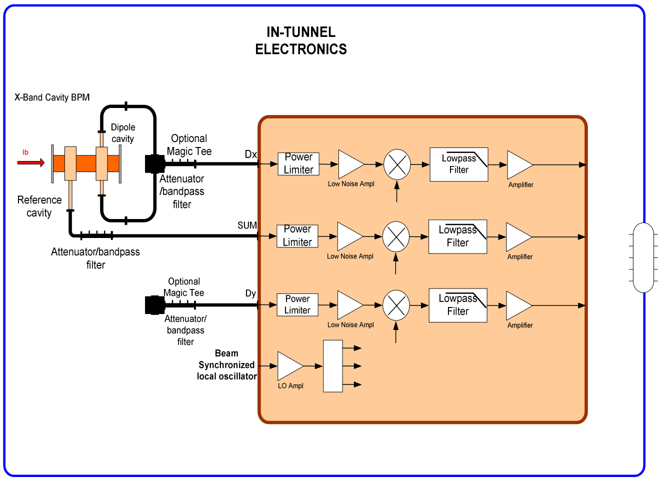

Figure 1: System block diagram.

---

*Work supported by U.S. Department of Energy, Office of Basic Energy Sciences, under Contract No. W-31-109-ENG-38.

X-BAND CAVITY DESIGN

The simplicity of fabrication and assembly of the X-band cavity BPM due to its cylindrical geometry make it our first choice for the LCLS undulator. The cavity BPM offers the advantage of being a small, compact detector that inherently reads zero when the beam is centered. Cavity BPMs show extremely good resolution and stability. The two-cavity BPM design shown in Fig. 2 illustrates the cross section of the detector. The beam passes through the monopole reference cavity, shown on the left, which excites the TM_{010} monopole mode signal at 11.384 GHz, proportional to the beam intensity or charge. The second cavity, 37 mm downstream through the 10 mm diameter beam pipe, is the TM_{110} dipole cavity shown at the far right. The output of the dipole cavity produces a signal that is dependent on the relative beam displacement r/r_{fix} shown in equation 1 [3]. Where R_s/Q is the normalized shunt impedance of the TM_{110} mode, Z is the output line impedance, Q_{ext} is the external quality factor and q is the charge. The voltage is linearly dependent on the offset and can be scaled.

$$V_{out} = \frac{\omega_0}{2}\sqrt{\frac{Z}{Q_{ext}}\left(\frac{R_s}{Q}\right)_{fix}}\,\frac{r}{r_{fix}}\,q \cdot \qquad (1)$$

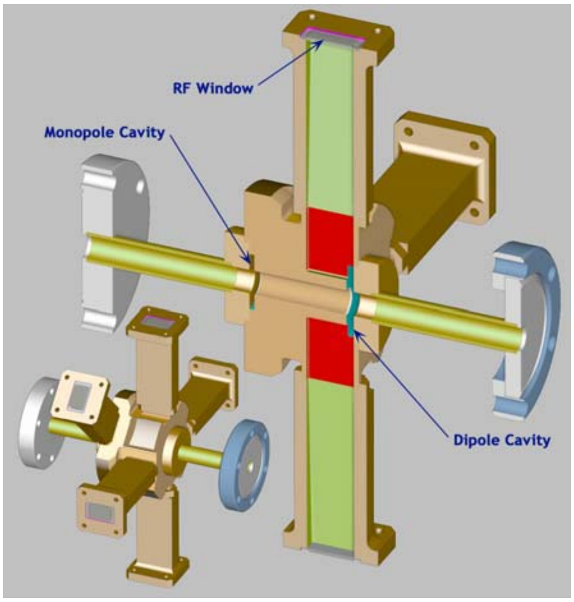

Figure 2: X-Band Cavity BPM Cross-Section.

The X-band cavity BPM inherently has the capability of resolving the beam position in the tens of nanometers, far exceeding the 1-micron resolution requirement indicated in Table 1. Equation 2 estimates the BPM thermal noise voltage output. Given the Bolzmann constant k, operating temperature T in Kelvin, impedance Z is 50 Ohms, the signal bandwidth B is about 2 MHz, and considering a system noise figure of 3 dB the minimum resolution would typically be less than 10 nm. The single-shot resolution will be limited by other processing and data acquisition electronic noise.

$$Vn \approx \sqrt{k \times T \times Z \times B} \qquad (2)$$

Horizontal and vertical position signals are generated from the two polarizations of the TM_{110} dipole mode. The polarized fields are coupled to four iris slots equally spaced around the cavity. The magnetic field of the dipole couples to the TM_{110} mode of the rectangular waveguide shown in Fig. 2. The distinctive modal patterns of the TM_{010} monopole and TM_{110} dipole modes make it possible to couple only to the dipole mode and reject the monopole mode. This selective coupling technique, pioneered by SLAC, has been incorporated in this design [4]. The iris couplers are precisely electrical discharge machined (EDM) into the solid copper block to ensured repeatable and accurate coupling. EDM provides the exceptional accuracy and repeatability that is critical for this device. This technique also ensures that the waveguide braze has little or no affect on the cavity performance from the migration of braze material. The two cavities are designed to operate at the same frequency and a small amount of tuning is provided for adjustment after brazing.

The outputs of the cavity are fed into 76-mm-long linear E-plane tapered waveguide transitions, which transform the cavity outputs (3 mm by 19.05 mm) to standard WR-75 waveguide (9.53 mm by 19.05 mm). The vacuum window shown in Fig. 3 is brazed into the WR75 waveguide flanges with a gold germanium filler alloy. The rf windows are made from glass fused onto a kovar base. The kovar is plated with nickel and then copper to facilitate brazing. The overall electrical performance of the transitions and windows together have a -20-db return loss with less than 0.2-dB insertion loss over a 200-MHz bandwidth centered at 11.384 GHz.

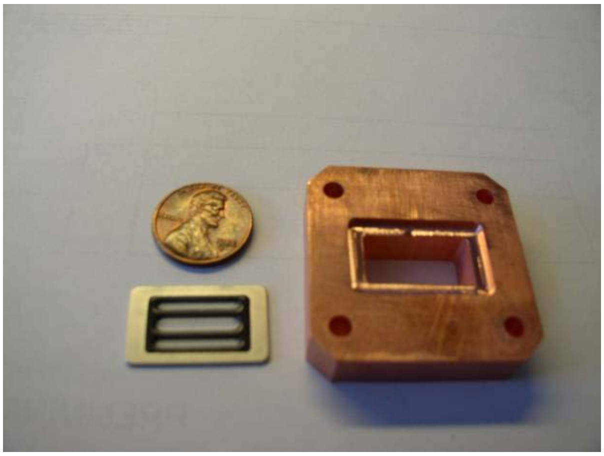

Figure 3: X-Band Cavity RF Window.

The BPM is a brazed assembly made up of the body, waveguide transitions, cavity end caps, rf windows, and end EVAC-type vacuum flanges. The 11.738-mm-radius monopole and 14.937-mm-radius dipole cavities are machined within a +0.000/-0.015-mm tolerance, with a surface finish of 0.1 µm (4 µin Ra) or better into a single piece of oxygen-free electronic copper. The machining tolerance deviation of +0.000/-0.015 mm will equate to a frequency increase of 7.5 MHz, which is within the system tuning capability. The final assembly is brazed in a vacuum furnace back-filled with dry hydrogen.

To facilitate installation alignment, the outer surface of the BPM body shown in Fig. 2 is machined to be concentric to the cavity to within 0.025 mm. This surface will be used as the fiducilization reference to align the BPM during installation.

There are two waveguide outputs for each plane on the dipole cavity. The output flanges are connected directly to the flexible WR75 waveguide shown in Fig. 4 to mechanically decouple any shock or vibration from the rest of the components. The waveguide provides an ideal transmission line for the X-band signals exhibiting very low loss and excellent radiation hardness. The original design concept incorporated optional magic tee power combiners at each pair of outputs on the dipole cavity. This effectively reduces the common mode noise generated by unwanted modes by about 20 db. It is expected that full compliance to the specification can be accomplished without the use of the combiner. This would facilitate the potential for using the unused or terminated ports for future diagnostics.

Each of the three inputs to the receiver is band limited by bandpass filters. The filters provide a 20-MHz bandwidth (-3 dB) centered at 11.384 GHz. The filters also provide a broadband -10 dB return loss match to the cavities. Out-of-band filtering of -60 db reduces unwanted modes from saturating the receiver input.

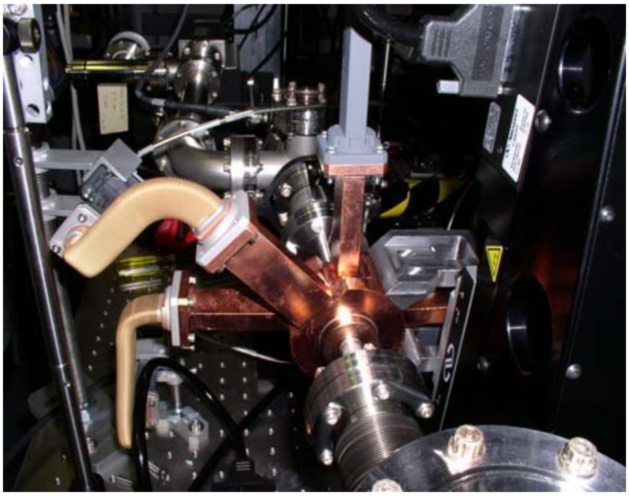

Figure 4: X-band cavity testing.

RECEIVER DESIGN

The receiver topology used is a single-stage three-channel heterodyne receiver shown in Fig. 1. The cavity BPM X-band signals are downconvertered to a 25- to 50-MHz intermediate frequency (IF) in the accelerator tunnel. The signals are first amplified in a low noise amplification (LNA) stage, then translated to a lower IF by mixing with a local oscillator (LO). The LO is a phase-locked dielectric resonate oscillator (PDRO) featuring low phase noise. One option is to lock the LO to the SLAC 119-MHz timing reference. This has the advantage of synchronizing the data with the beam. The other option would have the LO operate in a free-run mode. A single LO will drive all three channels and will be housed in the receiver chassis. The LNA is protected against high-power surges by a limiter that is rated at 50 W peak. After the X-band signals are down-converted, they are filtered and then amplified. The signals are then cabled out of the tunnel. The expected output of the receiver will be a bi-polar +/- 1-volt full-scale exponentially decaying sine wave between 175-260 ns (Q=2000-3000) in duration.

The receiver will be housed in an aluminum 3 in. high × 12 in. wide × 12 in. deep shielded enclosure. The unit will not dissipate more that 20 W and can be heat sunk. Special consideration is given to electro magnetic interference (EMI) susceptibility and emissions by using DC blocks on the inputs, EMI gaskets, feed through pins, and proper grounding. The receiver will be mounted in the tunnel below the undulator girder.

The data acquisition utilizes a commercially available ADC digitizer board. The ADC front end should have a minimum of 14-bit resolution and a sampling rate of 119 MSPS. The ADC clock will be synchronized to the frequency of the 119-MHz timing system of the SLAC linac. This will be considered the minimum requirement for the ADC and it is hoped that the performance requirement can be exceeded when the system is required.

The original plan for acquiring data for the prototype was to simply capture the exponentially decaying waveform and digitally peak detect the reference and position signals. The position and reference cavity IF signal data would then be fit to an exponential curve, with the position data being normalized to the reference.

Another processing algorithm being investigated is to digitally down-convert the IF signals. The raw digital waveform is multiplied point-by-point by a complex LO $e^{j\omega t}$ where ω is the IF frequency. A digital low-pass filter removes the 2ω component leaving a complex baseband signal. A quasi-Gaussian, symmetric, finite impulse response (FIR) digital filter is chosen to remove the 2ω product as well as out-of-band noise. The complex amplitude of the position signal is normalized by the reference cavity to remove bunch charge dependence (amplitude) and beam arrival time dependence (phase). Normalized phase and amplitude are converted to position via scaling and rotation by calibration data.

PROTOTYE RESULTS

Two X-band cavity BPMs have been prototyped and cold tested using a test fixture that precisely moves an $\frac{\lambda}{4}$ E probe driven by an Hp 8510 network analyzer that excites the cavity and then measures the response. Table 2 shows the predicted and measured results of a bolted-together prototype and brazed prototype. The monopole and dipole cavities were modeled using HFSS [5]. The difference of predicted vs. the measured frequency for the TM_{110} dipole mode was less than 0.2 % for both prototypes.

Table 2: Prototype cold test results.

Parameter (500 µm offset)	**Predicted**	**Measured Prototype # 1 bolted end caps**	**Measured Prototype # 2 brazed end caps**
Frequency TM_{010}	8.262 GHz	8.271 GHz	8.243 GHz
Coupling TM_{010}	-53 dB	-69 dB	-62 dB
Frequency TM_{110}	11.364 GHz	11.344 GHz	11.357 GHz
Coupling TM_{110}	-32 dB	-28 dB	-24 dB
Q (loaded) TM_{110}	2704	2086	2391
X/Y Isolation TM_{110}	-26 dB	-33 dB	-23 dB
Dipole to Monopole cavity Isolation	<-80 dB	<-85 dB	<-89 dB
Frequency TM_{020}	15.825 GHz	15.767 GHz	15.785 GHz
Coupling TM_{020}	-78 dB	-64 dB	-50 dB

The brazed prototype cavity BPM is presently installed in the Advanced Photon Source Injector Test Stand (ITS) shown in Fig. 4. The BPM is mounted on a precision 2-axis translation stage to test and calibrate the BPM. The ITS provides 1-nC single-bunch charge with bunch lengths 3-4 ps FWHM. The preliminary data shown in Table 3 indicates good correlation with the cold test and predicted values. An estimated voltage output of the dipole cavity was calculated to be 2.3 mV/µm/nC and the measured value was 1.22 mV/µm/nC. The current monitor used for this measurement has been recently recalibrated and the BPM output response will be re-measured.

Table 3. Prototype ITS test results.

Parameter	**Predicted**	**Cold Test**	**ITS Test**
Frequency	11.364 GHz	11.357 GHz	11.359 GHz
Loaded Q	2704	2391	2500
Isolation X/Y	-26 dB	-23 dB	-21 dB

CONCLUSIONS

X-band cavity BPM and receiver electronics have been designed and tested for micron-level resolution for eventual installation into the LCLS. Preliminary low-power test and beam test using the ITS have produced encouraging results in validating the design for achieving the stated goals. ITS testing is scheduled to continue to obtain valuable operational experience.

The second phase of testing will involve building three new BPMs and installing them at a fixed distance from each other in order to measure single-shot trajectories. The new BPMs will incorporate changes that will facilitate a small amount of cavity tuning. The BPMs will be installed in the APS LEUTL tunnel in October 2006. The testing objective is to provide a complete compliance table for the given specification given in Table 1. Beam conditions will be similar to the expected LCLS photo cathode beam. The prototype testing should be complete by early next year, followed by the production of 34 cavity BPMs.

ACKNOWLEDGMENTS

The authors would like to acknowledge Stephen Milton, John Carwardine, Glenn Decker, and Om Singh for many helpful discussions. The authors would also like to thank Randy Zabel for all his help with building and testing the prototypes.

REFERENCES

[1] R. Hettel, R. Carr, C. Field, and D. Martin, “Investigation of Beam Alignment Monitor Technologies for the LCLS FEL Undulator,” BIW 98, Stanford CA, May 1998, p. 413.

[2] P. Emma, J. Wu, “Trajectory Stability modeling and Tolerances in the LCLS,” EPAC 2006, Edinburgh, Scotland, June 2006.

[3] A.Liapine, www.hep.ucl.ac.uk/~**liapine**/part_one_ **waveguides**_and_cavities.doc

[4] Z. Li, R. Johnson, S. Smith, T. Naito, J. Rifkin, “Cavity BPM with Dipole-Mode-Selective Coupler,” PAC 03, Portland Oregon, May 2003.

[5] Ansoft HFSS, version 10.0, Ansoft Corporation, Pittsburgh, PA, USA, 2005.

NONINTERCEPTING BEAM SIZE AND POSITION MONITOR USING ODR FOR X-RAY FELS*

A.H. Lumpkin**, N.S. Sereno, W.J. Berg, D.W. Rule†, B.X. Yang, and C.-Y. Yao
Advanced Photon Source, Argonne National Laboratory, Argonne, IL 60439, U.S.A.
†Carderock Division, NSWC, West Bethesda, MD 20817 USA.

Abstract

Interest in nonintercepting (NI) beam size and position diagnostics between the undulators of x-ray free-electron lasers (XFELs) is driven by the requirement of beam-emittance matching and beam alignment, as well as by the need to minimize radiation damage to the undulator permanent magnets from scattered beam produced by the insertion of converter screens. For these reasons our investigations on optical diffraction radiation (ODR) as relative beam size and position diagnostics are particularly relevant to XFELs. We report the extensions of our studies at 7-GeV beam energy to aspects of the vertical and horizontal polarization components of the ODR near-field and far-field images. The near-field, vertically polarized data are particularly interesting because the vertical field lines at the metal more directly reflect the actual horizontal beam sizes. Although our experiments to date are with mm-scale beams and impact parameters of 1-2 mm, our analytical model indicates that this technique scales with beam size and has sensitivity at the 20- to 50-μm regime with an impact parameter, *d* = 5 times σ_y = 100 μm. This is the x-ray FEL intraundulator beam size regime.

INTRODUCTION

The interest in nonintercepting (NI) diagnostics for beam size and position in the undulators of x-ray free-electron lasers (XFELs) for beam match reasons is driven by the need to minimize the radiation damage to the undulator permanent magnets by scattering of beam by inserted converter screens. For such reasons our investigations on optical diffraction radiation (ODR) as NI relative beam size and position diagnostics [1-10] are particularly relevant. We reported initial experiments at FEL05 [11], and now we report the extensions of our studies at 7-GeV beam energy to aspects of the vertical and horizontal polarization components of the ODR near-field and far-field images. It appears that the near-field, vertically polarized data are particularly interesting. For our measurements of the beam size along the horizontal axis with a vertically displaced metal screen, the induced currents from the vertical field lines at the metal more directly reflect the actual beam size as revealed by scans of the upstream quadrupole fields. In addition, in our experimental configuration the vertical polarizer also rejects the strongest component of a weak background of visible-light optical synchrotron radiation (OSR) generated when the beam transits the horizontal bend dipole magnet that is 5.84-m upstream of the ODR station [12]. This same concept would be applicable to blocking the polarized visible undulator radiation co-propagating with the e-beam in an XFEL.

Although our experiments are with larger beams and impact parameters of 1-2 mm, our analytical model indicates that the technique scales with beam size and has sensitivity at the 20- to 50-μm regime with the impact parameter, d = 5 times σ_y = 100 μm. The beam size is similar to the 30-μm beam size in the XFEL intraundulator location. In addition, a direct comparison of the horizontal position readings of the nearby rf beam position monitor (BPM) and the ODR image centroid values during the scan of the upstream dipole current showed good agreement. The ODR data were also found to be very similar to an OTR image value during a similar dipole current scan. Our experimental results and some modeling results will be presented.

EXPERIMENTAL BACKGROUND

The Advanced Photon Source (APS) facility includes an injector complex with an rf thermionic cathode gun, an S-band linear accelerator, a particle accumulator ring (PAR) that damps the linac beam at 325 MeV, a booster injector synchrotron that ramps the energy from 0.325 GeV to 7 GeV in 220 ms, and the 7-GeV storage ring. At the exit of the booster, a dipole magnet allows direction of the beam to an alternate booster extraction beamline (BTX) that ends with a beam dump. This spur line has been used to develop our optical transition radiation (OTR) and our ODR diagnostics. The setup includes the upstream corrector magnets, two quadrupoles, and a dipole; and then, 5.8-m downstream the rf BPM (horizontal), the OTR/ODR imaging station, a localized beam-loss monitor based on a Cherenkov radiation detector, a Chromox beam-profiling screen, and the beam dump, as schematically shown in Fig. 1. An additional feature of the remote control of one strategic lens changes the optics from near-field to far-field imaging.

The ODR converter is a polished Al blade/mirror that is 1.5-mm thick, 30-mm wide, 30-mm tall, and it is mounted with its surface normal at 45° to the beam direction on a vertical stepper assembly. Its horizontal edge can be vertically positioned with an overall accuracy of ±10 μm over a span of 27.5 mm. The alignment of the optics with converter surface angle was done with an alignment laser placed on the surveyed beamline axis during an access

---

*Work supported by the U.S. Department of Energy, Office of Science, Office of Basic Energy Sciences, under Contract No. W-31-109-ENG-38.

**lumpkin@aps.anl.gov

period as described previously [12]. The near-field magnification resulted in calibration factors of 60-µm per pixel in x and 45-µm per pixel in y. Two 6-position filter wheels were used to select neutral density (ND) filters, bandpass filters, or two polarizers, which are oriented at 90 degrees to each other. The images are detected with a standard SONY charge-coupled device (CCD) camera, and the video is digitized with a MaxVideo MV200 digitizer interfaced to the Experimental Physics and Industrial Control Systems (EPICS) software architecture. The online image processing allows the selection of a region of interest, formation of the projected x and y profiles, and both a Gaussian fit to the profile and a numerical evaluation of the FWHM of the profile. The rms size is then the sigma of the Gaussian result or the estimated value found by dividing the numerically calculated FWHM by 2.35.

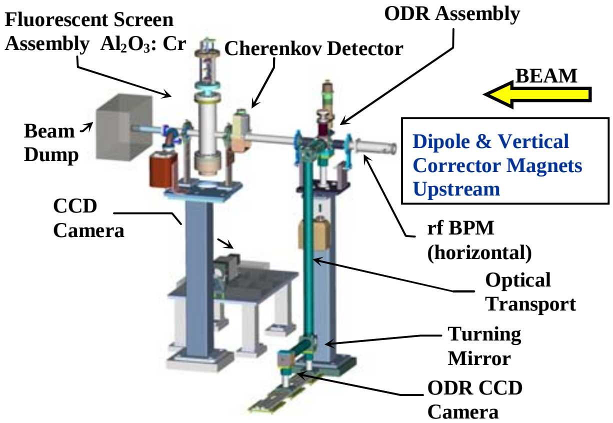

Figure 1: A Pro-E drawing of the OTR/ODR imaging station showing the rf BPM, the cube and stepper drive, the optical transport, the Cherenkov detector local loss monitor, and the Chromox profile monitor.

EXPERIMENTAL AND ANALYTICAL RESULTS

As mentioned in the previous section, the ODR profile results are referenced to complementary OTR profile results, and the image centroids are compared to the nearby, upstream rf BPM. The SDDS tools are used for the tracking of the process variables [13, 14].

The potential to monitor relative beam size has been discussed in our earlier papers [11, 12, 15]. However, in this case we now have the results of vertically polarized data. The OTR image profiles were first obtained by inserting the Al metal screen during a scan of the upstream AQ2 quadrupole field. This quadrupole strongly affects the horizontal beam size at our OTR/ODR station. Unfortunately, this is at a dispersive point in the lattice so we do not get emittance data cleanly from the quadrupole field scan. However, we do obtain a test of ODR as a relative beam size monitor. As seen in Fig. 2, the unpolarized, OTR-measured horizontal beam size varies from 2300 µm down to about 1300 µm. Results of both algorithms are shown, and they are seen to be in very good agreement because the beam shape is basically Gaussian when extracted from the 7-GeV booster synchrotron. Next, in Fig. 3, we show the observed vertically polarized ODR image profiles with an impact parameter of 1.25 mm during a similar quadruople field scan. The vertically polarized ODR horizontal image profiles track the beam size changes as seen qualitatively by the shape of the curve with AQ2 current. A direct comparison of the OTR and ODR is seen in the Fig. 4 combined plot of their fitted rms values. The ODR profiles are about 10% to 25% larger than the corresponding OTR profiles from the largest beam size to the smallest, respectively. The ratio of ODR/OTR for the size scan is next plotted in Fig. 5 to act as a lookup table for the beam-size monitor. As can be seen, at the minimum size of 1300 µm for the OTR, the ODR fit value is only 25% larger. This is much better than our factor of two results with unpolarized ODR observed on the same shift for this minimum beam focus and also reported at BIW06 [12]. The vertical polarization component would appear to be more reliable and direct in monitoring the actual beam size to better than 10% one has the ratio table or plot for these conditions.

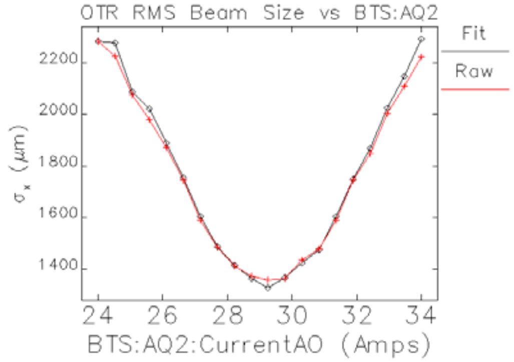

Figure 2: A plot of the OTR rms horizontal profile sizes for the upstream AQ2 quadrupole field scan. Both a Gaussian fit and a simple peak intensity to FWHM algorithm were used, which are in good agreement.

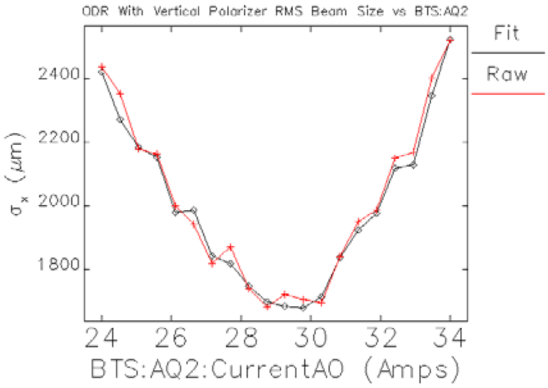

Figure 3: A plot of the vertically polarized ODR rms horizontal profile sizes for the upstream AQ2 quadrupole field scan. Both a Gaussian fit and a simple peak intensity to FWHM algorithm were used to measure image sizes, which are in good agreement.

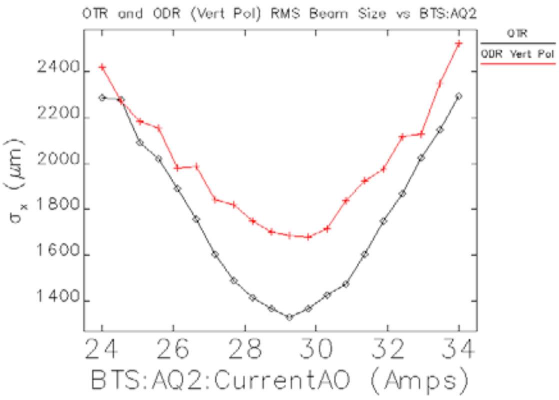

Figure 4: A direct comparison of the ODR (plus) and OTR (diamonds) Gaussian-fit horizontal profile size s during the quadrupole field scan. The vertically polarized ODR tracks the beam-size changes.

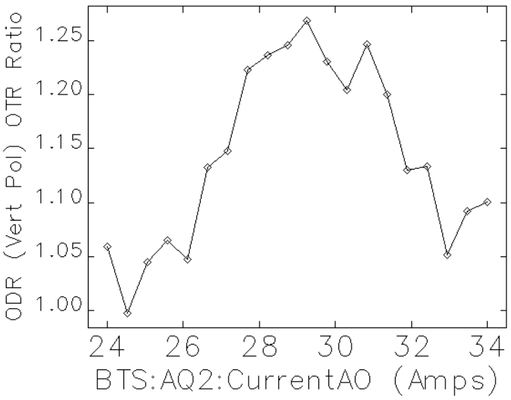

Figure 5: The ratio of ODR/OTR horizontal image sizes for different beam sizes during the AQ2 quadrupole scan. This ratio is noticeably smaller than for unpolarized data reported earlier.

In Fig. 6, we show the analytical results from our model described previously [11] for a beam size change of ±20% around the nominal σ_x=1300-µm value and the corresponding ODR image profile changes at the 1/e points in intensity. First, it is clear there is sensitivity to the beam-size changes that should be detectable in the camera images. Second, the HWHM values indicate an ODR profile of about 1.2 times the actual beam size as seen in the polarized data comparisons. These were done with a fixed σ_y = 200 µm. Initial vertical polarization effects have also been calculated, but further work is needed. The calculated ODR x width using the vertical polarization component was 20 to 50% narrower than that calculated using the horizontal component for *d* = 1000 and 2000 µm, respectively.

We also have calculated the sensitivity of ODR profiles to smaller beam sizes. In this case, we held the y size constant at 20 µm and varied the x-size from 20 to 50 µm using an impact parameter of 100 µm and beam energy of 7 GeV. In Fig. 7 it is clear that approximately a 25% increase in the ODR horizontal profile half width is calculated for the 50-µm beam size. Image processing should easily detect this change and use of polarization would improve the sensitivity. This should be a good match to monitoring beams of 30-µm size in the XFELs, subject to signal levels.

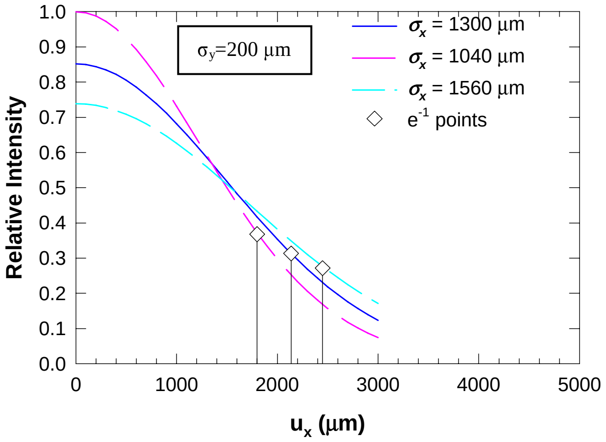

Figure 6: Analytical model results for the effects on the unpolarized ODR horizontal profiles for a variation of the beam size by ±20% around the 1300-µm value with *d*=1000 µm.

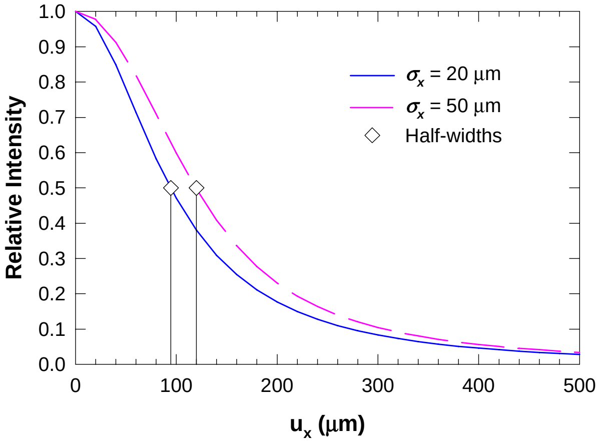

Figure 7: Analytical results for the change in unpolarized, horizontal ODR profiles for a change in beam size from 20 to 50 µm while holding the y value constant at 20 µm. The impact parameter is 100 µm for the 7-GeV beam. This is relevant to XFEL beam-size monitoring.

In addition, we repeated our relative beam position measurements first done with unpolarized ODR and compared to the rf BPM and OTR values [11]. In this case, we again used vertically polarized ODR with an impact parameter, *d* = 1.25 mm and a vertical size σ_y of 200 µm or less. The plot in Fig. 8 actually compares the centroid values from both OTR and ODR to the horizontal BPM readings. The OTR and ODR data overlap each other almost completely. This was done with the beam size σ_x = 1300 µm, the AQ2 quadrupole field set for the beam size minimum. Again, we believe the vertically polarized ODR component benefits the measurement sensitivity in the horizontal axis. Sensitivity at the 50- to

100-µm relative position level is attained. As in the case of beam size monitoring, for the much smaller beam and impact parameter in the XFEL case, we would expect much better position sensitivity (sub-10 µm) subject to signal level. Correspondingly, a vertical, single edge of a metal screen or aperture can be employed to obtain information on vertical position and beam size.

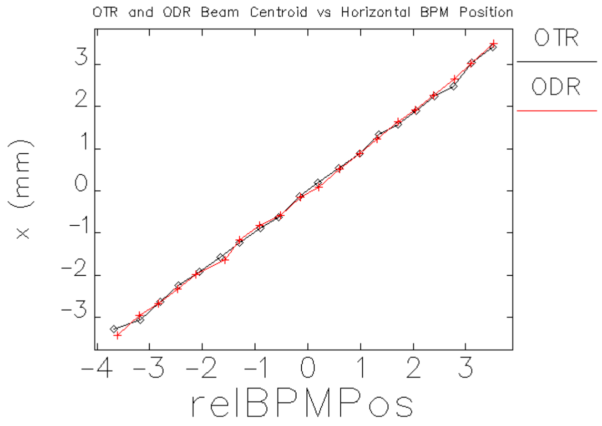

Figure 8: A plot of the OTR and ODR centroid value changes versus the nearby rf BPM values in mm during a scan of the upstream dipole current supply (and magnet fields). Horizontal position information can be reliably obtained from the vertically polarized ODR image centroids.

SUMMARY

In summary, we have extended our NI diagnostics techniques by evaluating the vertical and horizontal polarization components of near-field ODR images. As expected, the induced currents from the vertical field lines more directly represent the horizontal beam size in our configuration. Our results indicate that the tracking of relative beam size and position can be scaled down to address the potential needs of x-ray FELs. Complementary information on beam trajectory angle and beam divergence is being explored as well for higher average current beams.

ACKNOWLEDGMENTS

The authors acknowledge the support of Brian Rusthoven, Al Barcikowski, and Mike Bracken in the Mechanical Engineering Group, Joe Gagliano and Wayne Michalek in the Vacuum Group, Chuck Gold of the Diagnostics Group, and Bill Jansma and Horst Friedsam in the Survey Group for installation and resurvey, respectively, of the station in December 2005 and January 2006. The laser alignment proved to be a critical contribution to the new optics setup and the rotated BPM addressed the horizontal plane request.

REFERENCES

1. A.P. Kazantsev and G.I. Surdutovich, Sov. Phys. Sokl. **7**, 990 (1963).
2. M.L. Ter-Mikaelian, *High Energy Electromagnetic Processes in Condensed Media* (Wiley/Interscience, New York, 1972).
3. M. Castellano, Nucl. Instrum. Methods A **394**, 275 (1997).
4. Y. Shibata et al., Phys. Rev. E **52**, 678 (1995).
5. A.P. Potylitsyn, Nucl. Instrum. Methods B **145**, 169 (1998).
6. R.B. Fiorito, D.W. Rule, and W.D. Kimura, AIP Conf. Proc. **472**, 725 (1999); W.D. Kimura, R.B. Fiorito, and D.W. Rule, Proc. of the 1999 Particle Accelerator Conference, 487 (1999).
7. D.W. Rule, R.B. Fiorito, and W.D. Kimura, AIP Conf. Proc. **390**, 510 (1997).
8. R.B. Fiorito and D.W. Rule, Nucl. Instrum. Methods B **173**, 67 (2001).
9. T. Muto et al., Phys. Rev. Lett. 90(10) 104801-1 (2003).
10. P. Karataev et al., Phys. Rev. Lett. **93**, 244802 (2004).
11. A.H. Lumpkin et al., “Nonintercepting Electron Beam Diagnostics Based on Optical Diffraction Radiation for X-ray FELs,” Proceedings of the International FEL05 Conference, Stanford, CA, Aug. 21-26, 2005, JACoW/eConfC0508213, p. 604.
12. A.H. Lumpkin et al., “Developments in OTR/ODR Imaging Techniques for 7-GeV Electron Beams at APS,” submitted to Proceedings of BIW06, Batavia, Illinois, May 1-4, 2006.
13. L. Emery, M. Borland, H. Shang, R. Soliday, “User’s Guide for SDDS-Compliant EPICS Toolkit Version 1.5,” Advanced Photon Source, March 9, 2005.
14. H. Shang, Proc. of PAC2003, 3470 (2003).
15. A.H. Lumpkin et al., “Near-Field Imaging of Optical Diffraction Radiation Generated by a 7-GeV Electron Beam,” submitted to Phys. Rev.

INITIAL SEARCH FOR 9-keV XTR FROM A 28-GeV BEAM AT SPPS*

A.H. Lumpkin, J.B. Hastings,** and D.W. Rule***
Advanced Photon Source, Argonne National Laboratory
Argonne, IL 60439 USA

Abstract

The potential to use x-ray transition radiation (XTR) as a beam diagnostic and coherent XTR (CXTR) as a gain diagnostic in an x-ray FEL was proposed previously. At that time we noted that the unique configuration of the SLAC Sub-picosecond Photon Source (SPPS) with its known x-ray wiggler source, a special three-element x-ray monochromator, x-ray transport line, and experimental end station with x-ray detectors made it an ideal location for an XTR feasibility experiment. Estimates of the XTR compared to the SPPS source strength were done, and initial experiments were performed in September 2005. Complementary measurements on optical transition radiation (OTR) far-field images from a 7-GeV beam are also discussed.

INTRODUCTION

The use of x-ray transition radiation (XTR) as a beam diagnostic and coherent XTR (CXTR) as a gain diagnostic in an x-ray free-electron laser (XFEL) was proposed previously at FEL04 [1]. There have been a number of experiments to develop XTR as a source of x-rays in the past at several laboratories using moderate beam energies of a few hundred MeV to GeV [2-6], but there have been no applications in the FEL world to date. Partly based on recent experiments with a 7-GeV beam with optical transition radiation (OTR) and far-field or focus-at-infinity imaging [7], we projected that there should also be useful diagnostic information in the XTR field. In addition, we wanted to evaluate how to measure CXTR in an XFEL at 1.5 Angstroms. We identified the configuration of the SLAC Sub-picosecond Photon Source (SPPS) [8] with its known x-ray wiggler source, a special three-element x-ray monochromator, x-ray transport line, and experimental end station with x-ray detectors as a large-scale and ideal location for an XTR feasibility experiment. It was also the closest setup to what one might encounter in an x-ray FEL such as the Linac Coherent Light Source (LCLS) with its capability of translating in the 3-m undulator segments one at a time in the 100-m string of magnetic structures [9].

A test of XTR intensity with respect to the x-rays emitted by the SPPS wiggler when a 28-GeV beam transited it was proposed. Estimates of the XTR were done, the experiment proposal was approved, and initial experiments were performed in September 2005.

EXPERIMENTAL BACKGROUND

The OTR experiments were performed at the Advanced Photon Source (APS) as described elsewhere [7], and the XTR experiments were performed at the SPPS. The SPPS has been a short-pulse x-ray facility since 2004 [8]. The 28-GeV electron beam with a charge of $Q = 3$ nC, an emittance of 35 π mm-mrad, and bunch length of 230 fs was transported to the Final Focus Test Beam (FFTB) facility from the main SLAC accelerator [10] and through the single, permanent magnet wiggler as shown schematically in Fig. 1. The SPPS source was tuned to 9 keV by adjusting the wiggler gap, and a three-element x-ray monochromator is used to direct the x-rays down a 50-m long beamline to the end station. In addition, as noted in the schematic, there are several OTR stations with 1-µm-thick Ti foil installed in support of the series of experiments on beam driven plasma Wakefield acceleration by M. Hogan and his collaborators [11]. These Ti foils were used to generate the forward XTR for the trial experiments. A dipole at the end of the electron beam beamline directed the electrons to a beam dump.

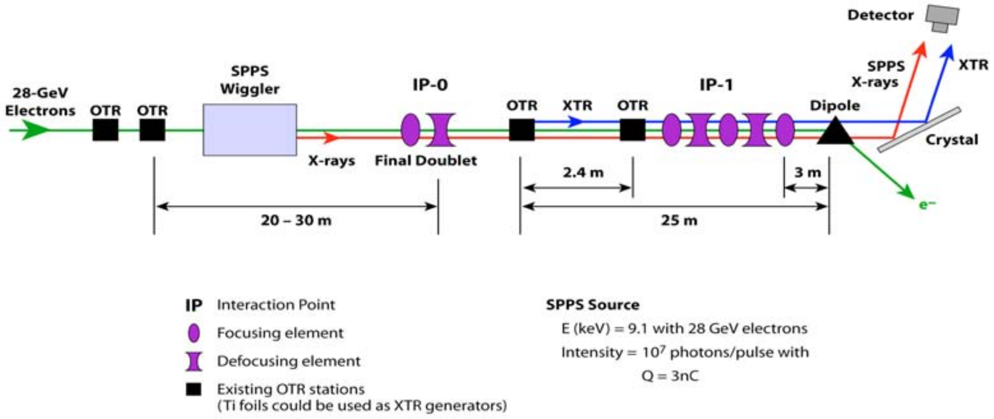

Figure 1: A schematic of the FFTB facility showing the beamline, SPPS wiggler, OTR stations, monochromator, and x-ray detectors.

---

*Work supported by the U.S. Department of Energy, Office of Science, Office of Basic Energy Sciences, under Contract No. W-31-109-ENG-38.
**SPPS/SLAC, Menlo Park, CA USA
***Carderock Division, NSCW, West Bethesda, MD USA

This dipole was the source of broadband x-ray synchrotron radiation (XSR) that also would be interacting with the three-element crystal monochromator. The three-element monochromator was adjusted to transport 9-keV x-rays from the wiggler using a series of x-ray detectors along the beamline.

At the end station an ANDOR x-ray CCD camera and Photonic Science X-Ray Eye intensified camera were used as the principle diagnostic components. The wiggler x-rays were also aligned based on a series of x-ray APDs along the beamline. The ANDOR camera is designed to be cooled to reduce read noise and dark current. Unfortunately on these particular experiments, a small vacuum leak in the camera prevented the final cool down, so we ran it at room temperature. The X-ray Eye was positioned about 1 meter downstream of the CCD camera and was used for initial wiggler beam and hence monochromator alignments. The attenuation of the SPPS source x-ray was done with various selections of Al foil thicknesses that were calculated to attenuate 9-keV x-rays by factors of up to 4000. At 10-keV x-ray energy the counts per detected photon was about 391, resulting in a dynamic range of 167. This assumed a 16-bit device and a gain of seven photoelectrons per count in the CCD.

Aspects of the possible eventual XTR application to LCLS are shown in Fig. 2. In the schematic the beam energy is 14 GeV and the OTR and XTR are generated by a thin foil (or foil stack). For OTR an off-axis mirror might be used, but for XTR an annular crystal would be used. The expected opening angle of the radiation cones in either case would be $1/\gamma = 35$ µrad. For OTR an imaging system would be used, and for XTR the YAG:Ce converter plus lens and CCD camera might be employed. A far-field imaging experiment with lenses appears feasible for the OTR. This would be done in a manner similar to our recent 7-GeV beam work at APS [7].

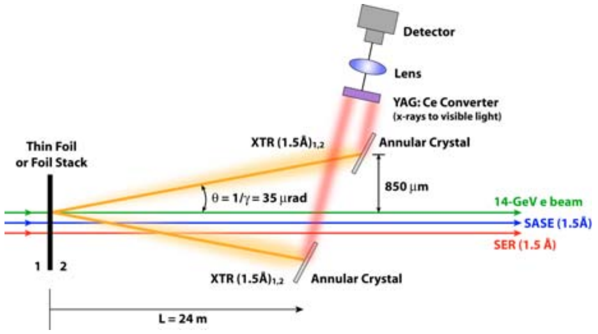

Figure 2: A schematic of the generation of XTR from a foil or foil stack from a 14-GeV beam and with competing wiggler x-rays or spontaneous emission in a SASE FEL.

EXPERIMENTAL RESULTS AND DISCUSSION

OTR Results at 7 GeV

As a point of reference, the results of complementary experiments on the 7-GeV beam at APS are included. In this case a single Al screen was used to generate the backward OTR. At this beam energy the expected OTR opening angle would be 70 µrad. This is within a factor of two of the angle in LCLS and of four in that for SPPS. In Fig. 3 we see the unpolarized, vertically polarized, and horizontally polarized images for the beam extracted from the booster synchrotron. For beam charges of 3 nC one could image these far-field angular distributions. The depth of the central minimum indicates the ensemble beam divergence is much smaller than 70 µrad, probably less than 10 µrad. An analytical model [12] was used to evaluate the expected profiles for different divergences. An example is shown in Fig. 4 for 3-µrad divergence.

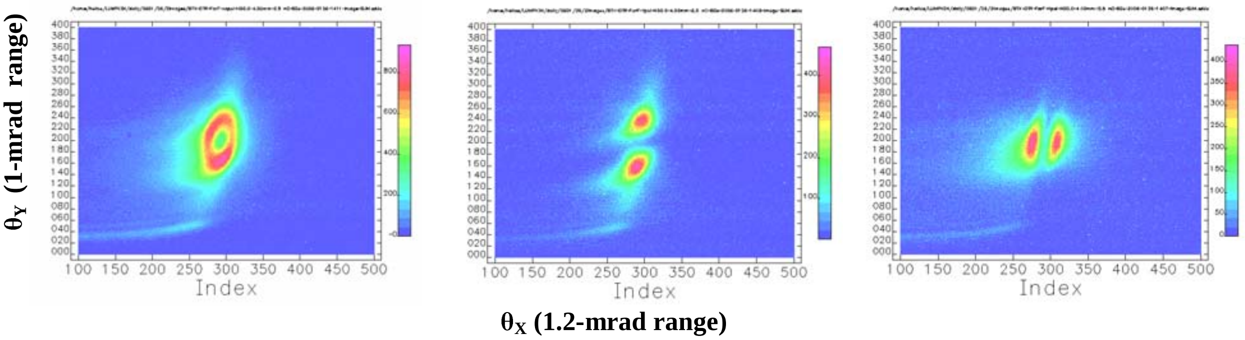

Figure 3: Example of far-field OTR images generated by a 7-GeV beam at APS; a) unpolarized, b) vertically polarized, and c) horizontally polarized.

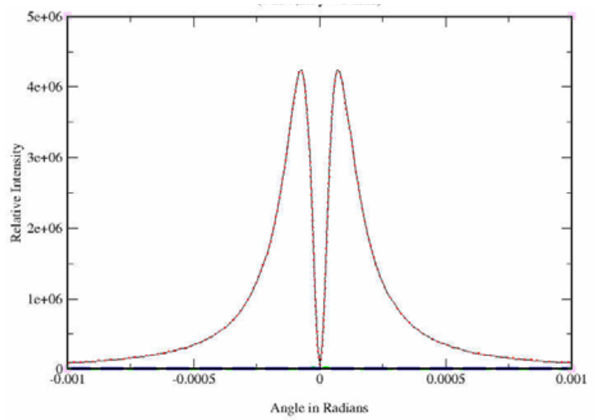

Figure 4: An analytical calculation of the OTR single foil angular distribution for a 7-GeV beam with 3-µrad divergence. The opening angle is ~70 µrad.

9-keV X-rays

In the case of the SPPS experiments we accepted the standard tuneup for 9-keV photons. The nominal intensity was projected to be 10^7 photons per 3 nC of charge. We had calculated the XTR yield from carbon foils as $\sim 10^3$ photons per 3 nC. The initial SPPS result is shown in Fig. 5 using the Al foil attenuation of 1000. The observed image corresponds to supported transport of 30×80 μrad^2. The three-element crystal monochromator is oriented in the horizontal plane with a spatial acceptance of about 1 mm, but subtends larger vertical angles. An example profile is shown in Fig. 6, indicating a vertical FWHM of about 20 µrad. In Fig. 7 we show the 9-keV x-ray image of the background XSR (attributed to the dipole upstream of the monochromator) obtained with the wiggler gap open and foils extracted. The gas nozzle from the experimental chamber just upstream of the x-ray CCD is actually inserted vertically from the top. It shadows the x-rays, and was seen in the horizontal axis because the CCD camera is rotated 90 degrees in the installation. The uniform stripe of the XSR from the vertically deflecting dipole is seen clearly. There is also a ghost image in the 10-shot average due to some camera trigger inconsistency.

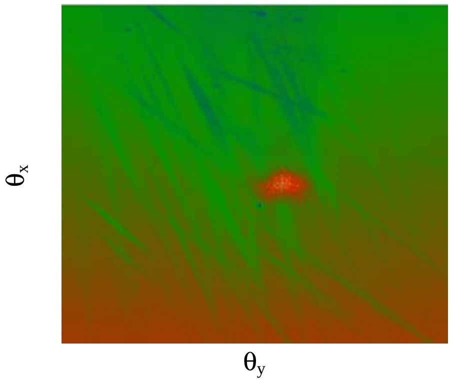

Figure 5: An x-ray CCD image of the SPPS 9-keV x-rays from the wiggler. The camera is rotated 90º so θ_y is along the image horizontal axis. The signal is attenuated by 1000.

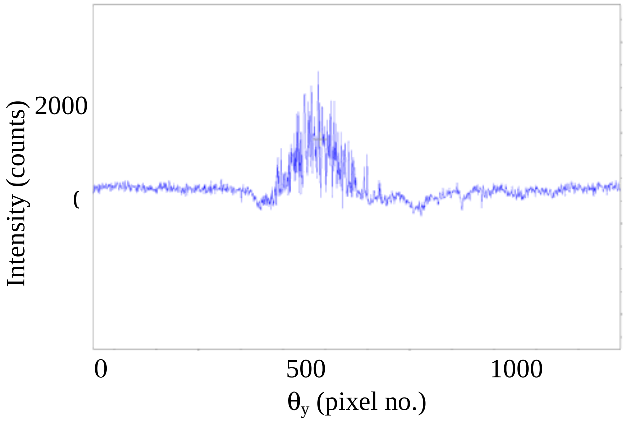

Figure 6: A vertical angular distribution profile from Fig. 5.

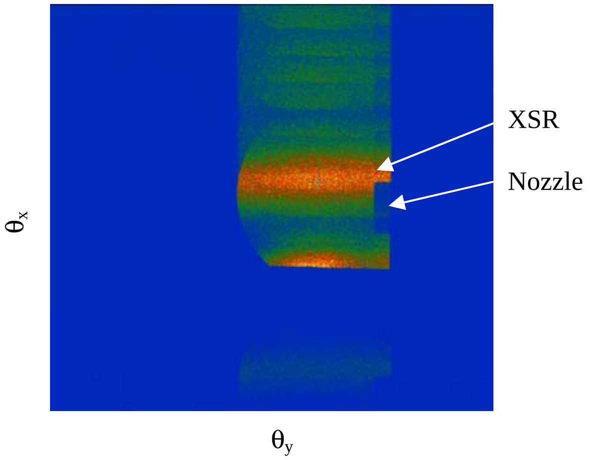

Figure 7: An x-ray CCD image of 9-keV XSR background coming down the beamline. The gas jet nozzle in a chamber upstream of the camera is shadowed. It is vertically insertable.

In Fig. 8 we show the observed x-ray image signal with all three foils inserted using a selected region of interest (ROI) with 4x4 pixel binning and with background subtraction of the signals with the wiggler gap open and all three foils out. This is a localized ROI pixel binning to improve statistics and camera sync. In Fig. 9 the profile in θ_y is shown. There is a hint of an annular shape, and the opening angles are marked on the profile as might be for the middle foil distance. Based on a calibration factor of 1.1 µrad per 4-pixel bin, the 18-µrad location is estimated for a foil at 80 m. In Fig. 10 a calculation for OTR from a 28-GeV beam is shown as a point of comparison for a divergence value of 5 µrad. The central minimum is deeper in the calculation than in the data profile.

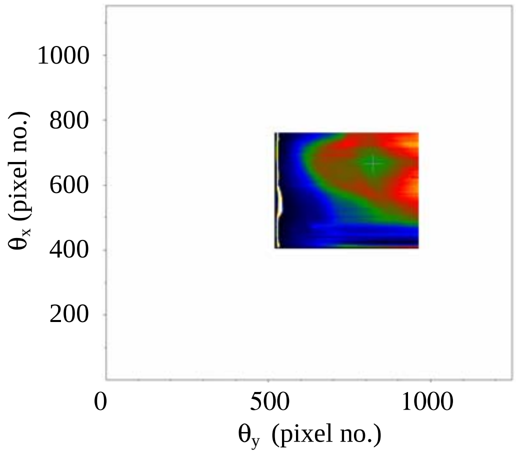

Figure 8: A background subtracted x-ray CCD ROI image of the 9-keV x-rays with three Ti foils inserted.

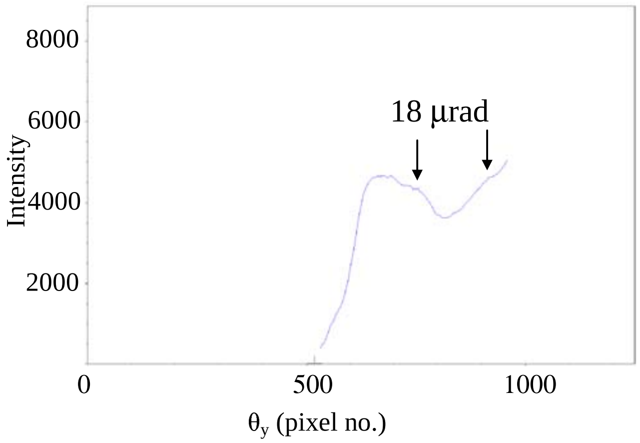

Figure 9: An x-ray CCD region of interest for the three XTR foils inserted case including background subtraction of the XSR source.

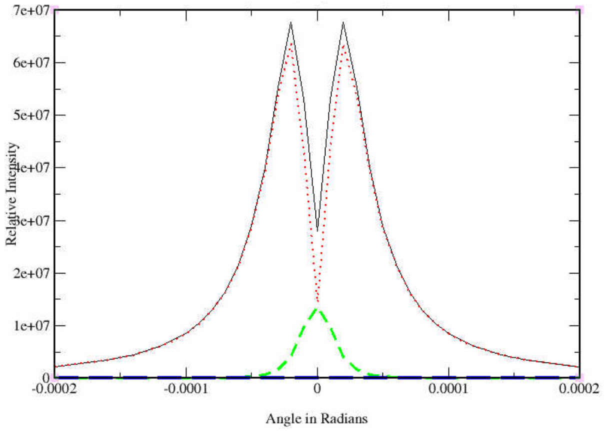

Figure 10: A calculation of the OTR angular distribution for a 28-GeV beam and 5-μrad divergence.

SUMMARY

In summary, we have shown the possibilities of OTR far-field imaging for a 7-GeV beam and report our initial attempts to extend such research to XTR from a 28-GeV beam. Due to the unfortunate event that the x-ray CCD camera could not be cooled during the XTR trials, the results are inconclusive. Certainly, XTR was generated by the Ti foils, but the unambiguous imaging of that radiation was problematical. The concept of a foil stack to enhance the XTR signal and the ability to actually cool the CCD were next on the agenda. The closing of the SPPS facility occurred before these experiments could be done, but the LCLS or SABER facilities at SLAC may provide a future opportunity to test the concepts.

ACKNOWLEDGMENTS

The authors acknowledge the assistance of Kelly Gaffney on the x-ray CCD, Aaron Lindenberg for borrowing the X-ray Eye, and the team of SPPS graduate students who rotated through the extended shifts at SLAC. They also thank Mark Hogan for use of the OTR stations in the FFTB.

REFERENCES

[1] A.H. Lumpkin, W.M. Fawley, and D.W. Rule, “A Concept for Z-dependent Microbunching Measurements with Coherent X-ray Transition Radiation in a SASE FEL,” Proceedings of the 2004 FEL Conference, Trieste, Italy, Editors: Bakker, Giannessi, Marsi, and Walker, 515 (2005).
[2] A.N. Chu et al., J. Appl. Phys. **51** (3) 1290 (March 1980).
[3] Michael J. Moran, Nucl. Instrum. Methods **B24/25** 335 (1987).
[4] Michael J. Moran, Nucl. Instrum. Methods **B33**, 18 (1988).
[5] M.A. Piestrup et al., Phys. Rev. **A 45** (2) 1183 (1992).
[6] H. Backe et al., Z. Phyz. **A 349** 87 (1994).
[7] A.H. Lumpkin et al., “Developments in OTR/ODR Imaging Techniques for 7-GeV Electron Beams at APS,” submitted to Proceedings of BIW06, Batavia, Illinois, May 1-4, 2006, AIP (in press).
[8] J.B. Hastings, “Sub-Picosecond Pulse Source: Recent Results,” presented at PAC2005, Knoxville, Tennessee, TOPB002.
[9] R.M. Bionta, “Characterization of X-ray FEL Radiation,” presented at FEL2005, Stanford, CA, THOB003.
[10] P. Emma et al., Proceedings of the PAC2003, 3129 (2003).
[11] M.J. Hogan et al., “Review of Beam-Driven Plasma Wakefield Experiments at SLAC,” presented at PAC2005, Knoxville, Tennessee, TOPA002.
[12] D.W. Rule, code Singlef, transported to APS Unix system 1992.

MODELING AND MEASUREMENT OF μ-METAL SHIELDING EFFECT ON THE MAGNETIC PERFORMANCE OF AN LCLS UNDULATOR[*]

Shigemi Sasaki, Isaac B. Vasserman, Emil Trakhtenberg
APS/ANL, Argonne, IL 60439, USA.

Abstract

In a previous paper [1], we presented results showing that the Earth's field might have a significant effect on the Linac Coherent Light Source (LCLS) undulator performance due to a large concentration of the field by the undulator poles. Based on the result of model calculation, we decided to shield the Earth's field by surrounding the undulator backing structure with a 1-mm-thick μ-metal sheet.

First, the effect of the shield was modeled using the code RADIA. According to the calculation, the shielding factor of a "C-shape" μ-metal shield was better than a factor of eight. Second, we measured the Earth's field shielding effect without an undulator. In our measurement laboratory, the vertical component of the Earth's field was about 0.5 gauss. It was suppressed down to smaller than 0.1 gauss with the shield. After these background measurements, we examined the effect of the shield with an undulator in place. The measurement results show very good agreement with the model calculation.

INTRODUCTION

For the commissioning of the Linac Coherent Light Source (LCLS), beam-based alignment will be used to correct the offsets of quadrupoles and beam position monitors. This strategy works only when the field integrals in each undulator segment are small enough [2]. Undulator segments will be measured and tuned in the magnetic measurement facility (MMF) at the Stanford Linear Accelerator Center and then installed on the iron girders and moved to the LCLS tunnel. Several sources of errors are possible here. The first one is due to the difference of the Earth's field at the locations of MMF and tunnel. This difference is exaggerated by a concentration of the Earth's field by vanadium-permendur poles of the device. Another possible source of error is the existence of the magnetic elements, such as iron, used in the support system and other elements of the tunnel. Based on the computer simulations using a simple model in the RADIA code [3], we decided to use the μ-metal sheet to shield unwanted external field effect.

EARTH'S FIELD MODELING

As shown in our previous paper [1], a seven-period undulator model with a large surrounding solenoid was used for simulating the Earth's field effect. By using this simple model, we found that the averaged field concentration factor was about 2.4, i.e., a 0.5-gauss external vertical dipole field gave a 1.2-gauss dipole field in an undulator. The horizontal component of Earth's field was found to be well suppressed on the undulator axis.

Because a dipole field above 0.7 gauss in an undulator gives an electron trajectory excursion of more than 2 μm from the undulator axis, this unwanted field needs to be suppressed or corrected. Figure 1 shows the model used for the calculation of shielding effect of μ-metal. The B-H curve of CO-NETIC sheet [4] was assumed for the calculation.

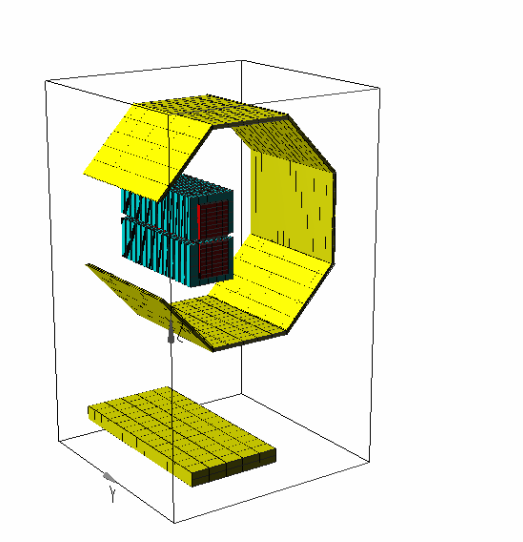

Figure 1: A μ-metal shield model used for the calculation.

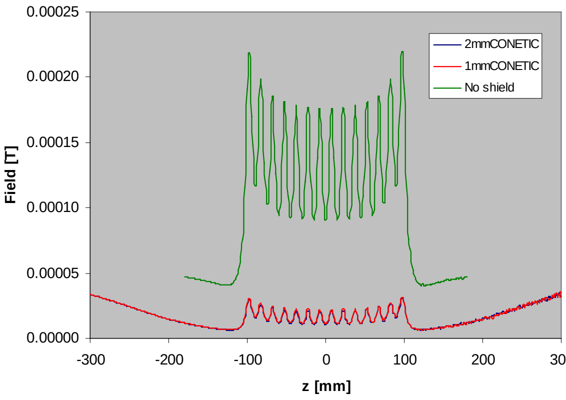

Figure 2: Summary of calculated results.

Figure 2 shows the summary of calculated results. The green curve represents the field change due to the 0.5-gauss external vertical field without a shield. In the central region, a field strength averaged over a half period is about 1.2 gauss. The red and blue curves are for 1-mm- and 2-mm-thick μ-metal shields, respectively. The

---

[*] Work supported by the U.S. Dept. of Energy, Office of Science, Office of Basic Energy Science, under Contract W-31-109-ENG-38.
[#] sasaki@aps.anl.gov

averaged field was 0.156 gauss for a 1-mm sheet and 0.147 gauss for a 2-mm sheet, respectively. Based on these calculations, we decided to use a 1-mm thick sheet for better cost performance. (A sheet with a double thickness provides only 6 % better shielding.)

From these results, we find that the concentration (enhancement) factor by the poles in an undulator is 2.4, and the suppression (damping) factor by the μ-metal shield is eight.

MEASURED RESULTS

The first and second articles of LCLS undulators were tuned in the magnetic measurement facility (MM1) at the Advanced Photon Source. Prior to the measurement, the background field along the measurement bench was measured with a moving coil. Figure 2 shows the Earth's field distribution along the z-axis.

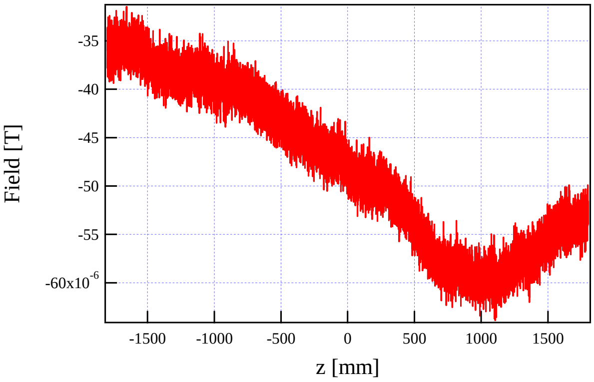

Figure 3: Earth's field distribution measured in MM1.

From this result, we can estimate the shielding effect by the μ-metal in an undulator based on the simulation result described in the previous section. Without the shield, the field, B_y, in an undulator due to the Earth's field is magnified by a factor of 2.4, i.e., $B_y = B_{EF} \times 2.4$. After applying the shield, the remaining field, B_{yrem}, is reduced by a factor of eight, i.e., $B_{yrem} = B_y/8$. Therefore, the signature of shield, B_{sig}, is: $B_{sig} = B_y - B_{yrem}$.

Figure 4 shows the signature of μ-metal shield. After measuring the undulator field without the shield, we can predict the field distribution with the shield by adding the shield signature to the raw data.

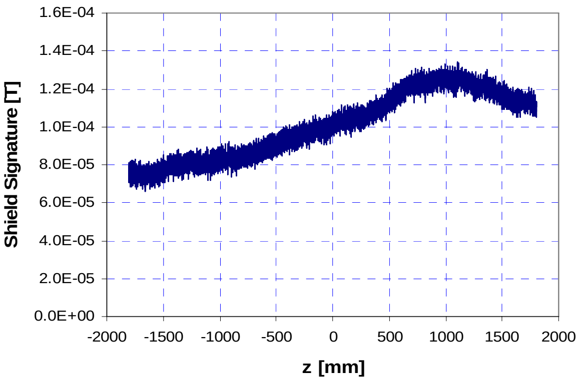

Figure 4: Signature of the μ-metal shield.

In Figure 5, the solid green curve is the second field integral of the raw data measured without the shield, and the blue broken curve is the prediction for after the shield is installed.

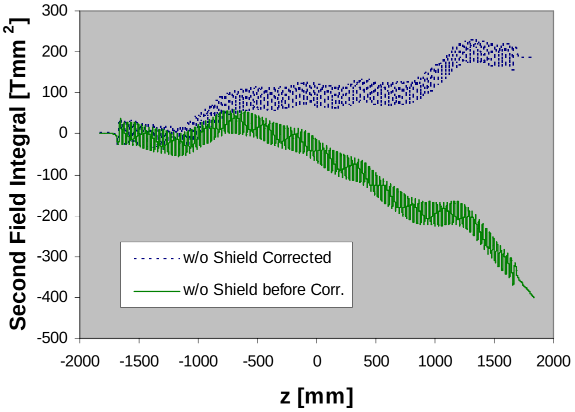

Figure 5: Second field integrals of raw data and corrected data.

Figure 6 shows the predicted second field integral and the integral measured after the shield was attached.

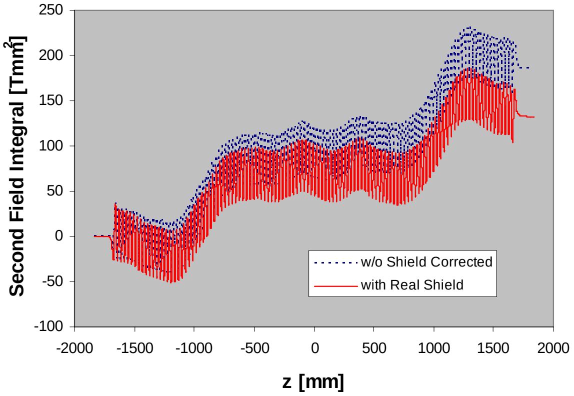

Figure 6: Second field integrals predicted from data without shield (blue broken line) and the data with the shield (red solid line), respectively.

The actual measured field data with the μ-metal shield is in good agreement with the corrected data based on simulation with a simple model.

DISCUSSION AND SUMMARY

In the example shown in this paper, we applied additional trajectory shims and phase shims to straighten the trajectory and to reduce the phase error after applying the μ-metal shield. Also, we corrected the first and second field integrals by applying appropriate shims at the entrance and the exit ends of undulator. Figure 7 shows the trajectory after the final tuning with the shield. The net kick (corresponding to the first integral) and the net displacement (corresponding to the second field integral) are well below the tolerances as shown. Also, the trajectory excursion in the undulator is well below the tolerances (2 μm).

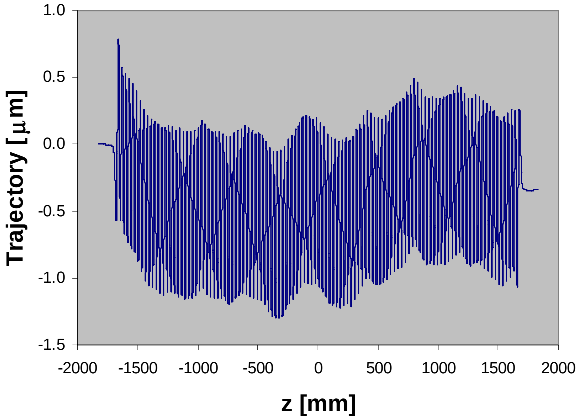

Figure 7: Trajectory of the first article undulator after final tuning.

In the example in this paper, we used the estimation procedures in a relatively early stage of the tuning process in order to demonstrate the effectiveness of this method. However, because the effectiveness of this method had been proven, we used it at the very end of the tuning process for the second article of LCLS undulators.

Here are the steps of the tuning procedures:

- Mechanically align an undulator to the Hall-probe measurement bench.
- Magnetically align the undulator axis to the Hall-probe.
- Set a proper gap by changing the thickness and/or the location of spacers (mechanical shims).
- Straighten the horizontal (x) trajectory by using trajectory shims.
- Minimize the phase errors by using phase shims.
- Straighten the vertical (y) trajectory.
- Apply shims to compensate multipoles.
- Apply μ-metal shield and do final measurements and tuning of field integrals.
- Do final fine tuning, if necessary.

REFERENCES

[1] S. Sasaki and I. B. Vasserman, Proceedings on 27th International Free Electron Laser Conference (FEL2005), Stanford, CA, August 2005.

[2] "Conceptual Design Report (CDR) for the Linac Coherent Light Source Project," SLAC-R-593, April 2002, http://www-ssrl.slac.stanford.edu/lcls/cdr .

[3] O. Chubar, P. Elleaume, J. Chavanne, J. Synchrotron Radiat. **5**, 481 (1998).

[4] http://www.magnetic-shield.com/ .

BEAM SPREADING AND EMITTANCE OSCILLATION OF AN INTENSE MAGNETIZED BEAM IN FREE SPACE*

Chun-xi Wang†, Kwang-Je Kim, ANL, Argonne, IL 60439, USA
Jack G. Zhang, IIT, Chicago, IL 60616,USA

Abstract

Intense beams with large angular momentum have important applications in electron cooling and in producing flat beams suitable for ultrafast x-ray generation, Smith-Purcell radiators, and possibly for a future linear collider. To gain a basic understanding of the influence of beam angular momentum in an otherwise space-charge-dominated beam, the behavior of such a beam in free space will be examined here, in particular, beam spreading due to space-charge force, as well as emittance oscillation. Drift space is an important part of a split photoinjector and plays a significant role in emitance compensation of a high-brightness photoinjector.

INTRODUCTION

By immersing the cathode in a magnetic field, beam with (large) angular momentum can be created and is referred to as "magnetized" beam. High-intensity magnetized beams have important applications in electron cooling and flat-beam generation. The emittance oscillation of a non-magnetized beam in the drift space of a split photoinjector has some generic properties such as the "double minimum" feature [1], which has been explained by space-charge induced beam spreadings of individual slices [2]. Here, we generalize the technique used in [2] to examine the influence of beam angular momentum on beam spreading and emittance oscillation in drift space.

For a round beam in an axisymmetric channel, the beam envelope is governed by the reduced beam envelope equation [3, 4]

$$\hat{\sigma}'' + \frac{\kappa}{\beta^2\gamma^2}\,\hat{\sigma} - \frac{\kappa_s}{\beta^2\gamma^2}\frac{1}{\hat{\sigma}} - \frac{\epsilon^2}{\hat{\sigma}^3} = 0. \qquad (1)$$

where $\hat{\sigma} = \sqrt{\beta\gamma}\,\sigma$ is the reduced envelope, κ represents the external focusing, and perveance $\kappa_s = I/2I_A$ gives the space-charge defocusing. Here, we consider uniform non-accelerating channels with constant κ and κ_s. In a drift space, $\kappa = 0$ and κ_s decreases somewhat due to longitudinal debunching, which will be ignored here. The emittance ϵ is conserved and may contain two parts: thermal emittance and angular momentum. Although angular momentum is correlated motion and intrinsically different from random thermal emittance, from the beam envelope evolution point of view, these two types of emittances make no difference. In high-brightness photoinjectors, the thermal emittance is sufficiently small such that a non-magnetized beam can be considered space-charge dominated. However, the existence of beam angular momentum qualitatively changed the property of the envelope equation by addding a significant emittance term. In the following, we present preliminary exploration of the effects of angular momentum. Because we will only consider non-accelerating beams, $\beta\gamma = 1$ is set in the following sections to simplify the notation. By the same token, we will use σ instead of $\hat{\sigma}$ for the reduced envelope as well.

BEAM SPREADING IN A UNIFORM NON-ACCELERATING CHANNEL

In a uniform non-accelerating channel, the coefficients in the beam envelope equation are all constants. The corresponding envelope Hamiltonian (with the setting $\beta\gamma = 1$)

$$H = \frac{p^2}{2} + \kappa\frac{\sigma^2}{2} - \kappa_s\ln(\sigma) + \frac{\varepsilon^2}{2\sigma^2} \qquad (2)$$

is a constant of motion, whose value can be expressed with the initial σ_0 and σ_0'. Thus, we have the first integral

$$\sigma'^2 + \kappa\sigma^2 - \kappa_s\ln\sigma^2 + \frac{\varepsilon^2}{\sigma^2} = \sigma_0'^2 + \kappa\sigma_0^2 - \kappa_s\ln\sigma_0^2 + \frac{\varepsilon^2}{\sigma_0^2}. \qquad (3)$$

The beam envelope is bounded by the potential well [4]. The lower bound is due to space-charge defocusing and emittance pressure. If any, the upper bound is due to external focusing. It reaches an extreme size σ_m at $\sigma' = 0$, which can be determined by

$$\sigma_0'^2 + \kappa\sigma_0^2 - \kappa_s\ln\sigma_0^2 + \frac{\varepsilon^2}{\sigma_0^2} = \kappa\sigma_m^2 - \kappa_s\ln\sigma_m^2 + \frac{\varepsilon^2}{\sigma_m^2}. \qquad (4)$$

Note that in drift space, i.e., without external focusing, $\sigma_m'' > 0$, there will be a beam waist for a converging beam. With external focusing, σ_m may be a minimum or maximum depending on the sign of σ_m''. From these equations, σ' can be solved as

$$\tilde{\sigma}' = \frac{\sigma'}{\sigma_m} = \pm\sqrt{\kappa\left(1-\tilde{\sigma}^2\right) + \frac{\kappa_s}{\sigma_m^2}\ln\tilde{\sigma}^2 + \frac{\varepsilon^2}{\sigma_m^4}\left(1-\frac{1}{\tilde{\sigma}^2}\right)}, \qquad (5)$$

where $\tilde{\sigma} \equiv \sigma/\sigma_m$. The sign depends on whether the beam is converging ($-$) or diverging ($+$). By integrating Eq. (5) we obtain the solution of the beam envelope as

$$s = \int_{\frac{\sigma_0}{\sigma_m}}^{1} \frac{\mathbf{sign}(\sigma_0')\,dx}{\sqrt{\kappa\left(1-x^2\right) + \frac{\kappa_s}{\sigma_m^2}\ln\left(x^2\right) + \frac{\varepsilon^2}{\sigma_m^4}\left(1-\frac{1}{x^2}\right)}} + \int_{1}^{\frac{\sigma}{\sigma_m}} \frac{\mathbf{sign}(\sigma')\,dx}{\sqrt{\kappa\left(1-x^2\right) + \frac{\kappa_s}{\sigma_m^2}\ln\left(x^2\right) + \frac{\varepsilon^2}{\sigma_m^4}\left(1-\frac{1}{x^2}\right)}}. \qquad (6)$$

---

* Work supported by U.S. Department of Energy, Office of Science, Office of Basic Energy Sciences, under Contract No. W-31-109-ENG-38.

† wangcx@aps.anl.gov; http://www.aps.anl.gov/~wangcx

This integral cannot be expressed with elementary functions. In the case $\kappa = \kappa_s = 0$, this integral yields the well-known hyperbola envelope for a bunch of free particles. For a space-charge dominated beam in free space ($\kappa = \epsilon = 0$), this integral yields the so-called universal beam-spreading curve for $\sigma/\sqrt{\kappa_s}$, which is independent of slice perveances. However, for a magnetized beam, there is a non-zero emittance term. Thus, the beam perveance can not be scaled away from the envelope equation. Therefore, beam spreading of a magnetized beam will have nontrivial dependence on beam perveance, and there is no universal beam-spreading curve anymore.

ENVELOPE EVOLUTIONS NEARBY A REFERENCE ENVELOPE

The relative motions of various beam slices are responsible for the variation of projected emittance in high-brightness photoinjectors. Thus, it is interesting to examine the evolution of envelopes nearby a reference envelope. Assuming small deviations, we expand a slice envelope around the reference envelope $(\bar{\sigma}, \bar{\sigma}')$ as

$$\begin{pmatrix} \sigma \\ \sigma' \end{pmatrix} = \begin{pmatrix} \bar{\sigma} \\ \bar{\sigma}' \end{pmatrix} + \sum_{\alpha} \begin{pmatrix} \partial_{q^\alpha} \bar{\sigma} \\ \partial_{q^\alpha} \bar{\sigma}' \end{pmatrix} \delta q^\alpha , \qquad (7)$$

where δq^α represents a small deviation in certain parameter q^α. Here, we consider the deviations in the initial values $\delta\sigma_0$ and $\delta\sigma_0'$, as well as the slice perveance $\delta\kappa_s$, assuming all slices have the same emittance and angular momentum.

To compute the partial derivatives with respect to σ_0, we take derivatives on both sides of Eq. (6) with respect to σ_0 and use Eq. (5) for simplification, which yields

$$0 = \frac{1}{\sigma'/\sigma_m} \partial_{\sigma_0} \frac{\sigma}{\sigma_m} - \frac{1}{\sigma_0'/\sigma_m} \partial_{\sigma_0} \frac{\sigma_0}{\sigma_m} + \frac{\partial_{\sigma_0}\sigma_m}{\sigma_m} F_x, \qquad (8)$$

where F_x denotes the integral,

$$F_x = \int_{\frac{\sigma_0}{\sigma_m}}^{1} \frac{\mathbf{sign}(\sigma_0') \left[\frac{\kappa_s}{\sigma_m^2} \ln\left(x^2\right) + 2\frac{\varepsilon^2}{\sigma_m^4}\left(1 - \frac{1}{x^2}\right)\right] dx}{\left[k\left(1 - x^2\right) + \frac{\kappa_s}{\sigma_m^2} \ln\left(x^2\right) + \frac{\varepsilon^2}{\sigma_m^4}\left(1 - \frac{1}{x^2}\right)\right]^{3/2}} + \int_{1}^{\frac{\sigma}{\sigma_m}} \frac{\mathbf{sign}(\sigma') \left[\frac{\kappa_s}{\sigma_m^2} \ln\left(x^2\right) + 2\frac{\varepsilon^2}{\sigma_m^4}\left(1 - \frac{1}{x^2}\right)\right] dx}{\left[k\left(1 - x^2\right) + \frac{\kappa_s}{\sigma_m^2} \ln\left(x^2\right) + \frac{\varepsilon^2}{\sigma_m^4}\left(1 - \frac{1}{x^2}\right)\right]^{3/2}}.$$

Thus, $\partial_{\sigma_0}\sigma$ can be solved as

$$\partial_{\sigma_0}\sigma = \frac{\sigma'}{\sigma_0'} + \frac{\sigma'}{\sigma_m} \partial_{\sigma_0}\sigma_m \left(\frac{\sigma}{\sigma'} - \frac{\sigma_0}{\sigma_0'} - F_x\right), \qquad (9)$$

where $\partial_{\sigma_0}\sigma_m$ can be obtained by differentiating Eq. (4) as

$$\partial_{\sigma_0}\sigma_m = \frac{\kappa\sigma_0 - \kappa_s/\sigma_0 - \varepsilon^2/\sigma_0^3}{\kappa\sigma_m - \kappa_s/\sigma_m - \varepsilon^2/\sigma_m^3} = \frac{\sigma_0''}{\sigma_m''}, \qquad (10)$$

which is non-zero unless staying at equilibrium.

Similarly, taking derivatives on both sides of Eq. (6) with respect to σ_0' yields the derivative $\partial_{\sigma_0'}\sigma$. Combined with Eq. (9), they give the first two expressions in the following sets of four derivatives:

$$\partial_{\sigma_0}\sigma = \frac{1}{\sigma_0'} \left(\sigma' - \sigma_0''\partial_{\sigma_0'}\sigma\right), \qquad (11)$$

$$\partial_{\sigma_0'}\sigma = \frac{\sigma_0\sigma' - \sigma_0'\sigma}{\sigma_m\sigma_m''} + \frac{\sigma_0'\sigma'}{\sigma_m\sigma_m''} F_x, \qquad (12)$$

$$\partial_{\sigma_0}\sigma' = \frac{1}{\sigma_0'} \left(\sigma'' - \sigma_0''\partial_{\sigma_0'}\sigma'\right), \qquad (13)$$

$$\partial_{\sigma_0'}\sigma' = \frac{\sigma_0\sigma''}{\sigma_m\sigma_m''} - \frac{\sigma_0'(\sigma\sigma'' - \sigma_m\sigma_m'')}{\sigma_m''\sigma_m\sigma'} + \frac{\sigma_0'\sigma''}{\sigma_m\sigma_m''} F_x. \qquad (14)$$

The last two expressions can be obtained by differentiating the first two expressions with respect to s. Clearly, these derivatives have the initial values $\partial_{\sigma_0}\sigma(0) = \partial_{\sigma_0'}\sigma'(0) = 1$ and $\partial_{\sigma_0'}\sigma(0) = \partial_{\sigma_0}\sigma'(0) = 0$. In the special case $\kappa = 0$ and $\varepsilon = 0$, these expressions reduce to the simple results of Eqs. (16) and (18) in [2], and $F_x = s$. It is important to note that, for a space-charge dominated beam where the emittance term can be neglected, all these expressions are independent of slice perveance, with or without external focusing. This property may play a significant role in emittance compensation of high-brightness photoinjectors. However, for a magnetized beam, these expressions will depend on the perveance of the (reference) slice.

To evaluate the effect of small perveance variations, we compute $\partial_{\kappa_s}\sigma$ and $\partial_{\kappa_s}\sigma'$ similarly. Differentiating Eqs. (3) and (4) yield, respectively,

$$\partial_{\kappa_s}\sigma' = \frac{1}{\sigma'}\left(\ln\frac{\sigma}{\sigma_0} + \sigma''\partial_{\kappa_s}\sigma\right), \qquad (15)$$

$$\partial_{\kappa_s}\sigma_m = \frac{1}{\sigma_m''} \ln\frac{\sigma_0}{\sigma_m}. \qquad (16)$$

Differentiating Eq. (6) with the help of function F_x and the above expression for $\partial_{\kappa_s}\sigma_m$ gives

$$\partial_{\kappa_s}\sigma = \frac{\sigma'}{\sigma_m\sigma_m''}\left(\frac{\sigma}{\sigma'} - \frac{\sigma_0}{\sigma_0'} - F_x\right) \ln\frac{\sigma_0}{\sigma_m} + \frac{\sigma'}{2}F_s, \qquad (17)$$

where the function F_s is defined the same as F_x except that $\kappa_s = 1$ and $\epsilon = 0$ are set in the numerators. (Thus, for a space-charge dominated beam, $F_x = \kappa_s F_s$.) The initial values of both $\partial_{\kappa_s}\sigma$ and $\partial_{\kappa_s}\sigma'$ are zero.

EMITTANCE OSCILLATION

From the envelope expressions in Eq. (7), assuming the various deviations from the reference envelope are uncorrelated, the emittance due to slice envelope variations can be calculated as [2]

$$\epsilon^{\mathrm{env}} \simeq \sqrt{\sum_{\alpha} W_{q^\alpha}^2 \left(\overline{(\delta q^\alpha)^2} \big/ \overline{q^\alpha}^2\right)}, \qquad (18)$$

where

$$W_{q^\alpha} \equiv (\bar{\sigma}\partial_{q^\alpha}\bar{\sigma}' - \bar{\sigma}'\partial_{q^\alpha}\bar{\sigma})\,\overline{q^\alpha}. \tag{19}$$

Here, the bar over δq^α and q^α indicates averaging over the slices.

Inserting the above partial derivatives into Eq. (19), we have

$$W_\sigma = \bar{\sigma}_0\left[\frac{\bar{\sigma}\bar{\sigma}'' - \bar{\sigma}'^2}{\bar{\sigma}_0'}\left(1 - \frac{\bar{\sigma}_0''}{\bar{\sigma}'}\,\partial_{\sigma_0'}\bar{\sigma}\right) - \frac{\bar{\sigma}\bar{\sigma}_0''}{\bar{\sigma}'}\right], \tag{20}$$

$$W_{\sigma'} = \bar{\sigma}_0'\left[\frac{\bar{\sigma}\bar{\sigma}'' - \bar{\sigma}'^2}{\bar{\sigma}'}\,\partial_{\sigma_0'}\bar{\sigma} + \frac{\bar{\sigma}\bar{\sigma}_0'}{\bar{\sigma}'}\right]. \tag{21}$$

These expressions reduce to the special results of Eqs. (17) and (19) in [2]. Since $\partial_{\sigma_0'}\bar{\sigma}$ equals zero at the beginning, we have the initial values

$$W_\sigma(0) = -W_{\sigma'}(0) = -\bar{\sigma}_0\bar{\sigma}_0'. \tag{22}$$

To examine the extreme values of $W_\sigma(s)$ and $W_{\sigma'}(s)$, we take the s-derivative of these functions and have, after some algebra,

$$W_\sigma' = \bar{\sigma}_0\,\frac{\bar{\sigma}\bar{\sigma}''' - \bar{\sigma}'\bar{\sigma}''}{\bar{\sigma}_0'\bar{\sigma}'}\left(\bar{\sigma}' - \bar{\sigma}_0''\,\partial_{\sigma_0'}\bar{\sigma}\right), \tag{23}$$

$$W_{\sigma'}' = \bar{\sigma}_0'\,\frac{\bar{\sigma}\bar{\sigma}''' - \bar{\sigma}'\bar{\sigma}''}{\bar{\sigma}'}\,\partial_{\sigma_0'}\bar{\sigma}. \tag{24}$$

It is easy to see that the factor

$$\frac{\bar{\sigma}\bar{\sigma}''' - \bar{\sigma}'\bar{\sigma}''}{\sigma'} = -2\left[\frac{\kappa_s}{\sigma} + 2\frac{\varepsilon^2}{\sigma^3}\right] \neq 0,$$

thus W_σ reaches the extreme value of $-\bar{\sigma}_0\bar{\sigma}_0''\bar{\sigma}/\bar{\sigma}'$ when $\bar{\sigma}' = \bar{\sigma}_0''\,\partial_{\sigma_0'}\bar{\sigma}$, and $W_{\sigma'}$ reaches the extreme value of $\bar{\sigma}_0'^2\bar{\sigma}/\bar{\sigma}'$ when $\partial_{\sigma_0'}\bar{\sigma} = 0$. Using Eq. (12) and the condition for the extreme, we can further express the extreme values W_σ^{m} as

$$W_\sigma^{\mathrm{m}} = -\bar{\sigma}_0\bar{\sigma}_0''\frac{\bar{\sigma}}{\bar{\sigma}'} = \frac{\bar{\sigma}_0}{\bar{\sigma}_0'}\left(\bar{\sigma}_m\bar{\sigma}_m'' - \bar{\sigma}_0\bar{\sigma}_0''\right) - \bar{\sigma}_0\bar{\sigma}_0''F_x, \tag{25}$$

$$W_{\sigma'}^{\mathrm{m}} = \bar{\sigma}_0'^2\frac{\bar{\sigma}}{\bar{\sigma}'} = \bar{\sigma}_0\bar{\sigma}_0' + \bar{\sigma}_0'^2F_x \tag{26}$$

where F_x integrates up to the extreme point. However, it is not obvious that the condition for the extremes can be satisfied (except the trivial case $W_{\sigma'}' = \partial_{\sigma_0'}\bar{\sigma} = 0$ at the beginning).

From these expressions, a few general properties can be drawn about emittance oscillation. In particular, for a beam focused into a drift, $\bar{\sigma}_0' < 0$, $\bar{\sigma}_0'' > 0$, $\bar{\sigma}_m\bar{\sigma}_m'' - \bar{\sigma}_0\bar{\sigma}_0'' > 0$, thus $W_\sigma(0) > 0$ and $W_\sigma^m < 0$, which leads to emittance minimum when W_σ crosses zero, as discussed in [2]. Furthermore, $W_\sigma^m < 0$ requires $\bar{\sigma}' > 0$ at that location, thus the emittance maximum due to W_σ is always located after the beam waist where $\bar{\sigma}' = 0$.

Similarly, W_{κ_s} can be worked out as

$$W_{\kappa_s} = \bar{\kappa}_s\left[\frac{\bar{\sigma}}{\bar{\sigma}'}\ln\frac{\bar{\sigma}}{\bar{\sigma}_0} + \frac{\bar{\sigma}\bar{\sigma}'' - \bar{\sigma}'^2}{\bar{\sigma}'}\,\partial_{\kappa_s}\bar{\sigma}\right], \tag{27}$$

where $\partial_{\kappa_s}\bar{\sigma}$ is given by Eq. (17). Clearly, $W_{\kappa_s}(0) = 0$.

EFFECTS OF BEAM ANGULAR MOMENTUM

To see the influence of beam angular momentum on the beam envelope spreading of an individual slice and on the emittance oscillation of a bunch of slices, we plot a set of five figures showing the quantities σ, σ', W_σ, $W_{\sigma'}$, and W_{κ_s}, using the expressions given above. In each figure, the red curve shows the evolution of a space-charge dominated beam and the blue curve shows the same beam but with an angular momentum term 10 times larger than the space-charge term at the beam waist (2 mm). The other parameters are $\sigma_0 = 9\,mm$, $\sigma' = -9.5\,mrad$, $\beta\gamma = 12$, $\kappa_s = 0.05$, which are adopted from an optimized SPARC photoinjector design.

Through this example and the above analysis, we see that, qualitatively speaking, the basic behavior of beam spreading and emittance oscillation in drift space are not changed by the large angular momentum, although there are significant quantitative changes. For example, the beam waist becomes much larger and is reached much quicker. Also, the emittance oscillation amplitude gets larger, and so on. From this point of view, W_{κ_s} may be an exception because there is no zero crossing anymore for the blue curve.

However, emittance compensation for magnetized beam [5] may be significantly different from conventional space-charge dominated beam. For example, there is no invariant envelope solution for the envelope equation in a booster when there is a significant emittance term. Thus, the matching condition for space-charge dominated beam may not be appropriate any more. Furthermore, the ability to compensate emittance may be limited by the fact that beam perveance cannot be scaled away from the envelope equation of a magnetized beam.

CONCLUDING REMARK

We developed a technique to examine the beam spreading and emittance oscillation of a magnetized beam in free space. Clearly, the technique also applies to a beam with significant thermal emittance and/or in a uniform focusing channel (we have kept both focusing κ and emittance ϵ in all the expressions). In a focusing channel, a beam may reach both minimum and maximum size because it is bounded by a potential well. For example, a diverging beam reaches a maximum beam size in the focusing solenoid for emittance compensation. The emittance evolution in the solenoid can be described by the same expressions presented above. Much more work is needed to understand emittance compensation of a magnetized beam.

REFERENCES

[1] M. Ferrario, J.E. Clendenin, D.T. Palmer, J.B. Rosenzweig, L. Serafini, SLAC-PUB-8400 (2000).

[2] C.-x. Wang, “Emittance oscillation in the drift space of split photoinjectors,” Proceedings of the 35nd Advanced ICFA

Beam Dynamics Workshop on Physics and Application of High-Brightness Electron Beam, October 2005.

[3] See, for example, J.D. Lawson, *The Physics of Charged Particle Beams*, 2nd ed. (Oxford University Press, New York, 1988).

[4] C.-x. Wang, Nucl. Instrum. Methods A**557**, 94 (2006).

[5] X. Chang, I. Ben-Zvi, J. Kewisch, BNL-73192-2004-CP.

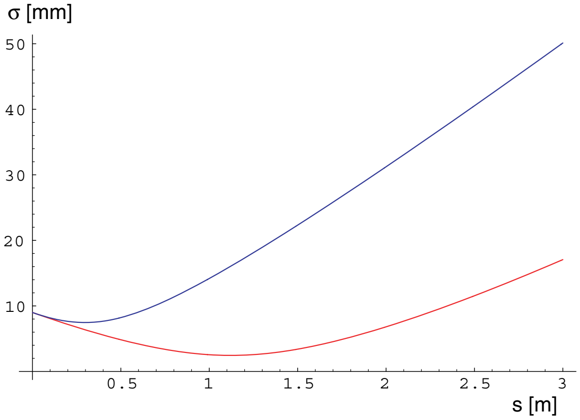

Figure 1: Reduced envelope in free space for space-charge dominated beam (red) and beam with large emittance (blue).

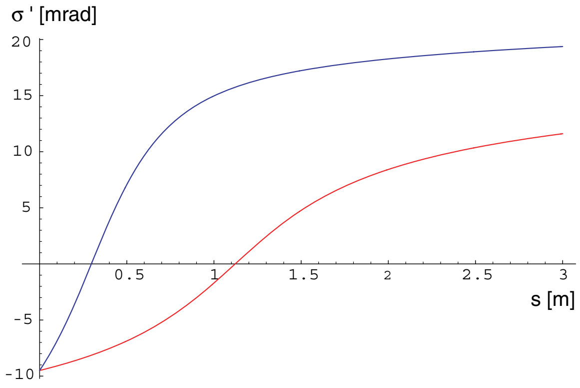

Figure 2: Reduced envelope slope in free space for space-charge dominated beam (red) and beam with large emittance (blue).

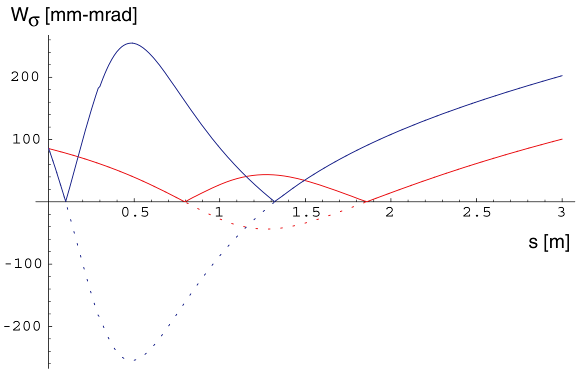

Figure 3: Emittance oscillation in free space due to initial slice envelope variation for space-charge dominated beam (red) and beam with large emittance (blue). The solid curves plot the absolute values.

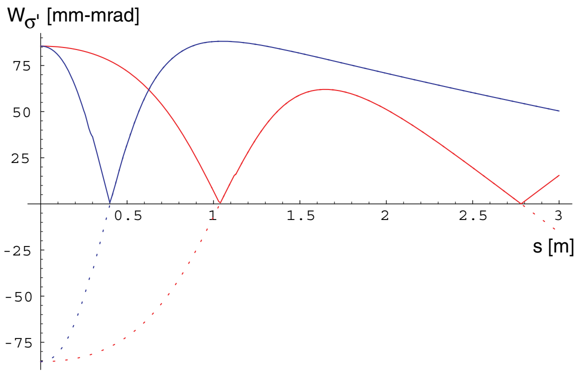

Figure 4: Emittance oscillation in free space due to initial slice slope variation for space-charge dominated beam (red) and beam with large emittance (blue). The solid curves plot the absolute values.

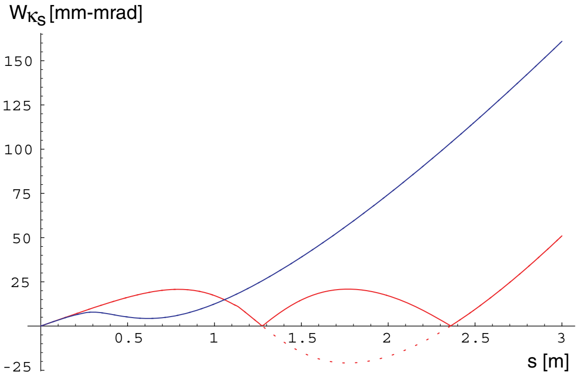

Figure 5: Emittance oscillation in free space due to slice perveance variation for space-charge dominated beam (red) and beam with large emittance (blue). The solid curves plot the absolute values.

ENERGY MODULATION OF THE ELECTRONS BY THE LASER FIELD IN THE WIGGLER MAGNET: ANALYSIS AND EXPERIMENT

A.A. Zholents#, LBNL, Berkeley, CA 94720, U.S.A.
K. Holldack, BESSY, 12489 Berlin, Germany.

Abstract

Energy modulation of the electron beam after the interaction with the laser field in the wiggler magnet can be calculated using interference of the laser field and the field of spontaneous emission in the far field region of wiggler radiation. Quite often this approach gives a deeper insight on the process than traditional calculations where the effect of the laser field on the electron energy is integrated along the electron trajectory in the wiggler. We demonstrate it by showing the agreement between the analytical model and the experiment involving wiggler scan measurements with large detuning from the FEL resonance producing more than one order of magnitude variations in the amplitude of the energy modulation. The high sensitivity was achieved using the THz radiation from a sub-mm dip in the electron density that energy modulated electrons leave behind while propagating along the storage ring lattice. All measurements were performed at the BESSY-II electron storage ring.

ENERGY MODULATION

The energy gain/loss obtained by the electron in the interaction with the laser field E_x polarized in the horizontal plane and co-propagating the planar wiggler magnet together with the electron in z direction can be found by solving the equation [1]:

$$\frac{d\gamma}{dz} = \frac{e}{mc^2} E_x \cdot \beta_x , \tag{1}$$

where γ is the relativistic factor, $\beta_x = v_x / c$, where v_x is the horizontal velocity of the electron and c is the speed of light, e, m are the electron charge and mass, and

$$E_x = E_0 / \sqrt{1+\left(z/z_0\right)^2} \sin[k\left(z-ct\right)+\psi] e^{-\tau^2/4\sigma_\tau^2} , \tag{2}$$

where k is the wave number of the laser field, $z_0 = ka_0^2/2$ is the Rayleigh length, a_0 is the waist size which is assumed to be in the center of the wiggler, $\psi = \psi_0 - \tan^{-1}\left(z/z_0\right)$, where ψ_0 is the phase of the wave at the beginning of the interaction with the electron at the entrance of the wiggler and σ_τ is the rms width of the laser pulse intensity.

For electron motion inside the wiggler one obtains:

$$\begin{aligned} \beta_x &= -\frac{K}{\gamma}\sin\left(k_w z\right), \\ \beta_z &= \sqrt{1-\frac{1}{\gamma^2}-\beta_x^2} \approx 1-\frac{1}{2\gamma^2}\left(1+K^2/2\right)+\frac{K^2}{4\gamma^2}\cos\left(2k_w z\right) \end{aligned} \tag{3}$$

where $k_w = 2\pi/\lambda_w$ and λ_w is the wiggler period, $K = eB_0/k_w mc$, B_0 is the peak magnetic field and β_z is the normalized velocity along the wiggler, *i.e.*:

$$z\left(t\right) = c\int_0^t \beta_z\left(t'\right)dt' \cong ct - \frac{1}{2\gamma^2}\left(1+\frac{K^2}{2}\right)ct + \frac{K^2}{8k_w\gamma^2}\sin\left(2k_w z\right) \tag{4}$$

In what follows we consider on-axis electrons only. This assumption can be extended to all electrons in the electron bunch if the electron beam size $\sigma_{x,y} << a_0$. Then, using (1) and (3) we write:

$$\begin{aligned} \frac{d\gamma}{dz} = \frac{eE_0 K}{2mc^2\gamma\sqrt{1+\left(z/z_0\right)^2}} &\left\{\cos\left(k\left(z-ct\right)+k_w z+\psi\right)\right. \\ &\left. -\cos\left(k\left(z-ct\right)-k_w z+\psi\right)\right\} e^{-\tau^2/4\sigma_\tau^2} \end{aligned} \tag{5}$$

It is further convenient to define the resonance electron energy, also called an FEL resonance energy, $\gamma_r^2 = \frac{k}{2k_w}\left(1+K^2/2\right)$ and assume a small energy spread $\Delta\gamma/\gamma_r$ such as to obtain:

$$k(z-ct) = -k_w z\frac{\gamma_r^2}{\gamma^2} - \frac{\xi}{2}\sin\left(2k_w z\right) \tag{6}$$

with $\xi = K^2/(2+K^2)$. Using a generation function for Bessel functions [2] we found:

$$\begin{aligned} &\cos\left[k_w z\left(1-\left(\gamma_r/\gamma\right)^2\right)-\xi/2\sin\left(2k_w z\right)+\psi\right]- \\ &\qquad \cos\left[k_w z\left(1+\left(\gamma_r/\gamma\right)^2\right)+\xi/2\sin\left(2k_w z\right)+\psi\right] \approx \\ &\left[J_0\left(\xi/2\right)-J_1\left(\xi/2\right)\right]\cos\left[k_w z\left(1-\left(\gamma_r/\gamma\right)^2\right)+\psi\right] \end{aligned}$$

where in the last step we retain only slowly varying terms with $1-\left(\gamma_r/\gamma\right)^2 << 1$. Finally, using dimensionless variables in Eq. (6) [3]: $\hat{z} = z/L_w$, $\nu = N2\delta\gamma/\gamma_r$, and $q = L_w/z_0$, where L_w is the length of the wiggler with N periods, $\hat{\sigma}_\tau = \sigma_\tau/\tau_0$ and $\tau_0 = 2\pi N/kc$, one obtains:

$$\frac{d\gamma}{d\hat{z}} = \frac{eE_0 KL_w}{2mc^2\gamma}\{JJ\}\frac{\cos\left(2\pi\nu\hat{z}-\tan^{-1}\left(q\hat{z}\right)+\psi_0\right)}{\sqrt{1+\left(q\hat{z}\right)^2}} e^{-\hat{z}^2/4\hat{\sigma}_\tau^2} \tag{7}$$

where definition $\{JJ\} = J_0\left(\xi/2\right)-J_1\left(\xi/2\right)$ is used following [4]. Introducing the laser pulse energy $A_L = \left(E_0^2/8\pi\right)\left(\pi a_0^2/2\right)\sqrt{2\pi}\sigma_\tau c$, Eq.(7) can be written as:

$$\begin{aligned} \left\langle\frac{d\gamma}{d\hat{z}}\right\rangle &= \frac{2}{mc^2}\sqrt{A_L\alpha\hbar\omega_{0s}\frac{K^2}{2+K^2}}\{JJ\} \\ &\times \sqrt{\frac{2q}{\left(2\pi\right)^{1/2}\hat{\sigma}_\tau}}\frac{\cos\left(2\pi\nu\hat{z}-\tan^{-1}\left(q\hat{z}\right)+\psi_0\right)}{\sqrt{1+\left(q\hat{z}\right)^2}} e^{-\hat{z}^2/4\hat{\sigma}_\tau^2} \end{aligned} \tag{8}$$

where α is the fine structure constant, ω_{0s} is central frequencies of the field of spontaneous emission, and $\langle ... \rangle$

AAZholents@LBL.GOV

defines averaging over one wiggler period. By integrating Eq.(8) one obtains for the amplitude of the energy modulation:

$$\Delta\gamma(q,\nu,\hat{\sigma}_\tau)=\frac{2}{mc^2}\sqrt{A_L\alpha\hbar\omega_{0s}\frac{K^2}{2+K^2}}\{JJ\}f(q,\nu,\hat{\sigma}_\tau) \quad (9)$$

where:

$$f(q,\nu,\hat{\sigma}_\tau)=\sqrt{\frac{2q}{(2\pi)^{1/2}\hat{\sigma}_\tau}}\int_{-0.5}^{0.5}\frac{\cos\left(2\pi\nu\hat{z}-\tan^{-1}(q\hat{z})\right)}{\sqrt{1+(q\hat{z})^2}}e^{-\hat{z}^2/4\hat{\sigma}_\tau^2}d\hat{z}$$

Figure 1 shows plots of $f(q,\nu,\sigma_\tau)$ for various q and ν and $\hat{\sigma}_\tau$. Using the maximum value of $f(q=8,\nu=-0.7,\hat{\sigma}_\tau=0.25)$ =2.2, one finds:

$$\Delta\gamma_{\max}\cong\frac{2}{mc^2}\sqrt{5A_L\alpha\hbar\omega_{0s}\frac{K^2}{2+K^2}}\{JJ\} \quad (10)$$

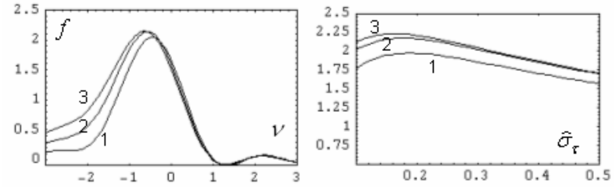

Figure 1. Function $f(q,\nu,\hat{\sigma}_\tau)$ for $\hat{\sigma}_\tau$=0.25 (left plot) and ν=-0.7 (right plot) and for q = 4, 6, and 8 (curves 1, 2, and 3).

Alternatively, the energy gain/loss obtained by the electron in the interaction with the laser field can be calculated considering the interference of the field of its spontaneous emission in the wiggler and the laser field. This technique takes it roots in a so-called acceleration theorem [5,6] declaring that the very existence of spontaneous emission is mandatory if the acceleration by the external field is employed in a linear order to this field. Following this idea and using Parseval's theorem, we write for the amplitude of the energy modulation:

$$\begin{aligned}mc^2\Delta\gamma_{\max}&=2\frac{\pi a_0^2c}{16\pi}\int E_s(t)E_L^*(t)dt=\\&2\frac{\pi a_0^2c}{16\pi}\int E_s(\omega)E_L^*(\omega)d\omega\end{aligned} \quad (11)$$

where $E_s(\omega)=\sqrt{2/\pi}E_{0s}\sin((\omega-\omega_{0s})\tau_0/2)/(\omega-\omega_{0s})$ is Fourier component of the field of spontaneous emission, $E_L(\omega)=E_{0L}\sqrt{2}\sigma_\tau\cdot e^{-(\omega-\omega_{0L})^2\sigma_\tau^2}$ is a Fourier component of the laser field, and ω_{0L} is the central frequency of the laser field. Further defining the energy of spontaneous emission (see, also [3]):

$$A_S=(E_s^2/8\pi)(\pi a_0^2/2)\tau_0c=5\alpha\hbar\omega_{0s}\frac{K^2}{2+K^2}\{JJ\}^2 \quad (12\}$$

radiating in the mode with a rms divergence of the intensity $\sigma_R'=\sqrt{2\lambda_s/\pi L_w}$, where $\lambda_s=2\pi c/\omega_{0s}$, one can obtain from (11):

$$\Delta\gamma_{\max}\cong\frac{2}{mc^2}\sqrt{A_L\,A_s}\left\{\sqrt{\hat{\sigma}_\tau}\int e^{-4(x-x_{0L})^2\hat{\sigma}_\tau^2}\frac{\sin(x-x_{0s})}{(x-x_{0s})}dx\right\} \quad (13)$$

where we used substitution $x=\omega\tau_0/2$ and $x_{0s}=\omega_{0s}\tau_0/2$ and $x_{0L}=\omega_{0L}\tau_0/2$. The entire expression inside the figure bracket shows the overlapping of the spectra of the laser signal and the spectra of spontaneous emission signal. This expression is normalized in such a way that it is approximately one when $\omega_{0s}=\omega_{0L}$ and $\hat{\sigma}_\tau$=0.25 corresponding to the optimal condition of the maximum energy modulation found previously. Finally we note that in the case of a large detuning from the FEL resonance a contribution of the second term with $\sin(x+x_{0s})/(x+x_{0s})$ could be comparable to a contribution of the main term with $\sin(x-x_{0s})/(x-x_{0s})$ and, thus, should be added to the overlapping integral.

EXPERIMENT

The energy modulation of electrons by the laser field was measured as a function of the detuning of the central frequency of the electron spontaneous emission in the wiggler from the central frequency of the laser field. The experiment was conducted at BESSY-II synchrotron light source [7]. The laser operated at a fixed wavelength of 800 nm while wiggler detuning covered large range of frequencies with the wavelengths changing from 200 nm to 1000 nm, *i.e.* in the range greatly exceeding the bandwidth of the laser pulse. As an illustration, Figure 2 shows normalized spectra of the laser field and the field of the electron spontaneous emission in the wiggler for a single set point during this scan.

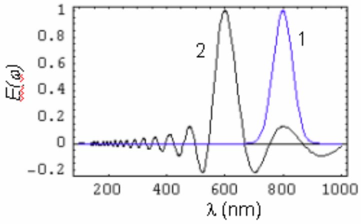

Figure 2. Spectra of the laser field (curve 1) and the field of spontaneous emission of electrons in the wiggler (curve 2).

Measurements of the energy modulation were performed indirectly using coherent THz radiation from a bending magnet 11 m downstream of the wiggler magnet. THz radiation was produced by the dip in the electron density distribution that energy modulated electrons leave behind after propagating the storage ring lattice with non-zero time-of-flight properties, a phenomena which is described elsewhere [8]. Use of the THz signal allowed us to obtain sufficient signal-to-noise ratio even with wiggler settings leading to very small amplitudes of the energy modulation. A typical example of THz spectra and the dip in the electron density distribution is shown in Figure 3.

The width and the magnitude of the dip are defined by the amplitude of the energy modulation of electrons and by time-of-flight parameters R_{51}, R_{52}, R_{56} of the lattice

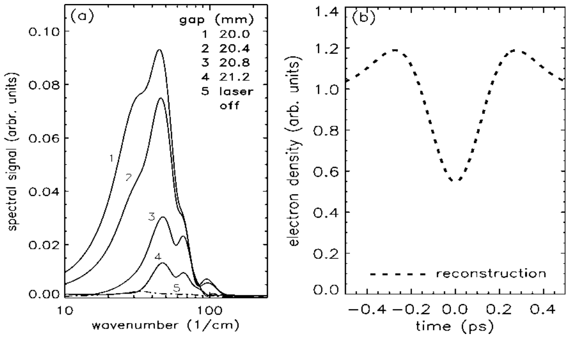

Figure 3. a) THz spectra for different wiggler gaps corresponding to different detunings near the FEL resonance, b) a dip in electron density determined from spectra measured at the FEL resonance and corrected for beamline transmission.

between the wiggler magnet and a source of the THz radiation. Figure 4 shows the magnitude of the dip calculated as a function of the amplitude of the energy modulation normalized on the relative energy spread of electrons σ_E. The following parameters were used: $\sigma_E = 10^{-3}$, R_{56}=-0.011 m, R_{51}= 5.5 10^{-5}, R_{52}= 0.53 m [9] , the electron beam size and angle in the wiggler magnet σ_x=320 μm and $\sigma_{x'}$ = 55 μrad.

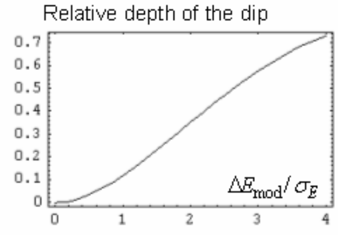

Figure 4. A relative magnitude of the dip as a function of the amplitude of the energy modulation ΔE_{mod}. The magnitude of one corresponds to 100% electron density modulation.

Variations in width and magnitude of the dip affect the THz signal, which was measured using an InSb-bolometer during the wiggler scan and plotted in Figure 5. Analyzing this measurement, we assumed that the THz signal is proportional to the square of the magnitude of the dip and that the magnitude of the dip itself is proportional to the amplitude of the energy modulation of electrons. We calculated the amplitude of the energy modulation using Eq. (13), which was, essentially, a calculation of the function $F(x_{0s}, x_{0L}, \hat{\sigma}_\tau)$, *i.e.* the overlapping area between two spectra shown in Figure 2. These calculations are more accurate than calculations using Eq. (9) because of the assumption of a small detuning used there does not work for a broad scan of the wiggler wavelength as used in the experiment.

The width of the dip defines the spectra of the emitted THz signal [8] and, therefore, indirectly impacts the measurement because of the spectral dependence of the detector and THz beamline transmission. We accounted for this effect using empirically defined coefficient 0.75 for calculated intensity of THz radiation when the amplitude of the energy modulation dropped below $\Delta E / \sigma_e$ <3. The other parameters used to obtain the fit were $N = 9.75$ (i.e. effective number of wiggler periods instead of 10 real periods), σ_τ = 45 fs and a floor level of 10^{-4} (defined in the units used in Figure 5) as given by incoherent synchrotron radiation from the regular bunch.

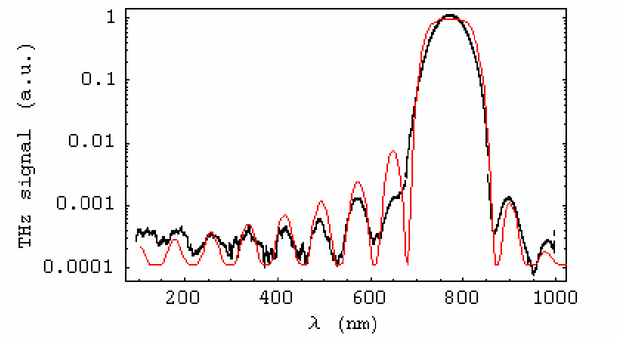

Figure 5. THz signal produced by the electron bunch with a dip in the electron density. The black curve shows the experimental result and the red curve the analytical fit.

CONCLUSION

Using a concept of the far field region we demonstrated that the energy modulation of electrons in the wiggler magnet by the laser light can be found by calculating the interference of the laser field and the field of the electron spontaneous emission in the far field region of the electron radiation in the wiggler. This allowed us to obtain a correct explanation for the measurements, where the wiggler detuning from the laser frequency covered a large range of frequencies exceeding the bandwidth of the laser field by many times.

Acknowledgement. A.Z. is grateful to M. Zolotorev for reading the manuscript and critical comments. K.H. is indebted to T. Quast, R. Mitzner, S. Khan and D.Ponwitz. This work was supported by U.S. DoE under Contract No: DE-AC03-76SF00098 and by the Bundesministerium für Bildung und Forschung and the Land Berlin.

REFERENCES

[1] J.B. Morphy, C. Pellegrini in: *Laser handbook,* vol 6, p.9, Elsvier Science Publisher, (1990).
[2] M. Abramovitz and I. Stegun, *Handbook of Math. Functions*, DOVER, New York, 1972, p.360;
[3] W.B. Colson, in: *Phys. of Quantum Electronic,* vol.5, p.157, Addison Wesley, (1978).
[4] K.-J. Kim, in: *AIP Conf. Proc., Am. Inst. Phys.*, New York, p.565, (1989); LBNL/PUB-490, Rev.2, (2001).
[5] R. B. Palmer, in, *AIP Conf. Proc.* No. 335,edited by P. Schoessow, , AIP, NewYork, (1995)90.
[6] Z. Huang, G. Stupakov, M. Zolotorev, Phys. Rev. Spec. Topics Acc. and Beams, 7, (2004)011302.
[7] BESSY-II, http://www.bessy.de/
[8] J. Byrd *et.al.*, Phys. Rev. Lett., **96**, (2006)164801; K. Holldack *et.al.*, Phys. Rev. Lett., **96** (2006)054601.
[9] courtesy G. Wüstefeld.

CALCULATION OF THE BEAM FIELD IN THE LCLS BUNCH LENGTH MONITOR

G. Stupakov, Y. Ding and Z. Huang
Stanford Linear Accelerator Center, Stanford University, Stanford, CA 94309, USA.

Abstract

Maintaining a stable bunch length and peak current is a critical step for the reliable operation of a SASE based x-ray source. In the LCLS, relative bunch length monitors (BLM) right after both bunch compressors are proposed based on the coherent radiation generated by the short electron bunch. Due to its diagnostic setup, the standard far field synchrotron radiation formula and well-developed numerical codes do not apply for the analysis of the BLM performance. In this paper, we develop a calculation procedure to take into account the near field effect, the effect of a short bending magnet, and the diffraction effect of the radiation transport optics. We find the frequency response of the BLM after the first LCLS bunch compressor and discuss its expected performance.

INTRODUCTION

Maintaining a stable bunch length and peak current is a critical step for the reliable operation of a SASE based x-ray source. In the LCLS, relative bunch length monitors (BLM) right after both bunch compressors are proposed based on the coherent radiation generated by the short electron bunch [1]. A similar diagnostic device is used in the operation of the DESY VUV-FEL (FLASH) [2].

In the previous calculations of the beam radiation [1] standard formulae for the synchrotron radiation in the far field were used. However, due to the close proximity of the reflecting mirror to the magnet, applicability of these formulae is not fully justifiable. An additional factor which complicates the radiation pattern is the short length of the magnet comparable to the formation length of the radiation with the wavelength of the order of the bunch length. To the authors' knowledge, the available computer codes for calculation of the beam radiation (*e.g.*, the Synchrotron Radiation Workshop [3]) cannot be used for our case because the beam passes through the hole in the mirror.

It is a goal of this paper to calculate the electromagnetic field of an electron bunch which takes into account the near field effect, the effect of a short bending magnet, and the diffraction of the radiation caused by reflection from the mirror. We find the energy spectrum intercepted by the mirror in the first LCLS bunch compressor (BC1). We carry out these calculation assuming radiation in free space and neglecting the effect on the radiation of the conducting walls of the vacuum chamber.

We use Gaussian units throughout this paper.

FORMULATION OF THE PROBLEM

A simplified layout of the problem is presented in Fig. 1. The beam passes through a short magnet (e.g., the last dipole of the first LCLS bunch compressor or BC1) of length l_m with the bending radius ρ and propagates along a straight line. A reflective mirror of diameter D with a circular hole of diameter d is located at a distance L from the exit edge of the magnet. The mirror is tilted at 45° and sends the beam field to the detector at the right angle to the beam trajectory. To simplify the calculation we, however, assume that the mirror's plane is perpendicular to the beam orbit (that is, it reflects the radiation back toward the magnet) and calculate the fields incident on as well as reflected from the mirror. Such modification of the geometry does not loose any significant physical effects of the problem.

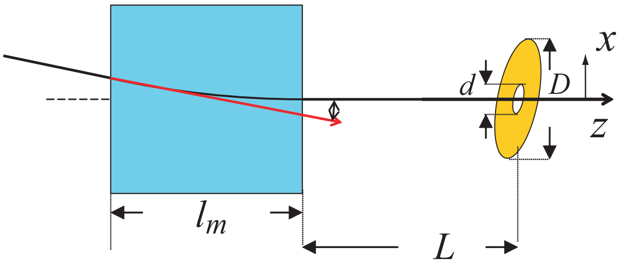

Figure 1: Layout of the bunch length monitor. The coordinate z is measured in the direction of beam propagation after the magnet with $z = 0$ at the exit edge of the magnet. The coordinate x is in the plane of the orbit, and the coordinate y is perpendicular to the plane.

We carried out calculations in the frequency domain. To calculate the Fourier component at frequency ω of the beam field on the surface of the mirror we used two approaches. In the first one, a standard expression for the electromagnetic field of an electron moving in free space was used (see, *e.g.*, [4])

$$\boldsymbol{E}(\boldsymbol{r},\omega) = \frac{e}{\gamma^2}\int_{-\infty}^{\infty} dt\, \frac{\boldsymbol{n}-\boldsymbol{\beta}}{R^2(1-\boldsymbol{n}\cdot\boldsymbol{\beta})^2} e^{i\omega(t+R/c)} + \frac{e}{c}\int_{-\infty}^{\infty} dt\, \frac{\boldsymbol{n}\times[(\boldsymbol{n}-\boldsymbol{\beta})\times\dot{\boldsymbol{\beta}}]}{R(1-\boldsymbol{n}\cdot\boldsymbol{\beta})^2} e^{i\omega(t+R/c)} \,. \qquad (1)$$

Here R, $\boldsymbol{n}$, $\boldsymbol{\beta}$ and $\dot{\boldsymbol{\beta}}$ are functions of time t: $\boldsymbol{R}$ is the vector connecting the current position of the electron with the observation point $\boldsymbol{r}$, with $R = |\boldsymbol{R}|$, $\boldsymbol{n}$ is the unit vector directed along $\boldsymbol{R}$, $\boldsymbol{\beta}$ and $\dot{\boldsymbol{\beta}}$ are the velocity and acceleration normalized by the speed of light, and $\gamma = (1-\beta^2)^{-1/2}$. The first term in Eq. (1) is usually referred to as the *velocity field*. Note that for a relativistic particle with $\gamma \gg 1$ the integrands in Eq. (1) have sharp narrow peaks in the direction for which $\boldsymbol{n}$ is parallel to $\boldsymbol{\beta}$ because in this direction the denominators $(1-\boldsymbol{n}\cdot\boldsymbol{\beta})^2 \sim 1/4\gamma^4$ become extremely small.

We remind the reader that the usual approximation for the *far zone* (FZ) is to neglect the velocity field and to take the limit $R \to \infty$:

$$\boldsymbol{E}_{\mathrm{FZ}}(\boldsymbol{r},\omega) \approx \frac{e}{cR}\int_{-\infty}^{\infty} dt\, \frac{\boldsymbol{n}\times[(\boldsymbol{n}-\boldsymbol{\beta})\times\dot{\boldsymbol{\beta}}]}{(1-\boldsymbol{n}\cdot\boldsymbol{\beta})^2} e^{i\omega(t+R/c)}\,.$$

In this expression, the value of R in front of the integral and the vector $\boldsymbol{n}$ are considered as constant but R in the exponential (and of course $\boldsymbol{\beta}$ and $\dot{\boldsymbol{\beta}}$) are functions of time. If one integrates this expression over a finite time interval from t_1 to t_2 the result is

$$\begin{aligned}\boldsymbol{E}_{\mathrm{FZ}}(\boldsymbol{r},\omega) = &-\frac{ie\omega}{cR}\int_{t_1}^{t_2} dt\, \boldsymbol{n}\times(\boldsymbol{n}\times\boldsymbol{\beta})e^{i\omega(t+R/c)}\\ &+\frac{e}{cR}\frac{\boldsymbol{n}\times(\boldsymbol{n}\times\boldsymbol{\beta})}{1-\boldsymbol{n}\cdot\boldsymbol{\beta}}e^{i\omega(t+R/c)}\bigg|_{t_2}\\ &-\frac{e}{cR}\frac{\boldsymbol{n}\times(\boldsymbol{n}\times\boldsymbol{\beta})}{1-\boldsymbol{n}\cdot\boldsymbol{\beta}}e^{i\omega(t+R/c)}\bigg|_{t_1}\,.\end{aligned}$$

The last two terms are responsible for the *edge* radiation in the far zone [5].

We found advantageous for numerical calculations to use another expression for the electromagnetic field of a moving point charge [6]:

$$\boldsymbol{E}(\boldsymbol{r},\omega) = \frac{ie\omega}{c}\int_{-\infty}^{\infty}\frac{dt}{R}\left[\boldsymbol{\beta}-\boldsymbol{n}\left(1+ic/\omega R\right)\right]e^{i\omega(t+R/c)}\,. \tag{2}$$

This is the underlying equation used in the Synchrotron Radiation Workshop code [3]. Although this equation looks very different from Eq. (1), they give the same result for $\boldsymbol{E}(\boldsymbol{r},\omega)$. The derivation of Eq. (2) using Lienard-Wiechert potentials can be found in Ref. [7]. In passing, we note that neglecting the velocity field in Eq. (1) is not justified in our situations and yields very different numerical results as compared to Eq. (2).

To integrate Eq. (2) over the particle's orbit we split the integration path into three pieces. The first one is a straight line before the entrance to the magnet, the second one is an arc of a circular orbit inside the magnet, and the third one comprises the part of the trajectory after the exit from the magnet. The first two integrals were computed numerically using the Mathematica built in integration routine [8] (in the first integral the lower limit of integration $-\infty$ was replaced by a large negative number). A direct numerical integration of the third integral turns out be slow and poorly convergent because of a fast variation of the phase in the integrand. To improve the speed of calculation we used a method described in Ref. [7], which is valid in the limit of large values of γ. Although formally the integration in Eq. (2) is extended beyond the position of the mirror, the dominant contribution to the integral comes from the part of the trajectory located in front of the mirror.

RESULTS OF THE CALCULATIONS

The quantity $c|E(\boldsymbol{r},\omega)|^2/8\pi$ can be considered as an energy flow of the electromagnetic field. We calculated this quantity at the location of the mirror for various frequencies ω and integrated it over the mirror surface. The resulting quantity is a measure of the energy reflected by the mirror in a unit interval of frequencies.

To illustrate the distribution of the spectral energy in the plane of the mirror, we plot in Fig. 2 the quantity $|E|^2$ (in arbitrary units) in the mirror plane at the distance $L = 22$ cm for $\omega/c = 50$ cm^{-1}. We also assume that the γ factor for the beam is equal to 500, the bending radius of the magnet is 2.5 m, and the magnet length $l_m = 22$ cm. The plot is truncated at small distances close to the trajectory of the beam after the magnet ($x = y = 0$) because the field has a singularity at the trajectory. Since the reflecting mirror has a hole for the passage of the beam, the field from this region is not reflected by the mirror.

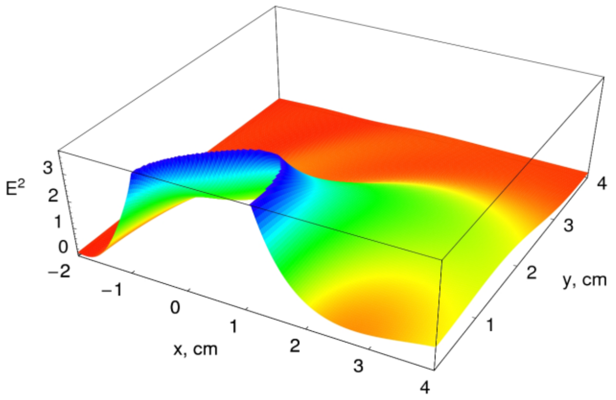

Figure 2: Square of the electric $|E|^2$ (in arbitrary units) in the observation plane x, y. The picture is symmetric with respect to the axis x. The color coding goes from red through yellow, green, and blue as the intensity increases.

Fig. 3 shows the same field as in Fig. 2 projected onto the surface of the mirror. The mirror outer diameter $D = 7.6$ cm, and the diameter of the hole is $d = 1.5$ cm. Note a complicated pattern of the field on the surface of the mirror.

We calculated the spectral energy $S(k)$ intercepted by the mirror as a function of the wavenumber $k = \omega/c$, $S(k) \propto \int_{\mathrm{mirror}} |E(\boldsymbol{r},k/c)|^2 d^2r$. It is normalized in such a way that the total energy reflected by the mirror due to the passage of a bunch with the longitudinal charge distribution $\lambda(z)$ ($\int\lambda(z)dz = 1$) is given by

$$\mathcal{E} = \int_0^{\infty} dk S(k)F(k)\,, \tag{3}$$

where $F(k)$ is the form factor related to the shape of the

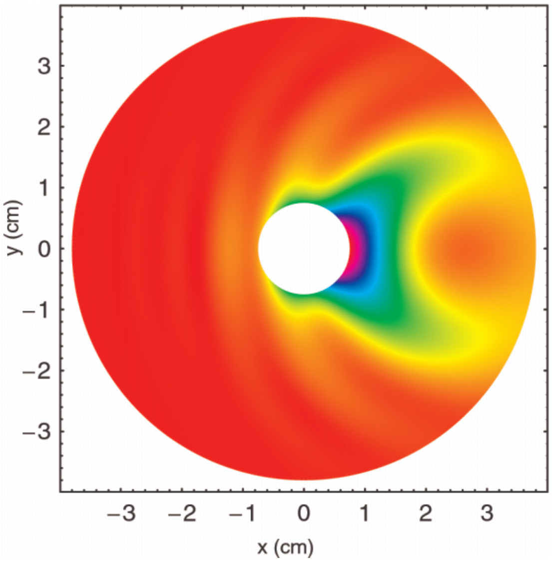

Figure 3: Distribution of the quantity $|E|^2$ on the surface of a round mirror. Shown is a hole at the center of the mirror for the beam passage.

electron bunch,

$$F(k) = \left| \int_{-\infty}^{\infty} \lambda(z) e^{ikz} dz \right|^2 . \quad (4)$$

The plot of the function $S(k)$ for the geometry of the mirror shown above is shown in Fig. 4.

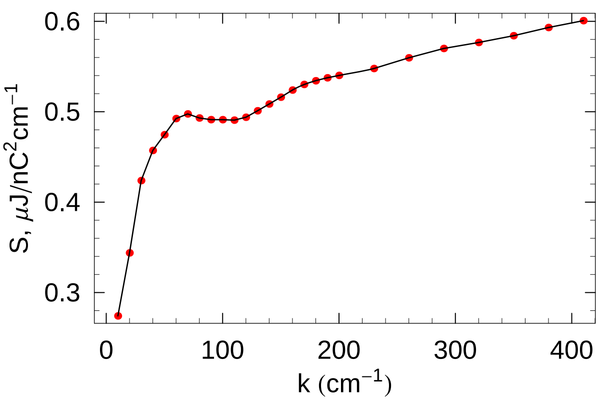

Figure 4: The spectral energy of the beam field intercepted by the mirror as a function of wavenumber $k = \omega/c$. The dots show the calculated values of S.

Using the calculated spectrum we computed the amount of energy intercepted by the mirror for various values of the bunch lengths, taking a parabolic bunch profile that is expected after BC1 [1]. This energy as a function of the compressed rms bunch length is shown in Fig. 5.

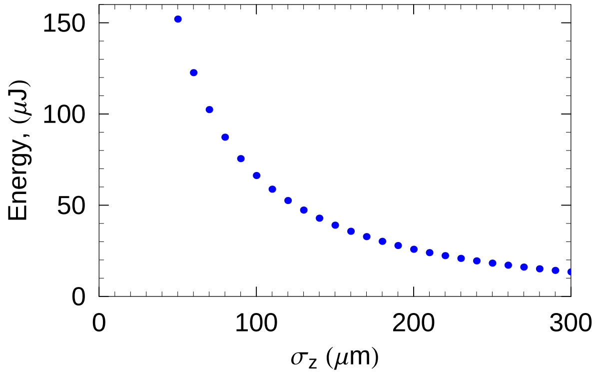

Figure 5: The reflected energy as a function of the compressed rms bunch length.

FIELD REFLECTED FROM THE MIRROR

To calculate the field reflected from the mirror, we use the vectorial diffraction theory as the wavelengths of interests (comparable to the bunch length) are much smaller than the size of the mirror [4]. The detector is assumed to be located far away from the mirror. Although there may be additional optical elements between the mirror and the detector, we neglect them here in order to illustrate the calculation method. According to the diffraction theory, the detected field is given by

$$\boldsymbol{E}_r = \frac{ie^{ikR_1}}{2\pi R_1} \boldsymbol{k} \times \int_{\text{mirror}} (\boldsymbol{n}_1 \times \boldsymbol{E}_s) e^{-i\boldsymbol{k}\cdot\boldsymbol{r}} d^2 r \, , \quad (5)$$

where R_1 is the distance between the detector and the mirror, $\boldsymbol{E}_s$ is the induced field at the mirror, and $\boldsymbol{n}_1$ is the unit vector perpendicular to the mirror surface dS. The induced field is defined as follows. The total electric field on the surface of the mirror is the sum of the beam field $\boldsymbol{E}$ (calculated in the previous section) and the induced field $\boldsymbol{E}_s$. Due to the boundary condition on the metal surface, the tangential component of this sum should vanish, $\boldsymbol{n}_1 \times (\boldsymbol{E}_s + \boldsymbol{E})_{\text{mirrror}} = 0$, which gives

$$(\boldsymbol{n}_1 \times \boldsymbol{E}_s)_{\text{mirrror}} = -(\boldsymbol{n}_1 \times \boldsymbol{E})_{\text{mirrror}} \, . \quad (6)$$

We will make the small angle approximation around the field propagation direction (for the mirror perpendicular to the beam orbit, the reflected field propagates in the direction opposite to the z axis). Using the cylindrical coordinate system r and ϕ in the mirror plane, we find the reflected field at the point with coordinates x and y in the detector plane as follows:

$$\boldsymbol{E}_r(x,y) = \frac{ike^{ikR_1}}{2\pi R_1} \int_{d/2}^{D/2} r dr \int_0^{2\pi} d\phi \boldsymbol{E}^{\text{tang}}$$
$$\times \exp\left[-i\frac{kr}{R_1}(x\cos\phi + y\sin\phi)\right] , \quad (7)$$

where the superscript “tang” indicates the component of the electric field tangent to the surface. Given the beam field $\boldsymbol{E}$ on the mirror as found in the previous section, we integrated Eq. (7) numerically to compute the detected signal. As a numerical example, Fig. 6 shows the reflected field intensity distribution at the distance $R_1 = 81$ cm from the mirror for $\omega/c = k = 50$ cm^{-1}. Note that the maximum of the field in the detector plane is shifted along the x coordinate. Equation (7) can be generalized to include a paraboloid mirror that focuses the radiation.

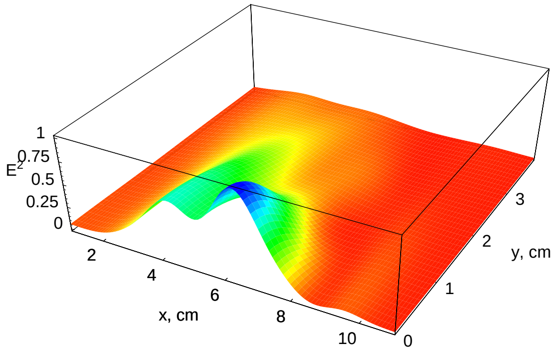

Figure 6: Square of the electric $|E|^2$ (in arbitrary units) in the detector plane x, y located 81 cm away from the mirror. The plot is symmetric with respect to the x axis.

CONCLUSION

We calculated the electromagnetic field intercepted and reflected by a metallic mirror for the geometry of the LCLS bunch length monitor. Unlike the previous calculations, we do not assume the far zone approximation for the radiation field. Our calculation takes into account the near field effect, the short length of the bending magnet (the so called “edge radiation” effect), and the diffraction of the radiation caused by reflection from the mirror.

Our calculations assume propagation of the beam in free space and neglect the effect on the radiation of the conducting walls of the vacuum chamber. In reality, those effects are not negligible, and our result should be considered as an approximation to the real spectrum.

ACKNOWLEDGMENT

We wish to thank P. Emma, H. Loos, and J. Wu for useful discussions. This work was supported by Department of Energy contract No. DE–AC02–76SF00515.

REFERENCES

[1] J. Wu, P. Emma, and Z. Huang, in *Proceedings of the 2005 Particle Accelerator Conference* (2005), p. 428.

[2] S. Casalbuoni, L. Fröhlich, O. Grimm, O. Peters, and J. Rossbach, in *Proceedings of the 2004 European Particle Accelerator Conference* (2004), p. 2586.

[3] O. Chubar and P. Elleaume, in *Proceedings of the 6th European Particle Accelerator Conference* (1998), p. 1177.

[4] J. D. Jackson, *Classical Electrodynamics* (Wiley, New York, 1999), 3rd ed.

[5] R. A. Bosch, Il Nuovo Cimento **20 D**, 483 (1998).

[6] O. V. Chubar, Rev. Sci. Instrum. **66 (2)**, 1872 (1995).

[7] G. Stupakov, Y. Ding, and Z. Huang, *Calculation of the beam field in the LCLS bunch length monitor*, Preprint SLAC-PUB-11890, SLAC (2006).

[8] S. Wolfram, *The Mathematica Book* (Wolfram Media/Cambridge University Press, 1999), 4th ed.

IN-SITU CLEANING OF METAL PHOTO-CATHODES IN RF GUNS

J.F. Schmerge, J.M. Castro, J.E. Clendenin, E.R. Colby, D.H. Dowell, S.M. Gierman, H. Loos,
M. Nalls, and W.E. White, SLAC, Menlo Park, CA, U.S.A.

Abstract

Metal cathodes installed in rf guns typically exhibit much lower quantum efficiency than the theoretical limit. Experimenters often use some sort of in situ technique to “clean” the cathode to improve the QE. The most common technique is laser cleaning where the laser is focused to a small spot and scanned across the cathode surface. However, since the laser is operated near the damage threshold, it can also damage the cathode and increase the dark current. The QE also degrades over days and must be cleaned regularly. We are searching for a more robust cleaning technique that cleans the entire cathode surface simultaneously. In this paper we describe initial results using multiple techniques such as keV ion beams, glow discharge cleaning and back bombarding electrons. Results are quantified in terms of the change in QE and dark current.

INTRODUCTION

The LCLS RF gun requires fields up to 120 MV/m to achieve the desired emittance of 1 μm with 1 nC of charge in a 10 ps bunch. The high field requires the use of a Cu cathode to avoid breakdown at the cathode joint. The LCLS laser can produce 250 μJ of energy at 255 nm which will require a QE of 2 10^{-5} to generate 1 nC of charge. In the case of the Gun Test Facility (GTF) drive laser operating at 263 nm, the theoretical QE for a clean Cu surface using a 263 nm photon is 33 10^{-5} with a 100 MV/m rf field and 8.4 10^{-5} with no applied field [1]. However, experience with multiple cathodes at the GTF indicate the QE of Cu can vary from as low as 10^{-6} to nearly 10^{-4} at 100 MV/m. In addition the QE is not constant over the laser spot leading to increased emittance from the non-uniform space charge forces.

Our experience with laser cleaning [1] has convinced us to search for a better technique that cleans the entire surface simultaneously, does not increase the dark current and is easily repeatable. Here we report QE and dark current measurements before and after using multiple techniques intended to clean the metal surface and increase the QE.

IN-SITU TECHNIQUES AND RESULTS

One of the simplest proposed cleaning methods is to heat the entire gun and drive off any surface contaminants with thermal energy. This was motivated by a test where a small Cu sample was heated in a vacuum chamber to 230 C for 100 minutes which increased the QE over 2 orders of magnitude [2]. All four Cu cathodes installed at the GTF have been baked after installation to 200 C for several days, resulting in measured QEs that range from 10^{-6} to nearly 10^{-4} at 60 MV/m.

Ion Beam Cleaning

Previously we reported QE measurements on Cu samples before and after exposing the sample to a few keV ion beam [3]. The measured QE as a function of illumination wavelength with no applied field agreed very well with the theoretical Cu QE [4] after dosing the sample with up to 10 mC of charge. X-ray photoelectron spectroscopy (XPS) measurements showed the primary contaminant was carbon.

This ion gun could not be installed on the GTF gun due to interference with the gun solenoid. The SLAC Accelerator Research Department B (ARDB) rf gun is nearly identical to the GTF gun but with more clearance between the gun and solenoid. Thus the ion gun, model number ZMB7C from Micro Photonics Inc., was installed on the ARDB rf gun. The two rf guns have interchangeable cathode plates but the lasers operate at slightly different wavelength. The ARDB drive laser wavelength is 266 nm and the GTF wavelength is 263 nm.

The ion gun was installed on one of the two laser ports in the half cell as shown in Figure 1. The beam has a direct line of site to the cathode through an oval opening in the cavity side wall measuring 0.433” X 0.25” with approximately a 70° angle of incidence at the cathode. The beam size at the cathode is approximately 1 cm in diameter.

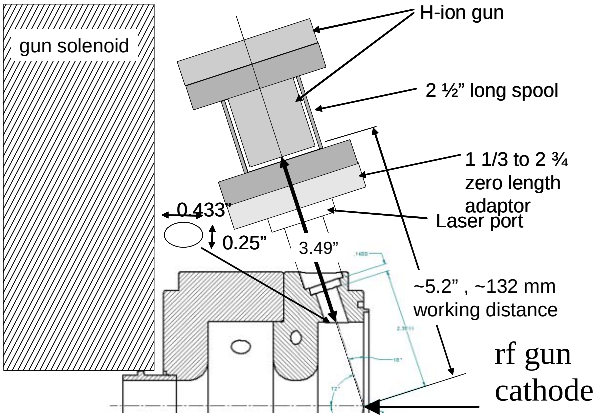

Figure 1: Layout of the ion gun and rf gun. The gun is installed on a laser port with a direct line of site to the cathode.

The QE was measured prior to the ion gun installation and was only 0.4 10^{-5} at 60 MV/m. The rf gun was vented using LN_2 tank boil-off and the ion gun installed. Before the ion gun was operated the QE was re-measured and found to have increased nearly an order of magnitude to 3 10^{-5}. The ion gun was then operated for 40 minutes at 2 keV and 2μA for a total integrated charge on the cathode of nearly 5 mC. After pumping out the hydrogen the QE was measured and found increased to 6 10^{-5} with no increase in the dark current. The ion gun was operated for a second time for 2 hours at 4 μA for a total dose of 29 mC but the QE decreased back to 3 10^{-5}. An additional 7 mC dose (1 hour at 2 μA) did not change the QE. The dark current was not affected by the hydrogen ion beam.

Although the QE increased initially after the first hydrogen ion beam cleaning, the subsequent QE was unchanged at 3 10^{-5} at MV/m. This is significantly lower than the 10 10^{-5} measured on the Cu samples at the same wavelength with no applied field [3]. The most interesting result was the substantial increase in QE after the gun was vented. This was also observed at the GTF and will be discussed in the next section.

The hydrogen was replaced with Argon and the ion gun operated for 30 minutes at 2-2.5 keV between 1.5-3 μA for a total dose of 3 mC. The dark current was measured but the rf system failed before the QE could be measured. The total integrated dark current more than doubled from 1.6 nC prior to the Argon cleaning to 3.4 nC after cleaning with a peak field of 105 MV/m. The peak dark current in the macropulse went from 1.1 mA to 2.6 mA.

The poor results compared to the test samples may partially be explained due to misalignment of the ion gun and thus limited cleaning at the center of the cathode. The 70° angle of incidence of the ion beam relative to the rf gun cathode is 33° larger than tested on the Cu samples which may limit the effectiveness of the ion beam cleaning. It is also theorized that contaminants removed from other areas exposed to the ion beam migrate to the cathode instead of getting pumped out of the gun.

Glow Discharge Cleaning

Glow discharges are commonly used to clean vacuum vessels [5-6] and optical components [7]. A possible advantage of this technique over the ion beam is that it cleans the entire surface of the gun which should reduce migration of contaminants and improve the cathode lifetime. Glow discharges have also been used to clean Cu accelerator structures such as the AFEL linac [8], an eleven cell photo-injector/linac. There it was observed that the glow was largely confined to a single cell, but could be moved to different cells through small changes in the rf drive frequency used to excite the glow discharge.

This technique was implemented on the GTF gun using both hydrogen and an oxygen-helium mixture (90% He and 10% O_2). Gas can flow into the gun through either the half cell via the laser port or the full cell via the waveguide and is pumped out the beam exit port of the gun with a scroll pump. The discharge is started using an rf source connected to the waveguide. We have used both a 26 W CW rf source and a pulsed 1 kW rf source with 30 μs pulse length, 200 Hz repetition rate and 5 W average power. The rf frequency can be adjusted to control the location of the glow discharge as determined by a visual inspection. Exciting the glow at the π mode frequency of 2856 MHz confines the glow to the full cell and exciting the 0 mode at 2852.5 MHz confines the glow to the half cell. However, atoms can move between cells through the cell to cell coupling aperture.

The QE of the cathode was 0.5 10^{-5} at approximately 80 MV/m after the gun was vented with LN2 boil-off to install the leak valve used to introduce the gas. The first discharge was on for roughly 1 hour using hydrogen flowing into the full cell with an inlet pressure of approximately 300 mTorr. The discharge was excited with the CW rf source at 2856 MHz. The QE increased significantly to 6 10^{-5} and further increased to 8 10^{-5} after a second hour with the glow discharge. Then we switched to the 0 mode frequency of 2852.5 MHz with all other parameters constant and the QE dropped over one order of magnitude to 0.3 10^{-5}. Multiple glows at 2856 MHz at pressures ranging from 30-600 mTorr had no effect on the QE. This was an attempt to control the mean free path and thus the number of ions that reach the cathode from the glow discharge in the full cell.

We theorized that with the glow in the half cell we had actually added carbon to the surface possibly by migration of carbon from the stainless tubes attached to the laser ports on the half cell to the cathode. We introduced oxygen to the system which is expected to bond with the carbon forming CO or CO_2 and accelerate the removal rate of surface carbon [5,7]. After a glow with the oxygen and helium gas at a pressure of 200 mTorr with the CW rf source at 2856 MHz the QE dropped to 0.01 10^{-5} which is the lowest value we have ever observed. An identical glow discharge with hydrogen restored the QE to 0.3 10^{-5}. It appears the oxygen attached to the Cu surface instead of the carbon and the hydrogen glow discharge removed the oxygen. Apparently the hydrogen ions are not energetic enough to remove the carbon. We tried to increase the hydrogen ion's energy by exciting the hydrogen with the 1 kW pulsed rf source for one hour and the QE increased to 0.8 10^{-5}. However later glows with the pulsed rf source caused the QE to decrease.

In an attempt to flow more hydrogen through the half cell we installed a leak valve on the laser port and then flowed directly into the half cell instead of into the full cell from the waveguide. However, the QE decreased every time we glowed with the gas flowing into the half cell possibly indicating some sort of contamination introduced through this leak valve. We also repeated the glow at 2852.5 MHz with the hydrogen flowing into the half cell instead of the full cell. This time the QE had an insignificant change compared to the previous glow at 2852.5 MHz when the QE decreased over an order of magnitude. This seems to indicate the flow rate is an important parameter and may help remove contaminants instead of relocating them.

One interesting result was an increase in the QE nearly every time we vented the gun with LN_2 boil-off. In one case the QE increased from 0.08 10^{-5} to 1 10^{-5} after venting and in another case it increased from 0.3 10^{-5} to 2 10^{-5}. The QE would slowly decrease after every glow and then increase once the gun was vented. We theorize that a contaminant in the LN2 boil-off attaches to the surface and reduces the work function or modifies the surface states to increase the QE [9]. Subsequent hydrogen glow discharges then remove this contaminant which reduces the QE but leave the primary contaminant, Which is assumed to be carbon, untouched. This “doping” of the surface was also observed on the ARDB cathode after venting the gun.

The dark current emitted from this cathode actually decreased during these tests. Prior to the glow discharge the total integrated dark current at a field of 95 MV/m was 250 pC with a peak current of 0.3 mA. The final charge was only 100 pC with a peak current of 0.1 mA. The Fowler-Nordheim field enhancement factor decreased from 120 to 90 but the emitting area increased nearly an order of magnitude. The dark current decrease occurred after the glow discharge at 2852.5 MHz.

Electron Bombardment of the Cathode Surface

The possibility of cleaning photo-cathodes with electrons was also investigated. A very simple method using electrons is possible by selecting a laser arrival time such that the electrons do not exit the gun but actually reverse direction and strike the cathode. These back bombarding electrons have been extensively studied in thermionic rf guns [10-11].

By adjusting the laser arrival time, the energy of the back bombarding electrons can be controlled as shown in Figure 2 where the energy of the electrons exiting the gun and those returning to the cathode are plotted as a function of laser phase for a peak field on axis of 95 MV/m. Electrons that reverse direction in the full cell are emitted at a laser phase between 93 and 117°. Electrons emitted at a phase greater than 119° reverse direction in the half cell and thus typically have lower energy at the cathode. Interestingly there are two narrow phase regions where the electrons actually reverse direction twice and finally exit the gun. This phenomenon is observed experimentally when the emitted charge versus laser phase is carefully measured. The emitted charge falls to zero around 115° and then a small peak reappears around 120°. Of course the exact phase where the charge turns on and off depends on the rf field amplitude and the laser pulse length.

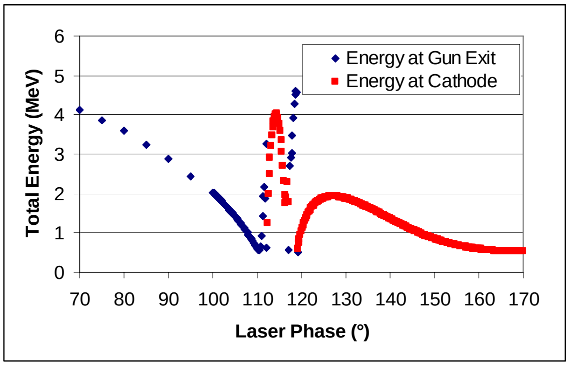

Figure 2: Simulation of the electron energy at the gun exit as a function of laser phase is plotted as diamonds. The squares show the energy of the electrons that return and strike the cathode.

Experiments were conducted with a Mg cathode and 3000 back-bombarding pulses with an estimated total charge of approximately 1 μC. The initial experiment used a laser phase of 140°, which should produce an electron with a kinetic energy of 0.85 MeV striking the cathode. No change in the QE was detected. The laser phase was adjusted to 160° and later to 125° corresponding to a kinetic energy of the bombarding electrons at the cathode of 0.076 MeV and 1.4 MeV. In all cases no measurable effect on the QE was observed. Back bombarding electrons also had no effect on the measured dark current.

The total dose of the electrons is over a factor of 1000 less than the ion beam dose and is possibly insufficient to produce a measurable effect on the QE. Plus the electron beam size may be larger when it returns to the cathode further limiting the total charge available for cleaning. The electrons may also penetrate too deep to remove surface contaminants.

CONCLUSIONS

Glow discharge cleaning appears to remove some surface contaminants without increasing the dark current. However, at least one contaminant, which is assumed to be carbon, was not removed but rather appears to have increased. Introduction of a small amount of water vapor may significantly improve the removal rate of surface carbon [7]. The hydrogen ion beam has the potential to remove all contaminants but the initial results showed no improvement in QE possibly due to misalignment of the ion beam or migration of contaminants. The electron beam bombardment had no effect on the QE or dark current possibly due to the low amount of charge per unit area incident on the cathode.

It is clear that additional diagnostics are necessary to understand the surface chemistry. We hope to add an RGA to the vacuum system to understand what species are present. Plus the surface contaminant coverage of the cathode should be measured using a technique such as XPS when the cathode is removed from the rf gun. It is important to understand which contaminants are present since this information can help determine what technique is best suited to remove them. In addition it is desirable to measure the QE versus wavelength to understand the contaminants effect on the emission process. The wavelength dependent QE gives detailed information regarding the work function and density of surface states.

Perhaps a combination of techniques such as heating, glow discharge, ion beams and doping will be required to produce a clean metal cathode with high QE. We will continue to study various cleaning techniques and the effect on the cathode QE, dark current and lifetime.

ACKNOWLEDGMENTS

We would like to acknowledge many helpful discussions and suggestions with R. Kirby and P. Pianetta at SLAC. Their surface science expertise has helped us better understand the cleaning process and guided us in choosing experimental parameters. This work was supported by Department of Energy contract DE-AC02-76SF00515.

REFERENCES

[1] J.F. Schmerge et al., proceeding of the SPIE Free Electron Laser Challenges II at Photonics West, San Jose, CA, 1999.

[2] D. Palmer et al., SLAC-PUB-11355, 2005.

[3] D.H. Dowell et al., Proceedings of the 27th Int. FEL Conf., Stanford, CA, 2005.

[4] D.H. Dowell et al., PRST-AB **9**,063502(2006);, SLAC-PUB-11788, 2006.

[5] H.F. Dylla, J. Vac. Sci. Tech. A, 6, 1276, (1988).

[6] E.Hoyt et al, SLAC PUB-95-6990, 1995.

[7] E.D. Johnson et al, Rev. Sci. Instrum., 58, 1042, (1987).

[8] R.L. Sheffield et al., Nucl. Instrum. and Meth. A, 318, 282, (1992).

[9] Q. Yuan et al., J. Vac. Sci. Tech. B, 21, 2830, (2003).

[10] H. Liu, Nucl. Instrum. and Meth. A, 302, 535, (1991).

[11] C.B. McKee and J.M.J. Madey, Nucl. Instrum. and Meth. A, 296, 716, (1990).

BUNCH LENGTH MEASUREMENTS AT JLAB FEL

P. Evtushenko, J. Coleman, K. Jordan, J. Michael Klopf, G. Neil, G. P. Williams
Thomas Jefferson National Accelerator Facility 12000 Jefferson Avenue, Newport News, VA 23606, U.S.A.

Abstract

The JLab FEL is routinely operated with sub-picosecond bunches. The short bunch length is important for high gain of the FEL. Coherent transition radiation has been used for the bunch length measurements for many years [1]. This diagnostic can be used only in the pulsed beam mode. It is our goal to run the FEL with CW beam and a 74.85 MHz micropulse repetition rate, which, with the 135 pC nominal bunch charge corresponds to the beam average current of 10 mA. Hence it is very desirable to have the possibility of making bunch length measurements when running CW beam with any micropulse frequency. We use a Fourier transform infrared (FTIR) interferometer, which is essentially a Michelson interferometer, to measure the spectrum of the coherent synchrotron radiation generated in the last dipole of the magnetic bunch compressor upstream of the FEL wiggler. This noninvasive diagnostic provides bunch length measurements for CW beam operation at any micropulse frequency. We also compare the measurements made with the help of the FTIR interferometer with data obtained using the Martin-Puplett interferometer [1]. Results of the two diagnostics agree within 15 %. Here we present a description of the experimental setup, data evaluation procedure and results of the beam measurements.

INTRODUCTION AND MOTIVATION

The Jefferson Lab Free Electron Laser (FEL) facility is a superconducting rf (SRF) energy recovery linac based light source [2]. It is capable of running CW electron beam with an average current of up to 10 mA. The nominal bunch charge is 135 pC. The maximum possible micro-pulse frequency is 74.85 MHz, which is the 20th subharmonic of the fundamental (1497MHz) frequency of the linac. The micro-pulse frequency can be reduced by a factor of 2n, where n is an integer ranging from 1 to 8. Thus the accelerator can be operated at the nominal bunch charge but at the lower average beam current that is essential for the machine setup and tuning. Another set-up used for tuning up the machine is pulsed beam mode, where the beam consists of 250 μs long macro pulses coming with a repetition rate of 2, 10 or 60 Hz. The micro-pulse frequency within such a macro pulse is not more than ~4.68 MHz. Thus the average beam current in the pulse beam mode is kept very low and this beam mode can be used for invasive measurements of the beam properties.

A modified Martin-Puplett interferometer built by U. Happek [1] has been used for several years for the bunch length measurements at JLab FEL. The interferometer is used with the coherent transition radiation (CTR). To generate the CTR, a view screen made of 100 μm thin gold plated silicon wafer is inserted in to the beam. This diagnostic is invasive and can be used only in pulsed beam mode. The challenge of the bunch length diagnostic was to be able to measure the bunch length when running CW beam with average beam currents from 0.5 mA to 10 mA.

The coherent synchrotron radiation (CSR) can be used for the bunch length measurements the same way as the CTR. The longitudinal bunch compression is finalized by the magnetic bunch compression placed upstream of the wiggler. The bunch length at the wiggler is almost the same as at the exit of the bunch compressor. In fact the amount of the CSR generated in the last dipole of the bunch compressor is very high. A beam line was built to transport the CSR to one of the FEL user labs where it will be used for user experiments [3]. We use a rapid-scan Michelson interferometer with the CSR for the noninvasive bunch length measurements when running CW beam.

USING COHERENT RADIATION FOR BUNCH LENGTH MEASUREMENTS

The underlining principals of using coherent radiation produced by an electron bunch for the bunch length measurements have been described in detail many times in the literature [4]. Here is a short summary of the principals upon which the measurements with coherent transition radiation, as well as for the ones with coherent synchrotron radiation, are based. Consider an electron bunch consisting of N_e electrons generating transition radiation (TR) or synchrotron radiation (SR). For a wavelength shorter than the bunch length, the radiation power is proportional to N_e, since for every electron there is on average another electron radiating in an opposite phase, and so the coherence term is zero. Both TR and SR are very broadband. For a wavelength much longer than the bunch length, all electrons radiate almost in one phase and, since the phase difference is constant, the radiation is coherent and therefore the power of the radiation is proportional to N_e^2. There is a transition region where the spectral power density changes from N_e to N_e^2. The position of this transition depends on the bunch length. Hence measurements of the radiation spectrum, which would cover the transition region, contain information about the bunch length. Rigorously it is expressed as follows, spectral power density associated with the radiation of the entire bunch is

$$P_b(\omega) = P_S(\omega)\left[N_e + N_e(N_e - 1)\left|\tilde{f}_b(\omega)\right|^2\right]$$

where $P_S(\omega)$ is the spectral density of a single electron radiation and $\left|\tilde{f}_b(\omega)\right|^2$ is the so-called longitudinal bunch form factor.

INTERFEROMETERS

The first device we use is a modified Martin-Puplett interferometer [1]. That is a step-scan device installed in the accelerator vault right next to the beam line. A lens made of polished Picarin is set in front of the interferometer and is used to transform the divergent TR into a nearly parallel beam going in to the interferometer. Wire grids made of 20 µm tungsten wire are used as the polarizing beam splitter and as the polarizer-analyzer. The period of the grid is 50 µm. A linear stage with a step motor is used to change the position of the movable mirror in the adjustable arm of the interferometer. An off-axis parabolic mirror is then used then to focus the radiation onto the input window of the Golay cell detector. Figure 1 shows an example of an interferogram measured with the interferometer and the corresponding spectrum, which, as will be explained later, is a Fourier transform of the interferogram.

Another interferometer, which we use for the measurements with the synchrotron light, is a rapid-scan device. This interferometer is commercially available from Thermo-Nicolet, and called a Nexus 670. The optical beam line used to transport the synchrotron radiation to the user lab is all reflective and is made of off-axis ellipsoidal and plane mirrors [3].

A synchrotron radiation opening angle of 150 milliradians is collected from the accelerator. The final beam is collimated into the Michelson using a 6” focal length off-axis paraboloid. For the measurements presented here we used a beam splitter made of silicon. For the measurements with the synchrotron radiation we used a PY55 detector in conjunction with a PAPY 1153 amplifier, both made by Goodrich [5]. One fundamental difference between the two interferometers is the determination of the path length difference. In the rapid-scan interferometer the path length is changed by a free running mirror, which moves with constant velocity during a scan. To measure the path difference in the interferometer there is one more interferometer built into it. The additional interferometer utilizes a HeNe laser, the fixed and the movable mirrors of the main interferometer and a beam splitter which is nested inside the main interferometer beam splitter. The detector for the HeNe laser light is placed at the output port of the interferometer. During the interferometer scan, the signal of the HeNe detector is a sine function with one period of the signal corresponding to a path length change of one wavelength of the HeNe laser, which is 632.8 nm. Thus the effective sampling frequency of the rapid-scan interferometer is much higher than the one of our step-scan interferometer. The frequency resolution of the measurements with a Michelson interferometer depends on the scan range and in our measurements is typically about 50 GHz.

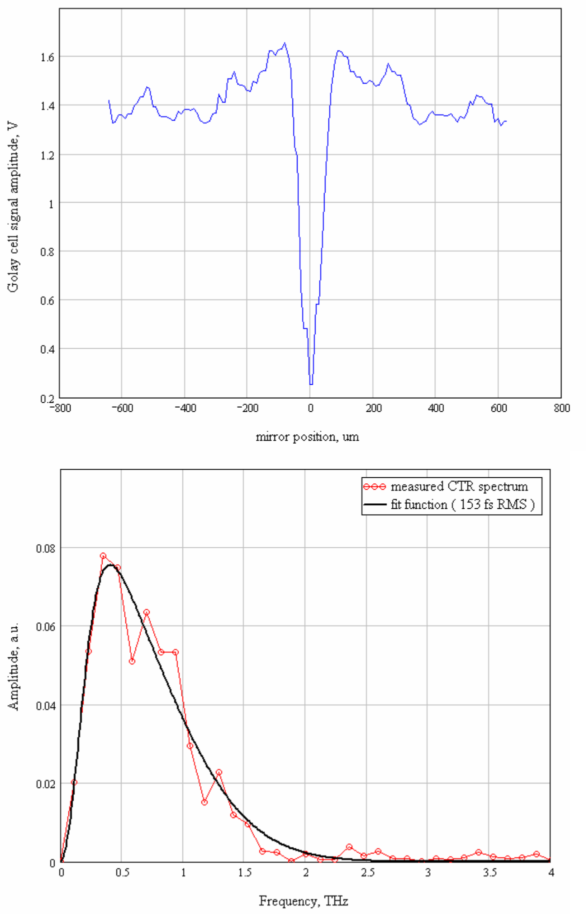

Figure 1: Interferogram measured with the modified Martin-Puplett interferometer and the corresponding spectrum.

In our measurements one scan of the rapid-scan interferometer takes about 2 seconds. Since both interferometers we use are essentially Michelson interferometers, the same data evaluation procedure for the bunch length reconstruction can be applied to the data obtained from either interferometer.

BUNCH LENGTH RECONSTRUCTION

We use the following data evaluation procedure for the bunch length estimation. The procedure is similar to the one described in [6]. According to the Wiener-Khintchine theorem [7], the autocorrelation function is the Fourier transform of the power spectrum. We use a Fast Fourier Transform (FFT) algorithm to calculate the powers spectrum from the interferogram since the data are discrete. The power spectrum defines uniquely the amplitude of the components of the frequency domain representation of the pulse. However, information about the relative phases of the different Fourier components is lost in the interferometric measurement. This is why a direct pulse shape reconstruction from the power spectrum is not possible.

We assume a Gaussian shape of the bunch, with the RMS bunch length σ_t. The Fourier transform of the distribution function is also a Gaussian function. Thus we can write the Gaussian bunch power spectrum as $\tilde{P}(\omega) = C \cdot e^{-(\omega\sigma_t)^2}$, where C is a constant. In the measured power spectrum, the intensity is strongly reduced below a certain threshold frequency as shown in Fig. 1. The reduction of the spectral density is due to diffraction losses. The general Huygens' integral can be used to describe the diffraction losses [8]. Result of the integration of the general Huygens' integral is not an analytical function and is not very convenient to use for further data evaluation. We approximate the low frequency cut-off function with the following analytical function $F_{filter} = 1 - e^{-(\omega/\omega_0)^4}$, where ω_0 is the characteristic cut-off frequency. The product of the Gaussian power spectrum and the filter function is the modified power spectrum

$$f_{fit}(\omega) = \left(1 - e^{-(\omega/\omega_0)^4}\right) \cdot C \cdot e^{-(\omega\sigma_t)^2} .$$

Once the modified power spectrum is expressed as an analytical function it can be used as a fit function with the nonlinear least square fit (NLSF) to approximate a measured power spectrum. From such a fit we can obtain σ_t, which we define as the RMS bunch length. There are several options regarding the characteristic cut-off frequency ω_0. The best would be to have it measured, but such a measurement in the frequency range of the interests is very difficult. Another option, which we have used so far, is to add in the effects of ω_0 to the fit parameter and to make sure it stays consistent during the measurements.

EXPERIMENTAL RESULTS

The accelerator setup is always done in diagnostic mode with pulsed beam. In this mode the modified Martin-Puplett interferometer is used for the bunch length measurements. We routinely operate the machine with an RMS bunch length of about 150 fs. However, dependent on the machine setup we have been measuring RMS bunch lengths in the range from about 100 fs up to 200 fs RMS. That implies that we do indeed successfully reconstruct the bunch lengths from the interferometer measurements as was described in the previous section. Figure 1 shows an example of an interferogram measured with the step-scan interferometer, while the corresponding spectrum also shows the fit function, which is the result of the data evaluation. For this particular measurement the fit gives the RMS bunch length of 153 fs.

When the accelerator is set up we can run CW beam and use the rapid-scan interferometer. Our experience is that the results of the measurements with two interferometers agree to within about 15 %. It is very important that with the Michelson interferometer and synchrotron radiation we can do bunch length measurements as a function of the average beam current. Figure 2 shows spectra of the CSR measured at 0.31 mA, 0.62 mA, 1.25 mA and 2.5 mA of beam average current and the measured CTR spectrum measured with pulsed beam, all the measurements were done with the same machine setup. The figure also shows the corresponding fit functions and the resulting RMS bunch length. The measurements show that the bunch length is not changing when the average beam current is increased. This is what one would expect, since the average current is increased by increasing the pulse repetition rate, keeping the bunch charge constant. However, at present the FEL efficiency has been decreasing with beam current and one explanation would be that it is due to an increase in bunch length. These measurements are therefore critical in ruling this out.

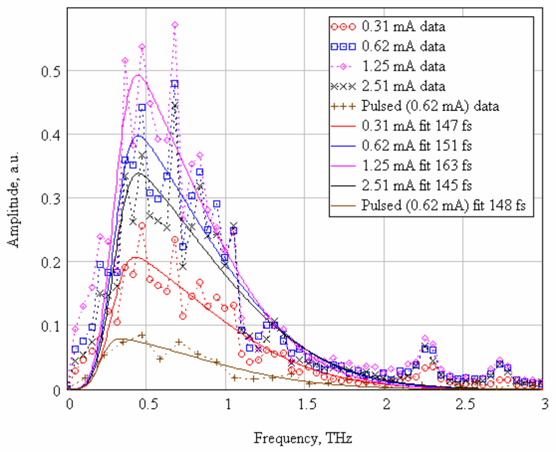

Figure 2: Spectra of the CSR measured at different average beam current with the CTR spectrum and the corresponding fit functions for bunch length reconstruction.

Another significant finding we have made is that the bunch length at the wiggler depends very strongly on the bunch charge. The bunch compression is normally optimized for the nominal bunch charge of 135 pC. When operating with much smaller bunch charge and without any changes in the machine setup, we have a much shorter bunch at the entrance to the linac. This results in a very small energy spread of the bunch at the exit of the linac. As a result, the M_{56} of the 180° bend and the chicane do not provide the same compression as for a bunch with nominal charge. As a result a bunch with a very small charge will be much longer at the wiggler than a nominal bunch. Figure 3.a shows measurements of the CSR spectrum of the nominal bunch, with an RMS bunch length of 129 fs, and that of a bunch with a very small charge where the RMS bunch length was measured to be 384 fs.

The rapid-scan interferometer provides more information than just a spectrum of CSR. Consider the interferometer scanning with the mirror velocity of 5mm/sec. Then the optical path length difference changes at a rate of 10 mm/sec. If the incoming radiation has, for example, a wavelength of 1 mm it will result in a modulation of the signal at the detector at a frequency of 10 Hz.

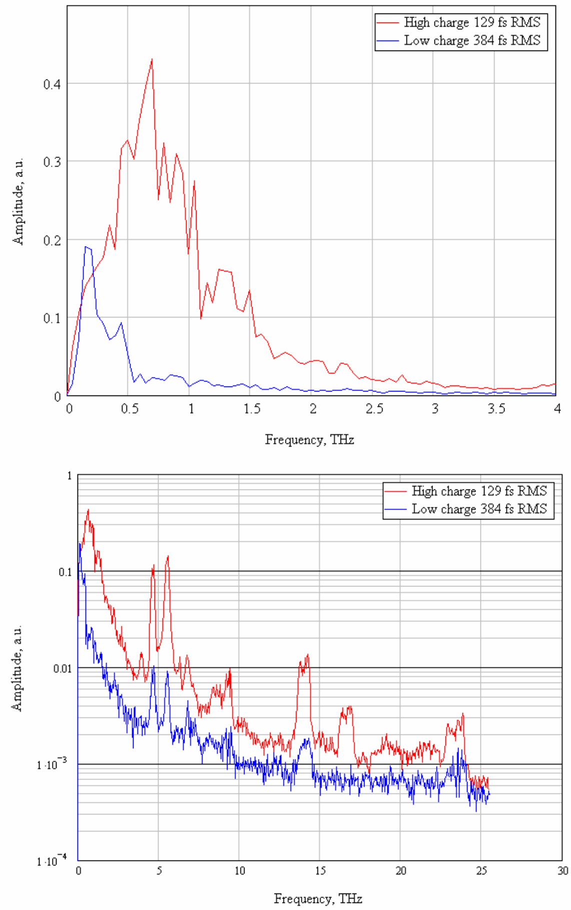

Figure 3: (a. top) spectra of the CSR measured at nominal bunch charge and much smaller bunch charge.;(b. bottom) the same data are shown on a logarithmic scale.

Thus different wavelengths measured by the interferometer be modulated at the detector at different frequencies. The frequency of the detector signal modulation is $f_M = 2v/\lambda$, where v is the velocity of the mirror during the scan and λ is the wavelength of the measured radiation. If the intensity of the incoming radiation is modulated, for instance due to a beam instability at some frequency, that will also result in modulation of the detector signal at that specific frequency. Hence the interferometer measurements also contain information about the beam stability. This technique has been used at numerous synchrotrons to diagnose and improve the beam stability [9]. Figure 3.b shows the data shown in Fig. 3.a on a logarithmic scale and over a bigger frequency span. The spectral power density peak at 4.69 THz corresponds to the radiation intensity modulation at 60 Hz; the next peak at 5.69 THz corresponds to the intensity modulation at 72.8 Hz and so on. We have yet to study in detail, the origin of all the observed beam modulations.

All the measured CSR spectra shown in Fig. 2 show local minima in the spectral power density, these are due to the water vapor absorption. This data corruption certainly reduces the accuracy of our bunch length reconstruction. To improve the setup we will switch to a newer Michelson interferometer operating in vacuum. It has been already demonstrated that such an interferometer can be operated in vacuum [10].

ACKNOWLEDGMENTS

We would like to thank S. Benson and D. Douglas for a numerous stimulating discussions and for operating the machine during measurements and systematic study of the interferometers.

This work supported by The Office of Naval Research the Joint Technology Office, NAVSEA PMS-405, the Air Force Research Laboratory, U.S. Army Night Vision Lab, the Commonwealth of Virginia, and by DOE Contract DE-AC05-84ER40150.

REFERENCES

[1] G. A. Krafft, P. Piot, K. Jordan, and J. Song, U. Happek and M. James, “Measuring and characterizing ultrashort bunches in the Jefferson Lab Free Electron Laser”, Proceedings of the EPAC98

[2] S. Benson, D. Douglas, M. Shinn, K. Beard, C. Behre, G. Biallas, J. Boyce, H. F. Dylla, R. Evans, A. Grippo, J. Gubeli, D. Hardy, C. Hernandez-Garcia, K. Jordan, L. Merminga, G. R. Neil, J. Preble, T. Siggins, R. Walker, G. P. Williams, B. Yunn, S. Zhang, H. Toyokawa, “High Power Lasing in the IR Upgrade FEL at Jefferson Lab”, Proceedings of the 2004 FEL Conference, Trieste, Italy, 229 (2004)

[3] S. Benson, D. R. Douglas, H. F. Dylla, J. Gubeli, K. Jordan, G. R. Neil, M. Shinn, S. Zhang and G.P. Williams, “High Power THz Generation from Sub-ps Bunches of Relativistic Electrons”, Mater. Res. Soc. Symp. Proc. 850, MM4.3.1 (2005)

[4] U. Happek, A.J. Sievers and E.B. Blum, Phys. Rev. Lett. 67, 2962 (1991)

[5] http://www.oss.goodrich.com/datasheets/oss/Goodrich_PAPY_DetectorPreamplifier.pdf

[6] A. Murokh, J.B. Rosenzweig, M. Hogan, H. Suk, G. Travish, and U. Happek, "Bunch Length Measurement of Picosecond Electron Beams from a Photoinjector using Coherent Transition Radiation", Nucl. Instr. Meth. A 410, 452 (1998)

[7] N. Wiener, Acta. Math. 55, 117, (1930)

[8] A. Siegman, Lasers, University Science Books, (1986)

[9] R. Biscardi, G. Ramirez and G.P. Williams, "Effects of RF Side-Bands on Spectral Reproducibility for Infrared Synchrotron Radiation", Rev. Sci. Instr. 66, 1856 (1995)

[10] P. Brierley, B. Badeau, P. Dumas, M. Smith, G. P. Williams, “Performance of a rapid-scan vacuum Michelson interferometer at the NSLS”, Review of Scientific Instruments 73, 1595-1598 (2002)

LONGITUDINAL PHASE SPACE CHARACTERIZATION OF ELECTRON BUNCHES AT THE JLAB FEL FACILITY

S. Zhang, S. Benson, D. Douglas, D. Hardy, G. Neil, and M. Shinn
TJNAF, Newport News, VA23606, USA

Abstract

We report longitudinal phase space measurements of short electron bunches at the 10kW Free-Electron Laser Facility at Jefferson Lab using broadband synchrotron radiation and a remotely controlled fast streak camera. Accurate measurements are possible because the optical transport system uses only reflective components that do not introduce dispersion. The evolution of longitudinal phase space of the electron beam can be observed in real time while phases of accelerator RF components are being adjusted. This fast and efficient diagnostic enhances the suite of machine setup tools available to JLab FEL operators and applies to other accelerators. The results for certain beam setups will be presented.

INTRODUCTION

High power Free-Electron Lasers (FELs) require very short electron bunches. The picosecond electron bunches produced by the DC high voltage GaAs photoguns must be accelerated and compressed to femto-second time scale using RF and magnetic compressors (for example, RF buncher cavities, off-crest acceleration, drift spaces and magnet chicanes). Setting and maintaining proper phase of the electron bunches with respect to the RF fields in the accelerating linac is critical for effective bunch compression and high power FEL operation. Longitudinal phase space (LPS) measurements provide extremely valuable correlated information between the temporal position of the electrons and their longitudinal momenta. Knowledge of LPS and perhaps more importantly, its evolution with time, helps during machine setup. We report a convenient and non-invasive means to monitor LPS in real-time using synchrotron radiation and a fast streak camera. This work builds upon work reported previously [1], and is part of an ongoing effort to enhance the diagnostic capabilities at the JLab 10KW FEL Facility. In this paper, we describe the measurement technique and discuss the results obtained under different beam setups.

SYSTEM DESCRIPTION

Figure 1 shows a schematic overview of the Jefferson Lab 10kW energy-recovery FEL facility which has been described in detail elsewhere [2]. Electron bunches from the gun are accelerated to 115MeV using a superconducting RF linac and turned 180 degree using a Bates-style arc magnet (ARC1) toward the FEL wiggler magnet located midway between the high-reflector and output-coupler mirrors. The electron beam then passes through a second 180 degree arc magnet for energy recovery through the linac.

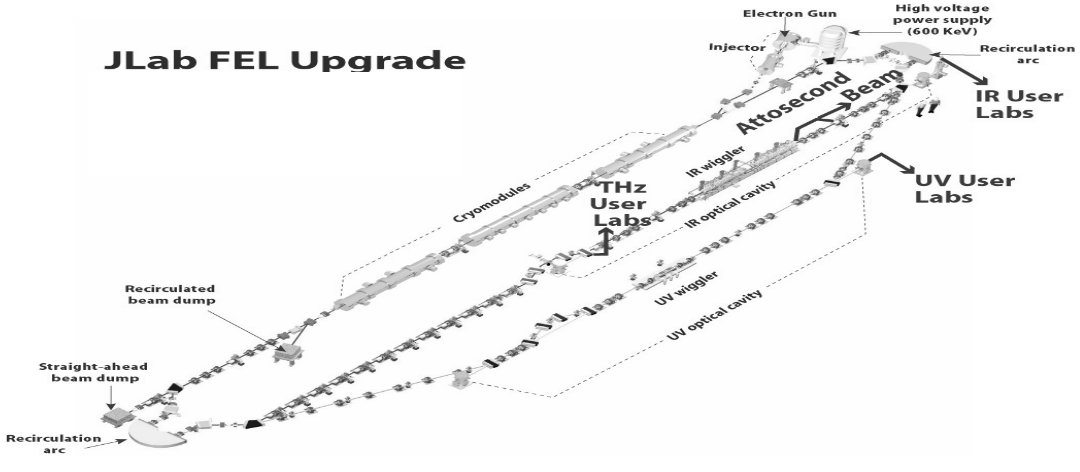

Figure 1: Layout of 10kW FEL facility at Jefferson Lab. The 1KW UV line is under construction. The linac consists of three cryo-modules. The ARC bending magnets are located at each end with ARC1 in the lower-left corner.

Managing the beam energy spread is critical for high current, high micro-bunch charge accelerator operation. In addition, it is particularly important to see how energy spread varies for the two states of accelerator operation: FEL on and off. As described in this paper, energy spread can be monitored non-invasively by monitoring the SR light emitted from the 180 degree bend magnets because electrons with lower energy travel a shorter radial path compared to electrons with higher energy. By monitoring the emission profile of the SR light in the horizontal plane, one can measure the size of the electron beam and therefore the beam energy spread.

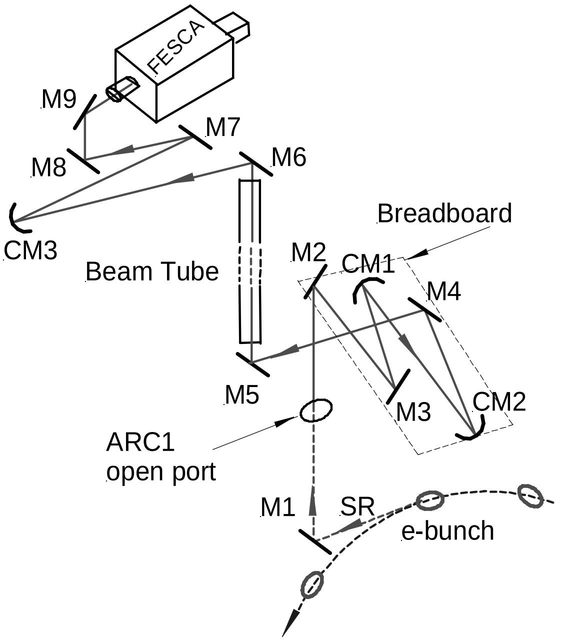

Figure 2: Schematic of the optical transport system (OTS). M, flat mirrors. CM, concave mirrors. Detailed description is given in the text.

For the measurement described here, SR light from the first 180 degree bend magnet (ARC1) was reflected upwards and out of the accelerator vault using an all-reflective optical transport system (Figure 2). The optical transport was designed to image-relay the bunch beam profile from outermost location of the beam orbit in ARC1 to the streak camera entrance slit. The SR light from the electron bunch is extremely broadband and it is important that transmission optics such as lenses are not used. Each mirror was coated with metallic coating to eliminate the dispersion effect. The three concave mirrors have radii of curvature of 200, 500 and 1000mm. Mirror M1 directs the SR beam from the bunch upwards through an open port to M2. The beam then reflects off several mirrors mounted on a small breadboard. The magnification can be adjusted by changing the distance between CM1 and CM2 in order to match the beam size to the camera cathode. The SR light propagates through a tube inserted into a penetration in the building floor. The final image at the streak camera was formed by the concave mirror CM3. A HeNe laser was available for rough pre-alignment of the system, but final alignment with SR light was time consuming, mostly because the distance between the bend magnet and the streak camera is long, more than 8m. Final optimization of the optical transport system was done with SR light during accelerator operations using several motorized mirrors.

The streak camera is a Hamamatsu Synchroscan FESCA system, the measured resolution is about 700fs. Having the streak camera outside the harmful environment of the accelerator vault is beneficial because sometimes local alignment of the camera must be performed, although data acquisition is completely remotely controlled.

MEASUREMENT AND DISCUSSION

Energy Calibration and Resolution

LPS measurements are presented on two-dimensional plots, showing energy spread along the temporal distribution of the electron bunch. Note however that what is actually measured is beam size versus the temporal distribution of the bunch. To convert beam size to energy requires calibration of the streak camera pixel display. This was accomplished using different beam energies and setups that provide minimum energy spread. Figure 3 shows five streak camera images for five different beam energies. The red curve is the initial energy set-point of 115MeV. The green (yellow) curve corresponds to higher (lower) with energy difference of 1.5%. The two peaks are separated by 391 pixels which yields a calibration factor of 0.00385% energy difference per pixel. Next, the pixel/energy resolution was studied using two energies separated by only 0.046%. The blue and pink peaks are separated by only 12 pixels but are clearly distinct. So the system resolution is definitely better than 0.05%.

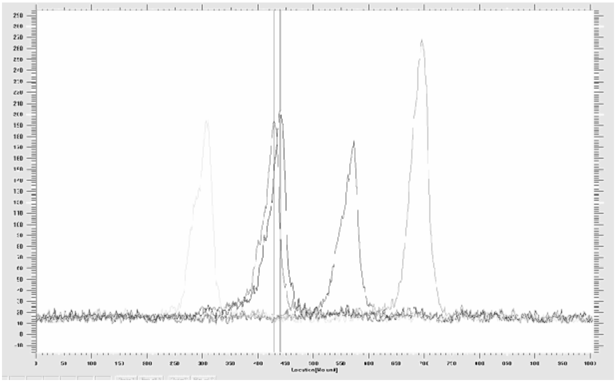

Figure 3. Streak camera images for five different beam energies. The yellow and green curves provide a calibration ratio, beam energy to pixel location. The pink and blue curves demonstrate the high degree of energy resolution of the system. The red curve is the nominal 115 MeV setpoint energy.

LPS vs. Linac Gang Phase

Production of high power FEL light requires off-crest operation of the accelerator. Deviations from this desired phase relationship may lead to reduced FEL output power. The phase relationship of the electron bunches relative to the linac gang phase can be quantified using LPS measurement and the SR light streak camera. This is dramatically evident in Figure 4 which shows streak camera data for different linac RF gang phases relative to on-crest operation. Each picture represents a snap-shot of data presented live within the FEL control room while the accelerator was running.

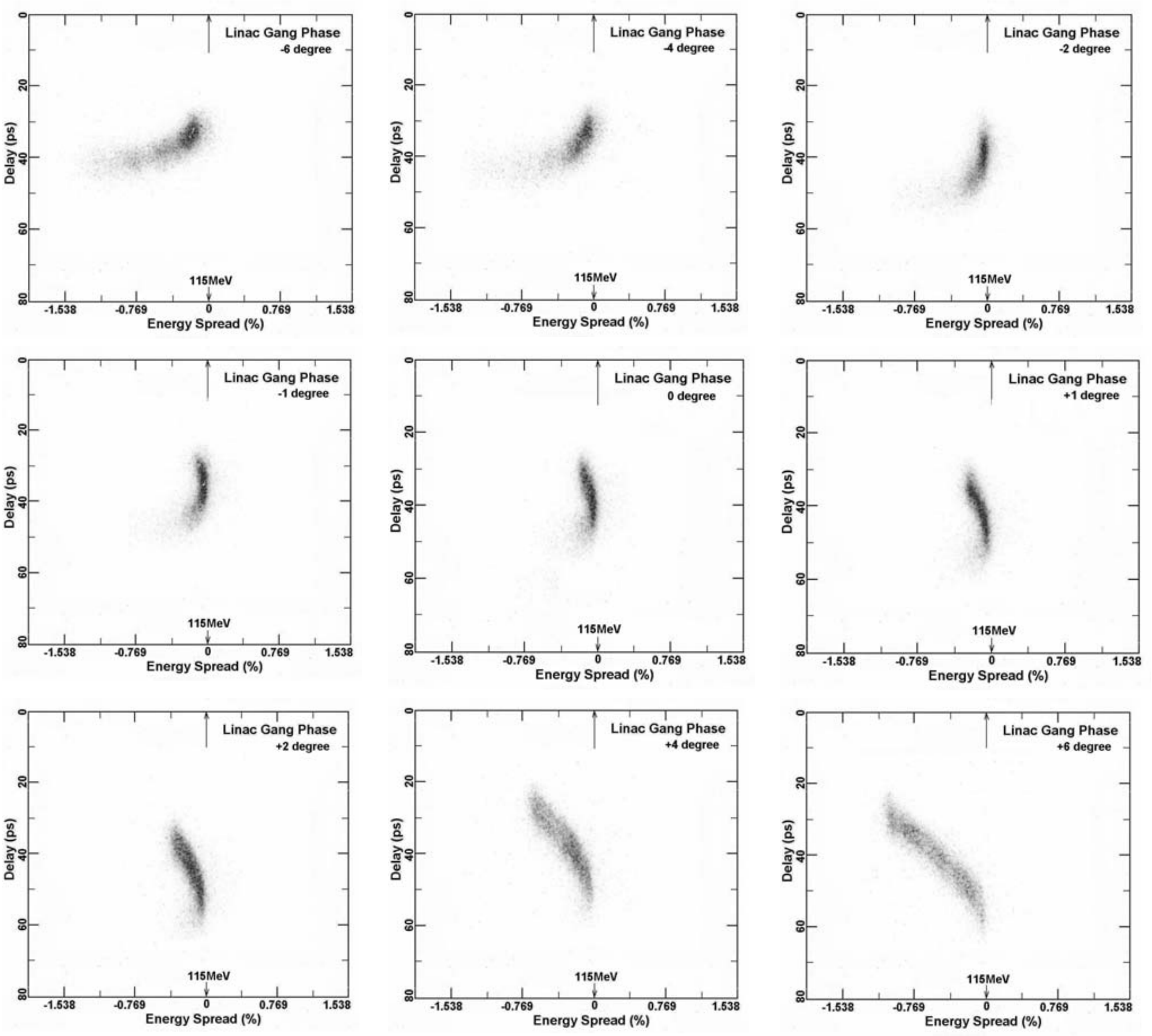

Figure 4: The LPS for different linac gang phase. Beam energy, 115MeV. Micro-pulse repetition rate: 9MHz. Macro-pulse, 1ms at 60Hz. Charge, 110pC per bunch.

From Fig.4, it is clear that the LPS can be quite different even if the bunches sit symmetrically on the two sides of the RF crest. This is the case when the phase angles are equal but have opposite signs. Apparently, a linear chirp and longer bunch length is obtained at 6 degree off-crest. At -6 degree off-crest, the bunch length becomes shorter but the shape is more like a banana, indicating high non-linearity. For on-crest operation, the bunches experience very little energy spread and the phase space is straight up with the least tilt.

LPS vs. Buncher Gradient

The whole injector of the JLab FEL facility consists of a high-voltage DC gun, a quarter cryo-unit followed by a transverse match section and an RF bunch compressor. The electron bunches from the photo-cathode initially have the same temporal length as the drive laser pulses but expand due to space charge effects. Passage through the quarter cryo-module also affects the electron bunch length. Optimum FEL operation requires the electron bunches be compressed before entering linac. We have observed that the gradient of the buncher can affect the phase space of the electron bunches. To investigate this phenomenon, we did LPS streak camera measurements while changing the buncher gradient (Figure 5).

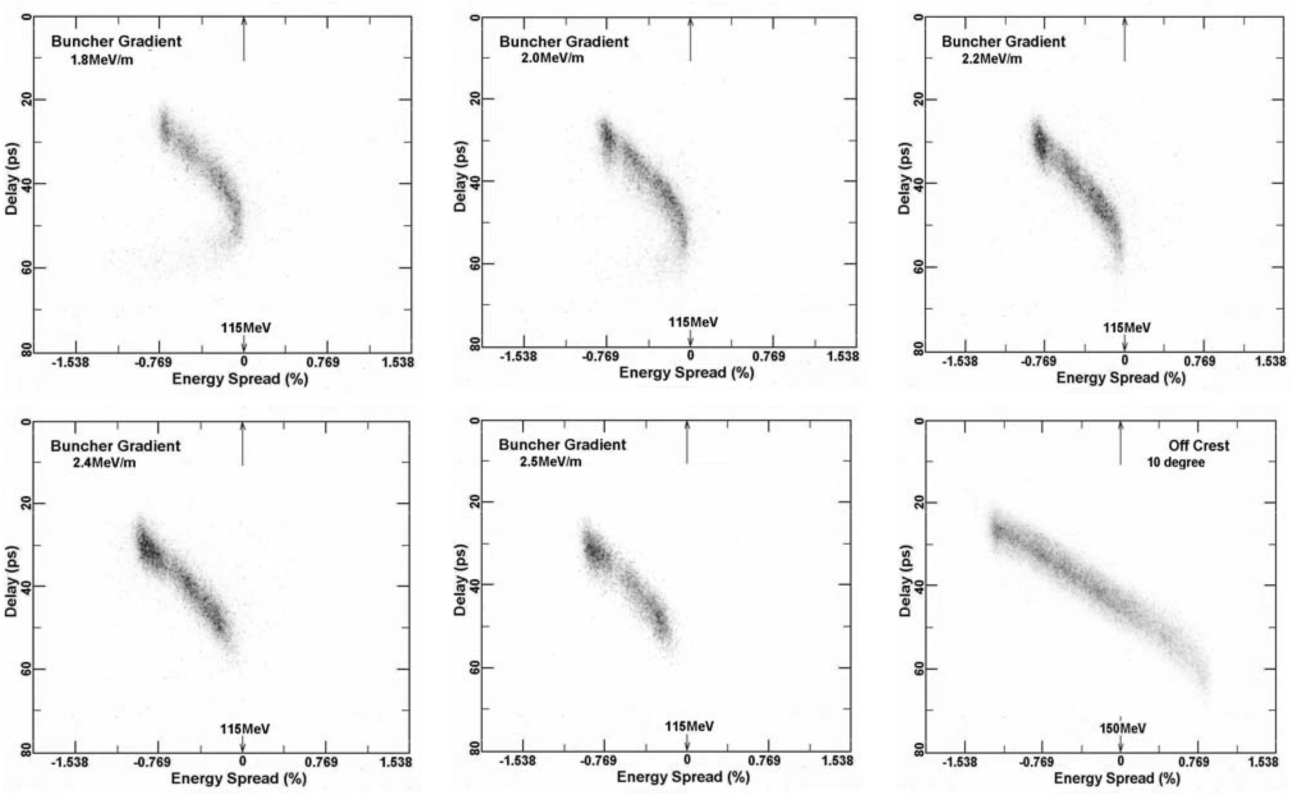

Figure 5: Longitudinal phase space for different buncher gradient. The beam energy, 115MeV. Micro-pulse repetition rate, 9MHz. Macro-pulse, 1ms at 60Hz. Charge, 110pC/bunch. The graph in lower right corner is explained in the text.

As the buncher gradient increases from low to high, the LPS trace gradually stretches out to become a linear chirp. The low energy head is basically preserved through the process while the curled tail disappears at 2.5MeV/m. The last graph in the lower right represents normal FEL operating condition. The excellent linear chirp can be seen across the whole 2.3% energy spread range.

A small part of the information at the two ends of the graph is lost, especially at low energy side of the plot. This is perhaps due to the limited energy window. This can be solved in the future by changing the optical demagnification at the expense of reduced resolution. We also used several band-pass filters with different bandwidth to see if there were dispersion effects induced in the optical transport. No difference was found with and without filters in the bean path, testament to the all-reflective nature of our design.

SUMMARY

We have established a diagnostic that provides real-time longitudinal phase space information without interruption to the accelerator operation. The longitudinal phase space was successfully measured with different linac gang phase and injector bunch gradient. The system was well calibrated with an energy resolution better than 0.05%. We are expecting to get better understanding on some important beam physics as we push toward high current beam and high power FEL on our facility in near future.

Acknowledgement

The authors would like to thank the FEL team, especially the I&C group. Thanks to M.Poelker for reviewing and extensive editing. This work is supported by the Office of Naval Research, Research, the Joint Technology Office, the Commonwealth of Virginia, the Air Force Research Laboratory, and by DOE Contract DE-AC05-84ER40150.

REFERENCES

[1] S. Zhang, et al., “Temporal Characterization of Electron Beam Bunches with a Fast Streak Camera at Jlab FEL Facility”, FEL2005, SLAC, August 2005, p.640.

[2] D.Douglas, et al., “Driver Accelerator Design for the 10kW Upgrade for the JLAB IR FEL”, LINAC2001, Monterey, CA 2001, p.867.

THE DEVELOPMENT AND APPLICATION OF A PHOTOEMISSION MODEL FOR CESIATED PHOTOCATHODE SURFACES

K. L. Jensen, J. E. Yater, J. L. Shaw, Naval Research Laboratory, Washington DC, 20375 USA
N. A. Moody, D. W. Feldman, P. G. O'Shea, University of Maryland, MD 20742, U.S.A.

Abstract

A theoretical photoemission model including thermal and field effects is presented. Particular attention is given to considering the impact of electron-electron and electron-lattice scattering and the development of an integrated absorption-transport-emission model developed to evaluate the moments of the electron emission distribution function. For the experimental conditions to which the theory is compared, there are no adjustable parameters. The performance of the model for the QE of bare metals and coated surfaces is discussed. A simple asymptotic model of emittance and brightness is given.[1]

INTRODUCTION

A high quantum efficiency (QE) photoemitter capable of in situ rejuvenation would fill a critical need in the development of high power FELs and linear accelerators. The demands placed on photocathode and drive-laser combinations by high power FELs are often both demanding and conflicting. Nano-Coulomb bunches in O(10) ps time scales require high quantum efficiency photocathodes, but such cathodes have traditionally degraded prematurely in vacuums characteristic of rf photoinjectors, whereas more rugged metal photocathodes require short wavelengths and therefore demand much of the drive lasers. The dispenser photocathode is intended to provide a rugged, low work function, long lived photocathode addressing these conflicting needs, and its development necessitated a validated photocathode model capable of analyzing data and predicting performance. A program to develop a controlled porosity dispenser (CPD) photocathode led to the creation and validation of a theoretical model that accounts for low work function surfaces from submonolayer coverage of alkali (and alkali earth) metals [i]. Efforts to extend and update that model have been in response to two needs: first, to provide theoretical support to an experimental CPD photocathode program by systematically studying cesiated surfaces, conventional sintered tungsten dispenser cathodes, and ultimately, custom engineered dispenser cathode; and second, to render the validated photoemission model in a form amenable to particle-in-cell (PIC) beam simulation codes [ii, iii] to predict performance of an rf injector gun using such a photocathode. Here the latest modifications to the model and its application are discussed.

Changes to the theoretical model are on two fronts. First, the scattering model affecting photoelectron excited transport to the surface has been revised. Second, the revisions motivated a moments-based emission model that is able to address cathode emittance. The beams of high power FEL's will be space charge dominated at some stage in the accelerator but especially in the gun. Non-uniform, transverse and temporal distributions affect emittance, and while the problem is of significant concern, predictive modeling efforts of device operation are compromised by the lack of adequate emission models in beam simulation codes. The photoemission models developed attempt to rectify the deficiency.

THE PHOTOEMISSION MODEL

Background

The photoemission model described in Ref. [i] represented quantum efficiency QE by

$$QE\left(T,F\right)=\frac{q}{\hbar\omega}F_{\lambda}(T)\left(1-R\right)P\left(\hbar\omega\right)$$
$$P\left(\hbar\omega\right)=\frac{U\left[\beta_T\left(\hbar\omega-\phi\right)\right]}{U\left[\beta_T\mu\right]} \qquad [1]$$

where $R(\omega)$ is the reflectivity of the surface, P is a probability of emission factor, U is the Fowler-Dubridge function, $\beta_T = 1/k_BT$ is the inverse temperature, ϕ is the barrier height above the Fermi level (work function minus Schottky barrier lowering factor, or $\Phi-\sqrt{4QF}$, where Q = 0.36 eV-nm and F is the product of electric field and electron charge). When coatings such as Cs are introduced, the work function Φ is dependent upon the degree of coverage θ in a manner predicted by Gyftopoulos-Levine theory. The scattering factor F_λ (not to be confused with field F) governs the probability that an electron will suffer a scattering event on its trajectory towards the surface and therefore be prevented from being photoemitted. It can be approximated by

$$F_{\lambda}\approx\frac{1}{\pi}\int_0^{\pi/2}\frac{\cos(\theta)}{\cos(\theta)+\left(\delta/l(E)\right)}d\theta \qquad [2]$$

where δ is the laser penetration depth, and the length $l(E)$ is the product of the electron velocity and relaxation time (the notation has changed from Ref. [i])

Amending recent work in measuring the QE of cesiated surfaces and the prediction of the QE of bare metals, we have revised components of the QE model by first, utilizing models of the relaxation rates τ implicit in f_λ at the electron energy augmented by the photon energy, and second, using a moments-based approach that changes the probability of emission term P. It is the moments-based approach that allows for transverse energy and velocity expectation values to be determined, from which estimates of the emittance and brightness can be made.

---

[1] Support by *Joint Technology Office* & *Office of Naval Research*

Scattering Rates and Their Determination

The relaxation time is taken to be the sum of three components:

$$\tau^{-1} = \tau_{ee}^{-1} + \tau_{ac}^{-1} + \tau_{imp}^{-1} \qquad [3]$$

where "*ee*" refers to electron-electron, "*ac*" refers to acoustic phonon, and "*imp*" to residual low temperature scattering due to impurities or defects. In the case of electron-electron scattering, the scattering rate is given by

$$\tau_{ee} = \frac{4\hbar K_s^2}{\alpha^2 \pi m c^2 (k_B T)^2} \left[\left(1 + \frac{E-\mu}{\pi k_B T} \right) \gamma\left(\frac{2k_F}{q_o} \right) \right]^{-1}$$
$$\gamma(x) = \frac{x^3}{4} \left(\tan^{-1} x + \frac{x}{1+x^2} - \frac{\tan^{-1}\left(x\sqrt{2+x^2} \right)}{\sqrt{2+x^2}} \right) \qquad [4]$$

where K_s is the dielectric constant, α is the fine structure constant, k_F is the Fermi wave vector, and q_o is the Thomas-Fermi screening length [iv] (the form given here corrects coefficient errors that exist in Ref. [iv]). To leading order, the Thomas-Fermi factor is given by

$$q_o^2 = \frac{4\alpha m c}{\pi \hbar^2 K_s} \sqrt{2m\mu} \qquad [5]$$

For acoustic scattering, the rate is given by [v]

$$\tau_{ac} = \frac{\pi \rho \hbar^3 v_s^2 \left(T_D / T \right)^5}{m k_B T k_F \Xi^2} \left(\int_0^{T_D/T} \frac{s^5 ds}{\left(e^s - 1 \right)\left(1 - e^{-s} \right)} \right)^{-1} \qquad [6]$$

where Ξ is the magnitude of the deformation potential, T_D is the Debye temperture, v_s is the velocity of sound, and ρ is the density. The Debye Temperature is given by

$$T_D = \frac{\hbar v_s}{k_B} \left(6\pi^2 N r \right)^{1/3} \qquad [7]$$

where N [#/cm^3] is the number density of the crystal, r is the (# of atoms / unit cell), and v_s is the sound velocity.

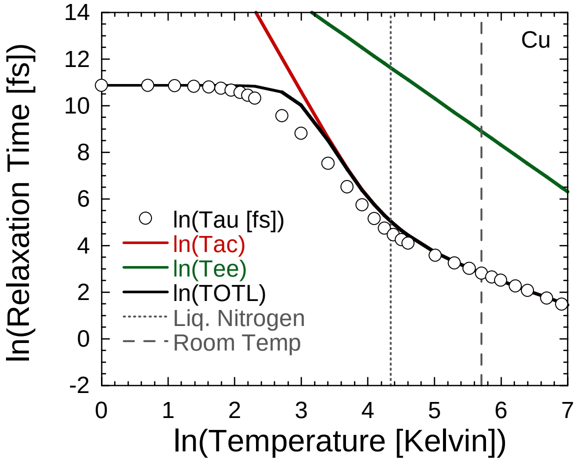

Figure 1: Determination of τ_{imp} and Ξ from thermal conductivity data from the literature.

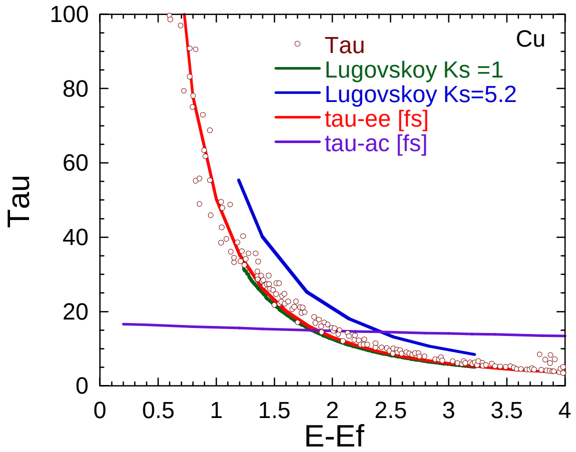

Figure 2: Determination of K_s from Monte Carlo simulations (red line) compared to parameters considered by Lugovskoy and Bray (green and blue)

Consequently, three parameters require an intricate simultaneous determination: τ_{imp}, K_s and Ξ. The values of τ_{imp} and Ξ are determined by low temperature thermal conductivity measurements after K_s is determined from Monte Carlo simulations in the literature [vi].

Comparison to Experiment

An example for Cu is shown in Figure 1 and 2. The procedure is reiterated for many metals, and in particular, for tungsten (W) and silver (Ag) which are the two cesiated metals experimentally examined [vii]. Parameters extracted from the literature become part of a library of material terms implicit in code and are not adjusted further. Comparisons of predictions of the resulting model with experimental data have been favorable for the cases of photoemission from copper [viii] and lead [ix] for a range of photon frequencies, as well as for other metals and particular frequencies discussed in the literature.

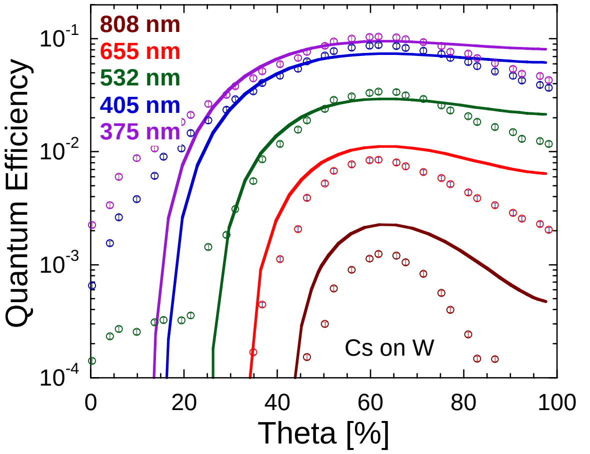

Figure 3: QE of Cs on W for low F and I_λ at 300 K versus fractional surface coverage (Ar-cleaned W). Symbols = experimental data; lines = theoretical model.

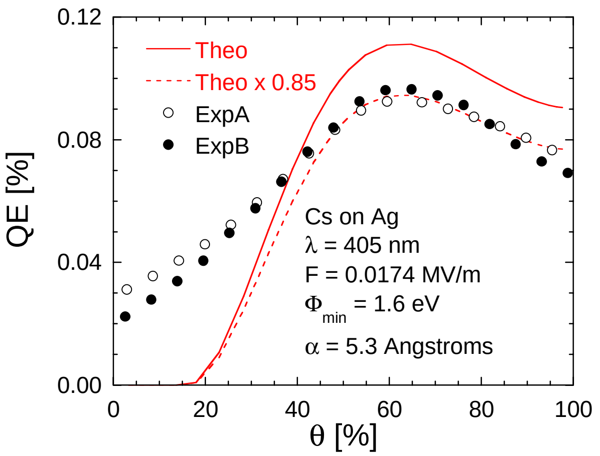

Figure 4: QE of Cs on Ag for conditions as in Fig. 3

Using the Gyftopoulos-Levine theory to relate the degree of surface coverage of Cesium on a bulk metal to the resulting work function [i], the prediction of QE for Cs on W and Cs on Ag was made and compared to experimental data. The results of that comparison are shown in Figures 3 and 4, respectively. The low coverage discrepancy shown in Fig. 4 is due to residual Cs on the surface from one experiment to the other. Issues of surface contamination led to investigations of cleaning using Ar ions, resulting in the better results for Cs on W shown in Fig. 3.

Origin Of Experimental-Theoretical Differences

The overall comparison between theory and experiment is shown to be remarkably good. Nevertheless, there are differences and an account of their probable origins is necessary. Theoretically, a simple nearly-free electron gas model is presumed, and so the significant complexities introduced by the density of states near the Fermi level are suppressed, and such complexities can matter for transition metals. Experimentally, in contrast to physical surfaces, the theoretical models are highly idealized. Cleaning is required to remove contaminants, and if due to sputtering, structure can be introduced. If the cathode is heated for cleaning, not all metals endure the necessary temperatures because of relatively low melting points (W can be strongly heated, whereas Ag cannot). Residual contamination can therefore remain in addition to what collects from an imperfect vacuum. Adsorbates often have higher work functions, *e.g.*, carbon-based contamination can induce local work functions of 5.5 eV. Assuming the surface is adequately cleaned, different exposed crystal faces can show markedly different work functions (*e.g.*, faces of Cu can vary by almost 0.8 eV): moreover, in Gyftopoulos-Levine theory, the exposed crystal plane affects the *f*-factor (see Ref. [i]: affects the number of Cs atoms per unit area) and which changes the shape of the QE hump: observations of the tungsten face, as shown in Figure 5, as well as considering other values of *f* suggest the generic (single) value chosen for *f* is not necessarily the optimal value when several faces are present.

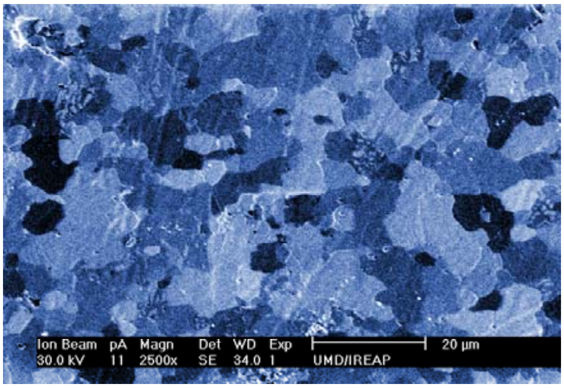

Figure 5: Image of sintered tungsten surface showing multiple crystal faces. Average grain size is O(10µm).

MOMENTS-BASED FORMULATION

The development of an energy-dependent relaxation time coincides with efforts to develop a modified emission probability model to replace Eq. [1], in which the energy of an incident electron affects its transmission probability *T(E)* over (or through for high fields) a barrier. By using a distribution function approach, parallel and transverse momentum expectation values are ascertained, the former used to evaluate the photoemission current, the latter to evaluated emittance (and both to evaluate brightness). Define the nth moment

$$M_n(x) = (2\pi)^{-3}\left(\frac{2m}{\hbar^2}\right)^{3/2}\int_0^\infty E^{1/2}dE \times$$

$$\int_0^{\pi/2}\sin\theta d\theta\left(\frac{2m}{\hbar^2}Ex^2\right)^{n/2} T\left\{(E+\hbar\omega)\cos^2\theta\right\}\times \qquad [8]$$

$$f_\lambda(\cos\theta, E+\hbar\omega)\, f_{FD}(E)\left\{1-f_{FD}(E+\hbar\omega)\right\}$$

where x = cos(θ) for parallel, and sin(θ) for transverse components. T is the transmission probability; f_λ is the integrand of F_λ, and the factor $f_{FD}(1\text{-}f_{FD})$ represents the probability that the initial state is occupied and the final state is not based on the Fermi Dirac distribution. The revised relaxation times are used in the determination of the f_λ factor. The inclusion of the transmission probability factor, and the impact on the integration limits it entails, generally results in current density estimates on the order of 30% less than the Modified Fowler-Dubridge approach, all other factors being equal. Methods to calculate Eq. [8] numerically rely on approximations to the transmission probability and models for the relaxation time in the scattering factor: below, however, an asymptotic case is considered so as to provide a simple model of emittance and brightness.

Under the Richardson approximation for the transmission coefficient and the zero-temperature approximation for the FD functions, the asymptotic expressions for the transverse (x = sinθ) moments are [x]

$$M_0 \approx \frac{1}{(2\pi)^2}\left[\frac{2m}{\hbar^2}\right]^{3/2} \frac{\mu^{1/2}(\hbar\omega-\phi)^2}{4(\mu+\phi)\left[p(\hbar\omega+\mu)+1\right]}$$
$$M_2 \approx \frac{2m\mu(\hbar\omega-\phi)}{3\hbar^2(\hbar\omega+\mu)}M_0 \qquad [9]$$

From the definition of the emittance [xi] as

$$\varepsilon_{n,rms}(z) = \frac{\hbar}{mc}\sqrt{\langle x^2\rangle\langle k_x^2\rangle - \langle xk_x\rangle^2} \qquad [10]$$

and following a derivation and approximations (uniform emission over a circular uniformly illuminated surface area) analogous to that leading to the widely-used thermal emittance relation

$$\varepsilon_{n,rms}(therm) = \rho_c / \left(4\beta_T mc^2\right)^{1/2} \qquad [11]$$

where ρ_c is the cathode radius and β_T is $1/k_BT$, it can be shown that $\varepsilon_{n,rms}(photo)$ is proportional to the illumination radius and the root of the 2nd and 0th moments, or

$$\varepsilon_{n,rms}(photo) \approx \frac{\rho_c}{2}\left[\frac{\mu(\hbar\omega-\phi)}{3mc^2(\hbar\omega+\mu)}\right]^{1/2}$$
$$\frac{B_n}{(1-R)I_\lambda A} \approx \frac{3qmc^2}{2\pi^2\mu^3\hbar\omega}\left(\frac{(\hbar\omega+\mu)(\hbar\omega-\phi)}{1+p(\mu+\hbar\omega)}\right) \qquad [12]$$

where B_n is the brightness [xii], R is the reflectivity, I_λ is the laser intensity per unit area, and A is the illuminated area. The brightness ratio in Eq. [12] is designed to forestall issues associated with reflectivity, laser particulars, and illumination area. Two observations are important: first, the emittance does not depend on the scattering factor to leading order (the brightness does through the p factor); second, the asymptotic form of B_n indicates that an optimal wavelength exits for which the brightness is maximized. The behavior of $\varepsilon_{\mathrm{n,rms}}$ and B_n are shown in Figure 6.

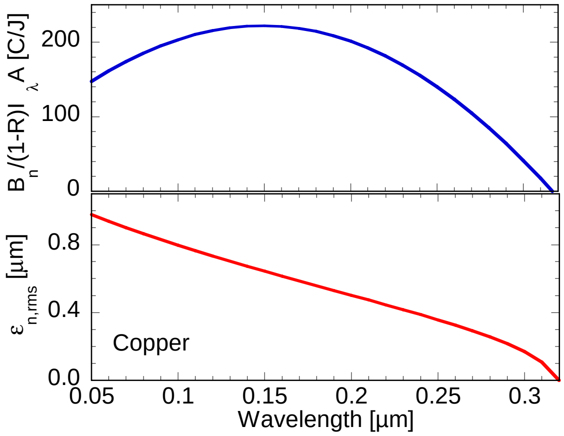

Figure 6: emittance and brightness ratio as a function of incident laser wavelength for copper parameters for conditions described in Ref. [viii].

Experimental values of emittance at 233 nm are approximately 50% larger than the theoretical value shown. The emittance of thermionic sources are generally within a factor of 2 larger than the theoretical estimate entailed by Eq. [11], and it is reasonable to presume similar explanations hold here: non-linear field components in the cavity, wakefields, non-uniformity of the illumination source (laser), thermal effects, quantum efficiency non-uniformity due to contamination or cathode structure, and space-charge effects occur for sufficiently high charge in the bunch, and likely some combination contribute to the theoretical-experimental differences between the simple asymptotic limit herein and experiment.

CONCLUSION

We have presented a revised photoemission model to account for theoretical-based scattering models and a moments-based approach for the evaluation of quantum efficiency. The revised scattering model enabled good agreement with experimental data of cesiated surfaces. The moments-based approach allowed for simple asymptotic expressions of emittance and brightness.

Acknowledgements

We gratefully acknowledge funding provided by the *Joint Technology Office* and the *Office of Naval Research*. In addition, we have benefited from interaction with many colleagues: in particular we thank (*alph*) C. Bohn, C. Brau, D. Dimitrov, D. Dowell, Y.Y. Lau, J. Lewellen, E. Nelson, J. Petillo, and J. Smedley.

REFERENCES

i K. L. Jensen, Donald W. Feldman, Nathan A. Moody, and Patrick G. O'Shea, Journal of Applied Physics 99, 124905 (2006).

ii J. J. Petillo, E. M. Nelson, J. F. DeFord, N. J. Dionne, B. Levush, *IEEE Trans. El. Dev.* **52**, 742 (2005).

iii D. A. Dimitrov, D. L. Bruhwiler, J. R. Cary, P. Messmer, P. Stoltz, K. L. Jensen, D. W. Feldman, P. G. O'Shea, *Conference Proceedings of the 27th Intl. Free Electron Laser Conference* (Stanford, CA, Aug. 21-25, 2005), paper TUPPE039.

iv A. V Lugovskoy, Igor Bray, *J. Phys. D: Appl. Phys.* **31** L78 (1998).

v Harald Ibach, Hans Lüth, *Sold State Physics* 2nd *Ed.*, (Springer-Verlag, Berlin, 1995).

vi F. Ladstädter, U. Hohenester, P. Puschnig, C. Ambrosch-Draxl, *Phys. Rev.* **B70**, 235125 (2004)

vii N. A. Moody, D. W. Feldman, P. G. O'Shea, K. L. Jensen, J. L. Shaw, J. E. Yater, (*Free Electron Laser Conference*, Berlin, Aug 27-Sep 1, 2006)

viii D. H. Dowell, F. K. King, R. E. Kirby, J. F. Schmerge, J. M. Smedley, *Phys. Rev. Spec. Top.*-AB 9, 063502 (2006)

ix Data from J. M. Smedley (*private communication*).

x K. L. Jensen, P. G. O'Shea, D. W. Feldman, N. A. Moody (*submitted to Appl. Phys. Letters*)

xi Patrick G. O'Shea, *Phys. Rev.* **E57**, 1801 (1998).

xii C. Brau, *Nucl. Inst. Meth. Phys. Res.* **A407**, 1 (1998).

EXPERIMENTAL PROGRESS TOWARD LOW WORKFUNCTION CONTROLLED POROSITY DISPENSER PHOTOCATHODES*

N. A. Moody[#], D. W. Feldman, E. J. Montgomery, A. E. Balter, P. G. O'Shea,
U. of Maryland, College Park, MD, USA
K. L. Jensen, J. E. Yater, J. L. Shaw, Naval Research Laboratory, Washington DC, USA.

Abstract

Photoinjectors for accelerator applications require long-lived photoemitters with high quantum yield in the visible range. Multi-alkali cesium-based photocathodes are frequently used but suffer from short lifetime, due to loss of cesium. A novel dispenser cathode is proposed and demonstrated that provides controlled delivery of cesium to the cathode surface at <200°C. This method allows for *in situ* rejuvenation of the photoemitting surface and could dramatically extend the effective lifetime of many alkali-based high-efficiency photocathodes.

INTRODUCTION

Laser-switched photoemitters are a source of electrons for high current applications such as free electron lasers [1],[2][3]. Photoinjector systems consist of a drive laser producing short bunches of photons and an efficient photocathode, which converts photon bunches into electron beam pulses [4]. Development of both technologies is required, but the scope of this project is restricted to improvement of the photocathode. Most high-efficiency photocathodes employ cesium-based surface coatings to reduce work function and enable efficient electron emission in the visible range. Lifetime is severely limited by the loss of this delicate coating, which degrades rapidly in practical vacuum environments. More robust photocathodes exist, but have much lower efficiency, and place unrealistic demands on drive laser power and stability. A common figure of merit for photocathodes is quantum efficiency: the ratio of the number of photoemitted electrons to incident photons. It is related to photocurrent J_e and optical intensity I_λ according to:

$$QE = \frac{\hbar\omega}{q}\left(\frac{J_e}{I_\lambda}\right) = 1.2398\,\frac{J_e\left[\mathrm{A/cm^2}\right]}{I_\lambda[\mathrm{W/cm^2}]\,\lambda\left[\mu\mathrm{m}\right]} \quad (1)$$

This research proposes a novel dispenser concept that dramatically extends the lifetime of high QE cesium-based cathodes by continuously or periodically restoring the cesium surface monolayer during an *in situ* rejuvenation process. A prototype dispenser cathode was fabricated and tested for two modes of operation: continuous and periodic near-room temperature rejuvenation. The data are compared with a photoemission model of partially covered surfaces under design for integration with existing beam simulations.

Overall performance suggests that this cesium-delivery mechanism can significantly enhance the efficiency and operational lifetime of a wide variety of present and future cesium-based photocathodes.

Dispenser Concept

A dominant degradation mechanism for high QE cesium-based cathodes is the loss of cesium either from a surface monolayer or a stoichiometric compound. Replenishing this layer with cesium continuously or periodically could restore cathode performance. Our concept of a cesium based dispenser photocathode involves three essential elements: a cesium reservoir, a photoemitting surface, and an interface between the two that controls the rate of cesium arrival. In this design, shown schematically in Figure 1, a small stainless steel cylinder contains a pellet of cesium chromate and titanium powders. A disk of made from 70% dense sintered tungsten (top) serves as both the photoemitting surface and the interface boundary [5]. During an initial heating process, the pellet breaks apart and releases elemental cesium, which diffuses through and across the sintered tungsten substrate to create a low workfunction photoemitting surface. This simple cesium-on-tungsten photocathode was used to characterize the behavior of the dispenser, but more complex cathodes such as cesium antimonide could also be built on the substrate.

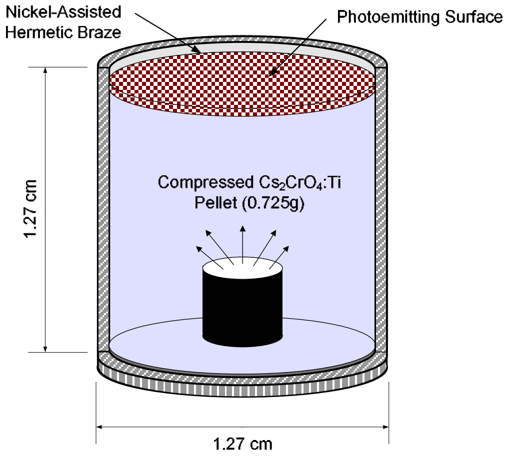

Figure 1: Schematic of Dispenser Cathode

Experimental Overview

In order to characterize the performance of the dispenser cathode, a detailed study of the photoemissive properties of cesium on tungsten was undertaken using the fabrication chamber shown in Figure 2.

---

*Work supported by Office of Naval Research, Joint Technology Office, and Directed Energy Professional Society

[#] nmoody@ieee.org

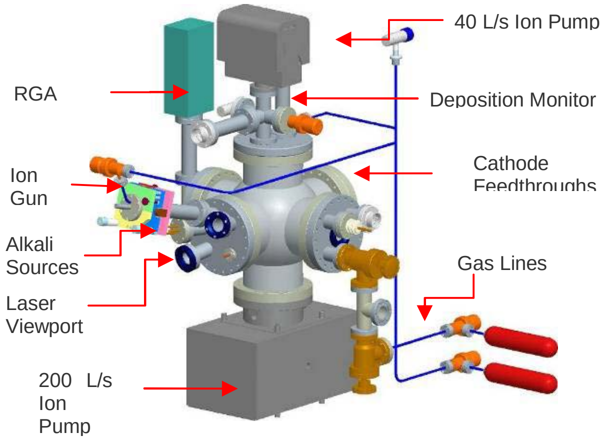

Figure 2: Vacuum Fabrication Chamber

Cesium was deposited externally using commercial sources onto a sintered tungsten disk identical to the one used to fabricate the dispenser cathode. QE was measured during deposition at several wavelengths as a function of cesium coverage, which was observed using a quartz crystal balance. Because cesium deposition occurred externally from an isotropic source, the resulting layer was assumed to be uniform. A characteristic curve was obtained whose shape and peak value depended upon the surface conditions of the cathode. Recall that for a dispenser cathode, cesium arrives at the surface through diffusion from within, so direct measurement of cesium coverage is not possible. Studying the effect of external, uniform deposition of cesium on tungsten, however, allows comparison of the dispenser's QE to that of a known system. This work is therefore divided in two parts: 1.) photoemission measurements of cesium on tungsten and 2.) characterization of the dispenser cathode.

Experimental Setup

Cesium is deposited onto the surface of a clean metal disk using SAES sources, while coverage is measured using an Inficon quartz crystal deposition monitor situated directly above the cathode. A circular anode biased at +186 volts is separated from the cathode by a distance of one centimeter. Photocurrent is measured across the anode-cathode gap using a Keithley 486 picoammeter. The entire circuit is isolated from the chamber and all connections are made using Triax to minimize noise and interference.

Five semiconductor CW lasers are sequentially shown onto the cathode while photocurrent, cesium coverage, laser intensity, background pressure, and cathode temperature are recorded using Labview. The lasers have output powers of 5mW with 2% stability at 355nm, 405nm, 532nm, 655, and 808nm. A Labview-controlled, motorized translation stage selectively positions a desired laser at the UHV chamber viewport, enabling QE measurement at multiple wavelengths during a single evaporation run. The laser spot is circular and expanded to a FWHM size of 1 cm.

Because a DC potential is used to extract charge from the cathode, ion back-bombardment occurs, where positively charged contaminants within the chamber accelerate toward and collide into the cathode, damaging and/or removing the surface layer of cesium [6]. Minimizing contaminants *during* evaporation is difficult because both the dispenser cathode and the cesium sources (having been exposed to atmosphere) contain trapped gases and traces of impurities that are emitted along with cesium. This effect is minimized by first outgassing the dispenser in a controlled manner at temperatures beneath that required to emit cesium.

EXPERIMENTAL RESULTS

Surface Metrology

The surface characteristics of sintered tungsten were studied in detail using optical, scanning electron, and focused ion beam microscopy. The porosity and thickness of the sintered disks used in the dispenser cathode were chosen such that extremes in either case were avoided. Figure 3 shows a side view of the sintered tungsten disk at 1000x magnification. Characteristic length scales of its polished surface were determined, including average pore diameter of 350nm, nearest-neighbor separation distance of 3.1µm, and average grain size of 4.8µm. The surface area each pore must coat with cesium was found on average to be 33.3µm^2 for uniform monolayer coverage. These lengths are significant because they estimate the surface diffusion length of cesium required to achieve complete coverage. Coverage uniformity is crucial because variation in the cesium surface coating causes similar variation in work function and electron emission.

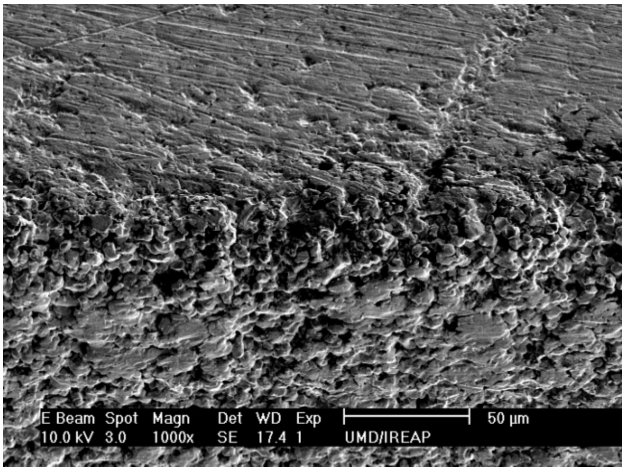

Figure 3: Side View of Dispenser Cathode

Cleaning Techniques

A standardized cleaning procedure using a 6.4keV ion argon beam was developed and shown to be remarkably effective in cleaning sintered tungsten. When cesium was deposited following the procedure, the effects of the treatment became apparent: a two-fold increase in QE with a peak QE of 0.11% in the UV, as shown in Figure 4.

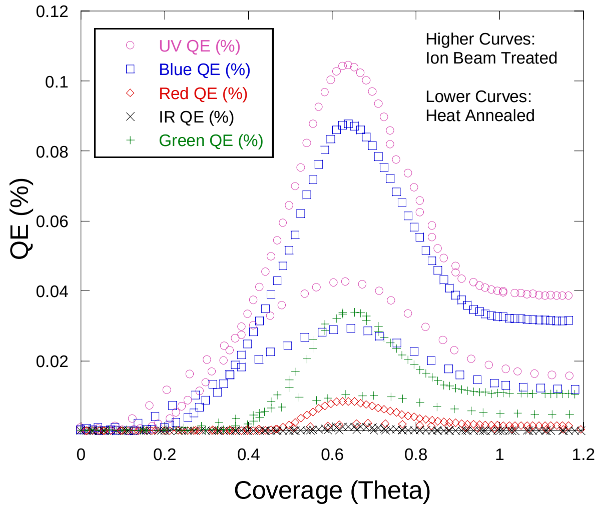

Figure 4: Effects of Ion Beam Cleaning

Coverage θ is reported in the above graph as a fraction of a monolayer, where $\theta = 0$ corresponds to bare tungsten and $\theta = 1$ is a full cesium monolayer. A single 45 minute treatment provided a 40mC dose of 6keV argon ions which was sufficient to produce apparent atomic cleanliness. This claim is justified because increasing the number of consecutive ion treatments and/or the energy of the ion beam did not produce further improvement in QE. Because cesium was deposited uniformly on an atomically clean surface, the QE of 0.11% can be said to be characteristic of a uniform, optimal cesium coating. This cleaning technique dramatically reduces the amount of time required to prepare a cathode for cesium deposition because it eliminates the need for a lengthy high temperature anneal.

Theory Comparison

The model used in this work is based upon the Fowler-DuBridge treatment of photoemission [6],[7] and follows the Gyftopolous-Levine approach of accounting for the effects of cesium coverage [9]. A distinguishing factor about the modified model is that an effort has been made to systematically reduce or eliminate unknowns, either by means of models or approximations, which were arbitrarily assigned or used as fit parameters in other treatments. The components of the model relevant to the experiments in this program are described in detail elsewhere [10]. Data describing the effect of surface cesium coverage on the work function and QE of metal photocathodes was compared to the model's predictions and found on average to be within 22% agreement, as shown in Figure 5. Similar agreement was found for cesium-on-silver and suggests that the theory is capable of predicting performance of metallic-based photocathodes. This experiment enables theory comparison for an important set of operation parameters: low drive laser intensity and low accelerating electric field. These parameters are typically much higher and are usually cited as reasons for drastic discrepancies between theory and experiment (e.g., laser heating, damage to cathode surface, etc.).

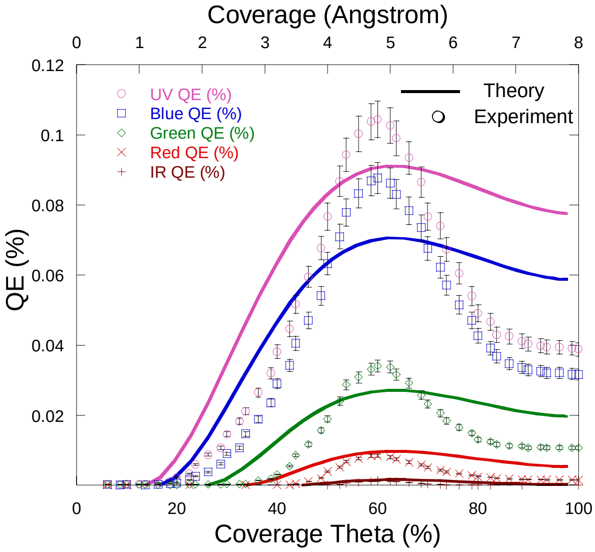

Figure 5: Comparison of Theory and Experiment

The inputs to the theory were simply generalized material parameters that could be widely applied to any number of different photocathodes.

Dispenser Cathode

The two basic procedures for operating the dispenser cathode are activation and rejuvenation. Activation occurs at higher temperatures and initiates a chemical reaction between the powders inside the cell, while rejuvenation occurs at much lower temperature and involves bringing atomic cesium to the surface in a controlled manner. Initial activation prepared the dispenser for use, as seen by the onset of photoemission at 425°C, followed by complete activation at 477°C, which produced a reduction in work function such that a large thermionic current was measured. Because of the elevated temperature, a significant amount of cesium was released throughout the chamber, producing up to a 50Å coating on an adjacent deposition monitor. This release is expected, however, and is not considered problematic because 1.) a large quantity of cesium remained within the dispenser following activation, and 2.) the activation procedure for a working dispenser cathode would most likely occur in a chamber separate from the actual electron gun (whose contamination with cesium would lead to field breakdown).

Following activation, the dispenser was allowed to cool and its 1/*e* lifetime was measured to be 5.2 days. After 65 hours of continuous operation, its QE decayed from its peak of 0.11% in UV to 0.06%. Complete rejuvenation was demonstrated when QE returned to its previous peak value of 0.11% upon heating to 140°C, as shown in Figure 6. Less than 3Å of cesium was deposited during this process, suggesting that *in situ* rehabilitation of the cathode is possible. Coverage at peak QE was indirectly measured to be about 64% using the relationship between cesium coverage and QE.

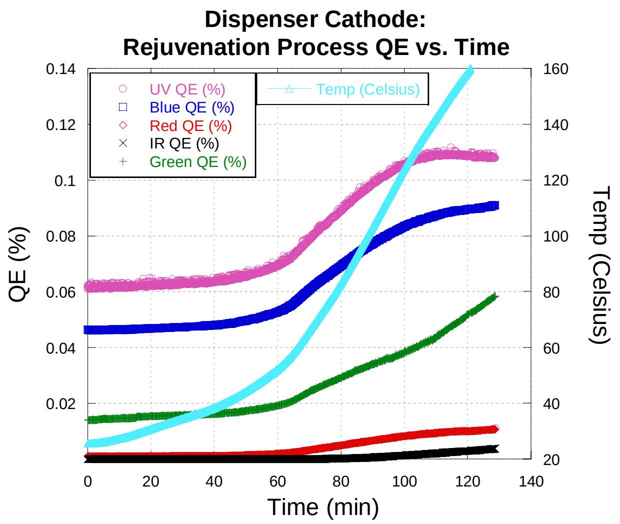

Figure 6: Rejuvenation of Cathode Surface

Two modes of cathode operation were demonstrated: periodic and continuous rejuvenation. For the continuous mode, temperature is held between 160-180°C, resulting in constant replenishment of the cesium layer. The 1/*e* effective (continuous duty cycle) lifetime in this mode was an astounding 47 days.

CONCLUSIONS

A prototype design for a near-room temperature dispenser cathode was proposed and demonstrated for the case of cesium-on-tungsten using commonly available components: thin-walled stainless steel and porous sintered tungsten. It is distinguished from other dispenser-type cathodes [11] by its low operating temperature, which makes it a good candidate technology where cathode thermal management is a concern. A method for conveniently integrating cesium chromate into the dispenser cell was demonstrated by forming the powder into a solid pellet under high pressure. The peak QE of the activated dispenser cathode, following an ion beam cleaning treatment, was 0.11%. This QE value was shown to correspond to that of a uniform, optimal cesium coating and suggests that the sintered tungsten interface facilitates uniform cesium coverage. This result suggests that the surface diffusion length of cesium across tungsten at temperatures ranging from 200-400°C is at least 5µm. The overall performance of the dispenser cathode suggests that its design could serve as a temperature-controlled cesium dispensing platform onto which a variety of high QE cesium-based photocathodes could be built.

REFERENCES

[1] P. G. O'Shea, H. P. Freund, Science **292**, 1853 (2001).

[2] D. H. Dowell, S. Z. Bethel, K. D. Friddell, Nucl. Instr. & Meth. in Phys. Res., A**356** 167 (1995).

[3] C. Travier, Nucl. Instr. & Meth. in Phys. Res. **A304**, 285 (1991).

[4] P. G. O'Shea, et. al., *Proc. Particle Accel. Conf.*, vol. 5, San Fran., May 6–9, 1991, pp. 2754–2756.

[5] Fabrication performed by B. Vancil, E-Beam Inc, Beaverton, OR.

[6] C. H. Garcia, C. A. Brau, Nucl. Instr. And Meth. in Phys. Res., A 475 (2001) 559-563.

[7] R. H. Fowler, Phys. Rev. 38, 45 (1931); L. A. DuBridge, Phys. Rev. 43, 727 (1933).

[8] J. H. Bechtel, W. L. Smith, and N. Bloembergen, Phys. Rev. B15, 4557 (1977).

[9] E. P. Gyftopolous and J. D. Levine, Jour. of App. Phys. **33**, 67 (1962).

[10] K. L. Jensen, D. W. Feldman, N. A. Moody, P. G. O'Shea, Jour. App. Phys., **99**, 1 (2006).

[11] R. E. Thomas, J. W. Gibson, G. A. Haas, and R. H. Abrams, IEEE Transactions on Electron Devices 37, 850 (1990).

OPTIMUM BEAM CREATION IN PHOTOINJECTORS USING SPACE-CHARGE EXPANSION*

J.B. Rosenzweig, A.M. Cook, M. Dunning, R.J. England
Particle Beam Physics Laboratory, Department of Physics and Astronomy
University of California Los Angeles, Los Angeles, CA 90095, USA

M. Bellaveglia, M. Boscolo, L. Catani, A. Cianchi, G. Di Pirro,
M. Ferrario, D. Filippetto, G. Gatti, P. Musumeci, L. Palumbo, C. Vicario
Istituto Nazionale di Fisica Nucleare, Laboratori Nazionale di Frascati
00044 Frascati (Roma), Italy

S. Jones
Jet Propulsion Laboratory, California Institue of Technology
4800 Oak Grove Drive, Pasadena, CA 91101, USA.

Abstract

It has recently been shown that by illuminating a photocathode with an ultra-short laser pulse of appropriate transverse profile, a uniform density, ellipsoidally shaped bunch is dynamically formed, which then has linear space-charge fields in all dimensions inside of the bunch. We study here this process, and its marriage to the standard emittance compensation scenario that is implemented in most modern photoinjectors. It is seen that the two processes are compatible, with simulations indicating that a very high brightness beam can be obtained. The scheme has produced stimulus for a series of experiments at the SPARC injector at Frascati in 2006-2007. An initial time-resolved experiment has been performed involving Cerenkov radiation produced at an aerogel. We discuss the results of this preliminary experiment, as well as plans for future experiments to resolve the ellipsoidal bunch shape at low energy. Future measurements at high energy based on fs resolution RF sweepers are discussed.

INTRODUCTION

In order to obtain the highest brightness electron beams from photoinjectors, it is most common to rely on the emittance compensation process [1]. Optimization of this process demands that the transverse fields be as uniform, and linear (in radius r) as possible. The existing studies of emittance compensation have, to that end, assumed use of a uniform density electron beam, having a cylindrical shape. However, this shape produces space-charge fields near the beam head and tail that have pronounced nonlinear dependencies on the spatial coordinates. These nonlinearities result in both transverse and longitudinal emittance growth.

It has been known for some time, however, that a uniform ellipsoidal density distribution yields space-charge fields that are linear in all dimensions [2]. Under such conditions, it is conceivable that one may obtain essentially emittance growth-free dynamics. How to produce such a distribution has, until recently, remained an unanswered question.

In 1997, Serafini proposed the dynamic creation of an ellipsoidal bunch by launching an ultra-short, radially shaped beam, which then evolves to achieve the desired longitudinal shape [3]. On the other had, it has recently been shown by Luiten, et al., that in obtaining the correct final ellipsoidal distribution, there is essentially no requirement on the shape of the initial laser pulse other than it be ultra-short (length τ_l much shorter than eventual beam length after space charge expansion) [4]. Thus such laser pulses are a natural, and technically achievable way of producing an ellipsoidally shaped, nearly uniform density beam.

As the beam dynamics just after photoemission are qualitatively different in the traditional emittance compensation scenario and in the Luiten-Serafini scheme, it is not immediately apparent that one may successfully combine the two. The UCLA-SPARC collaboration has recently shown [5] that this marriage is indeed possible; further, the combination of emittance compensation and dynamic creation of the ellipsoidal shaped beam produces results that in many ways are superior to those obtained in state-of-the-art designs. As the bunches that are produced are shorter than in standard cases, very high brightness beam creation is possible.

The basic idea behind the Luiten-Serafini scheme is simple: the beam profile expands and deforms longitudinally to produce, in the final state, a uniformly filled ellipsoid of charge. In the process, phase space rearrangements occur which degrade the emittances– especially in the longitudinal dimension. In order to understand this process, to specify experimental requirements, and to identify experimental signatures associated with the process, we have analyzed the dynamics of space-charge-dominated beam ex-

---

* Work supported by the US Dept. of Energy under grant DE-FG03-92ER40693, and the Italian Ministry.

pansion [5].

This analysis may be summarized in a few points:

First, the injected bunch surface charge density $\sigma_b = dQ_b/dA$ must not be too high, or image charge effects at the cathode distort the final pulse profile so that it is not ellipsoidal. This is quantified by the condition $\alpha \equiv 4\pi\sigma_b/E_0 \ << 1$.

Second, the beam must be much shorter than its eventual size in order to be able to ignore the details of the initial pulse profile. In practice, 300 fs laser pulses (typical of the limitations of the SPARC photocathode drive laser after conversion to UV) excite roughly the same length electron bunch, which expands to around 4 psec in our example cases. The pulse length after expansion is estimated as $L_b \approx 2\pi\sigma_b m_e c^2/E_0^2$.

The current density that is achieved after expansion is $J_z = eE_0^2/4\pi m_e c$, a constant dependent only on the applied electric field E_0. All beams become uniform in density. To achieve the desired ellipsoidal beam shape, one must choose the initial surface current density distribution correctly, which implies that $\sigma_b(r) = (3Q_b/2\pi a^2)\sqrt{1-(r/a)^2}$.

While the analysis of the beam dynamics is useful, the central issue of joining this regime with emittance compensation must be explored with simulations. The initial simulations begun in Ref. [5] that we have performed are in the context of the SPARC scenario, so that we may proceed directly to discussing the experimental tests of this new regime– now commonly known as the "blowout regime"– of the photoinjector there.

BLOWOUT REGIME WITH EMITTANCE COMPENSATION: GENERAL STUDY

We have performed initial UCLA PARMELA [6] simulations to explore joining the Serafini-Luiten scheme with the optimized emittance compensation working point of the SPARC injector at LNF. We assume that the gun (1.6 cell, 2856 MHz) and solenoid are the same, and run near to the standard conditions. Through trials, we have optimized the launch conditions of the beam. In order to have values of α which do not give excessive image charge effects, the beam charge is lowered and the beam radius is slightly enlarged. In the preliminary optimization, we launch a 0.33 nC beam with an initial longitudinal Gaussian distribution having $\sigma_t = 33$ fs beam, and a radial Gaussian with $\sigma_x = 0.77$ mm (cutoff at 1.8σ). The gun is run with a peak on-axis gradient of 120 MV/m; the beam is launched at 33 degrees forward of crest. This is a bit advanced in comparison to the nominal launch phase for a standard bunch, and serves to control the excessive beam energy spread after the gun. The emittance compensation solenoid is run with peak field $B_z = 2700$ G, which is slightly below the standard scenario, as the beam has slightly lower energy exiting the gun. We note that the peak value of α in our case is 0.11, as opposed to 0.42 in the LCLS design.

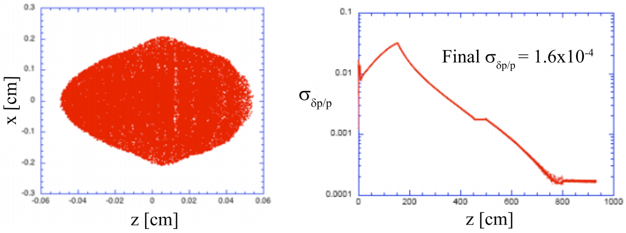

Figure 1: (left) PARMELA simulation results of electron bunch (x, z) distribution 133 cm from cathode (6.3 MeV energy), showing ellipsoidal beam boundary. (right) Evolution of $\sigma_{\delta p/p}$ in z for emittance compensation case, from PARMELA simulation.

The formation of the quasi-ellipsoidal bunch is clearly shown in Fig. 1, which displays the bunch (x, z) distribution at a point 133 cm from the cathode, in the drift space after the gun and just preceding initial traveling wave linac section. Here the beam has 6.3 MeV mean energy, and its transverse dynamics are space charge-dominated. Thus one sees clearly the "inflated" ellipsoidal beam shape. The final bunch length is 1.3 mm full width, corresponding to a peak current of 105 A. Thus even with one-third of the charge, this scheme should produce a higher current than obtained in simulations of the standard design.

Two notable defects are seen in the beam shape in Fig. 1. The first is the extension of the half-ellipsoid in the trailing part of the bunch as compared with the initial half– an asymmetry caused by image charge effects. This non-ideal behavior in fact gives the limit on σ; when one attempts to launch a higher surface charge density, the bunch deformation from the desired symmetric ellipsoid produces poor emittance performance. The second notable feature is the existence of an anomalous ring at the outer radial edge of the beam. This part of the beam has low surface charge density and experiences radially fringing fields due to its edge location. Because of these effects, it does not experience enough longitudinal expansion to keep pace with the rest of the bunch, but instead has a moderate amount of radial expansion.

As the longitudinal space-charge during much of the acceleration is also linear, and total pulse length T is short, the longitudinal phase space is very compact. The evolution of the relative momentum spread $\sigma_{\delta p/p}$ in z is shown in Fig. 1. The final achieved RMS value is $\sigma_{\delta p/p} = 1.6 \cdot 10^{-4}$, which is an order of magnitude smaller than that obtained in the standard LCLS type (or SPARC type) design.

The evolution of the RMS transverse beam size σ_x , and the RMS normalized emittance $\epsilon_{n,x}$ are shown in Fig. 2. While the behavior of σ_x is similar in most respects to the standard design, with the beam approximately matched at linac entrance to the invariant envelope, the emittance behavior is not as familiar. In the standard LCLS design, $\epsilon_{n,x}$ achieves a minimum value in the post-gun drift, rising to a local maximum at injection into the linac. The focusing and adiabatic damping of the motion in the linac then produce a

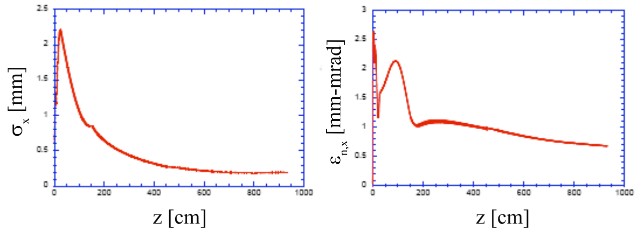

Figure 2: (left) The evolution of RMS transverse beam size σ_x for emittance compensation case, from PARMELA simulation. (right) Evolution of RMS normalized emittance $\epsilon_{n,x}$ for emittance compensation case.

monotonic decrease of $\epsilon_{n,x}$ in z. In our case, the transverse space-charge and thus the plasma/emittance oscillations do not "turn on" until after the longitudinal expansion is well underway, thus delaying the emittance minimum in Fig. 2 to occur inside of the linac. In order to produce faster emittance oscillations in the linac to strongly diminish $\epsilon_{n,x}$ before acceleration removes the plasma-dominated beam behavior, the solenoid field in the first linac section has been raised by 40$\%$ relative to the standard scenario. This ploy works well, as the final value (still slightly decreasing) of $\epsilon_{n,x}$ at the end of the second linac (84.5 MeV energy) is 0.68 mm-mrad. The thermal emittance at the cathode is 0.4 mm-mrad, and so the space-charge induced emittance is well compensated.

After acceleration to higher energy (84.5 MeV), the beam is not spacecharge dominated, and the (x, z) profile no longer ellipsoidal. Nonetheless, the beam has excellent emittance, and maintains a current profile with shape $I(t) \propto \sqrt{1-(2t/T)^2}$. With a high initial current, and low intrinsic energy spread, this beam may be compressed further, with very high final peak current achievable [7].

CONSIDERATIONS FOR SPARC EXPERIMENT

Laser and photocathode issues

Before discussing the planned electron beam measurements, we first review some experimental considerations specific to the use of such short lasers. First, we note that the laser pulse should be tailored, either by collimating and relay imaging, and that it must be quite short. In first measurements at SPARC, we have found, through cross-correlation measurements, that the UV pulse is difficult to make shorter than 300 fs using 3rd harmonic generation with noncollinear mixing in the conversion crystals. In order to obtain even this result, we must give up UV energy, going from 1.5 mJ to 0.2 mJ. While this energy is still adequate for obtaining 0.33 nC of charge using a metal cathode (Cu or Mg), to go shorter may be difficult. In order to check the effect of this extra pulse length on the scheme, we have performed simulations analogous to the original exploratory, indications are that the added length in the laser pulse does not affect the final electron beam configuration at this level.

The laser intensity needed for this scenario is a factor of 30-100 higher than in the LCLS case. The issue of laser damage at the cathode surface has been examined, and found based on previous experience at UCLA and at the BNL ATF to not be worrisome [7].

Experimental signatures and measurements

In the SPARC experiment, we plan first to image the beam (time-integrated) at low energy (5-7 MeV) in the region after the gun, using a YAG detector. For time resolved measurements we will first convert the beam spatial information to photons with a Cerenkov convertor. In order to have a manageably small angle of emission we use aerogel, which has a small index of refraction (n = 1.005-1.02). At 5 MeV the Cerenkov emission threshold is reached for $n = 1.005$; we may choose angles of emission from near zero at this threshold to up to 9 degrees with the aerogels that are presently in hand. The aerogels have been custom fabricated at the Jet Propulsion Laboratory.

Simulations consist of providing electrons (typically 40,000) from PARMELA to GEANT [8], which simulates the scattering of the electrons in the entrance foil and generates a collection of Cerenkov photons in the aerogel. The photon distributions that result are then passed to a *Mathematica* based, optical ray-tracing program, *Rayica*.

The streak camera at SPARC has 2 ps FWHM time resolution, which is on the border of resolution for the bunch length of interest. This will be handled in initial measurements by use of higher charges (above 1 nC), and thus longer beams, to test the longitudinal expansion dynamics of the beam. We thus must consider alternative schemes based on ultra-fast gating [7].

FIRST RESULTS

The first stage of experimentation on the blowout regime took place at INFN-LNF beginning at the end of March 2006. During commissioning of the SPARC RF photocathode gun, the UCLA-produced gun was conditioned quickly up to 11 MW, which produces 110 MV/m peak electric field, and a 5.7 MeV electron beam.

The laser was reconfigured for short pulses (less than 0.5 psec FWHM) and up to 1.6 nC of charge. The conditions for observing the dynamic creation of nearly uniformly filled ellipsoidal charge distributions were not quite present; in fact, the emittance was not of equivalent quality to that obtained in standard operation. Nevertheless, impressive first data was obtained.

Initial measurements of the longitudinal-transverse profile of the beam were made with aerogel with index $n = 1.008$, with the Cerenkov radiator placed 2.4 m away from the cathode, downstream of the slit-based emittance measurement system. Streak camera images were obtained using the transport system described in the previous section. Such a streak, after correction, is shown in Fig. 3.

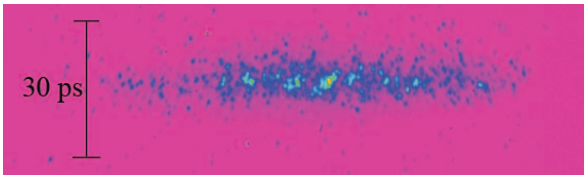

Figure 3: Streak image from SPARC experiment, after correction.

This image displays the profile obtained from a bunch with charge of 700 pC. A large charge is preferred in this case in order to discern information at a time scale longer over the streak camera resolution; the 700 pC case is expected to have expansion of approximately 7 psec FWHM, well in excess of this 2 psec FHWM resolution.

Streak images obtained in the highest temporal resolution mode are inherently noisy; this condition is required in order to avoid space-charge induced pulse distortion inside of the streak tube. Thus in order to extract information from single shots concerning the streak image– which should represent the beam density distribution in an (x, z) slice in the midplane of the bunch– we have adopted a maximum likelihood analysis to test for different assumed types of beam distributions.

The (x, z) slice distributions we have tested for consistency with the data include: (1) a bi-Gaussian (thermal-type) distribution; (2) a uniformly filled ellipse (assumed arising from a parent uniformly filled ellipsoid); and (3) a nearly uniformly filled ellipse with a tail, which we choose to represent as a Fermi-Dirac distribution.

As all of the distributions assumed have contours of constant density that are elliptical, a systematic statistical approach is possible, in which we look at the total integrated intensity inside of ellipses of size varying from zero area to an area covering the entire streak image. These ellipses are all required to have the same aspect ratio, which is given by the intensity profile itself, $R = \sigma_x / v_s \sigma_t$, where v_s is the streak velocity, and σ_t=3.45 psec for the streak in Fig. 3.

With these functions in hand, we can fit to the data given in the streak images to determine the likelihood that one of the assumed three profiles is more likely than the others. Such an exercise has been performed for the streak given in Fig. 3, with the results shown in Fig. 4. It can be seen the bi-Gaussian hypothesis can be rejected as the least likely model. While the uniformly filled ellipsoid gives a good fit near the distribution center, it is not very accurate at the edge, where one expects strong deviations in any case from this model. Finally, we note that the best fit obtained from the Fermi-Dirac model gives an excellent match to the data.

CONCLUSIONS

While the first measurements have established the soundness of the basic experimental approach, much more remains to be done. As of now, the SPARC injector is being modified to allow for near-axis (as opposed to 70 degree) injection. Additional improvements should also result from use of laser cleaning of the cathode. The SPARC injector will soon be completed with the addition of post-acceleration linacs and beam diagnostics (e.g. RF sweeper). In this fully mature experimental scheme, a complete test of the consistency of the Luiten-Serafini scheme with emittance compensation should be possible, using the large array of techniques described here. Further experiments will also emphasize the demonstration of high quality longitudinal phase space and concomitant low energy spread, as well as high compressibility.

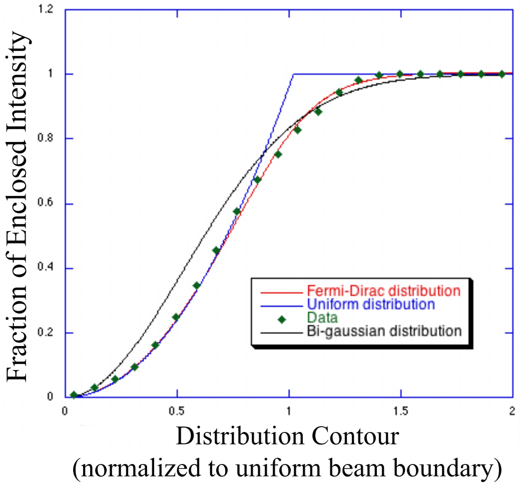

Figure 4: Analysis of streak data, with fraction of integrated intensity of data inside of elliptical contour shown. Best fit of data points to three models are shown: bi-gaussian distribution, uniform elliptical distribution, and Fermi-Dirac (uniform with tails) distribution.

ACKNOWLEDGEMENTS

The authors acknowledge useful interactions with Scott Anderson, Luca Giannessi, Marcello Quattromini, and Dirk Lipka.

REFERENCES

[1] L. Serafini and J.B. Rosenzweig, *Physical Review E* **55**, 7565 (1997).

[2] I.M. Kapchinskii and V.V. Vladimirskii, in *Proc. Int. Conf. High En. Accs.*, CERN, Geneva, 274, 1959.

[3] L. Serafini, *AIP Conf. Proc.* **413**, 321 (1997).

[4] O. J. Luiten, et al., *Phys. Rev. Lett.*, **93**, 094802-1 (2004).

[5] J. B. Rosenzweig, et al., *Nucl. Inst. and Meth. A*, **57** 87 (2006).

[6] E. Colby, *UCLA PhD Thesis*, FERMILAB-THESIS-1997-03 (FNAL, 1997).

[7] J.B. Rosenzweig, et al., *Proc. 2005 Phys. App. High Br. Beams*, Erice, 2006.

[8] S. Agostinelli, et al., *Nuc. Inst. and Meth. A* **506**, 250 (2003).

FREE ELECTRON LASERS IN 2006

W. B. Colson*, J. Blau, and A. Kampouridis
Physics Department, Naval Postgraduate School, Monterey CA 93943 USA

Abstract

Twenty-nine years after the first operation of the free electron laser (FEL) at Stanford University, there continue to be many important experiments, proposed experiments, and user facilities around the world. Properties of FELs operating in the infrared, visible, UV, and x-ray wavelength regimes are listed and discussed.

The following tables list existing (Table 1) and proposed (Table 2) relativistic free electron lasers (FELs) in 2006. A location or institution, followed by the FEL's name in parentheses, identifies each FEL; references are listed in Tables 3 and 4. Another good site for FEL references is http://sbfel3.ucsb.edu/www/vl_fel.html.

The first column of the table lists the operating wavelength λ, or wavelength range. The longer wavelengths are listed at the top with short x-ray wavelength FEL at the bottom of the table. The large range of operating wavelengths, seven orders of magnitude, indicates the flexible design characteristics of the FEL mechanism. In the second column, σ_z is the electron pulse length divided by the speed of light *c*, and ranges from almost CW to short sub-picosecond pulse time scales. The expected optical pulse length can be 3 to 5 times shorter or longer than the electron pulse depending on the optical cavity Q, the FEL desynchronism, and the FEL gain. The optical pulse can be up to 10 times shorter in the high-gain FEL amplifier. Also, if the FEL is in an electron storage-ring, the optical pulse is typically much shorter than the electron pulse. Most FEL oscillators produce an optical spectrum that is Fourier transform limited by the optical pulse length.

The electron beam energy E in MeV and peak current I in Amperes provided by the accelerator are listed in the third and fourth columns, respectively. The next three columns list the number of undulator periods N, the undulator wavelength λ_0, and the rms undulator parameter $K = eB\lambda_0/2\pi mc^2$ in cgs units, where e is the electron charge magnitude, B is the rms undulator field strength, and m is the electron mass. For an FEL klystron undulator, there are multiple undulator sections as listed in the N-column. Note that the range of values for N, λ_0, and K are much smaller than for the other parameters, indicating that most undulators are similar. Some exceptions are the long undulators containing many periods N that are being developed for the x-ray FEL amplifiers. Only a few of the FELs use the klystron undulator at present, and the rest use the conventional periodic undulator. Most of the undulators are configured to have linear polarization. The FEL resonance condition, $\lambda = \lambda_0(1+K^2)/2\gamma^2$ where γ is the relativistic Lorentz factor, provides a relationship that can be used to relate K to λ, E, and λ_0. The middle entry of the last column lists the accelerator type (RF for Radio Frequency Linear Accelerator, MA for Microtron Accelerator, SR for Storage Ring, EA for Electrostatic Accelerator), and the FEL type (A for FEL Amplifier, O for FEL Oscillator, S for SASE FEL, H for a high-gain high harmonic HGHG FEL). Most of the FELs are oscillators, but recent progress has resulted in short wavelength FELs using SASE (Stimulated Amplification of Spontaneous Emission) and high-gain harmonic generation (HGHG).

For the conventional undulator oscillator, the peak optical power can be estimated by the fraction of the electron beam peak power that spans the undulator spectral bandwidth, 1/(2N), or $P \approx EI/(8eN)$. For the FEL using a storage ring, the optical power causing saturation is substantially less than this estimate and depends on ring properties. For the high-gain FEL amplifier, the optical power at saturation can be substantially greater. The average FEL power is determined by the duty cycle, or spacing between the electron micropulses, and is typically many orders of magnitude lower than the peak power. The Jlab infrared FEL has now reached an average power of 10 kW with the recovery of the electron beam energy in superconducting accelerator cavities.

In the FEL oscillator, the optical mode that best couples to the electron beam in an undulator of length $L = N\lambda_0$ has Rayleigh length $z_0 \approx L/12^{1/2}$ and has a mode waist radius of $w_0 \approx N^{1/2}\gamma\lambda/\pi$. The FEL optical mode typically has more than 90% of the power in the fundamental mode described by these parameters.

This year the DESY FLASH FEL has reached the shortest wavelength ever for an FEL, $\lambda \approx 0.013$ μm. There are several other new lasings: Rossendorf (U-100) at $\lambda \approx 20$-150 μm, RIKEN (SCSS Prototype) at $\lambda \approx 0.049$ μm, and BNL (SDL FEL) at $\lambda \approx 0.198$ μm. New FEL lasings are highlighted in bold in Table 1.

ACKNOWLEDGMENTS

The authors are grateful for support from ONR, NAVSEA, and the JTO.

---

* Corresponding Author: 831-656-2765, Colson@nps.edu

Table 1: Free Electron Lasers (2006)

EXISTING FELs	**λ(μm)**	**σ_z(ps)**	**E(MeV)**	**I(A)**	**N**	**λ_0(cm)**	**K(rms)**	
Italy (FEL-CAT)	760	15-20	1.8	5	16	2.5	0.75	RF,O
UCSB (mm FEL)	340	25000	6	2	42	7.1	0.7	EA,O
Novosibirsk (RTM)	120-230	70	12	10	2x33	12	0.71	RF,O
Korea (KAERI-FEL)	97-1200	25	4.3-6.5	0.5	80	2.5	1.0-1.6	MA,O
Osaka (ISIR,SASE)	70-220	20-30	11	1000	32	6	1.5	RF,S
Himeji (LEENA)	65-75	10	5.4	10	50	1.6	0.5	RF,O
UCSB (FIR FEL)	60	25000	6	2	150	2	0.1	EA,O
Osaka (ILE/ILT)	47	3	8	50	50	2	0.5	RF,O
Osaka (ISIR)	32-150	20-30	13-19	50	32	6	1.5	RF,O
Tokai (JAEA-FEL)	22	2.5-5	17	200	52	3.3	0.7	RF,O
Bruyeres (ELSA)	20	30	18	100	30	3	0.8	RF,O
Osaka (FELI4)	18-40	10	33	40	30	8	1.3-1.7	RF,O
UCLA-Kurchatov	16	3	13.5	80	40	1.5	1	RF,A
LANL (RAFEL)	15.5	15	17	300	200	2	0.9	RF,O
Stanford (FIREFLY)	15-80	1-5	15-32	14	25	6	1	RF,O
Rossendorf (U-100)	**15-150**	**0.3-10**	**15**	**240**	**38**	**10**	**2.7**	**RF,O**
UCLA-Kurchatov-LANL	12	5	18	170	100	2	0.7	RF,A
Beijing (BFEL)	5-20	4	30	15-20	50	3	1	RF,O
Dresden (ELBE)	3-22	1-10	34	30	2x34	2.73	0.3-0.7	RF,O
Korea (KAERI HP FEL)	3-20	10-20	20-40	30	30x2	3.5	0.5-0.8	RF,O
Jlab (IR upgrade)	0.7-10	0.1	120	400	29	5.5	3	RF,O
Darmstadt (FEL)	6-8	2	25-50	2.7	80	3.2	1	RF,O
BNL (HGHG)	5.3	6	40	120	60	3.3	1.44	RF,A
Osaka (iFEL1)	5.5	10	33.2	42	58	3.4	1	RF,O
Tokyo (KHI-FEL)	4-16	2	32-40	30	43	3.2	0.7-1.8	RF,O
Nieuwegein (FELIX)	3-250	1	50	50	38	6.5	1.8	RF,O
Duke (MARKIII)	2.7-6.5	3	31-41.5	20	47	2.3	1	RF,O
Stanford (SCAFEL)	3-13	0.5-12	22-45	10	72	3.1	0.8	RF,O
Orsay (CLIO)	3-53	0.1-3	21-50	80	38	5	1.4	RF,O
Vanderbilt (FELI)	2.0-9.8	0.7	43	50	52	2.3	1.3	RF,O
Osaka (iFEL2)	1.88	10	68	42	78	3.8	1	RF,O
Nihon (LEBRA)	0.9-6.5	<1	58-100	10-20	50	4.8	0.7-1.4	RF,O
UCLA-BNL (VISA)	0.8	0.5	70.9	250	220	1.8	1.2	RF,S
BNL (ATF)	0.6	6	50	100	70	0.88	0.4	RF,O
Duke (OK-5)	0.45	0.1-10	270-800	35	2x32	12	0-4.75	SR,O
Dortmund (FELICITAI)	0.42	50	450	90	17	25	2	SR,O
BNL (SDL FEL)	**0.2-1.0**	**0.5-1**	**100-250**	**300-400**	**256**	**3.9**	**0.8**	**RF,A,S,H**
Orsay (Super-ACO)	0.3-0.6	15	800	0.1	2x10	13	4.5	SR,O
Osaka (iFEL3)	0.3-0.7	5	155	60	67	4	1.4	RF,O
Okazaki (UVSOR)	0.2-0.6	6	607	10	2x9	11	2	SR,O
Tsukuba (NIJI-IV)	0.2-0.6	14	310	10	2x42	7.2	2	SR,O
Italy (ELETTRA)	0.2-0.4	28	1000	150	2x19	10	4.2	SR,O
Duke (OK-4)	0.193-2.1	0.1-10	1200	35	2x33	10	0-4.75	SR,O
ANL (APSFEL)	0.13	0.3	399	400	648	3.3	2.2	RF,S
RIKEN(SCSS Prototype)	**0.05**	**1**	**250**	**800**	**600**	**1.5**	**1.3**	**RF,S**
DESY (FLASH)	**0.013**	**0.025**	**700**	**2000**	**984**	**2.73**	**0.81**	**RF,S**

Table 2: Proposed Free Electron Lasers (2006)

PROPOSED FELs	**λ(μm)**	**σ_z(ps)**	**E(MeV)**	**I(A)**	**N**	**λ_0(cm)**	**K(rms)**	
Tokyo (FIR-FEL)	300-1000	5	10	30	25	7	1.5-3.4	RF,O
Netherlands (TEUFEL)	180	20	6	350	50	2.5	1	RF,O
Romania (NILPRP)	60	10	7	2	100	2	0.4	RF,O
Dresden (ELBE)	20-150	1-10	20-40	30	38	10	0.3-2.7	RF,O
Novosibirsk (RTM1)	5-100	10	50	20-100	3x33	6	2	RF,O
Daresbury (4GLS-IRFEL)	3-75	0.5-1	18-50	70	27	2.7	2	RF,O
Novosibirsk (RTM)	2-11	20	98	100	4x36	9	1.6	RF,O
Frascati (SPARC)	0.533	0.1	142	500	6x71	3	1.3	RF,S
Hawaii (FEL)	0.3-3	2	100	500	84	2.4	1.2	RF,O
Jlab (UV FEL)	0.25-1	0.2	160	270	60	3.3	1.3	RF,O
Harima (SUBARU)	0.2-10	26	1500	50	33,65	16,32	8	SR,O
Shanghai (SDUV-FEL)	0.5-0.088	1	300	400	400	2.5	1.025	RF,O
Daresbury (4GLS-VUV)	0.4-0.1	0.1-1	600	300	150	5	2	RF,O
Daresbury (4GLS-XUV)	0.1-0.01	0.1-1	750-950	1500	1000	4.5	1-3.5	RF,S
Frascati (COSA)	0.08	10	215	200	400	1.4	1	RF,O
DESY (FLASH)	0.006	0.17	1000	2500	981	2.73	0.9	RF,S
Italy (SPARX)	0.0015	0.1	2500	2500	1000	3	1.2	RF,S
BESSY (Soft X-ray)	0.0012	0.08	2300	3500	1450	2.75	0.9	RF,S
Trieste (FERMI)	0.001-0.1	0.1	1200	500-2500	1140	3.5	1.2	RF,S
Pohang (PAL X-FEL)	0.0003	0.1	3000	4000	6000	1.5	1.1	RF,S
MIT (Bates X-Ray FEL)	0.0003	0.05	4000	1000	1500	1.8	2	RF,S
SLAC (LCLS)	0.00015	0.07	14350	3400	3328	3	3.7	RF,S
DESY (XFEL)	0.0001	0.08	17500	5000	4700	3.6	3.2	RF,S
RIKEN (SPring8 SCSS)	0.0001	0.5	8000	2000	1500	1.5	1.3	RF,S

Table 3: References and Websites for Existing FELs

EXISTING FELs	**Internet Site or Reference**
ANL (APSFEL)	J. W. Lewellen et. al., NIM **A483**, 40 (2002).
Beijing (BFEL)	http://bfel.ihepa.ac.cn
BNL (SDL FEL)	http://www.nsls.bnl.gov/facility/Accelerator/DUVFEL
BNL (ATF)	K. Batchelor et. al., NIM **A318**, 159 (1992).
BNL (HGHG)	A. Doyuran et. al., NIM **A475**, 260 (2001).
BNL (VISA)	A. Tremaine et. al., NIM **A483**, 24 (2002).
Bruyeres (ELSA)	P. Guimbal et. al., NIM **A341**, 43 (1994).
Darmstadt (FEL)	http://linaxa.ikp.physik.tu-darmstadt.de/richter/fel
DESY(FLASH)	http://flash.desy.de
Dortmund (FELICITAI)	http://www.delta.uni-dortmund.de/pub/fel/FEL.html
Dresden (ELBE)	http://www.fz-rossendorf.de
Duke (MARKIII)	http://www.fel.duke.edu/lightsources/mk3.html
Duke (OK-4, OK-5)	http://www.fel.duke.edu
Himeji (LEENA)	http://www.lasti.himeji-tech.ac.jp/NS/LEENA/LEENA_HP.html
Italy (ELETTRA)	http://www.elettra.trieste.it/projects/euprog/fel
Italy (FEL-CAT)	A. Doria et. al, Phys. Rev. Lett. **80**, 2841 (1998).
Jlab (IR upgrade)	http://www.jlab.org/FEL
Korea (KAERI HP FEL)	http://www.kaeri.re.kr/fel/index.php
Korea (KAERI-FEL)	http://www.kaeri.re.kr/fel/index.php
LANL (RAFEL)	http://www.lanl.gov/orgs/ibdnew/usrfac/userfac03.html
Nieuwegein (FELIX)	http://www.rijnh.nl/n4/n3/f1234.htm
Nihon (LEBRA)	http://www.lebra.nihon-u.ac.jp
Novosibirsk (RTM)	http://www.inp.nsk.su
Okazaki (UVSOR)	http://uvsor-ntserver.ims.ac.jp
Orsay (CLIO)	http://www.lure.u-psud.fr/CLIO.HTM
Orsay (Super-ACO)	M. E. Couprie et. al., NIM **A407**, 215-220 (1998).
Osaka (FELI4)	T. Takii et. al., NIM **A407**, 21-25 (1998).
Osaka (iFEL1)	http://www.fel.eng.osaka-u.ac.jp/english/index_e.html
Osaka (iFEL2)	http://www.fel.eng.osaka-u.ac.jp/english/index_e.html
Osaka (iFEL3)	http://www.fel.eng.osaka-u.ac.jp/english/index_e.html
Osaka (ILE/ILT)	N. Ohigashi et. al., NIM **A375**, 469 (1996).
Osaka (ISIR)	http://www.ei.sanken.osaka-u.ac.jp
RIKEN(SCSS Prototype)	http://www-xfel.spring8.or.jp
Rossendorf (U-100)	http://www.fz-rossendorf.de
Stanford (FIREFLY)	K. W. Berryman and T. I. Smith, NIM **A375**, 6 (1996).
Stanford (SCAFEL)	H. A. Schwettman et. al., NIM **A375**, 662 (1996).
Tokai (JAEA-FEL)	R. Hajima et. al., NIM **A507**, 115 (2003).
Tokyo (KHI-FEL)	M. Yokoyama et. al., NIM **A475**, 38 (2001).
Tsukuba (NIJI-IV)	K.Yamada et. al., NIM **A475**, 205 (2001).
UCLA-Kurchatov	http://pbpl.physics.ucla.edu
UCLA-Kurchatov-LANL	http://pbpl.physics.ucla.edu
UCSB (FIR FEL)	http://sbfel3.ucsb.edu
UCSB (mm FEL)	http://sbfel3.ucsb.edu
Vanderbilt (FELI)	http://www.vanderbilt.edu/fel

Table 4: References for Proposed FELs

PROPOSED FELs	**References for Proposed FELs**
BESSY (Soft X-ray)	M. Abo-Bakr et. al., Nucl. Inst. and Meth. **A483**, 470 (2002); Tsukuba Mo-P-07,Mo-P-08,We-P-51 (Sept 2003).
Daresbury (4GLS)	M. W. Poole and B. W. J. McNeil, Nucl. Inst. and Meth. **A507**, 489 (2003).
DESY (XFEL)	http://xfel.desy.de
DESY (FLASH)	http://flash.desy.de
Dresden (ELBE)	http://www.fz-rossendorf.de
Dresden (ELBE)	P. Michel et. al., FEL2004 (2004) p. 8, http://www.JACoW.org.
Frascati (COSA)	F. Ciocci et. al., A. Torre, IEEE J.Q.E. **31**, 1242 (1995).
Frascati (SPARC)	A. Renieri et. al., Nucl. Inst. and Meth. **A507**, 507 (2003).
Harima (SUBARU)	S. Miyamoto et. al., Report of the Spring-8 International Workshop on 30 m Long Straight Sections, Kobe, Japan (August 9, 1997).
Italy (SPARX)	A. Renieri et. al., Nucl. Inst. and Meth. **A507**, 507 (2003).
Jlab (UV FEL)	S. Benson et. al., Nucl. Inst. and Meth. **A429**, 27-32 (1999).
MIT (Bates X-Ray FEL)	http://filburt.lns.mit.edu/xfel
Netherlands (TEUFEL)	J. I. M. Botman et. al., Nucl. Inst. and Meth. **A341**, 402 (1994).
Novosibirsk (RTM)	N. G. Gavrilov et. al., Status of Novosibirsk High Power FEL Project, SPIE Proceedings, vol. **2988**, 23 (1997); N. A. Vinokurov et. al., Nucl. Inst. and Meth. **A331**, 3 (1993).
Novosibirsk (RTM1)	V. P. Bolotin et. al., Nucl. Inst. and Meth. **A475**, II-37 (2001).
Pohang (PAL X-FEL)	pal.postech.ac.kr/kor
RIKEN (SPring8 SCSS)	T. Shintake et. al., Nucl. Inst. and Meth. A507, 382 (2003); http://www-xfel.spring8.or.jp
Rocketdyne/Hawaii (FEL)	R. J. Burke et al, Proc. SPIE: Laser Power Beaming, Los Angeles, Jan. 27-28, 1994, Vol **2121**.
Romania (NILPRP)	Proceedings of FEL 2006; www.jacow.org
Shanghai (SDUV-FEL)	Z. T. Zhao et. al, Nucl. Inst. and Meth. **A528**, 591 (2004).
SLAC (LCLS)	M. Cornacchia, Proc. SPIE 2998, 2-14 (1997); LCLS Design Study Report, SLAC R-521 (1998).
Tokyo (FIR-FEL)	H. Koike et. al., Nucl. Inst. and Meth. **A483**, II-15 (2002).
Trieste (FERMI)	C. J. Bocchetta et. al., Nucl. Inst. and Meth. **A507**, 484 (2003); Tsukuba We-P-53 (Sept 2003).

OVERVIEW ON DIAGNOSTICS FOR X- AND XUV-FEL

Bernhard Schmidt*, DESY, Germany.

Abstract

Controlling and optimizing the SASE process of X-FEL and XUV-FEL requires detailed knowledge and information about the parameters of the driving electron beam which are of critical influence on the laser performance. Due to the very high peak current, collective phenomena have to be carefully measured and controlled while integral (projected) parameters are of limited use. This necessitates the development of a variety of diagnostics tools to monitor the electron bunch parameters in detailedness beyond the capabilities of conventional systems. Longitudinal bunch structures can be derived from time domain methods like electro optic techniques or using transverse deflecting RF-structures, and from frequency domain methods using coherent radiation. The paper will report on recent developments with special emphasis on single shot and online monitoring capabilities in this field. Other topics will be new concepts and experience in measuring the projected and time-sliced emittance of the beam, high precision beam position monitors and sub-picosecond beam phase and arrival time monitor systems.

INTRODUCTION

Diagnostics for X- and XUV-FEL is a very wide subject and can not, even rudimentary, be covered in a short conference contribution. This paper therefore concentrates on certain areas which are especially demanding and where new developments can be reported. Photon diagnostics is a separate important issue but is completely omitted here.

Single pass FEL, as they are used for the production of X- and XUV radiation, are challenging machines in terms of beam quality and parameter control. On one side, the lasing process depends more or less exponentially on beam parameters like emittance and peak current, on the other side are these parameters subject to a delicate balance between concurrent externally steered and uncontrolled collective effects. Diagnostics has to measure and to control these beam parameters such that optimum FEL operation is achieved. The feedback between the diagnostic tools measuring the parameters and the steering of the machine spans all time scales from the very slow experienced human advice to ultra fast intra-bunch feedback on the microsecond scale. A region of special importance is the longitudinal phase space, since the FEL operation requires high peak currents with good transverse emittance. All the compression mechanisms used and proposed so far will achieve these conditions only for a fraction of the entire bunch charge and the longitudinal diagnostic has to be sensitive to the parameters of this specific fraction.

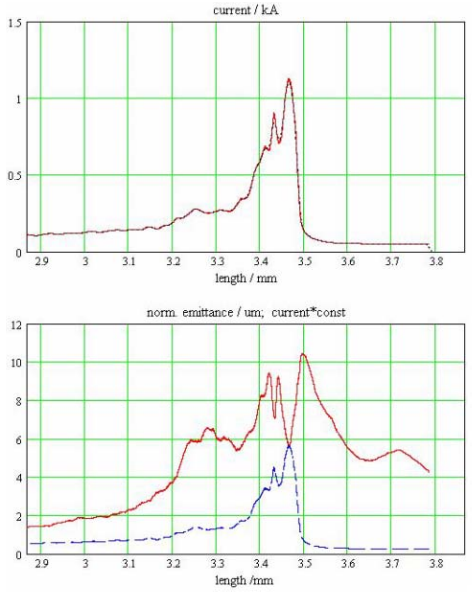

Figure 1: Simulated longitudinal bunch profile and emittance for a non-linear compressor scheme as used in FLASH. The influence of space charge effects and coherent synchrotron radiation on the bunch are included [1].

As an example, Fig. 1 shows the result of a comprehensive simulation of the longitudinal bunch profile and emittance for a non-linear compression scheme as used in FLASH [1]. Collective effects like space charge and coherent synchrotron radiation strongly influence the beam parameters and it becomes obvious, that projected values are of very limited use. Diagnostics has to reveal details of the bunch structure and to do so on a single bunch basis since the collective phenomena are of partially ’chaotic’ behavior.

BEAM POSITION MONITORS

SASE FEL are single pass machines and thus the trajectory of the electrons is not stabilized due to periodic boundary conditions. It is subject to shot to shot fluctuations and requires meticulous monitoring along the full lengths of the linac. The requirements on accuracy in the injector and main linac sections are of the order a few tens of micrometer which can be achieved by conventional button or resonant strip-line BPMs which are numerously used as workhorses in existing storage rings. Much higher demands on accuracy have to be faced in the undulators. Ac-

---

[*] bernhard.schmidt@desy.de

cording to simulations[2][10] , stable SASE operation at X-ray wavelengths (1 $\AA$) requires a well defined trajectory which is reproduced with an accuracy of a few micron. This means that undulator BPMs have to work with submicrometer resolution and an overall mechanical stability at the same level. The requirements can be met by cavity BMPs which have demonstrated nanometer resolution during prototype studies for the ILC[13] . For LCLS, X-band BPMs are under development at ANL and SLAC[6] while for the European XFEL, C-band structures working at 4.38 GHz are foreseen[7]. These BPMs will be used in a fast intra-bunchtrain feedback system to correct the beam trajectory actively [8]. Besides the monitors itself, maintaining the required mechanical accuracy requires sophisticated alignment tools and procedures for the undulator section; an overview on the status of the plans for LCLS has been given during this conference[3].

Two specialties in the field of beam position monitors should be mentioned here since they comprise new concepts. One idea is to use the beam induced higher order modes (HOM) in super-conducting cavities to derive information on the beam trajectory. The complex amplitude of the various HO modes depends on the transverse location of the trajectory inside the cavities as well as on its inclination with respect to the cavity axis. Accurate measurement of the HOM amplitude pattern therefor allows to derive these values with an accuracy of a few micrometer and μrad. Test measurements at FLASH[9] have shown the feasibility of the method and impressive first results.

The second field to be mentioned are large aperture BPMs to measure the beam position and size inside the dispersive section of the bunch compressors. The aim is to derive accurate information on the mean energy and energy spread of the beam with single bunch resolution. The accuracy required on the transverse beam center is of the order 5 micron for an energy resolution of 10^{-4} while the width of the beam is of the order 50 - 100 mm. An interesting technique which has been studied recently proposes to measure the arrival time of the signals on both ends of a transverse stripline across the compressor beam pipe with an accuracy on the 10 fs scale[4]. The sum of left and right timing provides the information on the transverse center of the charge and thus the mean energy while the timing difference contains information about the width of the distribution and thus the energy spread. The method to derive timing signals from beam pick-ups with fs accuracy will be described in the next section. An alternative method to measure the transverse distribution in the bunch compressors has been successfully investigated at FLASH; it is based on high resolution imaging of the synchrotron radiation in the UV range produced in the bunch compressor dipoles [5].

ARRIVAL TIME (BEAM PHASE) MONITORS

Monitoring the performance of the machine and providing high precision 'time stamps' for the FEL users requires to measure the arrival time of the electron bunches in front of the undulators with fs accuracy. This is well above the capabilities of conventional RF methods and requires either specialized longitudinal diagnostics (see section on electro-optic methods) or a new type of beam phase monitors as proposed in ref.[11]. These monitors use the rather large beam induced signals from conventional button or ring pick-up electrodes to modulate the intensity of a probe laser pulse with electro-optic modulators (based on 'Periodically Poled Lithium Niobate' structures). These modulators combine a bandwidth of several GHz with high sensitivity and allow to detect the zero crossing of the signal with an accuracy of a few femtoseconds. A test set-up at FLASH has demonstrated very promising resolutions recently. Fig. 2 shows the measured time difference between two bunches of the same bunch train at FLASH. The combined effect of real time jitter and resolution of the phase monitor is of the order 50 fs. A potential drawback of the method is, that it measures strictly the 'center of charge' of the bunch and not the actually lasing part. Ideally, the probing laser of the phase monitor is part of an optical timing system of the machine which avoids any additional timing jitter due to RF synchronization.

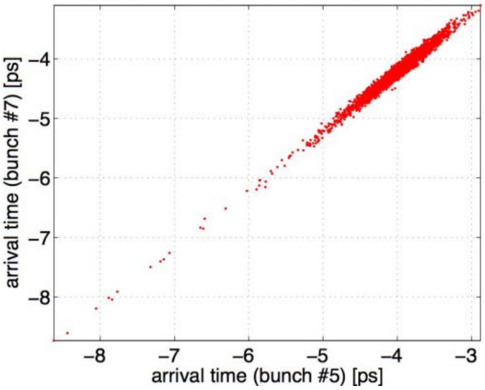

Figure 2: Time difference between two bunches of the same bunch train at FLASH, measured with a phase monitor using electro-optic detection of the zero crossing of a pick-up signal. The combined time jitter and monitor resolution is of the order 50 fs[12].

TRANSVERSE DEFLECTING STRUCTURES

Transverse deflection structures (TDS) are amongst the most powerful and developed tools to measure the phase space distribution of particle bunches. They have been developed at SLAC during the 60th[15] of the last century and used for both, beam separation and diagnostic purposes (e.g. [16]. Operating the deflecting structure close to the zero crossing of the RF, the bunches experience no net deflection but are streaked transversely. Adding a fast transverse kicker allows to send the streaked bunch to an off-axis screen independent of the streak power. If the transverse deflecting structure is combined with a FODO section, quadrupol scans allows to investigate the slice emittance of the bunches. In combination with a dispersive section, the streaked bunch images the slice energy spread of the beam. All future XFEL projects foresee transverse deflecting structures for diagnostic purposes. In the case of the European XFEL, multiple pairs of TDS are foreseen to allow measurements in both transverse planes at different locations along the injector section. An overview can be found in ref. [17].

For operation at zero crossing, the transverse deflection at the screen Δy depends on the longitudinal position Δz with respect to the center as

$$\Delta y = \Delta z \frac{eV}{E_0} \frac{2\pi}{\lambda_{HF}} \sqrt{\beta_c \beta_s} sin(\Delta\psi) \qquad (1)$$

with V the total deflection Voltage of the cavity, E_0 the beam energy and $\Delta\psi$ the phase advance between cavity center and screen. It depends on both β-functions at the cavity and the screen and since the temporal resolution of the method is determined by the ratio of $\Delta y/\Delta z$ to the unstreaked transverse size of the beam, the optimal optics for the TDS operation demands large β_c and small β_s. This has to be foreseen during the design of the machine and is not necessarily coincident with the optimal optics for FEL operation.

An S-band TDS operating at 2,856 GHz from SLAC (LOLA IV cavity) has been installed at the FLASH linac and is routinely used for beam diagnostic measurements and to develop the TDS method further. At optimized conditions, a streak power of more than $1mm$ per $100fs$ can be achieved which for a nominal beam diameter of $200\mu m$ would lead to a resolution of about $20fs$ (RMS). Under normal FEL operation conditions, the resolution observed is slightly less. The image of a typical, well compressed bunch is shown in Fig. 3, the width of the charge spike at the bunch head is of the order $150fs$ (FWHM). Fig. 4 shows a bunch fragmented by space charge and CSR due to too high compression (notice the difference in time scale compared to Fig. 3).

Scanning quadrupols in front and after the TDS, the slice emittance of the bunches can be measured; a detailed report on recent results has been given at this conference[18]. If the streaked bunch passes a dispersive section in front of the observation screen, the slice energy spread of the bunch can be derived with high accuracy. The example shown in Fig. 5 demonstrates the complex structure of the longitudinal distribution and the strong coupling between ΔE and z. The bunch head clearly has two well separated peaks in phase-space which almost coincide longitudinally. Such observations are in good agreement with start-to-end simulations and emphasise the necessity of powerful diagnostics for a detailed understanding of the machine. The TDS method can be called semi-parasitic since the observed bunches are lost from the FEL process. The read-out speed is limited by the complex imaging required, the information can not be used for fast feed-back systems.

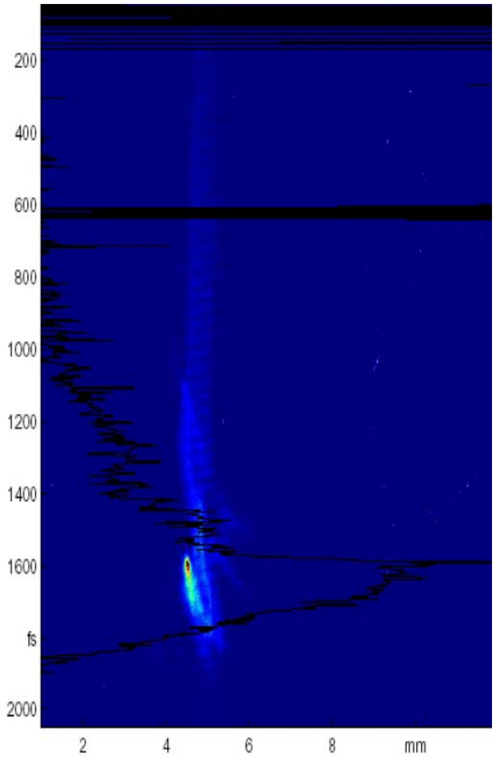

Figure 3: Image of a TDS streaked bunch at FLASH. The phase of the first accelerating module is set such to produce a well formed current peak[14].

ELECTRO OPTIC (EO) METHODS

The longitudinal charge profile of the bunches can be probed by detecting their relativistic Coulomb field by means of electro-optic crystals close to the beam trajectory. The optical properties (namely the birefringence) of the crystals is changed proportional to the electric field strength and the cumulative effect on a co-propagating short laser pulse can be detected. In this way, the temporal (longitudinal) structure of the bunch charge is impressed in a polarization modulation of the optical pulse. An overview on the different methods to decode this information is shown in Fig. 6. The scanning delay method is not single shot and can not be used if the temporal jitter of the mean time of the bunch is comparable or even larger than the length of the bunch. Single-shot EO bunch length measurements were pioneered at FELIX [20] with the spectral decoding method (EOSD), the more recently developed spatial decoding [22] and temporal decoding [23] techniques offer higher resolution at the price of enhanced complexity.

The spectral decoding method is of striking simplicity: the probing pulse is stretched to several ps by applying a linear chirp, that is a correlation between time and ’local’ wavelength. The polarization modulation due to the EO effect is translated into an intensity modulation by a

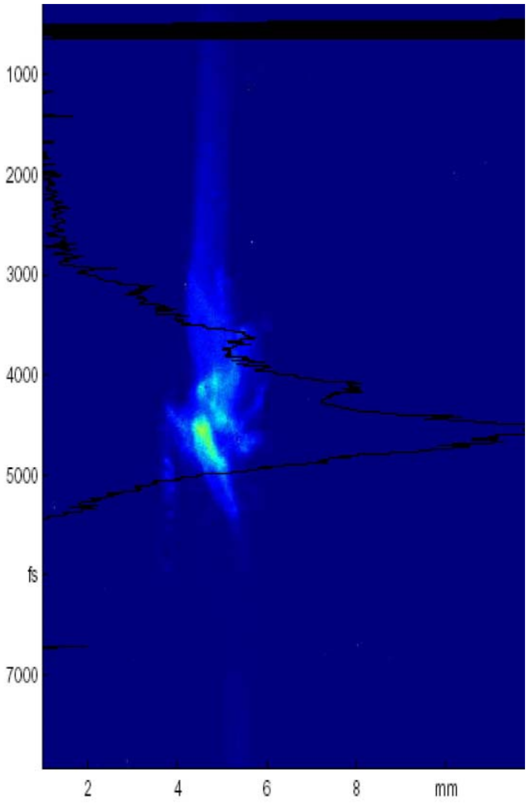

Figure 4: Image of a TDS streaked bunch at FLASH. The phase of the first accelerating module is set too much off-crest, the bunch is strongly distorted by space charge and CSR effects [14].

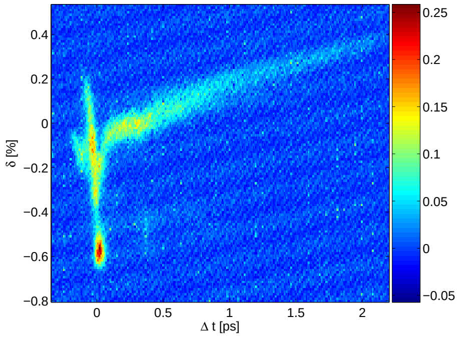

Figure 5: TDS streaked bunch with energy dispersion. The bunch head is contains two separated peaks, less than 100 fs apart and with an energy difference of 0.5 % [18].

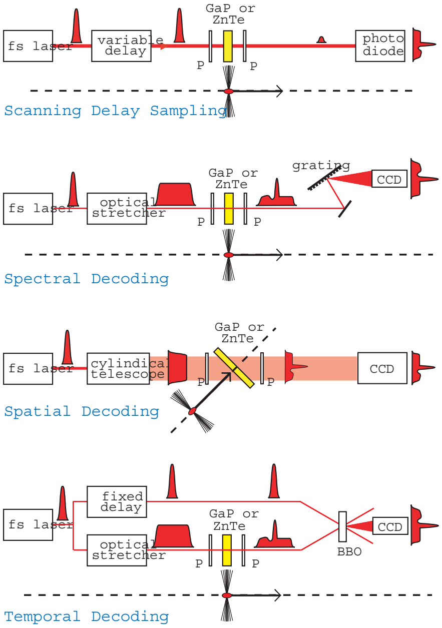

Figure 6: Overview on different methods to decode the temporal information form the laser pulse probing the EO crystal [19].

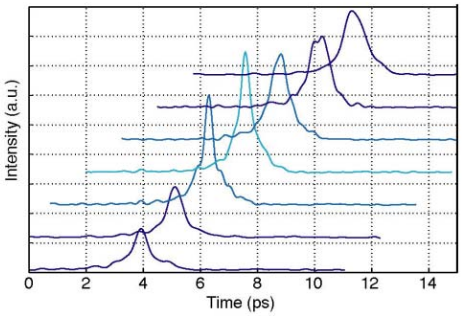

Figure 7: Single shot bunch profiles measured with electro-optic spatial decoding at the SLAC-FFTB using a ZnTe crystal [22].

set of crossed polarizers, the intensity as function of wavelength, measured with a conventional grating spectrometer, images the longitudinal charge profile. Unfortunately, the method has an intrinsic limitation: the amplitude modulation of the probe pulse creates unavoidably a spectral modulation which mixes with the linear chirp and thus spoils the 'decoding gauge'. For the very fast modulations (that is short pulses), this creates an apparent broadening of the pulse and even artificial temporal structures. For the typical optical wavelengths of 800 nm and a length of the chirped pulse of a few ps, structures shorter than about 200-300 fs (FWHM) can not be decoded correctly. Nevertheless, the centroid of the bunch can be detected with much higher accuracy (<50 fs) and coarse deterioration (double spikes etc.) can be easily detected. The method has the potential for further developments in the direction to become a routine on-line monitoring system. For that, the expensive and delicate Ti:Sa laser systems used so far have to be replaced by more robust devices (potentially fiber lasers). If the spectroscopy can be done by using a line camera with fast readout, multi-bunch capability can be envisaged for even the 200 ns bunch distance at the European XFEL.

Spatial decoding has been mainly developed at SLAC [22].

The spatially extended short probing laser pulse hits the EO crystal with non-perpendicular incidence, thus a spatial image of the crystal decodes the electric field a different points in time. The method has the great advantage to be free of the intrinsic limits of EOSD but relies on the spatial uniformity of the EO crystal which can be, especially for ZnTe, quite poor. It requires a quite complex optics and imaging system inside the accelerator tunnel but can operate with rather modest laser energy. Fig. 7 shows a result obtained at SLAC using a ZnTe crystal, the resolution of $270fs$ achieved is close to the limit for this material. At FLASH, a similar set up using GaP is installed and resolutions of the order $120fs$ have been demonstrated[21].

Temporal decoding is the most powerful and most complex EO method developed so far. The short laser pulse is split in two halves, one is chirped to a length covering the length of the electron bunch and passes the EO crystal in the beam line. The other one is kept short. The polarization modulation is transferred to an intensity modulation in the usual way, after that the probing pulse hits a non-linear crystal (SHG). There it is merged under a certain angle of inclination with the short 'gate' pulse from the same origin. In the SHG crystal, a second harmonic component is created proportional to the product of both laser intensities, leaving the crystal in a direction well separated from the two incoming components. The temporal information thus is decoded by optical cross correlation as shown in Fig. 8 schematically. Since a non-linear optical process is involved, the method requires much higher laser power (mJ) and thus a complex and expensive laser amplifier system. On the other hand, the method has demonstrated the best resolution so far. At an installation at FLASH, spike widths of the order 100 fs (FWHM) have been measured in good agreement with TDS data recorded simultaneously (Fig. 9).

Single-shot electro-optic diagnostic techniques are rather mature as experiments meanwhile but still in an infant state as routine operation tools. Since they are totally non-destructive and can be applied to any bunch, it is worthwhile to spend considerable efforts to overcome the technical problems to make them more robust an usable as continuously running monitoring tools. The development of optical synchronization systems makes them even more attractive, since they can be directly coupled to them by means of optical synchronization, avoiding any additional jitter introduced by RF components. They are ideal candidates to provide not only detailed information about the bunch structure online but as well to act as extremely precise bunch arrival time monitors and time stamp generators for pump-probe experiments.

COHERENT RADIATION DIAGNOSTICS

The relativistic electrons of the bunches radiate electromagnetic waves whenever their Coulomb field is subjected to changes: synchrotron radiation due to directional changes in the bending sections or transition and diffraction radiation if the field enters regions of changing dielectric properties. For wavelengths of the radiation longer than the distance of two electrons, these electrons radiate 'in phase' or coherently, the intensity of this coherent radiation scales with the square of the number of contributing electrons and can be a massive effect. More precisely, the radiated power per frequency interval can be written as

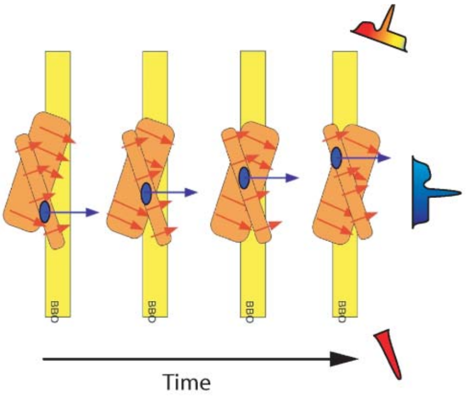

Figure 8: Temporal decoding of the intensity modulation of the probe pulse by spatial cross correlation in a second harmonic (SHG) crystal.

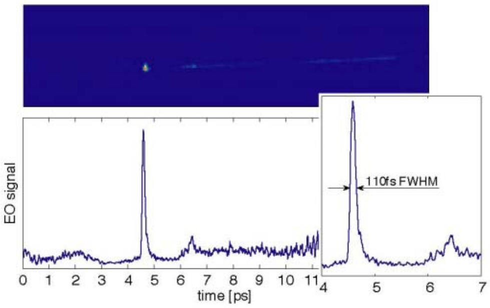

Figure 9: Longitudinal bunch profile measured at FLASH with the electro-optic temporal decoding technique using a 100μm thick GaP crystal [24].

$$\frac{dU}{d\omega} \propto N^2 |F_{long}(\omega)|^2 T(\omega, \gamma, r_b, \Theta, source) \qquad (2)$$

with

$$F_{long}(\omega) = \int_{-\infty}^{\infty} \rho(t) exp(-i\omega t) dt \qquad (3)$$

F_{long} is the longitudinal form factor of the bunch, the Fourier transform of the longitudinal charge distribution and T summarizes all other, potentially complex, properties of the radiation source.

The most popular application of coherent radiation diagnostics is to measure a global intensity of the radiation integrating over a certain (normally large) range of frequencies and use the signal strength as an index for the shortness (the 'compression') of the bunch. It should be kept in mind that the information on the bunch length obtained that way is restricted to the wavelength range

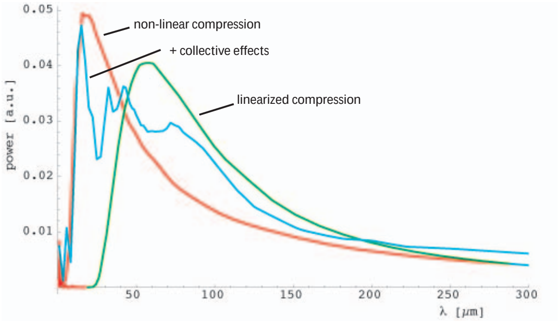

Figure 10: Simulated wavelength spectra of coherent transition radiation for two compression schemes without space charge and CSR effects and for an example of non-linear compression including space charge and CSR effect (data courtesy M. Dohlus).

covered by the radiation detector. If the coherent radiation intensity is observed spectrally resolved, information about the longitudinal form factor and thus the charge distribution can be obtained. For the typical bunch lengths between 10 fs and 100 fs contributing to the FEL process, the corresponding range of wavelengths is in the far infrared from 10 μm to 300 μm. As shown in Fig. 10, the wavelength spectra of coherent transition radiation from ideally compressed electron bunches strongly peak in the region below 200 μm, the position of the intensity maximum directly reflects the length of the current spike[1]. If the bunch is distorted by collective effects, the wavelength spectrum exhibits characteristic substructures which could be used to get information on the strength and nature of the collective phenomena. Despite the fact that a direct reconstruction of the bunch shape from radiation spectra is impossible due to the missing phase information, the wavelength spectra reveal sufficient information to act as 'fingerprints' of the longitudinal bunch structure.

The wavelength range of interest puts a few stringent boundary conditions to the experimental set up: conventional crystalline quartz windows are not transparent for wavelength shorter than about 80 μm and humid air absorbs below 300 μm even over short distances substantially. In consequence, the radiation has to be coupled out of the beam pipe by using a CVD diamond window and the entire coherent radiation set up has to be evacuated or flushed with a dry gas. Conventional IR spectrometers used so far in bunch length diagnostics are Michelson type interferometers measuring the autocorrelation function of the radiation. This method is intrinsically not single shot capable and the information has to be derived in a complex de-convolution process. Recently, a new type of spectrograph has been proposed[25] and assembled which is able to measure wavelength spectra over a sufficiently large range on a single shot basis. The central elements are gratings as dispersive elements and a multichannel detector with fast read out. In a first step, a set of reflective blazed gratings has been used to separate different wave length bands and to detect them with single element pyro-electric sensors. Such a device can be used as 'advanced bunch compression monitor' which is much more sensitive to the actually lasing part of the bunch than conventional integrating devices. It has been tested at the THz beam line[28] of FLASH using coherent transition radiation and proven capabilities. More details can be found in ref. [**?**].

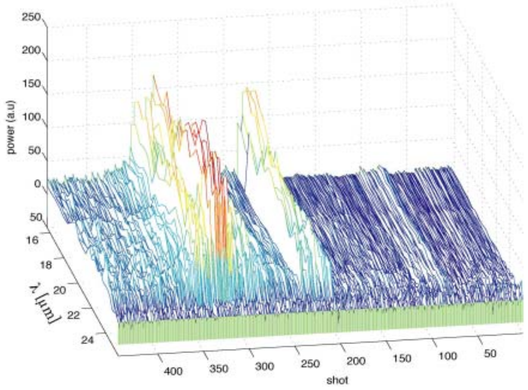

Figure 11: A set of successively recorded single shot spectra in the wavelength range 16-26 μm from coherent transition radiation at FLASH. While recording from right to left, the off-crest phase of the first accelerating module was scanned from zero to about -8 degrees.

The development of a 30 channel fast read out pyro-electric sensor at DESY[29] made it possible to record coherent radiation spectra for single shots online. The device has a sensitivity of about 300 pJ per channel (5σ noise-level) and is almost free of disturbing 'etalon' resonances in the sensitivity in the interesting wavelength range from 1 μm to $1mm$. For this, newly designed pyro-electric sensors have been developed together with industry. The device has been used together with transmission gratings and reflective gratings for fist online single-shot spectroscopy at the FLASH THz beamline[2]. As an example, Fig. 11 shows a set of successively recorded spectra in the range of 16-26 μm while the phase of the first accelerating module was scanned over 8 degrees[27]. Radiation in this wavelength range is produced in two (probably three) narrow regimes of the off-crest phase. One of them is usually used for FEL operation. In contrast to this, fig. 12 shows the equivalent scan for very short wavelengths between 5 μm and 8 μm. No such pronounced bands are seen, the intensity pattern fluctuates from shot to shot and the overall intensity increases with larger off-crest phase angles. This is a very clear indication for micro-bunching on a few femtosecond scale.

Single shot coherent spectroscopy has made a step forward but still to prove its benefits for bunch profile diagnostics and online monitoring. Transmission gratings

---

[1] For a Gaussian bunch, the position of the intensity maximum in wavelength space depends linearly on the temporal width of the bunch

[2] The evacuated beamline images transition or diffraction radiation from an off-axis screen over a distance of 20m to outside the linac tunnel. A fast kicker is used to kick individual bunches to the screen, thus the measurements can run in parallel to normal FEL operation.

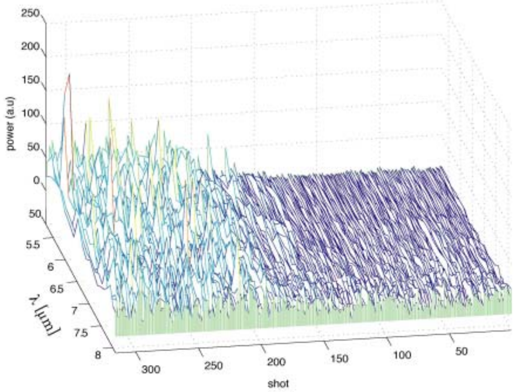

Figure 12: A set of successively recorded single shot spectra in the wavelength range 5-8 μm from coherent transition radiation at FLASH. While recording from right to left, the off-crest phase of the first accelerating module was scanned from zero to about -8 degrees.

offer a wider spectral range but can not reach the shortest wavelengths, reflective gratings span only about one octave in wavelength but have higher efficiency and are available down to the UV region. The natural next step is to 'stage' several reflective gratings with a final transmission grating to span the full range of interest simultaneously. Equipped with fast read-out, these devices can be used even for fast feedback systems.

SUMMARY

Diagnostics for XUV and XFEL requires a variety of new developments on various fields to cope with the very demanding challenges of these machines. Considerable progress has been made during the past years for beam position monitors and especially on the field of longitudinal phase space diagnostics and arrival time monitors. But most of the new methods are still not mature and more or less far from being applicable as routine online tool to control and steer the machine. This is a reach and challenging field for the next years. On top of this, even more sophisticated techniques like the "optical replica synthesizer" are on their way to be explored [30][31].

REFERENCES

[1] M. Dohlus, "Modeling of Space Charge and CSR Effects in Bunch Compressor Systems", Proceedings EPAC2006, MOPCH015.

[2] W. Decking, X-FEL Project Team at DESY, private communication.

[3] H.D. Nuhn, "Electron Beam Alignment Strategy in the LCLS Undulators", Proceedings FEL06, THBAU02.

[4] K.E.Hacker et al., "Large Aperture BPM for use in Dispersive Regions of Magnetic Chicanes", Proceedings FEL06, TUPPH054.

[5] C.Gerth, "On-line Energy Spread Measurements Using Synchrotron Radiation in the Bunch Compressors at FLASH", Proceedings FEL06, THPPH011.

[6] R.M.Lill et al., "Linac Coherent Light Source (LCLS) Undulator BPM System", FEL06, THPPH054.

[7] D. Noelle et al., "First Ideas for the XFEL BPM System", FEL06, THPPH014.

[8] B. Keil et al., "An Intra Bunch Train Feedback System for the European XFEL", Proceedings FLS06, WG521.

[9] J. Frisch et al.,"High Precision SC Cavity Alignment Diagnostics with HOM Measurements", Proceedings EPAC06, TUYPA02.

[10] J. Wu and P. Emma, "Trajectory Stability Modeling and Tolerances in the LCLS",Proceedings EPAC06, MOPCH049.

[11] F. Loehl et al. , "A Sub 100 fs Electron Bunch Arrival-time Monitor System for the VUV-FEL", Proceedings EPAC06, THOBFI01.

[12] F. Loehl , private communication.

[13] S. Walston et al., "Performance of a Nanometer Resolution BPM System", Proceedings EPAC06, TUPCH105.

[14] courtesy Holger Schlarb, DESY.

[15] O.H. Altenmueller, R.R. Larsen and G.A. Loew, "Investigation of Traveling-Wave Separators for the Stanford Two-Mile Linear Accelerator", The Review of Scientific Instruments, Vol. 35, Number 3, April 1964.

[16] R. Akre, L. Bentson, P. Emma and P. Krejcik, "Transverse RF Deflecting Structure or Bunch Length and Phase Space Diagnostics", Proceedings PAC 2001, p. 2353.

[17] C. Gerth, M.Roehrs and H. Schlarb, "Layout of the Diagnostic Sections for Emittance and Energy Spread Measurements at teh European XFEL", Proceedings FEL06, THPPH010.

[18] C. Gerth, M.Roehrs and H. Schlarb, "Investigations of the Longitudinal Electron Bunch Structure at the FLASH Linac with a transverse deflecting RF-Waveguide.", Proceedings FEL06, TUBAU06.

[19] S.P. Jamison et al., "Femtosecond bunch length measurements", Proceedings EPAC2006, TUYPA01.

[20] I. Willke et al., "Single-shot electron-beam bunch length measurements", Phys. Rev. Lett. 88, 124801, 2002.

[21] H. Schlarb et al., "Comparative Study of Bunch length and Arrival Time Measurements at FLASH", Proceedings EPAC2006, TUPCH024.

[22] A.L. Cavalieri et al., "Clocking Femtosecond X Rays", Phys. Rev. Lett. 94, 114801 (2005).

[23] G. Berden et al., "Electro-optic techniques with improved time resolution for realtime, nondestructive single-shot measurements of femtosecond electron bunch profiles", Phys. Rev. Lett. 93, 114802, 2004.

[24] B. Steffen at al. , "Single Shot Longitudinal Bunch Profile Measurements at FLASH using Electro-Optic Techniques", Proceedings EPAC2006, TUPCH026.

[25] H. Delsim-Hashemi et al., "Broadband Single Shot Spectrometer", Proceedings FEL2005, THPP029.

[26] H. Delsim-Hashemi et al., "Bunch Compression Monitor", Proceedings EPAC2006, MOPTH016.

[27] H. Delsim-Hashemi et al., ”Single-Shot Longitudinal Diagnostics with THz radiation at the Free-Electron Laser FLASH”, Proceedings FEL2006, THPPH018.

[28] S. Casalbuoni et al., ”Far-infrared transition and diffraction radiation Part II: the Thz beamline at the VUV-FEL linac”, TESLA FEL 2006-04.

[29] B. Schmidt et al. , ”A 30 channel pyro-electric line detector with MHz read out for mid and far infrared detection”, in preparation.

[30] E. Saldin et al. , ”A simple method for the determination of the structure of ultrashort relativistic electron bunches”, Nucl. Instr. Methods A 539, 499 (2005).

[31] P. van der Meulen et al. , ”Technical aspects of the Integration of the Optical Replica Synthesizer for the Diagnostics of Ultra-short Bunches into FLASH at DESY”, Proceedings FEL2006, TUBAU05.

LOW EMITTANCE INJECTOR AT SCSS

Hitoshi Tanaka*[,A,B)], Kazuaki Togawa[A)], Hitoshi Baba[A)], Toru Hara[A,B)], Atsushi Higashiya[A)],
Takahiro Inagaki[A)], Hirokazu Maesaka[A)], Hiroshi Matsumoto[B,C)], Kazuyuki Onoe[A)], Yuji Otake[A)],
Katsutoshi Shirasawa[A)], Takashi Tanaka[A,B)], Takanori Tanikawa[A)],
Makina Yabashi[A,B)], Tsumoru Shintake[A)],

A) RIKEN/SPring-8, 1-1-1, Kouto, Sayo, Hyogo, 679-5148, Japan
B) JASRI/SPring-8, 1-1-1, Kouto, Sayo, Hyogo, 679-5198, Japan
C) KEK, 1-1, Oho, Tsukuba, Ibaraki, 305-0801, Japan.

Abstract

The SPring-8 compact SASE source (SCSS) project aims at SASE-based FEL at wavelength region of 1 angstrom. To generate a high quality electron beam, a low emittance injector comprising of a 500 kV pulsed electron gun, beam deflector and three-stage velocity bunching process has been investigated [1, 2]. To confirm beam performance of the injector, the SCSS prototype accelerator with the identical injector system was constructed [3]. Via beam tuning of the prototype accelerator over half a year, the first stage beam commissioning was completed successfully and SASE at wavelength of about 50 nm was observed in June 20th, 2006 [3]. The analysis of experimental SASE data predicts that essential beam quality, i.e., "effective electron beam brilliance" reaches to the target value, 200 A/π^2mm^2·mrad^2. In this paper, we describe the injector design of the SCSS prototype accelerator and show the achieved beam performance.

INTRODUCTION

In order to achieve SASE-based x-ray FEL, normalized slice emittance of ~1 πmm.mrad is required with a high peak current of a few kA. For this purpose, it has been believed that a photo-cathode RF electron gun (RF-gun) based system is the most promising. The RF-gun based system has been thus adopted as the injector for the LCLS [4] and XFEL [5] projects.

In the SCSS project, we however took a different approach to this problem. A conventional technology-based injector, which comprises of a pulsed electron gun with a thermionic-cathode, a beam deflector and three-stage velocity bunching process was chosen [1, 2]. This choice is due to potentiality achieving simultaneously high stability and tunability, which are critically important for realization of "stable" x-ray FEL. This injector system is free from the dark current from the cathode, which could be a serious problem in the RF-gun based system.

In the SCSS injector system, basic functions on beam handling such as emission of electrons, beam pulse processing, beam acceleration and bunch compression are separated. Machine parameters in each function are thus adjustable independently, which assures wide tunability in operation. This is an advantage when compared to the RF-gun based system, where these functions are tightly coupled. Furthermore, the RF-gun based system has to use a state of the art laser system to extract electrons from the cathode, which may cause instability in the initial beam condition.

Although the SCSS injector system has an advantage on the electron beam stability and operation tunability, there remains the question whether "emittance conservation" through the injector is a sufficient level or not under the practical error condition. To reply this, in other words, to confirm beam performance of the injector and investigate hidden problems in operation, the SCSS prototype accelerator was constructed and has been tested.

OUTLINE OF INJECTOR SYETEM

Figure 1 shows the schematic view of the injector system of the SCSS prototype accelerator. Since the SCSS injector is basically the same as that of the prototype accelerator, we explain beam handling over the injector by using Fig. 1.

Electron beams are extracted from the single crystal CeB_6 cathode by a 500 kV pulse voltage (1 in Fig. 1) [6]. The repetition rate is 60 Hz at most and the electron pulse width is about 2 μsec. The theoretical thermal emittance is 0.4 πmm.mrad. The initial beam energy is 500 keV and peak current is 1 A.

The developed beam deflector (2 in Fig. 1) cuts out about 1 nsec short pulse from the extracted beam. Due to the fast rising and falling time of the deflector electric field, 1 nsec beam pulse has a beam tail of about 100 psec, in front of and behind the beam. The deflector has a collimator with a hole of which diameter is 5 mm and the beam is collimated into a cylindrical shape with a transversally hard edge.

Owing to the high beam energy of 500 keV, a conventional solenoid coil, which covers a wide beam path, is unnecessary. Instead of the solenoid, a special magnetic lens, where the solenoid coil is covered by an iron york, has been developed (3 in Fig. 1). This magnetic lens has two significant advantages: (1) Due to the localized focusing field, three functions, beam focusing, beam acceleration and bunch compression can be separated. (2) Due to the properly large aperture, nonlinear fringe fields are suppressed enough to avoid the

---

[*] E-mail: tanaka@spring8.or.jp

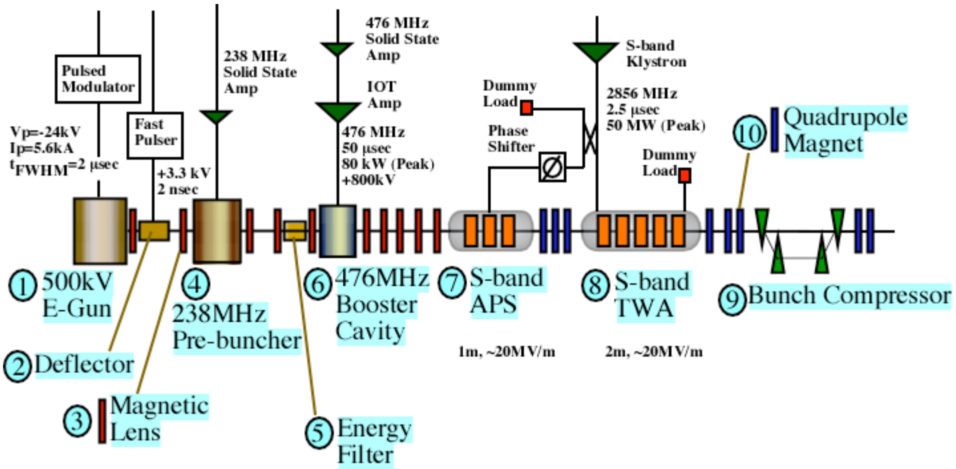

Fig. 1: Schematic drawing of SCSS injector system.

emittance growth. The former advantage is quite important for precise beam tuning.

The cylindrical beam with the pulse width of 1 nsec receives energy modulation, about 400 keV in a peak-to-peak value, in the 238 MHz pre-buncher (4 in Fig. 1). The energy modulated beam develops the density modulation when passing through a 1.6 m drift section. The energy filter (5 in Fig. 1) is now not used. In front of the booster, the average beam energy is ~0.43 MeV and the peak current reaches to 5 A (~200 ps). Then, in the 476 MHz booster cavity (6 in Fig. 1), the beam energy is boosted up to ~1 MeV to suppress the space charge effect and to linearlize the velocity gradient. In the velocity bunching process, both the voltage and phase of the two cavities are crucial for the bunching performance. Structures of both cavities were therefore carefully designed so that the frequency and gap-voltage are not sensitive against a vibration and temperature change. The peak current increases up to 50 A (~10 ps) while the 1 MeV electron beam flights over 1.3 m from the booster to the first S-band acceleration tube (7 in Fig. 1).

The energy of the electron beam is boosted by the two S-band accelerating tubes (7 and 8 in Fig. 1) up to ~41 MeV with the design bunching phase and up to~50 MeV with the crest phase. To suppress the emittance growth due to the symmetry-break of the first acceleration tube, APS structure was adopted. The velocity bunching process completes by the end of the first tube, where the peak current reaches to ~80 A (~6 ps).

Downstream of the first S-band accelerator tube, the beam energy is higher than 10 MeV and a quadrupole magnet (10 in Fig. 1) is used to focus the beam instead of the magnetic lens.

In the SCSS prototype accelerator, the beam is further compressed for SASE experiments by the bunch compressor, which comprises of four identical rectangular magnets (10 in Fig. 1). The deflecting angle is 0.1 rad and the maximum linear dispersion is about 110 mm. After the bunch compression, the peak current reaches to ~800 A (~0.7 ps).

The injector system is divided into three main parts, the electron gun, the beam deflector and three-stage velocity bunching process. Details of each part are described in the following three sections.

500 KV PULSED ELECTRON GUN

To constantly obtain low emittance electron beam with high beam current of 1~3 A, the electron gun was significantly improved from conventional electron guns. Table 1 lists the main electron gun parameters and Fig. 2 shows the CeB_6 cathode assembly (left) and the cathode being heated in the test chamber. The major improvements are:

- A small sized single crystal CeB_6, of which diameter is 3mm, was used as a cathode.
- The control grid was removed from the cathode, because the grid increases beam emittance by distorting the electric field.
- The gun voltage was raised up to 500 kV to suppress a space charge effect and remove troublesome solenoid coils.
- The cathode was stably heated up to high temperature as 1400~1600 deg.C by use of graphite heater.

Table 1: Gun Parameters

Beam Energy	500 keV
Peak Current	1~3A
Pulse Width (FWHM)	2 μsec
Repetition Rate	60 Hz
Cathode Temperature	1400~1600 deg.C
Cathode Diameter	3mm
Theoretical Thermal Emittance (rms)	0.4 πmm.mrad
Measured Normalized Emittance (rms, 90% particles)	0.6 πmm.mrad [7]

- The graphite sleeve surrounding the cathode was adopted to reduce beam halo.
- The flat Wehnelt was used as the anode to reduce emittance growth and to enlarge dynamic range of the peak current.

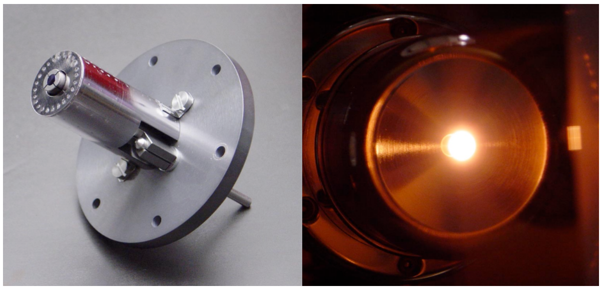

Fig. 2: Cathode assembly (left) and heated cathode (right).

BEAM DEFLECTOR

Since the control grid was removed from the developed electron gun to suppress beam emittance growth, beam deflector, which cuts out a 1nsec short pulse from the long one, is indispensable for the SCSS injector system. Figure 3 shows the principle of the beam deflector. The deflector comprises of two parallel electrode plates and one steering coil. The coil generates a DC magnetic field in the horizontal plane, which deflects the beam vertically and dumps it by using the narrow physical aperture as shown in the figure. The short pulsed electric field in the vertical plane, which cancels out the vertical kick by the DC magnetic field, achieves gating of ~1 nsec. The driving pulse has a fast rising and falling time, ~200 psec, which can generate a well-edged electron beam with a short tail. The flatness of the pulsed electric fields at the flat top determines the emittance degradation in the deflector. Hence, to achieve the sufficient field quality, impedance matching was fully considered in the design of the electric circuit and the parallel electrode plates including the casing chamber.

THREE-STAGE VELOCITY BUNCHING

The SCSS injector starts beam compression from the low beam energy of a 500 keV and reduces the bunch length by a several hundredth as the energy increases up to a few tens MeV. In the design of the SCSS injector, it is thus important to suppress emittance growth caused by a space charge force. On the other hand, the high compression ratio, higher than hundred, is required. Hence, handling of nonlinearity in the compression process is important.

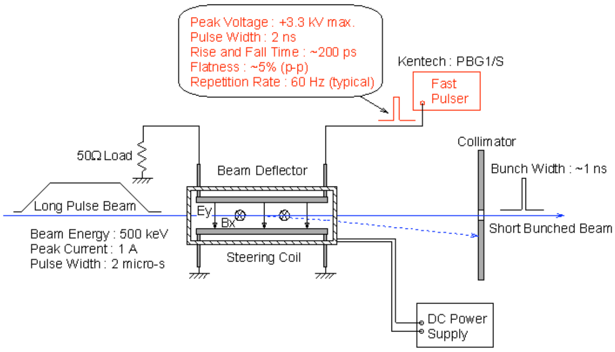

Fig. 3: Schematic drawing of beam deflector.

Suppression of Emittance Growth

Assuming that the beam transverse shape is round and hard-edged and all electro-magnetic potentials are axial-symmetric, equation of motion under a space charge force is described in a cylindrical coordinate by [8]

$$r'' + \frac{\gamma'}{\beta^2\gamma} r' + \frac{\gamma''}{2\beta^2\gamma} r + \left(\frac{qB}{2m_0c\beta\gamma}\right)^2 r - \left(\frac{p_\theta}{m_0c\beta\gamma}\right)^2 \frac{1}{r^3} - \frac{2I}{(\beta\gamma)^3 I_A}\frac{r}{r_m^2} = 0, \tag{1}$$

where r, β, γ, B, p_θ, I, I_A and r_m are the electron radius, relative velocity, relative energy, longitudinal magnetic field, azimuthal momentum, peak current and Alfven current, respectively. The last term in L.H.S. shows the space charge force acting on the electron beam, suggesting that the guideline on the bunch compression is the ratio of γ^3. For example, when γ increases from 1 to 2, criterion on the compression ratio is $(2/1)^3=8$. This idea was first proposed by T. Shintake [1].

The bunch compression in the SCSS prototype accelerator however, apparently exceeds the above guideline and the simulation code, PARMELA predicts that the emittance growth is larger than that in 8-GeV SCSS. Because the injector parameters of the prototype accelerator were optimized not for SASE in wavelength region of 1 angstrom, but for in VUV region under the limited boundary condition, the peak current rather than the slice emittance was pursued. In the 8-GeV SCSS design, RF parameters, especially the RF voltage of 238 MHz pre-buncher will be re-optimized and the use of L-band accelerators instead of the S-band (7 and 8 in Fig. 1) is under investigation.

Nonlinearity Handling

To achieve the high compression ratio, suppression of nonlinearity in the bunch compression process, which originates from a RF voltage and velocity dependence on relative energy of the beam, is the key. For the simple system comprising of a RF potential, drift space and initially mono-energetic beam, the condition achieving the linear velocity distribution against time can be easily solved by neglecting a space charge force and expressed using only three parameters: an initial beam energy, peak RF voltage and RF phase. By using 500 keV and 209 kV as the initial beam energy and peak RF voltage of the pre-buncher, respectively, the linear distribution is obtained at about -125 deg. from the crest phase. Since the injector of the prototype accelerator has the 476 MHz booster cavity downstream of the pre-buncher, the condition for the linear distribution becomes more complicated at the exit of the booster, i.e., it also depends on the booster parameters. Figure 4 shows the velocity distribution dependence on RF phase of the pre-buncher behind the booster, which was calculated with the injector parameters of the prototype accelerator. In this case the phase between -100 and -120 deg. is found to be optimum. In consideration of the experimental results obtained at the prototype accelerator, all the parameters relating to the three-stage velocity bunching process have been re-investigated.

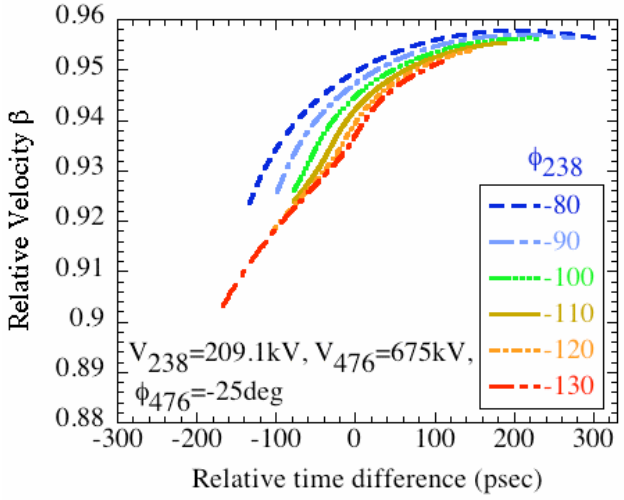

Fig. 4: Velocity distribution dependence on RF phase of the pre-buncher behind the booster calculated with the injector parameters of the prototype accelerator.

SCSS PROTOTYPE ACCELERATOR

The SCSS prototype accelerator comprises of the low emittance injector, bunch compressor with a magnetic chicane, C-band acceleration system, and two in-vacuum undulators as shown in Fig. 5. To verify the injector capability providing the high quality electron beam, the design target of the normalized slice emittance and peak current was set at 2 πmm.mrad and 800 A, respectively. Attainment of the target confirms that the beam performance for x-ray FEL is reachable by smooth extension of the prototype accelerator. And also, the target performance is enough for SASE lasing at wavelength of 40 ~ 60 nm.

Since both the injector and bunch compressor were already described in the previous sections (see Fig. 1), we start a brief explanation of the prototype accelerator from the C-band acceleration system. The system is divided into two acceleration units. Each unit has two 1.8 m-long choke-mode type traveling wave acceleration (TWA) tubes [9] driven by a 3/4π mode. Each unit has one 50MW C-band klystron. The RF power from the klystron is boosted up by a factor of 3.4 by the RF pulse compressor and equally fed to the two acceleration tubes. In the prototype accelerator, different compressors, SKIP [10] and SLED [11] were adopted for the first and second units, respectively, to compare the performance of the two compressors. The nominal accelerating field gradient is about 30 MV/m when the beam is accelerated at the crest phase and in this operating condition RF power fed to each acceleration tube is 46 MW on average of 300 nsec filling time.

The undulator part is divided into two identical in-vacuum undulators of 4.5 m. The permanent magnet material is NdFeB and magnet structure is a 45-deg. tilted Halbach type [12]. Minimum, nominal and fully opened gaps are 2, 3 and 25 mm, respectively. At the minimum (nominal) gap K-value reaches to about 1.8 (1.3) and the wavelength of the first harmonic is about 80 (60) nm with the beam energy of 250 MeV. The period length is 15 mm and the number of periods is 300 per undulator. To keep a small beam size in the horizontal plane, one focusing quadrupole locates between two undulators. In front of the first undulator, a magnet chicane is installed to protect the undulator permanent magnets from accidental electron bombardments and dark currents from the C-band accelerators.

The symbol “M” in Fig. 5 shows a chamber port for a usual beam profile measurement with fluorescence and optical transition radiation. In the beam tuning, these ports are also used to measure a longitudinal beam density distribution by using coherent transition radiation because evolution of the longitudinal distribution is quite important for setting RF parameters in the velocity bunching process. The symbol “S” shows a transverse beam slit to collimate the beam in energy and transverse space.

TUNING STRATEGY OF SCSS PROTOTYPE ACCELERATOR

In the beam tuning, the following points were well considered, because there is no diagnostics to measure the slice emittance directly.

(1) Suppression of slice emittance growth by a space charge force: Over-focusing of the beam causes the emittance growth by a space charge force and hence, it is important to tune the real beam envelope same as the calculation. To this end, initial condition of the real beam from the electron gun should be fixed. We made series of systematic measurements on the beam profiles by changing strengths of the plural magnetic lenses one by one without RF power of both the 238 MHz pre-buncher and 476 MHz booster. By analyzing the data, the virtual beam source was thus determined for the prototype accelerator.

(2) Suppression of slice emittance growth by over-bunching: RF voltage and phase were calibrated and set based on the real beam response for the pre-buncher, booster and S-band accelerators. As the beam response, dependences of the bunch compression on these two parameters were measured. The measurements were performed with the developed microwave spectrometer and the detection system combining the wide frequency band diode detector [13] with a high-pass mesh filter. For

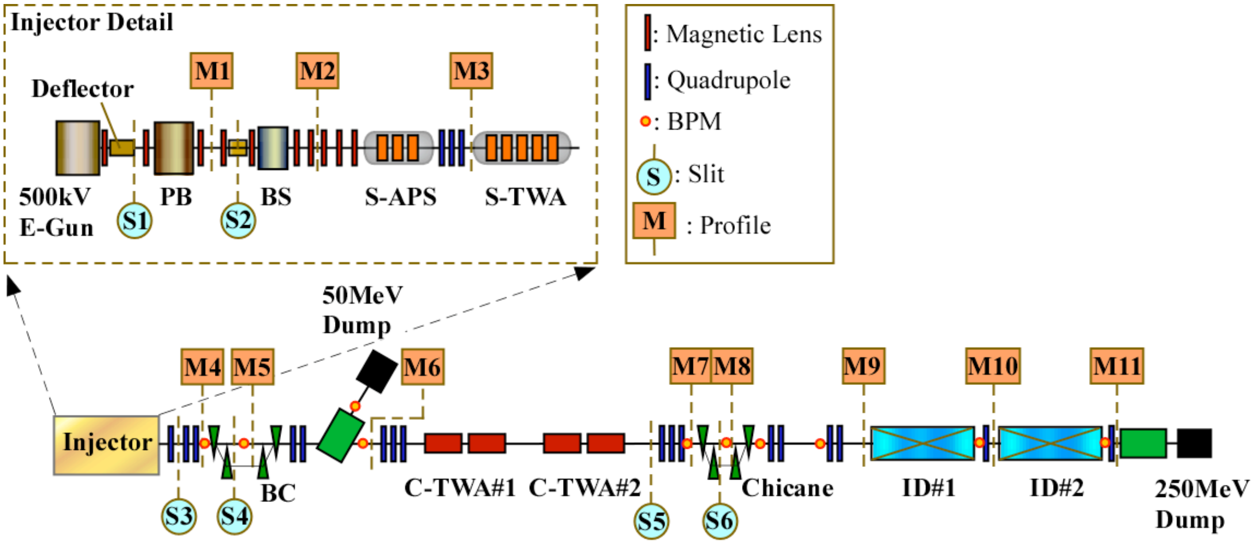

Fig. 5: Schematic drawing of SCSS prototype accelerator.

the crest phase detection, we used the following three methods depending on the condition; beam induced field method [14], the method based on the maximum beam transmission and the method based on the maximum displacement at the dispersive section.

(3) Suppression of slice emittance growth by nonlinear fields: Nonlinear fields at both fringes of the magnetic lenses and RF cavities increase the slice emittance. To suppress this growth, electron beam centering to each device is important. We centered the beam on each device by dithering, i.e., by observing the beam responses against the current and acceleration phase modulation.

(4) Confirmation of slice emittance: Condition of the transverse phase space was indirectly confirmed by comparing the measured data with the simulated ones. For the comparison, five beam profiles upstream of the C-band acceleration system and three kinds of projected emittance were used.

EXPERIMENTAL RESULTS OBTAINED AT SCSS PROTOTYPE ACCELERATOR

In this section, we summarize the obtained results, i.e., the projected emittance, bunch length, dark current, stability and electron beam brilliance.

Projected emittance

The projected emittance values were measured under the following three conditions: (1) 500 keV beam with the pulse-width of 1nsec after the beam deflector (M2 in Fig. 5), (2) 50 MeV beam accelerated at the crest phase of the S-band TWA tube (M6 in Fig. 5), and (3) 250 MeV beam accelerated at the bunching phase (crest -30 deg.) of the S-band TWA tube and at the crest phase of the C-band TWA tubes (M9 in Fig. 5). The emittance of condition (1) was estimated from the beam size and angular divergence measured by the horizontal slit scan. On the other hand, the emittance of the conditions (2) and (3) were estimated by a conventional Q-scan method. Table 2 lists the estimated emittance values together with the calculated ones. The measured emittance of the long pulse beam emitted from the electron gun is also shown. Comparing the emittance values with and without the deflector, we see that the emittance growth by the deflector is not significant. We also see that the estimated values have good agreement with the calculation at the beam energy of 50 and 250 MeV.

Fig. 6 shows the beam size dependences obtained by the Q-scan method at the beam energy of 50 MeV. Each point represents the average of 10 data. The solid and dashed lines represent the fitting curves of which form is determined by linear beam theory. Since scattering of 10 data is smaller than the radius of the plotted circles, it was neglected in the figure. The error bar represents 1σ of a fitting error. We see that the all data points over the wide range of the focusing strength are well fitted by the parabolic curve. These facts show that the electron beam is stable enough for this kind of measurement.

Bunch length

Bunch length was measured with a femto-second streak camera (Hamamatsu Photonics FESCA-200, temporal resolution of 200 fs). Cherenkov radiation from conically shaped BK7 glass was observed for the 41MeV electron beam and optical transition radiation (OTR) from an Au

Table 2: Estimation of normalized emittance

Beam Energy [MeV]	Norm.Emittance $(\varepsilon_x, \varepsilon_y)$ [πmm.mrad]	Calculation $(\varepsilon_x, \varepsilon_y)$ [πmm.mrad]
0.5(bef.deflector)	(0.6, -)	-
0.5(aft.deflector)	(1, -)	-
50	(3, 3)	(2.8, 2.6)
250	(4, 2)	(2.3, 2.3)

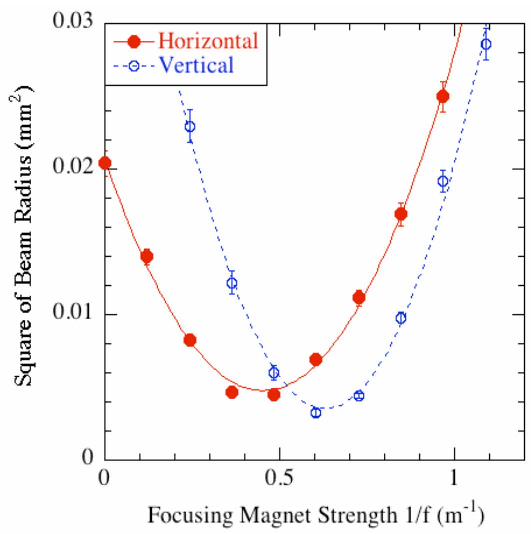

Fig. 6: Measured data by the Q-scan method at the beam energy of 50 MeV.

thin film was observed for the 250 MeV electron beam. The results are 5 psec (41 MeV) and 2 psec (250 MeV) in 1σ, which are much larger than the simulated bunch length of 1 psec. As causes of this discrepancy, we presently predict that the transverse beam size enlarges the pulse length of Cherenkov radiation. And also, in respect to measurement with OTR, we doubt that the optics including streak camera system enlarges the pulse length.

We measured bunch length with another method, where the pulse length of beam is converted to a systematic energy chirp by using a RF field gradient [15]. In our case, the second C-band acceleration unit (C-TWA#2 in Fig. 5) is operated at a zero-crossing phase to generate a systematic energy chirp. Beam density distribution projected to the horizontal plane is then observed with OTR from the Au thin film located in the middle of the chicane (M8 in Fig. 5). The linear dispersion at the OTR screen is about 150 mm. Figure 7 shows the measured density profiles under three different operating conditions of the second C-band unit, i.e., RF turned off and at the crest ± 90 deg. accelerating phase. By using the RF parameters and dispersion value, the full pulse width is estimated to be about 1.1 ps, which agrees well with the simulation.

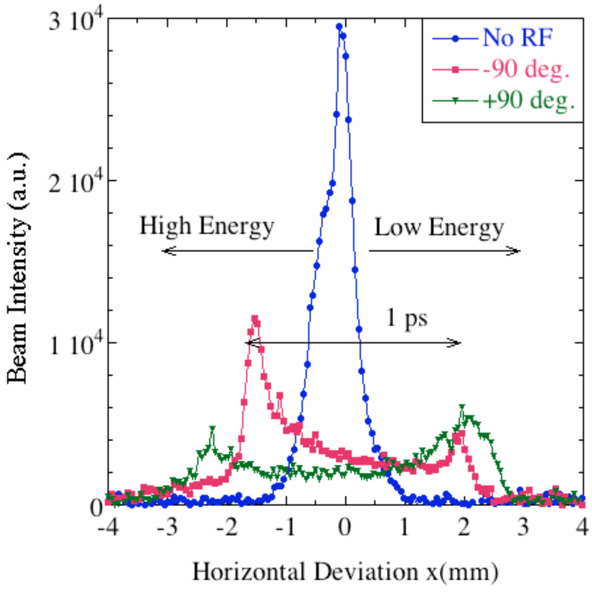

Fig. 7: Measured beam density profile projected on the horizontal plane with three different operating conditions.

Dark current

When the deflector is switched on, dark current downstream of the pre-buncher is invisible on a fluorescence screen of M1 in Fig. 5. It is true that the dark current from the electron gun is negligible for any beam tuning. Quantitative measurements are planned in next operation period after the summer shutdown.

Stability

Long-term stability of the electron beam or the prototype accelerator is the following. The standard SASE lasing is basically reproduced by reloading the nominal parameter set of the magnets and RF systems. At present, the SCSS prototype accelerator has not been operated continuously over a long period, but operated day by day. In 2 to 3 hr after the operation starts in the morning, we suffer the slow drifts of some parameters such as the high voltage of the electron gun, etc, which is so far adjusted manually. Introduction of slow feedback controls is thus under investigation.

With respect to short-term stability of the electron beam, the stability of the beam energy is 0.37 % in full-width downstream of the second C-band acceleration unit. This was estimated by using the shot-by-shot fluctuation of the horizontal position at M8 in Fig. 5. The beam orbit stability was measured by using the beam position monitor (BPM) [16] at the entrance of the first undulator, where no linear dispersion exists in the design. The horizontal and vertical orbit stabilities at this position are 13 and 21 μm in 1σ, respectively. These values are smaller than a fifth of the beam size.

With respect to lasing stability, the peak performance has not been achieved routinely. In order to maximize the laser amplification, slight tuning is needed for the pre-buncher phase, S-band TWA phase, position and width of the slits, S4 and S6 in Fig. 5. Figure 8 shows the shot-by-shot lasing stability measured by the photodiode (International Radiation Detectors Inc. SXUV100) in the VUV beamline [17]. The energy per pulse was measured by integrating the photogenerated charge of the photodiode. The lasing wavelength is about 60 nm and the repetition rate was 5 Hz. The data however were taken asynchronously at 3 Hz due to the reading speed of the temporary data acquisition system. We see that relatively strong lasing occurred in all shots over the period of measurement without any feedback correction.

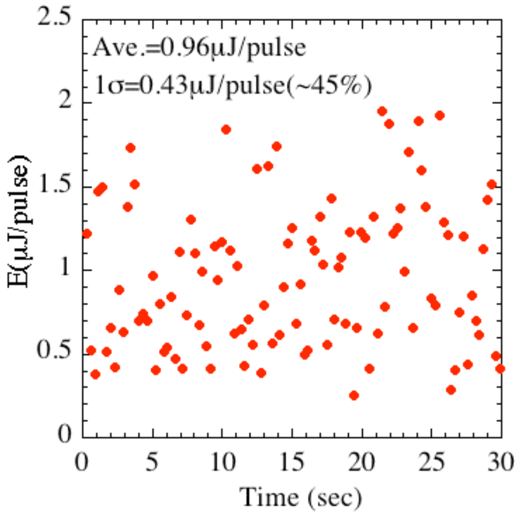

Fig. 8: Shot-by-shot stability of lasing. The beam energy is 250 MeV and the undulator gap is 3 mm.

Electron beam brilliance

Effective electron beam brilliance, the ratio of a peak current to 4-dimensional transverse phase space volume, is estimated by the following two approaches. One is to reproduce the measured dependence of the laser amplification on the peak current by using the 1-D model [18]. The other is to reproduce the measured dependence of the laser amplification on the K-value by using the 3-D simulation code, SIMPLEX [19].

(1) Estimation with 1-D model: The bunch current was controlled with the slit S4 in Fig. 5. Through the bunch length measurement with a systematic energy chirp, we confirmed that the local density peak in the bunch depends on the slit width of S4. Figure 9 shows the dependence measured by the photodiode in the VUV beamline. The filled circles and error bars represent the average and 1σ of 100 data, respectively. In this measurement, the gaps of both undulators were closed to 4 mm and the beam energy was accelerated up to the nominal energy, 250 MeV. Hence, the lasing wavelength is 49nm.

In the 1-D model, the total radiation intensity I is written by the sum of the spontaneous radiation intensity I_N and coherent radiation intensity I_L as

$$I = I_L + I_N = I_{L0}\exp\left(z/L_{1G}\right) + I_N, \qquad (2)$$

where z and L_{1G} represent the total length of the undulators and the 1-D gain length, respectively. Assuming that the horizontal normalized slice emittance is the same as the vertical one, L_{1G} is expressed by using the beam parameters as

$$L_{1G} = \frac{150.2}{\left(\dfrac{H}{\left\langle\beta_x^{1/2}\right\rangle\left\langle\beta_y^{1/2}\right\rangle}\right)^{1/3}},\ H = \frac{I_p}{\varepsilon_{ns}}. \qquad (3)$$

Here, ε_{ns} and I_p represent the normalized slice emittance and peak current, respectively. β_x and β_y are the horizontal and vertical betatron functions, respectively. The bracket < > represents the average of the inside parameter over the undulator length. First we determined the betatron functions experimentally. Then, we fitted the experimental data by using H as only a parameter in consideration with the dependence of Eq. (2) and (3) on the beam charge. The solid line in Fig. 9 shows the result, which agrees well with the experimental data. The ratio of I_p to ε_{ns}, namely H is estimated to be 480 A/πmm·mrad. Assuming that ε_{ns} is the design value, 2 πmm·mrad, the electron beam brilliance becomes 240 A/π^2mm^2·mrad^2.

(2) Estimation with 3-D model: Fixing the electron beam condition, we measured the dependence of the angular photon flux density on the K-value by changing the gap of the first undulator only. To extract the core photon beam, the horizontal acceptance was limited within ±100μm from the beam center by using the horizontal slit in the VUV beamline. Then, the horizontally narrow beam was monochromatized and detected by the CCD camera [17]. We further set a small window on the CCD image for limiting the bandwidth and the vertical acceptance. The angular photon flux density was finally obtained by integrating the intensities in the window. Figure 10 shows the measured dependence of the angular flux density on the K-value with the filled circles. Each data was taken by the integration time of 10sec, i.e., the integration of 50 data. The vertical axis represents the ratio of the flux density to that of the spontaneous radiation. The spontaneous radiation data were measured for each K-value by operating S-band TWA at the de-bunching phase.

Assuming that the normalized slice emittance and momentum spread are the design values, 2 πmm.mrad and 0.1 % (1σ), respectively, we simulated the

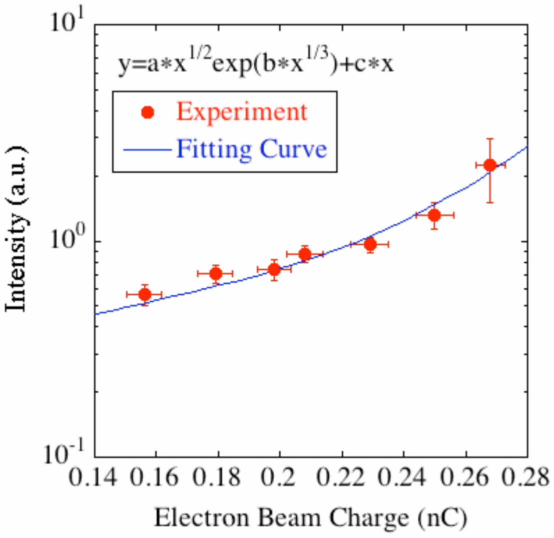

Fig. 9: Dependence of laser amplification on the beam charge.

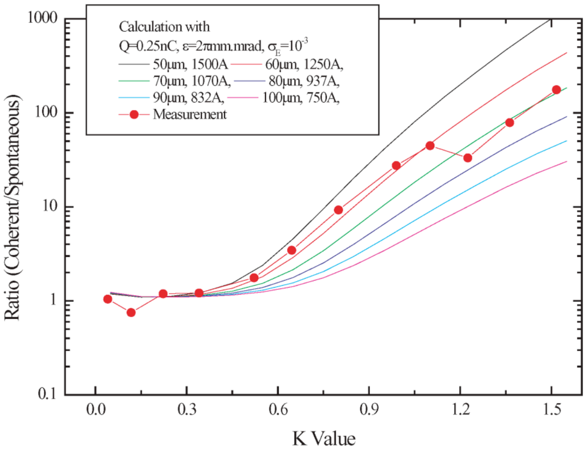

Fig. 10: Dependence of laser amplification on the K-value.

dependence on the K-value with SIMPLEX. Here, the peak current was used as a parameter. The solid lines in Fig. 10 show the results. By comparing the simulation and experimental data, we see that the experimental data locate between the two lines obtained with 1070A and 1250A. The electron beam brilliance is estimated to be 270 ~ 310 A/π^2mm^2·mrad^2.

SUMMARY

The SCSS injector system was designed to achieve the stable and flexible beam operation satisfying the high beam quality required for SASE-based x-ray FEL. On the other hand, our design needs the bunch compression of relatively long electron beam in a low energy regime ranging from 500 keV to a few MeV, with suppressing the emittance growth due to a space charge force and non-linearity. This is quite challenging and there remains the question whether "emittance conservation" through the injector is a sufficient level or not under the practical error condition. To confirm beam performance of the injector, the SCSS prototype accelerator was constructed.

Owing to careful beam tuning based on the emittance conservation, SASE lasing in the wavelength ranging from 40 to 60nm has been stably obtained at the SCSS prototype accelerator. We analysed the reproducible SASE lasing data by the 1-D model and 3-D simulator. As a result, we found that electron beam brilliance is estimated to satisfy the design target, 200A/π^2mm^2·mrad^2.

This experimental result shows that PARMELA gives a good design guideline in our case and concludes that the beam performance for x-ray FEL is reachable by the smooth extension of the prototype accelerator.

REFERENCES

[1] T. Shintake et al., “SPring-8 Compact SASE Source (SCSS)”, SPIE, Optics for Fourth-Generation X-Ray Sources, Bellingham, August 2001, p. 12.
[2] ”SCSS X-FEL Conceptual Design Report”, RIKEN/SPring-8, May 2005, Mikazuki, Japan, http://wwwxfel.spring8.or.jp/.
[3] T. Shintake, “Status of the SCSS Test Accelerator and XFEL Project in Japan”, EPAC’06, Edinburgh, June 2006, p. 2741; http://www-xfel.spring8.or.jp/fist_lasing/FirstLasingofSCSS.html.
[4] “Linac Coherent Light Source (LCLS) Conceptual Design Report”, SLAC-R-593, April 2002.
[5] “TESLA Technical Design Report, PART V, The X-ray Free Electron Laser”, ed. G. Materlik and Th. Tschentscher, March 2001.
[6] K. Togawa et al., “CeB6 Electron Gun for the Soft X-ray FEL Project at SPring-8”, NIMA, **528** (2004) 312.
[7] K. Togawa et al., “Emittance Measurement on the CeB$_6$ Electron Gun for the SPring-8 Compact SASE Source”, FEL’04, Trieste, August 2004, p.351.
[8] M. Reiser, “Theory and Design of Charged Particle Beams”, John Wiley & Sons, Inc., New York, 1994, p. 210.
[9] T. Shintake et al., "HOM-Free Linear Accelerating Structure for e+e- Linear Collider at C-band", PAC’95, Dallas, May 1995, p. 649.
[10] T. Sugimura et. al, “SKIP–A Pulse Compressor for SuperKEKB”, LINAC’04, Lübeck, August 2004, p.754 (2004).
[11] T. Shintake et al., “A New RF Pulse-Compressor Using Multi-Cell Coupled-Cavity System”, EPAC’96, Sitges, June 1996, p. 2146.
[12] T. Tanaka et al., “Development of the short-period undulator for the X-ray FEL project at SPring-8”, SRI’03, San Francisco, August 2003, p. 227.
[13] International Radiation Detector Inc., http://www.ird-inc.com/.
[14] R. B. Neal, “The Stanford Two-Mile Accelerator-I”, W. A. Benjamin, Inc., New York, 1968, p.383.
[15] L. Rivkin et al., “Bunch Lengthening in the SLC Damping Ring”, EPAC’88, Rome, June 1988, p.634.
[16] T. Shintake, “Development of Nanometer Resolution RF-BPMs”, HEACC’98, Dubna, October 1998, http://lcdev.kek.jp/Conf/HEACC98/133.PDF .
[17] M. Yabashi et al., in these proceedings.
[18] R. Bonifacio et al., “Collective Instabilities and High-Gain Regime in a Free Electron Laser”, Opt. Commun., **50** (1984) 373.
[19] SIMPLEX was developed by Takashi Tanaka (RIKEN/SPring-8), http://radiant.harima.riken.jp/simplex/.

Operational Experience with the Emittance-Meter at SPARC*

L. Catani†, A. Cianchi, INFN-Roma Tor Vergata, Roma, Italy
C. Ronsivalle, ENEA C.R. Frascati, Roma, Italy
P. Musumeci, M. Petrarca, INFN-Roma, Roma, Italy
M. Bellaveglia, R. Boni, M. Boscolo, M. Castellano, E. Chiadroni, L. Cultrera,
G. Di Pirro, A. Drago, M. Ferrario, D. Filippetto, V. Fusco, A. Gallo, G. Gatti,
F. Tazzioli, C. Vaccarezza, M. Vescovi, C. Vicario, INFN-LNF, Frascati, Roma, Italy
M. Migliorati, L. Palumbo, University La Sapienza, Roma, Italy.

Abstract

We report the operational experience of the movable emittance meter at SPARC. It is based on the well-known technique of pepper pot measurements (1-D slits in our case) but, in addition, it allows moving the measuring device along the beam line from about 840 mm to 2200 mm from the cathode, following the emittance oscillations. More than a simple improvement over conventional, though non-trivial, beam diagnostic tools this device defines a new strategy for the characterization of high performance photo-injectors, providing a tool for detailed analysis of the beam dynamics, over a section of the accelerator where emittance compensation take place. With this device we planned to perform detailed and systematic studies on beam dynamics with particular attention to the transverse parameters as well as longitudinal.

INTRODUCTION

The aim of the SPARC [1] project is to promote R&D towards high brightness photo-injectors to drive a SASE-FEL experiment. The 150 MeV SPARC photo-injector consists of a 1.6 cell RF gun operated at S-band (2.856 GHz, of the BNL/UCLA/SLAC type) and high-peak field on the cathode incorporated metallic photo-cathode of 120 MV/m, generating a 5.6 MeV, 100 A (1 nC, 10 ps) beam.

The beam is then focused and matched into 3 SLAC-type accelerating sections, which boost its energy to 150-200 MeV. The first phase of the SPARC Project was dedicated to the beam RMS emittance measurement along the drift space following the RF gun, where the emittance compensation process occurs.

The complete characterization of the beam parameters at different distances from the cathode is important to define the injector settings optimizing emittance compensation and for code validation. For this measurement, a dedicated moveable (in z, z being the distance from the cathode, measured along the accelerator axis) emittance measurement device [3] (emittance-meter) is used allowing to measure the RMS emittance in the range from about z=86 cm to z=210 cm.

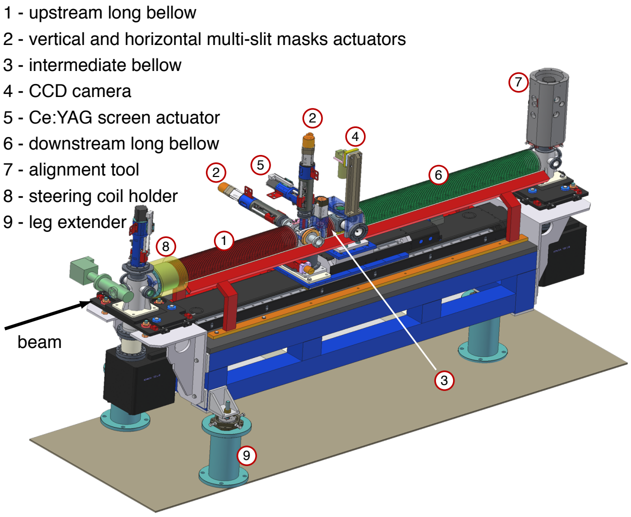

Figure 1: 3D mechanical drawing of the SPARC emittance-meter

The technique to measure the beam emittance and the phase space, in both the horizontal and vertical planes, makes use of a double system of horizontal and vertical slit masks [2]. Each mask consists of a slits array (7 slits, 50 μm width spaced of 500 μm, 2 mm thick) and two single slits, 50 and 100 μm width. The slits are realized by photo-chemical etching providing, compared to mechanical machining, higher precision and improved smoothness of slits edges. The multislits are used for single shot measurements, provided the beam size is large enough for an adequate beam sampling by the slit array. Alternatively, a single slit can be moved across the beam spot. In this case the accuracy of transverse sampling can be freely chosen adjusting the step between the different positions of the slit. This measurement is an integration over many pulses.

Linear actuators with stepper motors are used to control the insertion of the slits masks into the beamline. A differential encoder and a reference end switch guarantee reproducibility and accuracy of the movement to better than 2 μm, required for single-slit multi-shots measurements.

The projected cross-section of beamlets emerging from the slit-mask are measured by means of a downstream

---

* This work has been partially supported by the EU Commission in the sixth framework program, contract no. 011935 EUROFEL-DS1.

† luciano.catani@roma2.infn.it

Ce:YAG radiator. Because beam size and divergence depend on the longitudinal position, the slit to screen distance must be properly adjusted in order to optimize the accuracy of the beamlets profile measurement as the movable device is placed at different z. A bellow is therefore interposed between the slit mask and the screen, allowing their relative distance to be changed while keeping the masks at a fixed position with respect to the gun. This solution allows to set the length of drift between slit mask and the screen that best fits the different scenarios: converging beam, diverging beam, single or multi-slits. Refer to Fig.1 for a schematic drawing of the emittance meter.

Radiation emitted in the forward direction from the Ce:YAG crystal is collected by a 45 degrees mirror downstream from the radiator. The back face of the transparent crystal radiator is observed, thus minimizing degradation of the spatial resolution due to the depth of field of the optics.

Beam images are acquired using digital CCD cameras equipped with a 105mm ”macro” type objective. The magnification of 0.66 gives a resolution of 15.4 μm per pixel.

Beam charge is measured by means of a Faraday cup, placed in a cross together with a chrome-oxide screen to image the beam at 60 cm from the cathode. This screen is also used to monitor the position of the laser spot on the cathode. The emittance-meter is followed by a magnetic spectrometer measuring the beam energy and energy spread

DETAILS ON MEASUREMENTS WITH THE MOVABLE EMITTANCE-METER

The movable emittance-meter was built to perform a detailed characterization of the SPARC photo-injector studying the beam dynamics as function of relevant parameters such as the solenoid field, the beam charge and size, the laser pulse length and its shape. Refer to [4] for more details.

Beam Envelope

Evolution of the bunch transverse size along the photo-injector is a important, though simple, measurement we regularly perform with the emittance-meter. It takes less than 5 minutes to complete the measurement consisting of continuously changing the z-position of the movable system between the upper and lower ends to grabb beam images at various position. These images are on-line processed to filter out the background noise and to calculate the RMS value of the beam size. In Fig.2 are shown results of measurements of the RMS beam size vs z for different values of the solenoid field at the gun. The measurement procedure is a completely automatic one-click operation of the control system.

At a glance we can guess the solenoid current that gives the waist in the required z position or, by comparing x and y envelopes curves, check for the causes that might produce beam envelope irregularities, laser or solenoid misalignment for instance. The different curves in Fig.2 show how the beam waist and its position in z are changed as consequence of the different solenoid currents.

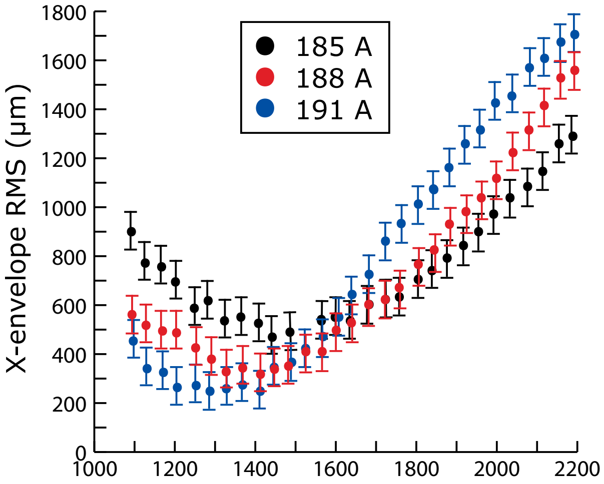

Figure 2: Envelope of the beam (x-plane) along z for different solenoid currents

Emittance

The emittance can be measured, in both x and y planes, at different positions along the emittance-meter. The beam size and its divergence are expected to change as the distance from the cathode changes: the beam is converging at the beginning of the emittance-meter and diverging in the second half. Different measurement strategies are then implemented to achieve the best accuracy of the emittance calculation algorithm.

When the beam is close to the waist, its size is small and the multi-slits mask is not suited because it produces a limited number of beamlets. The single-slits multi-shot measurement is also preferable in the region close to the end of the emittance-meter where the beam size is typically larger than the part of the mask covered by the slit-array and when the beam is strongly converging because profiles of beamlets produced by the multi-slits mask might overlap. Typical values of the sampling distance between the slit positions ranges from 110 μm to 380 μm. At least nine beamlets are always collected with the single slit. In all of the other conditions the multi-slits mask provides fast single-shot measurements, while the single-slit is preferred for accurate analysis.

It’s worth mentioning that, for given beam conditions, results produced by both single-slit and multi-slit measurement have always been fully consistent. A simple check of results produced by the emittance calculation algorithm consists in comparing the RMS beam size at the slit-mask (measured by moving the screen at the longitudinal position of the slit-mask during emittance measurement) against the value of beam size estimated by the emittance calculation algorithm. We always obtained an excellent agreement between the two results.

Fig.3 shows an example of emittance measurements at different positions along the emittance-meter. In this case the beam charge was 700 pC and the energy 5.14 MeV with a longitudinal profile σ= 4.35 psec.

A typical emittance measurement with the single-slit mask consists of collecting 15 beam images for each slit position. The center of mass and RMS size of beamlets are calculated for each image and averaged. We verified t larger statistic doesn't significantly improve the accura of results. In details, from each beamlets image we cal late the projection on the axis, subtract the baseline, tr gaussian fit to find the best position for the center of int sity distribution, reduce the number of the relevant poi skipping these that are outside the 3 standard deviati from the centre and only on the remaining points we cal late the RMS parameters.

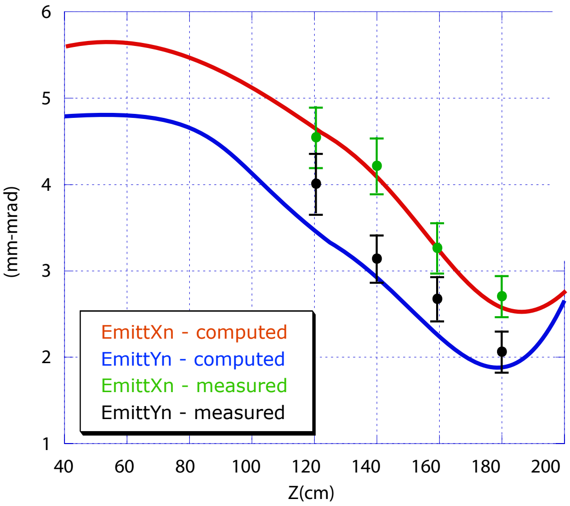

Figure 3: Emittance measurements along the e-meter

The high magnification optical system, the high efficiency YAG screen and a CCD with a remotely controlled gain always provide a good signal to noise ratio and large number of sampling point for every beamlet in all the conditions.

Transverse phase space

The measurement of RMS Twiss parameters and emittance with the single-slit mask allow, as a side-product, the reconstruction of the beam transverse phase space [5]. For each slit position, the beamlet profile on the screen yelds the divergence distribution of particles at the given x position, i.e. those emerging from the slit-mask. Interpolation of the different profiles produces the two dimensional x - x' distribution.

In Fig.4 we show the phase-space measured at different positions along the emittance-meter for a low charge (100 pC) beam. Clearly the beam is going through a focus evolving from convergent to divergent. On the other hand, as the photoinjector theory predicts, the evolution has many differences from that in a linear optics crossover. In a "standard" drift the particles being on the left (negative x) move to the right crossing the origin thus following the lines of motion of constant x. Here the particles that are on left at the beginning of the beamline stay on the left. They get close to the origin (both in x and x') without crossing it and after the laminar space charge dominated waist they move back (still negative x) changing the sign of their divergence

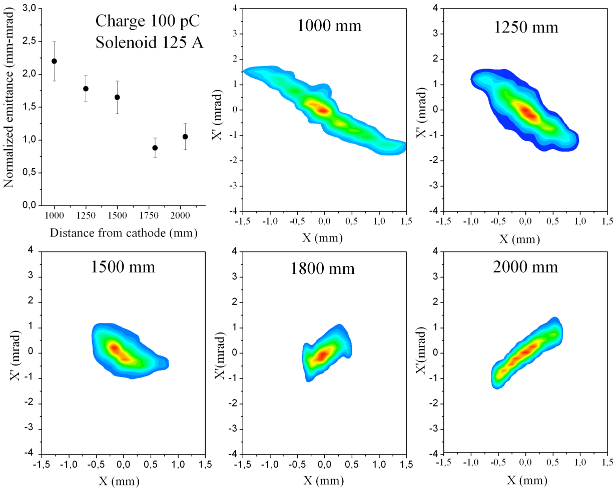

Figure 4: Phase space measure along the e-meter

subsectionBeam energy and energy spread

The e-meter gives also the possibility to investigate the longitudinal dynamics and correlation between transverse and longitudinal planes.

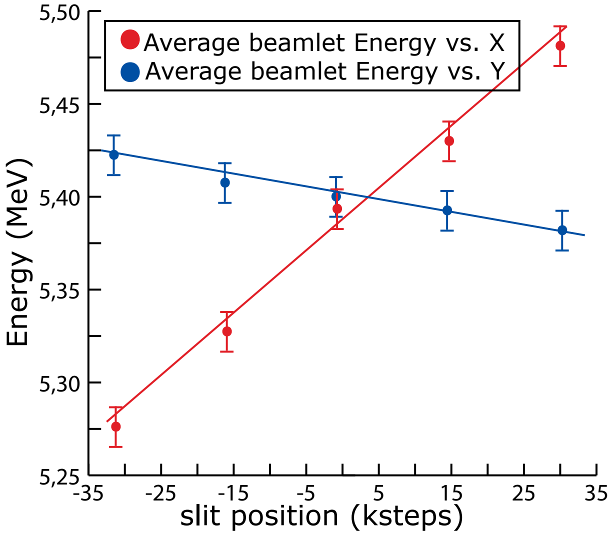

Figure 5: Beamlet energy vs transverse position

Moving the x or y single-slit across the beam and measuring the energy at the spectrometer gives evidence of a possible correlation between particles transverse position and their energy. The measurements in Fig.5 show a variation of beamlets mean energy when the position of the vertical single-slit is changed moving it across the beam in the horizontal direction. The correlation, clearly stronger in the x-direction, suggest as possible cause the non-normal incidence of the laser beam on the cathode in the y=0 plane.

As a final example of the extended diagnostic capabilities of the emittance-meter we report in Fig.6 the evolution of the energy spread measured for the central beamlet (i.e. with the vertical single-slit centered on the beam center of mass) as function of the position along z of the slit mask.

Note that all the points in the graph, except the last one representing the energy spread of the whole beam obtained removing the slit-mask from the beam path, correspond to positions within the high impedance bellows. Inside the long bellows the wakefields contribution to the energy spread adds to the longitudinal space charge effect and the energy spread grows faster. These effects significantly contribute to the energy spread up to the slit-mask while for the low charge beamlet the wakefields and space charge effect are practically negligible. As consequence an increasing energy spread is expected as the distance of the slit-mask from the cathode became larger. It is clearly confirmed by

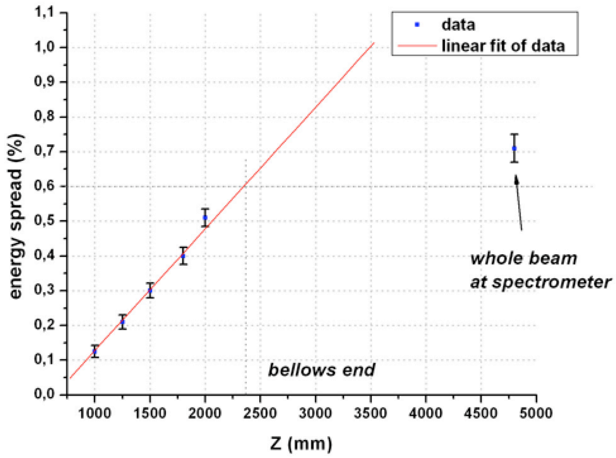

Figure 6: Contribution of bellows to energy spread is evidenced selecting a small portion of the beam with the singl-slit mask and moving it at different Z.

CONCLUSION

The final task of the SPARC photo-injector commissioning is to provide a complete sets of measurements (including transverse and longitudinal profiles of the laser) allowing a complete characterization of the beam dynamics by following the evolution of all the beam parameters.

As it appears from the previous paragraphs, beam dynamics in a photo-injector is a non trivial problem that critically depends on many variables. In systems equipped with a single (at a given longitudinal position) emittance diagnostic station, beamline parameters like solenoid strength or laser launching phase are varied to obtain emittance values that can be checked against those predicted by simulation codes. Unfortunately, the changing of a set-point is often hindering a cross-talk between different simulation parameters which so far has been taken into account somewhat externally (for example varying the gun phase affects the extracted charge, and varying the solenoid strength changes the quadrupole component effect).

The clear advantage in characterizing a photo-injector with the SPARC movable emittance-meter is that once the working point is set, a single simulation run generates results which reproduce the evolution of the experimental data (beamsize, emittance, energy spread) taken with the movable measurement device at the different positions along the beamline. In other words a single simulation run can be checked against a number of experimental points, not just a single one, all representing, or measured with, the same identical photo-injector working point.

Further work, more detailed and accurate measurements, is foreseen in order to approach such ambitious goal, fully understand the system, and validate the prediction capabilities of the modeling codes.

REFERENCES

[1] D. Alesini et al., Nucl. Instr. & Meth. In Phys. Res. A 507 (2003) 345-349C.

[2] M. Zhang, FERMILAB-TM-1988, Oct 1996.

[3] L.Catani et.al., Rev. Sci. Instrum. 77, 093301 (2006).

[4] M. Bellaveglia ”Commissioning of SPARC Photoinjector”, these Proceedings.

[5] S. G. Anderson et al. ”Space-charge effects in high brightness electron beam emittance measurements”, Phys. Rev. ST Accel. Beams 5, 014201 (2002).

HIGH CURRENT ELECTRON EMISSION FROM MICROSCOPIC TIPS

R. Ganter, R.J. Bakker, M. Dehler, J. Gobrecht, C. Gough, E. Kirk, S.C. Leemann, K. Li, M. Paraliev, M. Pedrozzi, F. Le Pimpec, J.-Y. Raguin, L. Rivkin, V. Schlott, H. Sehr, S. Tsujino, A. Wrulich, Paul Scherrer Institut, Villigen CH 5232, Switzerland.

Abstract

In order to find electron sources with low intrinsic emittance (< 5.10^{-8} m.rad) and high brigthness (B > 5.10^{13}A.m^{-2}.rad^{-2}), single tip field emitter as well as Field Emitter Arrays (FEAs) are investigated. By field emission very high current densities can be obtained (up to 10^{12}A.m^{-2}) from extremely small source sizes. Illumination of such field emitting sources by laser pulses (photo-field emission) gives in addition the possibility to pre-bunch the emission to very short pulse lengths. Maximum peak currents, measured from single tips of ZrC with a typical apex radius around one micrometer are presented. Voltage pulses of two nanoseconds duration and up to 50 kilovolts amplitude lead to field emission currents of several hundreds of milliamperes. By combining these electrical pulses with laser pulses, peak currents of several amperes were extracted from the tip apex. This high current emission mode is different from field emission or photo-field emission and has many similarities with the so-called explosive electron emission.

INTRODUCTION

Reducing the beam emittance while keeping high brightness is the most direct way to reduce cost and size of Free Electron Lasers (FELs). In linear accelerators, the parameters of the accelerated beam depend strongly on the performances of the electron gun. The beam emittance in the electron gun is ultimately limited by the intrinsic emittance at the electron source which can be expressed as follow [1,2]:

$$\varepsilon_{n,rms} = \frac{R}{2}\sqrt{\frac{2E_{kin}}{3mc^2}} \qquad (1)$$

where R is the beam radius in the case of a uniform radial distribution and E_{kin} is the mean transverse kinetic energy of emitted electrons (Maxwell energy distribution), m is the electron mass and c the speed of light. In order to reduce the thermal emittance one can either reduce the beam size (R) and/or the mean transverse kinetic energies (E_{kin}) of produced electrons. Field emitter arrays should be capable of producing electron beams with extremely low transverse kinetic energy due to a focusing electrode positioned just one micrometer after the emitting point [3-5]. A single tip electron source should also produce low emittance beam because of the extremely small emitting area (<1µm^2) [6]. Indeed, current densities as high as 10^{12} A.m^{-2} can be achieved by field emission [7]. In practice, the strong dependence of the field emitted current on the local field enhancement factor (down to nanometric scale) and on the local work function (which depends on contaminants, crystal orientation) makes this emission very difficult to control (breakdowns) and to stabilize (fluctuations). Laser illumination of field emission electron sources gave encouraging results in stabilising and increasing the total current emission [8]. If the regime of emission is dominated by photo-field emission, it should become possible to pre-bunch the emission down to 10-30ps with picosecond lasers while keeping high current densities.

LOW EMITTANCE GUN PROJECT

The goal of the Low Emittance Gun (LEG) Project [9] at Paul Scherrer Institute (PSI) is to produce electron bunches of 15ps rms duration with a normalized transverse emittance of 5.10^{-8}m.rad and a minimum peak current of 5.5A at an energy of 4 MeV (see also companion paper [10]). The requirement in peak current is already quite challenging for both FEAs and single tip cathodes. Furthermore, if the electron source is capable of reaching the targeted emittance then the acceleration of such a beam into the relativistic regime without emittance blow up remains very difficult. The LEG concept will combine diode and RF acceleration. A few millimeters gap will separate the electron source from the first radio frequency (RF) cavity. Voltage pulses of 0.5MV and 250ns duration will be applied across this diode gap at a repetition rate of 10Hz. The resulting high accelerating gradient should minimize the emittance growth caused by space charge forces. Comissioning of this high voltage pulser is under way at PSI [9]. After the diode gap the electron beam will enter the RF cavities. A two-frequencies RF cavity (1.5GHz and 4.5GHz) has been designed in order to obtain flat top acceleration waves which minimize the emittance dilution due to RF acceleration [11].

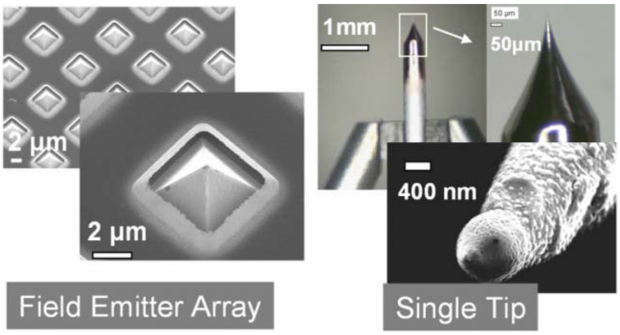

Figure 1: Field Emitter Array produced at PSI and single tip of ZrC from AP Tech Inc. .

The maximum peak current reached with commercial FEAs [12] was around 120 mA [8] for a one millimeter diameter array with 50000 tips. The main limitation comes from the non uniformity of the emission from tip to tip. The intrisic emittance of the same commercial single gated FEAs (no focusing grid) has recently been measured to be around 2.10^{-6}m.rad [13] for a one millimeter diameter cathode. Performances achieved with commercially available FEAs enabled us to better define the ideal FEA for LEG. PSI is currently developping an own production of FEAs based on a self aligned moulding technique. With this technology, pyramid shaped tips can be produced (see Fig. 1) which should better dissipate the heat and thus be able to carry more current. Since FEAs are still under development at PSI the rest of the paper will focus on single tip electron sources.

Single tips are produced by etching a wire which is then inserted in a so called Vogel mounting (see Fig. 1). This mounting allows current circulation and thus tip flash heating as well as field forming [14] of the apex. Metal carbides, like ZrC, are conductors with lower work functions (~ 3.5 eV) than commonly used W or Mo surfaces [15]. ZrC surfaces are also known to be more resistant against sputter damage and the threshold temperature for surface migration (~ 1500 K) is higher than for W or Mo surfaces [16]. We used commercially available ZrC tips from APTech Inc. [17] (McMinnville, USA). Field emission is always localised to small surface imperfections which have a smaller work function and / or a more favorable geometry for field enhancement so that current density goes rapidly to values as high as 10^{12} A/m^2 [7]. The consequence is a fast local heat up with an increased risk for a vacuum arc. The best way to limit the heat up is to emit during very short pulses and at low repetition rates. Nanosecond voltage pulses were applied to a ZrC tip in order to increase the emission current.

EXPERIMENTAL SETUP

Fig. 2 represents the experimental setup used to measure the emitted current from single tips of ZrC [17]. A fast pulser from the company FID GmbH delivering pulses up to 100 kV in amplitude and with 2ns duration (FWHM) at 10 Hz was connected to the tip. A special broad bandwidth (up to 1 GHz) coaxial vacuum feedthrough has been designed to feed the ZrC tip. The tip has a fairly large apex radius (r ~ 1 µm) and is positioned 1 mm behind an aluminium gate electrode (see inset in Fig. 2). The gate has a 2 mm diameter hole and is grounded. The faraday cup is also grounded and about 5 mm away from the tip apex on the same axis.

FIELD EMISSION FROM SINGLE TIPS

Fig. 3 represents the current pulses collected by the faraday cup when voltage pulses of amplitude V_{Tip} were applied to the tip.

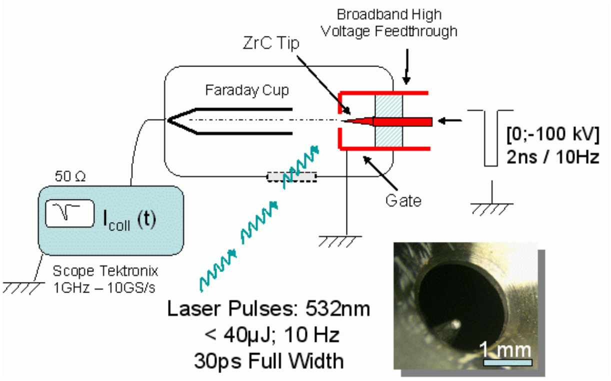

Figure 2: Experimental setup for pulsed field emission and photo-field emission tests.

Field emitted current starts to be detected at voltages around 20 kV (Fig. 3); peak currents as high as 460 mA were measured for applied voltages around 50kV. At this level of current, amplitude fluctuations became relevant (as illustrated by the two pulses at 51kV on Fig.3, left graph) and a monotonic decay of the amplitude was observed. Fluctuations usually indicate that the surface temperature became high enough to activate surface migration of contaminants which in turn change the field emission properties. At lower currents (Fig. 3, right graph), the emission was more stable and the current - voltage characteristics could be measured. These measurements are also represented in a Fowler-Nordheim (F-N) plot (Fig. 4, right graph). From the F-N plots, one can estimate the field enhancement factor β as well as the emitting area [18,19]. The local electric field F_{loc} at the tip apex is then defined as $F_{loc}= \beta.V_{Tip}$. A linear fit (see Fig. 4) of measured values gives $\beta \sim 2.10^5$ m^{-1} and an emitting area around S ~10^4 nm^2 (assuming a work function of 3.5eV for ZrC). This is consistent with a tip radius of 1 µm. With such a small emitting area and if we assume a divergence of sixty degrees [20] a rough estimate gives a normalized emittance less than 5.10^{-8}m.rad and a beam brightness around: B ~10^{13} A.m^{-2}.rad^{-2}.

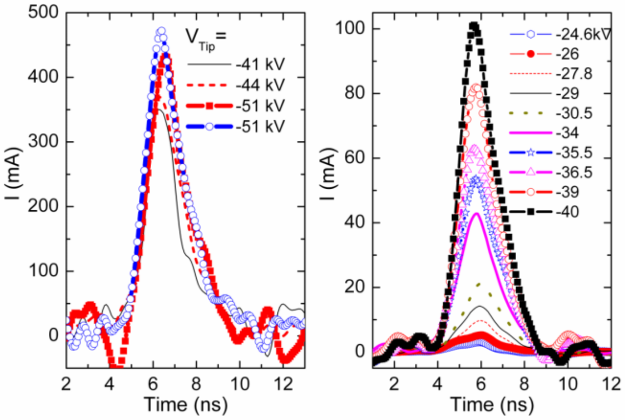

Figure 3: Current pulses collected on the faraday cup for different voltage pulse amplitudes V_{Tip}.

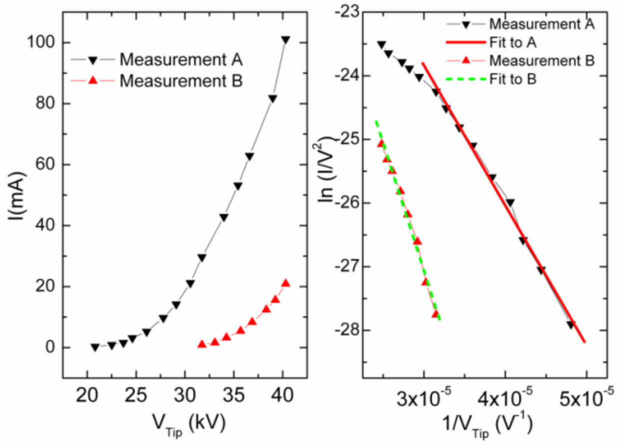

Figure 4: Current voltage characteristics acquired at 5 min interval (left) and Fowler-Nordheim representation of the same curves (right).

With the use of short (2ns) high voltage pulses at low repetition rate, it has been possible to limit the heat up of the tip and to increase the current that can be extracted from a ZrC tip up to 470 mA. For comparison, with a DC electric field, only currents below 10 µA could be safely extracted. However, these high current field emitted pulses revealed strong fluctuations in amplitude. The illumination of the tip with picosecond laser pulses should help to increase the stability and to reach higher peak currents.

LASER ASSISTED ELECTRON EMISSION

Laser assisted field emission [21] [22] is an interesting approach to combine the advantage of field emission (high brigthness) and laser photo-emission (stability, short time modulation). In the photo-field emission regime, the high electric field around the apex lowers the potential barrier of the crystal so that photoemission with large wavelength (λ>532nm) becomes possible and efficient. In previous experiments, similar ZrC tips were illuminated by laser pulses while a DC electric field was applied [8]. Peak currents as high as 580 mA were reached with 10ns long laser pulses of 532nm wavelength. Shorter laser pulses of 1ns (FWHM) at 1064nm produced photo-field current pulses of similar duration [23] suggesting the possibilty to pre-bunch the emission to even shorter levels. In consequence, we recently combined the voltage pulser presented in the first part of the paper with a picosecond laser from the company Time Bandwith Products (see Fig. 2).

The laser system provides 30 ps long laser pulses at 532 nm with a maximum energy per pulse of 40 µJ. The laser was focused on the tip apex with a lens positioned at the focal distance (200 mm) from the tip outside the vacuum chamber. Nanosecond voltage pulses were applied to a ZrC tip while laser pulses were illuminating the tip apex at a repetition rate of 10Hz. If emission is dominated by photo-field emission then the expected current pulse should be as short as 30 ps (FWHM). Unfortunately the bandwidth of our faraday cup (< 1GHz) limits the detection of such short current pulses. The incident laser energy per pulse can be varied between 1 and 40µJ. At low laser energy (<5 µJ/pulse) no change from the pure field emission mode was observed. Above 5 µJ, the current increased suddenly by one order of magnitude leading to the current pulses shown on Fig. 5.

Figure 5 represents the current pulses measured by the faraday cup when laser pulses (532 nm, 20 µJ, 10^8-10^9 W.cm^{-2}) were synchronised with the high voltage pulses for different voltage amplitude V_{Tip}. The collected peak current was as high as 5.5 A at a repetition rate of 10 Hz. The shape of the current pulse follows the applied voltage pulse (the satellite peak at t=3ns corresponds to a similar reflexion in the applied voltage). No significant jitter or amplitude variations were observed as it would be the case for vacuum breakdowns. No decay of the amplitude was observed after several hours of 10 Hz operation and pressure was stable around 10^{-8} mbar. This electron emission was probably not resulting from photo-field emission since it was lasting several nanoseconds. The dependence of the extracted current on laser energy (step like dependence) indicates that there is a threshold above which this large current emission is detected. This has much in common with the so called explosive electron emission (EEE) which is a kind of stable vacuum arc regime. EEE has been largely described by Mesyats [24] and Fursey [7,25]. EEE takes place when a large amount of energy is concentrated into a small volume (by joule effect or laser heating) which eventually explodes and generates a large flow of electrons together with other particles. The difference between this regime of EEE and normal vacuum arcs is the very good reproducibility and stability of the process. The quasi-stationary behaviour is based on the fact that at each explosion the surounding surface melts and some new micro protrusions (and nearly identical) arise which serve as new emitting centers.

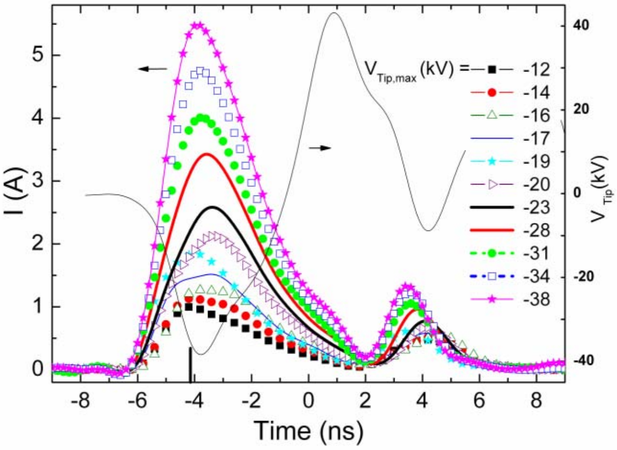

Figure 5: Current collected on the faraday cup when picosecond laser pulses were synchronised (at t ~ -4ns) with high voltage electrical pulses. One example of the voltage applied to the tip is also represented.

The current density during EEE can be extremely high usually above 10^{12} A.m^{-2} so that the size of the emitting center is small (around 1 μm). Further tests are required to better understand and estimate the interest of these large current pulses for a low emittance gun application.

CONCLUSION

Field emission naturally produces very large current density beam so that good performances in terms of beam emittance and beam brightness can be expected from a single tip. The consequence of large current density emission is a high risk of overheating with generation of vacuum arcs. For accelerator application field emission sources must provide a minimum peak current of several amperes. Pulsed field emission at low repetition rate showed that larger peak currents (from 10 μA in DC to almost 500 mA in pulsed mode) can be extracted from a single tip of ZrC. In order to reach LEG goals, photo-field emission is an attractive mechanism which allows time modulation with fast lasers. Preliminary tests of illumination of a tip with picosecond laser pulses while nanosecond voltage pulses are applied have been made. An interesting regime of electron emission (similar to explosive electron emission) delivering stable current pulses of several amperes has been observed. Further tests are still required to see if it has some relevance for a low emittance gun application.

REFERENCES

[1] S. Humphries, *Charged Particle Beams* (John Wiley & Sons, 1990).

[2] J. E. Clendenin *et al.*, NIM A **455,** 198-201 (2000).

[3] A. E. Candel, Ph. D. Thesis, ETHZ, 2005.

[4] A. E. Candel *et al.*, Nuclear Instruments and Method in Physics Research A **558,** 154-158 (2006).

[5] M. Dehler *et al.*, J. Vac. Sci. Technol. B **24,** 892-897 (2006).

[6] V. M. Zhukov *et al.*, Radioteckhnika i elektronika **10,** 2153-2162 (1988).

[7] G. Fursey, *Field Emission in Vacuum Microelectronics* (Plenum Publishers, New York, 2005).

[8] R. Ganter *et al.*, J. Vac. Sci. Technol. B **24,** 974-979 (2006).

[9] http://leg.web.psi.ch.

[10] R. J. Bakker, this Conference, 2006.

[11] J.-Y. Raguin *et al.*, in *Progress in the design of a two-frequency RF cavity for an ultra-low emittance pre-accelerated beam*, Proceedings of the EPAC06 Conference, Edinburgh, Scotland, 2006.

[12] http://www.sri.com/psd/microsys/.

[13] S. C. Leemann *et al.*, in *First measurement results at the LEG Project's 100 keV DC gun test stand* Proceedings of the EPAC06 Conference, Edinburgh, Scotland, 2006.

[14] B. Grishanov *et al.*, Radiotekhnika i Elektronika **23,** 575 (1978).

[15] W. A. Mackie *et al.*, J. Vac. Sci. Technol. B **12,** 722-726 (1994).

[16] F. M. Charbonnier *et al.*, J. Vac. Sci. Technol. B **19,** 1064-1072 (2001).

[17] http://www.a-p-tech.com/.

[18] W. Zhu, *Vacuum Microelectronics* (John Wiley & Sons, 2001).

[19] A. Brenac *et al.*, Revue Phys. Appl. **22,** 1819-1834 (1987).

[20] F. Charbonnier, Appl. Surf. Sci. **94/95,** 26-43 (1996).

[21] M. Boussoukaya *et al.*, Nucl. Instr. and Meth. A **279,** 405-409 (1989).

[22] C. H. Garcia *et al.*, Nucl. Instr. and Meth. A **483,** 273-276 (2002).

[23] R. Ganter *et al.*, Nuclear Instruments and Method in Physics Research A **In Press** (2006).

[24] G. A. Mesyats, Plasma Phys. Control. Fusion **47,** A109-a151 (2005).

[25] G. N. Fursey *et al.*, Applied Surface Science **215,** 286-290 (2003).